



Novel Photocatalytic Processes Mediated by Carbon Nitride Photocatalysis

Dissertation

zur Erlangung des akademischen Grades

"doctor rerum naturalium"

(Dr. rer. nat.)

in der Wissenschaftsdisziplin "Organische Chemie"

eingereicht an der

Mathematisch-Naturwissenschaftlichen Fakultät

der Universität Potsdam

von

Stefano Mazzanti

Potsdam 2021

Unless otherwise indicated, this work is licensed under a Creative Commons License Attribution 4.0 International.

This does not apply to quoted content and works based on other permissions.

To view a copy of this licence visit:

<https://creativecommons.org/licenses/by/4.0>

Published online on the

Publication Server of the University of Potsdam:

<https://doi.org/10.25932/publishup-54209>

<https://nbn-resolving.org/urn:nbn:de:kobv:517-opus4-542099>

Table of contents

Foreword and goal of this thesis	1
1. Introduction	3
1.1. Photocatalysis and Electron transfer	4
1.2. Overview of photocatalytically active materials	5
1.3. General mechanism in molecular and semiconductor photocatalysis ...	10
1.4. Synthesis and structure of carbon nitride materials.....	12
1.5. Optical and photoredox properties.....	16
1.6. Illumination-Driven Electron Accumulation in Semiconductors and Exploitation (IDEASE).....	17
1.7. Energy transfer in Carbon Nitrides.....	23
1.8. Flow chemistry	26
2. Dichloromethylation of enones by carbon nitride photocatalysis.....	31
3. Photocatalysis Goes Thinner Than a Hair: Carbon Nitride Thin Films as All- in-one Technology for Photocatalysis.....	45
4. Multisite Proton Coupled Electron Transfer with Long-lived Radicals of Poly(Heptazine Imide)s for Uphill Organic Synthesis.....	61
5. All-organic Z-scheme photoreduction of CO ₂ with water as the donor of electrons and protons	75
6. Overall conclusions and outlooks	93
7. Appendix – Supplementary material.....	96
7.1 General methods and materials	96
7.2 Dichloromethylation of enones by carbon nitride photocatalysis	99

7.3 Photocatalysis Goes Thinner Than a Hair: Carbon Nitride Thin Films as All-in-one Technology for Photocatalysis.....	244
7.4. Multisite Proton Coupled Electron Transfer with Long-lived Radicals of Poly(Heptazine Imide)s for Uphill Organic Synthesis.....	329
7.5. All-organic Z-scheme photoreduction of CO ₂ with water as the donor of electrons and protons	345
8. Abbreviations	398
9. References.....	403
From Italy to a PhD in Germany, what a journey!.....	418

Foreword and goal of this thesis

In the field of catalysis, energy in different forms is employed to overcome kinetic and/or thermodynamic barriers, to transform a reagent into a desired product using a catalyst. Its role is to focus the given energy to direct the reaction coordinate towards desired products, while lowering the energy necessary to operate such transformation.

During such a process the catalyst temporarily loses its nature, changing its physical state (excited states) or chemical state (bond formation/cleavage), which is restored with a successive step. All these phases form the catalytic cycle.

In this way, reactions can be performed in a selective and efficient manner.

When light is the chosen energy to activate such a cycle, the phenomenon is defined as photocatalysis. Reactions can also happen only with light in absence of the catalyst using photosensible substrates, in which case the process is defined as photochemical.

Most literature in photocatalysis is based on the employment of metals, transition metal complexes, or finely designed organic photocatalysts. Despite their high reactivity, they are rather expensive, unstable, or not recyclable.

For this reason, a heterogeneous catalyst is highly desirable, as it is more stable and can be recycled. In the galactic variety of photoactive materials, carbon nitrides (CN) can be considered among the most valid candidates to fulfill its purpose in sustainability with the environment. Strong point for their employment is the cost, generally lower than other common photocatalysts. Lastly, CN are very ductile materials, as morphology can be engineered, properties can be tuned, and CN based technology can be shaped for the specific task.

Therefore, the aim of this work is to overcome limitations and uncover new trails for research in photocatalysis, synthetic methodology, and chemical technology within the application of carbon nitride materials and the investigation of chemical and physical processes involved. Thereby, seen the broad scope of the goal, all topics have been studied with a multidisciplinary approach focused on organic chemistry between the edges of material chemistry and heterogeneous photocatalysis.

The thesis starts with the introduction (chapter 1). Following, experimental projects are presented showing the employment of carbon nitride photocatalysts in different applications (chapter 2-5). Compound names, figures, and tables are numbered restarting for every chapter. They are also accompanied by extensive supplementary material, which can be found in the appendix (section 7), where each chapter is paired. Example: chapter 2, Supplementary Table 1 can be found in appendix section 7.2 with the same name.

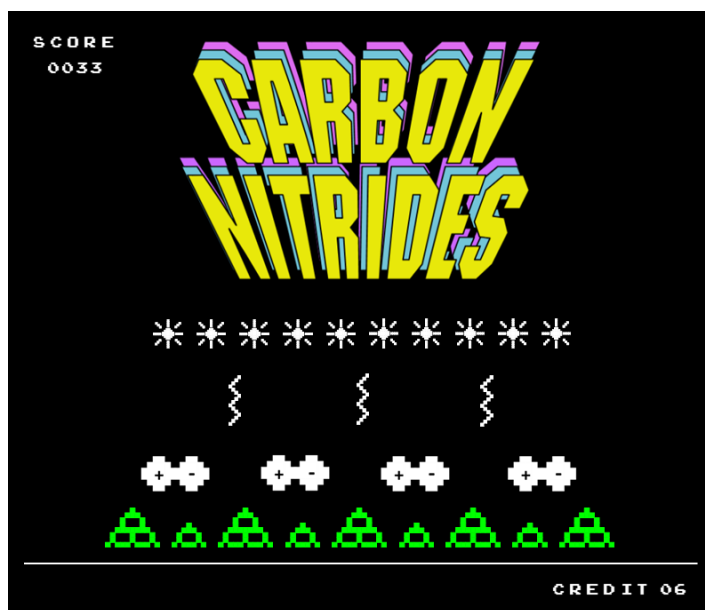
Finally, overall conclusions and outlooks (chapter 6) are given, taking into account all the work accomplished.

1. Introduction

Overview

Herein, an introduction is given to the readers, to provide all the tools to understand the work performed in this thesis.

Starting from principles of electron transfer processes, which represents a main core in photocatalysis, an overview of photoactive materials and working mechanisms is provided. Then, carbon nitrides are classified based on their unique properties, structure, and redox potentials. Afterwards, recently emerged concepts in heterogeneous carbon nitride photocatalysis are introduced, emphasizing the synthesis of organic compounds: 1) Illumination-Driven Electron Accumulation in Semiconductors and Exploitation (IDEASE); 2) singlet-triplet intersystem crossing in carbon nitride excited states and related energy transfer; 3) architectures of flow photoreactors.



This chapter is an adapted version of the review:

S. Mazzanti, A. Savateev, Emerging Concepts in Carbon Nitride Organic Photocatalysis.
ChemPlusChem 2020

1.1. Photocatalysis and Electron transfer

Electron transfer is a universal method to activate organic molecules that can be triggered, for example, by chemical oxidants/reductants, or employing mechanoredox catalysis,^[1] electrocatalysis,^[2] and photoredox catalysis.^[3]

The aforementioned catalytic approaches require a material (the catalyst) to convert a specific type of energy into the driving force for substrate oxidation and reduction. In mechanoredox catalysis – piezoelectric materials and mechanical energy, in electrocatalysis – electrically conductive materials and electric current, in photoredox catalysis – light responsive molecules and photons (electromagnetic radiation) represent the catalyst and energy, respectively. Catalytic redox approaches are more material efficient compared to purely chemical approaches, as they ideally require energy only, which can be derived from renewable sources and the catalyst. However, these approaches come with some drawbacks, such as the employment of sacrificial agents, and degradation of electrodes. Nevertheless, Reisner et al. demonstrated that biomass can be employed as a sustainable electron donor in net-reductive reactions.^[4]

On the other hand, this purely chemical approach would require employment of toxic or explosive agents, and generate considerable amounts of waste derived from auxiliary agents. Taking into account all these pros and cons, the catalytic approach appears to be much more appealing.^[5]

While mechanoredox catalysis is a very recent concept that has not been investigated extensively in preparative organic chemistry, electrocatalysis and photoredox catalysis radically changed the field of catalysis; including how organic chemists conceive of strategies for synthesis or functionalization of a desired molecule.^[6, 7]

Verschueren and Borggraeve indicated the shared attributes of these approaches,^[8] but they also possess unique features. For example, a photoredox approach functions better in overall redox neutral reactions, due to the fact that oxidation and reduction steps are executed by

the same species, while electrocatalysis offers a greater tolerance to functional groups due to precise control over electrolysis parameters, namely voltage or current. Except few reports, electro- and photocatalysis are employed separately in synthesis of organic molecules, but develops conjunctly, as photoelectrocatalysis in water splitting and CO₂ conversion.^[9]

Growth of concepts related to the synthesis of organic molecules in the past two decades have benefitted from the large number of tunable parameters accessible in photocatalysis. For example, photocatalyst redox potentials as well as the energy and intensity of incident light; utilized for energy transfer in photocatalytic systems,^[10] multiphoton/chromoselective catalysis,^[11] and proton coupled multielectron transfer.^[12]

To properly explore these and other concepts in photocatalysis, a brief overview of materials used as photocatalysts is given showing their key features and advantages.

1.2. Overview of photocatalytically active materials

Although, Ir(III) and Ru(II)^[13] complexes were among the first redox active sensitizers in organic synthesis, their high cost motivated scientists to develop alternatives based on earth abundant transition metals,^[14] metal free organic dyes such as flavins,^[15, 16] and other commercially available compounds.^[17] Higher thermal and chemical stability, ease of recovery from the reaction mixture, and recyclability make semiconductor materials more attractive in comparison to molecular systems.^[18] Processability of semiconductors alongside insolubility within common solvents make them extremely useful for the fabrication of nano-, micro-, and macro-structures with applications in photocatalysis as coatings in microfluidic reactors,^[19] active layers in photoelectrocatalysis,^[20] photocatalytically active monoliths^[21], and aerogels.^[22]

Based on elemental composition, semiconductor materials can be divided into several classes: inorganic materials, represented by metal oxides and chalcogenides,^[23] as well as

perovskites,^[24] metal organic frameworks, composed of metal linker and organic ligand^[25] and organic materials, built exclusively from organogenic elements.

Although unitary metal oxides, such as TiO₂^[26] have been one of the mainly used photoactive materials since 1970, binary and ternary metal oxides hold promise in photocatalytic applications. Primarily, this is due to precise tuning of the optical band gap as it has been shown by Le Bahers and Takanabe, and higher efficiency, as demonstrated by Kudo's group.^[27] Furthermore, Marschall et al. synthesized a series of pyrochlores (compounds with brutto formula A₂M₂O₆X in which A and M are cations and X is the counter ion) featuring enhanced absorption up to near IR due to the presence of defects,^[28] while CaFe₂O₄ with a hierarchical pore morphology and spinel ferrites ZnFe₂O₄ and MgFe₂O₄ were used for the fabrication of photoelectrodes.^[29] Mixed metal oxides have additionally been employed in different photocatalytic devices including large scale solar-driven redox photovoltaic-electrochemical systems.^[30]

Purely organic semiconductors differentiate themselves from inorganic materials in terms of improved ability for design.^[31] Indeed, even when taking only commercially available building blocks into account, there is an overwhelming amount of materials with specific structures adjusted for a specific application.^[32] Related to organic photoredox catalysis, in a series of works Zhang et al. used covalent triazine frameworks in the synthesis of benzophosphole oxides,^[33] porous polybenzobisthiadiazole network in the dehalogenation reaction of α - bromoacetophenones,^[34] donor-acceptor COFs in coupling of heteroarenes with diethyl bromomalonate,^[35] and poly(benzothiadiazole) in [2+2] cycloaddition of styrene. ^[36] Benzo-thiadiazole-based microporous organic polymers were also used in bromination of electron rich-aromatic compounds^[37] and poly-benzobis-thiadiazoles in the synthesis of fused 1,2,3,4-tetrahydroquinolines, respectively,^[38] while in-depth mechanistic studies revealed the formation of singlet oxygen (¹O₂) in these reactions which univocally confirmed the energy transfer path.

Carbon nitrides (CNs) stand out from transition metal free heterogeneous photocatalysts due to the alternating C–N bonds in their structure. CNs are a family of materials composed of polymeric chains and graphitic layers of N-rich aromatic rings with monomeric units constituted by triazine or heptazine units linked together by N bonds (sp^3) with an ideal ratio in graphitic carbon nitride structure of 3:4 C/N.^[39] They are prepared by the calcination of N-rich compounds, such as urea and melamine, producing architectures which absorb light in the visible range. Over years of research, different approaches for CNs preparation have emerged. Thus, Shalom et al. introduced a concept of supramolecular preorganization of monomers, such as cyanuric acid and melamine.^[40] This approach was later employed in the synthesis of CN of different morphologies, such as micron-sized CN tubes for dye degradation,^[41] micron-sized sheets for dye adsorption and degradation,^[42] continuous 500 nm-10 μ m thick CN films for photoelectrochemistry (PEC),^[43] hierarchically structured nanoporous CN with edelweiss-like morphology,^[44] and 1D nanofibers for O₂ liberation from water.^[45]

Apart from supramolecular preorganization of monomers, several methods such as using appropriate starting precursors,^[46, 47] template,^[48] pre- or post-treatment,^[49] metal- or nonmetal- and molecular doping^[50, 51-53] are commonly employed to adjust CNs properties. The following paragraphs highlight some of these strategies in greater detail.

Although, melamine and urea are the cheapest commercial precursors for CNs preparation using more complex but easily accessible molecules such as 3-amino-1,2,4-triazole oligomer,^[54] they can be beneficial to transfer morphology of the precursor to the final CN via the ‘topotactic-like’ phase transition as has been shown by Dontsova et al.^[55]

Templating is a commonly used method to increase surface area of carbon nitrides and, in general, an indispensable tool in materials chemistry. The development of porous carbon nitrides is essential to overcome restrictions related to low surface area, and suppress charge recombination for application in heterogeneous photocatalysis.^[56, 57] Vinu et al.

synthesized a class of CN materials with different carbon-to-nitrogen ratios. In this manner optoelectronic and physicochemical properties of CN materials can be modulated for different applications.^[56, 58] Thus, C_3N_5 material has been prepared by self-condensation of 3-amino-1,2,4-triazole inside confined mesopores of KIT-6 silica at 500 °C. Higher nitrogen content resulted in enhanced rate of H_2 production due highly ordered 3D structure with a high surface area, reduced band-gap with improved absorption in the visible solar spectrum, and by capturing more photons due to a light scattering effect inside the pores. Even more nitrogen enriched materials, i.e. C_3N_6 , were synthesized by the same group with a similar template method, employing aminoguanidine hydrochloride as the precursor, which also displayed higher activity toward H_2 production compared to carbon nitride with the C_3N_4 stoichiometry. The field is still expanding toward materials with a higher C/N ratio, such as C_3N_7 , finding application in electrochemical oxygen reduction.^[59]

Heteroatom doping is a reliable method to introduce different elements into the CN backbone, effectively changing electrical, optical, and morphological properties of the material. Heating trithiocyanuric acid at 650 °C was reported to yield sulfur doped CN. The photocatalyst prepared via this straightforward approach presented a 12 times higher activity in hydrogen evolution reaction (HER) and a 5 times higher activity in oxygen evolution reaction (OER). Doping of CN with sulfur also allowed the material to perform OER without the employment of any metallic cocatalyst.^[52]

Boron carbon nitride can be prepared from boron oxide and melamine in bulk at 650 °C, achieving better photodegradation of Rhodamine B compared to undoped material.^[47]

Other nonmetal atoms, such as halides, may be employed in heteroatom doping of CNs. Iodine doped carbon nitride can be obtained by heating dicyanamide with ammonium iodine at 550 °C. This doping extends the UV-vis absorption spectrum up to 600 nm compared to g-CN and doubles H_2 production rates.^[51] Beyond the edges of photocatalysis, mesoporous CNs doped with sulfur and phosphorus also found application in energy storage.^[60]

Zhang and Wang employed different approaches to tune CNs properties by introducing electron deficient monomers into the CN structure to enhance photocatalyst performance in HER^[61] constructing internal triazine–heptazine donor–acceptor (D-A) heterostructure to reach AQY 60% in HER^[62] using elemental doping with selenium for bio applications.^[63]

Finally, a heterojunction between two or more semiconductors is used to improve performance of the hybrid material by reducing the recombination rate of photogenerated charge carriers. For example, Yu and Zhang developed a 0D/2D S-Scheme heterojunction material composed of CeO₂ quantum dots and CN for photocatalytic deactivation of bacteria.^[64] Zou and Shi designed a complex Zn_xCd_{1-x}In₂S₄ solid solution coupled with CN nanosheets as a 2D/2D heterostructure,^[65] a material possessing heterojunction between CdS, WO₃ and CN,^[66] and ultrathin CN nanosheets modified with Cu₂MoS₄ for H₂ liberation.^[67]

Recapitulating available literature, it was concluded that, in general, CN-based photocatalysts of sophisticated structure, such as those featuring heterojunction and exquisite morphology, are employed in water splitting and environmental applications (model reactions), while CNs photocatalysts with large surface area and stoichiometry close to C₃N₄ are commonly employed in organic synthesis.

Finally, it is important to point out that the application of carbon nitrides in light energy conversion extends beyond organic synthesis. They are also used as a radical photoinitiator^[68, 69] in construction of photo-electrochemical and electrochemical devices,^[70] sensors, photonics, and hydrogels.^[71, 72]

Remarkable progress in the field of CN-based photocatalysis clearly demonstrates the ever-growing interest of the scientific community in this class of materials. Continuing with the next chapters, CN materials are classified into ionic and covalent structures based on chosen preparation methods and their properties. Thereafter, emerging fields, namely the application of CN materials and their long-lived radicals in energy transfer and flow chemistry are explored in a concept-wise approach.

1.3. General mechanism in molecular and semiconductor photocatalysis

To give a better description of carbon nitride photocatalysis, in this paragraph, differences and similarities are shown between the general mechanism used in molecular photoredox catalysis and semiconductor photocatalysis. An in-depth understanding of the mechanism guarantees exploration of new reaction pathways in organic synthesis and avoids the pitfalls of data interpretation. Photoredox catalysis enables selective generation of open-shell species via a sequence of processes summarized in Figure 1.^[73] This process starts with the excitation of the photocatalyst (PC) from the ground state to the excited state (PC*). Here, an electron is promoted to the LUMO creating a vacancy in the HOMO thus giving rise to a more active redox agent. Afterwards, in the presence of substrates with suitable redox properties the photocatalyst undergoes photoinduced electron transfer (PET), a process generally exploited to generate open-shell species.^[74] In all elementary steps shown in Figure 1, the substrate is either a synthetically useful organic molecule or sacrificial electron donor/acceptor. If a photocatalytic reaction requires sacrificial electron donors, such as amines or alcohols, the process is defined as 'net reductive'. If electron acceptors, for example O₂, PhNO₂ or (NH₄)₂S₂O₈, the reaction is 'net oxidative'. If no sacrificial agent is added, the process is 'net redox-neutral'.^[75] When the excited state of the photocatalyst is oxidized (formation of PC^{•+}) by the substrate or sacrificial electron acceptor, (and turnover is completed by oxidation of the sacrificial electron donor or another substrate), the pathway is called oxidative quenching (Figure 1a).

Oxidative quenching is operative, for example with phenanthrene,^[76] 9-mesityl-10-methylacridinium perchlorate (Mes-Acr-Me),^[77] eosin Y,^[78] and Ir(dF(CF₃)ppy)₂(dtbbpy)PF₆ in the corresponding chemical transformations.^[79]

On the other hand, if the catalyst is first reduced (formation of PC^{•-}) by the substrate, or sacrificial electron donor (and turnover is then completed by reduction of another substrate or electron acceptor), the pathway is called reductive quenching (Figure 1b).^[80] Reductive

quenching has been reported, for example for 1,4-dicyanonaphthalene (DCN),^[81] 9,10-dicyanoanthracene (DCA),^[82] 2,4,6-tri(p-tolyl)pyrylium tetrafluoroborate (p-Me-TPT),^[83] 3-cyano-1-methylquinolinium perchlorate (QuCN⁺ClO₄⁻),^[84] 9-mesityl-10-methylacridinium perchlorate (Mes-Acr-Me),^[85] eosin Y, and Ru(bpy)₃²⁺.^[80, 86] Overall, the redox properties of the photocatalyst with respect to the redox properties of the substrates define whether oxidative or reductive quenching takes place in the specific reaction.

Photoinduced electron transfer pathways

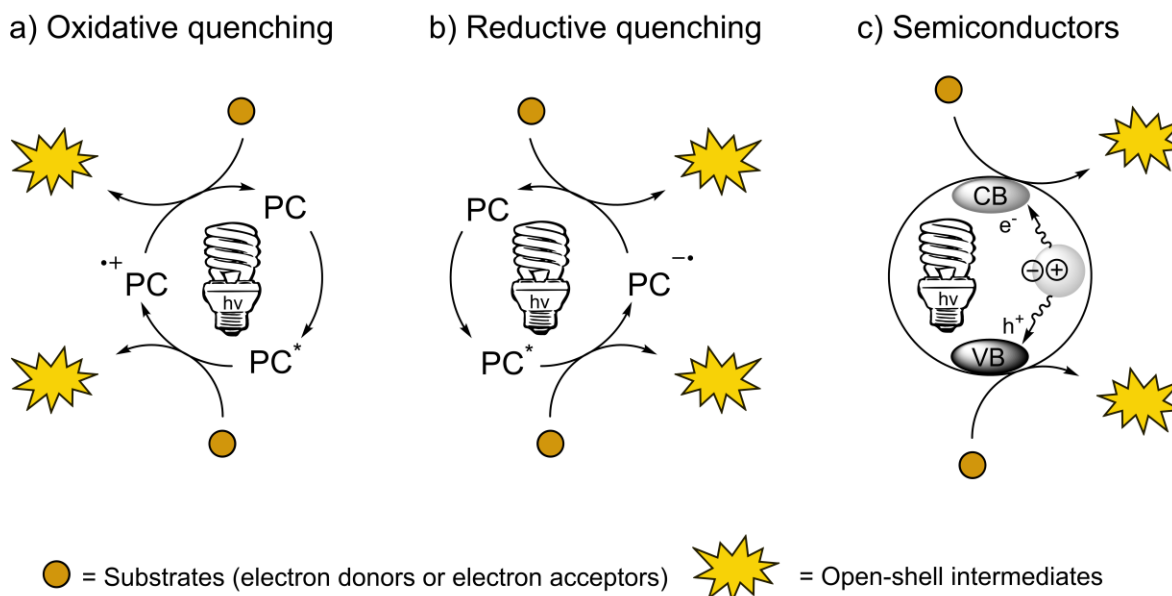


Figure 1. Photoredox mechanism comparing molecular photocatalysts and semiconductors.

Nevertheless, in both pathways substrates are converted to radical ions, which are more reactive compared to their neutral precursors. In semiconductor photocatalysis, the terms valence band (VB) and conduction band (CB) are used to denote 'sites' on the energy scale for substrate oxidation and reduction, respectively. The bands edges VB maximum and CB minimum can be considered as equivalents of HOMO and LUMO. When an incident photon interacts with the surface exciton it splits into a hole and electron establishing charge

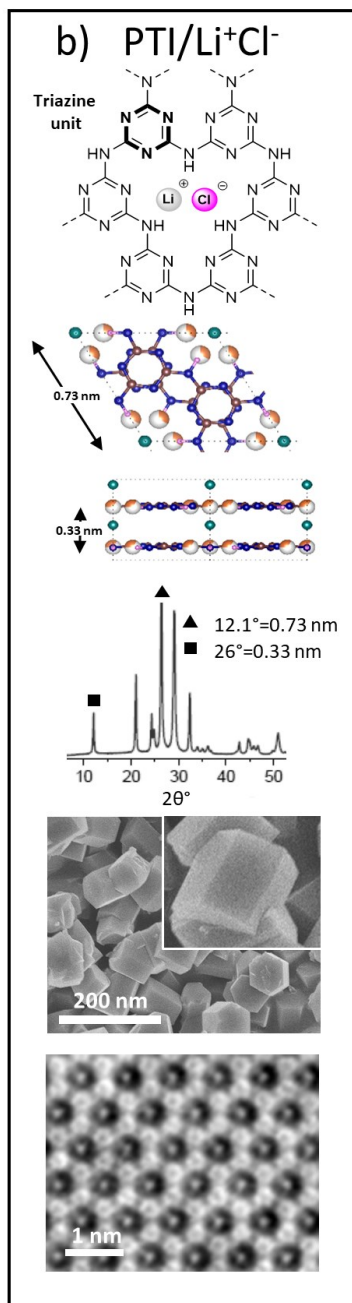
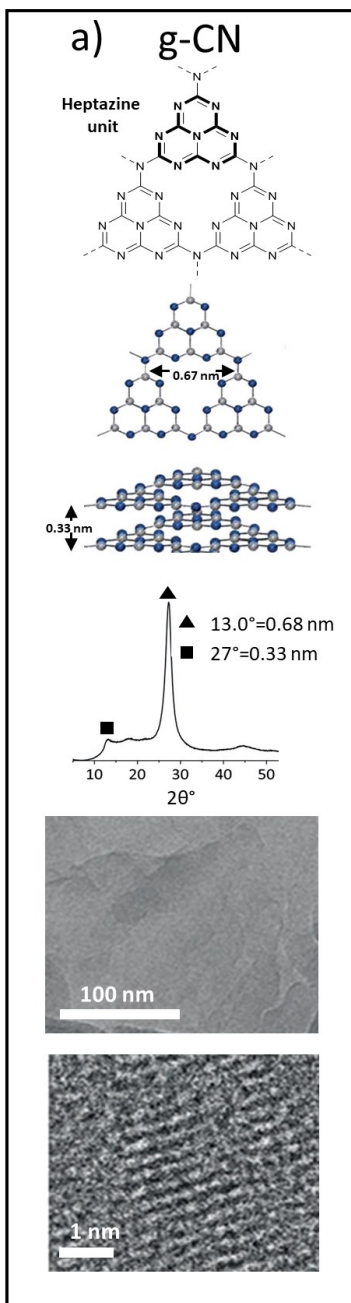
separation between VB and CB. Unlike to molecular photocatalysis that considers formation of $PC^{\bullet-}$ and $PC^{\bullet+}$ and, therefore, implies stepwise mechanism, in semiconductor photocatalysis PET substrate oxidation and reduction occur simultaneously (Figure 1c).

1.4. Synthesis and structure of carbon nitride materials

Chemical composition, morphology, and properties of CNs depend on the synthetic approach. Indeed, material engineering is a key step to tune the material toward specific applications. The great ensemble of materials with a general name of carbon nitrides can be divided into two categories: covalent and ionic CNs (Figure 2).^[87, 88]

The crucial difference is that covalent CNs do not have ionic N bonds – they possess only covalent C–N bonds or contain equal amount of cations and anions that are delocalized and intercalated between the π -conjugated layers and N-H functionality.^[89] On the other hand, ionic CNs have negatively charged N atoms bonded with metal cations.^[90] Powder X-ray diffraction (PXRD), scanning electron microscopy (SEM), and transmission electron microscopy (TEM) can be considered as the fingerprints to identify the type of synthesized CN (Figure 2). In general, graphitic CN (g-CN),^{[91] [88] [92, 93, 94]} mesoporous graphitic CN (mpg-CN),^[95, 96, 97, 98] and poly(triazine imide) intercalated with LiCl (PTI/Li⁺Cl⁻),^[99, 100, 101] are representative model examples covalent CNs. Preparation of paterfamilias g-CN is the most straightforward – melamine, or analogous precursors, is simply calcinated at 550-600 °C to obtain a metal free polymeric semiconductor. In PXRD, g-CN is characterized by peaks at 13° and 27°, due to in-plane periodicity formed by tri-substituted heptazine units and inter-layer stacking similar to that in graphite, respectively (Figure 2a). g-CN is a mainly amorphous material as typically seen from SEM and TEM images. Higher intensity of the diffraction peak at 27° indicates a preference of g-CN to form layered structure due to π - π stacking, which can be verified in TEM image (Figure 2a) as a stack of 5- 10 layers. At the same time, relatively low intensity of the diffraction peak at 13° indicates relatively few repeating units in the plane.

Covalent Carbon Nitrides



Ionic Carbon Nitrides

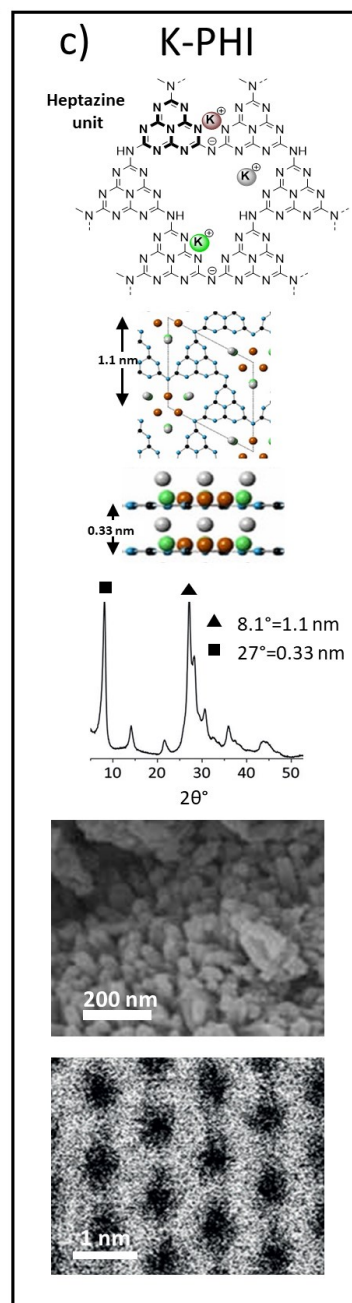


Figure 2. Carbon nitride model materials. Following in vertical order: structure representation, PXRD, SEM, and TEM. a) g-CN. Reproduced and modified from reference [50, 139] with permission from The Royal Society of Chemistry and Wiley-VCH Verlag GmbH & Co. KGaA, Weinheim, respectively. b) PTI/Li⁺Cl⁻. c) KPHI. Reproduced and modified from reference [139, 106] with permission from Wiley-VCH Verlag GmbH & Co. KGaA, Weinheim.

mpg-CN has a similar chemical structure to the graphitic predecessor, but has greater catalytic activity due to a larger surface area >200 m²g⁻¹.^[102] Preparation of mpg-CN belongs to the hard template synthesis method, which employs cyanamide as the precursor and colloidal silica aqueous solution followed by calcination at 550 °C and washing with ammonium bifluoride for template removal.^[98]

PTI/Li⁺Cl⁻ is a more crystalline member of covalent CNs (Figure 2b). It is composed of tri-substituted triazine units and can be prepared by calcining dicyanamide in a LiCl/KCl eutectic salt mixture at 400-600 °C.^[101] In this case, the eutectic salt mixture serves as a template and directs precursor polymerization toward PTI/Li⁺Cl⁻ instead of g-CN. PXRD spectrum of this material shows many intense peaks, whereby 12.1° and 26° have been assigned to in-plane periodicity and layers stacking respectively, which were also confirmed by high resolution TEM.^[101, 103] SEM images show beautiful crystallites of tridimensional hexagonal shape with diameter ~1 μm. Structure is further confirmed by aberration corrected integrated differential phase contrast TEM (AC-iDPC TEM) imaging showing the interconnected triazine pattern. Even though PTI/Li⁺Cl⁻ shows highly geometrical and beautiful structure, its application at this moment is limited to HER only. Nevertheless, due to its highly organized structure, PTI/Li⁺Cl⁻ offers an excellent platform to study reactivity of different facets in photocatalysis as has been demonstrated by Lin and Wang.^[103]

In the other category, ionic CNs are constituted by poly(heptazine imide)s (PHIs) and cyanamide surface-functionalized melon-type carbon nitride (N₃CN₂)_x.^[104] Heptazine units are the building blocks in these materials. Potassium PHI (K-PHI) has been selected as a model material because of its broadly documented application in organic synthesis and in depth characterization (Figure 2c).^[87, 104-119] The structure is highly ordered compared to g-

CN, although still possessing a large amount of structural defects such as unit cell distortions, faults in the sequences of CN-layer stacking, edge and screw dislocations, as well as rippling of CN-layers.^[106] The ordered motifs of K-PHI are constructed from six heptazine units observed as a honeycomb structure in TEM images. In PXRD, KPHI can be easily recognized by the appearance of a diffraction peak at 8° . The peak at 27° , attributed to layer stacking that is a common feature for all types of CNs, and in general for graphite like materials, is also observed in the K-PHI PXRD pattern. From SEM images, it appears as nanospherulites with a diameter in the range of 30 to 300 nm. For K-PHI, three main preparation methods have been reported: 1) mechanochemical pretreatment of 5-aminotetrazole in LiCl/KCl eutectic mixture followed by calcination at 550°C ;^[120] 2) from dicyanamide, KSCN and potassium melonate penta-hydrated calcinated at 500°C ;^[116] 3) from trichloromelamine, KSCN, and LiCl calcinated at 550°C .^[121]

At the same time, alkali metal poly(heptazine imide)s (M-PHIs) are prepared via an ionothermal approach employing Na, K, and Cs based salts.^[120] Such cations compensate the negative charges of deprotonated amino functionalities mediating the interaction between different layers and giving rise to a more ordered structure. Once PHIs are synthesized, they can undergo cation exchange and, if treated with HCl, are converted into H-PHI or covalent CN in the notation of this thesis. Vice versa, treating H-PHI or CN oligomeric precursors with alkali metal sources is another approach for PHIs preparation.^[90, 104, 108, 119, 122] It should be noted that modification of synthesis conditions of the discussed herein classes of carbon nitride materials have tremendous impact on material fingerprints such as PXRD pattern (diffraction peak position and relative intensity), or morphology observed by SEM and TEM. Indeed, there is a continuum of materials with the stoichiometry close to C_3N_4 . Therefore, to assign a proper chemical structure to the CN material, it is essential to consider structural features derived from physical methods, such as PXRD, TEM, solid state NMR, X-Ray

photoelectron spectroscopy, together with materials chemical properties such as the ability to store electrons under light irradiation (discussed below) and ion exchange.

1.5. Optical and photoredox properties

In general, g-CN absorbs light with $\lambda \leq 460$ nm that gives optical band gap of 2.7 eV (Figure 3a), while the absorption coefficient exceeds 10^5 cm⁻¹.^[71] However, by selecting an appropriate preparation method, the absorption edge can be shifted up to near IR, while the optical band gap narrows to 1.5 eV.^[55, 123] The g-CN emission maximum is located at 470 nm (figure 3b). K-PHI optical band gap is similar to g-CN, but features extended absorption up to 750 nm, attributed to the presence of intraband states (Figure 3a).^[106] K-PHI emission is observed at 500 nm (Figure 3b). g-CN has VB located at +1.82 V and CB at -0.88 V vs. RHE while VB potential in K-PHI is shifted to +2.54 V and CB to -0.09 V vs. RHE (Figure 3c).

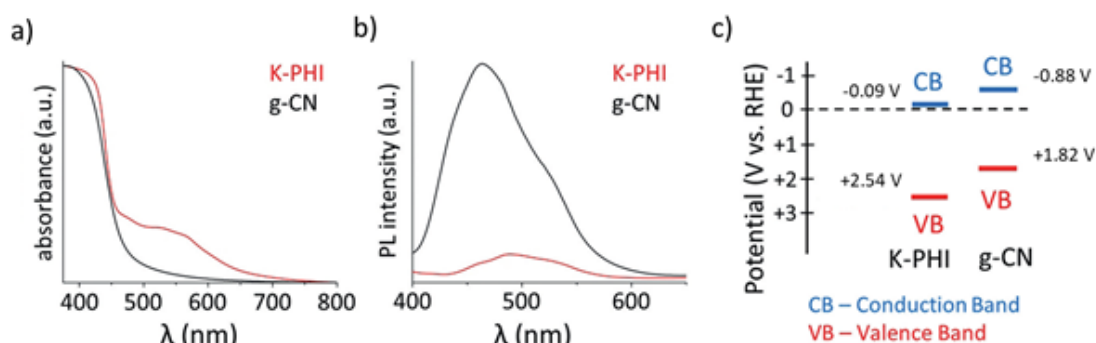


Figure 3. Optical properties of g-CN and K-PHI. a) DRUV-vis spectra. b) Photoluminescence spectra. c) VB and CB. Reproduced and modified from reference [139] with permission from Wiley-VCH Verlag GmbH & Co. KGaA, Weinheim.

Depending on the preparation method, PTI/Li⁺Cl⁻ have a band gap of 2.8-3.2 eV,^[99] while the position of VB and CB have not yet been determined.^[124]

Although steady state absorption and fluorescence spectroscopy can provide basic information related to CNs optical properties, advanced spectroscopic analysis are required to obtain a more comprehensive picture. Transient absorption spectroscopy (TAS) and time

resolved photoluminescence (tr-PL) are indeed useful tools for this purpose.^[125, 126] With these techniques, Merschjann and co-workers analyzed different CN samples.^[127] They concluded that electrons are transported predominantly perpendicular to graphitic sheets, which is in clear contrast to conductivity in graphene and related materials. From this perspective, AAA stacking of carbon nitride layers is beneficial for electronic transport.^[128] These findings led to the conclusion that surface area in heterogeneous carbon nitride photocatalysis correlates rarely with the material photocatalytic activity. Another important conclusion is that nanostructure of CNs, in particular number of layers in c-direction, defines material photocatalytic activity. Indeed, based on tr-PL data, Zhang et al. concluded that decreasing layer distance in CNs promotes higher electronic transport that leads to higher catalytic activity.^[122] Furthermore, with these techniques, Durrant et al. showed that CN materials can accumulate long-lived electrons in deep traps that are not reactive in HER.^[129] Using the spectroscopic study and photocatalytic activity data in HER, they concluded that CNs prepared at lower temperature possess a larger number of NH₂-groups, which act as trapping states and decrease activity in HER.

Overall, TAS and tr-PL are powerful spectroscopic techniques, which give valuable insights into understanding the influence of CNs structural parameters on catalytic activity.

1.6. Illumination-Driven Electron Accumulation in Semiconductors and Exploitation (IDEASE)

In semiconductor photocatalysis, the reaction mechanism implies simultaneous reduction and oxidation of the substrates by photogenerated electrons and holes (Figure 1c). In other words, PET and photocatalyst turnover steps are merged in one synchronous process. This general mechanism has been successfully adopted for covalent CN photocatalysis. However, deviation from this classical mechanism becomes particularly evident, when ionic carbon nitrides are employed in net reductive processes. While covalent CNs participate in photocatalytic transformations via the mechanism proposed by Kisch and depicted in Figure

1c,^[130] PHIs (in particular K-PHI) behave quite differently, due to the aforementioned structural and morphological features, namely the negatively charged polymeric scaffold and arrangement of heptazine units in a honeycomb-like structure. PHIs change color from yellow to green-blue in the presence of electron donors under light irradiation. Reaction mixture staining, as shown in Figure 4a, is a clear sign of long-lived radical accumulation on the surface and in the bulk of the material (Figure 4a).

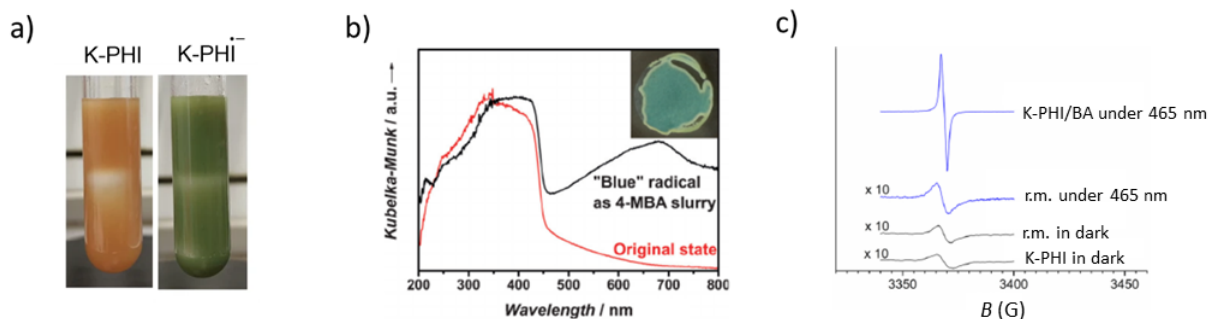


Figure 4. Carbon nitride radical anion. a) K-PHI before (left) and after light irradiation (right). Reproduced and modified from reference [105] with permission from Springer Nature b) Absorption spectra of long-lived radical in NCN-CN_x. Reproduced and modified from reference [118] with permission from Wiley-VCH Verlag GmbH & Co. KGaA, Weinheim. c) EPR spectra of K-PHI radical anion. Reproduced and modified from reference [108] with permission from Elsevier B.V.

Steady state absorption spectroscopy shows the rise of an absorption band around 600-700 nm, as the result of such drastic color change (Figure 4b). The EPR spectrum, a sharp uncoupled peak, as a singlet, can be observed as proof of radical formation (Figure 4c).

In-depth EPR studies have shown that there are different kinds of paramagnetic species.^[106, 111, 116, 121] Indeed, they can be attributed to unpaired electrons in carbons within the aromatic ring and to ammoniated electrons.^[53, 131]

Spectra from continuous wave EPR also showed anisotropic strains indicating the presence of several types of radicals, which differ slightly in their electronic structure. Furthermore, DFT simulation of hyperfine coupling between unpaired electrons resulted in about 0.7% spin density on the s orbital and about 10% spin density on the p orbital of the ¹⁴N nucleus,

which in turn indicates spin localization at one heptazine repeat unit with slight delocalization at the neighboring heptazine units. This data is also in agreement with the work by Markushyna and co-workers in which it was found that every 4th heptazine unit stores one electron, [131] as further proof of charge delocalization to the neighboring units. Figure 5a compares capacity of different carbon nitride materials – amount of electrons in μmol stored in 1 g of the material. Thus, capacity of ionic carbon nitrides, such as PHIs, is 20 times higher than that of mpg-CN.

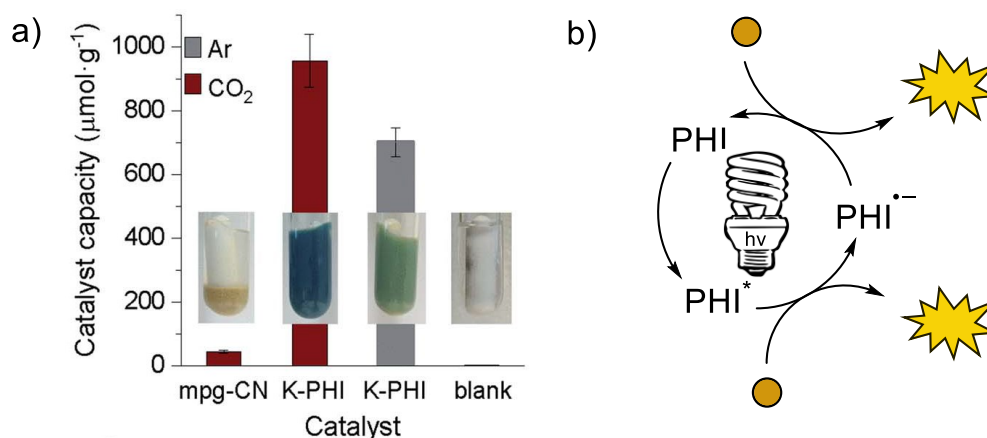


Figure 5. Display of PHIs unique feature to form long-lived radical. a) Capacity of covalent (mpg-CN) ionic (K-PHI) carbon nitrides under Ar and CO_2 . Capacity is expressed as the amount of electrons that can be stored in the material ($\mu\text{mol}(e^-)\text{g}^{-1}$). Reproduced and modified from reference [111] with permission from The Royal Society of Chemistry. b) Reductive quenching mechanism of PHI excited state.

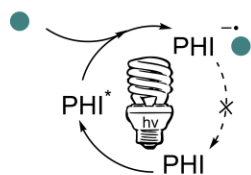
In this way, when discussing the mechanism of net reductive photocatalytic reaction mediated by PHIs, reductive quenching is obviously operative as depicted in Figure 5b.[75] In this view, behavior of K-PHI and related CN-based materials is similar to homogeneous photoredox catalysis rather than inorganic semiconductors, such as TiO_2 (Figure 1a). One can consider CNs, able to store electrons upon light irradiation, as finely designed enzyme-like architectures, which brings us to the concept of IDEASE, Illumination-Driven Electron Accumulation in Semiconductors and Exploitation. The analogy becomes more evident if one

refers to photosynthesis, which can be schematically represented as a two-step process. In phase I, or the light phase, CNs accumulate electrons, in the process under the IDEAS acronym,^[111] as previously introduced by Savateev and co-workers. After that follows phase II, or the Dark phase. Here the stored electrons are exploited in different ways (Figure 6a). Depending on the use of these stored charges, different applications are found in literature and even more can be created. It should be noted that charge and discharge processes in PHI materials differ from previously reported semiconductor-metal composites, since in this case it is more appropriate to talk about solvated electrons delocalized over organic heteroaromatic heptazinic units, rather than metal nanoparticles studied earlier by Kamat et al.^[132-134]

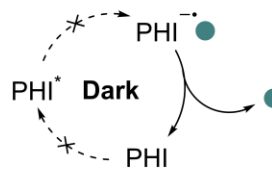
Therefore, the acronym IDEASE is a convenient and short term to define such a biomimetic multi step process.^[111, 117, 118] Lotsch, Jeschke, Reisner, and co-workers found that during the dark phase, once charged with electrons during irradiation in presence of benzylic alcohol, CN materials enable HER with the aid of colloidal Pt (Figure 6b).^[104] Thanks to this work, it is now possible to brand photocatalytic net reductive reactions, in which a photocatalyst turnover is accomplished in the dark, with the name “Dark Photocatalysis”. It has been also shown that the long-lived radicals can be generated by applying cathodic voltage. The continuous charging can be seen as a supercapacitor suggesting that energy transfer via carbon nitride in a sort of solar battery may be possible.

Indeed, straight after the discovery of “Dark Photocatalysis”, Lotsch and co-workers built a solar half-battery based on cyanamidefunctionalized PHI (NCN-PHI) (Figure 6c).^[117] When a NCN-PHI based electrode is illuminated in the presence of benzylic alcohol, the voltage in open circuit potential (OCP) measurements raises up to -0.6 vs. NHE and can be discharged in the dark. It is also possible to perform charge and discharge cycles only using electricity as the driving force (in permanent dark conditions).

a) ————— **IDEASE** —————



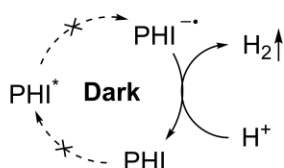
I - Light phase



II - Dark Phase

————— **Lotsch, Jeschke, Reisner 2017** —————

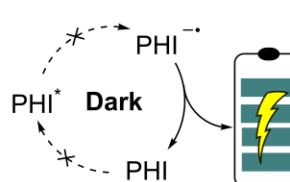
b)



HER - Dark photocatalysis

————— **Lotsch 2018** —————

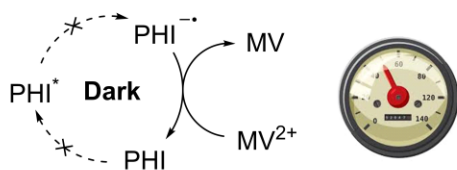
c)



Charge storage and discharge - Solar battery

————— **Savateev 2019** —————

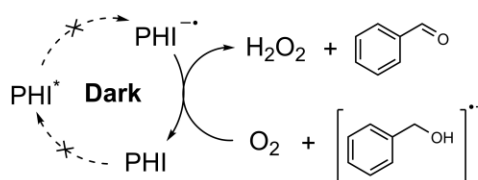
d)



Charge storage and quantification - IDEAS

————— **Wang 2019** —————

e)



Benzylic alcohol oxidation - Ammoniated electrons

Figure 6. Various examples of IDEASE concept.

Furthermore, it must also be pointed out that PHIs are able to absorb light and store/discharge photoinduced electrons in one single carbon nitride material with no need of further electron shuttles.

Savateev and co-workers quantified the capacity of PHI materials in IDEAS by titration of the long-lived radical with methyl viologen (MV^{2+}) (Figure 6d).^[111] In their work, they used K-PHI and benzyl amine as an electron donor. Experimentally, it was found that 1 gram of K-PHI is able to store up to at least 0.95 mmol of electrons corresponding to one uncoupled electron per four heptazine units. Wang and co-workers exploited the discussed phenomenon in the reduction of molecular oxygen in the presence of a proton source for the generation of H_2O_2 , using benzyl alcohol as hole scavenger, which is further oxidized to benzaldehyde (Figure 6e).^[121] Therefore, it may be considered as another example of Dark Photocatalysis. Although such long-lived radicals have been known for a discrete amount of time and not only related to CN materials,^[135] the combination of this feature with other properties of carbon nitrides will yield a number of applications in photocatalysis and beyond.

1.7. Energy transfer in Carbon Nitrides

Energy transfer is defined as the photophysical process where an excited state of a molecular species (donor) is quenched by another molecule (acceptor) increasing its energy.^[136] In photocatalytic context, the term 'donor' refers to photocatalyst or photosensitizer.

For this process to happen, it is fundamental that the photocatalyst, once in its excited state, is able to perform an intersystem crossing (ISC) forming a triplet excited state (S_1 - T_1 transition). Relaxation of the photocatalyst triplet to the ground state (T_1 - S_0 intersystem crossing) is spin forbidden and is therefore a much slower process compared to S_1 - S_0 transition, which guarantee extensive excited state lifetime to participate in bimolecular quenching processes.^[137] The employment of a visible light photosensitizer is convenient as they are able to access the triplet excited state under less energetic electromagnetic radiation, which is beneficial for higher selectivity and the scope of functional groups tolerated in the specific photocatalytic reaction.^[138] Energy transfer processes are also differentiated in two categories: 1) Förster Resonance Energy Transfer (FRET) due to dipole-dipole interactions, a process which plays an important role in photosynthesis, fluorescence Labeling, and bioimaging; 2) Dexter Energy transfer, due to a simultaneous exchange of electrons between acceptor ground state and donor excited state respectively, a process which dominates photosensitized organic reactions in solution.^[10]

One peculiarity of the photocatalytic mechanism based on energy transfer is that it does not generate charged ions, which nevertheless are implied in the mechanism based on electron transfer (Figure 7a).^[102] Extensive literature analysis suggests that a vast majority of photocatalytic reactions mediated by carbon nitrides are explained in terms of pure electron transfer, while energy transfer is not even considered.^[139] However, the conjugated polymer structure of carbon nitrides is similar to that of polyaromatic compounds, which might be beneficial for singlet-triplet ISC (Figure 7b).^[10]

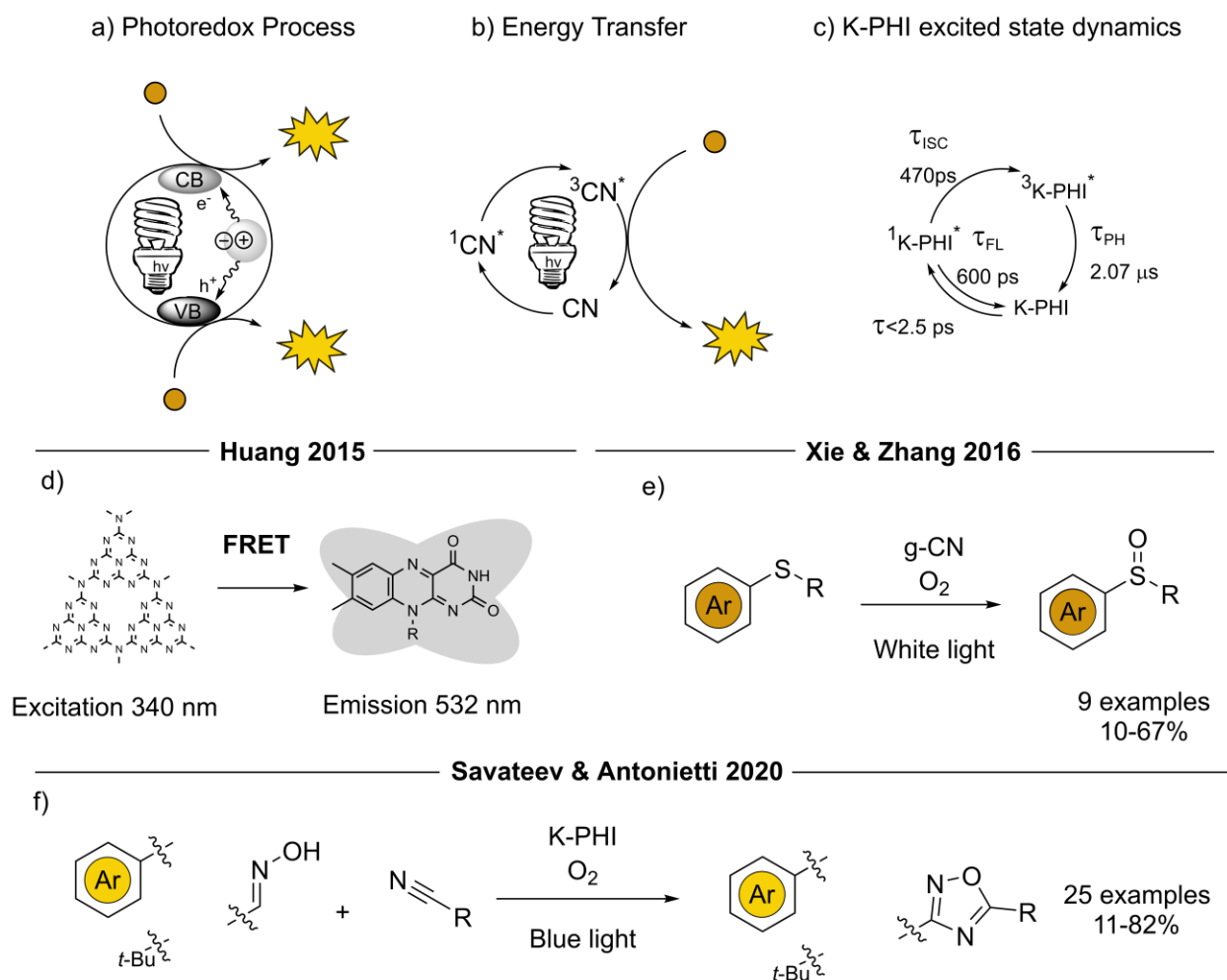


Figure 7. Schematic mechanisms overview and energy transfer processes reported in literature. a) Photoredox catalytic process in semiconductors. b) Energy transfer process; c) K-PHI excited state dynamics; d) FRET between g-CN and riboflavin. e) Generation of $^1\text{O}_2$ for the synthesis of sulfoxides; f) generation of $^1\text{O}_2$ for the preparation of oxodiazoles and isoxazoles.

Therefore, the energy transfer mechanism for carbon nitriles can also be operative. K-PHI is characterized by a relatively short fluorescence lifetime (S_1 - S_0 transition) $\tau_{\text{FL}} = 600$ ps and a fluorescence quantum efficiency (QE) $< 0.1\%$ that supports the existence of non-radiative pathways of the excited state relaxation.^[106] At the same time, for covalent carbon nitriles typically $\tau_{\text{FL}} > 2$ ns and fluorescence QE $> 10\%$ have been reported.^[126, 140] Since the yield of

free ions is higher for triplet contact radical ion pair,^[75] the ability of the sensitizer to form a long-lived triplet state, which can be achieved by decreasing singlet-triplet energy gap, is beneficial for the photocatalytic reaction. For K-PHI as well as covalent carbon nitrides, such singlet-triplet energy gap has been determined to be ~ 0.2 eV.^[138] Overall, materials with long τ_{FL} and τ_{PH} , short τ_{ISC} are beneficial for the application in photocatalysis.

Taking K-PHI as an example and using TAS, Strauss and Guldi confirmed singlet-triplet ISC and described excited state dynamics with the corresponding lifetimes (Figure 7c).^[128] Compared to ionic carbon nitride such as K-PHI, in which ISC occurs within $\tau_{ISC} = 470$ ps and a phosphorescence lifetime of $\tau_{PH} = 2.07$ μ s, in covalent carbon nitride, prepared via calcining melamine, ISC has been reported to occur within few ps, while the phosphorescence lifetime is ~ 124 μ s.^[126] Although both ionic and covalent carbon nitrides belong to the same class of materials, this example illustrates that exciton dynamics in carbon nitrides could be tuned in a broad range. Huang and co-workers found that CNs can act as photosensitizers when excited with photons at 340 nm.^[141] This leads to a fluorescence resonance energy transfer (FRET) to riboflavin (RF), with green emission at 532 nm (Figure 7d). After such discovery, the authors applied this concept for the development of an analytical method for the determination of RF in complex matrix samples, based on fluorescence ratiometric detection. By this method, they were able to quantify RF amount in milk and commercial vitamin drinks in a simple, economical, and sensitive manner. This represent a brilliant example of using CNs as photochemical sensors. Then, Xie, Zhang, and co-workers proved that oxygen can serve as energy acceptor in combination with CN materials.^[142] They showed that in situ generated singlet oxygen (1O_2) can be used to oxidize sulfides to sulfoxides (Figure 7e). Savateev and Antonietti used K-PHI in synthesis of highly valuable active pharmaceutical ingredients (APIs), such as oxadiazoles-1,2,4 and isoxazoles, via a cascade of energy transfer, which involves sensitization of 1O_2 and [3+2]-cycloaddition reaction (Figure 7f).^[128] Although only few papers report using CNs in energy transfer processes, the authors foresee

the application of this feature to expand a portfolio of organic reactions mediated by $^1\text{O}_2$ or combining CNs with other energy acceptors.

1.8. Flow chemistry

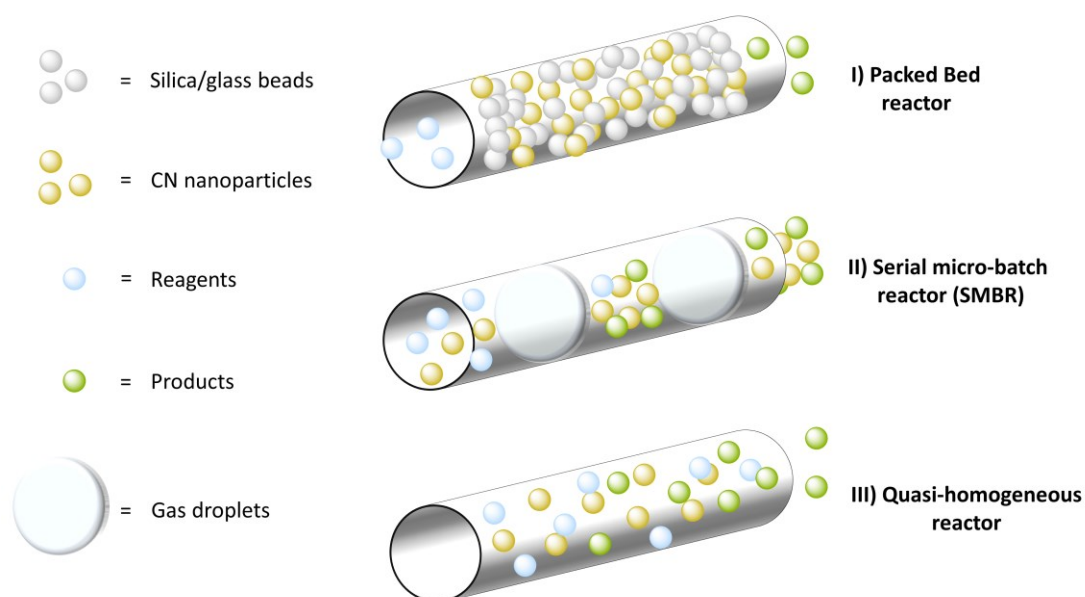


Figure 8. Overview of different technologies in carbon nitride flow photocatalysis.

Flow chemistry is a chemical technology involving the employment of channels or tubing to conduct a reaction in a continuous stream, and is quickly becoming an indispensable tool and widespread technology among laboratories.^[143] It guarantees unique control of key reaction parameters ensuring efficient mixing and heat transfer, unmatched by batch technology from this point of view.^[144] It is also an opportunity to scale-up reactions easily increasing productivity by lowering the reaction times.^[145] Flow technology can also be coupled with other techniques, such as organic synthesis under microwave irradiation, as has been studied in depth by Barham et al.^[146]

Despite the enormous amount of literature published in the field of photocatalysis and photoredox catalysis, industrial applications, except few examples, are scarce.^[147] The reason behind this is attributed mainly to a Beer-Lambert law limitation,^[148] whereby increasing the size of the vessel decreases the light penetration, and thus, the net photocatalytic activity.^[149] In addition, considering that photocatalysts usually employed in organic synthesis include expensive metals, synthesis of APIs by this approach become expensive.^[150] In this context, CNs can be up to three orders of magnitude less expensive than other photocatalysts and, more importantly, can be recycled.^[87] Efforts have been undertaken to establish CN photocatalysis in large scale.^[151] The coupling of carbon nitride photocatalysis with a flow approach is envisioned as a promising solution to replace expensive metal photocatalysts. Colloid dispersions, such as suspension of semiconductor in liquid phase, vastly decrease light penetration due to back-scattering, observed in UV-vis absorption spectra as significant absorption in the full optical range.^[105] Scattering also results in a higher absorption coefficient in the Beer-Lambert equation.^[13] Therefore, in heterogeneous photocatalysis, to ensure efficient light delivery into the bulk of the reaction mixture, thin flow photoreactors are a preferential choice in scale-up strategies. Three main technologies have been adopted so far in CN photocatalysis in flow (Figure 8). I) Packed bed reactors, in which the catalyst is immobilized or grafted inside the tube and reagents are pumped through the reactor. It can be considered as a simple and steady solution preventing the catalyst separation step, although these type of reactors are known to have great pressure drops, which requires high inlet pressure. In addition, clogging often occurs upon prolonged usage.^[152] They also have great limitations due to light penetration – light reaches only the outside layers of the catalyst, which are closer to the reactor walls. II) Serial micro-batch reactor (SMBR), in which segmented gas-slurry stream is passed through the tubular reactor, is a convenient solution to mitigate the no-slip condition. However, such systems have a long onset time. Afterwards, since productivity correlates with the flow rate,

increasing the reaction time might lead to CN deposition. III) Quasi-homogeneous photocatalysis, in which stable colloid solution composed of carbon nitride and reagents in polar solvent is pumped through the tubing, identical to the reactor configuration in homogeneous photocatalysis. The approach is similar to SMBR, without the employment of a gas line. The strategy is still convenient for scaling up reactions avoiding clogging, and having good irradiation surface. In the first approach, Blechert and co-workers used a packed bed reactor filled with mpg-CN, silica, and glass beads (to reduce back pressure).^[97] This technology was tested in radical cyclisation of 2-bromo-1,3- dicarbonyl compounds (Figure 9a). Using the flow reactor, reaction time was shortened by about fifty times, 5 min versus 4 h, compared to the reaction in batch.

Years later Rueping et al. reported an analogous technology by using a chromatography column with a similar filler composition, but employing g-CN as the photocatalyst (Figure 9b).^[93] Accordingly, the flow approach reduced reaction time by about six times, 3 h versus 17 h, in the photocatalyzed desilylative addition of α -silylamines.

Reisner and co-workers built a packed bed photoreactor similar to the aforementioned one, but employed it in a triphasic gas-liquid-solid flowsystem with oxygen as the gaseous phase.^[95] Overall, this technology demonstrated 3-6 times higher productivity, with higher conversion of benzylamines in homocoupling and benzylic alcohols oxidation (12 examples), but lower selectivity compared to the reaction in batch (Figure 9c).

Wang, Zhang, and co-workers grafted CN material as a film on silica beads in order to increase catalyst surface area and the area exposed to light.^[153] This approach increased productivity by 10 times compared to the reaction in batch in the [2+2] dimerization of α -sarone in gram scale (Figure 9d).

Pieber and Gilmore developed SMBR concept in decarboxylative fluorination of carboxylic acids.^[154] In decarboxylative fluorination of phenoxyacetic acid to (fluoromethoxy)benzene, as an example, the productivity was increased 5 times compared to the approach in batch

(Figure 9e). The approach allows for efficient mixing inside the individual slurry segment,^[152] while segmented flow eliminates the problem of no-slip condition, reactor clogging, catalyst leaching, and deposition. In addition, due to higher interface area between gaseous and liquid phase, the approach holds promise for photocatalytic reactions employing O₂.

Krivtsov, Beranev, and co-workers introduced the 'quasihomogeneous photocatalysis' concept according to which heptazine-based polymeric carbon nitrides nanoparticles with size 10±3 nm are used as water-soluble photocatalyst, but at the same time can be recovered by simple modulation of the ionic strength of the medium.^[155]

However, obtaining such stable colloid solution is not simple, especially when nanoparticles are bigger and tend to agglomerate. Therefore, instead of exploitation of material properties, tailored setups can help reaching such phase homogeneity. Following this approach, Kappe, Pieber, and co-workers employed an oscillatory plug flow photoreactor in order to maintain a stable dispersion in the heterocoupling of alkyl amines with aryl bromides (Figure 9f).^[156] Authors reached grams-per-hour productivity, which is 24 times higher compared to the reaction in batch. This particular approach is free of moving parts, allows for the pumping of dispersion containing reagents and CN catalyst directly through the reactor and prevents settling of solid material.

All flow technologies described above univocally support higher productivity (gram of product per hour) of flow approach compared to the reaction in batch. ^[143, 157] CN flow chemistry ensures much higher photon efficiency compared to batch reactions. Future development of this field combined with CNs will soon be extended in combination with the expanding topics of gas-liquid phase photoredox catalysis and PEC.^[6, 158]

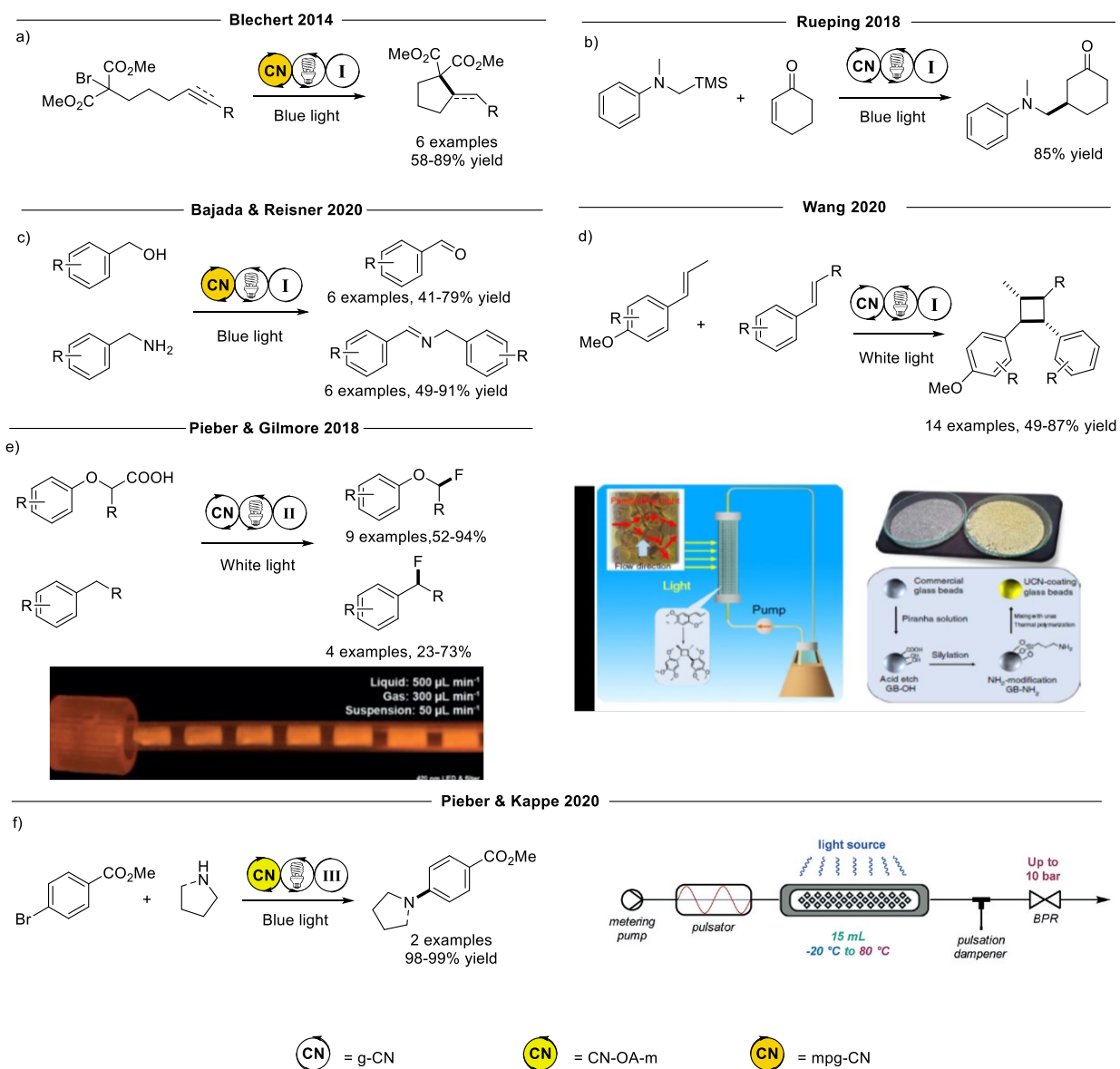
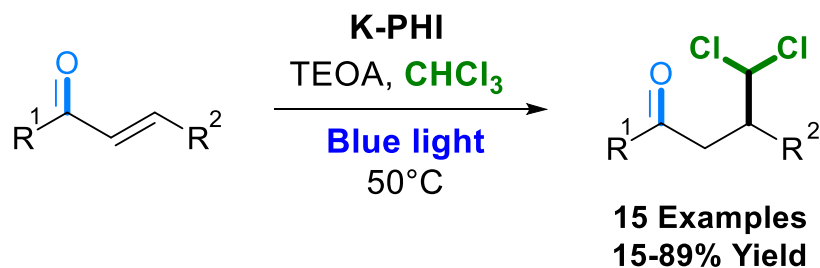


Figure 9. CN photo-flow chemistry. Different scale-up methodologies for photochemical reactions and improve productivities. Inset in d) is reproduced and modified from reference [153] with permission from Springer Nature. Inset in e) is reproduced and modified from reference [154] with permission from Wiley-VCH Verlag GmbH & Co. KGaA, Weinheim. Inset in f) is reproduced and modified from reference [156] with permission from The Royal Society of Chemistry.

2. Dichloromethylation of enones by carbon nitride photocatalysis

Overview

Small organic radicals are ubiquitous intermediates in photocatalysis and are used in organic synthesis to install functional groups and to tune electronic properties and pharmacokinetic parameters of the final molecule. Development of new methods to generate small organic radicals with added functionality can further extend the utility of photocatalysis for synthetic needs. Here, a new method to generate dichloromethyl radicals from chloroform is presented using K-PHI photocatalyst under visible light irradiation for C1-extension of the enone backbone.



This chapter is an adapted version of the article:

S. Mazzanti, B. Kurpil, B. Pieber, M. Antonietti, A. Savateev, Dichloromethylation of enones by carbon nitride photocatalysis. *Nature Communications* 11, 1387, 2020.
<https://doi.org/10.1038/s41467-020-15131-0>

Results and discussion

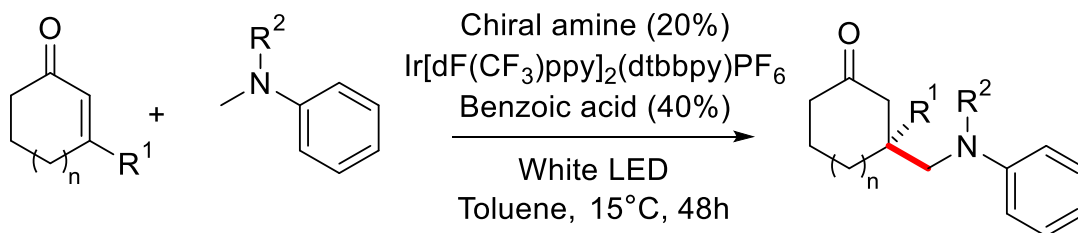
Small organic radicals, such as CH_3 , CF_3 , CHF_2 ^[160] and perfluoroalkyl,^[161] CH_3O ^[91] etc. are used for the functionalization of the organic molecules in order to tune steric and electronic properties. Furthermore, the lipophilicity and metabolic stability of pharmaceuticals may be adjusted in this way.^[162] Despite their importance for medicinal chemistry, CF_3 , alkyl, and CH_3O groups are chemically stable. Therefore, further diversification of the molecule at these newly formed sites is problematic. For example, cleavage of C-F bond in CF_3 -group is extremely demanding.^[163] The same applies to C-O bond in the CH_3O -group.^[164]

Conversely CHCl_2 radical from the pool of small organic radicals is synthetically more useful. It enables the installation of an electrophilic carbon, and the C-Cl bonds can be conveniently cleaved using weak nucleophiles. In other words, the CHCl_2 radical allows for C_1 -extension of the substrate framework, while simultaneously adding a chemically active functionality.^[165] From this point of view, the CHCl_2 radical can be regarded as a 'small functional radical'.

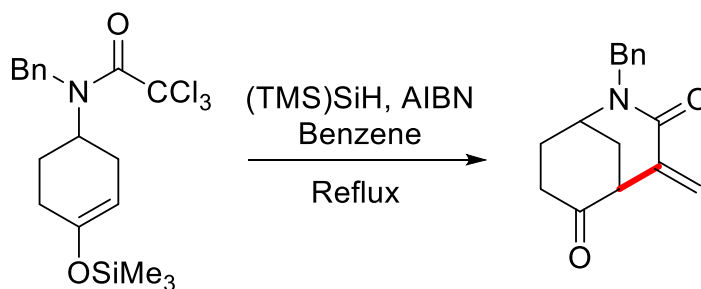
Despite the obvious synthetic utility of the dichloromethyl radical, literature is still lacking reactions using dichloromethyl moieties in conjugate additions – the kind of reaction resembling a traditional polar Michael addition. The latter was well studied in photoredox catalysis.^[166] An example shown in Figure 1a employs methyl groups in tertiary amines and C=C double bond as coupling partners. The chemistry of dichloromethyl radicals is restricted to a few examples, while such radicals are generated predominantly by catalyst containing rare precious metals or dangerous chemicals (Figure 1 b,c).

It has been hypothesized that chloroform can be used as atom efficient source of CHCl_2 radicals. Although chloroform readily gives dichlorocarbene in the presence of strong bases, the photocatalyst will alter the path of chloroform decomposition. Formation of the dichloromethyl radical thereby may be achieved by one-electron reduction of chloroform followed by elimination of a chloride anion.

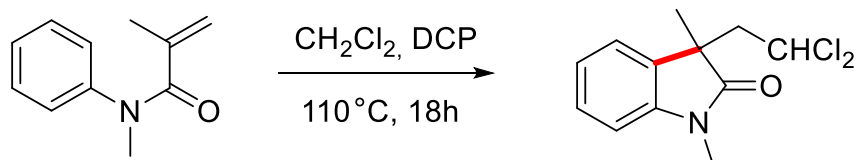
a) Photocatalyzed conjugated addition to enones



b) Cyclisation of trichloroacetamides



c) Preparation of dichlorinated oxindoles



d) This work - Dichloromethyl radical addition to enones

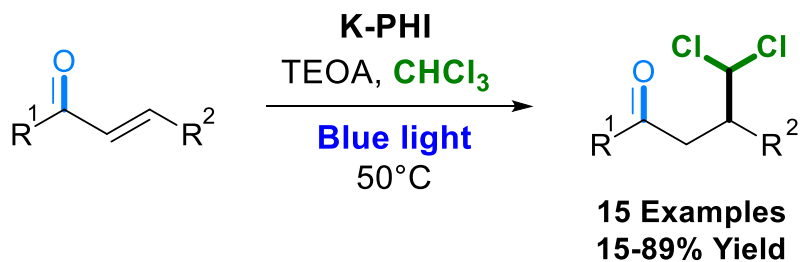
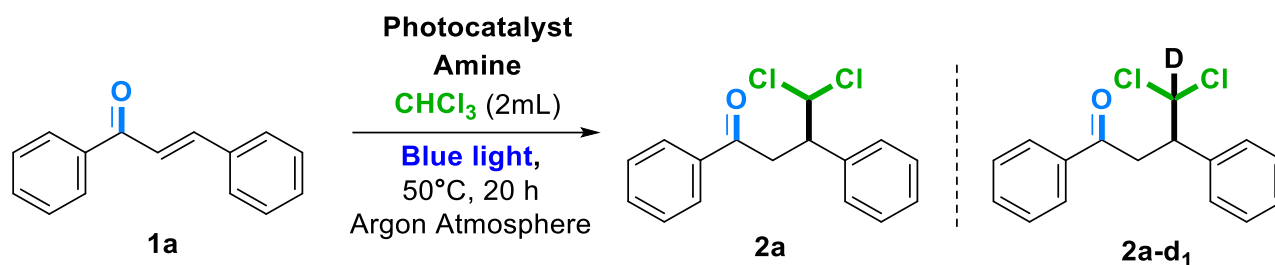


Figure 1. Previous works related to the designed reaction are presented. a) Conjugate addition to enones. b) Cyclisation of trichloroacetamides. c) Synthesis of dichlorinated oxindoles. d) Photocatalytic reaction developed in this work.

In order to trigger this process, the first experiment employed chalcone **1a**, chloroform, tetrahydroisoquinoline (THIQ) as an electron donor, and K-PHI as the photocatalyst, under blue light. Dichloroketone **2a** was synthesized initially with 17% yield when 1 equivalent of THIQ was used (Table 1, entry 1).



Entry	Amine	Photocatalyst	Yield (%) ^b
1	THIQ (1 eq, 0.05 mmol)	K-PHI (5 mg)	17
2	THIQ (2 eq., 0.1 mmol)	K-PHI (5 mg)	33
3	THIQ (4 eq., 0.2 mmol)	K-PHI (5 mg)	51
4	TEOA (3 eq., 0.15 mmol)	K-PHI (5 mg)	62
5	TEOA (10 eq., 0.5 mmol)	K-PHI (5 mg)	97
6	TEOA (10 eq., 0.5 mmol)	-	-
7 ^c	TEOA (10 eq., 0.5 mmol)	K-PHI (5 mg)	-
8	-	K-PHI (5 mg)	-
9 ^d	TEOA (10 eq., 0.5 mmol)	K-PHI (5 mg)	99
10	TEOA (10 eq., 0.5 mmol)	Na-PHI (5 mg)	49
11	TEOA (10 eq., 0.5 mmol)	mpg-CN (5 mg)	85
12	TEOA (10 eq., 0.5 mmol)	CdS (20% mol)	70
13 ^e	TEOA (10 eq., 0.5 mmol)	TiO ₂ (20% mol)	94

14	TEOA (10 eq., 0.5 mmol)	Ir(ppy) ₃ (2.5% mol)	97
15	TEOA (10 eq., 0.5 mmol)	[Ru(bpy) ₃]Cl ₂ (2.5% mol)	8

Table 1. Screening of reaction conditions. a) Reaction conditions: 1 eq., 0.05 mmol, 10.4 mg of **1a**; under light irradiation ($\lambda = 461$ nm, 51 ± 0.03 mW cm⁻², blue LED; b) Yields estimated by GC-MS; c) no light; d) Reaction performed in CDCl₃; e) reaction performed under UV light ($\lambda = 365$ nm, 17.5 ± 0.03 mW cm⁻²).

By increasing the amount of THIQ gradually to four equivalents, the yield of **2a** was increased to 51% (entry 3). However, an even higher yield (62%) of **2a** was achieved by using 3 equivalents of triethanolamine (TEOA) as electron donor (entry 4). The optimum conditions include 10 equivalents of TEOA under which 97% yield was achieved (entry 5). The reaction does not proceed without catalyst, light, or a sacrificial electron donor (entry 6-8). CDCl₃ is a suitable source of CDCl₂ radicals offering a route for *d*-labeled dichloroketones **2a-d**₁ with 99% yield (entry 9). Also the robustness of the reaction was evaluated using different alcohols as hole scavengers observing the formation of the desired product in all cases, albeit in lower yield (Table S1, entry 11-14). These results illustrate the better ability of amines to donate electrons compared to alcohols, due to lower oxidation potentials (*e.g.* +0.5 V for TEOA, +1.5 V for benzyl alcohol, and +1.9 V for MeOH, EtOH, *i*PrOH (Supplementary note 1). It is also supported by a higher H₂ production rate over carbon nitride materials using TEOA as electron donor compared to MeOH and EtOH^{[167],[61]} and comparative tests of benzyl alcohol oxidation versus benzylamine.^[168] Moderate heating (50°C) facilitates the reaction, as the yield of **2a** was 64% when reaction was performed at 20°C (Supplementary Table 1, entry 21). The catalytic activity was compared with other materials and photoredox complexes. Na-PHI gave **2a** with 49% yield (entry 10).^[169] Similar behavior was already observed during the photocatalytic synthesis of thioamides.^[113] Mesoporous graphitic carbon nitride (mpg-CN) gave **2a** with comparable yield 85% (entry 11). The inorganic semiconductors CdS and TiO₂ gave **2a** in 70% and 94% yield, respectively (entries 12, 13).

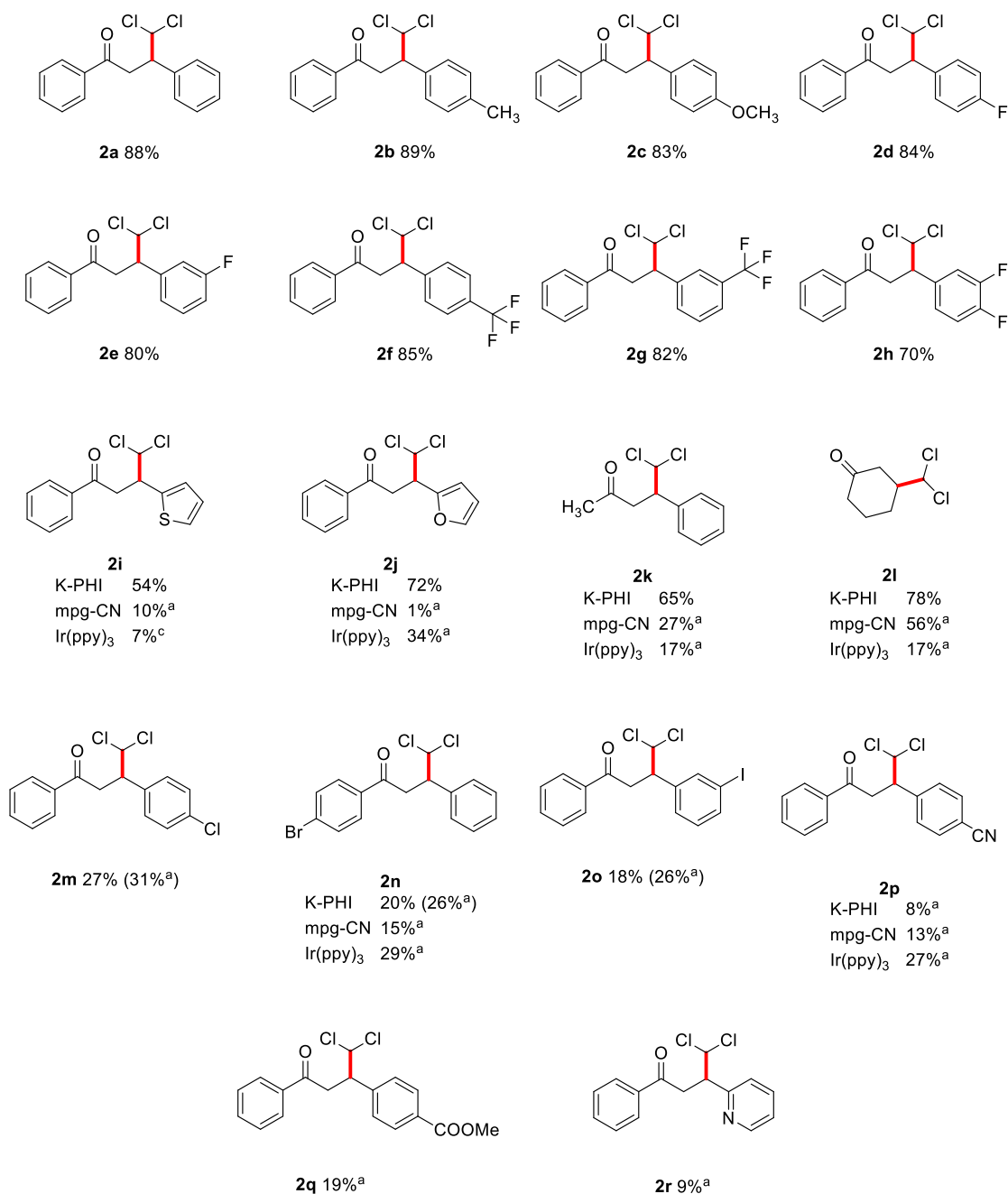


Figure 2. Scope of enone substrates. Reaction conditions: enone **1** (1 eq., 0.05 mmol); TEOA (10 eq., 0.5 mmol, 67 μ L); CHCl_3 (2 mL); Argon atmosphere; under light irradiation ($\lambda = 461 \text{ nm}$, $51 \pm 0.03 \text{ mW cm}^{-2}$, blue LED), isolated yields. Superscript "a" indicates the yields determined by $^1\text{H NMR}$ using 1,2,3-trimethoxybenzene as internal standard.

Homogeneous Ir(ppy)₃ gave **2a** with 97% yield (entry 14), while [Ru(bpy)₃]Cl₂ only resulted in 8% of **2a** (entry 15). Furthermore, it was also shown that recycled K-PHI remains photocatalytically active for at least two further cycles (Supplementary Table 2).

Using the optimized conditions fifteen dichloroketones have been isolated with 18-89% yield (Figure 2, **2a-2o**). The characterization of products was conducted by NMR analysis. Dichloroketones **2** do not give stable molecular ions in the mass spectra (electron ionization). For example, the expected m/z value for **2a** is 292. However, a signal with m/z 221 was detected (Supplementary Figure 2). The latter corresponds to 2,4-diphenylfuran. In general, 2,4-diarylsubstituted furans are products of oxygen nucleophilic attack at CHCl₂-group followed by elimination of two molecules HCl under the conditions of GC-MS data acquisition. Below, the reactivity of CHCl₂ group was employed in the synthesis of pyrroles and furans. Nonetheless, elemental analysis of **2a** revealed chlorine content in excellent agreement with the calculated content confirming the proposed structure. A further proof of the product structure it was observed in the rise of the triplet in the ¹³C NMR spectrum in the *d*-labeled compound (**2a-d₁**) using deuterated chloroform as dichloromethyl source.

Dichloromethylated chalcones bearing strong electron withdrawing groups, *i.e.* CN-, MeO₂C- and pyridin-2-yl, **1p-r**, gave the corresponding products **2p-r** in low yields as analyzed by ¹H-NMR spectrometry of the crude reaction mixture (Supplementary Note 2). Nevertheless, it is envisioned as the toolbox of synthetic organic chemistry to be useful for further diversification of the products structures employing, for example, methyl-group in **2b**, F-atoms in **2d,e,h**, and intrinsically reactive sites in **2i,j**. Common reactive Michael acceptors, such as methyl vinyl ketone and acrylonitrile gave only trace amounts of CHCl₂ addition to the double bond as evidenced by GC-MS (Supplementary Note 3). Even more reactive Michael acceptors, *i.e.* methacrolein, methyl acrylate, and 2-furanone, gave a complex mixture and the desired products could not be identified (Supplementary Note 4).

Analysis of the substrates scope suggests that diarylsubstituted enones in general are more suitable substrates for photocatalytic dichloromethylation than terminal alkenes. Nevertheless, the advantages of the developed method are a simpler protocol and safer conditions. For example, the synthesis of **2a** and **2l** was described earlier using exotic reagents such as dichloromethylithium^[170]. A comparison of K-PHI, mpg-CN, and Ir(ppy)₃ photocatalysts using selected enones, **1i-l,n,p**, revealed that K-PHI in general gives the products in higher yields.

In the course of studying suitable reagents to install C_xHal_yH_z-groups in the enone **1a**, other halogenated reagents were tested including dichloromethane, bromoform, iodoform, 1,1,2,2-tetrachloroethane, and tetrachloromethane (Supplementary Table 1). Careful analysis of the reaction mixture revealed that addition of CHBr₂-, CHI₂-, and C₂HCl₄-groups to enone **1a** indeed took place. However, the products are not stable and undergo further chemical transformations, such as HX elimination and subsequent cyclizations to 2,4-diphenylfurane derivatives (in case of bromoform and iodoform) or dichlorodihydropyranes (in case of tetrachloroethane) (Supplementary note 5). Compared to bromoform and iodoform, chloroform is beneficial due to higher selectivity in the reaction of enones C1 backbone extension.

Scaling the dichloromethylation reaction of **1a** in batch led to gradual decrease of the dichloroketone yield from 88% (on 0.05 mmol scale) to 23% (on 5 mmol scale) (Supplementary Table 3). After careful investigation, it was concluded that the origin for such drastic drop of the product **2a** yield is poor light penetration in the depth of the batch reactor due to light back-scattering by suspended semiconductor particles (Supplementary Note 6).^[171]

In order to overcome limitations of the batch approach, the reaction was performed in a continuous flow reactor made out of thin (inner diameter 1.6 mm) fluorinated ethylene propylene (FEP) tubing (Figure 3). The use of carbon nitrides has been reported in serial

micro-batch reactors,^[154] that use gas-liquid segments to avoid clogging. A simplified system is applicable for K-PHI due to relatively small particle diameter (100 nm) and negative zeta-potential (ζ) (Figure 3a). Electrostatic stabilization allows pumping colloidal solution (Figure 3b, Supplementary Note 7) without using a gas-liquid system (Figure 3c). Using flow approach, **2a** was obtained with 57% yield. Considering convenience of K-PHI suspension pumping through thin FEP tubing along with easiness of the photocatalyst recovery, the entire system enables quasi-homogeneous photocatalysis in flow.^[155]

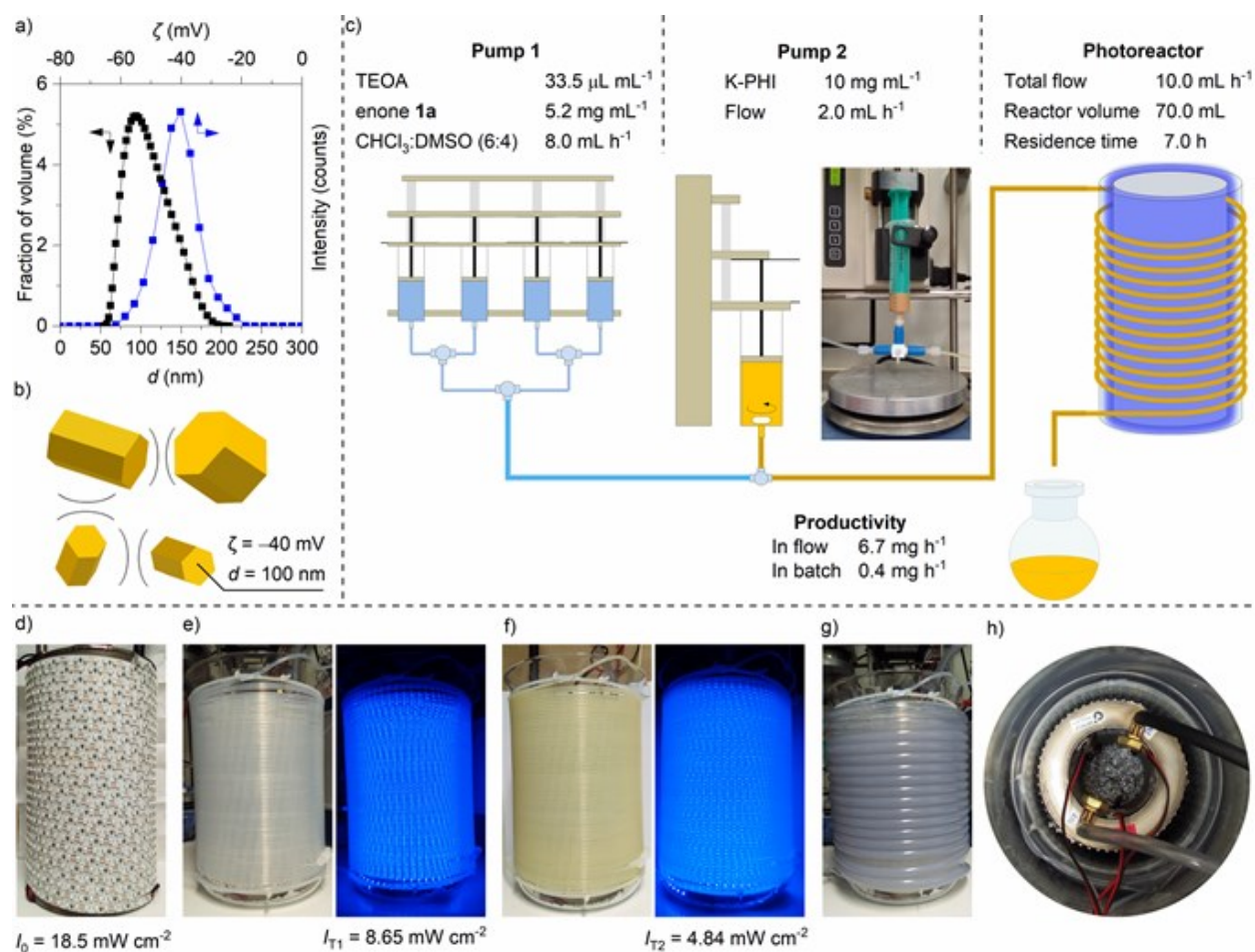


Figure 3. K-PHI colloidal solution properties and flow photoreactor design used in this work. a) Zeta-potential (ζ) and hydrodynamic diameter (d) of K-PHI particles suspended in water. b) Schematic representation of colloidal solution stabilization by electrostatic repulsion. c) Schematic representation of the reactor setup and reaction parameters. Yield was determined by GC-MS collecting

the solution for 30 minutes from the photoreactor; comparison between flow and batch are made considering the optimized reaction conditions in batch. d) The light source was built by wrapping self-adhesive LED stripes around a hollow steel cylinder shell equipped with inlet and outlet for water-cooling. Incident light intensity (I_0) measured at zero distance from the light source 18.5 mW cm^{-2} . e) Light source placed inside a glass beaker wrapped with FEP tubing under day light and blue light source. Transmitted light intensity (I_{T1}) was measured at zero distance from the FEP tubing. f) FEP tubing filled with a reaction mixture under day light and blue light source. Transmitted light intensity (I_{T2}) was measured at zero distance from the FEP tubing. g) Photoreactor wrapped with PVC tubing to maintain the desired temperature during the experiment. h) View from the top on the assembled flow photoreactor immersed into a glass beaker. The space between the beakers is filled with cooling agent (water).

As seen from the light intensity measurements (Figure 3d-f), the FEP tubing filled with the reaction mixture absorbs 74% $[(I_0 - I_{T2})/I_{T0}]$ of light. These results suggest that by performing the reaction in flow, more homogeneous irradiation of K-PHI particulate is achieved compared to the reaction in batch (Supplementary Note 6). Furthermore, the problem of poor light permeability was solved through a semiconductor suspension and increased the productivity of γ,γ -dichloroketone **2a** synthesis by a factor of 19.

Finally, the γ,γ -dichloroketones obtained by the photocatalytic generation and addition of dichloromethyl radicals to enones were used to install other reactive functional groups. As a practical example, dichloroketone **2a** was converted to β -formyl ketone **3a** by simple hydrolysis with 60% yield (Figure 4). The ketoaldehyde **3a** was then transformed into multi-substituted heterocycles (**4a-6a**) using microwave assisted condensations with a series of nucleophiles. For instance, furan and pyrrole scaffolds have been used in synthesis of bioactive substances.^[172]

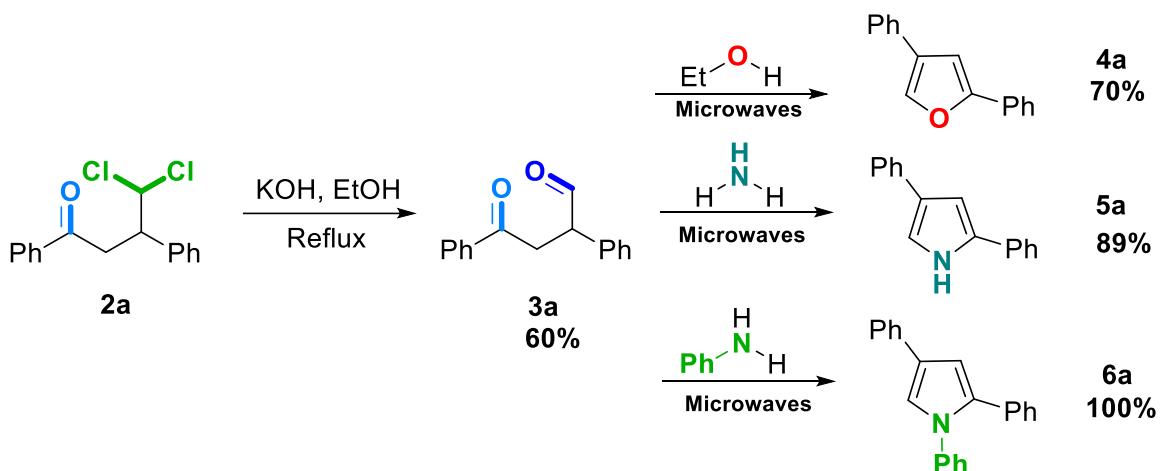


Figure 4. Preparation of different heterocyclic bioactive compounds from enones. Isolated yields are shown.

To support the role of chloroform as electron acceptor, a method for oxidative coupling of benzylamines was developed (Figure 5).^[173] As example, four imines with 83-100% yield were synthesized. These results offer an alternative route for such transformations using chloroform as a solvent and electron acceptor.

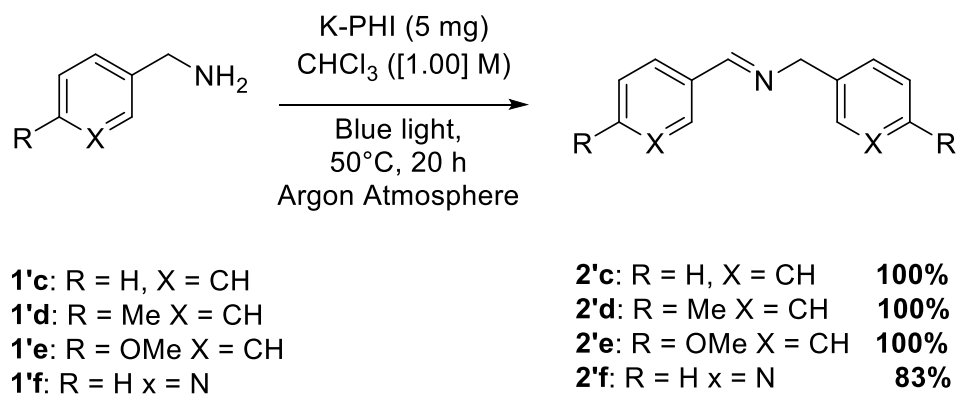


Figure 5. Oxidative coupling of benzylamines. GC-MS yields are shown.

The proposed mechanism of the reported photocatalytic reaction is shown in Figure 6a. In the first step, K-PHI is excited by blue photons giving excited state of the photocatalyst (K-PHI*). Removal of an electron from TEOA by K-PHI* (reductive quenching of the photocatalyst), leads to the formation of the long-lived radical anion K-PHI^{•-}, that has the typical deep green color.^[110, 114] Chloroform is subsequently oxidized by a single electron transfer event forming the chloroform radical anion that eliminates a chloride anion resulting in a dichloromethyl radical. Addition of the dichloromethyl radical to the β -carbon atom of the enone gives intermediate **i-1**. Abstraction of hydrogen from TEOA leads to the desired product **2**. While TEOA acts as hole scavenger, chloroform simultaneously acts as solvent and electron acceptor to complete the photocatalytic cycle, as it was already proposed by Chen et al.^[174] It is also possible to detect traces of different chlorinated compounds, that result from side radical reactions of the dichloromethyl radical, via GC-MS. By running experiments in the absence of the enone, the formation of halogenated compounds including hexachloroethane that is likely formed via a homocoupling of dichloromethyl radicals was observed (Figure 6b, Supplementary Table 4, Supplementary Figure 4, 5). However, investigating the mechanism of benzylamine coupling, no halogenated compounds have been detected, because of the different role of dichloromethyl radical, which acts as hydrogen abstractor, forming dichloromethane, undetectable via GC-MS (Figure 6c).

Conclusions

In this chapter, the library of small organic radicals available for photocatalytic synthesis was extended to dichloromethyl radicals that can be conveniently generated from chloroform. The method was validated in a 1,4 addition of dichloromethyl radicals to enones. The process is photocatalyzed by the heterogeneous, metal free carbon nitride photocatalyst K-PHI. Fifteen γ,γ -dichloroketones were isolated in moderate to excellent yield. The possibility to use other polyhalogenated compounds such as bromoform, iodoform, and 1,1,2,2-tetrachloroethane has been demonstrated. Light scattering by carbon nitride particles has been identified as limiting factor for scaling these transformations. The results suggest that, in a typical photocatalytic experiment using 2.5 mg mL^{-1} of semiconductor particles, the penetration depth of light is only 3 mm. In polar solvent, such as DMSO, nanoparticles of K-PHI give stable suspension that was pumped through a thin (1.6 mm internal diameter) tubing. γ,γ -dichloroketone **2a** has been also synthesized using quasi-homogeneous photoreactor. The γ,γ -dichloroketones obtained were proved to be useful building blocks with applications in the synthesis of bifunctional compounds that can be used for the preparation of heterocyclic bioactive compounds. The use of chloroform as solvent and electron acceptor was also demonstrated in the oxidative coupling of benzylamines.

3. Photocatalysis Goes Thinner Than a Hair: Carbon Nitride Thin Films as All-in-one Technology for Photocatalysis

Overview

Herein, an innovative approach is presented using carbon nitride thin films prepared via chemical vapor deposition (CVD) at different vessel walls and using them as batch and microfluidic photoreactors. These morphological changes are employed to maximize the performance of the materials in photocatalytic reactions, in which the carbon nitride thin films show at least one orders of magnitude higher activity per area unit compared to photocatalysis using suspended particles.



This chapter is an adapted version of the article:

S. Mazzanti, G. Manfredi, A.J. Barker, M. Antonietti, P. Giusto, A. Savateev, Photocatalysis Goes Thinner Than a Hair: Carbon Nitride Thin Films as All-in-one Technology for Photocatalysis, *ChemRxiv*, **2021**, Preprint. <https://doi.org/10.26434/chemrxiv.14198357.v1>

Results and discussion

A unique feature of heterogeneous photocatalysis is tuning properties of the employed material, which typically is a semiconductor by adjusting its morphology. In other words, semiconductor particles with essentially the same bulk chemical composition, but having, for example, variable diameter,^[175] aspect ratio between different facets of the single crystal,^[176] just to name a few,^[177] possess different photophysical properties and therefore demonstrate different activity.

Despite an outcome of a certain photocatalytic reaction mediated either by homogeneous or heterogeneous photocatalyst is the same, the underpinning mechanism is quite often different.^[178] In homogeneous organic photoredox catalysis represented, for example, by organic dyes, triplet excited states of the sensitizer with lifetime in μs -ms range are often engaged.^[10] While inorganic semiconductors do not possess triplet states, organic π -conjugated systems fall in between inorganic semiconductors, in terms of their heterogeneous nature and processability, and molecular sensitizers due to similarities of their local structures.

Semiconductor photocatalysis also offers multiple engineering solutions.^[179] For example, coating of the photoreactor wall with semiconductor particles is an appealing feature in combination with flow technology.^[180] In this regards, Wang et al. recently reported on a fixed-bed flow system employing CN supported on glass fibers and beads.^[153] However, backscattering from the surface limits accessibility of photons and reduces efficiency of the reactor.

For high throughput screening (HTS) in photocatalysis and flow technology, an ideal solution would be a thin transparent layer of semiconductor deposited at the inner wall of the photoreactor. Very recently, a method to obtain highly homogeneous CN thin films over areas of several dozens of cm^2 on different substrates was reported, regardless of their shape and surface topology by means of chemical vapor deposition (CVD).^[69, 181] The high

homogeneity and flatness allowed to apply these CN thin films in optics showing that they have a very high refractive index comparable to that of diamond in the visible range.

Seen the rich experimental data of using CN particles in photocatalysis, as well as unique opportunities offered by this class of materials in combination with the CVD, 4 mL glass vials have been coated, with the CN thin film.^[69, 181] In this way, visible batch wall reactors (Vis-BWR) were fabricated (Figure 1a). Deposition of the CN film on the reactor wall after the CVD is seen with naked eye by its typical yellowish color, photonic reflections, and the deep blue fluorescence when the Vis-BWR is exposed to UV light (Figure 1b).* The CN film strongly absorbs photons with wavelength ≤ 420 nm as confirmed by the UV-vis absorption spectrum (Figure S1a). In the steady-state photoluminescence spectrum, the maximum is observed at 470 nm (Figure S1b).

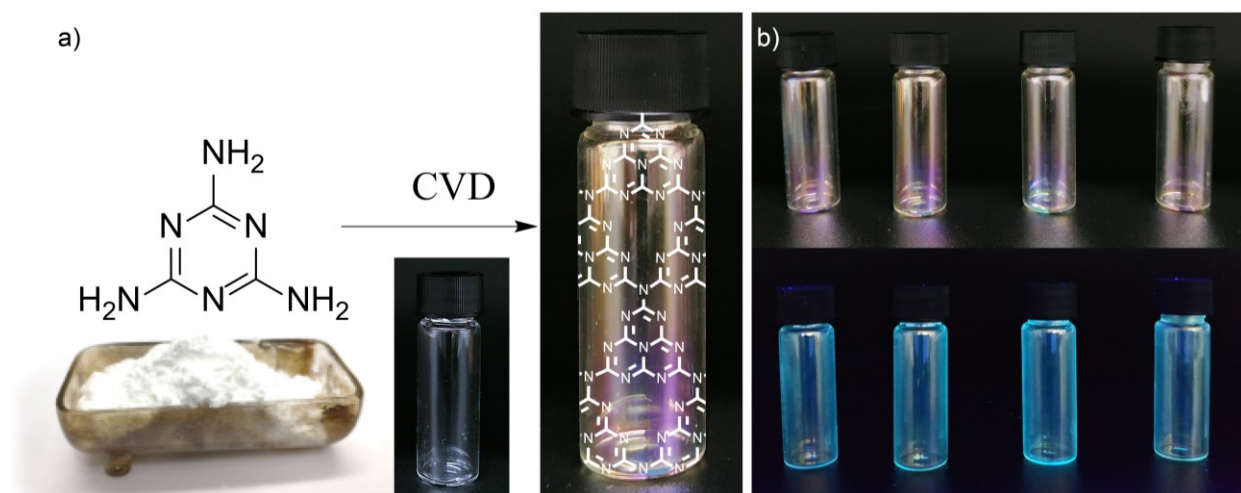


Figure 1. Fabrication of Vis-BWR and their appearance. a) Schematic representation of the CVD process of vial coating with CN, showing the ideal heptazinic structure. b) Vis-BWR under visible and 365 nm light.

* Despite CN film prepared by CVD has been characterized earlier, we consider it necessary to provide full characterization data as properties of the films may depend on the employed substrate.

A CN film with a thickness of about 170 nm was obtained as evidenced by atomic force microscopy (AFM) (Figure 2a). CN coating in the Vis-BWR is homogeneous and flat, while surface roughness is < 1 nm over the field of view $5 \times 5 \mu\text{m}^2$, as confirmed by AFM (Figure S2) and scanning electron microscopy (SEM, Figure 2b). Despite fluorescence quantum yield of the CN films is relatively low ($< 0.6\%$), emission can be observed even by naked eye. For further analysis, the CN film was completely removed from the selected area of the vial by mechanical treatment. By comparing the cleaned area of the vial with the untreated area after the CVD, the presence of the CN film on the glass surface was confirmed by energy-dispersive X-ray spectroscopy (EDX) mapping (Figure 2c-e).[†] At the nanoscale, the film reveals the presence of a layered structure, where each shade of grey represent a stack of graphitic layers (Figure 2f). Graphitic-like structure was further confirmed by X-ray diffraction, where the π - π stacking peak at 27.4° is identified (Figure S4). Based on interlayer distance of 0.33 nm and film thickness of 170 nm, the average number of layers in the CN film to be ca. 500 was estimate. Electron energy loss spectroscopy (EELS) reveals the presence of carbon (as a peak at 287 eV) and nitrogen (400 eV), which are integrated in strongly sp^2 -conjugated structure as confirmed by pronounced π^* peak (Figure 2g). The surface of the CN film is free of oxygen contaminations as concluded from the absence of a peak at ca. 532 eV (Figure 2g), which is in good agreement with previous results.^[181] The high quality of the deposition achieved on the vials provides a solid evidence to transform, in principle, every piece of lab glassware, such as vials, test tubes, or flasks into a Vis-BWR according to the reaction requirements.

[†] Signal of silicon (Figure 2e) and oxygen (Figure S3f) originate from the substrate and greatly enhanced at the area, where the film has been removed.

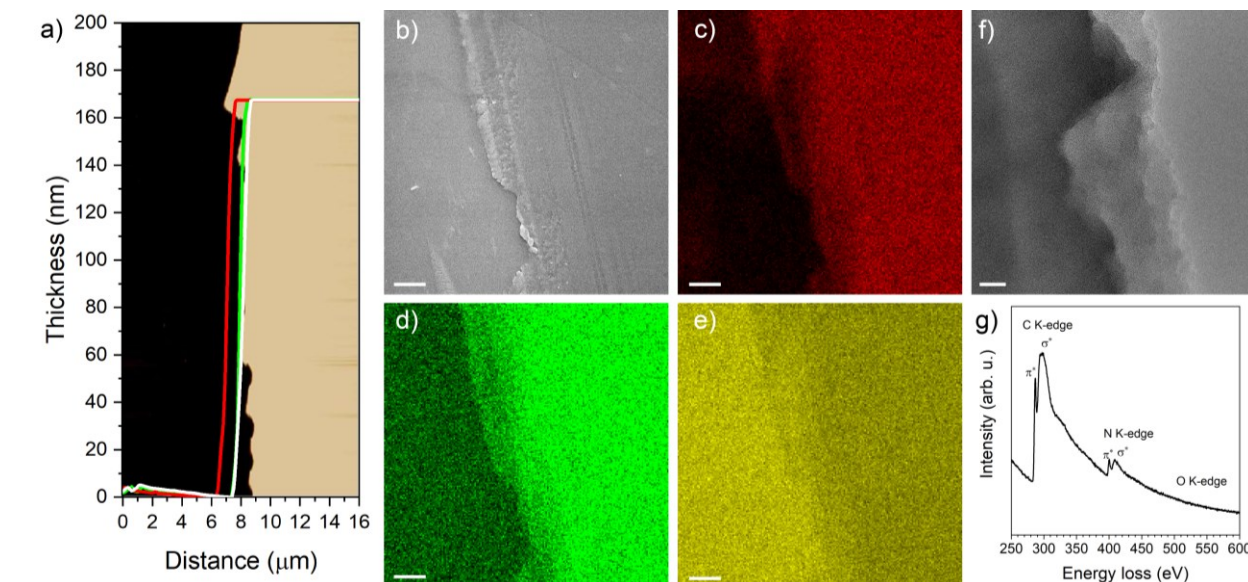
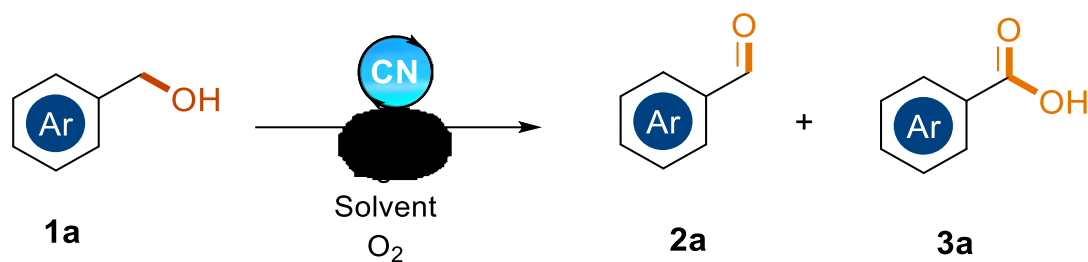


Figure 2. CN film characterization. a) AFM step-height analysis of the CN thin film deposited on the 4 ml vial (background is the original image obtained from the AFM, superimposed with the graph). b) SEM image of a scratched area of the coated vial; c-e) SEM-EDX mapping of carbon (in red), nitrogen (in green) and silicon (in yellow); scale bar 2 μm. f) TEM image of the CN thin film (scale bar 20 nm) and g) EELS core loss spectrum.

CVD allows growing CN thin films, while at the same time the technique does not alter substantially positions of HOMO and LUMO,^[181] which in combination with numerous earlier reports using suspended CN particulate enables us to consider such films as very promising candidates for using them as photocatalyst in net oxidative reactions under visible light. The oxidation of benzyl alcohols to benzoic acid was chosen as a benchmark reaction to compare performance of the CN thin films and Vis-BWRs with other photocatalysts and photocatalytic systems. Acetonitrile was selected as a solvent due to its polarity and high capacity towards dissolution of oxygen and high chemical stability against reactive oxygen species, such as superoxide radicals and singlet oxygen.^[182] Thorough optimization of reaction conditions is given in Table 1.



Entry	BA (mmol)	Solvent	Time (h)	Light	Yield 2a (%)	Yield 3a (%)
1	0.05	CH ₃ CN	20	365 nm	3	n.d.
2	0.05	CH ₃ CN	20	400 nm	10	n.d.
3	0.05	CH ₃ CN	20	White	-	n.d.
4	0.05	CH ₃ CN	20	525 nm	-	n.d.
5	0.025	CH ₃ CN	20	400 nm	14	n.d.
6	0.025	EtOH	20	400 nm	7	n.d.
7	0.025	<i>i</i> PrOH	20	400 nm	8	n.d.
8	0.025	H ₂ O	20	400 nm	7	n.d.
9 ^a	0.025	CH ₃ CN	20	400 nm	29	n.d.
10 ^{ab}	0.025	CH ₃ CN	20	400 nm	27	n.d.
11 ^{abc}	0.025	CH ₃ CN	20	400 nm	38	n.d.
12 ^{abc}	0.025	CH ₃ CN	20	400 nm x2	56	15
13 ^d	0.01	CH ₃ CN	24	400 nm x2	14	81 (87)
14 ^{d,e}	0.01	CH ₃ CN	24	400 nm x2	-	-
15 ^{d,f}	0.01	CH ₃ CN	24	No light	-	-

Table 1. Optimization of reaction conditions of benzyl alcohol (BA) oxidation. Yields have been estimated via GC-MS and in parenthesis via ¹H NMR with internal STD a) 2 cm distance from the LED b) Without stirring. c) Carbon nitride layer that was deposited in the CVD furnace on the outer surface of the vial was removed by sequential treatment with DMSO, followed by polishing with paper cloth and glass paper. d) reaction conditions as reported in the general procedure for benzyl alcohol oxidation e) reaction performed using a glass vial without CN coating. f) vial was wrapped in aluminum foil

Control experiments confirmed that the reaction is purely photocatalytic. Thus, no benzoic acid was obtained in the absence of the CN films excluding the thermal effects induced by heating originating from the light source as potential driving force (entry 14). Reaction did not proceed in dark either (entry 15). Under optimized conditions benzoic acid was obtained in 87% yield along with quantitative conversion of benzyl alcohol under illumination with 400 nm LED for 24 hours.[‡]^[183] Recently Hutchings et al. showed that benzyl alcohol acts as a quencher of the radical species in the thermal oxidation of benzaldehyde to benzoic acid even at very low concentrations, which explains formation of benzaldehyde in our case as well (entries 1-12).^[184]

After finding optimal reaction conditions, the scope of benzyl alcohols was expanded (Figure 3). The method provides a simple procedure for the preparation of substituted benzoic acids. Substrates bearing poorly electron donating or electron withdrawing group at the aromatic ring have been converted into the corresponding benzoic acids in good and high yields (**3a-g**). On the other hand, alcohols bearing strong electron donating groups were fully consumed, but the corresponding acids were obtained in poor or no yields (**3h-k**). Lower tolerance of the functional groups to reactive oxygen species is apparently responsible for lower selectivity in these cases.^[95]

As suggested by electron microscopy and AFM, CN films deposited at the glass surface are dense and non-porous (Figure 2). Therefore, the surface area of the sensitizer is defined by geometric area of the coating that is in contact with the reaction mixture in the photocatalytic experiments.

[‡] The reaction was conducted without stirring (Table 1 entry 9-10). Prolonged stirring actually causes damage of the Vis-BWRs coating (Figure S5)

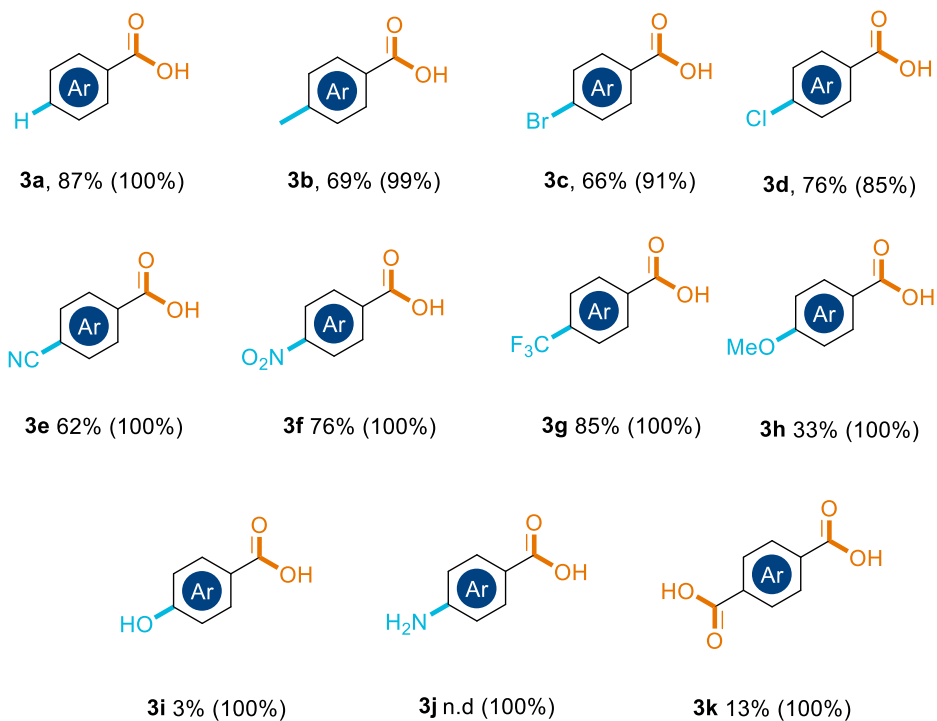
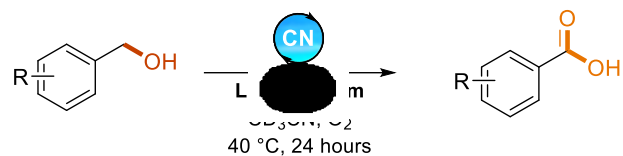


Figure 3. Scope of benzyl alcohols. Reaction conditions: alcohol (0.01 mmol), CD_3CN (3 mL), O_2 (1 bar), reaction was conducted in 4 mL Vis-BWR. See experimental procedure for details in ESI. Yields and conversions (in parentheses) have been determined using 1,3,5-trimethoxybenzene as internal standard by ^1H NMR.

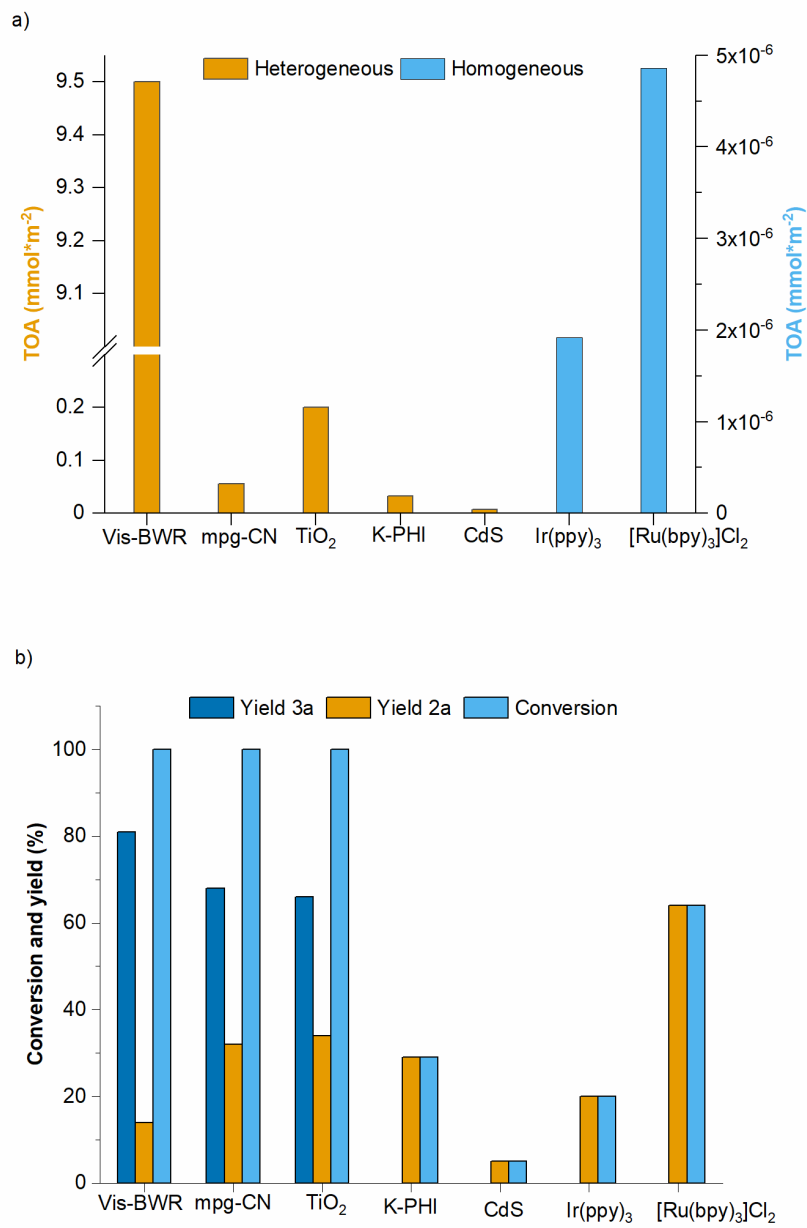


Figure 4. Catalyst screening. TOA and yields comparison. Reaction details as reported in Table S2

To evaluate the performance of the CN films and compare it with other photocatalysts, the number of benzyl alcohol molecules converted by a surface area unit was calculated and expressed in mmol m^{-2} for several standard photoredox catalysts under the same conditions (Table S2, Figure 4a). For the Vis-BWR reactor, such parameter is 9.5 mmol m^{-2} , for suspended photocatalyst particulate it is $\text{ca. } 10^{-2} \text{ mmol m}^{-2}$ and for common homogeneous Ir and Ru complexes is $\text{ca. } 10^{-6} \text{ mmol m}^{-2}$. Such difference point to substantially faster reaction kinetics in case of using the semiconductor thin film created under controlled conditions of the CVD. Furthermore, higher selectivity was achieved in case of Vis-BWR (Figure 4b). Explanation for such a remarkable enhancement of the activity is given below taking into account results of time-resolved spectroscopic characterization of the CN thin films. Conventional CVD method also allows fabricating several vials at once with high reproducibility, which makes the technology highly relevant to the needs of high-throughput photocatalysis (Figure 5a).^[185] In addition, Vis-BWR coated with CN thin film are stable and can be reused many times, here proven only for three catalytic cycles (Figure 5b). Immobilization of the CN films at glass surface simplifies work up procedure and more importantly eliminates the necessity of photocatalysts separation. These features prompted us to study the CN films in combination with flow technology. Microfluidic systems are a promising class of chemical reactors, which offer significant advantages as compared to batch reactors, such as larger scale production (seamless scalability), precise control over the residence time and local stoichiometry.^[186] Here, two mirror parts of a microfluidic reactor (channel diameter $250 \mu\text{m}$) were coated homogeneously with the CN thin films on the channel walls, to obtain a visible (microfluidic) flow wall reactor (Vis-FWR) (Figure 5c). The Vis-FWR was again tested in oxidation of benzyl alcohol under illumination with 400 nm . In this setting, the main product is benzaldehyde (Figure 5d).

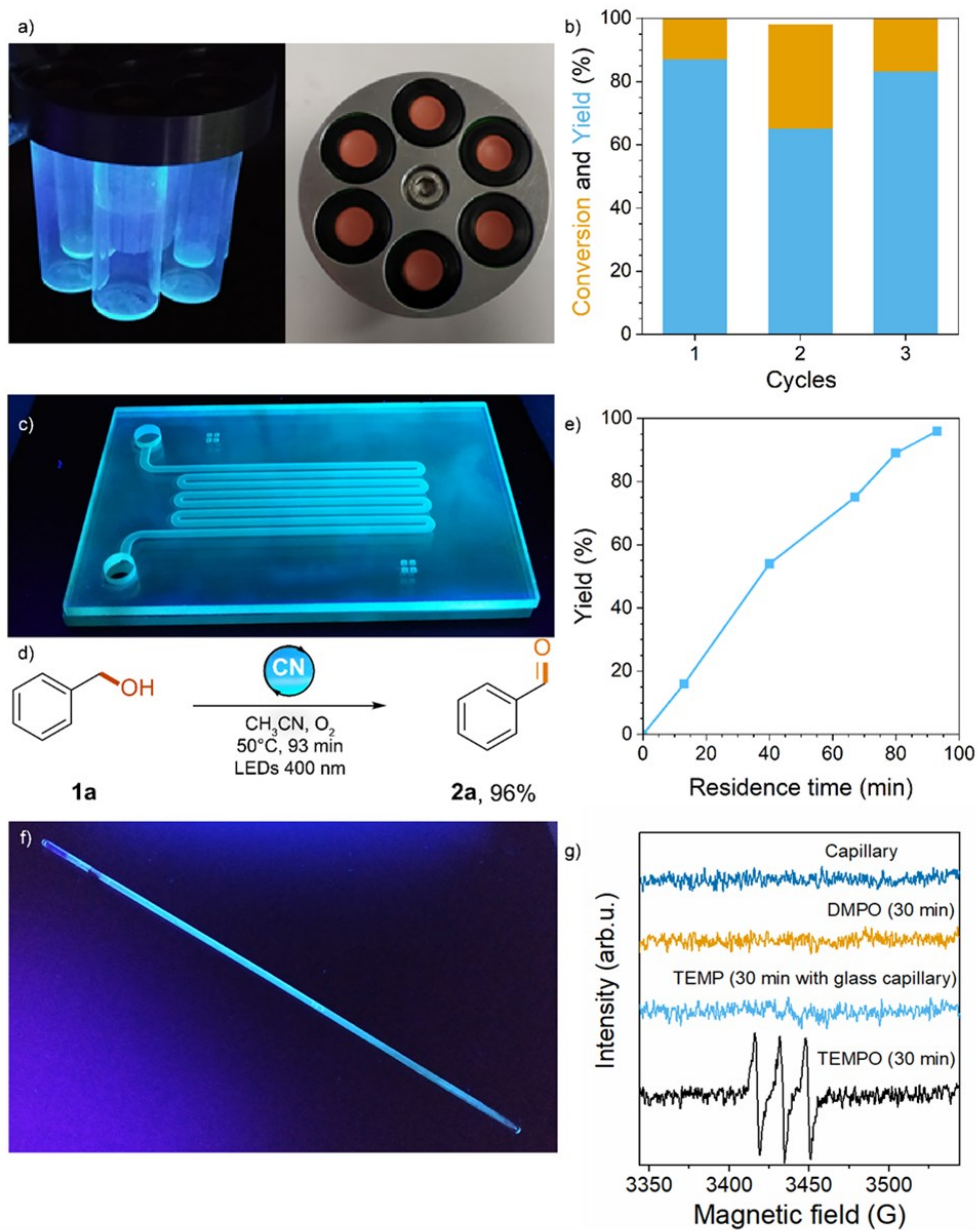


Figure 5. Application of the CN thin film in photocatalysis. a) Vis-BWR for high-throughput screening. b) Recyclability of Vis-BWR. c) Half cell of Vis-FWR coated with CN film under 365 nm light. d) Scheme of the reaction in flow. e) Yield optimization. f) Coated capillary. g) TEMPO generation and detection via in-situ EPR.

Therefore, depending on the reactor configuration, one can select which type of product to synthesize. The optimization of the reaction conditions led to linear dependence of the yield versus the residence time implying that the reaction follows zero-order kinetics with the respect of benzyl alcohol (Figure 5e). Apparently, the reaction depends on O₂ concentration, which may explain the formation of benzaldehyde as the main product. Applying recirculation of the reaction mixture, the yield of benzaldehyde reached 96% after 93 minutes (Figure 5d,e).

To gain insight into the nature of reactive oxygen species in the photocatalytic oxidation of benzyl alcohol and to propose a mechanism, it was applied in-situ EPR spectroscopy using a glass capillary coated with the CN film by CVD, in the same way as the Vis-BWR and Vis-BFR were produced (Figure 5f). The capillary was charged with the solution of 2,2,6,6-tetramethylpiperidine in O₂ saturated solution of MeCN followed by irradiation with 415 nm in the cavity of the EPR spectrometer. Appearance of TEMPO signal indicates that in this set of experiments, CN films sensitize singlet oxygen (¹O₂) (Figure 5g, see appendix for further details).

Eventually, time-resolved spectroscopy was used to gain insights into the changes of CN excited state dynamics, which result from the assembly of this material into thin films. Thus, photophysics of the excited state was investigated using time-correlated single photon counting (TC-SPC) time-resolved photoluminescence (tr-PL) and transient absorption spectroscopy (TAS). PL decay is well fitted ($R^2 > 0.99$) using a single stretched exponential function with a time exponent of $\frac{1}{2}$ and a lifetime of ~ 0.6 ns (Figure S7, Table S3). Such behavior is common for polymer systems that present defects and traps, in good agreement with the recorded relatively low internal quantum efficiency (IQE) of 0.6% (Figure S1b).^[187] According to the TAS data acquired under N₂ (Figure S8), excitation of the CN film leads to the appearance of a broad band in the observed wavelength range (500–750) nm ascribed

to excited states absorption (ESA).[§] Such behavior of the CN thin films is significantly different from the dispersion of CN in liquid phase reported earlier.^{[129],[106]} Therein, a negative photoinduced ΔOD signal in the visible range was attributed to ground state bleaching (GSB) of the CN, whereas a positive ΔOD signal from the CN thin films can be observed indicating a transient photoinduced absorption.^[129] Therefore, in case of the CN film, the net signal composed of the CN GSB and ESA is positive.

Analysis of the ESA decay in the femto-to micro-second time scale suggests that the process is characterized by two lifetimes (Figure S9). The faster process is described by the same parameters ($\beta = 1/2$, $\tau = 0.6$ ns) as tr-PL, which suggest that the singlet excited states (S_1) of the CN possess broad absorption in the visible range (Table S4). It is assumed that the depopulation of S_1 in the CN film proceeds via three pathways: i) radiative relaxation, ii) singlet-triplet ISC, and iii) non-radiative recombination. Taking into account extremely low fluorescence quantum yield, <0.6% (Figure S1b), the first pathway is not dominant. The second, slower process, of the CN ground state recovery corresponds to the depopulation of the triplet excited states (T_1) in the CN film. Furthermore, a channel by which T_1 is converted back into S_1 , such a triplet-triplet annihilation (TTA, which would exhibit a density-dependent rate) explains the intensity dependence of TA recombination rate in nano- to micro-second time scale (Figure S10) and the longer time constants obtained, when the CN film was in degassed acetonitrile (Table S5).^[126] TTA also contributes to the tail of long-lived emission seen in tr-PL, although the significant stretching rates of both PL and TA kinetics is likely due more to disorder in the excitonic landscape of CN materials.^[188] Absence of noticeable peak shift in the TAS indicate vanishingly small singlet-triplet energy gap, which might be the additional pathway of S_1 - T_1 interconversion.

[§] Changes in absorbance maximum from one sample to the other can be attributed to changes in the grating position whose efficiency greatly drops near the edges of the studied wavelength intervals.

Overall, different photophysics of the CN thin films, compared to the reported earlier, obviously stems from different synthesis conditions – polycondensation of the precursor in bulk at atmospheric pressure (used earlier)^[129] and polycondensation-deposition of carbon nitride in thin layers from vacuum under the controlled conditions in the CVD system (gas-to-solid reaction in this work). Apart from being indispensable to create durable technological devices, CVD also produces the CN material with narrow ΔE_{ST} , which facilitates singlet-triplet ISC. Until now, CN materials prepared by condensation of the precursors in bulk have been reported to have ΔE_{ST} of 0.156-0.248 eV.^[106] Furthermore, absence of voids in the structure of the CN thin film is also beneficial to suppress non-radiative recombination of triplet excited states (vibrational relaxation) by decreasing free volume in the crystal lattice.^[189] These differences strongly point that a strict control over reaction conditions defining how the nanostructure of the sensitizer influences the material photophysical properties to achieve high activity in photocatalytic reactions that involve EnT.

The results of spectroscopic study were combined with experimental data and propose the following mechanism of benzyl alcohols oxidation by the CN thin films (Figure 6a). Absorption of light by the CN thin film leads to the formation of the CN singlet excited states (S_1). Part of the singlet excited states undergo ISC to form triplet excited states (T_1) characterized by lifetime, which are long enough to interact with O_2 via EnT mechanism. Indeed, tr-PL data acquired for the CN thin films in oxygenated and degassed CH_3CN , clearly indicate that singlet excited states are not quenched by oxygen – S_1 life time is ca. 0.6 ns regardless of the environment (Table S3). On the other hand, TAS data indicate that O_2 does quenches triplet excited states as their lifetime decreases from 238 ns to 158 ns (Table S4). Once formed, 1O_2 reacts with benzyl alcohol producing benzaldehyde and presumably H_2O_2 .^[190] Then, benzaldehyde is converted to benzoic acid either via thermal or photocatalytic pathway (Figure 6b).

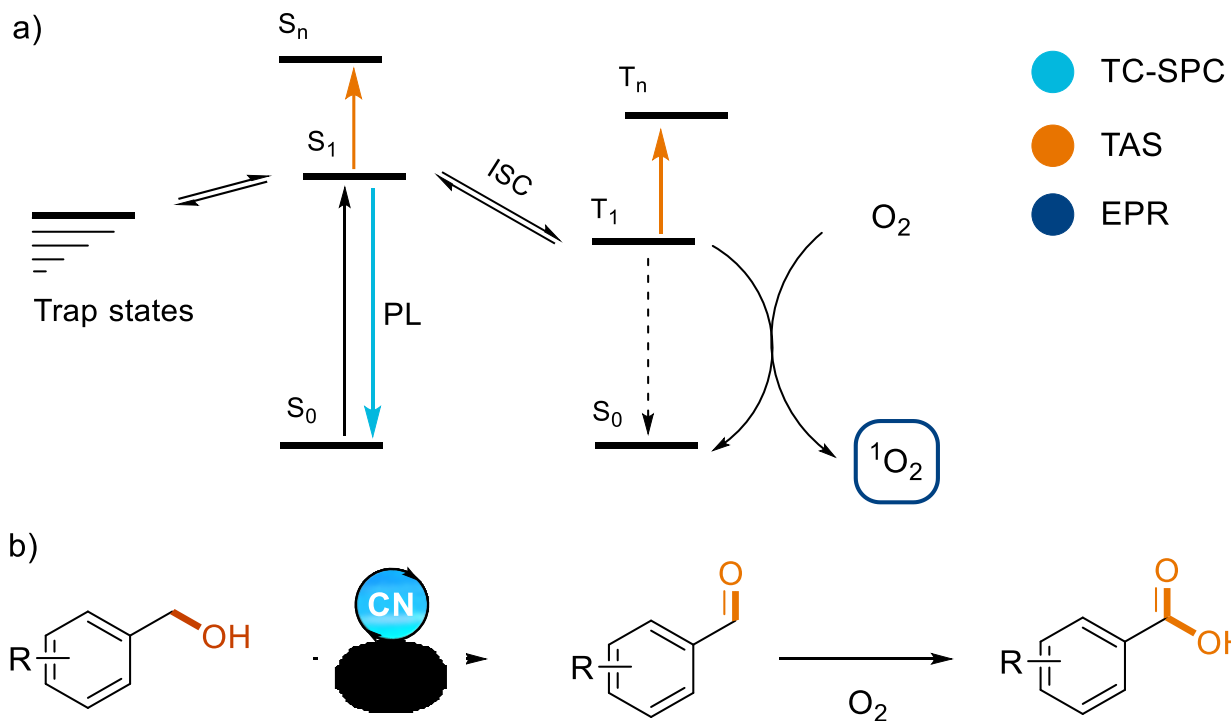


Figure 6. Mechanism of benzyl alcohol oxidation using thin CN films. a) Proposed photophysical mechanism. b) Photocatalytic mechanism of benzyl alcohol oxidation to benzaldehyde and subsequent thermal oxidation to benzoic acid.

Hence, the developed technology not only makes the Vis-BWR a convenient choice to conduct a photocatalytic reaction, it is also more efficient compared to the analogous dispersion of photocatalyst in liquid medium.

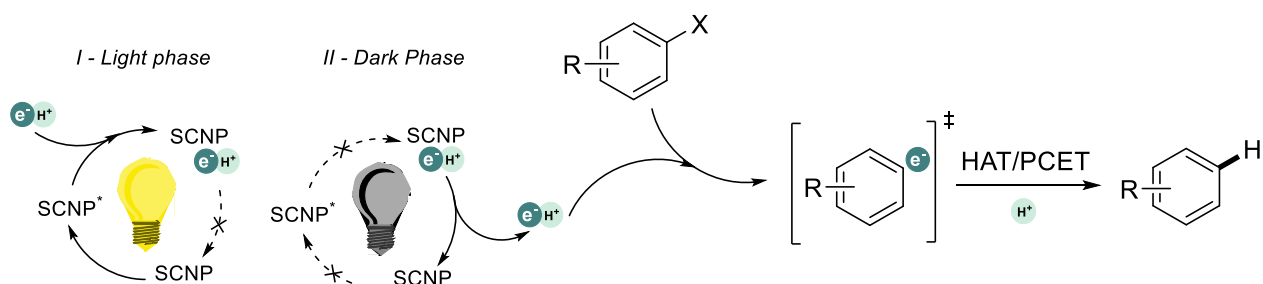
Conclusions

In this chapter, an innovative approach is presented in visible photocatalysis exploiting CN thin films. A common lab vial was coated employing CVD becoming a reusable reactor itself. The as-coated vials were exploited as photoreactors in the one-step oxidation of ten alcohols, in which corresponding benzoic acids have been obtained with up to 87% yield in 24 hours. Based on EPR, time resolved emission and absorption spectroscopy, oxidation of benzyl alcohols mediated by the CN thin films involves singlet oxygen, which is sensitized via energy transfer from triplet excited states. Furthermore, this technology was applied also to microfluidic systems by coating the two mirror parts of a microfluidic flow reactor. The latter was successfully tested for the oxidation of benzyl alcohol leading to benzaldehyde with the yield linearly increasing up to 96% in ca. 90 minutes. It is believed that the technology developed herein is a significant step forward for the improvement of photocatalysis both at a research and industrial level. Indeed, the utilization of thin film technology allows to truly implement photocatalysis in automated labs, such as HTS, as no time-demanding post-separation steps of the heterogeneous photocatalysts are required, such as filtration or centrifugation. Furthermore, typical problems occurring also in microfluidic flow reactors with heterogeneous photocatalyst can be overcome, such as fouling and clogging of the reactor and/or pumping system. Exploiting CN thin films would also allow to make more complicated tandem or cascade reaction setups by combining different flow reactors, or graft-from the surface desired functional species in a desired position, such as small molecules, polymers, and eventually enzymes. Beyond that, the presented technology can be exploited not only for photocatalysis, but furthermore in electro- and thermo- catalysis, or any of their combination. Eventually, the presented technology will pave the way for new, safer, more sustainable, and thereby exciting chemistry combining the advantages of thin films and (photo-)catalysis, whereby limits are dictated by scientists imagination.

4. Multisite Proton Coupled Electron Transfer with Long-lived Radicals of Poly(Heptazine Imide)s for Uphill Organic Synthesis

Overview

A combination of photochemistry and proton coupled electron transfer (PCET) is a primary strategy employed by the biological objects and synthetic chemistry to enable uphill reactions under mild conditions. Degenerate nanometer-sized n-type semiconductor nanoparticles (SCNPs) with the Fermi level above the bottom of the conduction band are strongly reducing and act more like metals than semiconductors. Application of the degenerate SCNPs is limited to few examples. Herein, K-PHI microporous are loaded with electrons (e^-) and charge balancing protons (H^+) in light phase using sacrificial agents. e^-/H^+ in the degenerate K-PHI nanoparticles are weakly bound and therefore used in a range of PCET reactions in dark, such as generation of aryl radicals from aryl halides.



This chapter is an adapted version of the article (*manuscript in preparation*):

S. Mazzanti, C. Schritt, M. Antonietti, A. Savateev, Multisite Proton Coupled Electron Transfer with Long-lived Radicals of Poly(Heptazine Imide)s for Uphill Organic Synthesis

Results and discussion

Photochemistry and proton coupled electron transfer (PCET) – combination of these two approaches is the only efficient strategy to enable uphill reactions under mild conditions, employed both in natural photosynthesis and photocatalysis.^{[191],[192]} Indeed, electronic energy is insensitive to temperature change as inferred from Boltzmann constant, $8.5 \cdot 10^{-5} \text{ eV K}^{-1}$, while PCET reactions are characterized by lower activation energy compared to stepwise electron transfer (ET)/proton transfer (PT) as it avoids formation of high-energy intermediates.^{[193],[194],[195]}

It has been known as early as 1980th that n- and p-type semiconductor nanoparticles (SCNPs) are able to accumulate either electrons or holes.^{[196],[197],[132, 133]} The process of SCNPs ‘charging’ is triggered by irradiation with light in the presence of sacrificial agents, while the stored charges can then be employed under dark conditions for either reduction or oxidation of the substrates.^{[133],[198]} In the context of this work, hereafter the discussion is narrowed to n-type SCNPs with excess of electrons in the CB. This concept has already been explained in the introduction, as IDEASE and it is intriguing since it offers a way to decouple light and dark phases in photocatalysis, mimic natural photosynthesis, and potentially explore unknown pathways in organic synthesis (Figure 1a).^{[199],[200]} A remarkable feature of such charged (degenerate or heavily doped) SCNPs, is higher reduction power due to shift ($E_F - E_C$) of the Fermi level above the bottom of the CB (Figure 1c),^[201] which makes them more similar to metals than semiconductors. The shift could be as high as -1 eV , for example, for CdS nanoparticles with the diameter of 1.5 nm, but it vanishes quickly as the diameter of the SCNP exceeds 5-10 nm.^[202]

In the degenerate nanoparticles of inorganic semiconductors, such as TiO_2 , negative charge caused by the excess of electrons in the CB is compensated by protons (H^+), which are stored in the double layer and can be used collectively in reductive PCET.^[203] Up to date at least a dozen of articles use electrons stored in the SCNPs, without addressing explicitly the role of

protons, which obviously contribute to the reactivity in dark. It is not surprising that many reactions employing degenerate SCNPs in dark also deal with transfer of H^+ – hydrogen evolution reaction,^{[204],[205]} reduction of O_2 to H_2O_2 ^{[121],[206]} and others.^{[207],[87],[199]} From the first chapter it has been shown that degenerate SCNPs are integrated into the photoredox cycle under continuous light irradiation, namely K-PHI longed-lived radicals, to facilitate the generation of dichloromethyl moieties.^{[139],[208]} Furthermore, it has been reported in literature that K-PHI can also mediate reduction of α,β -unsaturated ketones to ketyl radicals (via transfer of e^-/H^+)^[110] and enable condensation of α,β -unsaturated ketones with tetrahydroisoquinolines.^[109]

Higher activity of the degenerate nanoparticles of K-PHI and related organic semiconductors in PCET reactions in dark obviously stem from a combination of the properties: i) conjugated negatively charged microporous structure (Figure 1b), with the pore diameter of ca. 0.8 nm that hosts both e^- and H^+ ;^{[106],[209]} ii) highly positive potential of the VB (+2.2 V vs. NHE)^[114] facilitates fast ($k \sim 10^5$ - $10^{12} s^{-1}$)^{[104],[210]} quenching of holes. Higher degree of K-PHI doping with electrons, up to $0.5e^-/0.5H^+$ per unit cell,^[111] can be achieved even for particles with the diameter >100 nm, which is only possible when e^-/H^+ are stored in the micropores.

Plentiful reports of using K-PHI nanoparticles in net-reductive reactions and their high capacity in charge storage has led to investigate degenerate K-PHI nanoparticles as multisite (MS) PCET reductants in dark. In MS-PCET approach, electrons are stored in the π -conjugated structure of K-PHI, while H^+ are located either on the surface or in the micropores. Therefore, e^-/H^+ are transferred to the substrate from different sites, which is different compared to conventional hydrogen atom transfer (HAT) catalysts.^{[211],[212],[213]}

Aryl halides are synthetically useful precursors of aryl radicals in photoredox catalysis.^{[214],[215]} Aryl radicals can be obtained from the corresponding arylhalides upon photolysis.^{[216],[217]} One-electron reduction of arylhalides to aryl radicals occurs at potential of -1 to -2 V vs SCE,^[218] which makes ET in this case ca. +23 to +46 kcal mol⁻¹ endergonic,

and can be accomplished employing strongly reducing photoredox catalysts.^{[219],[220]} Alternatively, MS-PCET, in which e^- is transferred to the aryl moiety, while H^+ is added to Br^- , is $-5.2 \text{ kcal mol}^{-1}$ exergonic (Figure 1d, see appendix for thermochemical calculations).^{[221],[222]}

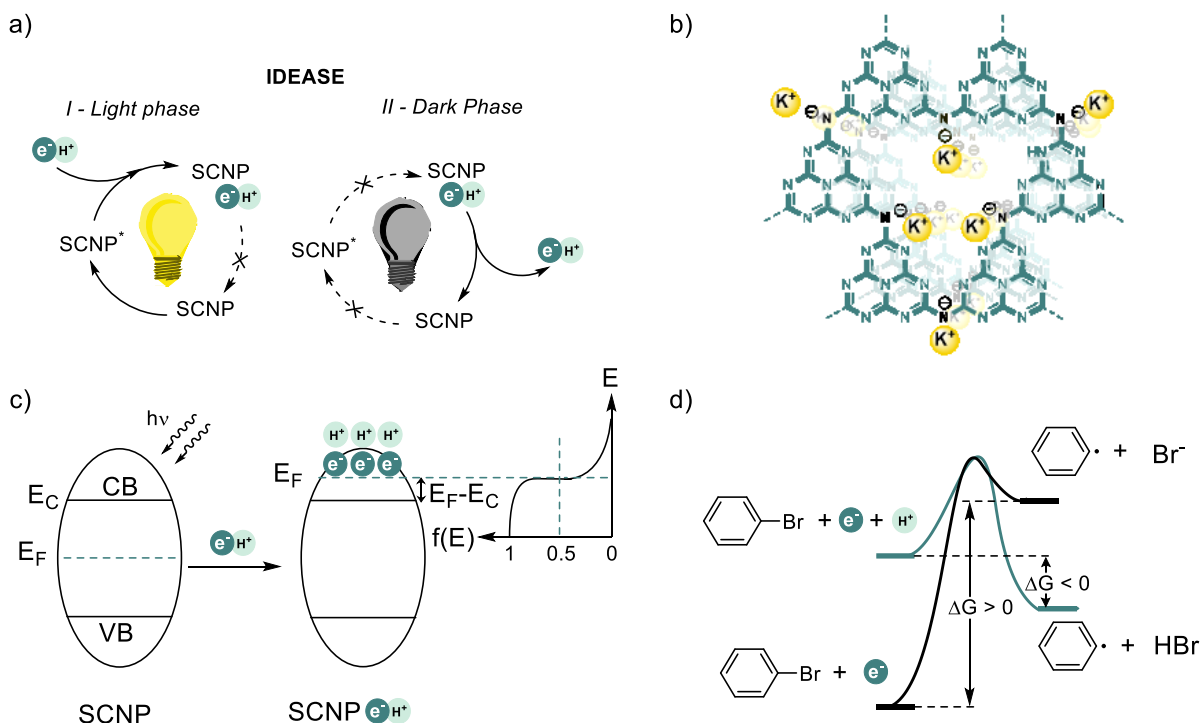
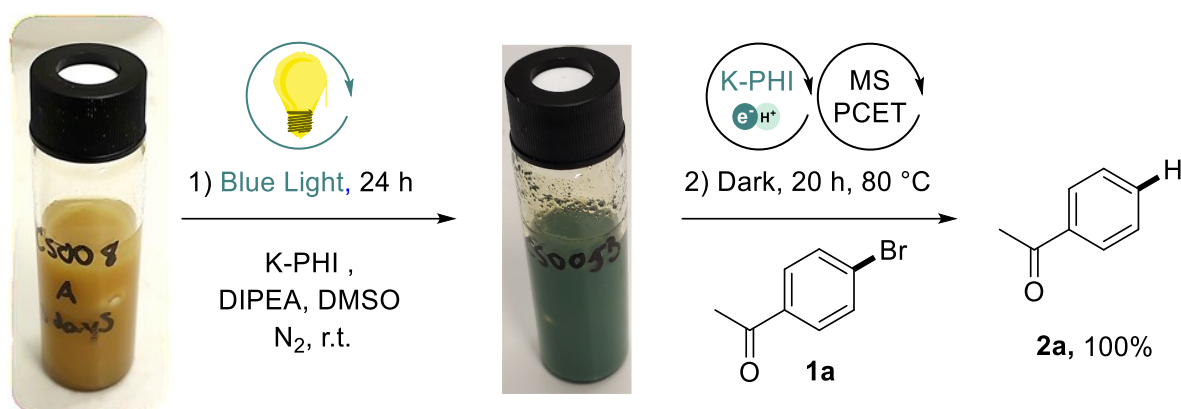


Figure 1. Background and concept of this work. a) Decoupling of light and dark phases in photocatalysis through IDEASE. b) Structure of K-PHI. c) Irradiation of the SCNP in the presence of e^-/H^+ donors triggers accumulation of electrons in the CB and H^+ at the surface of the SCNP. d) Generation of aryl radicals via ET and MS-PCET.

In this chapter, a two-step method is reported to generate aryl radicals from the corresponding arylhalides. In the first step, K-PHI is loaded with e^-/H^+ under light irradiation in the presence of the sacrificial donor. In the second step, arylhalide is reduced via MS-PCET by e^-/H^+ stored in K-PHI nanoparticles in dark. Thermochemical calculations suggest that e^-/H^+ in K-PHI are weakly bound, which makes them useful for reduction of classes of organic

compounds, such as generation of ketyl radicals and even $6e^-/6H^+$ reduction of nitrocompounds to anilines in dark.

For reduction of arylhalides via MS-PCET, a two-step procedure was developed: 1) irradiation of the reaction mixture with blue light for time τ_1 at temperature $T_1^\circ\text{C}$ in the presence of sacrificial agent to load K-PHI with e^-/H^+ ; 2) addition of aryl halide to K-PHI(e^-/H^+) and maintaining the reaction mixture in dark for time τ_2 at temperature $T_2^\circ\text{C}$. While a complete data set of reaction conditions optimization is given in the Table S1-S8, Table 1 highlights the most important findings.



Entry	1a (mmol)	Semiconductor	Amine	Solvent	τ_1 (h)	τ_2 (h)	T_1 ($^\circ\text{C}$)	T_2 ($^\circ\text{C}$)	Yield (%)
1 ^a	0.025	K-PHI (20 mg)	TEA (350 μL)	DMSO (1 mL)	25	20	RT	50	6
2 ^a	0.025	K-PHI (40 mg)	TEA (350 μL)	DMSO (1 mL)	25	20	RT	50	15
3 ^a	0.025	K-PHI (80 mg)	TEA (350 μL)	DMSO (1 mL)	25	20	RT	50	22
4 ^a	0.025	K-PHI (20 mg)	TEA (350 μL)	DMSO (1 mL)	16	5	RT	80	14
5 ^b	0.025	K-PHI (20 mg)	DIPEA (140 μL)	DMSO (1 mL)	22	19	RT	80	67
6 ^b	0.025	K-PHI (80 mg)	DIPEA (140 μL)	DMSO (1 mL)	22	19	RT	80	31
7 ^b	0.025	K-PHI (80 mg)	DIPEA (140 μL)	DMSO (3 mL)	22	20	RT	80	71
8 ^b	0.05	K-PHI (80 mg)	DIPEA (560 μL)	DMSO (3 mL)	24	20	RT	80	100
9 ^b	0.05	K-PHI (80 mg)	DIPEA (560 μL)	DMSO (3 mL)	24	20	RT	RT	7

10 ^c	0.05	K-PHI (80 mg)	DIPEA (560 μ L)	DMSO (3 mL)	24	20	RT	80	traces
11 ^b	0.05	None	DIPEA (560 μ L)	DMSO (3 mL)	24	20	RT	80	traces
12 ^b	0.05	Na-PHI (80 mg)	DIPEA (560 μ L)	DMSO (3 mL)	24	20	RT	80	61
13 ^b	0.05	mpg-CN (80 mg)	DIPEA (560 μ L)	DMSO (3 mL)	24	20	RT	80	12
14 ^b	0.05	TiO ₂ (80 mg)	DIPEA (560 μ L)	DMSO (3 mL)	24	20	RT	80	Traces
15 ^{b,c}	0.05	K-PHI (80 mg)	DIPEA (560 μ L)	DMSO (3 mL)	24	/	RT	/	100
16 ^{b,d}	0.05	K-PHI (80 mg)	DIPEA (560 μ L)	DMSO (3 mL)	24	20	RT	80	49

Table 1. Optimization of reaction conditions. a) Blue light (5 cm distance, 49 mW \cdot cm⁻²). b) Blue light (1 cm distance, 470 mW \cdot cm⁻². c) Vial wrapped in aluminum foil (no light).) Reaction performed in one step (only light). d) Reaction performed using recycled K-PHI

The screening of the reaction conditions started with triethylamine (TEA) as a sacrificial e⁻/H⁺ donor and DMSO as solvent. 4-bromoacetophenone (**1a**) was selected as the model aryl halide to be added in step 2. Time of the light phase was chosen to be 25 h and temperature T₁ = 25°C, while the parameters of the dark phase were τ_2 = 20 h and T₂ = 50°C. Thus, acetophenone **2a** was obtained with 6% yield (Table 1, entry 1). By increasing the amount of K-PHI the yield reached 22% (entry 2-3). It was found that crucial parameter to accelerate the reaction was raising the temperature in the dark phase to T₂ = 80°C (entry 4). Screening the amount and type of amine (Table S2), led to DIPEA as the optimum sacrificial electron donor (Table 1, entry 5). Taking into account high extinction coefficient of carbon nitrides, >10⁵ cm⁻⁵,^[71] further improvement in the yield of **2a** was achieved by decreasing optic density of the solution and increasing light intensity (Table 1, entry 7). After further screening of DIPEA amount and duration of τ_1 and τ_2 (Table S5-S6), 100% yield of **2a** was achieved (Table 1, entry 8). Control experiments confirmed that photocharging of K-PHI proceeds only upon irradiation with light (Table 1, entry 10-11). Under optimized conditions, ionic carbon nitride, such as Na-PHI, gave **2a** in 61% yield, while mesoporous

graphitic carbon nitride (mpg-CN) gave **2a** in 12% yield (entry 12-13), which underlines essential role of negatively charged framework and microporous structure of ionic carbon nitrides in storage of protons (Figure 2).^{[106],[223]} **

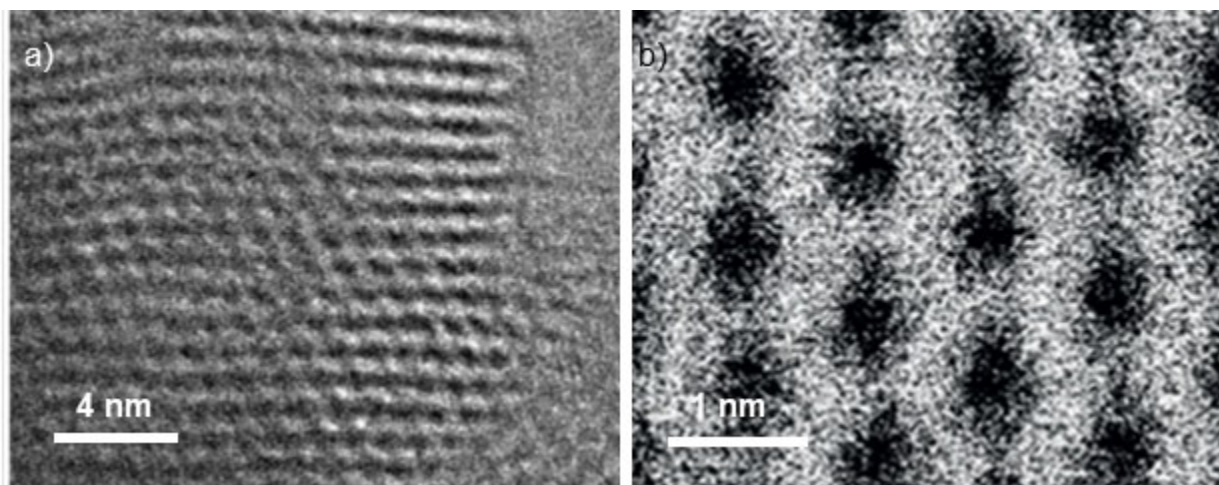


Figure 2. AC-HRTEM images of K-PHI microporous structure. Reproduced with permission from [106, 139]

TiO₂ did not give **2a** either (entry 14), which is explained by low amount of (e⁻/H⁺) stored in this material as surface area nor morphology have been optimized. The color of K-PHI(e⁻/H⁺) dispersion depends on the used solvent and is the most pronounced in case of using DMSO (Figure S3a). Remarkably, K-PHI(e⁻/H⁺) is able to reduce **1a** even after storage of 7 days under O₂ free conditions (Table S9, entry 1-3).^{††[224]}

** Being a protic solvent, little amount of water slightly promotes reduction of **1a** to **2a**, which is in agreement with MS-PCET mechanism (Table S8, entry 7-9).

†† Slightly decreased yield of **2a**, 51%, is explained by partial oxygen leakage inside the vial and quenching electrons stored in K-PHI (Figure S3b).

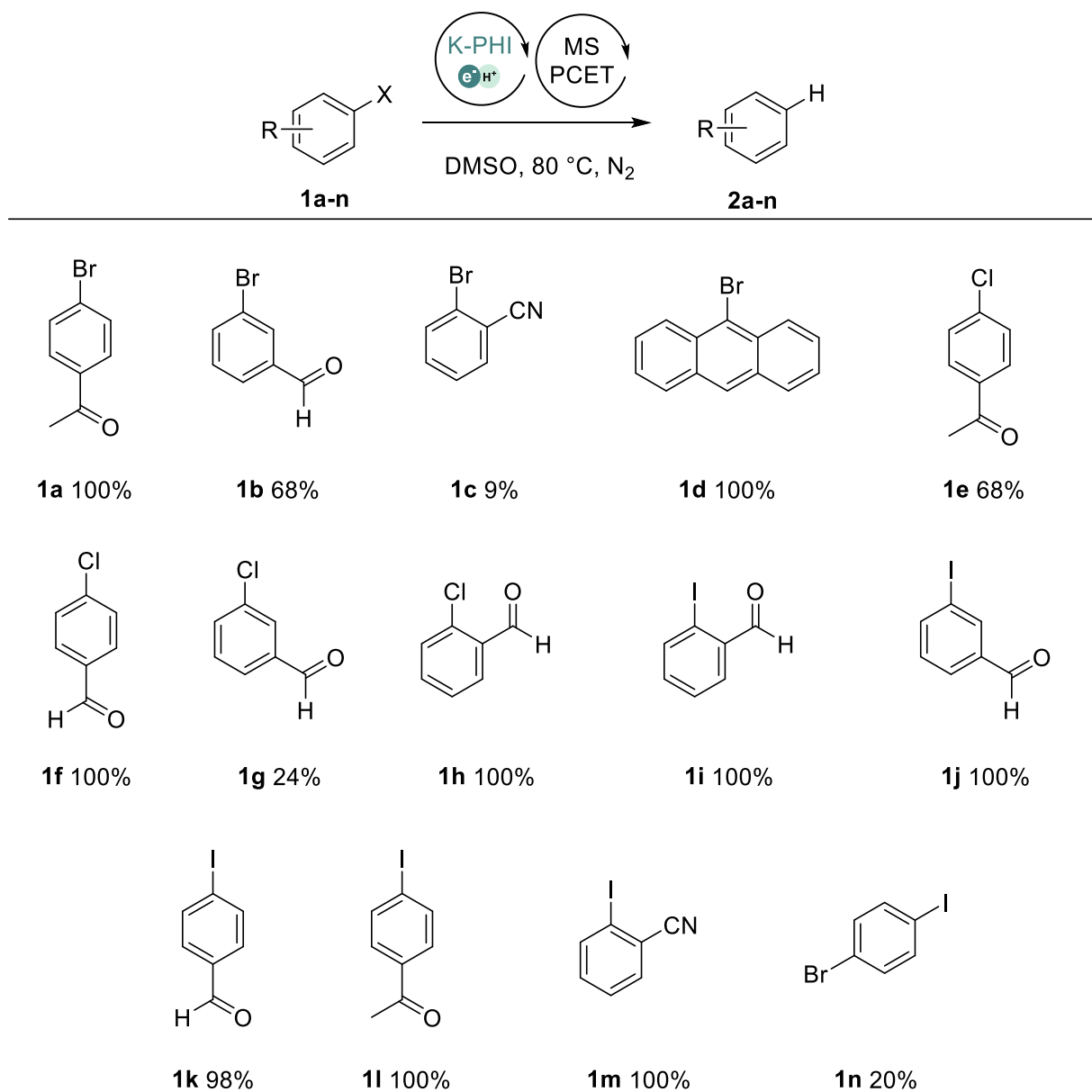


Figure 3. Scope of aryl halides in MS-PCET using K-PHI(e^-/h^+). Conditions: 1) 80 mg K-PHI, 3 mL DMSO, Blue light ($490 \text{ mW}\cdot\text{cm}^{-2}$), 24 hours (τ_1), RT (T_1); 2) 0.05 mmol aryl halide (**1a-n**) in 1 mL of DMSO, 20 hours (τ_2), 80 °C (T_2). See standard procedure in the appendix for further details. Yields determined by GC-MS.

In the second run, recovered K-PHI nanoparticles gave **2a** in 49% yield, implying that the material is stable and does not degrade (Table 1, entry 16).

Optimized conditions were applied to generate aryl radicals from other aryl halides. Fourteen substrates were converted into the corresponding aromatics in 9-100% yield (Figure 3).

In general, aryl iodides gave the corresponding hydrocarbons in higher yields compared to aryl bromides and aryl chlorides due to weaker C–I bond (**1i-1m**). Aryl chlorides (**1e-1h**), which are considered to be less reactive substrates,^[225] due to stronger C–Cl bond, were reduced as well.

Higher yields in case of *ortho*- **1h** and *para*-substituted **1e-f** arylchlorides, compared to the *meta*-substituted one **1g**, is explained by resonance stabilization of the intermediary radical by the electron withdrawing group. On the other hand, *para*-bromobenzonitrile **1o** (Figure S4), which has reduction potential similar to **1a** (Table S10), did not give the product, while the reduction product of *ortho*-bromobenzonitrile **1c** with yield of 9% was obtained. Other aryl halide tested did not react as expected, whose explanation remain elusive (Figure 4 **1o-1s**). Substrate bearing EDG group also did not react according to higher reduction potential (Figure 4, **1t**).

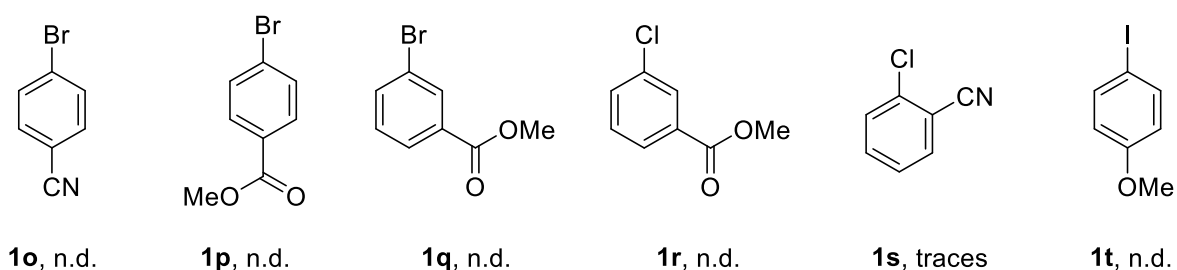


Figure 4. Structure of aryl halides that did not react under the standard conditions. n.d. – the product of arylhalide reduction was not detected in the GC-MS chromatograms.

The mechanism of the two-step generation of aryl radicals is shown in Figure 5. Excitation of K-PHI leads to the formation of K-PHI* excited state with electron and hole located in CB and VB. Reduction of K-PHI* by DIPEA leads to the formation of the degenerate K-PHI (e^-/H^+). Taking into account highly positive VB potential of K-PHI (+2.2 V vs NHE) and earlier reports on reductive MS-PCET using tertiary amines, such as $(n\text{Bu})_3\text{N}$,^[226] charging of the SCNP proceeds via stepwise $1e^-$ oxidation of DIPEA followed by abstraction of H^+ from α -carbon atom of the $[\text{DIPEA}]^{+\cdot}$ and transfer to K-PHI.

In the dark cycle, transfer of H^+ to halide (X) and e^- to aryl moiety leads to the formation of HX, which is trapped by excess of DIPEA and the aryl radical. Given that $\text{BDFE}[\text{C-H}]$, for example, in benzene is $104.4 \text{ kcal mol}^{-1}$,^[222] once formed aryl radical abstracts e^-/H^+ (or H^\bullet) either from charged K-PHI(e^-/H^+) or other components of the reaction medium.

Thermochemical calculations suggest that e^-/H^+ are bound to K-PHI only weakly – $\text{BDFE}[\text{K-PHI}(e^-/H^+)]$ is $< 5.2 \text{ kcal mol}^{-1}$ (see thermochemical calculations in the appendix). Such BDFE value is much lower than that in ketyl radicals (ca. $26\text{-}30 \text{ kcal mol}^{-1}$).^{[227],[192]} It is also lower than BDFE in superoxide radical ($42.7 \text{ kcal mol}^{-1}$)^[228] or H_2O_2 ($79.6 \text{ kcal mol}^{-1}$),^[228] which are the intermediates of O_2 reduction to H_2O_2 . Therefore, charged K-PHI(e^-/H^+) nanoparticles are very strong reductants. Indeed, such conclusions agree with earlier reports of using charged K-PHI(e^-/H^+) or related materials in reduction of O_2 to H_2O_2 in dark.^{[121],[206]}

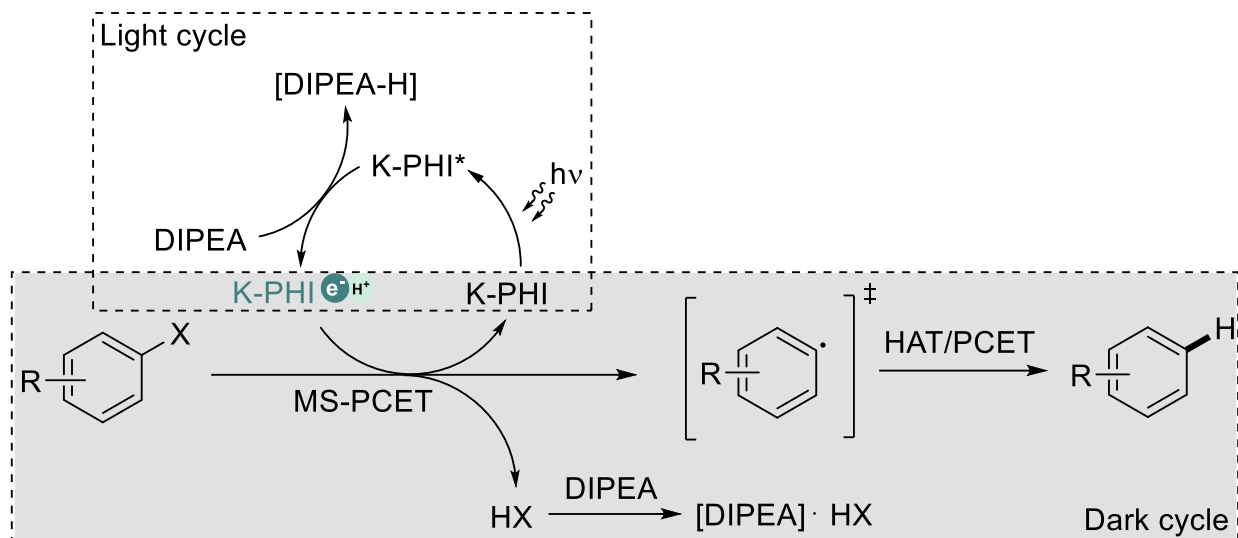


Figure 5. A proposed mechanism of aryl halides reduction via MS-PCET using K-PHI(e^-/H^+).

It was proved experimentally that K-PHI(e^-/H^+) nanoparticles reduce chalcone to the ketyl radical, which is followed by coupling with a second molecule of the chalcone, gives cyclopentanol with the yield of 30% (under non-optimized conditions, Figure 6a). Finally, reduction of nitrobenzene is known to terminate at the step of diazo- and/or azoxy-compounds,^[151] while $6e^-/6H^+$ reduction to aniline can be accomplished using K-PHI nanoparticles under continuous light irradiation (in this case K-PHI(e^-/H^+) are constantly recovered) in the presence of formic acid as sacrificial donor of electrons and protons.^[229] Here, nitrobenzene was reduced to aniline with 100% selectivity and 7% yield (under non-optimized conditions) with pre-synthesized K-PHI(e^-/H^+) in dark (Figure 6b).

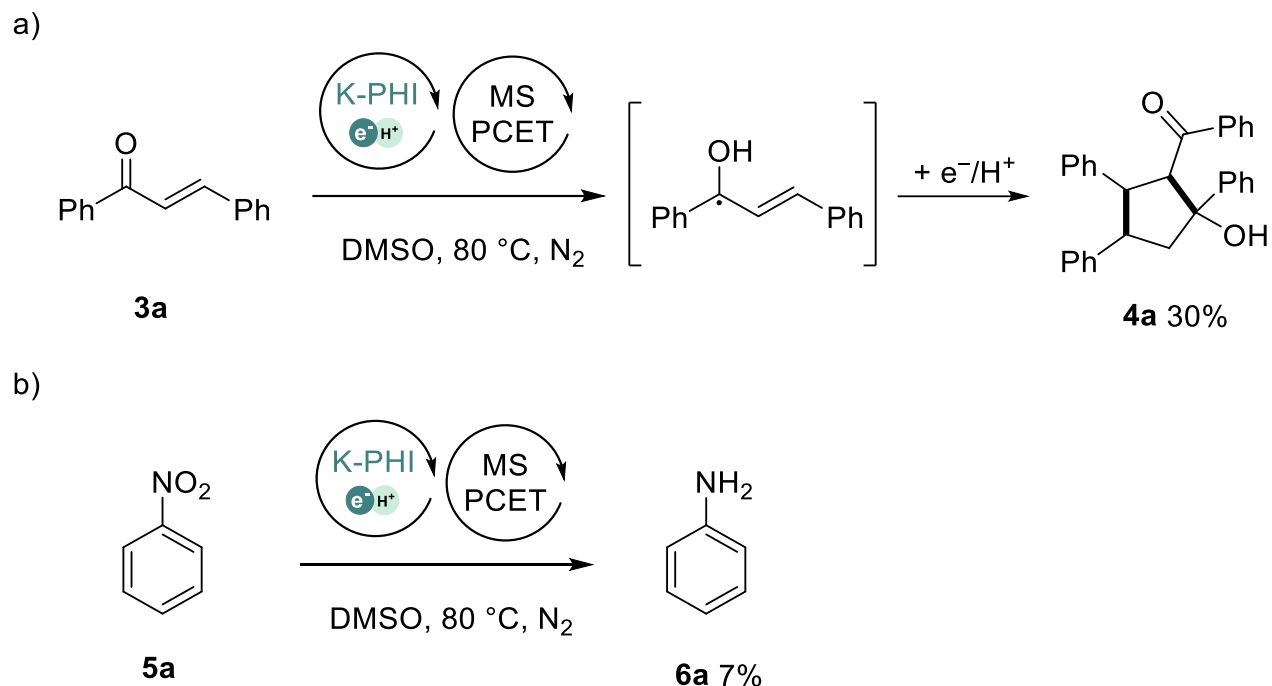


Figure 4. Scope of the MS-PCET reactions mediated by K-PHI(e^-/H^+) in dark. a) Generation of the ketyl radical from chalcone followed by its cyclization to the cyclopentanol. b) Reduction of nitrobenzene to aniline via MS-PCET using K-PHI(e^-/H^+) in dark. Conditions: 1) 80 mg K-PHI, 3 mL DMSO, Blue light ($490 \text{ mW}\cdot\text{cm}^{-2}$), 24 hours (τ_1), RT (T_1); 2) 0.05 mmol substrate (**3a** or **5a**) in 1 mL of DMSO, 20 hours (τ_2), 80 °C (T_2). See standard procedure in the appendix for further details. Yields determined by GC-MS.

Collectively, the examples illustrate remarkable reduction power of K-PHI(e^-/H^+) to drive uphill processes via MS-PCET.

Overall, negatively charged microporous structure of the SCNP is the most crucial parameter that explains high performance of K-PHI nanoparticles in the MS-PCET reactions. It gives degenerate semiconductor with higher degree of doping with electrons (and charge-compensating H^+), 1 mmol g^{-1} or ca. 10^{21} cm^{-3} ,^[111] compared to mpg-CN (ca. $6\cdot 10^{19} \text{ cm}^{-3}$),^[111] and non-porous inorganic SCNPs, such as TiO_2 (10^{18} cm^{-3})^[230] and ZnO (ca. $2\cdot 10^{19} \text{ cm}^{-3}$),^[231] which correlates with the yield of **2a** (Table 2).

Entry	SCNP	Diameter, nm	Doping degree, [electrons]·cm ⁻³	Yield of 2a, %
1	K-PHI	100	ca. 10 ²¹ [a]	100%
2	mpg-CN	–	ca. 6·10 ¹⁹ [a]	12%
3	TiO ₂	–	ca. 10 ¹⁸ [b]	Traces ^[d]
4	ZnO	4.6	2·10 ¹⁹ [c]	–[e]

Table 2. Correlation of SCNPs doping degree with the yield of **2a** under the optimized conditions. [a] Calculated using the equation: $N = d \cdot C \cdot N_A$, where d – density of carbon nitride, 2.336 g cm⁻³,^[232] C – concentration of electrons in the carbon nitride, mol g⁻¹. Data is taken from the reference ^[111]. N_A – Avogadro number, 6.02·10²³ mol⁻¹. [b] Data is taken from the reference ^[230]. [c] Data is taken from the reference ^[231]. [d] Commercial TiO₂. [e] Not evaluated in this work.

Considering that up-shift of the Fermi level in semiconductors is proportional to the concentration of charge carriers (n), $E_F - E_C \sim n^{2/3}$,^[202] higher doping degree affords material with stronger reduction power. Upon partial discharging, Fermi level shifts downwards and reduction power of the SCNP(e⁻/H⁺) decreases.

Under the optimized conditions (with respect to the yield of **2a**, 100%) the efficiency of e⁻/H⁺ harvesting in dark phase by the aryl halide is 63%, which is explained by a decrease of the reduction power of K-PHI(e⁻/H⁺) once the SCNP is partially discharged in dark. From the practical point of view, MS-PCET using K-PHI under continuous light irradiation is more convenient since K-PHI(e⁻/H⁺) nanoparticles are constantly recharged at the expense of a sacrificial agent.

Conclusions

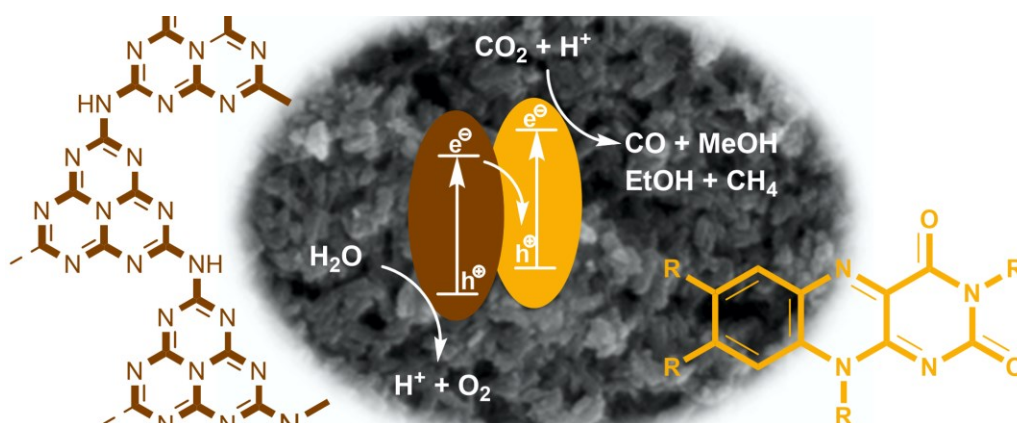
Ionic carbon nitrides, represented by K-PHI nanoparticles, direct energy of electromagnetic radiation to drive uphill processes via MS-PCET with electrons stored in the π conjugated structure and protons either in the micropores or on the surface of the material. Based on thermochemical calculations, the binding energy of e^-/H^+ in charged K-PHI nanoparticles is $<5.2 \text{ kcal mol}^{-1}$, which makes the material a very potent reductant. Using charged K-PHI(e^-/H^+) nanoparticles, 14 aryl halides have been reduced with 9-100% yield of the corresponding aromatic.

Scope of the methodology has been expanded to $6e^-/6H^+$ reduction of nitrobenzene to aniline and generation of ketyl radical from the chalcone followed by cyclodimerization to cyclopentanol in dark. The integration of several features that until now were intrinsic for plants and natural photosynthesis, into a nanomaterial composed of abundant C,N,K elements offers a powerful tool for synthetic organic chemistry. The concept developed herein has high potential for 'storage' of natural sunlight and subsequent use in synthetically useful uphill processes in the flask.

5. All-organic Z-scheme photoreduction of CO₂ with water as the donor of electrons and protons

Overview

Carbon nitrides and flavins are two classes of easy accessible transition metal-free, photoactive materials. Their photocatalytic efficiency to enable a variety of chemical reactions is well documented. Here, their combination in one photocatalytic system by designing biomimetic non-spherical core-shell architectures comprising micro-sized crystals of flavins decorated by potassium poly(heptazine imide) nanoparticles on the surface is reported. The designed non-spherical core-shell composites are tested in the photocatalytic CO₂ reduction to CH₄, MeOH, EtOH and CO using water vapor as a donor of electrons and protons at the gas-solid interface.



This chapter is an adapted version of the article:

S. Mazzanti, S. Cao, K. ten Brummelhuis, A. Völkel, J. Khamrai, D.I. Sharapa, S. Youk, T. Heil, N.V. Tarakina, V. Strauss, I. Ghosh, B. König, M. Oschatz, M. Antonietti, A. Savateev, All-organic Z-scheme photoreduction of CO₂ with water as the donor of electrons and protons, *Applied Catalysis B: Environmental*, 285, 119773, 2021

Results and discussion

Extensive, anthropogenic combustion of fossil fuels into CO₂ is the main contributor to global warming^[233] and artificial photosynthesis is considered as one of the most promising approaches to address the involved problems.^[234] Previous research in artificial photosynthesis proved that a series of valuable chemicals, for example, CO,^[94] methanol,^[235] ethanol,^[151] can be prepared from CO₂ using synthetic materials as photocatalysts, while water is the most attractive donor of electrons and protons.^[236] Many materials have been reported to promote CO₂ reduction under light irradiation,^[236] but limited stability and efficiency of the process limit applications.^[237]

Riboflavin (vitamin B2) and its derivatives are eco-friendly, cheap,^[238] non-toxic redox active dyes.^[239] They have been employed mostly as homogeneous photocatalysts to perform photo-oxidations,^[15, 238, 240, 241] but were also reported in heterogeneous photocatalysis, here supported on nanostructured metal oxide films for the oxidation of alkylbenzenes.^[241] In addition, riboflavin tetrabutryrate was used as emission layer in OLEDs.^[242] However, photocatalytic reduction reactions mediated by flavins have not been explored.^[243]

On the other hand, the larger class of carbon nitride (CN) materials, after uprising in H₂ evolution under visible light, has also been applied in organic synthesis^[87, 93, 120, 139, 153, 208, 244] and in solar energy storage applications.^[245] Several methods have been developed to tune physical and chemical properties of CNs, and as a result, to enhance the photocatalytic activity in a certain reaction.^[88] However, even though construction of donor-acceptor conjugated polymers has been widely used,^[31, 246, 247] this last strategy has been seldom applied to CNs based material.

K-PHI is thereby a promising candidate for construction of such donor-acceptor composites.^[87, 115, 247] The small particle size of K-PHI can be considered also beneficial to ensure a high interface area between two components when constructing heterogeneous donor-acceptor composites.

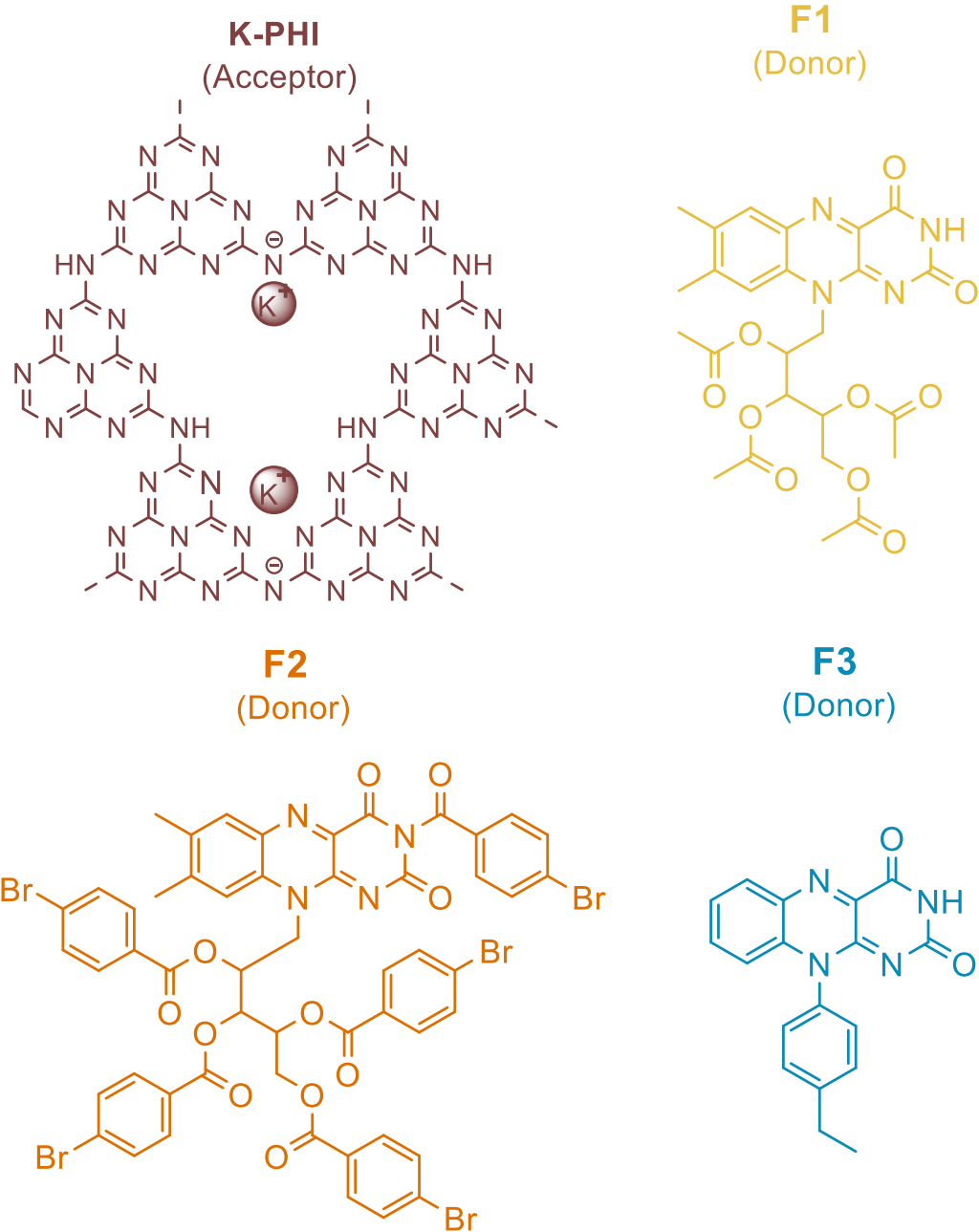


Figure 1. Chemical structures of K-PHI and flavins employed.

Herein, the two classes of materials are brought together – flavins and K-PHI to design donor-acceptor composites.

The composites (C1, C2, and C3) were prepared via self-assemble by in situ crystallization of the corresponding flavins (F1, F2, and F3, see Figure S1-S2 for their preparation) from methanol solution upon concentration in vacuum followed by spontaneous deposition of K-PHI nanoparticles as a type of Pickering stabilizer (Figure 2). The molar ratio between K-PHI and flavins has been chosen to 2:1 (assuming a repetitive molar weight of K-PHI of 500 g mol⁻¹) to ensure a complete coverage of the flavin microcrystals with K-PHI nanoparticles and to achieve a high interface area between the donor and acceptor in solid state.

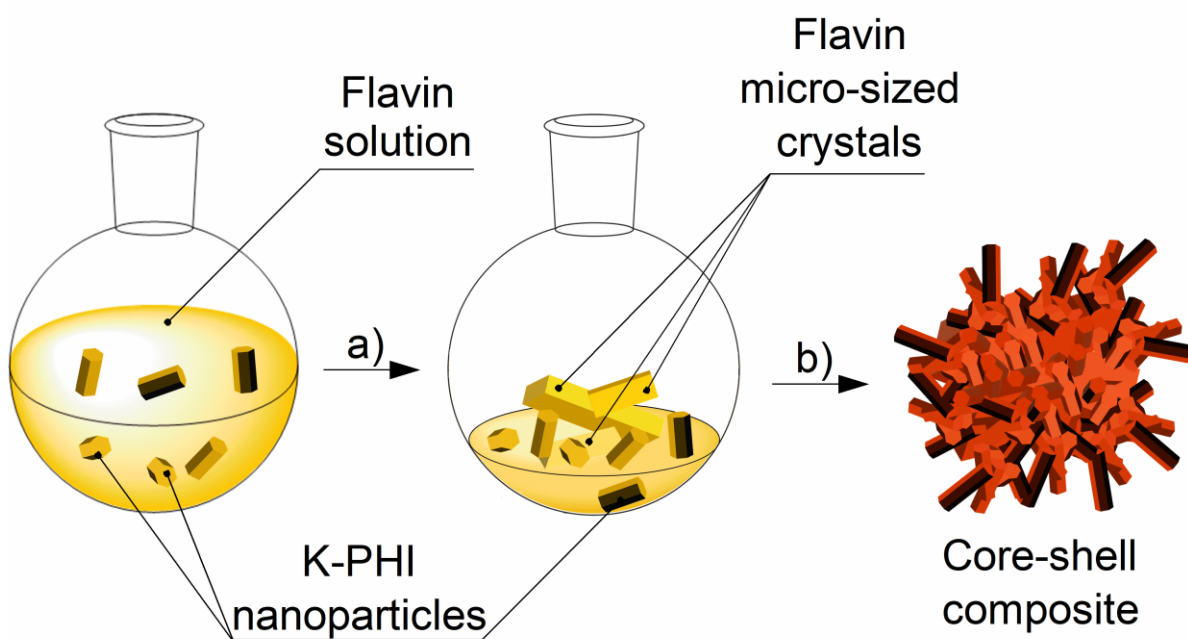


Figure 2. Schematic procedure of non-spherical core-shell composite preparation and schematic representation of the composite morphology. Color staining of the composite illustrates red-shifted onset of light absorption in the heterojunction as evidenced by DRUV-vis spectroscopy (see below). Schematic representation of flavin and the non-spherical core-shell composite morphology as evidenced by the SEM images of flavin F3 and composite C3. Step a) denotes stirring a colloidal solution of K-

PHI nanoparticles and flavin in MeOH followed by concentration under reduced pressure b) denotes grinding in mortar followed by annealing in air oven at 150 °C.

Figure 3 shows the morphology of flavins and the composites. The morphology of flavin F1 is represented by thin plates (Figure 3a), flavin F2 by sharp-edged particles of irregular shape, and flavin F3 by rectangular bricks. The SEM images of composites C1, C2, and C3 do not show morphological features of the pure flavins, but are rather identical to that of pure K-PHI – assembly of nanoparticles with the diameter 100-200 nm (see also Figure S3-S9 for overview images), which means that flavin crystals are indeed completely covered by the K-PHI colloidal stabilizer. Thus, SEM provides the first piece of evidence that flavins and K-PHI form core-shell structures, albeit non-spherical, upon self-assembly – flavin crystals in the core, while the shell is constructed from K-PHI particles. To get more insights about the structure of the obtained composites at the nanoscale, transmission electron microscopy and energy-dispersive X-ray (EDX) analysis were used. The later allows clear distinguishing between different part of the composites, since bromine is present exclusively in flavin and potassium – in K-PHI. Figure S10 shows a typical amorphous particle of flavin F2 with a diameter of about 500 nm. In the corresponding C2, composite large amorphous particles of flavin F2 are decorated with nanocrystalline K-PHI nanoparticles (typically <100 nm in diameter) (Figure 3g,h, S11).^[105] Analysis of HRTEM images and corresponding FFT transforms allows to conclude that formed K-PHI particles crystallize in hexagonal structure, with $a = 12.6 \text{ \AA}$, $c = 3.3 \text{ \AA}$ (Figure 3i-k).^[106, 116] EDX spectra obtained from different parts of non-spherical core-shell structures have different K:Br ratios; thus crystalline parts exhibit a higher K content (Figure S12c) while the amorphous part, the flavin-rich region, display a higher Br signal (Figure S12f).

PXRD analysis of K-PHI nanoparticles reveals a typical pattern for this material with a pronounced peak at 8° , due to the in-plane periodicity, and the peak at 28° due to graphitic packing (Figure S13a) [47].^[248] Flavins F1 and F3 are crystalline powders, while F2 is

amorphous (Figure S13b, d, f). Higher crystallinity of flavins F1 and F3 is explained by a smaller and more regular shape of the molecule, i.e., a lower number of degrees of freedom that facilitates crystallization. Composites C1 and C2 are amorphous with respect to the flavin core, but all composites show pronounced peaks related to the presence of K-PHI nanoparticles (Figure S13c, e, g), while intensity of the diffraction peaks depends of K-PHI content in the composites (Figure S14, Table S1).

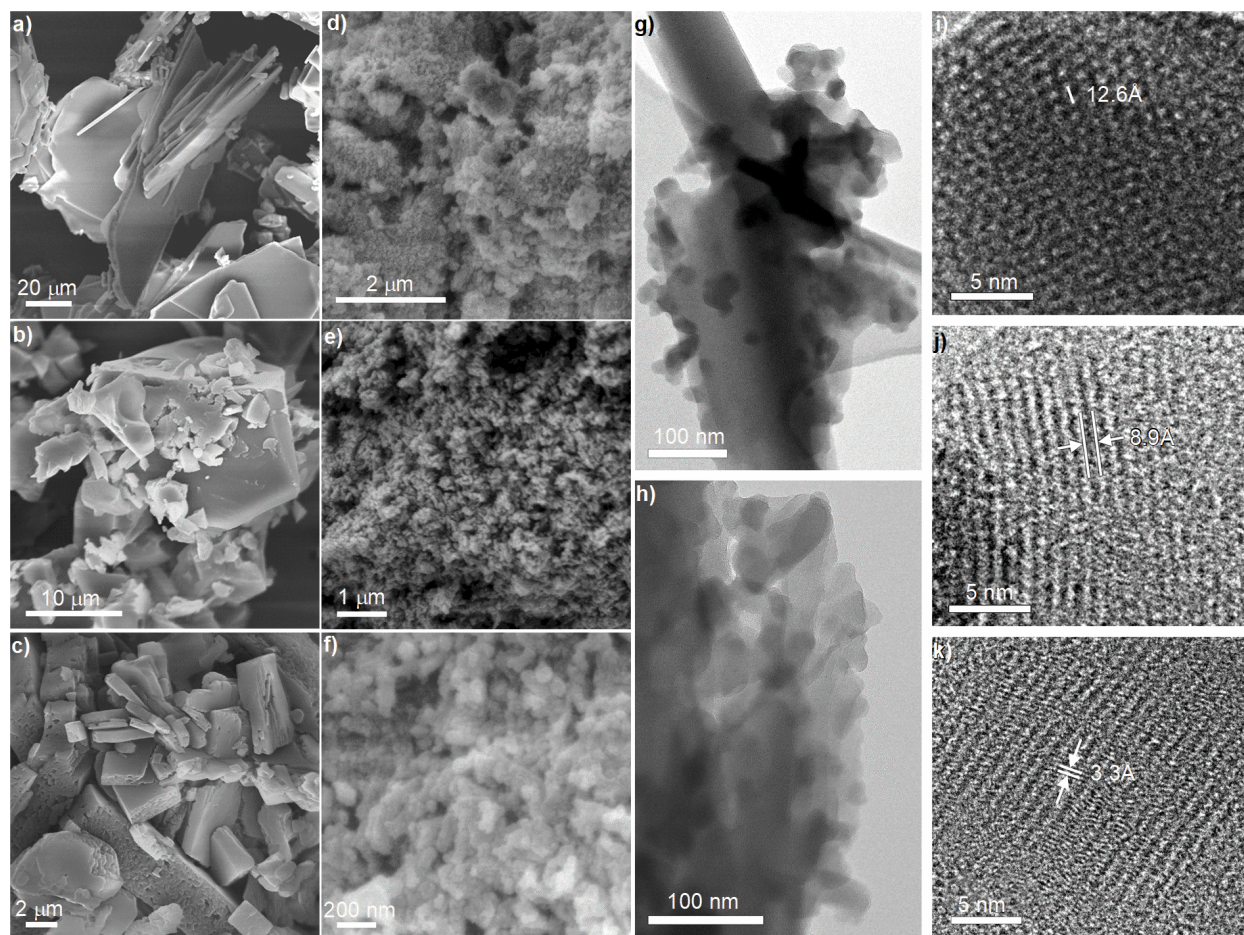


Figure 3. Electron microscopy images of the flavins and their composites. SEM images of: a) Flavine F1; b) Flavine F2; c) Flavine F3; d) Composite C1; e) Composite C2; f) Composite C3; g, h) overview TEM images of the composite C2. i, j, k) HR-TEM images of K-PHI nanoparticles in the composite C2 taken along different crystallographic directions.

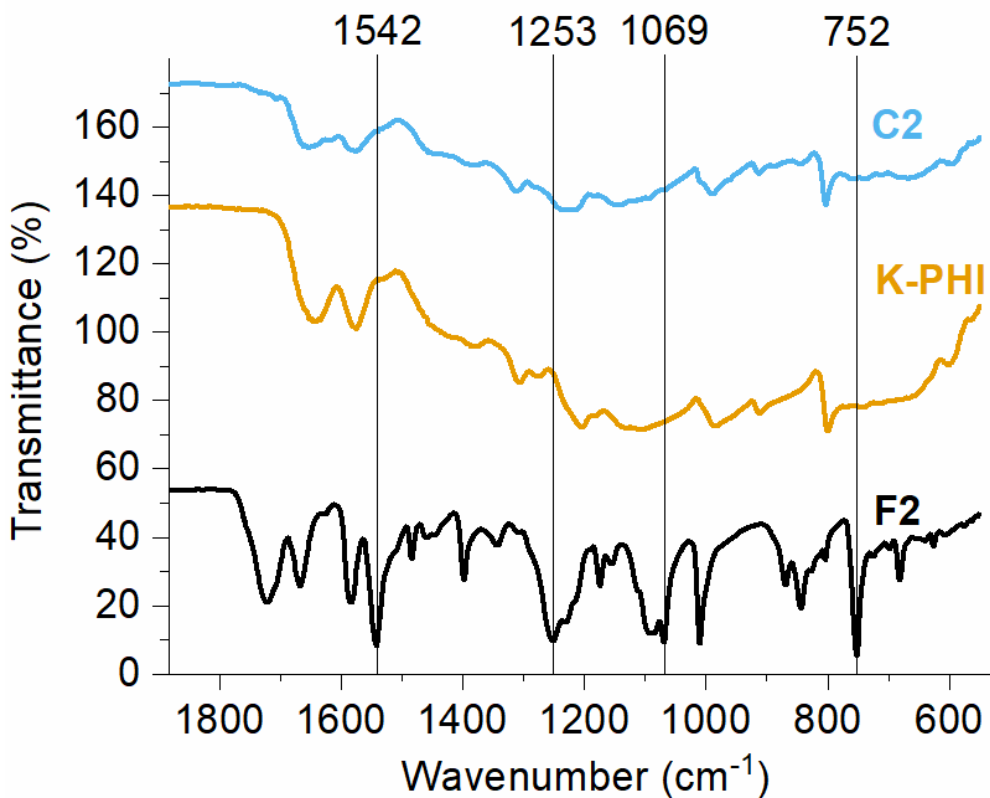


Figure 4. FT-IR spectra of flavin F1, K-PHI and composite C1 in comparison. Selected vibrational peaks of flavin are labeled.

Fourier-transform infrared (FT-IR) spectra of the composites are very similar to that of K-PHI, while vibration peaks related to the flavins are mainly absent (Figure 4, Figure S15). FT-IR data provide a second piece of evidence supporting the formation of the core-shell structure. In this architecture, the flavin core is covered by the K-PHI shell. As a result, the vibrational peaks of the shell are predominantly seen in the IR spectra.

The solid-state emission spectra of the flavins, K-PHI and their composites are shown in Figure 5a and Figure S16. Pure flavins have fluorescence Internal Quantum Efficiency (IQE) 2.0–7.7%, while K-PHI has an IQE of 0.19% (Table S2). Practically complete fluorescence quenching is observed for composites in the solid state – composites IQEs are only 0.1-0.4%

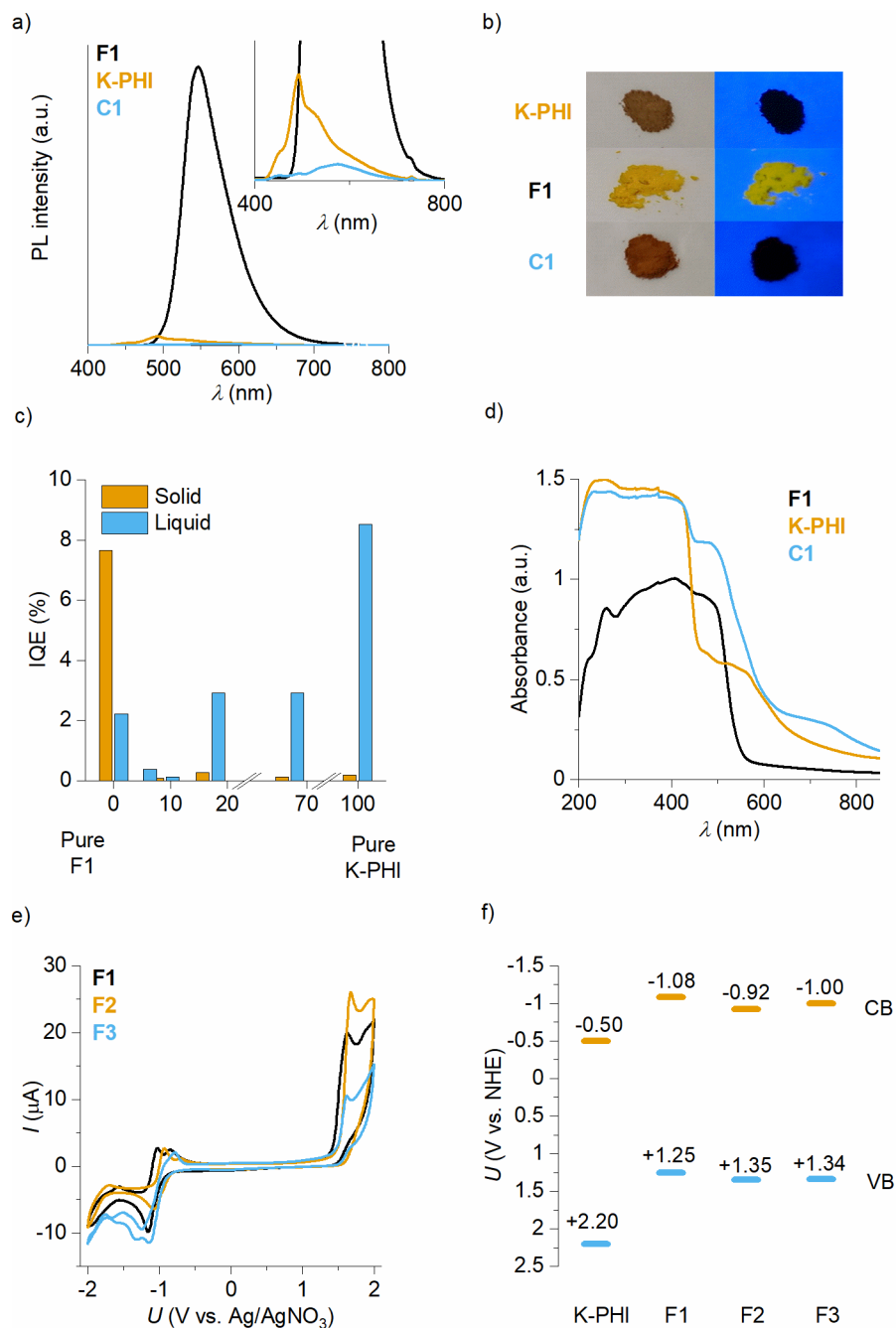


Figure 5. Optical properties of flavins and composites. a) Solid state PL spectra of F1, K-PHI and the composite C1. Inset shows magnified PL spectra of K-PHI and the composite C1. b) Powder of K-PHI, flavin F1 and the composite C1 under ambient day light and under 365 nm irradiation. c) IQE of composites in solid state and dispersions in DMSO. X-axis represents K-PHI

content. d) DRUV-vis absorption spectra of F1, K-PHI and composite C1. e) CV curves recorded using 2 mM solution of flavin in MeCN. Glassy carbon (diameter 3 mm) was used as a working electrode (WE), Ag wire in AgNO₃ (0.01M) with (nBu)₄N⁺ClO₄⁻ (0.1M) in MeCN – as a reference electrode (RE) and Pt wire – as a counter electrode (CE). f) CB and VB potentials of K-PHI are taken from the literature.^[114] For flavins, CB and VB refer to HOMO and LUMO potentials determined from CV curves (Figure 5e).

(Table S2). Titration experiments showed that the composite with only 9% K-PHI content already shows complete fluorescence quenching (Figure 5c). These results give a third piece of evidence supporting the formation of an electronically active structure. Taking into account the results of the electron microscopy study and FT-IR, electronic interaction between the partners of the composite is obviously the most efficient when they are assembled in core-shell structure. A similar behavior has been reported for flavin-graphene composites.^[249]

However, dispersions of the composites C1 and C3 in DMSO do not exhibit fluorescence quenching (Figure S17) suggesting that polar solvent disrupts the interaction between the flavins F1 and F3 and K-PHI particles. In addition, dispersion of the composite C1 in DMSO followed by filtration resulted in a yellowish solution implying the dissolution of the flavin F1 in DMSO (Figure S18). Furthermore, IQE of a series of K-PHI/F1 mixtures in DMSO with different K-PHI content shows an opposite trend compared to the measurements in solid state (Figure 5c), i.e. higher IQE (8.5%) for pure K-PHI suspension. On the other hand, flavin F1 showed lower IQE (2.2%) compared to that in solid state (7.7%), which is explained by an agglomeration induced emission phenomenon.^[250] Since the synthesized composites are applied in the photocatalytic CO₂ reduction in the gas-solid interface, spectroscopic data obtained in the solid state are considered to be more relevant to the study.

Thermogravimetric analysis (TGA) of C2 demonstrates lower mass loss in the composite compared to the calculated value suggesting that the shell made of thermodynamically stable K-PHI nanoparticles stabilizes the flavin core in the composite (Figure S19). Overall, observation of the composites morphology directly from the electron microscopy images,

FT-IR data, strong fluorescence quenching in the composites, and TGA data, collectively support the formation of non-spherical core-shell structures.

In agreement with earlier reports, K-PHI has an onset of absorption at 700 nm that is assigned to $n-\pi^*$ transitions,^[251] but the main contribution to light absorption originates from the $\pi-\pi^*$ transitions observed as a band at 460 nm, i.e., the band gap, as concluded from the diffuse reflectance (DR) UV-vis absorption spectra (Figure 5d). In the solid state, all flavins have the onset of absorption at 540 nm that corresponds to the optical band gap of ca. 2.3 eV (Figure S20). Similar band gap values of flavins, despite different backbone structure, i.e. protected ribose backbone (in case of F1 and F2) and 4-ethylphenyl substituent (in F3), support the fact that the isoalloxazine core acts as the chromophore.

Band gap values derived from the DRUV-vis spectra are close to that obtained from the cyclic voltammetry (CV) measurements of the flavins in MeCN solution, 2.27-2.34 eV (Figure 5e). Considering the relative alignment of the frontier orbitals energy levels in flavins and CB/VB energy levels in K-PHI (Figure 5f), the designed composites can be regarded as being able to follow a Z-scheme activation, if it is compared with all-semiconductor systems. The Z-scheme rationalizes the complete fluorescence quenching observed in the composites in the solid state. Indeed, this is due to the selective charge recombination at the interface, while energy transfer is suppressed, as already reported for a flavin-graphene composite^[249] and for a carbon nitride-carbon composite.^[252]

Direct charge transfer in the composites C1 and C2 is supported by the appearance of the additional absorption band, albeit weak, with the onset at 800 nm (Figure 5d). DFT calculations also predicted Bader charge shift between flavin F3 and K-PHI of 0.023 electrons (see appendix for computational details).

Transient photocurrent measurements are indispensable to investigate light response properties of semiconductors, such as K-PHI.^[253] Such measurements are typically done by immersing an electrode (typically FTO glass) coated with the analyzed material into the

aqueous electrolyte. However, this approach was not suitable for the studied materials. Due to partial solubility of flavins in water, the coated FTO glass is not stable. Binders, such as PVDF, gave stable electrodes, but conductivity was too low to record reliable data.

The solution was found employing thin layers of conductive hydrogel between the electrodes that serve as the electrolyte (Figure 6, Figure S21-22, see experimental procedure in the appendix for details of the device fabrication). The developed architecture allows preserving the morphology of the analyzed material for hours due to low diffusion of the flavins into the bulk of the hydrogel. Compact size, thickness of only 10 mm, absence of electrolyte leakage, and good light permeability are additional advantages of the fabricated device. The photoelectrodes in such architecture are stable for at least a few hours (Figure S23).

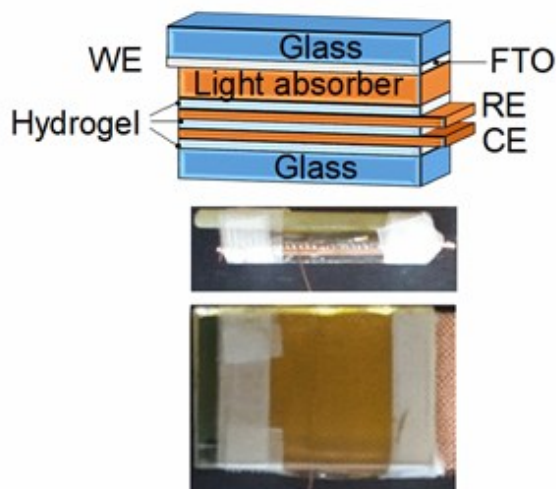


Figure 6. Electrochemical measurements. a) Representative scheme of the electrochemical cell employing hydrogel layers as the electrolyte. Schematic representation, side and front views of the ready device; b) Illuminated OCP experiment. The experiment was performed in dark (30 s) followed by irradiation with white LED (10 s, 467 mW cm⁻²). Seven cycles were recorded for each material. The temperature was kept at 25-30°C by using air fan. Geometric area of the working electrode was 3.2 cm².

With the electrochemical device in hands, different electrochemical tests were performed: illuminated open circuit potential (OCP), linear sweep voltammetry (LSV), chronoamperometry (CA), and chronopotentiometry (CP) (Figure 7).

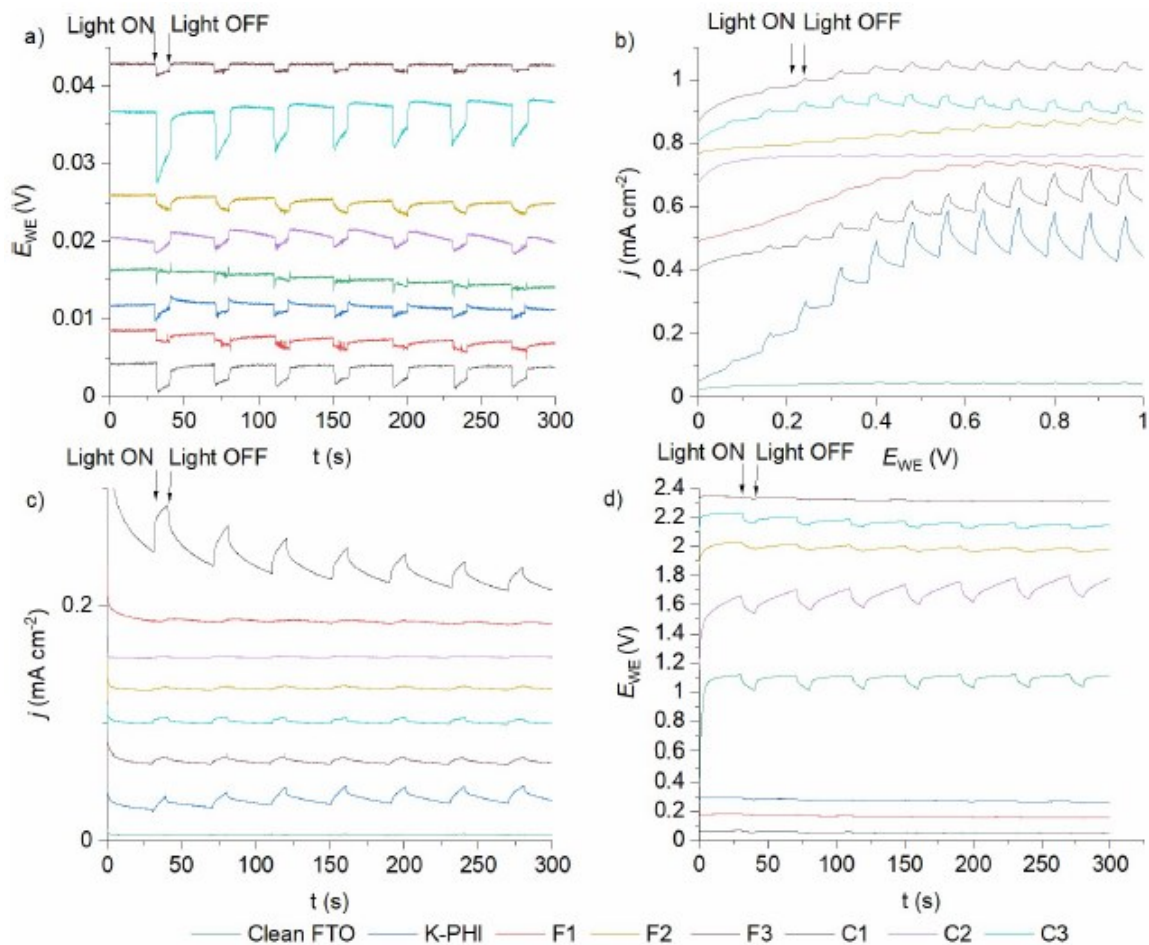


Figure 7. Electrochemical measurements. Herein data is plotted in stack. Electrochemical device was cooled with axial fan. Irradiation using White LED 467 mW cm^{-2} at 3 cm distance. a) Open circuit voltage. b) Linear sweep Voltammetry c) Chronoamperometry. Voltage 0.5 V. d) Chronopotentiometry. Current $10 \mu\text{A}$.

Thus, illuminated OCP experiment showed a negative shift suggesting that all tested materials possess n-type conductivity, [254] while in CA experiments a positive photocurrent densities of 2-22 $\mu\text{A cm}^{-2}$ were registered. Therefore, once irradiated, materials resistance decreases due to increase of charge carriers concentration. For pure K-PHI and its composites, these findings are in agreement with the reported earlier positive slope in the Mott-Schottky plot.[123] However, to the best of author's knowledge, there is no data for flavins in solid state. The amplitude of the OCP change increases in the sequence K-PHI \approx flavin < composite (Figure 8) due to the introduction of the additional light absorber, a flavin ($\lambda_{\text{onset}} \leq 540$ nm). Analysis of the CA data (Figure 9) reveals that pure K-PHI shows higher photocurrent densities compared to pure flavins. At the same time, composite C1 shows twice higher photocurrent compared to pure K-PHI and 14 times higher photocurrent compared to pure flavin F1 supporting the existence of charge transfer between the two components of the composite.

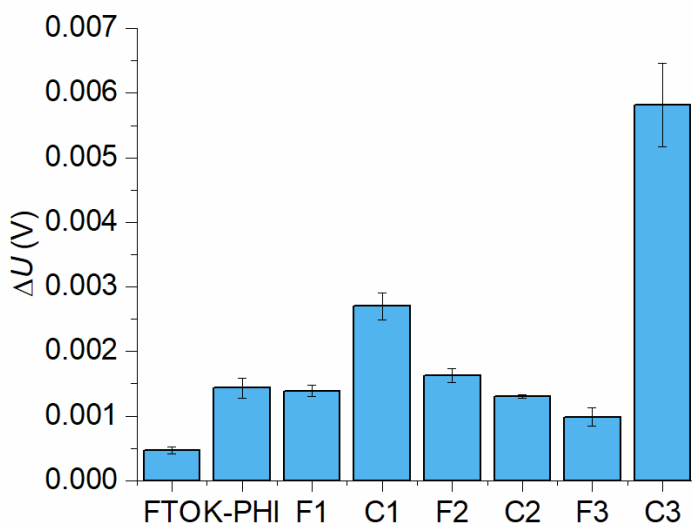


Figure 8. OCP change under light irradiation. Mean values were calculated based on 7 cycles. Error bars correspond to standard deviation calculated based on the data of 7 cycles.

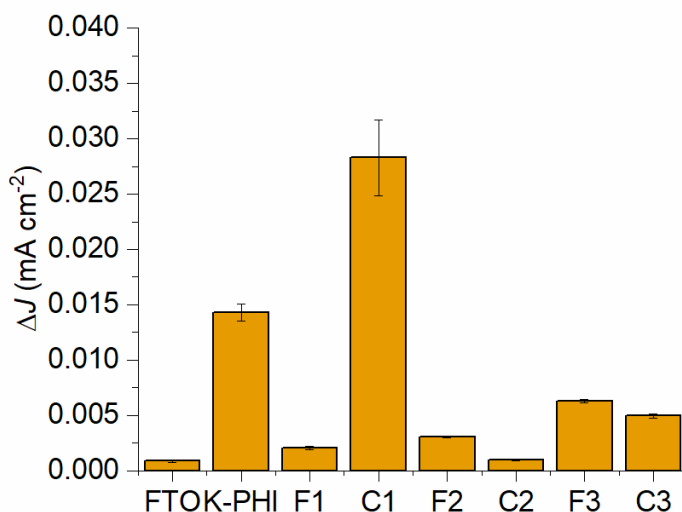


Figure 9. Photocurrent density change in the chronoamperometry (CA) experiments. Mean values were calculated based on 7 cycles. Error bars correspond to standard deviation calculated based on the data of 7 cycles. Larger error bars in case of composite C1 is explained by lower stability of the electrode during the electrochemical measurements.

Composites C2 and C3, however, showed lower photocurrents compared to the individual components. Analysis of absolute current densities (Figure S27) suggests that surface properties of the photoelectrode have clear impact on the overall conductivity. Thus, K-PHI (hydrophilic), the flavin F1 (partially soluble in water) and their composite C1 show not only the highest photocurrent, but also the highest dark current in the series of studied materials. On the other hand, the flavin F2 (large hydrophobic molecule due to presence of multiple Br atoms) and its composite show the lowest dark current.

Since a Z-scheme relies on the excitation of both the composite components (K-PHI and flavin), here with two photons with different wavelength (due to different optical band gaps), the photocatalytic properties of the prepared composites under white light irradiation in a gas-solid batch photoreactor was investigated. The photocatalytic CO₂ reduction reaction was performed using water vapor as the electron and proton donor.

The formation of CO, CH₄, MeOH, and EtOH was monitored – common products of CO₂ reduction. In addition, no H₂ formed due to the fact that the investigated system is free of transition metal co-catalyst, which otherwise would facilitate hydrogen evolution.

Figure 10 shows the yield of the products obtained using pure K-PHI, flavins and their composites. Pure K-PHI and flavins F1 and F2 show selectivity toward alcohols, methanol, and ethanol. The same trend is conserved in the composites. Therefore, reduction selectivity of the composite is largely defined by the property of the incorporated flavin. Thus, considering photocatalytic reduction of CO₂ to CH₄, the productivity of the composite C3 is 15% higher compared to the flavin F3, while composite C2 showed 2.5 times higher activity compared to the flavin F2. On the other hand, the productivity of photocatalytic reduction to CO can be increased by 27% employing composite C2 compared to flavin F2 and 3 times using composite C3 compared to flavin F3.

Thermal response measurements recording the temperature of the materials during adsorption were conducted to probe the interaction of CO₂ and H₂O with the surface of K-PHI, flavin F1, and the composite C1, as an example, (Figure S29, S30).^[255] Dry CO₂ has very low affinity to these materials (Figure S31). When CO₂ saturated with water vapor at room temperature, significantly more heat is released due to additional adsorption of water. When helium instead of CO₂ is used as a carrier gas exemplarily for composite C1, the individual contribution of water adsorption can be estimated. The heat released is far less than in the presence of CO₂ and the difference is much larger than the contribution from dry CO₂ adsorption. Therefore, water vapor serves not only as electron and proton donor in the photocatalytic CO₂ reduction, it also enhances adsorption of CO₂ at the photocatalyst surface.

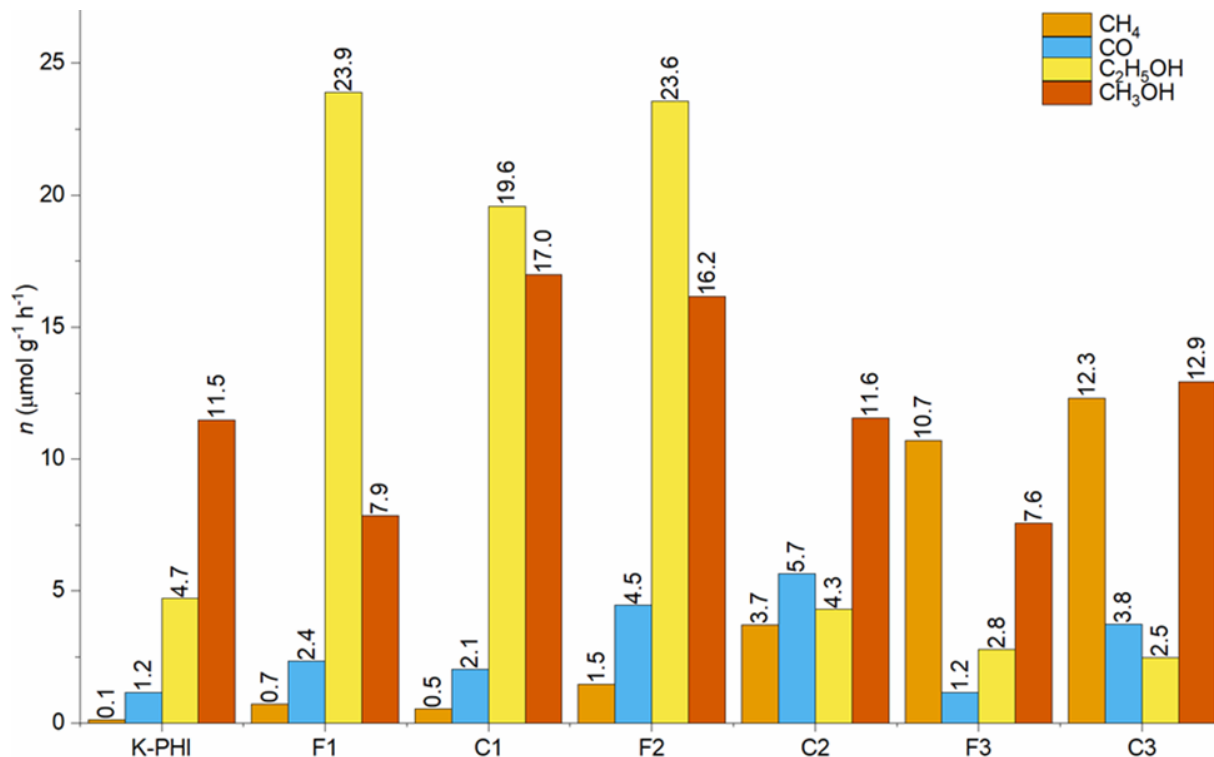


Figure 10. Photocatalytic CO₂ reduction experiments comparing different catalysts.

Furthermore, adsorption of CO₂ and H₂O at the composite C1 is defined by the surface properties of K-PHI rather than flavin F1, as the integrated peak area is comparable to that of pure K-PHI, which gives another factor for the activity of the core-shell structure of the composite with K-PHI particles outside. However, the total amount of CO₂ molecules converted by the composite C1 is similar to that of the flavin F1 (Figure S32), while CO₂ shows relatively weak affinity implying that the band structure of the flavin determines the rate of the overall photocatalytic activity and selectivity towards a certain product.

From the results of photocatalytic tests, it is concluded that selectivity of CO₂ photocatalytic reduction can be tuned by using composites of K-PHI and flavins. The forged Z-scheme heterojunction between K-PHI and flavins provides a material with the reducing properties of pure flavin and oxidative properties of pure K-PHI. This phenomena, combined with

longer life-times of excited states due to interface charge recombination, promotes the improvement of photocatalytic activities, compared to pure flavins(Figure 11). [256]

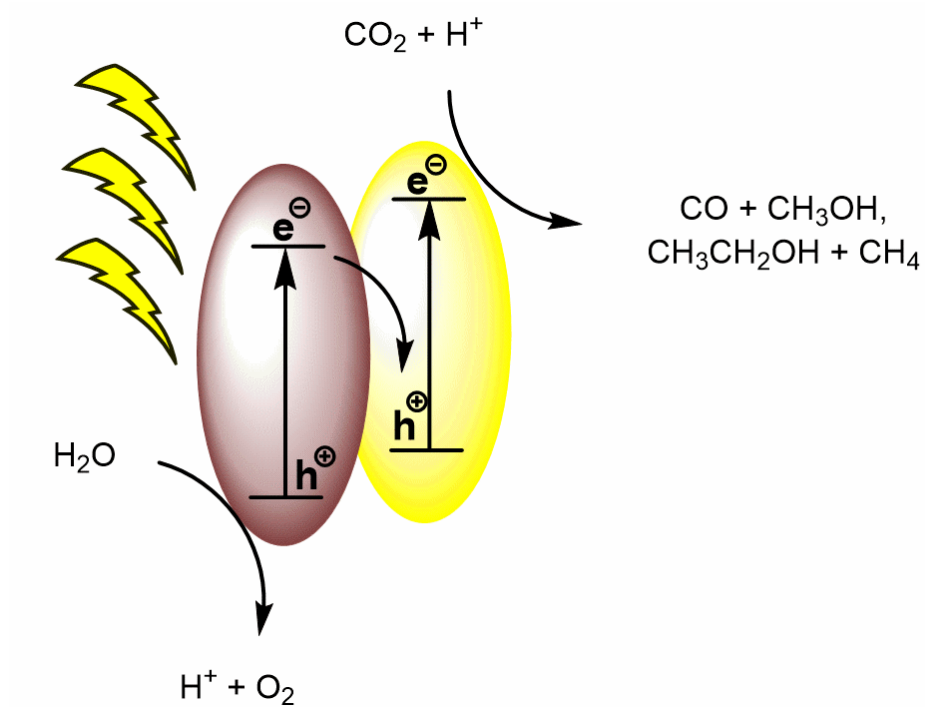


Figure 11. Proposed mechanism of CO₂ reduction. Brown phase represent K-PHI. Yellow phase represent flavins.

Conclusions

In this chapter, three different composites made by K-PHI nanoparticles and flavins have been prepared by a simple and straightforward co-precipitation/stabilization approach. The properties of the composites were investigated by SEM, XRD, TEM, EDX, IR and PL, while the results suggest the formation of a spontaneous heterojunction between the core and the shell. The photocatalytic activity of the composites has been evaluated in reduction of CO₂ to CO, CH₄, MeOH, and EtOH. The results suggest that the selectivity of the composites toward specific products is largely defined by flavins, i.e. the flavins constitute the reduction side. The K-PHI shell presumably promotes the liberation of oxygen by its very positive HOMO, accelerates the reaction, and changes the product distribution presumably by kinetic effects. Photoelectrochemical performance of flavins powder and their composites have been investigated using a dedicated electrochemical device employing a thin layer of conductive hydrogel as polymer electrolyte. In particular, a riboflavintetracetate-based composite showed a photocurrent two times higher than that of pure K-PHI and 14 times higher than pure riboflavintetracetate suggesting higher charge mobility.

6. Overall conclusions and outlooks

Carbon nitride is full of intriguing possibilities to adjust to the needs of photocatalysis. This work analyses some possible improvements for the field.

These types of materials are unique, cheap photocatalysts enabling the development of new synthetic routes for the making of building blocks to be used for the productions of active pharmaceutical compounds. Indeed, thanks to the invention of K-PHI, the creation of a new synthetic strategy was possible by the proposed dichloromethylation of enones (chapter 1). While analyzing K-PHI nanoparticles properties, it was found that stored charges can be used in different contexts, for instance in the field of dark photocatalysis.

New insights have been gained regarding multisite proton coupled electron transfer processes, thanks to mechanistic investigations concluding that material morphology, namely microporous layered structure in the case of K-PHI, contributes to the storage of charges, weakly adsorbed and therefore promptly reactive in the reduction of organic substrates.

The potential of this approach is very wide and places K-PHI on the edge to be an alternative sustainable reducing agent, thus becoming a useful tool for synthetic chemistry, while being then independent of sunlight discontinuity issues (chapter 4).

K-PHI also represent a platform that can be coupled to obtain composite material with unique properties, as highlighted in the photoreduction of CO₂ to more valuable chemicals. Given the simplicity of flavins and carbon nitride synthesis, the presented approach lays a foundation for the construction of a library of composites for task-specific applications in photocatalysis. Three structurally different core-shell composites constructed from micro-sized crystals of flavin (the core) and decorated with K-PHI nanoparticles (the shell) have been prepared and the spontaneous formed heterojunction contributed tuning selectivity and improving photocatalytic activity in the CO₂ reduction to CO, CH₄, MeOH, and EtOH (chapter 5).

Continuing the discovery in CN photocatalysis, the ductility of these materials combined with CVD preparation method allowed to shape carbon nitride to coat lab vials, EPR capillaries, and flow reactor showing the great potential of such flexible technology.

Also, further spectroscopic tools can be designed, such as coated NMR tubes, cuvettes, and electrodes, for mechanistic investigations. In these vials, it has been highlighted that the material morphology was responsible for improved photocatalytic activity, proofed by catalytic experiments and photophysical investigations (chapter 2).

Then, the implementation of carbon nitride in flow, as thin films (chapter 2) or in quasi-homogeneous configuration (chapter 1), provides a new technology for process scale-up and further development. For example, a multi step reaction with heterogeneous catalysts usually requires different packed bed reactors in series and different catalysts. A possible advantage of using K-PHI in a quasi-homogeneous configurations allows the dispersed catalyst to be pumped into reactors bearing different conditions allowing the performance of different chemical functionalization in a series of plug flow reactors, reducing the number of fixed bed reactors employed.

Looking towards other possible follow-ups, there is still a deep gap in the understanding of certain underpinning mechanisms. Indeed, while in depth explanations are provided regarding reaction mechanism or material morphology, studies of surface interaction between CN photocatalysts and substrates just started to appear.^[257]

Understanding heterogeneous catalytic mechanism on solid surfaces is a very challenging topic, that combined with the employment of light is made even harder.

Considering the chemical reactions reported in this work, one can observe substantial differences to the (thermal) catalytic processes. Indeed, in heterogeneous catalysis, substrates tend to react with other molecular species on the surface of the catalyst.

On the other hand, in photocatalysis, small but highly reactive intermediate are generated, due to catalyst interaction, which then can react with organic substrates. This process does

not necessarily involve a surface bimolecular reaction. Therefore, it is no surprise that practical photocatalytic methods are almost segregated to the functionalization of bioactive scaffold for drugs production, where selectivity and reactivity are chosen with the right combination of compatible conditions and substrates.

Otherwise, the wandering of such reactive species in the reaction mixture is difficult to control, easily leads to poor selectivity.

This explains why the majority of research work on heterogeneous photocatalysis is based on the degradation of pollutants, whereby controlled and uncontrolled species devouring pollutants is a desirable activity.

Therefore, understanding interactions between organic substrates and solids at the interface in photocatalysis would grant great advancements in the development of finely designed photocatalytic materials, capable to guarantee selectivity to the highly reacting species generated via photocatalytic approach.

In this way, photocatalysis could be developed towards the production of bulk chemicals, whereby the restriction of substrates would be balanced by selective photocatalysts.

Concluding, new applications of CN materials have been developed in this thesis, opening interesting outlooks for further research pathways.

The key to reach such achievements can be placed in the multidisciplinary approach used during all the chapters, whereby catalytic activities have always been correlated to material analysis and reaction mechanism investigation.

7. Appendix – Supplementary material

7.1 General methods and materials

¹H and ¹³C NMR spectra were recorded on Agilent 400 MHz (at 400 MHz for Protons and 101 MHz for Carbon-13). Chemical shifts are reported in ppm versus solvent residual peak: chloroform-*d* 7.26 ppm (¹H NMR), 77.1 ppm (¹³C NMR); acetonitrile-*d*₃ 1.94 ppm (¹H NMR), 118.3 ppm (¹³C NMR); *DMSO-d*₆ 2.50 ppm (¹H NMR), 39.52 ppm (¹³C NMR)

Irradiance of the LED modules was measured using PM400 Optical Power and Energy Meter equipped with integrating sphere S142C.

Powder X-Ray diffraction patterns were measured on a Bruker D8 Advance diffractometer equipped with a scintillation counter detector with CuK α radiation ($\lambda = 0.15418$ nm) applying 2θ step size of 0.05° and counting time of 3s per step.

Nitrogen adsorption/desorption measurements were performed after degassing the samples at 150 °C for 20 hours using a Quantachrome Quadrasorb SI-MP porosimeter at 77.4 K. The specific surface areas were calculated by applying the Brunauer-Emmett-Teller (BET) model to adsorption isotherms for $0.05 < p/p_0 < 0.3$ using the QuadraWin 5.11 software package.

Mass spectral data were obtained using Agilent GC 6890 gas chromatograph, equipped with HP-5MS column (inner diameter=0.25 mm, length=30 m, and film=0.25 μ m), coupled with Agilent MSD 5975 mass spectrometer (electron ionization).

Scanning electron microscopy (SEM) images were obtained on a LEO 1550-Gemini microscope.

The X-ray photoelectron spectroscopy (XPS) measurements were carried out in an ultrahigh vacuum (UHV) spectrometer equipped with a VSW Class WA hemispherical electron analyzer. A dual anode Al K α X-ray source (1486.6 eV) was used as incident radiation. Survey and high resolution spectra were recorded in constant pass energy mode (44 and 22 eV, respectively). During the UPS (He I excitation energy $h\nu=21.23$ eV)

measurements a bias of 15.32 V was applied to the sample, in order to avoid interference of the spectrometer threshold in the UP spectra. The values of the valence band maximum (VBM) are determined by fitting a straight line into the leading edge.

Optical absorbance spectra of powders were measured on a Shimadzu UV 2600 equipped with an integrating sphere.

Emission spectra, Internal and External Quantum Efficiency (IQE/EQE) were recorded on Jasco FP-8300 instrument. The excitation wavelength was set at 360 nm.

Energy dispersive X-Ray (EDX) analysis was performed on JEOL JSM-7500F electron microscope equipped with two Oxford Instruments EDX detectors, located at opposite sides from the sample. The angle between the sample film surface and EDX detector axis was 28°.

The TEM measurements were acquired using a double-corrected Jeol ARM200F, equipped with a cold field emission gun and a Gatan GIF Quantum. The used acceleration voltage was 200kV and the emission was set to 10 μ A in order to reduce beam damage. An objective aperture with a diameter of 60 μ m was introduced into the beam to improve the contrast while still allowing for atomic resolution.

Zeta-potentials were measured in aqueous colloidal solution of K-PHI using a Malvern Zetasizer instrument.

Hydrodynamic diameter of K-PHI particles in water was measured using Malvern Zetasizer instrument.

Carbon nitride photocatalysts synthesis and characterization

K-PHI

Potassium poly(heptazine imide) (K-PHI) was synthesized according to the previously described procedure.^[115] Mixture of lithium chloride (3.71 g), potassium chloride (4.54 g) and 5-aminotetrazole (1.65 g) was grinded in ball mill for 5 min at the shaking rate 25 s⁻¹. Reaction mixtures were transferred into porcelain crucibles and covered with lids. Crucibles were placed in the oven and heated under constant nitrogen flow (15 L·min⁻¹) and

atmospheric pressure at a following temperature regime: heating from room temperature to 550 °C for 4 hours, annealing at 550 °C for 4 hours. After completion of the heating program, the crucibles were allowed to cool slowly to room temperature under nitrogen flow. The crude products were removed from the crucibles, washed with deionized water (100 mL) for 3 hours in order to remove salts, then filtered, extensively washed with deionized water and dried in a vacuum oven (20 mbar) at 50 °C for 15 h.

mpg-CN

Cyanamide (3.0 g) and Ludox HS-40 (7.5 g) were mixed in a 10 mL glass vial. The mixture was stirred at room temperature for 30 min until cyanamide has completely dissolved. The resultant solution was stirred at +60°C for 16 h until water has completely evaporated. Magnetic stir bar was removed and white solid was transferred to the porcelain crucible and heated under N₂ flow in the oven. The temperature was increased from room temperature to 550°C within 4 h and maintained at 550°C for 4 h. The crucible was spontaneously cooled to room temperature. The solid from the crucible was briefly grinded in the mortar and transferred to the polypropylene bottle. A solution of (NH₄)HF₂ (0.24 g·mL⁻¹, 50 mL) was added and suspension was stirred at room temperature for 24 h. The solid was filtered, thoroughly washed with water, once with ethanol and dried in vacuum (55°C, 20 mbar) overnight.

g-C₃N₄

Diacyandiamide (15.0 g) was calcined at 600°C for 4 h under flow of nitrogen (15 L min⁻¹) in a porcelain crucible. Yellow solid was ground in mortar.

7.2 Dichloromethylation of enones by carbon nitride photocatalysis

Chlorine elemental analysis was performed by company MikroLab.

Microwave reactions were carried out in a CEM Discover® SP System microwave reactor.

Cyclic voltammetry (CV) measurements were performed in a glass single-compartment electrochemical cell. Glassy carbon (diameter 3 mm) was used as a working electrode (WE), Ag wire in AgNO₃ (0.01M) with tetrabutylammonium perchlorate (0.1M) in MeCN as a reference electrode (RE), Pt wire as a counter electrode. Each compound was studied in a 50 mM concentration in a 0.1 M tetrabutylammonium perchlorate (TBAP)/chloroform electrolyte solution (10 mL). Before voltammograms were recorded, the solution was purged with Ar, and an Ar flow was kept in the headspace volume of the electrochemical cell during CV measurements. A potential scan rate of 0.050 V s⁻¹ was chosen, and the potential window ranging from +2.5 V to -2.5 V (and backwards) was investigated. Cyclic voltammetry was performed under room-temperature conditions (~20-22 °C).

Light scattering by K-PHI suspension

Light scattering by K-PHI particles has been evaluated using two methods. In the first method transmittance spectrum of K-PHI suspension (2.5 mg mL⁻¹) in CHCl₃:DMSO (9:1) have been acquired in the range of wavelength 400-1100 nm using a UV-vis spectrometer T70+. Four cuvettes made of optical glass with optical path 1 mm, 2 mm, 5 mm and 10 mm were first filled with CHCl₃:DMSO (9:1) mixture and used to acquire the baseline. Solvent was removed and cuvettes were refilled with K-PHI suspension in CHCl₃:DMSO (9:1). Transmittance of the suspension at 461 nm was used in the discussion.

In the second method, transmittance of K-PHI suspension (2.5 mg mL⁻¹) in CHCl₃:DMSO (9:1) was calculated by measuring the light intensity passed through the cuvette using blue light (461±20 nm, $I_0 = 10.6 \text{ mW cm}^{-2}$) from the external light source. Light source from Jasco FP-

8300 fluorescence spectrometer was used for this purpose. Excitation and emission bandwidths were set to 20 nm. Transmittance of the K-PHI suspension was calculated as $I/I_s \cdot 100\%$, where I – light intensity measured by the optical power meter after light passed through the cuvette filled with K-PHI suspension, mW cm^{-2} ; I_s – light intensity measured by the optical power meter after light passed through the cuvette filled with K-PHI CHCl_3 :DMSO (9:1) mixture, mW cm^{-2} . Supplementary Figure 86 shows the experimental setup for measurement of light intensity using a 5 mm cuvette as an example.

Flow photoreactor

Design of the flow photoreactor, i.e. tubings and fittings, used in this work is based on the reported in the literature.^[154]

The flow photoreactor consist of the following parts:

A. Light source. Self-adhesive LED stripe (Luminous Flux 1820 lm/m, distance between individual LEDs 8.4 mm, Input Voltage 12V DC, Current 4 A, Power 48 W, dominant wavelength 460 nm, length 500 mm) fabricated by JKL Components (Manufacturer Part No. ZFS-85000HD-B) were used as a light source. Three LED stripes were attached with the displacement between the leading ends of stripes ca. 120° to the home-made hollow steel cylinder (external diameter 140 mm, height 230 mm, wall thickness 1 mm) equipped with inlet and outlet (both with external diameter 8 mm, wall thickness 1 mm) for supplying cooling water. Each piece of the LED stripe is powered by a constant voltage LED driver (manufacturer Mean Well, Manufacturer Part No. LPV-60-12, Output voltage 12 V, Output current 5 A, Maximum output power 60 W). Total length of the LED stripe is 12.22 m, total number of LEDs 1437, output power at zero distance from the light source 18.5 mW cm^{-2} (Supplementary Figure 87).

B. Photoreactor. Photoreactor was made by wrapping the tubing (tetrafluorethylene/hexafluorpropylene copolymer (FEP), manufacturer Bohlender,

Manufacturer Part No. S1815-08, external diameter 3.2 mm (1/8"), internal diameter 1.6 mm (1/16")) around the glass beaker (purchased from Fischerbrand Catalogue No. FB33119, external diameter 170 mm, height 270 mm, capacity 5000 mL). Total length of the reactor is 35 m, volume 70 mL (Supplementary Figure 88).

C. Cooling module. Huber Ministatic cc (Manufacturer Peter Huber Kältemaschinen GmbH, Manufacturer Part No. 37791/98, temperature range $-25^{\circ}\text{C}...+125^{\circ}\text{C}$) was used.

D. External shell (Supplementary Figure 89). External shell of the photoreactor was made by wrapping aluminium foil around a glass beaker (purchased from Fischerbrand Catalogue No. FB33183, external diameter 217 mm, height 350 mm, capacity 10000 mL).

E. Reaction mixture supply module (Supplementary Figure 90). The module consists of Syringe pump (World Precision Instruments, Model No. AL-1600), 4 Luer Lock Syringes (Capacity 20 mL, manufacturer B. Braun, Manufacturer part No. 4606205V), 4 Luer Adapters (1/4-28 Female to Female Luer, Material Tefzel, Manufacturer Upchurch Scientific, Manufacturer Part No. UPP-678), 3 Tee Assemblies (for tubing 1/16", Material Tefzel, Manufacturer Upchurch Scientific, Manufacturer Part No. UPP-632), 8 Ferrules (for tubing 1/16", 1/4-28, Material Tefzel, Manufacturer Upchurch Scientific, Manufacturer Part No. UPP-200N), 8 Nuts (for tubing 1/16", 1/4-28, Material Tefzel, Manufacturer Upchurch Scientific, Manufacturer Part No. UPP-245), 1 Ferrule (for tubing 1/8", 1/4-28, Material Tefzel, Manufacturer Upchurch Scientific, Manufacturer Part No. UPP-300N), 1 Nut (for tubing 1/8", 1/4-28, Material Tefzel, Manufacturer Upchurch Scientific, Manufacturer Part No. UPP-345), 6 pieces of FEP tubing (tetrafluorethylene/hexafluorpropylene copolymer (FEP), manufacturer Bohlender, Manufacturer Part No. S 1815-04, external diameter 3.2 mm (1/16"), internal diameter 1.6 mm (1/32"), total length ca. 500 mm), 1 piece of FEP tubing (tetrafluorethylene/hexafluorpropylene copolymer (FEP), manufacturer Bohlender, Manufacturer Part No. S1815-08, external diameter 3.2 mm (1/8"), internal diameter 1.6 mm (1/16"), length ca. 500 mm).

F. Photocatalyst supply module (Supplementary Figure 91). The module consists of Syringe pump (KD Scientific, Model No. 789100B), Magnetic stirrer (IKA RCT classic), PTFE coated magnetic stir bar (Length 15 mm, Diameter 5 mm, manufacturer Bohlender, Manufacturer Part No. C354-08), 1 Luer Lock Syringe (Capacity 20 mL, manufacturer B. Braun, Manufacturer part No. 4606205V), 1 T-connector (Manufacturer Kinesis, Manufacturer Part No. 001109, Material PTFE), 1 Luer adaptor (Female Luer to 1/4-28, Material Tefzel, Manufacturer Upchurch Scientific, Manufacturer Part No. P-624), 2 Ferrules (for tubing 1/8", 1/4-28, Material Tefzel, Manufacturer Upchurch Scientific, Manufacturer Part No. UPP-300N), 2 Nuts (for tubing 1/8", 1/4-28, Material Tefzel, Manufacturer Upchurch Scientific, Manufacturer Part No. UPP-345).

G. Reaction mixture receiver. Glass vials or flask.

Photoreactor assembly.

Cooling water inlet of the light source (A) was connected to the cooling module outlet (C) using PVC tubing (inner diameter 8 mm, outer diameter 12 mm, length ca. 1.5 m, Purchased from Carl Roth GmbH & Co. KG). Outlet of the light source (A) was connected to the cooling module inlet (C) using PVC tubing (inner diameter 8 mm, outer diameter 12 mm, length ca. 5 m, Purchased from Carl Roth GmbH & Co. KG). Longer piece of the PVC tubing was wrapped around the photoreactor (B). The photoreactor (B) and the PVC tubing was placed inside the external shell (C). Deionized water was added to the space between the external shell (C) and the photoreactor (B) until all FEP tubing of the photoreactor (B) is completely covered with water. Outlet of the photoreactor (B) was placed into the reaction mixture receiver (G). Inlet of the photoreactor (B) was connected to the outlet of the photocatalyst supply module (F). Inlet of the photocatalyst supply module (F) was connected to the outlet of the reaction mixture supply module (E).

Synthesis of dichloroketone 2a in flow photoreactor.

The syringes of the reaction mixture supply module (E) were first filled with a homogeneous solution prepared by mixing 520 mg of chalcone 2a, 3.35 mL of TEOA in 100 mL of CHCl₃/DMSO (6:4) solution. The syringe of the photocatalyst supply module (F) was filled with a dispersion of K-PHI in DMSO (10 mg/mL), previously sonicated for 20 minutes for optimal dispersion. Stirring bar was added to the syringe. The syringe was fixed into the syringe pump. The stirring plate was turned on in order to maintain K-PHI suspended. The cooling system was turned on, while the temperature was set to 20 °C. The space between the photoreactor (B) and external shell (D) was filled with deionized water. The light source (A) was turned on. The flow rate of the reaction mixture supply module (E) syringe pump was set to 8 mL h⁻¹ and the pump was enabled. When the reaction mixture solution reached the T-connector of the photocatalyst supply module (F), the flow rate of the syringe pump was set to 2 mL h⁻¹ and the pump was enabled. After passing through the flowreactor (reaction time of 7 hours), the solution was collected into glass vials for 1 h 30 min. Fractions between minutes 30 and 60 were combined and analyzed by GC-MS to give 57% yield.

General method for chalcone (1a-j) preparation

To a mixture of acetophenone (1g, 8.3mmol) and corresponding aldehyde (9.1mmol) in 50 mL of mixture methanol/water (1:4), solution of sodium hydroxide (667mg, 16.6mmol) in 2 ml of water was added dropwise at room temperature and resulted solution was stirred for 20 hours at room temperature, in case of chalcones **1c,j** or 20 hours at reflux. Then reaction mixture was cooled to room temperature and for chalcones **1a-f,h** 50ml of water was added, obtained precipitate was filtered, washed with water (3 x 15ml) then with 10ml of mixture water/ethanol (4:1) and dried on air to give product as solid material. In case of chalcones **1g**, precipitate after filtration was redissolved in 30ml of mixture ethanol and aq. (2N) hydrochloride acid (1:1) and refluxed for 2 hours, then cooled to room temperature, diluted

with 50ml of water and obtained precipitate was filtered, washed with water (3 x 15ml) then with 10ml of mixture water/ethanol (4:1) then dried on air to give product as solid material.

Preparation of chalkone 1k

To stirring mixture of benzaldehyde (12g, 0.11mol) and acetone (40g, 0.68mol) in water (20ml), aqueous (20%) solution of sodium hydroxide (1.5ml) was added dropwise at 25°C. after addition reaction mixture was stirred for another 2 hours at 25°C. Then mixture was diluted with water (100ml) and acidified with aq. (2N) hydrochloride acid to pH=5, then extracted with chloroform (3 x 15ml), all organic solutions were combined, washed with brine (2 x 10ml), dried over Na₂SO₄. Residue after evaporation was redissolved in 50ml of mixture ethanol and aq. (2N) hydrochloride acid (1:1) and refluxed for 2 hours. Then cooled to room temperature, diluted with 50ml of water, extracted with chloroform (3 x 15ml), all organic solutions were combined, washed with brine (2 x 10ml), dried over Na₂SO₄, evaporated to give as residue orange oil, vacuum distillation of which gives pure chalcone 1k (yield 74%).

General method for chalcone (1m, n, o, p, q) preparation

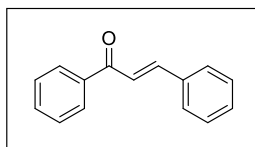
To a 100 mL flask, the corresponding aldehyde (10,4 mmol) and acetophenone (10.5 mmol, 1.22 mL) are stirred in 30 mL of EtOH. Then the solutions is kept at 0 °C with an ice bath and slowly added an aqueous solution of NaOH (0.8g in 30 mL). The solution is then stirred at room temperature for 3 hours. The precipitate formed is then filtered, washed with water and ethanol. Finally the solid obtained is purified by recrystallization in ethanol.

Preparation of chalkone 1r

In a flask charged with CH₃OH (0.5 mL), NaOH (1 N, 5.8 mL) and picolinaldehyde (1.80 mL, 1.0 equiv.) at 0 °C, it was added acetophenone (1.1 mL, 0.5 equiv). The solution was left to

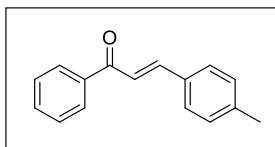
react overnight. Then ice water (10 mL) was added and the mixture was stirred vigorously. The resulting solid was filtered, washed with cold water, dried and purified by silica gel column chromatography (EtOAc/hexanes) to provide compound 1o (1.4 g, 76% yield) as a pale yellow solid.

(E)-chalcone (1a).^[258]



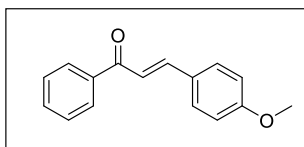
Yellowish solid (yield 73%). ¹H NMR (400 MHz, CDCl₃) δ 8.03 (dd, *J* = 8.3, 1.3 Hz, 2H), 7.82 (d, *J* = 15.7 Hz, 1H), 7.65 (dd, *J* = 6.8, 2.8 Hz, 2H), 7.60 (t, *J* = 7.3 Hz, 1H), 7.57 – 7.49 (m, 3H), 7.45 – 7.40 (m, 3H). ¹³C NMR (101 MHz, CDCl₃) δ 190.5, 144.8, 138.2, 134.9, 132.8, 130.5, 128.9, 128.6, 128.5, 128.4, 122.1.

(E)-1-phenyl-3-(p-tolyl)prop-2-en-1-one (1b).^[259]



Yellowish solid (yield 82%). ¹H NMR (400 MHz, Chloroform-*d*) δ 8.05 – 8.00 (m, 2H), 7.81 (d, *J* = 15.7 Hz, 1H), 7.62 – 7.47 (m, 6H), 7.23 (d, *J* = 8.0 Hz, 2H), 2.40 (s, 3H). ¹³C NMR (101 MHz, CDCl₃) δ 190.7, 145.0, 141.1, 138.3, 132.7, 132.1, 129.7, 128.6, 128.5, 128.5, 121.1, 21.6.

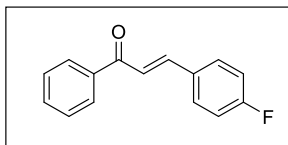
(E)-3-(4-methoxyphenyl)-1-phenylprop-2-en-1-one (1c).^[258]



Yellowish solid (yield 82%). ¹H NMR (400 MHz, CDCl₃) δ 8.01 (dd, *J* = 8.3, 1.3 Hz, 2H), 7.79 (d, *J* = 15.6 Hz, 1H), 7.63 – 7.55 (m, 3H), 7.49 (t, *J* = 7.4 Hz, 2H), 7.42 (d, *J* = 15.6 Hz, 1H), 6.93

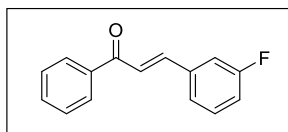
(d, $J = 8.8$ Hz, 2H), 3.85 (s, 3H). ^{13}C NMR (101 MHz, CDCl_3) δ 190.6, 161.7, 144.7, 138.5, 132.6, 130.28, 128.6, 128.4, 127.6, 119.7, 114.4, 55.5.

(E)-3-(4-fluorophenyl)-1-phenylprop-2-en-1-one (1d).^[260]



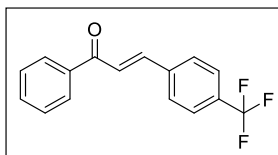
White solid (yield 85%). ^1H NMR (400 MHz, CDCl_3) δ 8.03 – 8.01 (m, 2H), 7.78 (d, $J = 15.7$ Hz, 1H), 7.69 – 7.55 (m, 3H), 7.54 – 7.41 (m, 3H), 7.12 (t, $J = 8.6$ Hz, 2H). ^{13}C NMR (101 MHz, CDCl_3) δ 190.35, 164.07 (d, $J = 251.9$ Hz), 143.56, 138.11, 132.90, 131.13 (d, $J = 3.4$ Hz), 130.38 (d, $J = 8.5$ Hz), 128.69, 128.50, 121.74 (d, $J = 2.3$ Hz), 116.17 (d, $J = 21.9$ Hz).

(E)-3-(3-fluorophenyl)-1-phenylprop-2-en-1-one (1e).



White solid (yield 80%). ^1H NMR (400 MHz, Chloroform- d) δ 8.06 – 8.00 (m, 2H), 7.76 (d, $J = 15.7$ Hz, 1H), 7.64 – 7.57 (m, 1H), 7.57 – 7.47 (m, 3H), 7.44 – 7.32 (m, 3H), 7.12 (t, $J = 8.9$ Hz, 1H). ^{13}C NMR (101 MHz, Chloroform- d) δ 190.19, 163.05 (d, $J = 246.9$ Hz), 143.32 (d, $J = 2.7$ Hz), 137.92, 137.13 (d, $J = 7.6$ Hz), 133.05, 130.54 (d, $J = 8.3$ Hz), 128.73, 128.55, 124.60 (d, $J = 2.8$ Hz), 123.16, 117.41 (d, $J = 21.5$ Hz), 114.49 (d, $J = 21.9$ Hz).

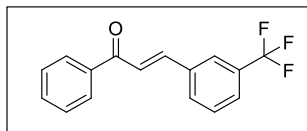
(E)-1-phenyl-3-(4-(trifluoromethyl)phenyl)prop-2-en-1-one (1f).^[261]



White solid (yield 81%). ^1H NMR (400 MHz, CDCl_3) δ 8.04 (d, $J = 7.5$ Hz, 2H), 7.81 (d, $J = 15.7$ Hz, 1H), 7.77 – 7.65 (m, 4H), 7.62 – 7.58 (m, 2H), 7.54 – 7.51 (m, 2H). ^{13}C NMR (101 MHz,

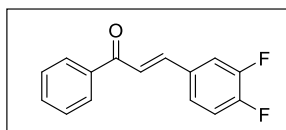
CDCl₃) δ 190.1, 142.8, 138.3, 137.8, 133.2, 131.9 (q, J = 32.3 Hz), 128.8, 128.6, 128.5, 125.9 (q, J = 4 Hz), 124.2, 123.8 (q, J = 272 Hz).

(E)-1-phenyl-3-(3-(trifluoromethyl)phenyl)prop-2-en-1-one (1g).^[262]



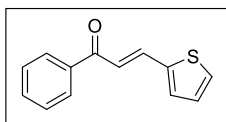
White solid (yield 78%). ¹H NMR (400 MHz, Chloroform-*d*) δ 8.07 – 8.02 (m, 2H), 7.89 (s, 1H), 7.85 – 7.79 (m, 2H), 7.69 – 7.50 (m, 6H). ¹³C NMR (101 MHz, CDCl₃) δ 190.05, 142.87, 137.79, 135.66, 133.16, 131.68, 131.50 (q, J = 32.3 Hz), 129.56, 128.77, 128.59, 126.87 (q, J = 4 Hz), 124.70 (q, J = 4 Hz), 123.82 (q, J = 273.7 Hz), 123.61.

(E)-3-(3,4-difluorophenyl)-1-phenylprop-2-en-1-one (1h).



White solid (yield 78%). ¹H NMR (400 MHz, Chloroform-*d*) δ 8.04 – 7.99 (m, 2H), 7.71 (d, J = 15.7 Hz, 1H), 7.63 – 7.58 (m, 1H), 7.55 – 7.42 (m, 4H), 7.40 – 7.34 (m, 1H), 7.21 (dt, J = 9.7, 8.3 Hz, 1H). ¹³C NMR (101 MHz, Chloroform-*d*) δ 189.94, 151.64 (dd, J = 254.5, 13.1 Hz), 150.66 (dd, J = 250.5, 13.1 Hz), 142.36 (t, J = 2.0 Hz), 137.84, 133.11, 132.13 (dd, J = 5.9, 4.0 Hz), 128.75, 128.53, 125.36 (dd, J = 6.6, 3.4 Hz), 122.83 (d, J = 2.4 Hz), 117.94 (d, J = 17.7 Hz), 116.51 (d, J = 17.6 Hz).

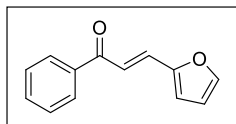
(E)-1-phenyl-3-(thiophen-2-yl)prop-2-en-1-one (1j).^[263]



Orange solid (yield 68%). ¹H NMR (400 MHz, CDCl₃) δ 8.01 (dd, J = 8.3, 1.3 Hz, 2H), 7.95 (d, J = 15.3 Hz, 1H), 7.61 – 7.55 (m, 1H), 7.53 – 7.47 (m, 2H), 7.43 (d, J = 5.0 Hz, 1H), 7.37 (d, J =

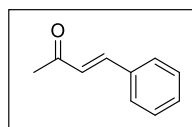
5.0 Hz, 2H), 7.10 (dd, $J = 5.0, 3.6$ Hz, 1H). ^{13}C NMR (101 MHz, CDCl_3) δ 189.9, 140.4, 138.1, 137.3, 132.8, 132.2, 128.9, 128.7, 128.43, 128.41, 120.7.

(E)-1-phenyl-3-(thiophen-2-yl)prop-2-en-1-one (1k)^[263]



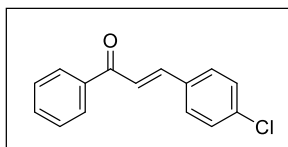
Orange oil (yield 62%). ^1H NMR (400 MHz, CDCl_3) δ 8.06 – 8.00 (m, 2H), 7.64 – 7.43 (m, 6H), 6.72 (d, $J = 3.4$ Hz, 1H), 6.52 (dd, $J = 3.4, 1.8$ Hz, 1H). ^{13}C NMR (101 MHz, CDCl_3) δ 189.9, 151.7, 145.0, 138.2, 132.9, 130.8, 128.7, 128.5, 119.3, 116.4, 112.8.

(E)-4-phenylbut-3-en-2-one (1l)^[264]



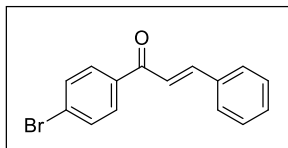
Yellow solid (yield 74%). ^1H NMR (400 MHz, Chloroform- d) δ 7.57 – 7.49 (m, 3H), 7.43 – 7.38 (m, 3H), 6.72 (d, $J = 16.3$ Hz, 1H), 2.39 (s, 3H). ^{13}C NMR (101 MHz, CDCl_3) δ 198.54, 143.52, 134.39, 130.57, 129.00, 128.28, 127.14, 27.56.

(E)-3-(4-chlorophenyl)-1-phenylprop-2-en-1-one (1m)



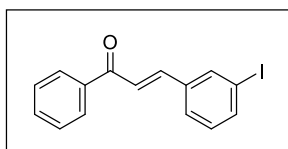
Pale yellow solid (69% yield). ^1H NMR (400 MHz, Chloroform- d) δ 8.05 – 7.99 (m, 1H), 7.76 (d, $J = 15.7$ Hz, 1H), 7.63 – 7.56 (m, 2H), 7.55 – 7.49 (m, 2H), 7.42 – 7.38 (m, 1H). ^{13}C NMR (101 MHz, CDCl_3) δ 190.41, 143.49, 138.14, 136.58, 133.49, 133.10, 129.75, 129.40, 128.83, 128.65, 122.56.

(E)-1-(4-bromophenyl)-3-phenylprop-2-en-1-one (1n)



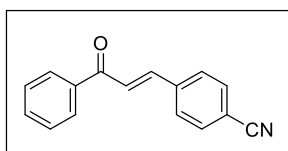
Pale yellow solid (64% yield). ^1H NMR (400 MHz, Chloroform-d) δ 7.93 – 7.87 (m, 1H), 7.82 (d, J = 15.7 Hz, 1H), 7.70 – 7.61 (m, 2H), 7.48 (d, J = 15.7 Hz, 1H), 7.45 – 7.41 (m, 2H). ^{13}C NMR (101 MHz, CDCl_3) δ 189.57, 145.59, 137.03, 134.79, 132.08, 130.93, 130.18, 129.16, 128.67, 128.06, 121.57.

(E)-3-(4-iodophenyl)-1-phenylprop-2-en-1-one (1o)



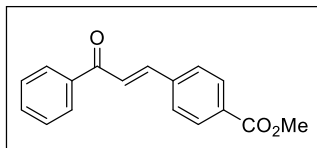
Pale yellow solid (47%). ^1H NMR (400 MHz, Chloroform-d) δ 8.05 – 7.98 (m, 1H), 7.77 – 7.66 (m, 1H), 7.64 – 7.56 (m, 1H), 7.55 – 7.48 (m, 1H), 7.16 (t, J = 7.8 Hz, 0H). ^{13}C NMR (101 MHz, CDCl_3) δ 190.24, 143.06, 139.33, 138.01, 137.19, 136.94, 133.18, 130.73, 128.85, 128.69, 127.98, 123.23, 94.93.

(E)-4-(3-oxo-3-phenylprop-1-en-1-yl)benzonitrile (1p)



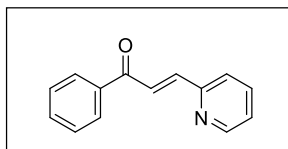
Pale yellow solid (53% yield). ^1H NMR (400 MHz, Chloroform-d) δ 8.06 – 8.01 (m, 1H), 7.78 (d, J = 15.7 Hz, 0H), 7.76 – 7.70 (m, 2H), 7.65 – 7.58 (m, 1H), 7.53 (ddt, J = 8.2, 6.6, 1.2 Hz, 1H). ^{13}C NMR (101 MHz, CDCl_3) δ 189.91, 142.68, 142.24, 139.32, 137.72, 133.47, 132.85, 128.95, 128.85, 128.72, 125.16, 118.56, 113.63, 109.59.

methyl (E)-4-(3-oxo-3-phenylprop-1-en-1-yl)benzoate (1q)



White solid (43% yield). ^1H NMR (400 MHz, Chloroform- d) δ 8.11 – 8.06 (m, 1H), 8.06 – 8.01 (m, 1H), 7.82 (d, J = 15.8 Hz, 1H), 7.74 – 7.68 (m, 1H), 7.65 – 7.58 (m, 1H), 7.56 – 7.48 (m, 1H), 3.95 (s, 2H). ^{13}C NMR (101 MHz, CDCl_3) δ 120.32, 96.61, 73.38, 69.24, 67.99, 63.24, 61.65, 60.30, 58.88, 58.71, 58.40, 54.23.

(E)-1-phenyl-3-(pyridin-3-yl)prop-2-en-1-one (1r)^[265]

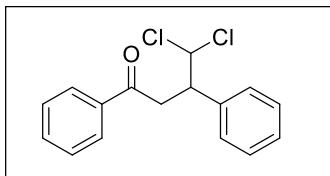


Pale yellow solid (yield 76%). ^1H NMR (400 MHz, Chloroform- d) δ 8.71 – 8.66 (m, 1H), 8.17 – 8.06 (m, 3H), 7.81 – 7.71 (m, 2H), 7.63 – 7.55 (m, 1H), 7.55 – 7.46 (m, 3H), 7.30 (ddd, J = 7.7, 4.8, 1.2 Hz, 1H). ^{13}C NMR (101 MHz, CDCl_3) δ 190.55, 153.22, 150.21, 142.79, 137.89, 137.11, 133.22, 128.86, 128.77, 125.69, 125.59, 124.58.

General method for γ,γ -dichloroketones (2a-r) preparation

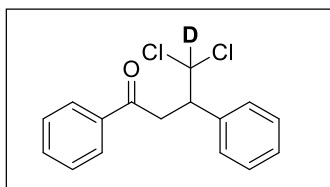
A glass tube with rubber-lined cap was evacuated and filled with argon three times. To this tube triethanolamine (74.6 mg, 66 μL , 0.5 mmol), corresponding chalcone (50 μmol), K-PHI (5 mg) and chloroform (2 mL) were added. Resulting mixture was stirred at 50°C under irradiation with Blue LED ($\lambda=461\text{nm}$) for 20 hours. Then reaction mixture was cooled to room temperature and centrifuged, clear solution was separated and solid residue was washed with chloroform (2 mL) and centrifuged again. Organic solutions were combined and evaporated to dryness. Residue after evaporation was purified by silica gel column chromatography using mixture of hexane/diethyl ether (98:2) as an eluent.

4,4-dichloro-1,3-diphenylbutan-1-one (2a)



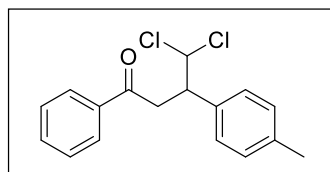
Yellow oil (yield 88%). ^1H NMR (400 MHz, Acetonitrile- d_3) δ 8.00 – 7.95 (m, 2H), 7.64 – 7.59 (m, 1H), 7.53 – 7.47 (m, 2H), 7.43 – 7.38 (m, 2H), 7.36 – 7.27 (m, 3H), 6.28 (d, J = 4.9 Hz, 1H), 4.10 (dt, J = 9.3, 4.9 Hz, 1H), 3.87 – 3.67 (m, 2H). ^{13}C NMR (101 MHz, CD_3CN) δ 197.2, 138.4, 136.7, 133.4, 129.3, 128.7, 128.3, 128.0, 127.8, 77.1, 50.8, 39.4. Elemental analysis calculated for $\text{C}_{16}\text{H}_{14}\text{ClO}_2$ Cl 24.18 found 24.77 ± 0.01 . GC-MS: m/z 221.2 [M-2HCl]

4,4-dichloro-1,3-diphenylbutan-1-one (2a-d₁)



Yellow oil. ^1H NMR (400 MHz, Acetonitrile- d_3) δ 8.01 – 7.93 (m, 2H), 7.65 – 7.59 (m, 1H), 7.53 – 7.47 (m, 2H), 7.43 – 7.39 (m, 2H), 7.36 – 7.26 (m, 3H), 4.09 (dd, J = 8.7, 4.9 Hz, 1H), 3.87 – 3.66 (m, 2H). ^{13}C NMR (101 MHz, CD_3CN) δ 198.10, 139.25, 137.58, 134.31, 130.18, 129.61, 129.14, 128.90, 128.65, 78.01-77.46 (t, J = 27.866 Hz), 51.54, 40.31.

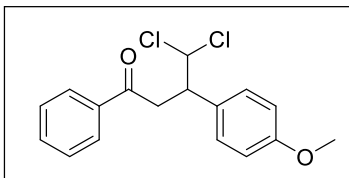
4,4-dichloro-1-phenyl-3-(p-tolyl)butan-1-one (2b)



Yellow oil (yield 89%). ^1H NMR (400 MHz, Acetonitrile- d_3) δ 7.99 – 7.94 (m, 2H), 7.64 – 7.59 (m, 1H), 7.52 – 7.47 (m, 2H), 7.30 – 7.26 (m, 2H), 7.14 (d, J = 7.9 Hz, 2H), 6.25 (d, J = 4.8 Hz, 1H), 4.05 (dt, J = 9.2, 4.8 Hz, 1H), 3.85 – 3.63 (m, 2H), 2.29 (s, 3H). ^{13}C NMR (101 MHz, CD_3CN)

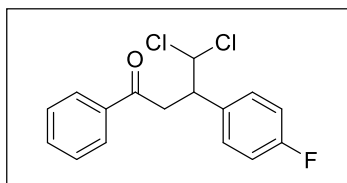
δ 197.3, 137.6, 136.7, 135.3, 133.4, 129.2, 128.9, 128.7, 128.0, 77.3, 50.4, 39.4, 20.1. GC-MS: m/z 234.1 [M-2HCl]

4,4-dichloro-3-(4-methoxyphenyl)-1-phenylbutan-1-one (2c)



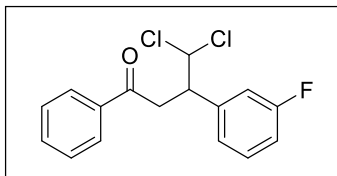
Yellow oil (yield 83%). ^1H NMR (400 MHz, Acetonitrile- d_3) δ 7.99 (d, $J = 7.2$ Hz, 2H), 7.68 – 7.62 (m, 1H), 7.53 (t, $J = 7.7$ Hz, 2H), 7.38 – 7.32 (m, 2H), 6.93 – 6.86 (m, 2H), 6.26 (d, $J = 4.7$ Hz, 1H), 4.07 (dt, $J = 9.1, 4.8$ Hz, 1H), 3.84 – 3.76 (m, 4H), 3.70 (dd, $J = 17.8, 5.0$ Hz, 1H). ^{13}C NMR (101 MHz, CD_3CN) δ 197.3, 159.2, 136.7, 133.4, 130.4, 130.1, 128.7, 128.0, 113.5, 77.5, 54.9, 50.0, 39.4. GC-MS: m/z 250.1 [M-2HCl]

4,4-dichloro-3-(4-fluorophenyl)-1-phenylbutan-1-one (2d)



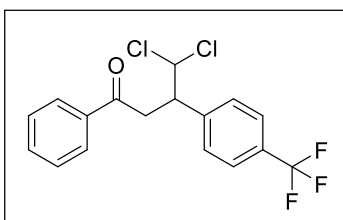
Yellow oil (yield 84%). ^1H NMR (400 MHz, Acetonitrile- d_3) δ 8.00 (dd, $J = 8.4, 1.3$ Hz, 2H), 7.68 – 7.62 (m, 1H), 7.56 – 7.50 (m, 2H), 7.49 – 7.44 (m, 2H), 7.14 – 7.07 (m, 2H), 6.29 (d, $J = 4.7$ Hz, 1H), 4.13 (dt, $J = 8.4, 5.0$ Hz, 1H), 3.85 – 3.70 (m, 2H). ^{13}C NMR (101 MHz, Acetonitrile- d_3) δ 197.1, 162.2 (d, $J = 244.2$ Hz), 136.6, 134.3 (d, $J = 3.3$ Hz), 133.5, 131.2 (d, $J = 8.2$ Hz), 128.7, 128.0, 114.9 (d, $J = 21.5$ Hz), 76.9, 49.9, 39.7. ^{19}F NMR (376 MHz, Acetonitrile- d_3) δ -116.45 (tt, $J = 8.9, 5.4$ Hz). GC-MS: m/z 238.1 [M-2HCl]

4,4-dichloro-3-(3-fluorophenyl)-1-phenylbutan-1-one (2e)



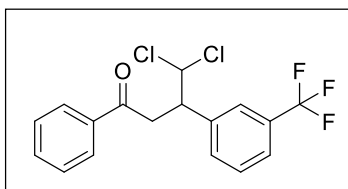
Yellow oil (yield 80%). ^1H NMR (400 MHz, Acetonitrile- d_3) δ 8.01 (dt, $J = 8.5, 1.6$ Hz, 2H), 7.68 – 7.63 (m, 1H), 7.56 – 7.51 (m, 2H), 7.38 (td, $J = 8.0, 6.2$ Hz, 1H), 7.28 (d, $J = 7.8$ Hz, 1H), 7.23 (dt, $J = 10.5, 2.1$ Hz, 1H), 7.11 – 7.03 (m, 1H), 6.31 (d, $J = 4.8$ Hz, 1H), 4.15 (dt, $J = 8.5, 5.0$ Hz, 1H), 3.88 – 3.72 (m, 2H). ^{13}C NMR (101 MHz, Acetonitrile- d_3) δ 196.9, 162.4 (d, $J = 243.4$ Hz), 141.1 (d, $J = 7.4$ Hz), 136.6, 133.5, 130.0 (d, $J = 8.3$ Hz), 128.7, 128.0, 125.5 (d, $J = 2.8$ Hz), 116.1 (d, $J = 22.2$ Hz), 114.5 (d, $J = 21.1$ Hz), 76.5, 50.3, 39.5. ^{19}F NMR (376 MHz, Acetonitrile- d_3) δ -114.90 – 115.03 (m). GC-MS: m/z 238.1 [M-2HCl]

4,4-dichloro-1-phenyl-3-(4-(trifluoromethyl)phenyl)butan-1-one ((2f))



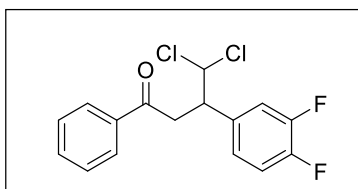
Yellow oil (yield 85%). ^1H NMR (400 MHz, Acetonitrile- d_3) δ 8.00 – 7.95 (m, 2H), 7.68 – 7.59 (m, 5H), 7.53 – 7.47 (m, 2H), 6.32 (d, $J = 4.8$ Hz, 1H), 4.20 (dt, $J = 8.9, 4.9$ Hz, 1H), 3.89 – 3.73 (m, 2H). ^{13}C NMR (101 MHz, CD_3CN) δ 196.8, 142.9, 136.5, 133.5, 130.2, 129.1 (q, $J = 37$ Hz), 128.7, 128.0, 125.0 (q, $J = 4$ Hz), 124.3 (q, $J = 37$ Hz), 76.3, 50.4, 39.6. ^{19}F NMR (376 MHz, Acetonitrile- d_3) δ -114.90 – 115.03 (m). GC-MS: m/z 288.1 [M-2HCl]

4,4-dichloro-1-phenyl-3-(3-(trifluoromethyl)phenyl)butan-1-one (2g)



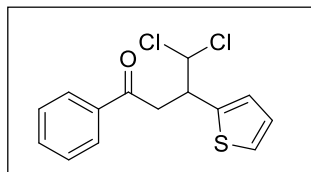
Yellow oil (yield 82%). ^1H NMR (400 MHz, Acetonitrile- d_3) δ 8.02 – 7.94 (m, 2H), 7.77 (s, 1H), 7.70 (d, $J = 7.7$ Hz, 1H), 7.65 – 7.60 (m, 2H), 7.56 – 7.47 (m, 3H), 6.32 (d, $J = 4.8$ Hz, 1H), 4.20 (dt, $J = 8.3, 5.0$ Hz, 1H), 3.90 – 3.72 (m, 2H). ^{13}C NMR (101 MHz, CD_3CN) δ 196.89, 139.58, 136.49, 133.53, 133.40, 129.72 (q, $J = 32.3$ Hz), 129.03, 128.72, 128.39, 128.05, 126.20 (q, $J = 4$ Hz), 124.53 (q, $J = 4$ Hz), 124.34 (q, $J = 273$ Hz), 76.38, 50.35, 39.59. ^{19}F NMR (376 MHz, cd_3cn) δ -63.03. GC-MS: m/z 288.1 [M-2HCl]

4,4-dichloro-3-(3,4-difluorophenyl)-1-phenylbutan-1-one (2h)



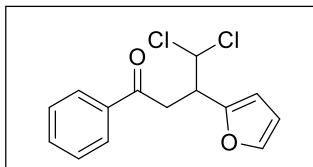
Yellow oil (yield 70%). ^1H NMR (400 MHz, Acetonitrile- d_3) δ 8.02 – 7.94 (m, 2H), 7.65 – 7.60 (m, 1H), 7.53 – 7.48 (m, 2H), 7.42 – 7.34 (m, 1H), 7.26 – 7.21 (m, 2H), 6.26 (d, $J = 4.7$ Hz, 1H), 4.10 (dt, $J = 7.8, 5.2$ Hz, 1H), 3.76 – 3.71 (m, 2H). ^{13}C NMR (101 MHz, CD_3CN) δ 196.8, 150.8 (m), 148.4 (m), 136.5, 135.7 (m), 128.7, 128.0, 126.2 (m), 118.4 (d, $J = 18.2$ Hz), 116.9, 118.4 (d, $J = 17.2$ Hz), 76.4, 49.7, 39.7. ^{19}F NMR (376 MHz, Acetonitrile- d_3) δ -140.02 – 140.20 (m), -141.30 – 141.47 (m). GC-MS: m/z 256.1 [M-2HCl]

4,4-dichloro-1-phenyl-3-(thiophen-2-yl)butan-1-one (2i)



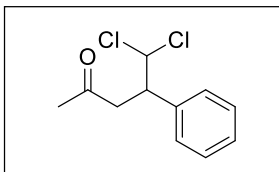
Yellow oil (yield 54%). ^1H NMR (400 MHz, Acetonitrile- d_3) δ 8.01 – 7.96 (m, 2H), 7.66 – 7.60 (m, 1H), 7.54 – 7.48 (m, 2H), 7.32 (dd, J = 5.1, 1.2 Hz, 1H), 7.13 – 7.09 (m, 1H), 6.99 (dd, J = 5.1, 3.6 Hz, 1H), 6.31 (d, J = 3.7 Hz, 1H), 4.42 (dt, J = 8.4, 4.2 Hz, 1H), 3.84 – 3.63 (m, 2H). ^{13}C NMR (101 MHz, CD_3CN) δ 196.7, 140.4, 136.5, 133.6, 128.8, 128.1, 127.5, 126.7, 125.4, 76.6, 46.1, 41.0.

4,4-dichloro-3-(furan-2-yl)-1-phenylbutan-1-one (2j)



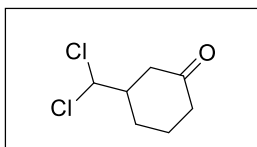
Yellow oil (yield 72%). ^1H NMR (400 MHz, Acetonitrile- d_3) δ 8.01 (d, J = 7.2 Hz, 2H), 7.67 – 7.62 (m, 1H), 7.52 (t, J = 7.7 Hz, 2H), 7.45 – 7.42 (m, 1H), 6.37 (dd, J = 3.2, 1.8 Hz, 1H), 6.33 (d, J = 3.2 Hz, 1H), 6.30 (d, J = 3.8 Hz, 1H), 4.28 – 4.19 (m, 1H), 3.78 (dd, J = 18.0, 8.8 Hz, 1H), 3.61 (dd, J = 18.0, 4.3 Hz, 1H). ^{13}C NMR (101 MHz, CD_3CN) δ 196.8, 151.9, 142.3, 136.5, 133.5, 128.8, 128.1, 110.6, 108.4, 75.2, 44.8, 37.8.

5,5-dichloro-4-phenylpentan-2-one (2k)



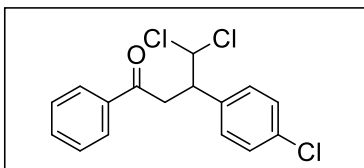
Yellow oil (yield 54%). ^1H NMR (400 MHz, Acetonitrile- d_3) δ 7.39 – 7.26 (m, 5H), 6.16 (d, J = 4.8 Hz, 1H), 3.93 – 3.81 (m, 1H), 3.19 (dd, J = 6.8, 2.8 Hz, 2H), 2.07 (s, 3H). ^{13}C NMR (101 MHz, CD_3CN) δ 206.1, 138.2, 129.2, 128.3, 127.8, 77.0, 50.3, 43.8, 29.6. GC-MS: m/z 194.1 [$\text{M}-\text{HCl}$]

3-(dichloromethyl)cyclohexan-1-one (2l)



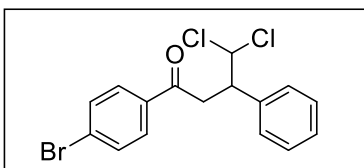
Yellow oil (yield 78%). ^1H NMR (400 MHz, Chloroform-*d*) δ 5.79 (d, $J = 2.9$ Hz, 1H), 2.70 – 2.62 (m, 1H), 2.50 – 2.38 (m, 3H), 2.32 (td, $J = 14.2, 13.6, 6.3$ Hz, 1H), 2.22 – 2.10 (m, 2H), 1.76 – 1.64 (m, 2H). ^{13}C NMR (101 MHz, CDCl_3) δ 209.2, 76.4, 48.5, 42.8, 40.9, 26.8, 23.9. GC-MS: m/z 180.0

4,4-dichloro-3-(4-chlorophenyl)-1-phenylbutan-1-one (2m)



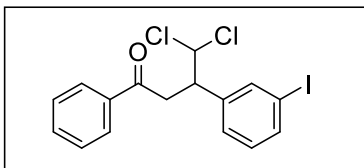
Yellow oil. ^1H NMR (400 MHz, Chloroform-*d*) δ 8.00 – 7.94 (m, 1H), 7.62 – 7.57 (m, 1H), 7.51 – 7.44 (m, 1H), 7.31 (s, 2H), 6.08 (d, $J = 4.0$ Hz, 0H), 4.13 (ddd, $J = 8.0, 5.4, 4.0$ Hz, 1H), 3.80 – 3.63 (m, 1H). ^{13}C NMR (101 MHz, CDCl_3) δ 196.78, 136.48, 134.06, 133.77, 133.50, 130.56, 129.04, 128.91, 128.82, 128.73, 128.20. GC-MS: m/z 254.1 [M-2HCl]

1-(4-bromophenyl)-4,4-dichloro-3-phenylbutan-1-one (2n)



Yellow oil. ^1H NMR (400 MHz, Chloroform-*d*) δ 7.86 – 7.80 (m, 1H), 7.64 – 7.59 (m, 1H), 7.38 – 7.29 (m, 2H), 6.09 (d, $J = 4.1$ Hz, 0H), 4.14 (ddd, $J = 7.7, 5.5, 4.1$ Hz, 1H), 3.76 – 3.63 (m, 1H). ^{13}C NMR (101 MHz, CDCl_3) δ 196.10, 137.95, 135.38, 132.31, 132.22, 132.17, 130.75, 130.24, 130.15, 129.73, 129.05, 129.00, 128.85, 128.70, 128.42, 128.21. GC-MS: m/z 298 [M-2HCl]

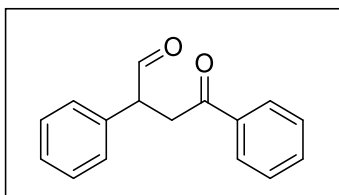
4,4-dichloro-3-(3-iodophenyl)-1-phenylbutan-1-one (2o)



Yellow oil. ^1H NMR (400 MHz, Chloroform- d) δ 8.03 – 7.93 (m, 1H), 7.73 (t, J = 1.8 Hz, 1H), 7.66 – 7.57 (m, 1H), 7.52 – 7.46 (m, 1H), 7.36 (dt, J = 7.7, 1.4 Hz, 1H), 7.07 (t, J = 7.8 Hz, 1H), 6.08 (d, J = 4.0 Hz, 1H), 4.09 (ddd, J = 7.8, 5.3, 4.0 Hz, 1H), 3.82 – 3.61 (m, 1H). ^{13}C NMR (101 MHz, CDCl_3) δ 196.67, 140.39, 138.08, 137.24, 136.48, 133.78, 130.27, 128.91, 128.58, 128.23, 94.49. GC-MS: m/z 346.0 [M-2HCl]

Preparation of *dichloro-ketone* derived compound (3-6a)

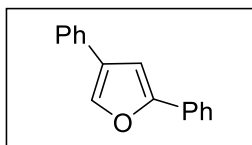
4-oxo-2,4-diphenylbutanal (3a)



In a sealed glass tube, it was added 4,4-dichloro-1,3-diphenylbutan-1-one (2a) (0.05 mmol, 14.66 mg), KOH (100 mg), EtOH (3 mL). The reaction vessel has then been kept to react for 1 hour in an oil bath at 100 °C. After, the reaction was left to cool down to room temperature. Afterwards, ice was added to the reaction mixture before adding concentrated HCl. The mixture was then neutralized with NaHCO_3 and extracted with EtOAc and washed with brine. Collected organic solutions were evaporated, dissolved in CH_2Cl_2 and dried over Na_2SO_4 . At this stage, the yield of 3a was recorded measuring ^1H NMR with 1,3,5-trimethoxybenzene as internal standard. The crude obtained has been purified with a chromatographic column Hexane/EtOAc (9:1).

Yellow oil (yield 60%). ^1H NMR (400 MHz, Chloroform- d) δ 9.81 (d, J = 0.7 Hz, 1H), 7.98 (dd, J = 8.4, 1.4 Hz, 2H), 7.59 – 7.54 (m, 1H), 7.48 – 7.43 (m, 2H), 7.42 – 7.37 (m, 2H), 7.35 – 7.31 (m, 1H), 7.30 – 7.27 (m, 2H), 4.47 (dd, J = 8.5, 4.9 Hz, 1H), 3.96 (dd, J = 18.0, 8.5 Hz, 1H), 3.23 (ddd, J = 18.1, 4.8, 0.6 Hz, 1H). ^{13}C NMR (101 MHz, CDCl_3) δ 199.07, 197.34, 136.46, 135.47, 133.39, 129.34, 129.15, 128.67, 128.17, 127.97, 127.23, 53.69, 39.49.

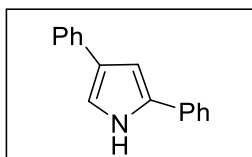
2,4-diphenylfuran (4a)



For the preparation of this compound it was followed a slightly different synthesis already report in another work^[165]. In a glass tube with a Teflon-lined snap cap, it was added 4-oxo-2,4-diphenylbutanal (3a) (0.1 mmol, 23.8 mg), EtOH (1 mL), HCl 1 M (0.1 mL). The vessel has then been place in the microwave reactor at 150 °C for 15 minutes. The reaction mixture was diluted with EtOAc and then washed with a saturated solution of NaHCO₃ and then with Brine. Collected organic solutions were evaporated, dissolved in CH₂Cl₂ and dried over Na₂SO₄. At this stage, the yield of 4a was recorded measuring ¹H NMR with 1,3,5-trimethoxybenzene as internal standard. The crude obtained has been purified with a chromatographic column Hexane/EtOAc (99:1).

Colorless crystals (yield: 70%). ¹H NMR (400 MHz, Chloroform-d) δ 7.77 (d, J = 0.9 Hz, 1H), 7.76 – 7.71 (m, 2H), 7.58 – 7.53 (m, 2H), 7.45 – 7.39 (m, 4H), 7.34 – 7.27 (m, 2H), 6.98 (d, J = 0.9 Hz, 1H). ¹³C NMR (101 MHz, CDCl₃) δ 154.98, 138.03, 132.49, 130.78, 128.98, 128.86, 128.49, 127.74, 127.27, 125.94, 123.98, 104.11.

2,4-diphenyl-1H-pyrrole (5a)

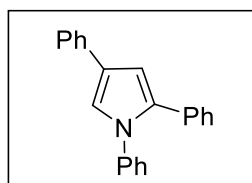


In a glass tube with a Teflon-lined snap cap, it was added 4-oxo-2,4-diphenylbutanal (3a) (0.1 mmol, 23.8 mg), a mixture THF:AcOH (1:1, 1 mL), AcONH₄ (0.4 mmol, 31 mg). The vessel has then been place in the microwave reactor at 170 °C for 15 minutes. The reaction mixture was diluted with EtOAc and then washed with a saturated solution of NaHCO₃ and then with Brine. Collected organic solutions were evaporated, dissolved in CH₂Cl₂ and dried over Na₂SO₄. At this stage, the yield of 5a was recorded measuring ¹H NMR with 1,3,5-

trimethoxybenzene as internal standard. The crude obtained has been purified with a chromatographic column Hexane/EtOAc (85:15).

White solid (yield: 89%). ^1H NMR (400 MHz, Chloroform-d) δ 8.46 (s, 1H), 7.61 – 7.55 (m, 2H), 7.55 – 7.50 (m, 2H), 7.38 (ddd, J = 10.4, 8.4, 7.0 Hz, 4H), 7.30 – 7.18 (m, 2H), 7.15 (dd, J = 2.7, 1.7 Hz, 1H), 6.84 (dd, J = 2.8, 1.7 Hz, 1H). ^{13}C NMR (101 MHz, CDCl_3) δ 135.60, 133.20, 132.58, 129.10, 128.81, 126.73, 126.64, 125.89, 125.31, 123.99, 115.68, 104.09.

1,2,4-triphenyl-1H-pyrrole (6a)



In a glass tube with a Teflon-lined snap cap, it was added 4-oxo-2,4-diphenylbutanal (3a) (0.1 mmol, 23.8 mg), a mixture THF:AcOH (1:1, 1 mL), phenylamine (0.2 mmol, 18 μL). The vessel has then been placed in the microwave reactor at 170 $^\circ\text{C}$ for 15 minutes. The reaction mixture was diluted with EtOAc and then washed with a saturated solution of NaHCO_3 and then with Brine. Collected organic solutions were evaporated, dissolved in CH_2Cl_2 and dried over Na_2SO_4 . At this stage, the yield of 6a was recorded, measuring ^1H NMR with 1,3,5-trimethoxybenzene as internal standard. The crude obtained has been purified with a chromatographic column Hexane/EtOAc (85:15).

White solid (yield: 100%). ^1H NMR (400 MHz, Chloroform-d) δ 7.66 – 7.61 (m, 2H), 7.45 – 7.30 (m, 5H), 7.30 – 7.18 (m, 9H), 6.78 (d, J = 1.8 Hz, 1H). ^{13}C NMR (101 MHz, CDCl_3) δ 140.42, 135.26, 134.88, 132.80, 129.20, 128.84, 128.43, 128.26, 126.93, 126.68, 125.98, 125.79, 125.65, 125.24, 121.01, 108.86.

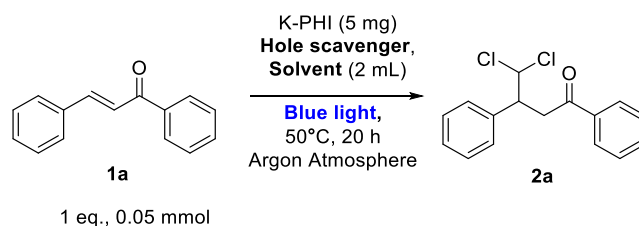
General method for imines preparations (2'a-f)

A glass tube with rubber-lined cap was evacuated and filled with argon three times. To this tube, corresponding amine (0.1 mmol for 1'a-b, 0.2 mmol for 1'c-f), K-PHI (5 mg) and chloroform (2 mL) were added. Resulting mixture was stirred at 50 $^\circ\text{C}$ under irradiation with

Blue LED ($\lambda = 461\text{nm}$) for 20 hours. Then reaction mixture was cooled to room temperature and centrifuged, clear solution was separated and solid residue was washed with chloroform (2 mL) and centrifuged again. Organic solutions were combined and evaporated to dryness (Supplementary Figure 92, Supplementary Figure 93).

Supplementary Tables

Supplementary Table 1. Screening reactions^{a,b}



Entry	Hole Scavenger	Solvent	Yield, %
1	THIQ (1 eq, 0.05 mmol)	CHCl ₃	17
2	THIQ (2 eq, 0.1 mmol)	CHCl ₃	33
3	THIQ (3 eq, 0.15 mmol)	CHCl ₃	41
4	THIQ- <i>d</i> ₂ (3 eq, 0.15 mmol)	CHCl ₃	36
5	THIQ (4 eq, 0.2 mmol)	CHCl ₃	51
6	TEOA (3 eq., 0.15 mmol)	CHCl ₃	62
7	TEOA (10 eq., 0.5 mmol)	CHCl ₃	97
8 ^b	TEOA (10 eq., 0.5 mmol)	CHCl ₃	96
9	TEA (10 eq., 0.5 mmol)	CHCl ₃	37

10	DiPEA (10 eq., 0.5 mmol)	CHCl ₃	+
11	MeOH (10 eq., 0.5 mmol)	CHCl ₃	10
12	EtOH (10 eq., 0.5 mmol)	CHCl ₃	7
13	iPrOH (10 eq., 0.5 mmol)	CHCl ₃	6
14	BnOH (10 eq., 0.5 mmol)	CHCl ₃	8
15	TEOA (10 eq., 0.5 mmol)	DMF	-
16	TEOA (10 eq., 0.5 mmol)	Triethyl orthoformate	-
17	TEOA (10 eq., 0.5 mmol)	CH ₂ Cl ₂	+
18 ^c	TEOA (10 eq., 0.5 mmol)	CH ₂ Cl ₂	-
19	TEOA (10 eq., 0.5 mmol)	CH ₂ Cl ₂	-
20	TEOA (10 eq., 0.5 mmol)	C ₂ H ₂ Cl ₄	-
21 ^d	TEOA (10 eq., 1 mmol)	CHCl ₃	64
22	TEOA (10 eq., 0.5 mmol)	CH ₂ Cl ₂	-
23	TEOA (10 eq., 0.5 mmol)	CHCl ₃ /DMSO 1:1	47

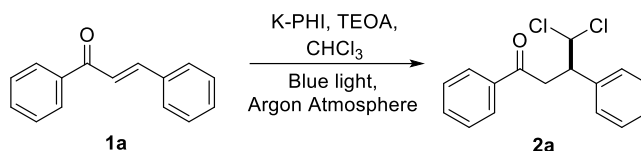
a) Reaction conditions: 1 eq., 0.05 mmol, 10.4 mg of **1a**; under light irradiation ($\lambda = 461 \text{ nm}$, $51 \pm 0.03 \text{ mW cm}^{-2}$, blue LED; b) Yields were recorded by GC-MS. When the chromatogram was not possible to estimate yields in this way, GC-MS was used only as qualitative analysis with the following reported signs in the table: +) product formation is observed at the end of reaction; -): product formation is not observed at the end of reaction; b) reaction performed under air; c) 100mg of CHI₃ were dissolved in the solvent; d) reaction performed with 'coold finger' at 20 °C, 1 eq., 0.1 mmol, 20.8 mg of **1a**, 4 mL of solvent.

Supplementary Table 2. Catalyst recycling.

Entry	K-PHI refill	Yield (%) ^a
1	-	97
2	+1.5 mg	96
3	2.5 mg	97

a) Yields were calculated by GC-MS. After following the general procedure for the preparation of dichloroketones (section 5), the residual catalyst was washed with water (2 mL) and centrifuged for two times. The residue was then placed overnight in the vacuum oven at 50°C. Before reuse, the lost mass has been refilled with fresh catalyst.

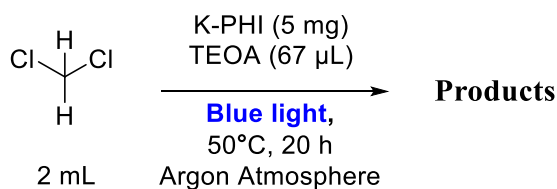
Supplementary Table 3. Scale-up experiment.^a



Entry	1a, mmol (mg)	K-PHI, mg	TEOA, mL	CHCl ₃ , mL	Scale factor ^b	Time, h	Yield of 2a, ^c %
1	0.05 (10.4)	5	0.066	2	1	20	88
2	0.25 (52)	25	0.335	10	5	20	43
3	0.25 (52)	25	0.335	10	5	40	71
4	0.50 (104)	50	0.67	20	10	20	38
5	5.00 (1040)	250	6.6	100	100	20	23

^a Reaction conditions: blue LED ($\lambda = 461 \text{ nm}$, $51 \pm 0.03 \text{ mW cm}^{-2}$); ^b with respect to enone **1a**; ^c determined by GC-MS

Supplementary Table 4. Screening reaction with chloroform alone.



Entry	K-PHI	TEOA	Light	Major products ^a
1	-	+	+	-

2	+	+	+	C ₂ H ₂ Cl ₄ , C ₂ HCl ₅ , C ₂ HCl ₃ , C ₂ Cl ₄
3	+	-	+	C ₂ Cl ₆
4	-	-	+	-
5	-	+	-	-
6	+	+	-	-
7	+	-	-	-
8	-	-	-	-

a) Only a qualitative analysis by GC-MS was possible because of multiple peaks in chromatogram.

Supplementary Notes

Supplementary Note 1

It was investigated the reasons why TEOA is better hole scavenger than alcohols. As an example, in Supplementary Figure 94 is reported cyclic voltammograms, comparing oxidation potential of TEOA and benzyl alcohol. It is clear that TEOA has much lower oxidation potential than benzylic alcohol, +0.5 V vs +1.5 V. Therefore TEOA is oxidized faster, leading to the formation of much higher amount of K-PHI radical anion species to carry on the reaction.

Supplementary Note 2

Enones **1p-r** gave dichloro ketones **2p-r** as evidenced by ¹H NMR spectra of the reaction mixture (Supplementary Figure 95-100). Formation of these products was supported by the presence of doublet at 6.08-6.20 ppm in the ¹H NMR spectrum assigned to the CHCl₂ group, which is similar to the synthesized dichloro ketone **2a-l**

The attempts to isolate CN-, CO₂Me- and pyridine-substituted dichloro ketones **2p-r** by column chromatography were not successful.

Relatively low yields of dichloroketones **2p-r** bearing strong electron withdrawing groups (CO₂Me, CN, pyridine), it is attributed to two factors. Firstly, electron withdrawing groups activate C=C bond for reduction, i.e. in the gas chromatograms of the reaction mixture the detected products of chalcones **1p-1r** C=C bond reduction. Similar behavior of electron deficient chalcones was observed earlier when studied their cyclodimerization.¹² In other words, addition of CHCl₂-group to the C=C bond competes with the reduction of C=C bond. Secondly, higher lability of dichloroketones **2p-r** toward nucleophiles creates difficulties for these compounds isolation by column chromatography due to irreversible interaction with OH-groups of silicagel. It is also found that reversed phase chromatography (C18 modified stationary phase, eluent – acetonitrile:water in different ratios) is not suitable for γ,γ -dichloroketones purification either.

It should be pointed out that even a relatively weak nucleophile such as oxygen of the carbonyl group in dichloroketones **2** capable for triggering the intramolecular cyclization followed by elimination of two molecules HCl. Therefore, in the GC-MS (electron ionization) have not a signal with m/z of dichloroketones, e.g. m/z 292 for **2a**, but always observed signal of the furans generated from the corresponding dichloroketone, e.g. m/z 220 for 2,4-diphenylfuran.

Supplementary Note 3

Supplementary Figure 101 shows a list of Michael acceptor that were used as substrates in the dichloromethylation reaction.

The reaction mixture was analyzed by GC-MS. Please note that all Michael acceptors gave quite complex mixture. Therefore, it is provided only mass spectra of the dichloromethylated products that it was possible to identify. Assignment of the specific structure to the chromatogram peak was made taking into account isotope distribution of the molecular ion

(denoted as Exp. or E.). Theoretical isotope distribution (denoted as Theor. or T.) was calculated using ChemDraw 17.1.0.105 (19) software (see Supplementary Figures 102-103). In the GC-MS of the reaction mixture using methylvinyl ketone as a substrate, it was identified 1) tetrachloroethane – the product of two dichloromethyl radicals coupling, 2) product of triethanol amine dehydrogenation,¹² 3) residual triethanolamine and 4) a small amount of dichloromethylated product **2s**. Isotope distribution in the mass spectrum of **2s** molecular ion matches well with the calculated one (Supplementary Figure 102).

In the GC-MS of the reaction mixture using acrylonitrile as a substrate, it was identified 1) tetrachloroethane – the product of two dichloromethyl radicals coupling, 2) product of triethanol amine dehydrogenation,¹² 3) residual triethanolamine and 4) a small amount of dichloromethylated product **2t**. Isotope distribution in the mass spectrum of **2t** molecular ion matches well with the calculated one (Supplementary Figure 103).

Any attempts to separate compounds **2s** and **2t** from the reaction mixture by column chromatography were not successful (Supplementary Note 4).

Other Michael acceptors did not give the desired product even in trace quantity.

Supplementary Note 4

It is assumed that high reactivity of the Michael acceptors **1s-1w** is responsible for either low or no yield of the products **2s-2w**. Many of compounds **1s-1w** are used as polymer precursors due to reactive C=C bond. Therefore, in the photocatalytic reaction that involves radical intermediate, they most probably undergo polymerization.

Another reason for low or no yield of the products **2s-2w** may consist in high reactivity of these compounds toward nucleophiles, e.g. hydroxyl groups of triethanolamine during synthesis, silicagel hydroxyl groups during purification. Worth mentioning that reversed phase chromatography (C18 modified stationary phase, eluent – acetonitrile:water in different ratios) was not suitable for dichloroketones purification either.

Finally, the conclusions about high reactivity of dichloromethylated compounds **2s-w** are supported by absence of almost any data regarding synthesis of these compounds obtained from SciFinder and Reaxys (Supplementary Figure 104-113). With surprise, SciFinder output as of 24.10.2019 showed that only one article mentions methyl 4,4-dichlorobutanoate **2v** – a product of CHCl_2 addition to the β -carbon atom of methacrylate **1v** (Supplementary Figure 107). [Acta Chemica Scandinavica, Series B: Organic Chemistry and Biochemistry, B35(3), 175-8; 1981]. However, no NMR data is given for the title compound neither yield.

Compounds **2s-2u** and **2w** that would have expected to be obtain from the suggested Michael acceptors upon addition of CHCl_2 -moiety, have not been reported earlier (Supplementary Figure 104-106, 108).

Similar results were obtained from Reaxys (Supplementary Figure 109-113)

Taking into account absence of any data regarding the dichloromethylated Michael acceptors **2s-2u** and **2w**, it was concluded that synthesis of such compounds is not a trivial task. Despite high attractiveness for organic synthesis they have not been synthesized so far.

It is important to point out that most of dichloroketones prepared in this work have not been reported either. However, success in dichloromethylation of enones bearing aromatic substituent is explained by higher stability of these molecules compared to small Michael acceptors under the reaction conditions. Due to steric hindrance and resonance stabilization of the aromatic substituents, diarylsubstituted enones are less susceptible for polymerization. Therefore, the path of CHCl_2 -moiety addition to the $\text{C}=\text{C}$ bond becomes dominant. Furthermore, isolation of dichloromethylated ketones is possible, but until the point when the structure becomes too electron deficient and hence susceptible for nucleophilic attack (see Supplementary Note 2).

Supplementary Note 5

Several halogenated compounds have been investigated as possible sources of $C_xHal_yH_z$ groups to introduce into enone **1a**. Reaction mixtures were analyzed by GC-MS. Assignment of the specific structure to the chromatogram peak was made taking into account isotope distribution of the molecular ion (denoted as Exp. or E.). Theoretical isotope distribution (denoted as Theor. or T.) was calculated using ChemDraw 17.1.0.105 (19) (Supplementary Figure 114-115, 117-118, 120).

The experiment using dichloromethane as solvent showed traces of the product. There are also intense peak of TEOA (broad due high concentration) and starting chalcone (Supplementary Figure 114).

In case of using bromoform, in the reaction mixture it was identified the following major products: 1) residual bromoform, 2) compound with a brutto formula C_2HBr_3 , presumably 1,1,2-tribromoethene, 3) tetrabromoethene, 4) tetrabromoethane, 5) compound with a brutto formula C_9H_7OBr , presumably cinnamoyl bromide, 6) unreacted chalcone **1a**, 7) 2,4-diphenylfuran, 8) 4-bromo-1,3-diphenylbutan-1-one (Supplementary Figure 115).

Formation of tetrabromoethane suggests that similarly to chloroform, in the photocatalytic reactor bromoform yields dibromomethyl radical. Two of such radicals recombine and give detectable products in GC-MS, i.e. tetrabromoethane, 1,1,2-tribromoethene.

Formation of 4-bromo-1,3-diphenylbutan-1-one suggests that addition of dibromomethyl radical to the C=C bond of enone **1a** took place. Reduction of the intermediary dihaloketone yields 4-bromo-1,3-diphenylbutan-1-one. Furthermore, intermediary dibromoketone undergoes intramolecular cyclization, i.e. nucleophilic attack of the carbonyl oxygen atom at the carbon atom of $CHBr_2$ -group, followed by elimination of two molecules HBr and yields 2,4-diphenylfuran (Supplementary Figure 116).

This mechanism is further supported by the fact that no triethanolamine was detected in the reaction mixture by GC-MS – it has been converted to the salt. After the photocatalytic

experiment it was observed formation of gum-like residue. Therefore, only soluble fraction of the reaction mixture was analyzed by GC-MS (Supplementary Figure 116).

In case of iodoform, i.e. solution in CH_2Cl_2 , it was observed formation of small amount of 2,4-diphenylfurane implying that tentative CHI_2 -radical has been attached to the enone **1a**. Similarly to bromoform, no triethanolamine or its dehydrogenation products were detected in gas chromatogram suggesting acidification of the reaction mixture and subsequent binding triethanolamine to the insoluble salt (Supplementary Figure 117).

Analysis of the GC-MS data of the reaction mixture using 1,1,2,2-tetrachloroethane as a solvent revealed that this halogenated solvent partially underwent chemical transformation. The following products have been identified of tetrachloroethane conversion: 1) trichloroethene, 2) trichloroethane and 3) tetrachloroethene. Cis-isomer of chalcone **1a** was detected in the GC-MS of the reaction mixture (Supplementary Figure 118). In addition, two compounds, presumably isomers, with m/z 304 and similar retention times, i.e. 10.650 min and 10.996 min, were detected. Based on the analysis of the isotope distribution in the molecular ion, it was assigned brutto formula $\text{C}_{17}\text{H}_{14}\text{Cl}_2\text{O}$ to these compounds. The compounds with the brutto formula $\text{C}_{17}\text{H}_{14}\text{Cl}_2\text{O}$ might be the products of tetrachloroethane addition to the $\text{C}=\text{C}$ bond of enone **1a** according to Supplementary Figure 119).

Elimination of two HCl molecules mediated by TEOA followed by one of the $\text{C}=\text{C}$ bonds reduction yields the two products with brutto formula $\text{C}_{17}\text{H}_{14}\text{Cl}_2\text{O}$ that were detected in the GC-MS. Acidification of the reaction mixture was concluded based on the fact that TEOA was not detected by GC-MS. Instead it was converted to gum-like residue, similarly to the experiments with bromoform and iodoform, upon protonation with the generated HCl .

Reaction in tetrachlorometane led to isomerization of chalcone **1a**. Similarly to the experiments with bromoform, iodoform and tetrachloroethane, triethanolamine was converted to gum-like residue insoluble in tetrachloromethane (Supplementary Figure 120).

Overall, it is concluded that K-PHI may be used to generate $C_xHal_yH_z$ radicals from the respective halogenated compounds and potentially used to extend the backbone of enones.

Supplementary Note 6

A series of experiments were performed in the batch reactor scaling up proportionally the amount of reagents/catalyst/solvent. The smallest amount of enone **1a** was 0.05 mmol and the largest amount – 5 mmol. The yield of dichloroketone **2a** (η) decreases gradually as the amount (n) of reagents, i.e. chalcone **1a**, increases (Supplementary Figure 121).

These results can be explained by the fact that the surface area of the liquid phase exposed to the light scales lower than the volume of the reaction mixture. Therefore, only a small fraction of the catalyst (close to the surface of the reaction) receives sufficient number of photons to mediate the reaction. The highest surface-area-to-volume ratio ($A = 4.57$) was for the reaction performed on 0.05 mmol scale, the lowest, $A = 1.37$, was for the reaction performed on 5 mmol scale. Assuming that the yield (η) of dichloroketone **2a** will approach zero in infinitely large photoreactor due to infinitely small number of photocatalyst located at the near surface layer and exposed to light, η versus A can be fitted with the linear function $\eta = 18.47 \times A$ ($R^2=0.995$) (Supplementary Figure 122).

In order to elucidate the origin of this effect, further investigation were conducted.

Carbon nitride particles strongly absorb and scatter light (Supplementary Figure 17-18 in the ESI therein). Therefore, it was conceded that the chemical reaction occurs only in a thin layer located close to the surface of the liquid phase. On the other hand, the central area of the batch photoreactor remains in 'dark' and therefore no photocatalytic reaction occurs there. When reaction is performed on 0.05 mmol scale using 2 mL of solvent in a glass tube of 10 mm in diameter, most of the photoreactor volume is exposed to light, therefore average photoreactor productivity is high. On the other hand, on the 5 mmol scale using 200 mL of solvent in a glass tube of 30 mm in diameter, only a small volume of the batch photoreactor

is effectively irradiated by light, while most of the reactor volume remains in dark. As a result average productivity of the photoreactor is low.

In order to find a distance from the reactor wall to the point in the bulk of the reaction mixture below which photons cannot penetrate, light transmittance measurements of K-PHI suspension were performed in CHCl₃:DMSO (9:1) in 1 mm, 2 mm, 5 mm and 10 mm cuvettes using convenient UV-vis spectrometer. Ten percent of DMSO has been added to delay sedimentation of K-PHI particles during the measurements.

The data in the graphs (Supplementary Figure 123) show that 1 mm thick layer of K-PHI suspension absorbs 94.50% of blue photons ($\lambda = 461$ nm), 2 mm thick layer absorbs 99.15%, 5 mm thick layer absorbs 99.45% and 10 mm thick layer absorbs 99.50% of light. Transmittance measurements were corrected taking into account absorption of pure solvent.

Comparable results were obtained when it was measured a fraction of light intensity (461 ± 20 nm, $I_0 = 10.6$ mW cm⁻²) passed through the cuvettes of variable length (1 mm, 2 mm, 5 mm and 10 mm) filled with K-PHI suspension.

These reference measurements show that higher light intensity allows for better light delivery in the bulk of the reaction mixture. However, even using relatively high light intensity (10.6 mW cm⁻²) compared to that in the UV-vis spectrometer, 95% of photons do not penetrate into the reaction mixture deeper than 3 mm.

Having this data, it was calculated a specific absolute yield (N) of dichloro ketone **2a** (mmol of dichloro ketone **2a** produced by 1 gram of K-PHI) assuming that the 'active' volume of the batch reactor is limited by 3 mm thick cylinder shell. Supplementary Figure 124 shows specific absolute yield (N) of dichloro ketone **2a** versus enone **1a** amount (n, mmol) taken for the experiment.

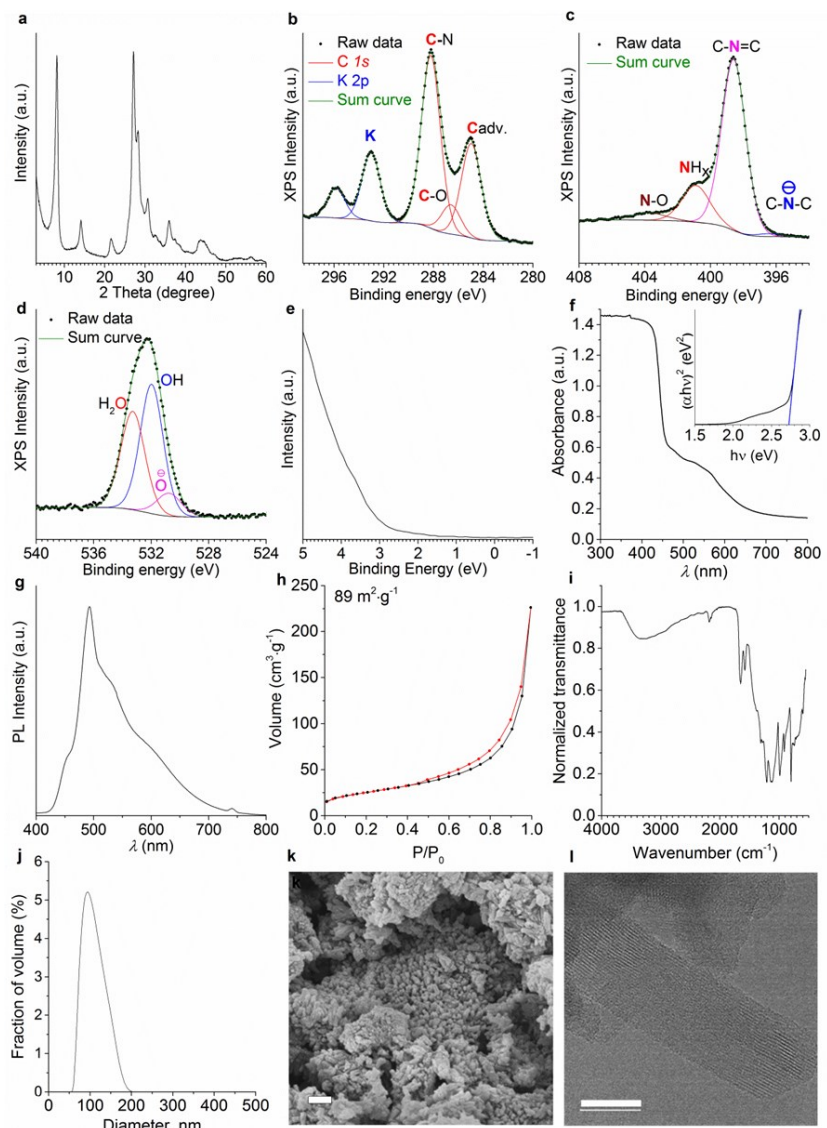
In this case the yield of **2a** is 7.05 ± 0.5 mmol g⁻¹ and depends weakly on the amount of enone **1a** taken for the experiment. Relative standard deviation in this case is 7.2%.

All in all, it is concluded that the main limitation of scaling up the photocatalytic reaction mediated by the heterogeneous photocatalyst in batch is poor light penetration into the bulk of the reaction mixture.

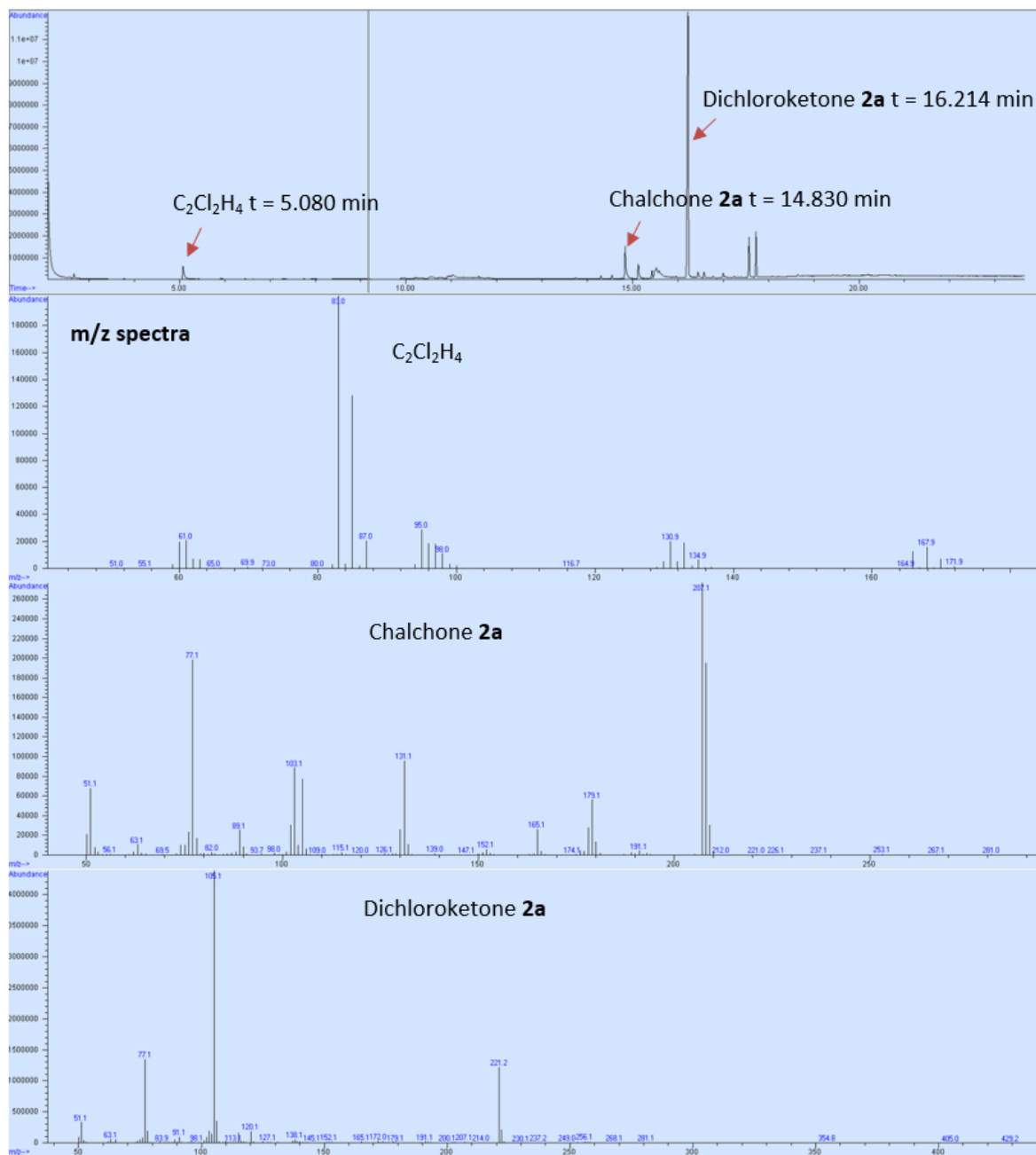
Supplementary Note 7

To further investigate colloidal properties of K-PHI nanoparticles, it was conducted a deposition test, to compare its properties with other carbon nitrides, such as g-CN and mpg-CN. It was proceeded by adding the selected photocatalyst (5 mg) in a mixture of CHCl₃/DMSO (3:2, 2 mL), sonicated for 10 minutes and stirred for another 10 minutes. Suspensions were left standing without agitation. Pictures were taken at different times to observe solid precipitation (Supplementary Figure 125). From this experiment it clear as K-PHI also has superior capacity to stay dispersed in solution.

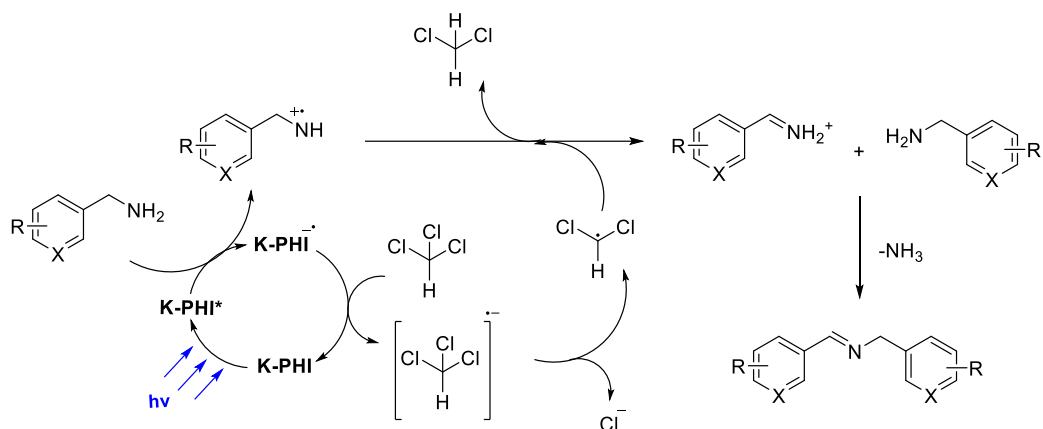
Supplementary Figures



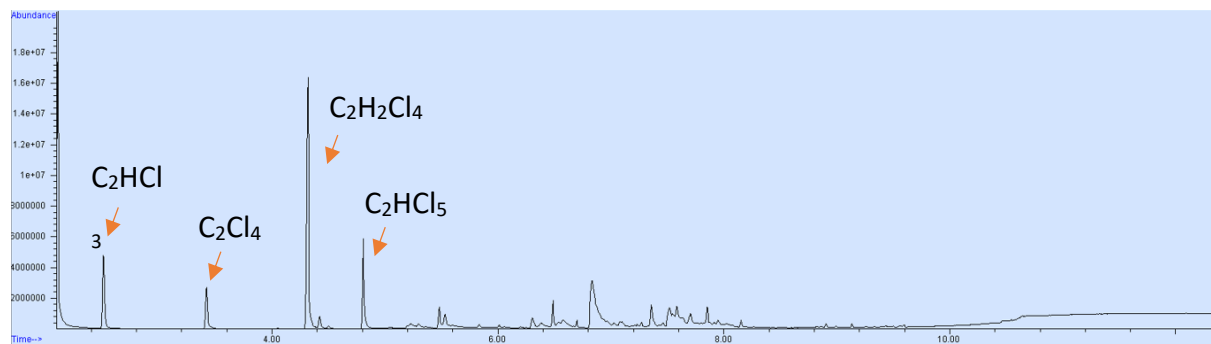
Supplementary Figure 1 K-PHI characterization. a) PXRD pattern of K-PHI; b) XPS C 1s and K 2p spectra of K-PHI; c) XPS N 1s spectrum of K-PHI; d) XPS O 1s spectrum of K-PHI; e) UPS spectrum of K-PHI; f) UV-vis absorption spectrum of K-PHI with Tauc plot as inset assuming that K-PHI is a direct semiconductor; g) room temperature PL spectrum of K-PHI obtained upon excitation with 350 nm wavelength; h) N_2 sorption isotherm measured at 77 K. BET surface area; i) FT-IR spectrum of K-PHI; j) DLS analysis of K-PHI suspension in water; k) representative SEM image of K-PHI photocatalyst. Scale bar 200 nm; l) AC-HRTEM image of K-PHI photocatalyst. Scale bar 20nm. Source data are provided as a Source Data file.



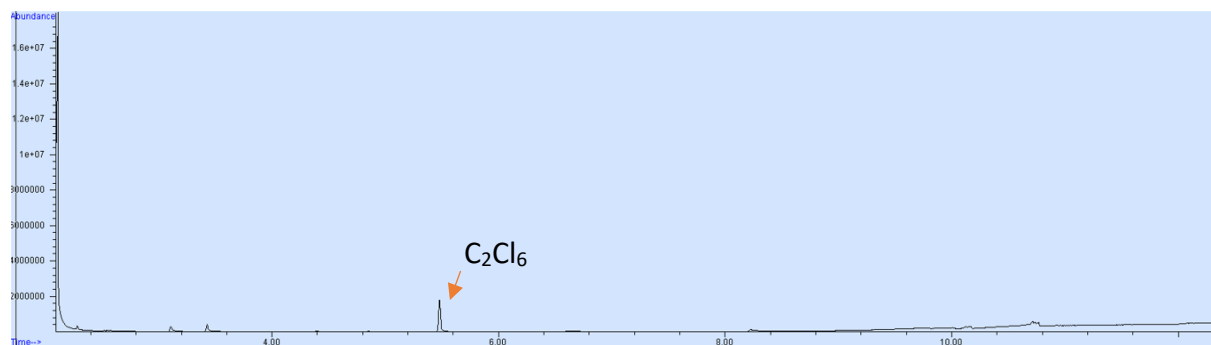
Supplementary Figure 2. Typical chromatogram during reaction screening



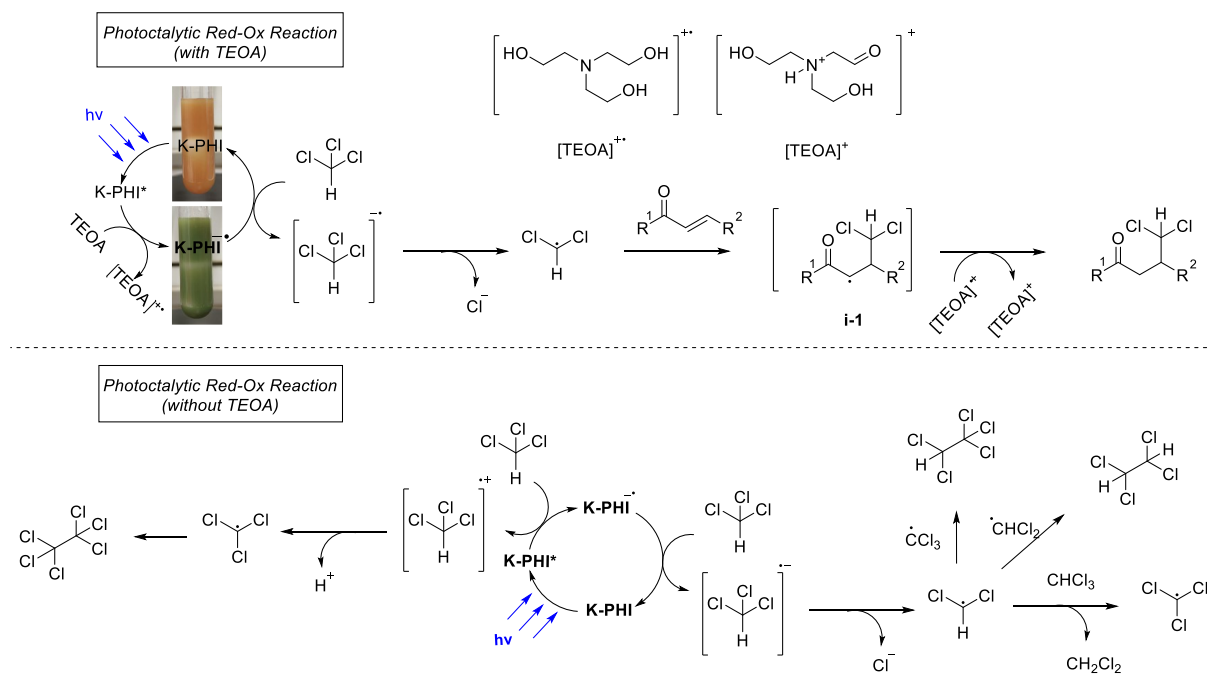
Supplementary Figure 3. Detailed mechanism proposed for oxidative coupling of benzylamines.



Supplementary Figure 4. Chromatogram after reaction of entry 2 (Supplementary Table 4).

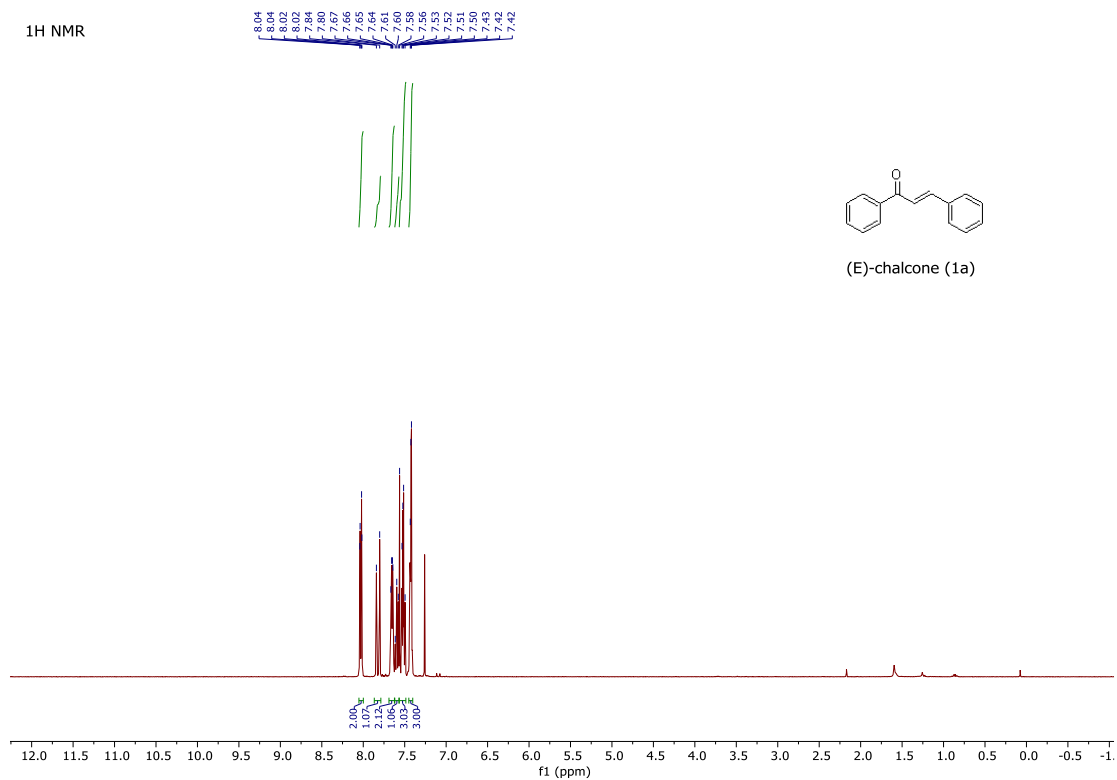


Supplementary Figure 5. Chromatogram after reaction of entry 3 (Supplementary Table 4).



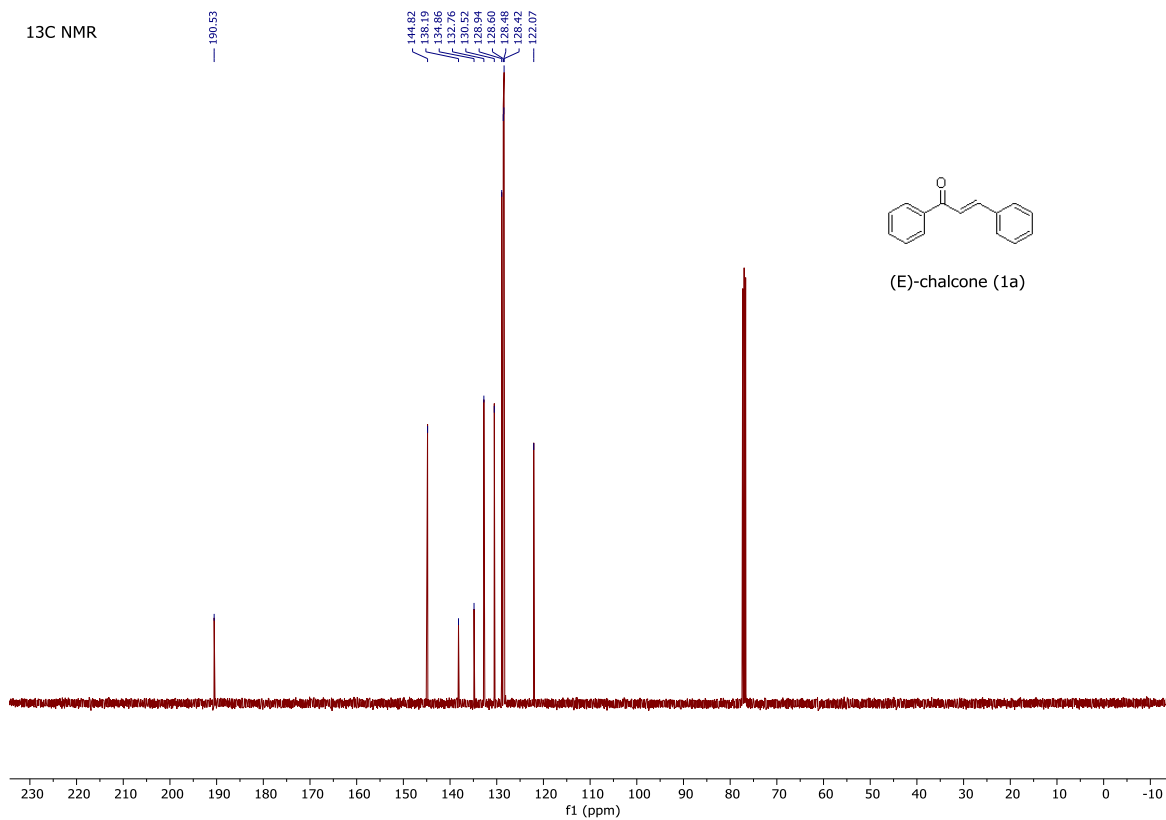
Supplementary Figure 6. Detailed mechanism proposed for dichloromethyl radical addition to enones and also for the formation of the different halogenated hydrocarbons.

¹H NMR



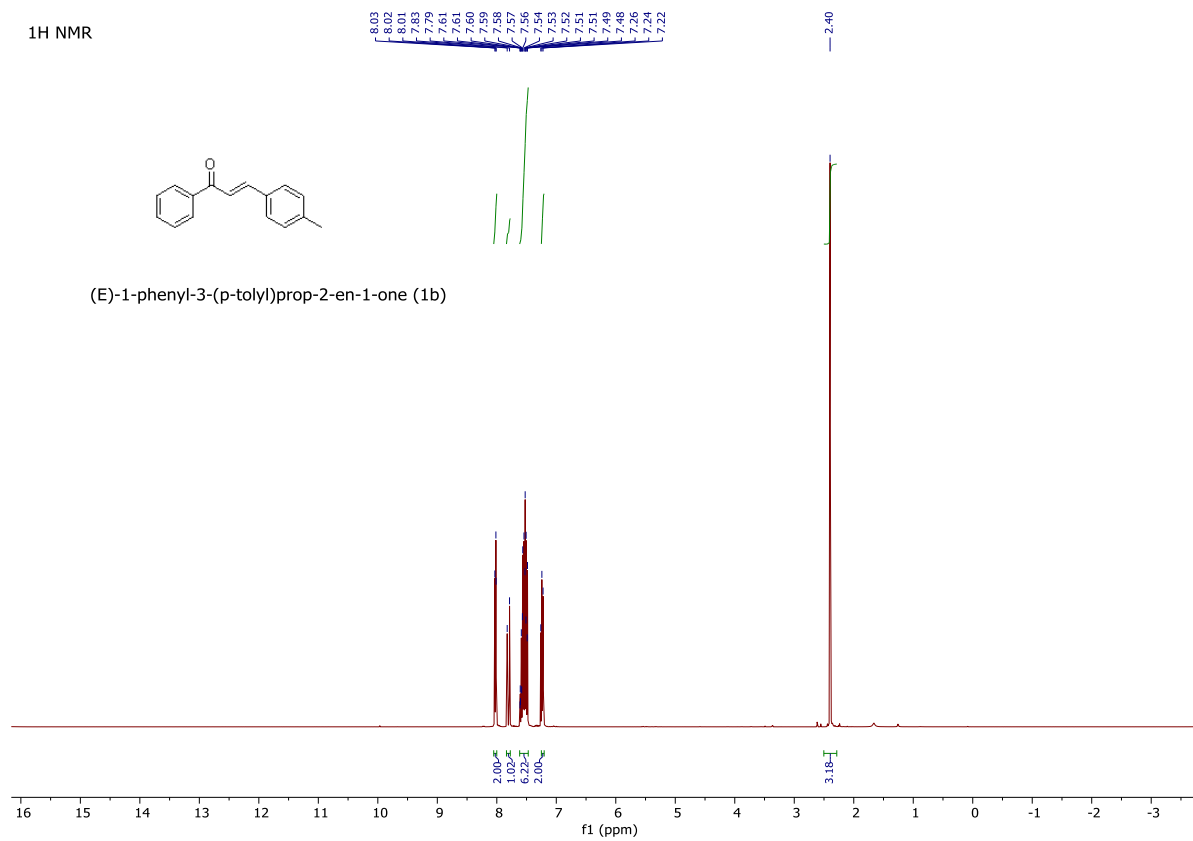
Supplementary Figure 7. NMR spectrum of 1a.

13C NMR

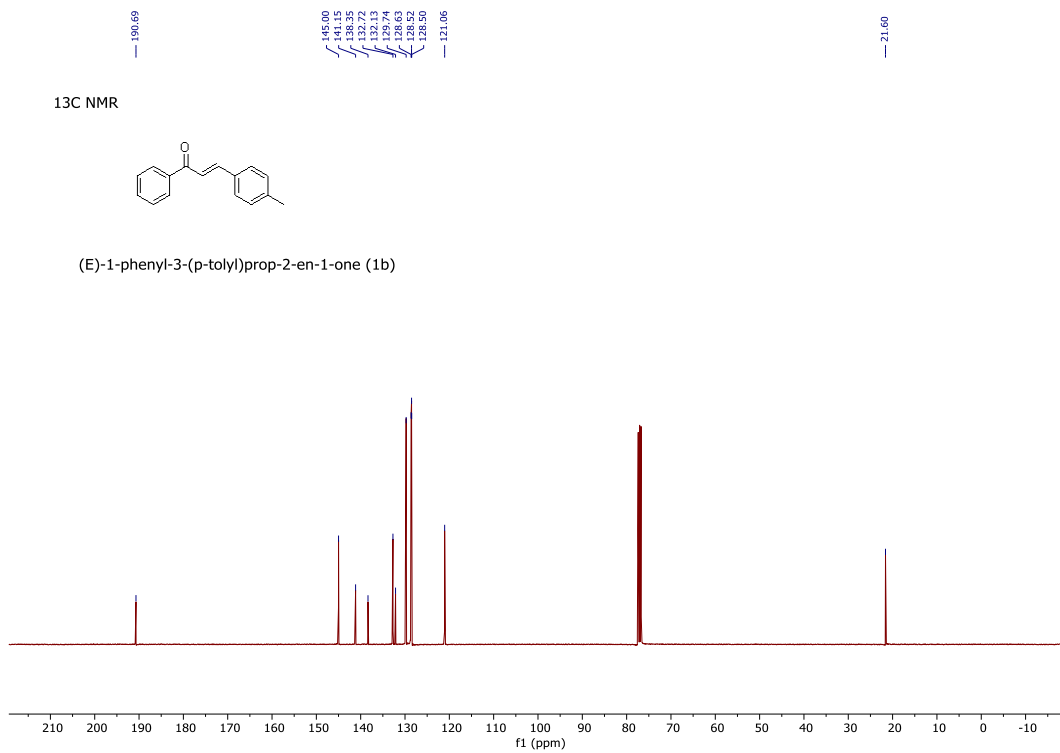


Supplementary Figure 8. NMR spectrum of 1a.

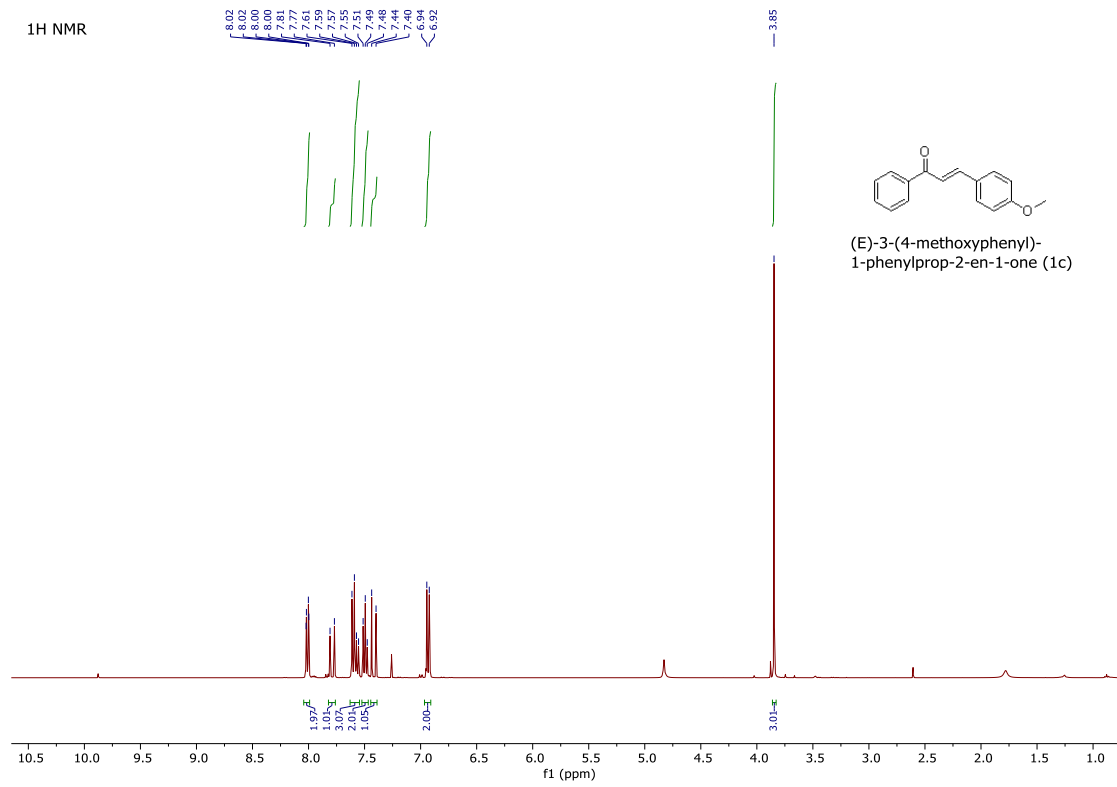
¹H NMR



Supplementary Figure 9. NMR spectrum of 1b.

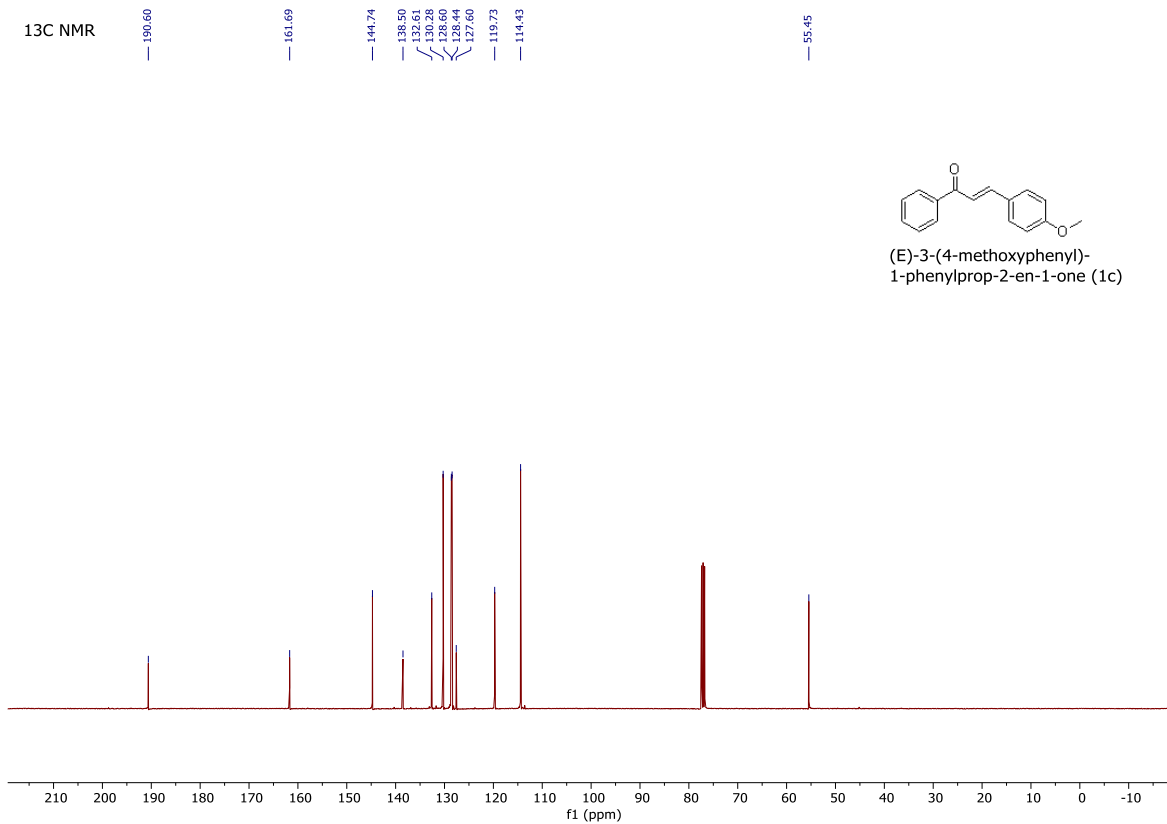


Supplementary Figure 10. NMR spectrum of **1b**.



Supplementary Figure 11. NMR spectrum of 1c.

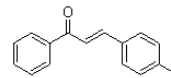
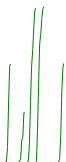
13C NMR



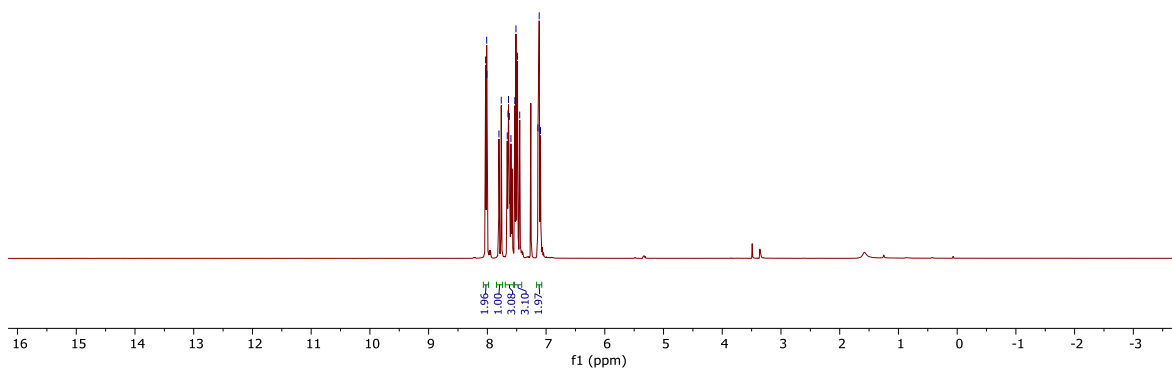
Supplementary Figure 12. NMR spectrum of 1c.

¹H NMR

8.03
8.01
7.80
7.76
7.66
7.64
7.63
7.60
7.53
7.51
7.49
7.34
7.12
7.10

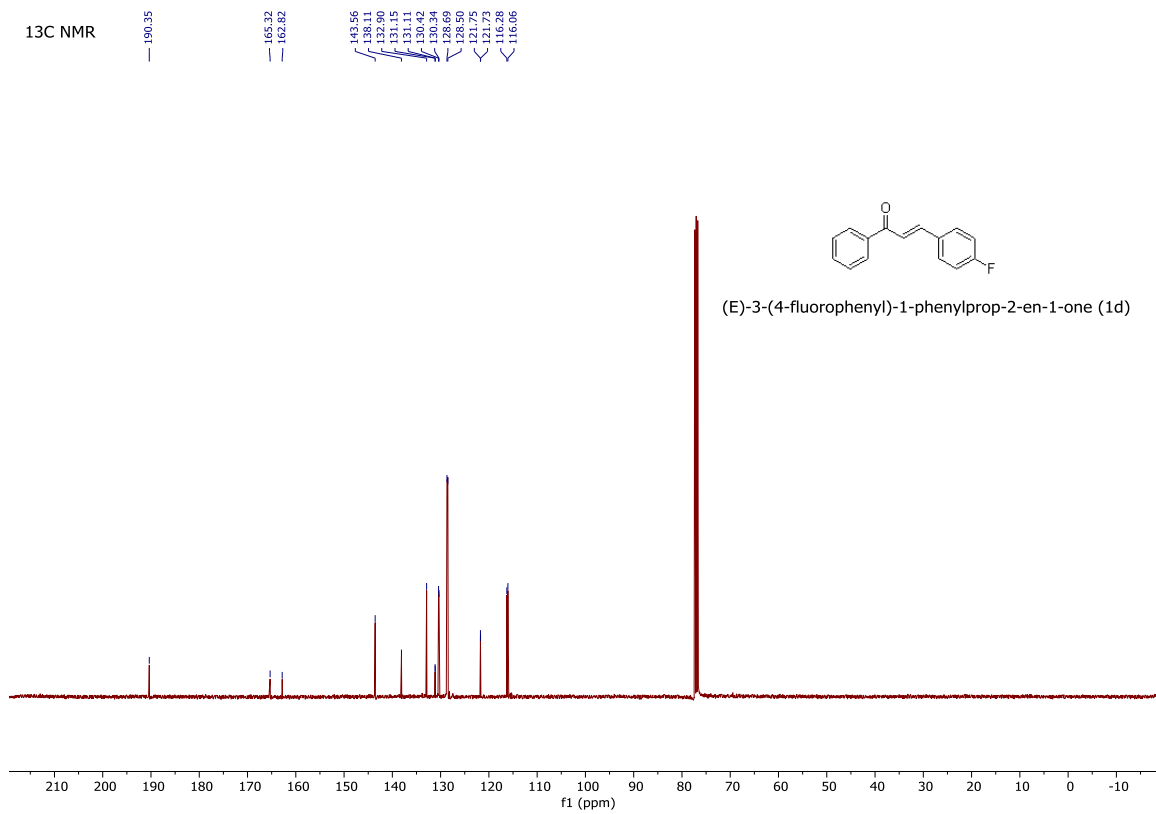


(E)-3-(4-fluorophenyl)-1-phenylprop-2-en-1-one (1d)



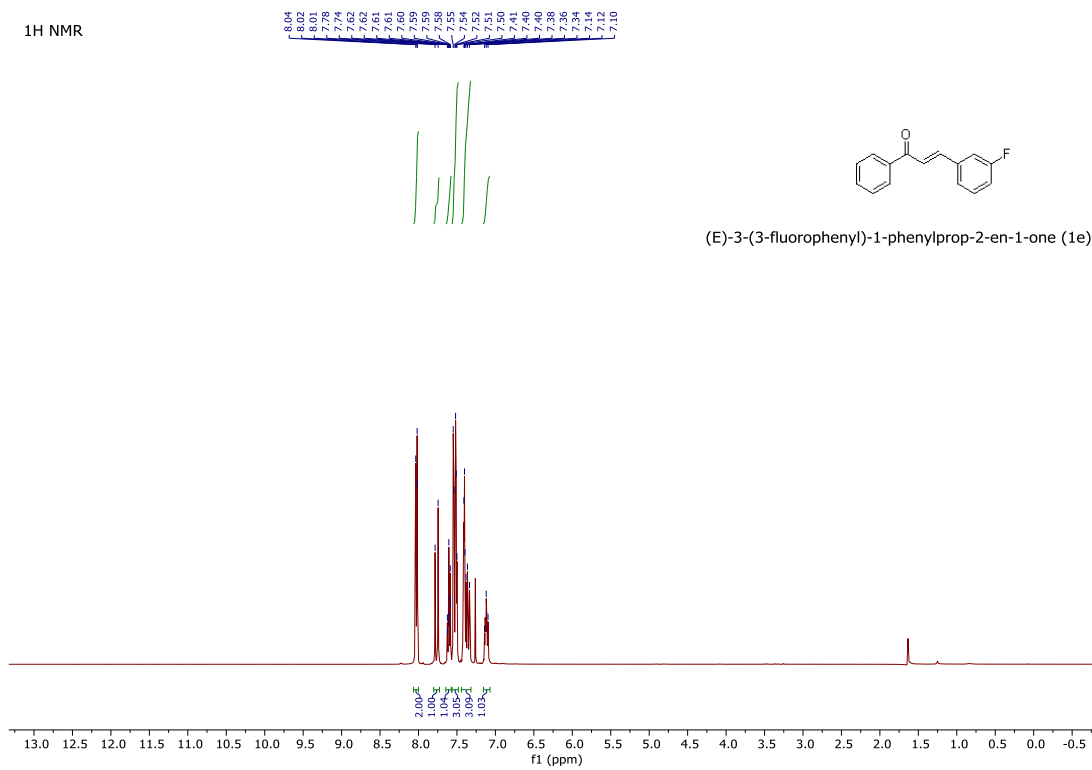
Supplementary Figure 13. NMR spectrum of 1d.

13C NMR

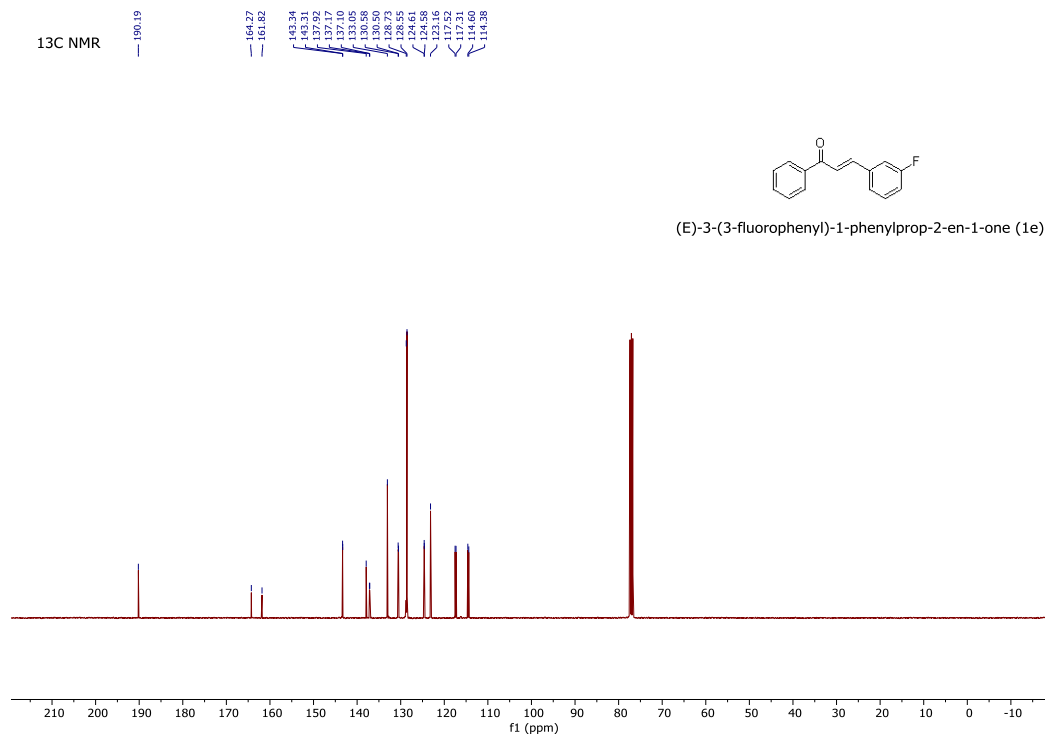


Supplementary Figure 14. NMR spectrum of 1d.

¹H NMR

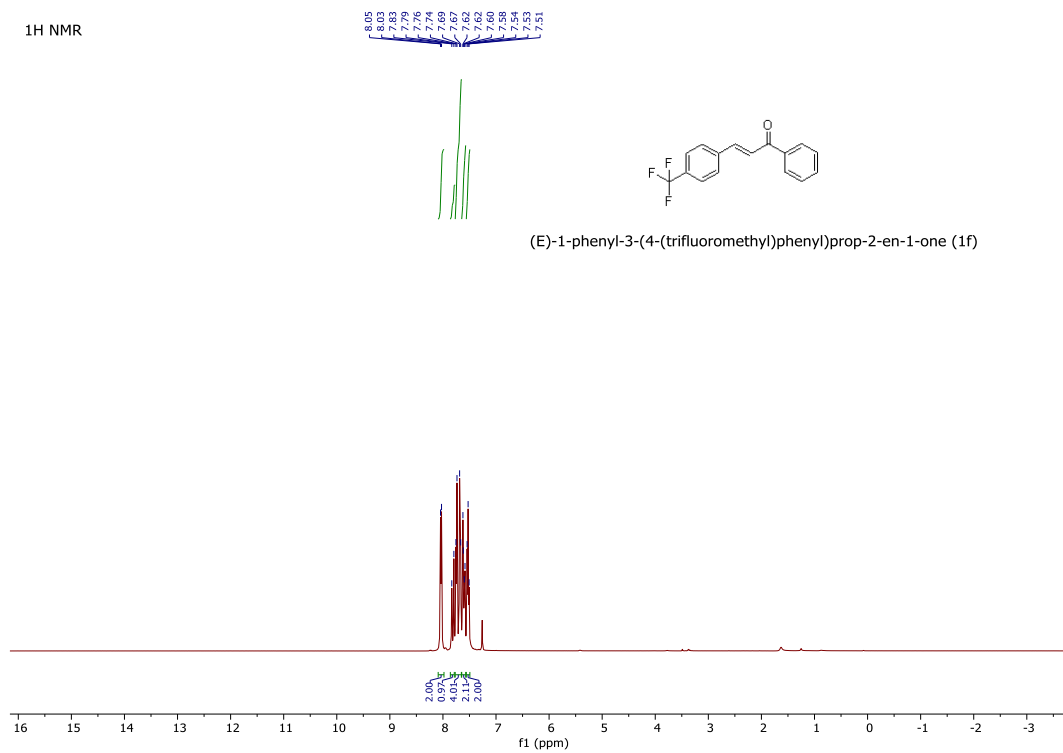


Supplementary Figure 15. NMR spectrum of 1e.



Supplementary Figure 16. NMR spectrum of 1e.

¹H NMR

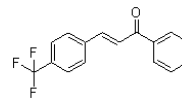


Supplementary Figure 17. NMR spectrum of **1f**.

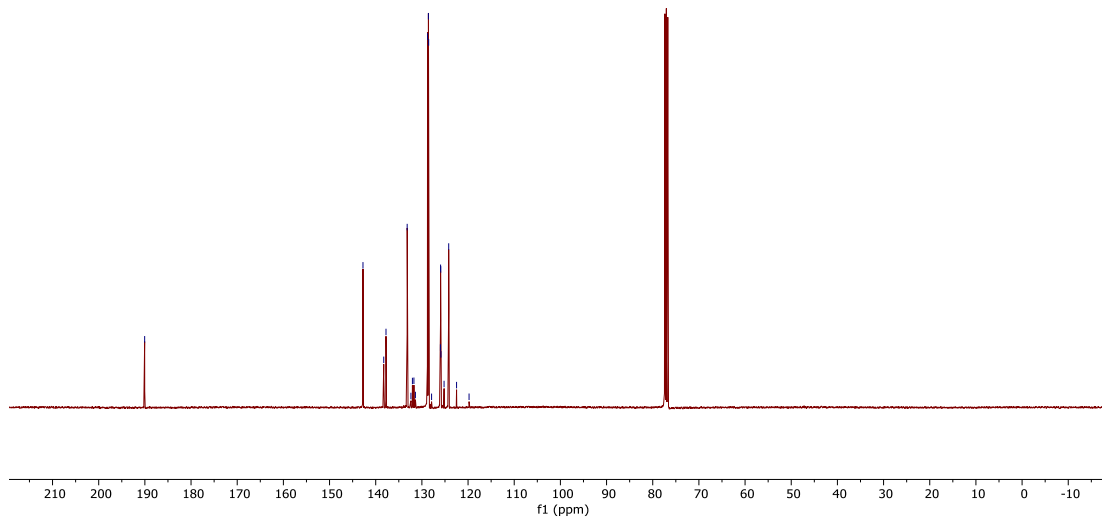
¹³C NMR

— 190.05

145.76
145.74
137.77
133.19
132.38
131.95
131.93
131.40
128.77
128.58
127.95
127.90
125.99
125.95
125.91
125.89
124.19
122.49
119.78

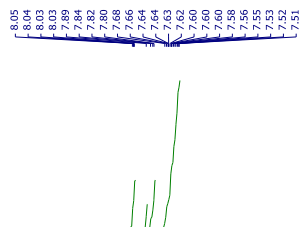


(E)-1-phenyl-3-(4-(trifluoromethyl)phenyl)prop-2-en-1-one (**1f**)

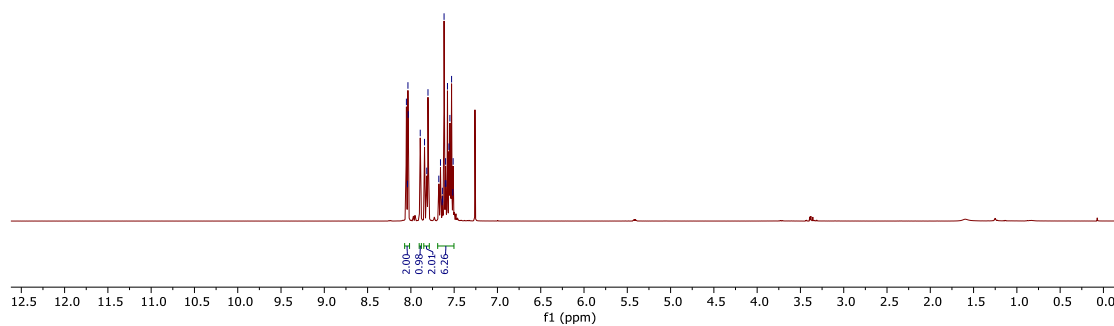


Supplementary Figure 18. NMR spectrum of **1f**.

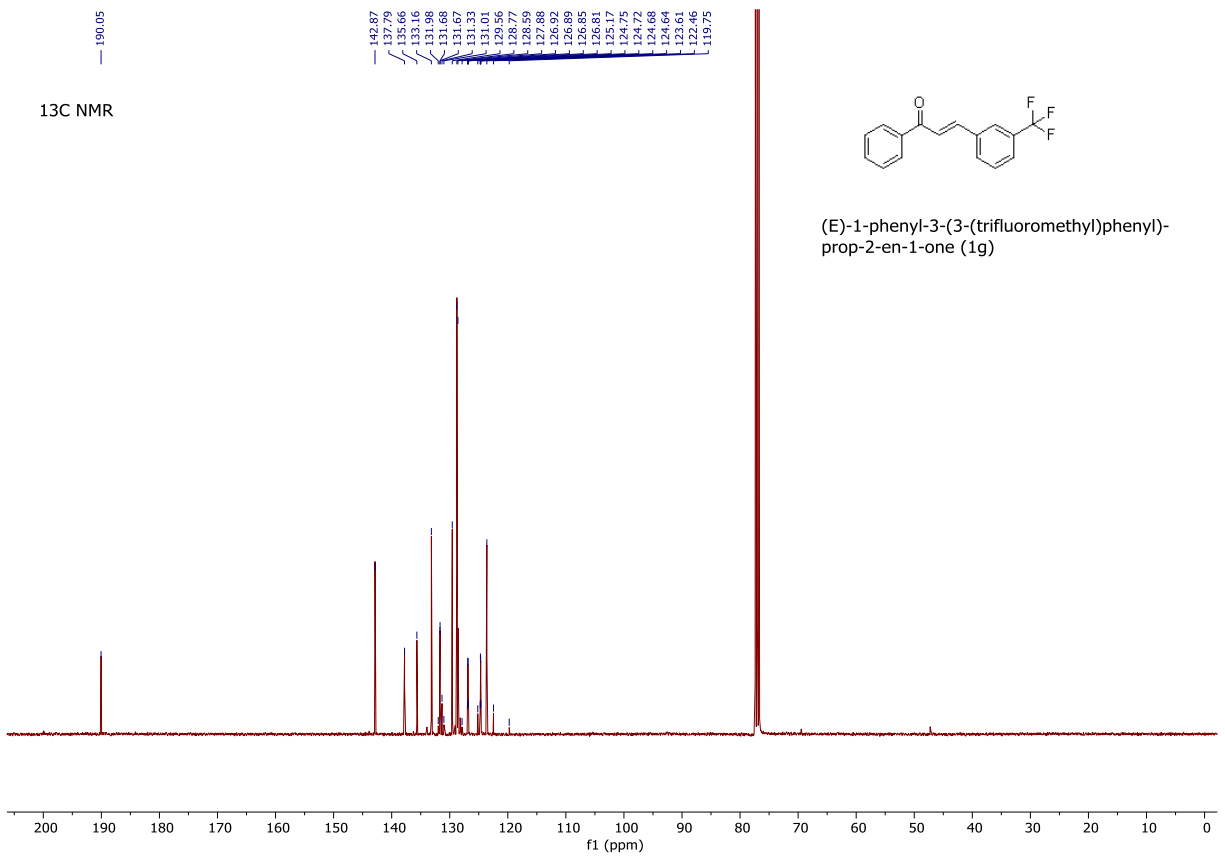
¹H NMR



(E)-1-phenyl-3-(3-(trifluoromethyl)phenyl)prop-2-en-1-one (1g)



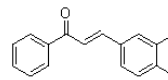
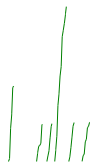
Supplementary Figure 19. NMR spectrum of 1g.



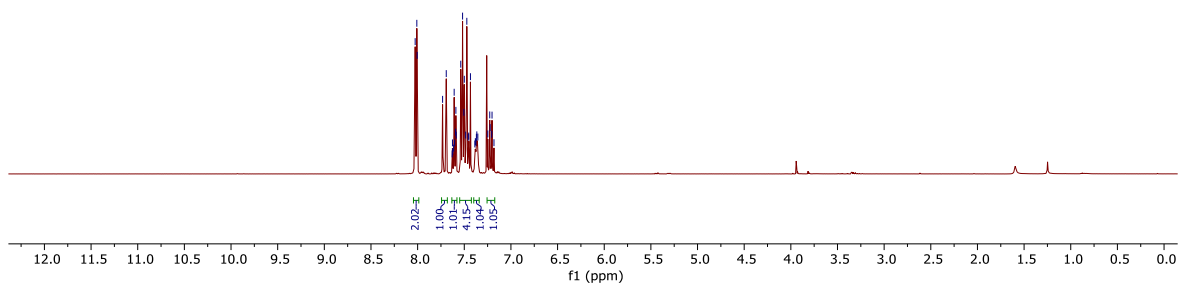
Supplementary Figure 20. NMR spectrum of 1g.

¹H NMR

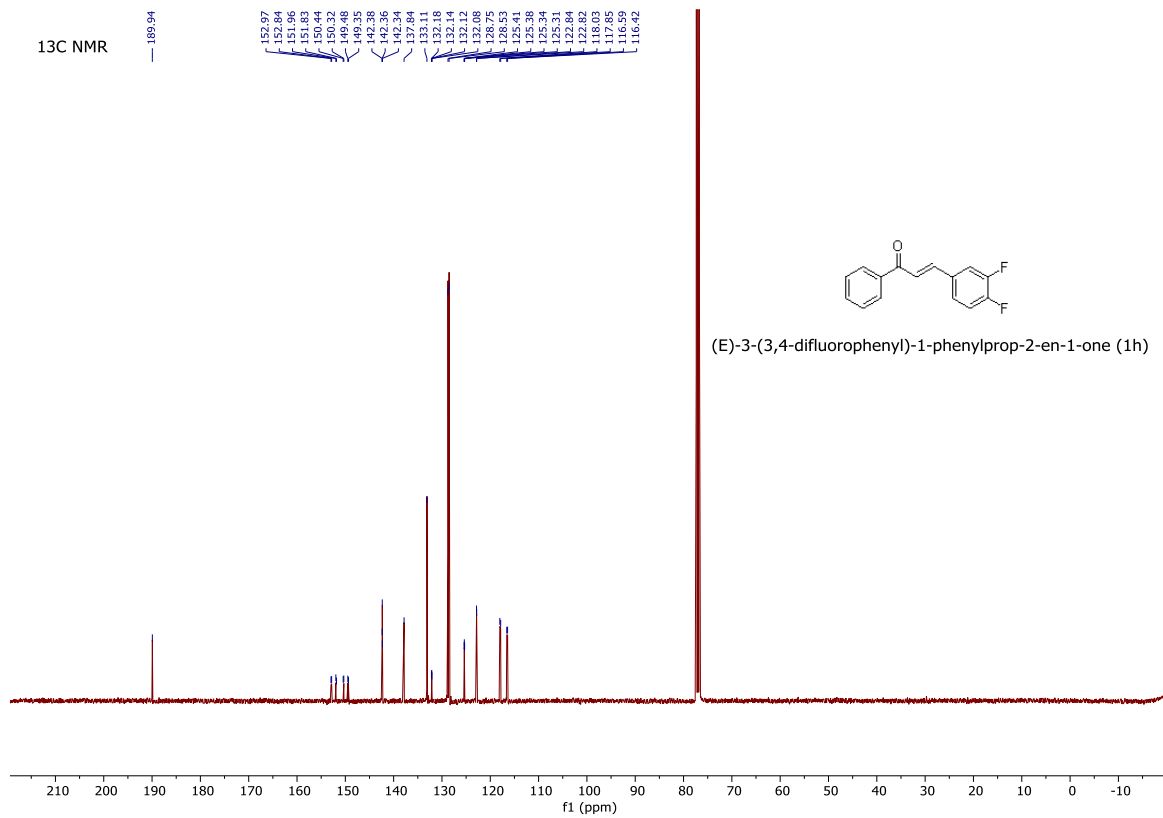
8.03
8.01
8.00
7.73
7.69
7.63
7.62
7.61
7.60
7.59
7.59
7.54
7.52
7.50
7.50
7.47
7.47
7.46
7.45
7.43
7.39
7.38
7.37
7.37
7.35
7.25
7.23
7.21
7.20
7.18



(E)-3-(3,4-difluorophenyl)-1-phenylprop-2-en-1-one (1h)



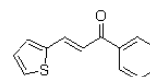
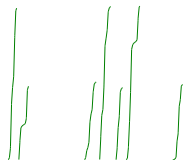
Supplementary Figure 21. NMR spectrum of 1h.



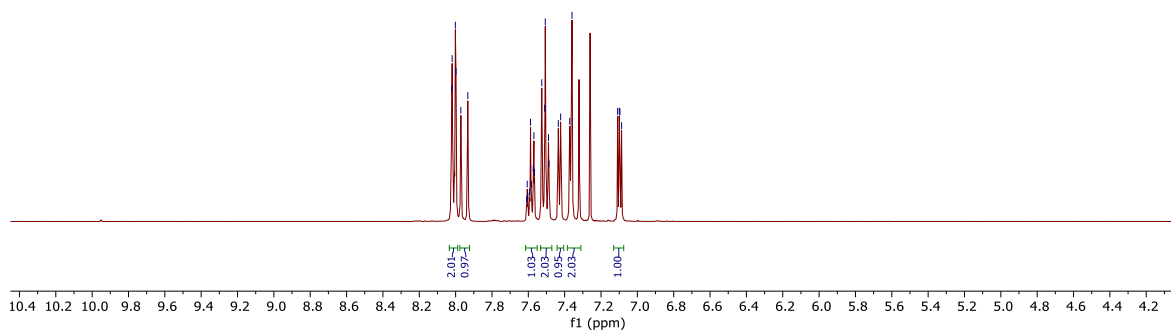
Supplementary Figure 22. NMR spectrum of 1h.

¹H NMR

8.02
8.00
8.00
7.97
7.61
7.61
7.60
7.59
7.58
7.57
7.57
7.53
7.51
7.49
7.49
7.42
7.37
7.36
7.11
7.10
7.09

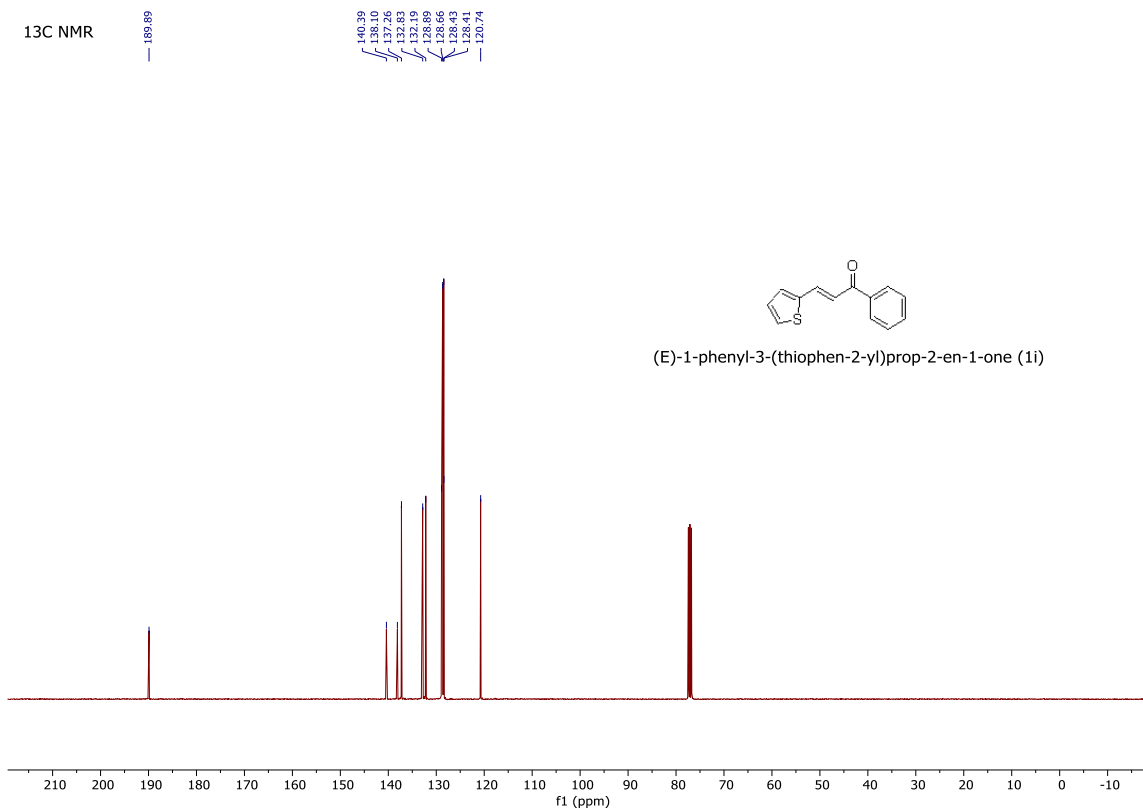


(E)-1-phenyl-3-(thiophen-2-yl)prop-2-en-1-one (**1i**)



Supplementary Figure 23. NMR spectrum of **1i**.

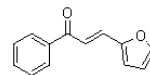
13C NMR



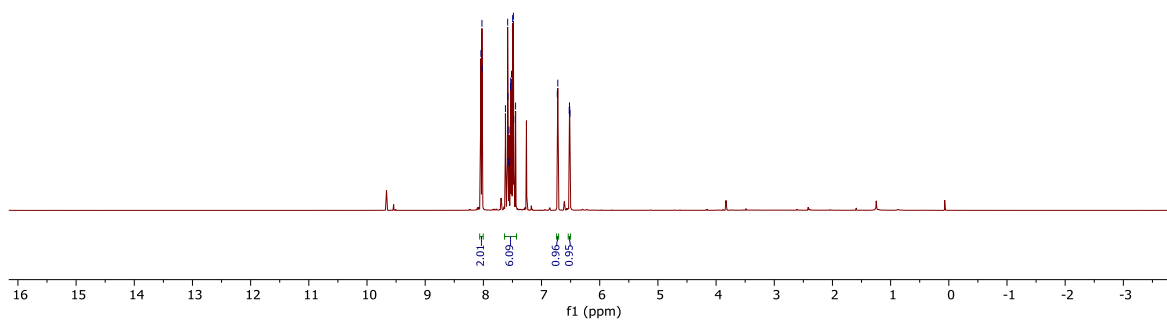
Supplementary Figure 24. NMR spectrum of **1i**.

¹H NMR

8.04
8.02
7.98
7.96
7.95
7.95
7.93
7.90
7.88
7.85
6.72
6.52
6.52
6.51

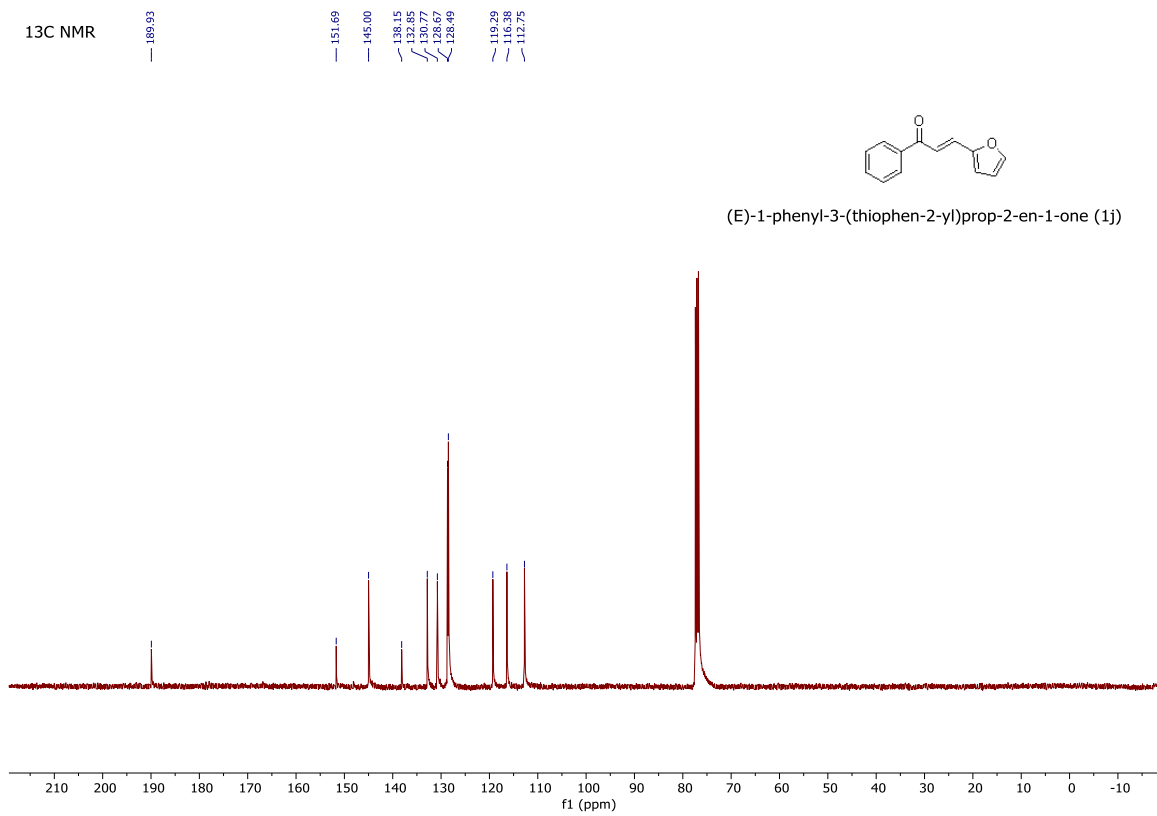


(E)-1-phenyl-3-(thiophen-2-yl)prop-2-en-1-one (**1j**)

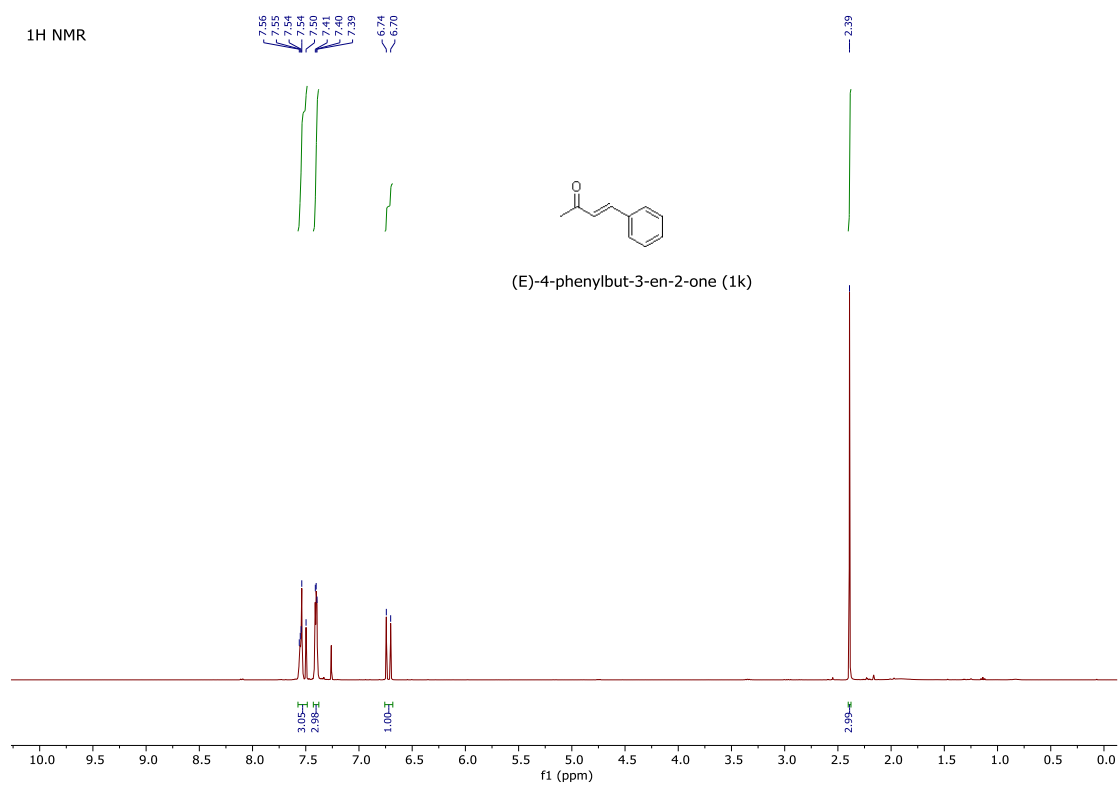


Supplementary Figure 25. NMR spectrum of **1j**.

13C NMR



Supplementary Figure 26. NMR spectrum of **1j**.

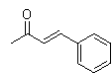


Supplementary Figure 27. NMR spectrum of 1k.

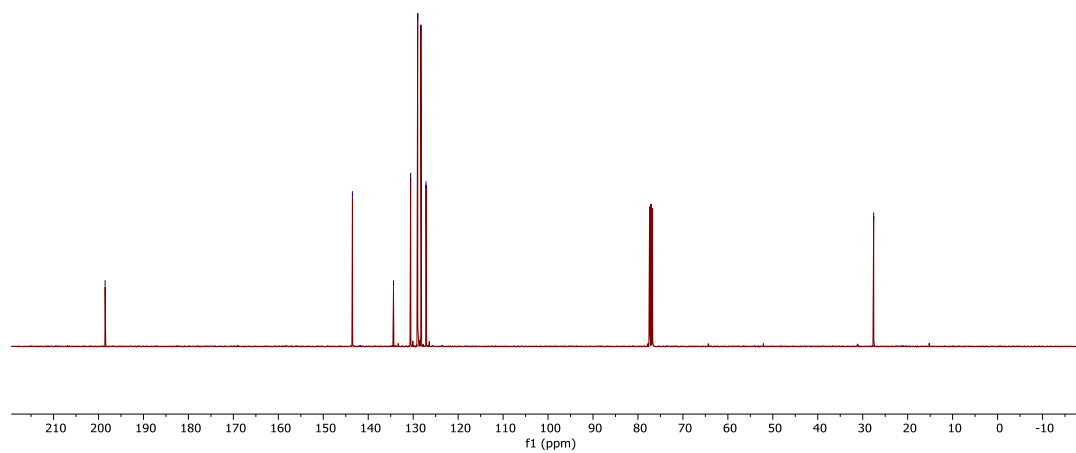
13C NMR
— 198.54

— 143.52
— 134.39
— 129.72
— 128.10
— 128.28
— 127.14

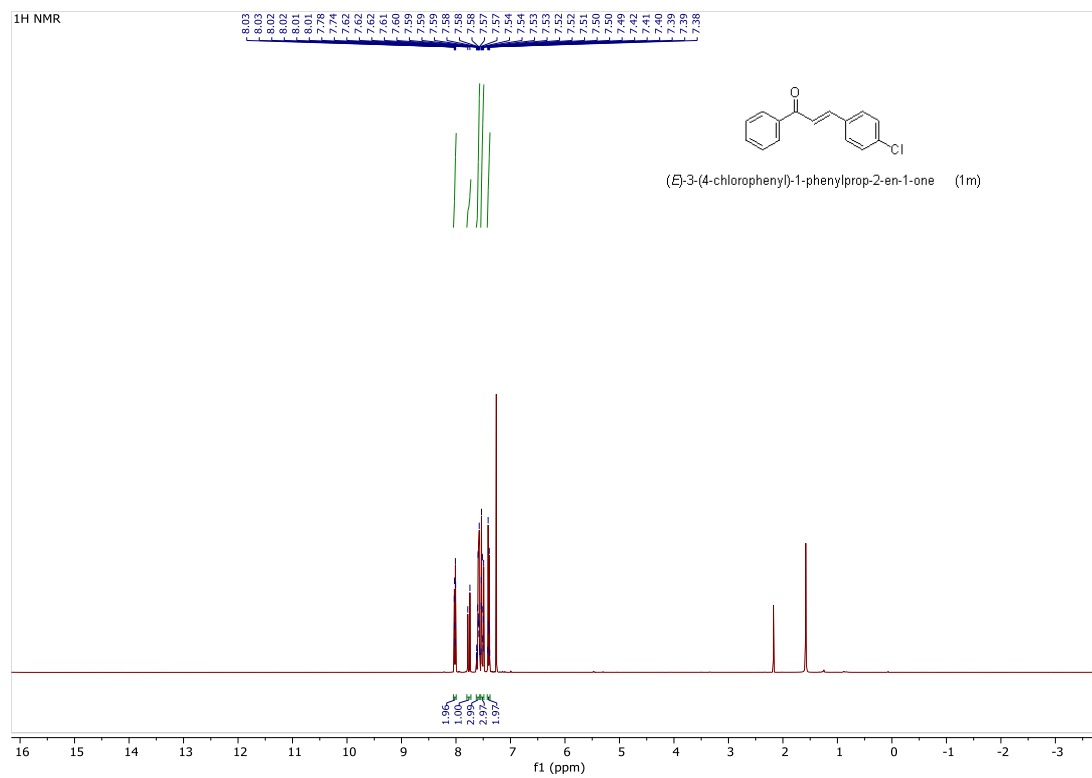
— 27.56



(E)-4-phenylbut-3-en-2-one (1k)

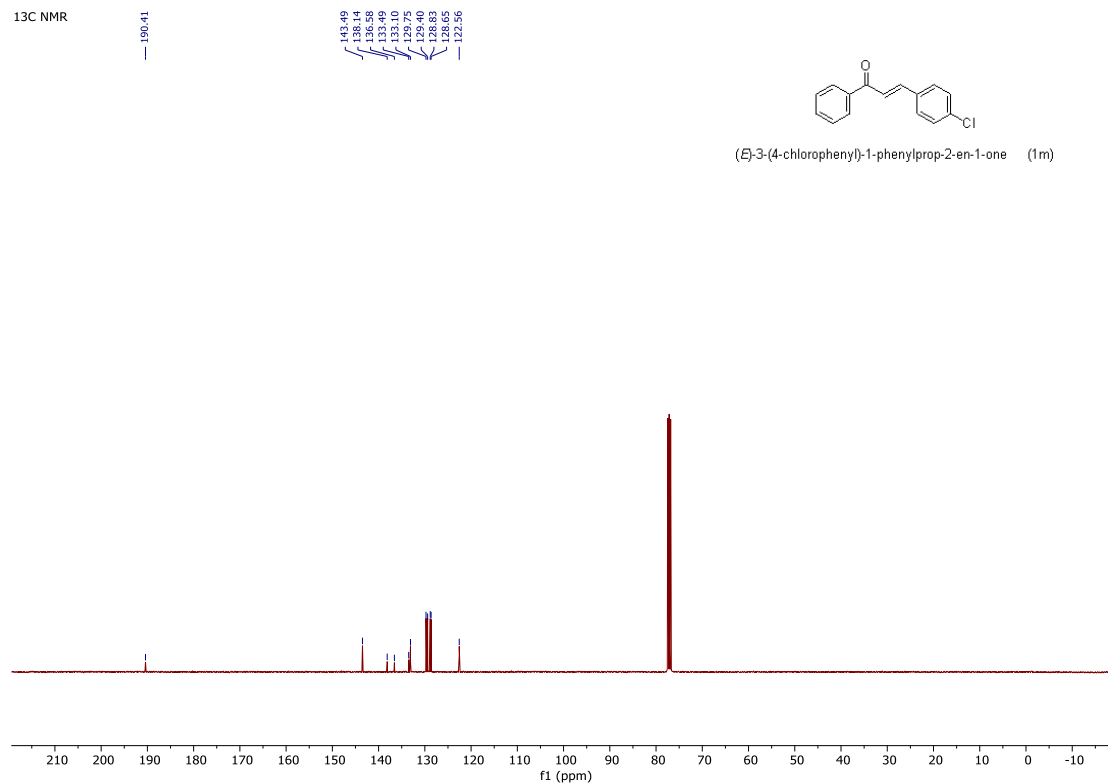


Supplementary Figure 28. NMR spectrum of 1k.



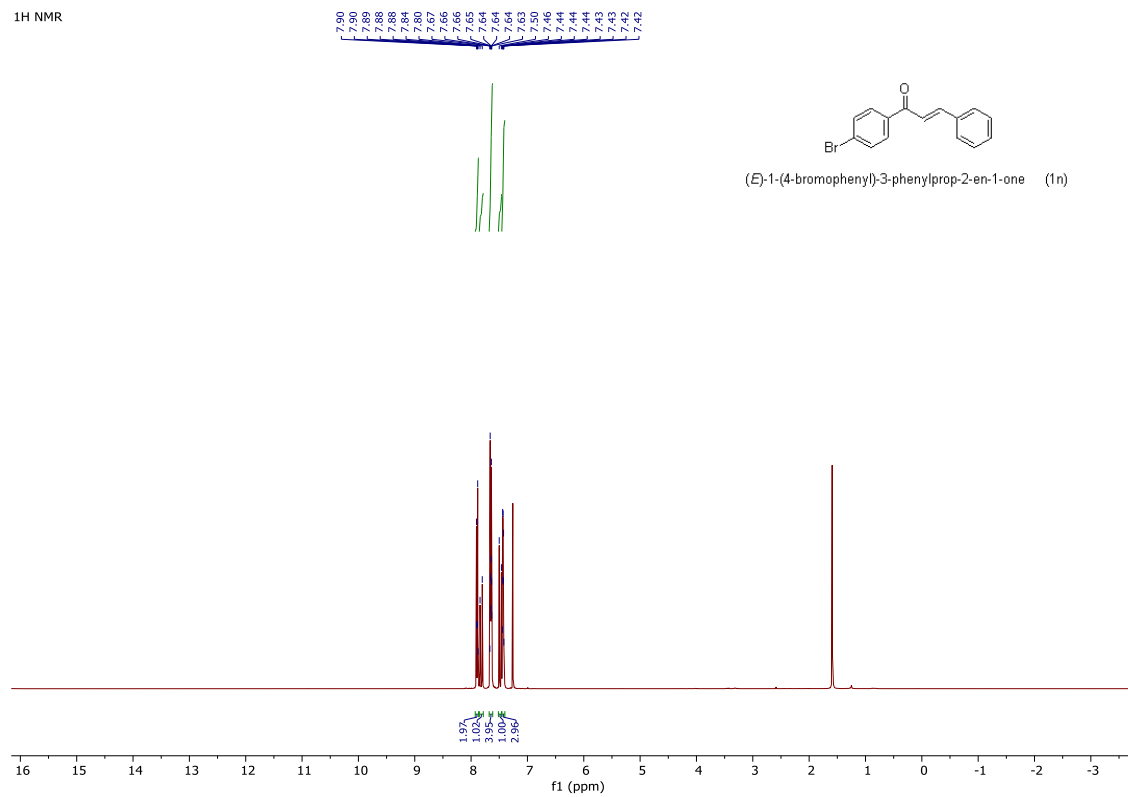
Supplementary Figure 29. NMR spectrum of 1m.

¹³C NMR



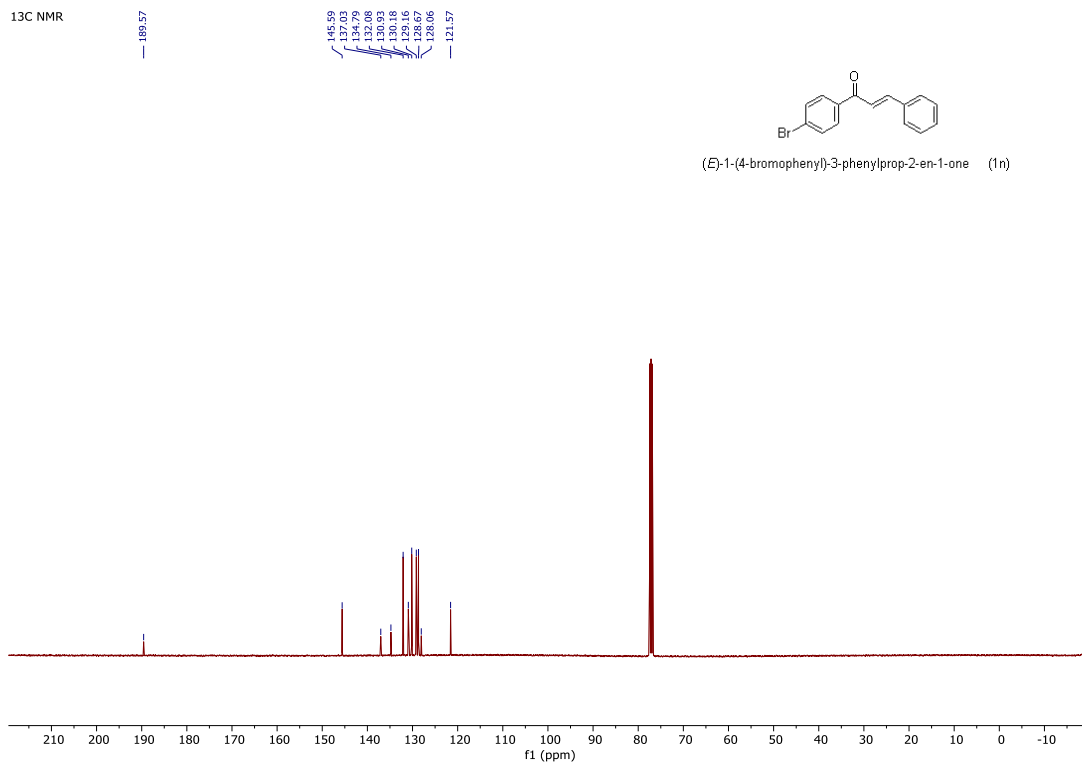
Supplementary Figure 30. NMR spectrum of 1m.

¹H NMR



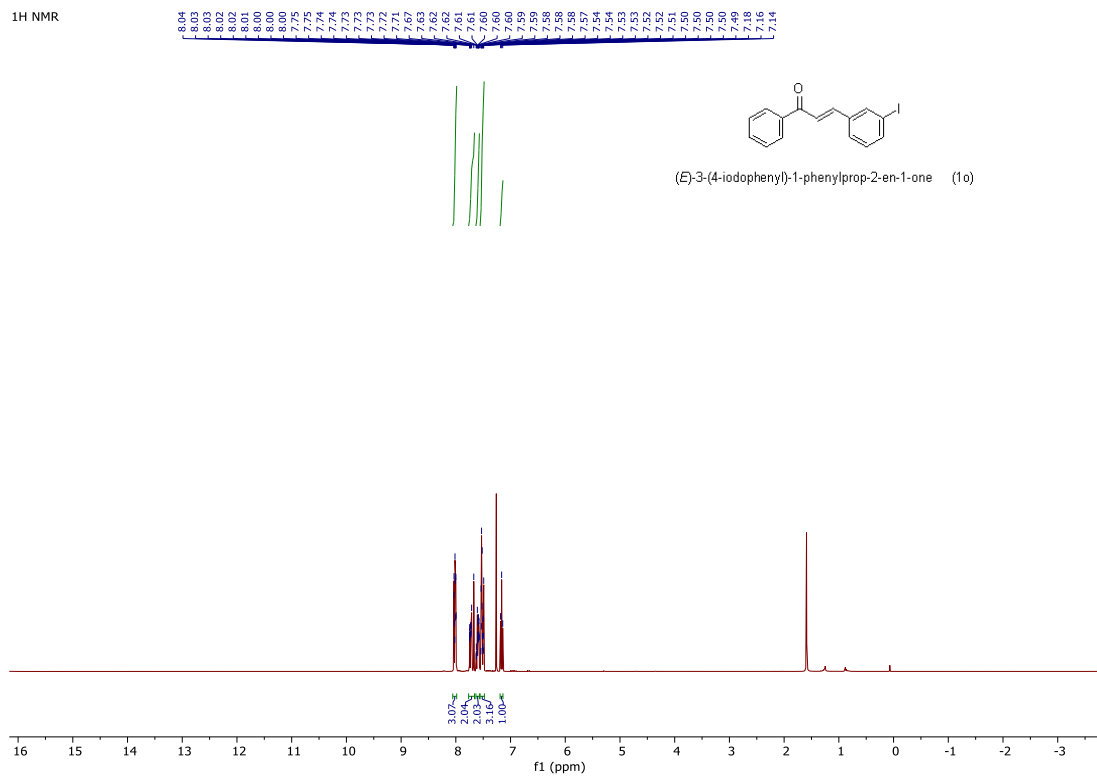
Supplementary Figure 31. NMR spectrum of 1n.

¹³C NMR



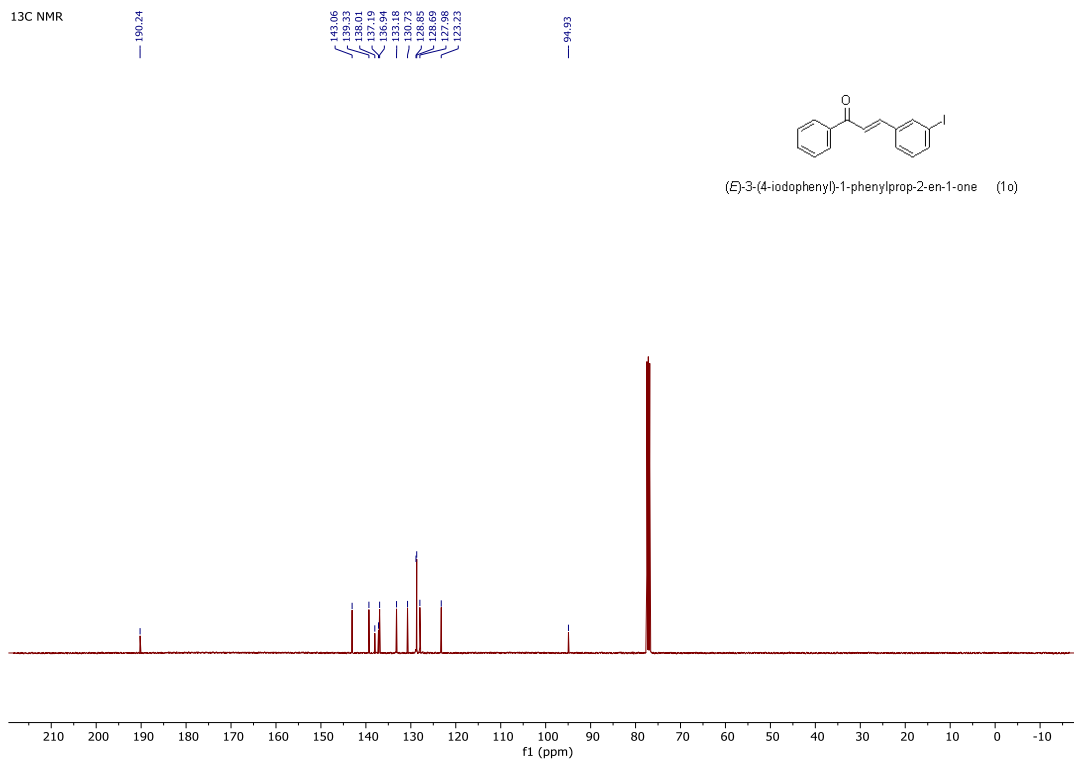
Supplementary Figure 32. NMR spectrum of 1n.

¹H NMR

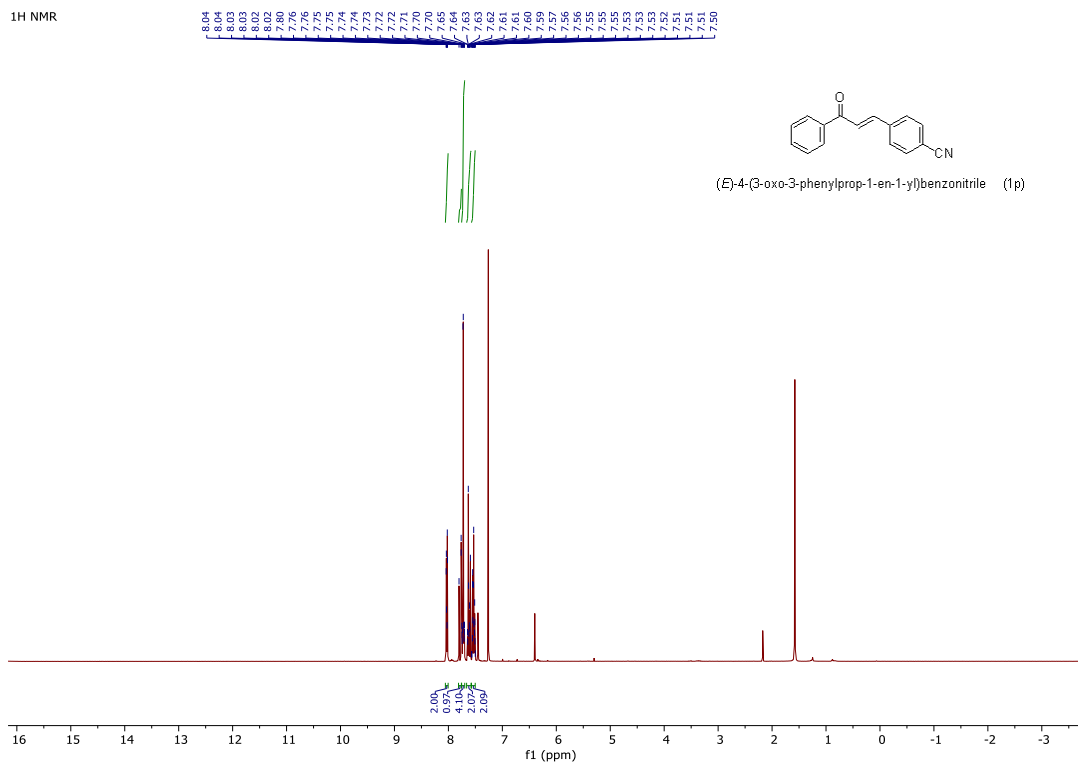


Supplementary Figure 33. NMR spectrum of 1o.

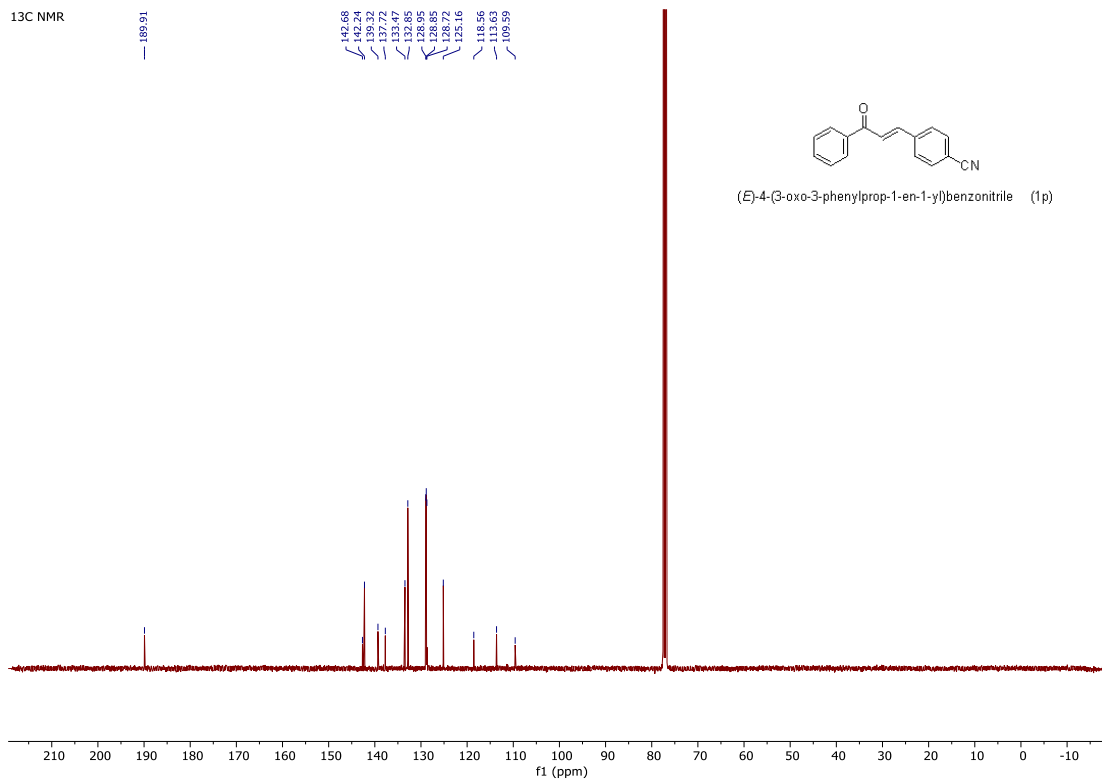
¹³C NMR



Supplementary Figure 34. NMR spectrum of 1o.

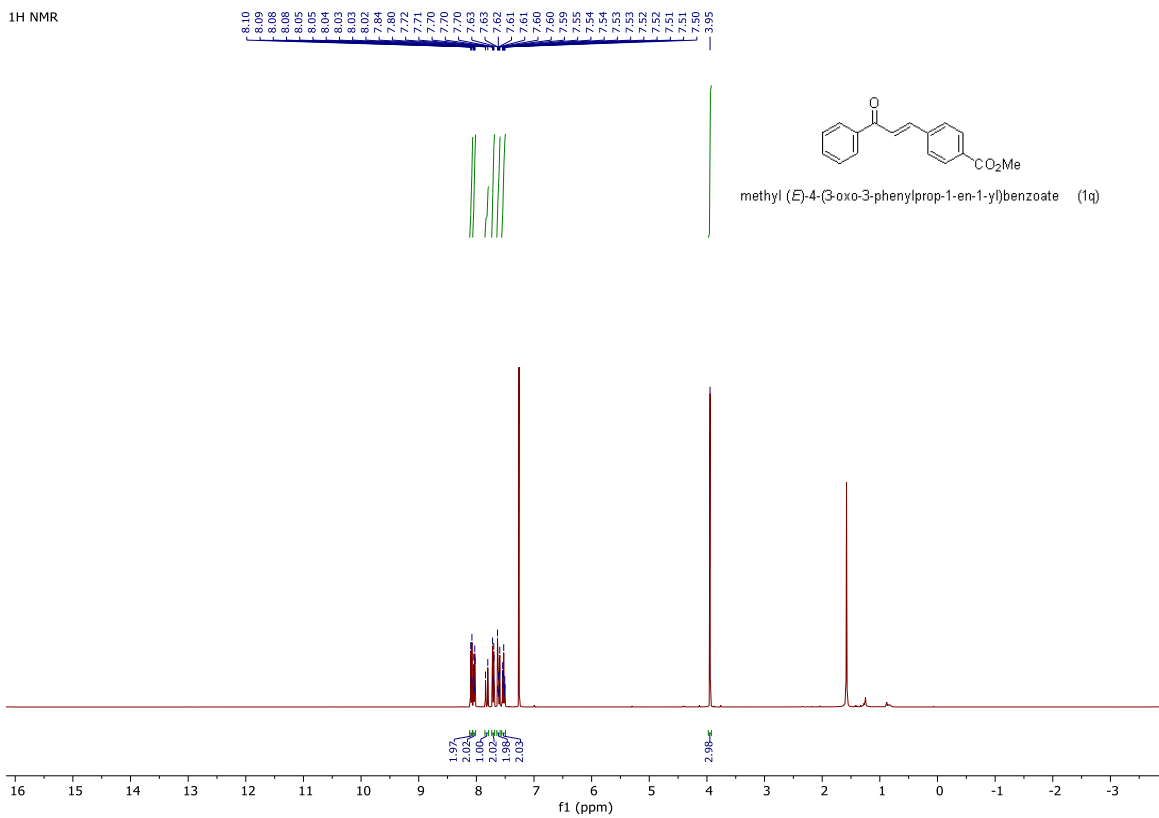


Supplementary Figure 35. NMR spectrum of 1p.



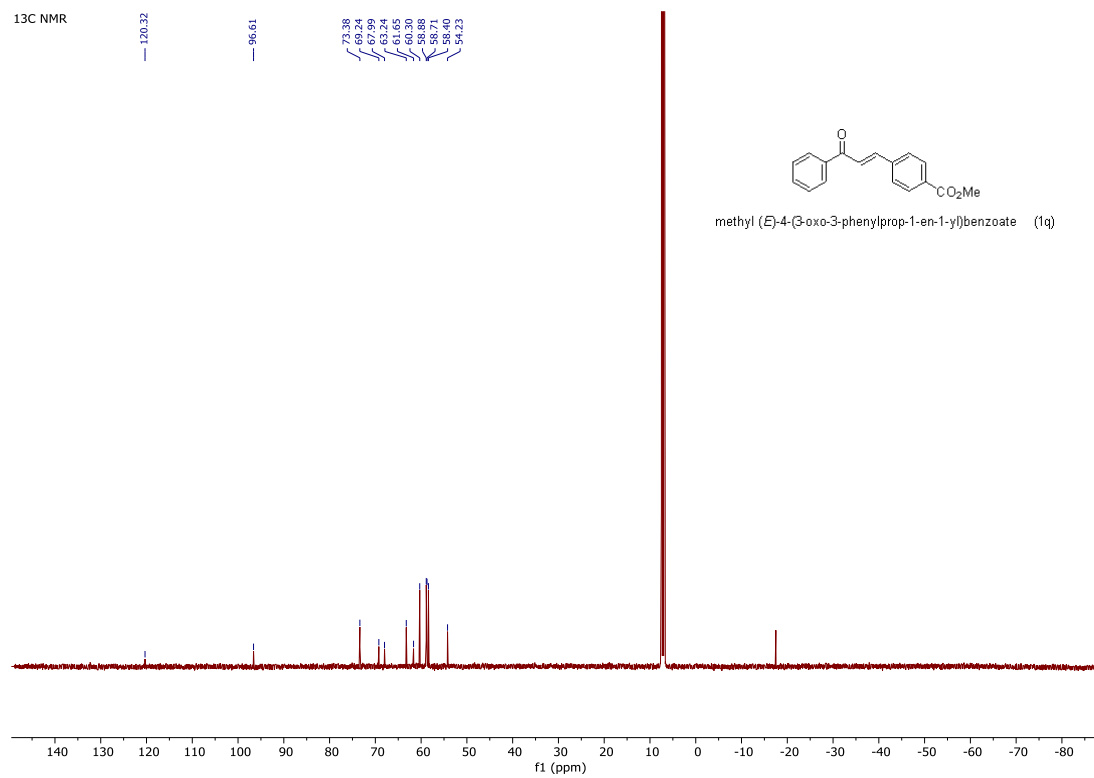
Supplementary Figure 36. NMR spectrum of 1p.

¹H NMR

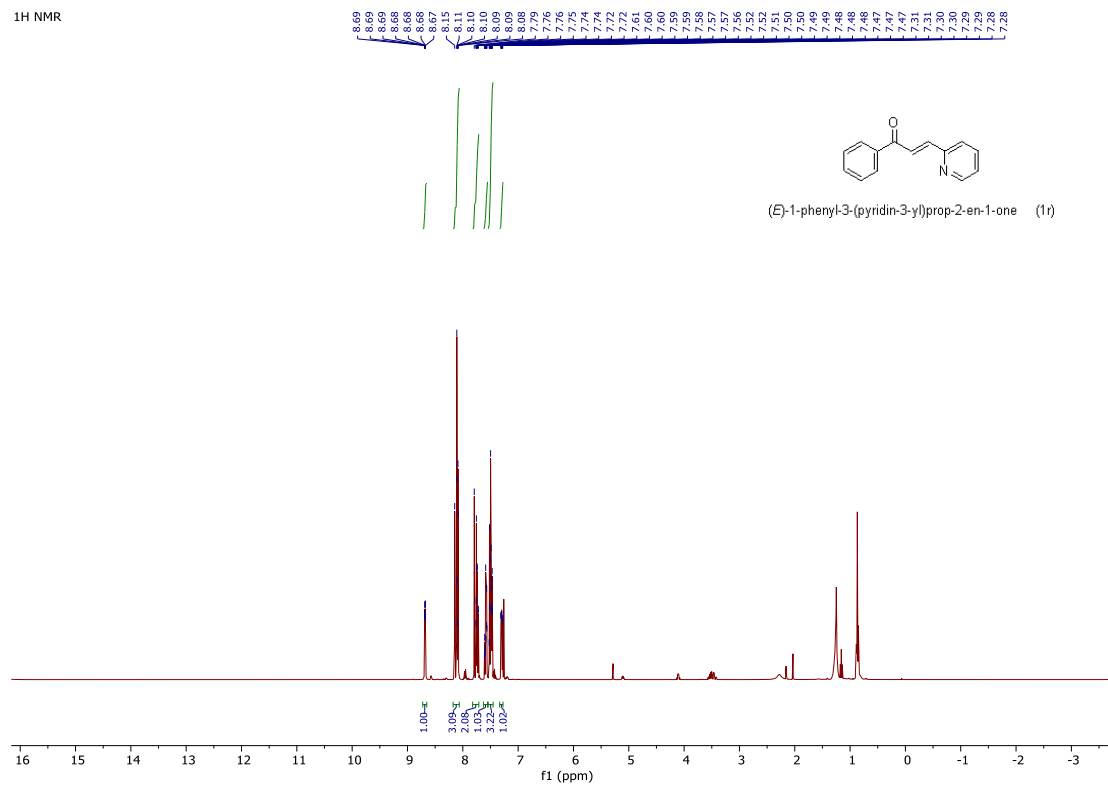


Supplementary Figure 37. NMR spectrum of 1q.

13C NMR

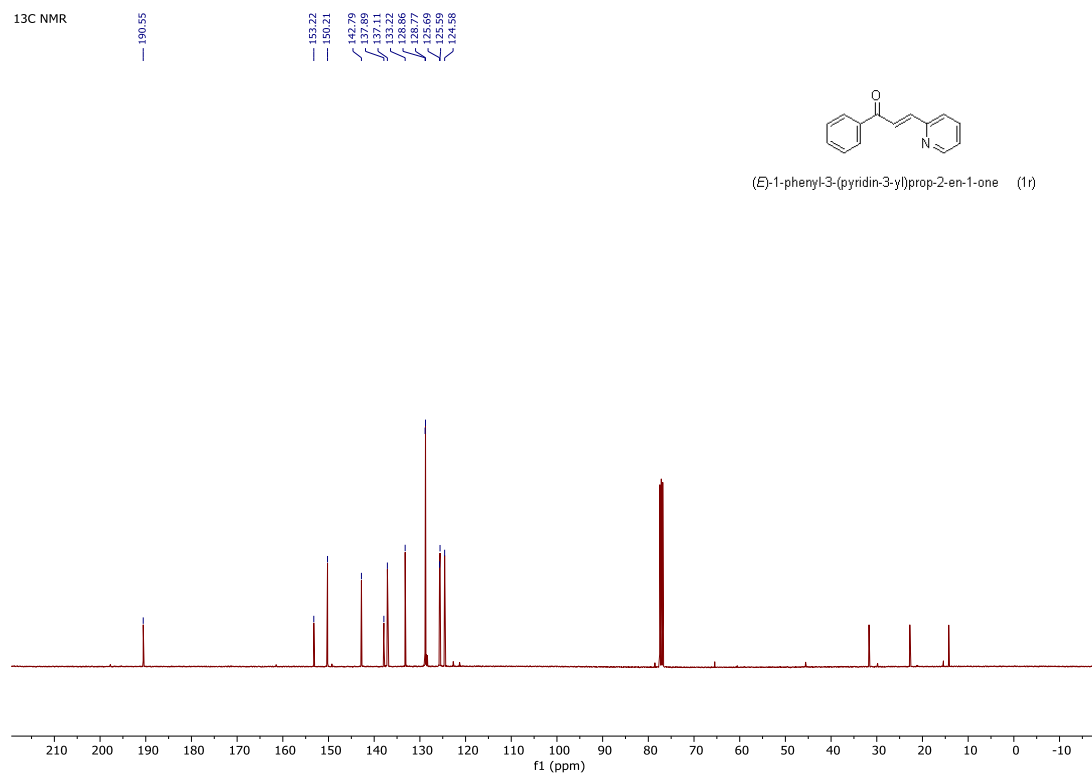


¹H NMR



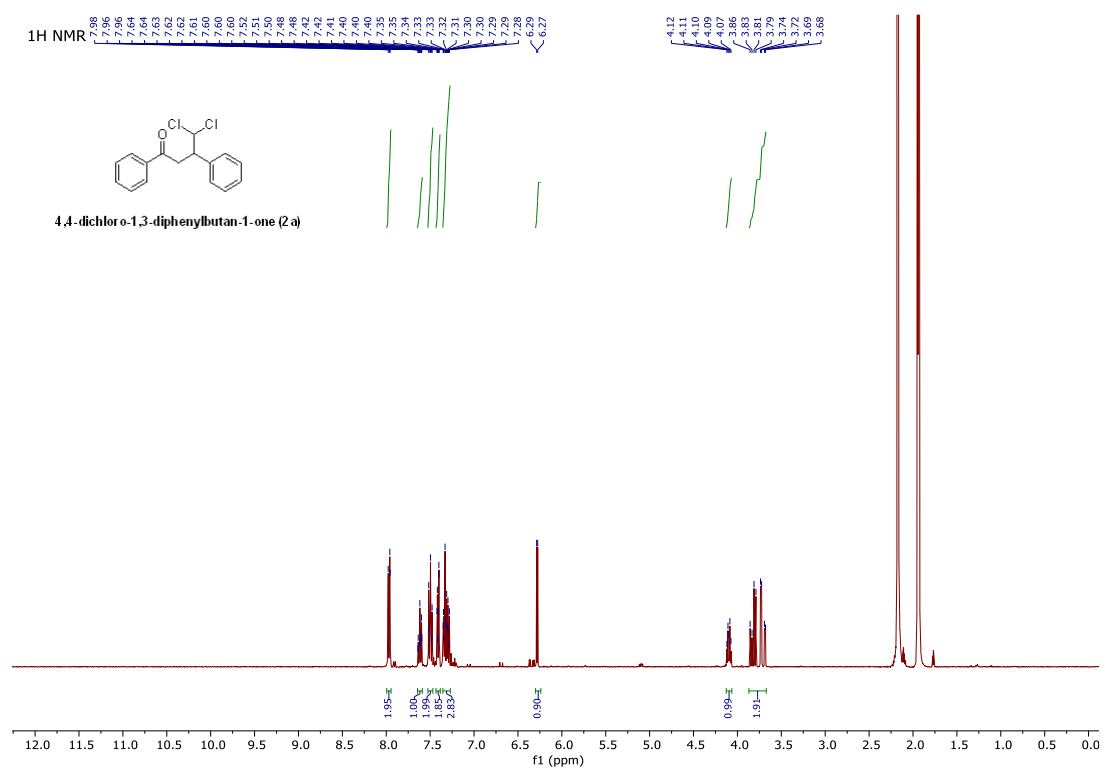
Supplementary Figure 39. NMR spectrum of 1r.

¹³C NMR

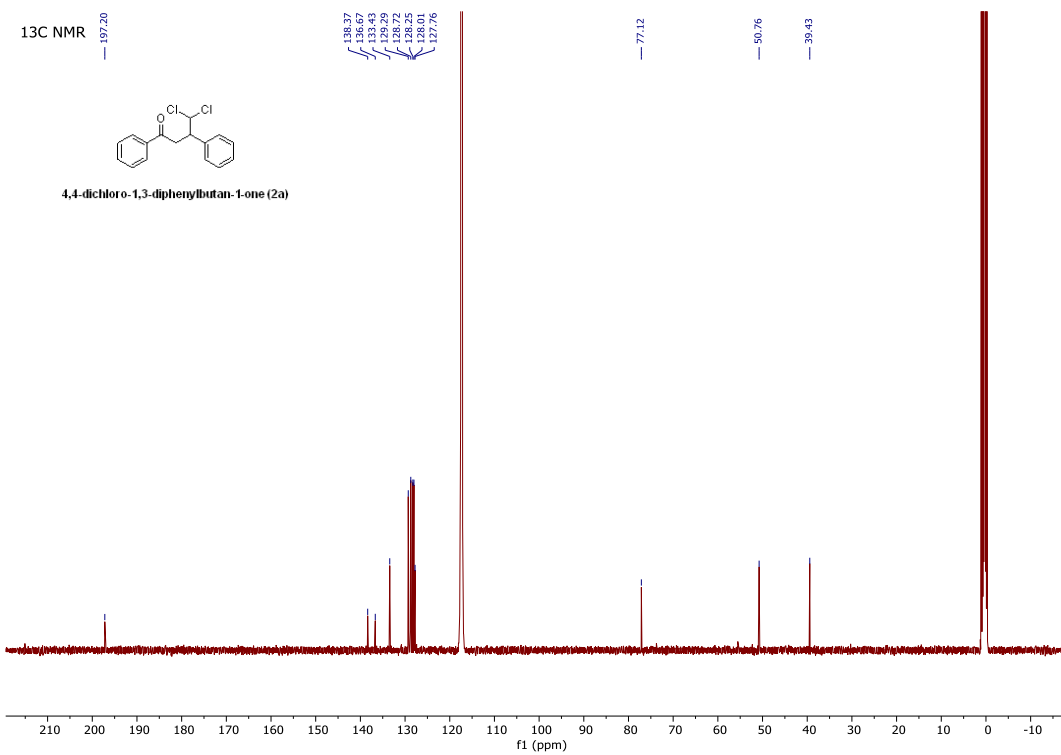


Supplementary Figure 40. NMR spectrum of 1r.

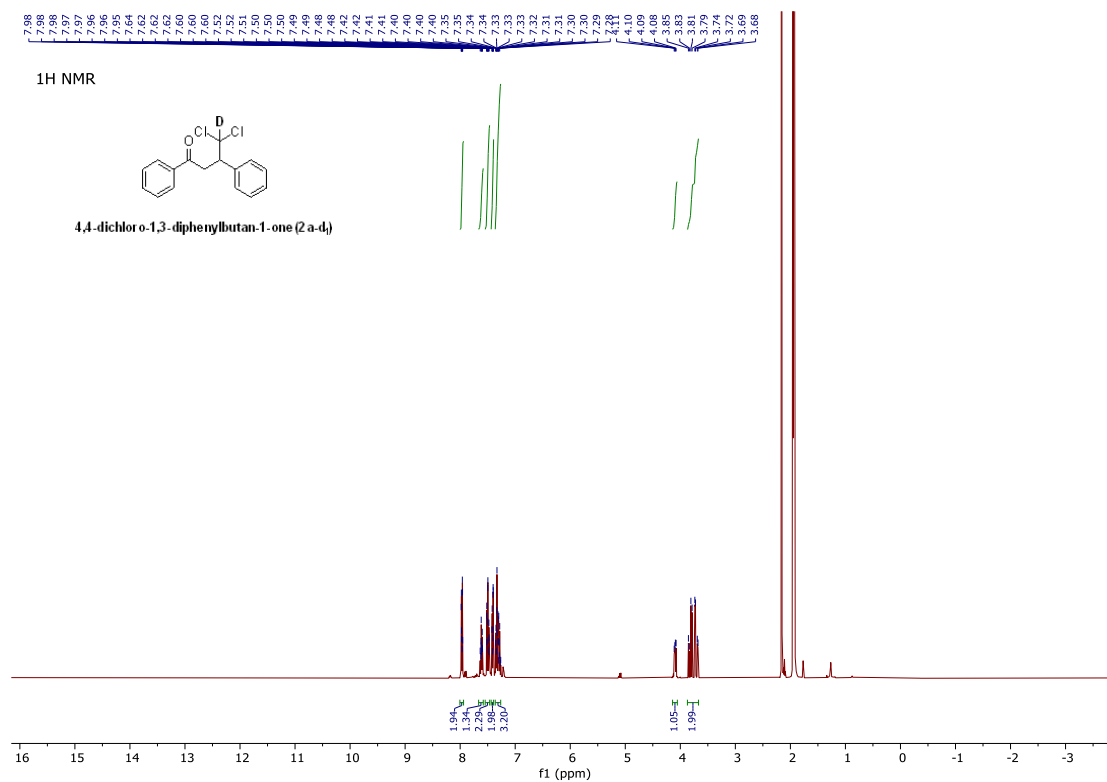
^1H , ^{13}C and ^{19}F NMR spectra of γ,γ -dichloroketones (2a-o)



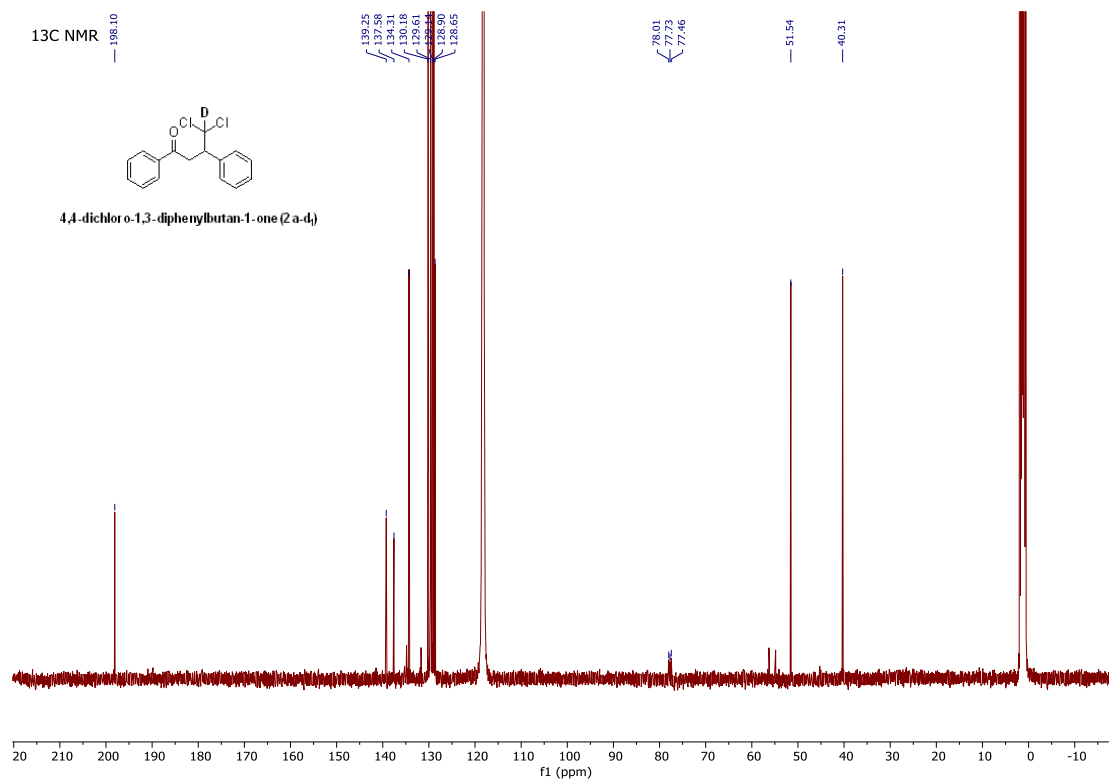
Supplementary Figure 41. NMR spectrum of 2a.



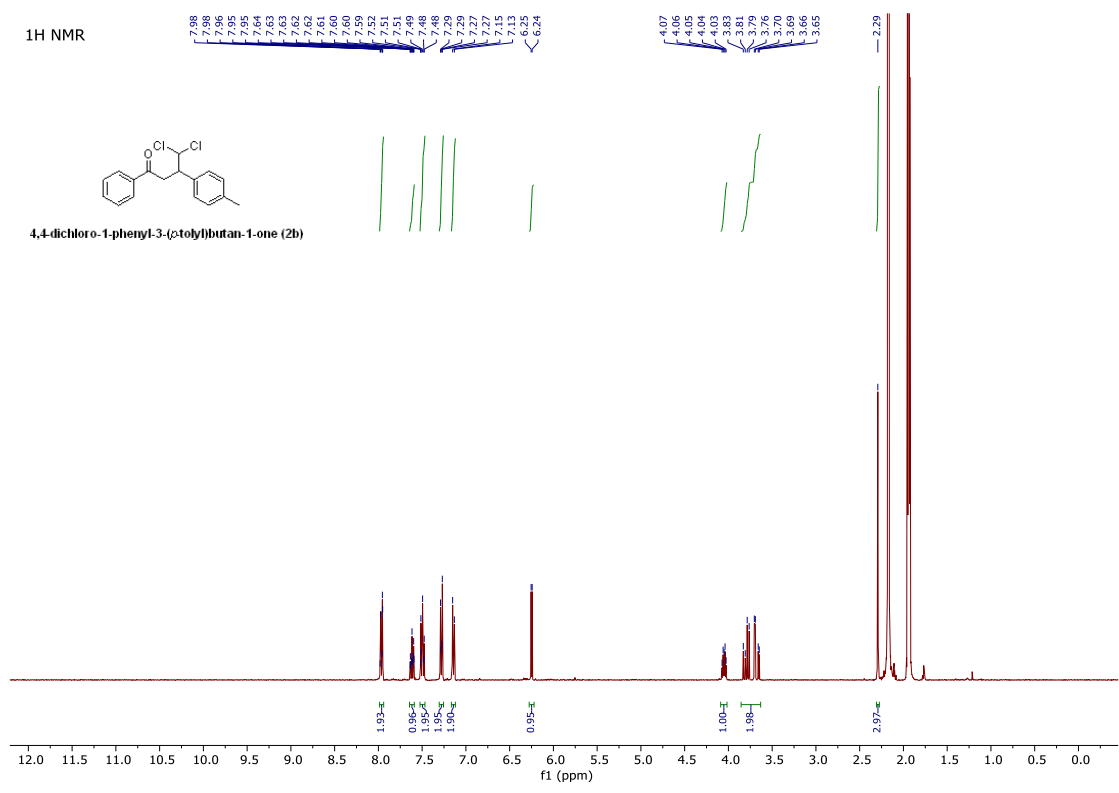
Supplementary Figure 42. NMR spectrum of 2a.



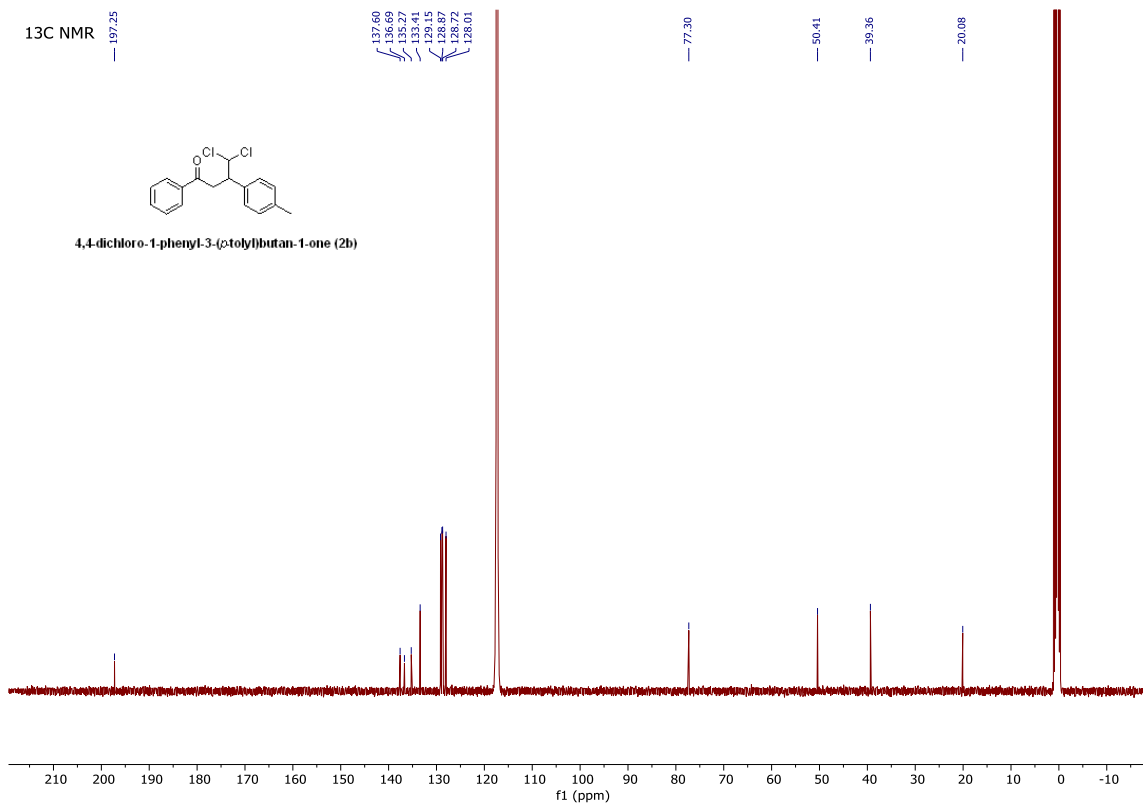
Supplementary Figure 43. NMR spectrum of 2a-d₁.



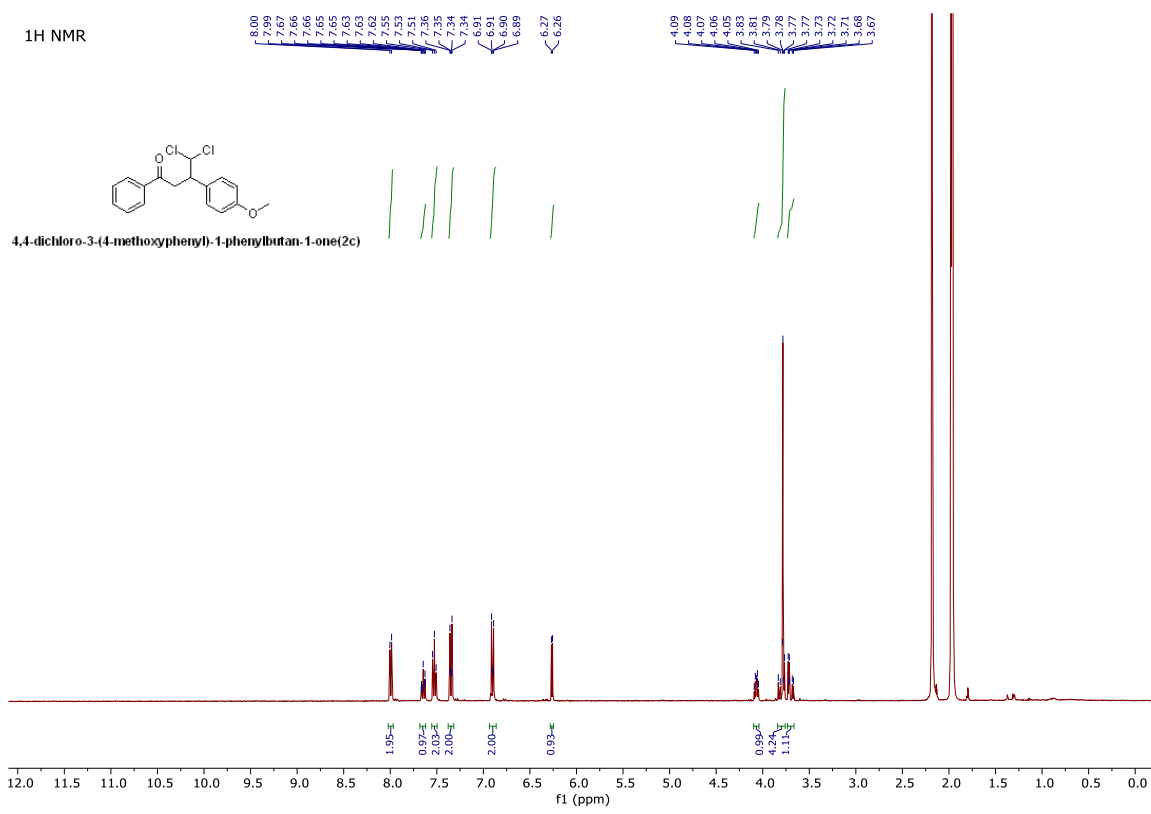
Supplementary Figure 44. NMR spectrum of 2a-d₁.



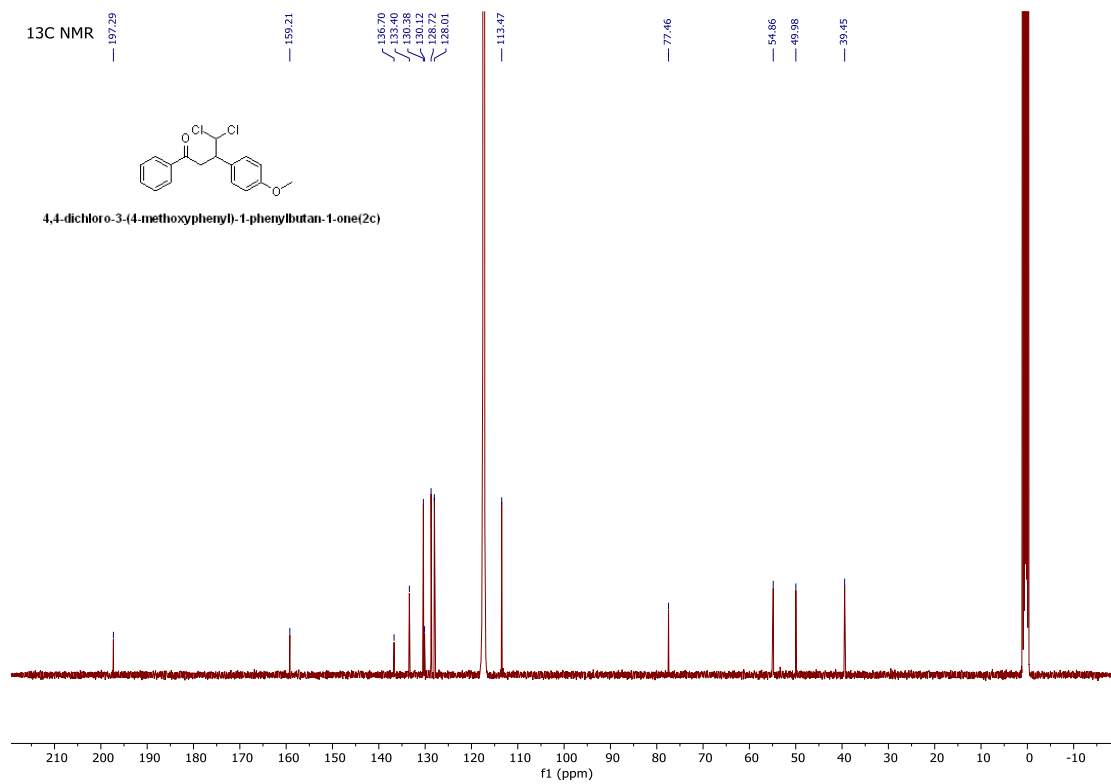
Supplementary Figure 45. NMR spectrum of 2b.



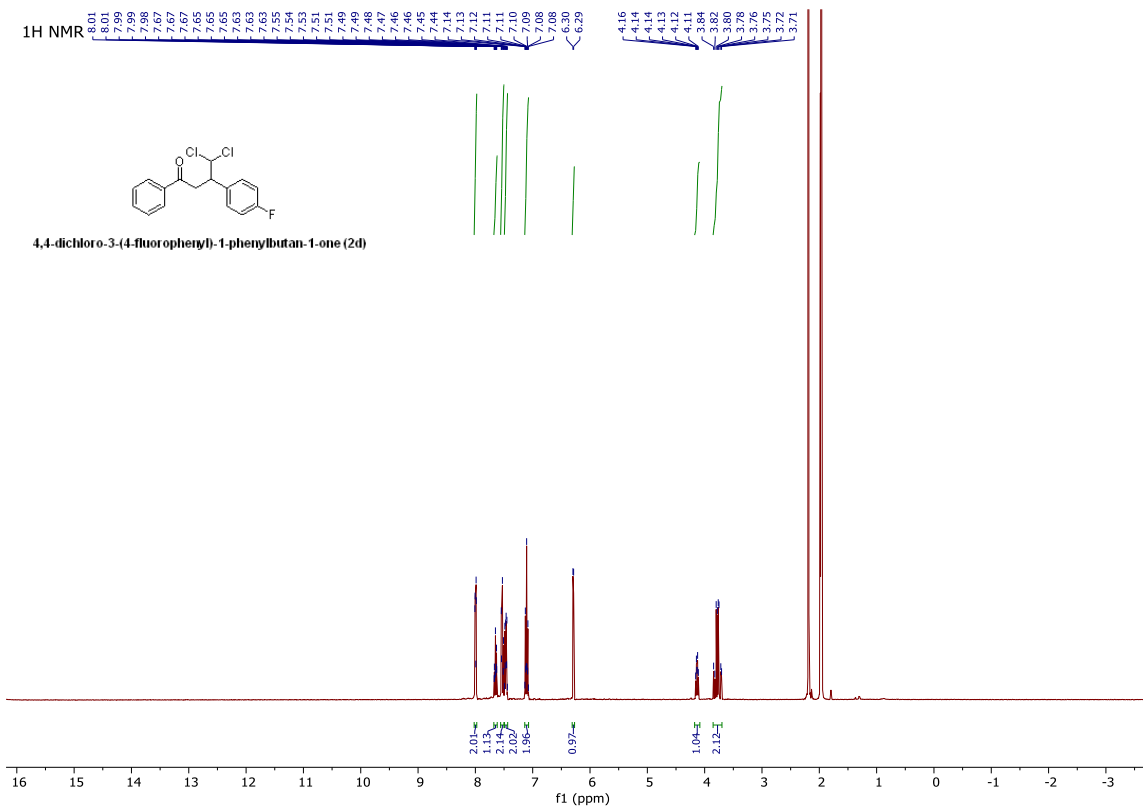
Supplementary Figure 46. NMR spectrum of 2b.



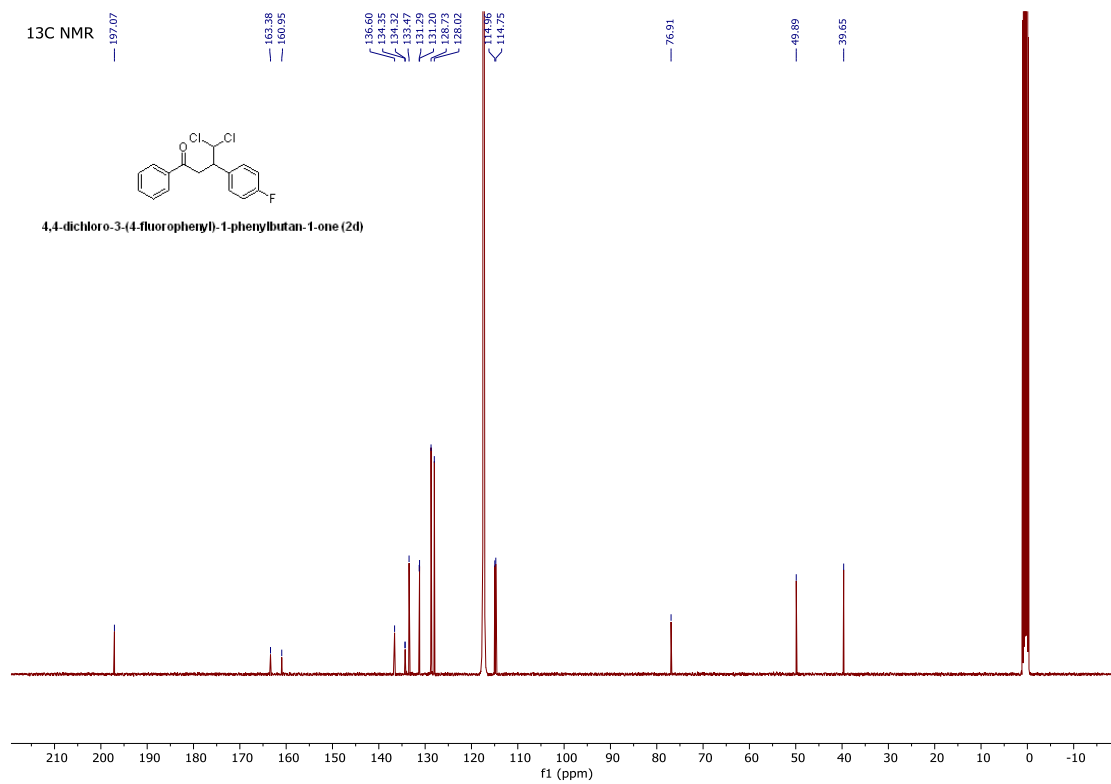
Supplementary Figure 47. NMR spectrum of 2c.



Supplementary Figure 48. NMR spectrum of 2c.

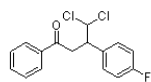


Supplementary Figure 49. NMR spectrum of 2d.

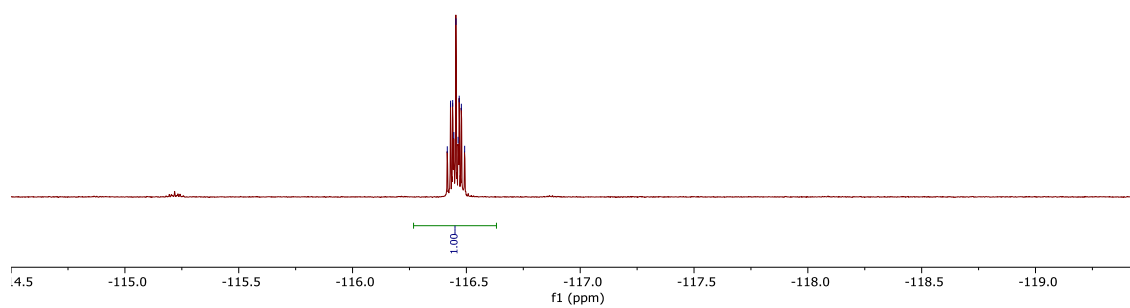
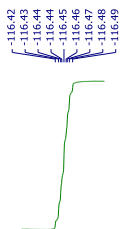


Supplementary Figure 50. NMR spectrum of 2d.

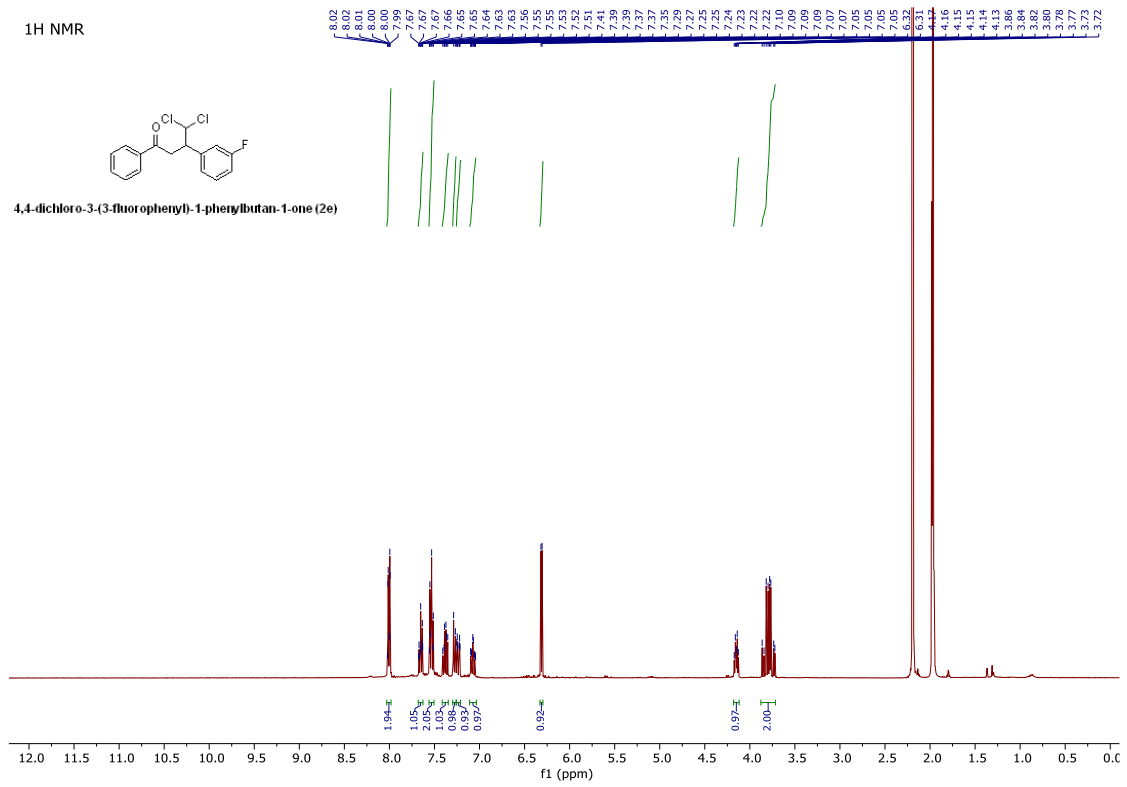
19F NMR



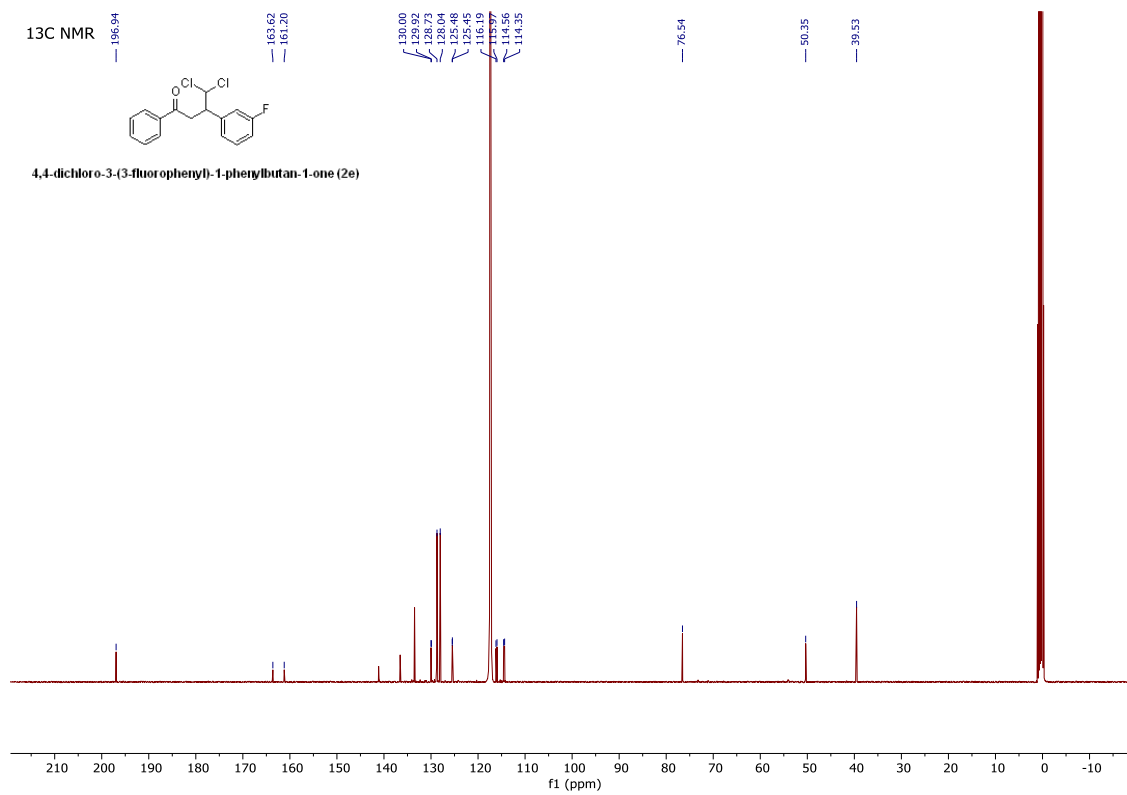
4,4-dichloro-3-(4-fluorophenyl)-1-phenylbutan-1-one (2d)



Supplementary Figure 51. NMR spectrum of 2d.

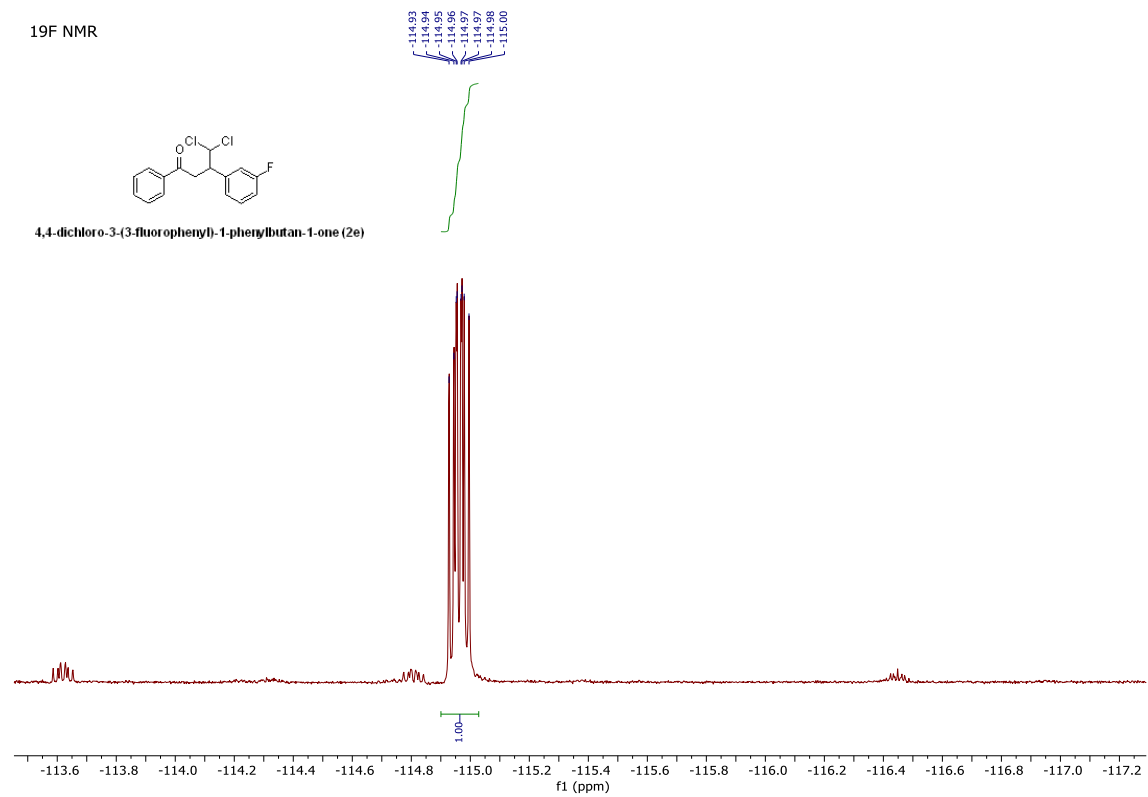


Supplementary Figure 52. NMR spectrum of 2e.



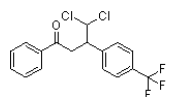
Supplementary Figure 53. NMR spectrum of 2e.

19F NMR

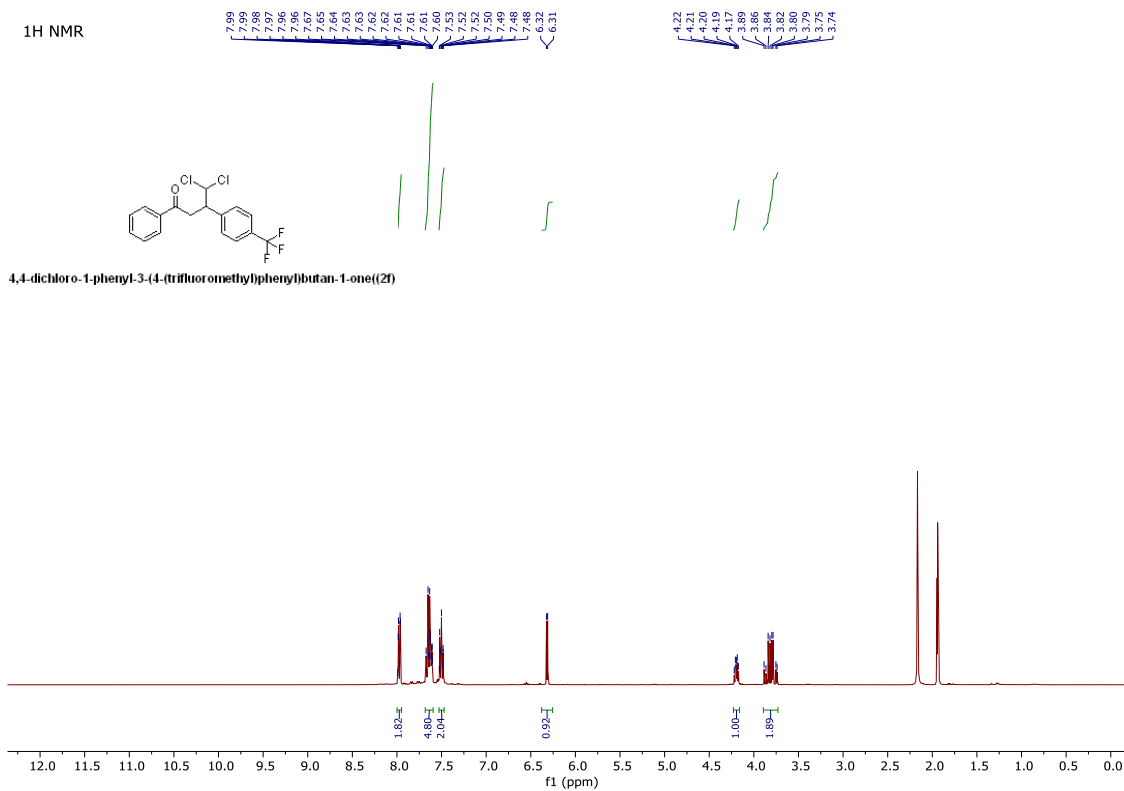


Supplementary Figure 54. NMR spectrum of 2e.

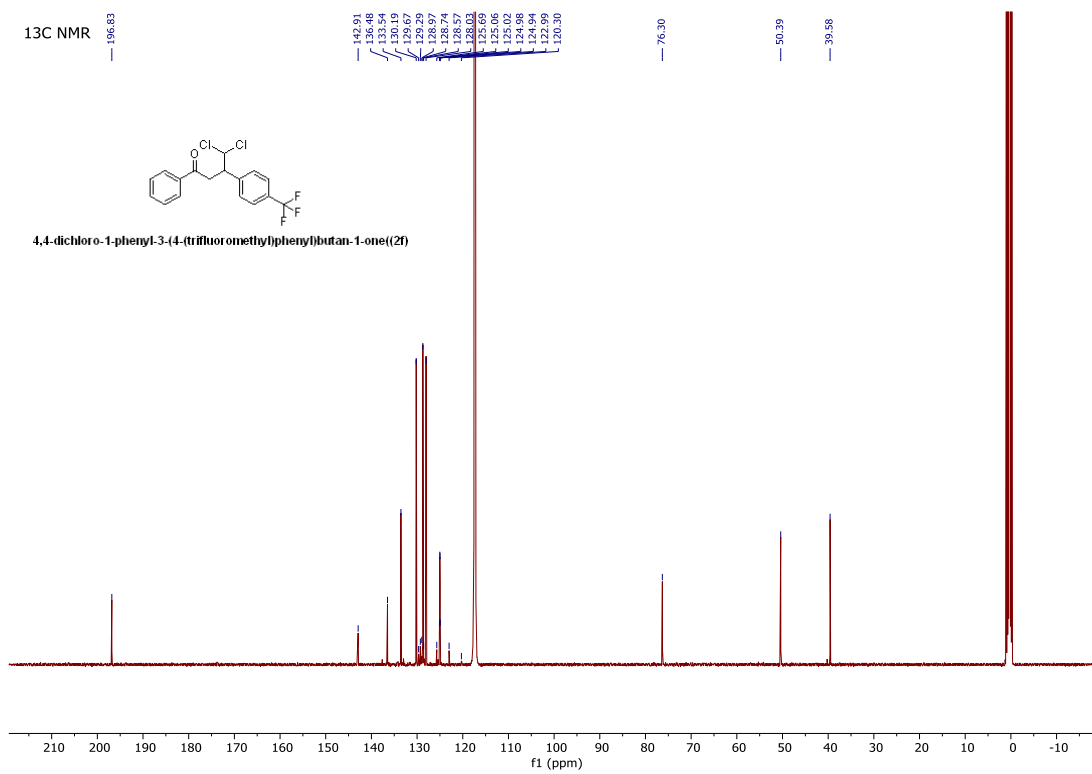
¹H NMR



4,4-dichloro-1-phenyl-3-(4-(trifluoromethyl)phenyl)butan-1-one (2f)



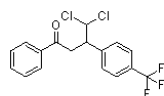
Supplementary Figure 55. NMR spectrum of 2f.



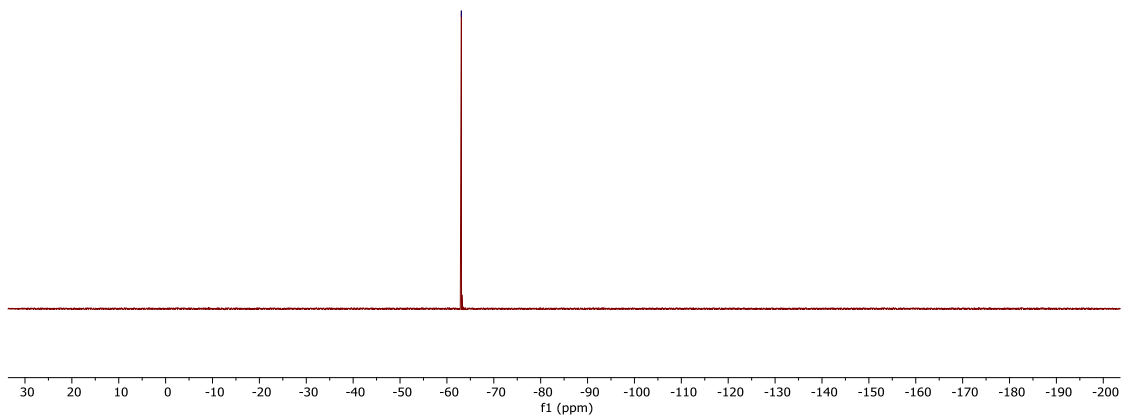
Supplementary Figure 56. NMR spectrum of 2f.

19F NMR

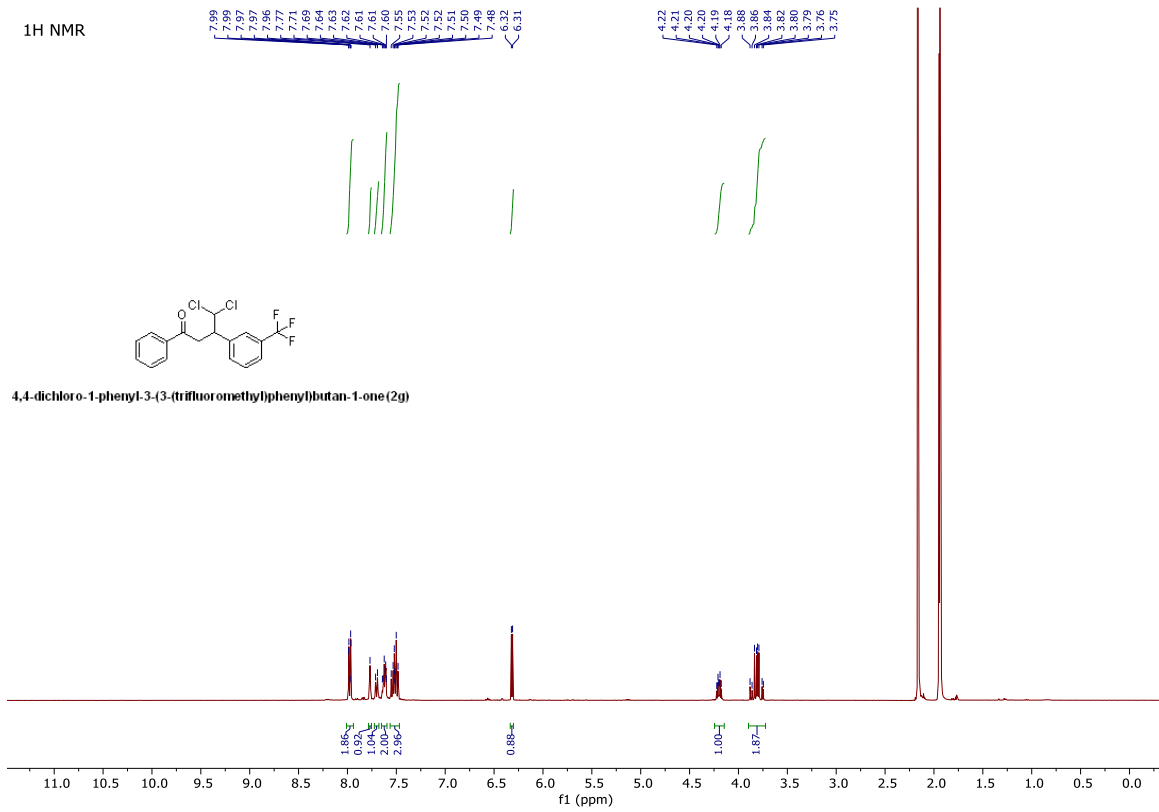
— 63.08



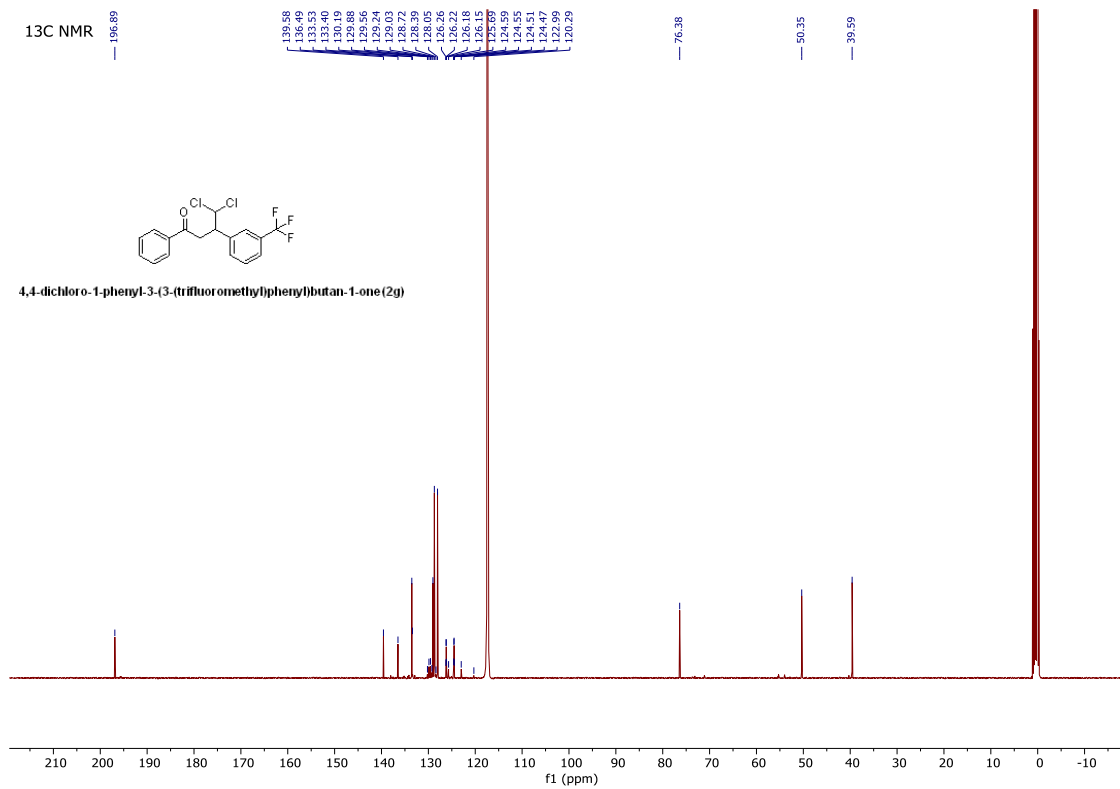
4,4-dichloro-1-phenyl-3-(4-(trifluoromethyl)phenyl)butan-1-one(2f)



Supplementary Figure 57. NMR spectrum of 2f.



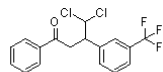
Supplementary Figure 58. NMR spectrum of 2g.



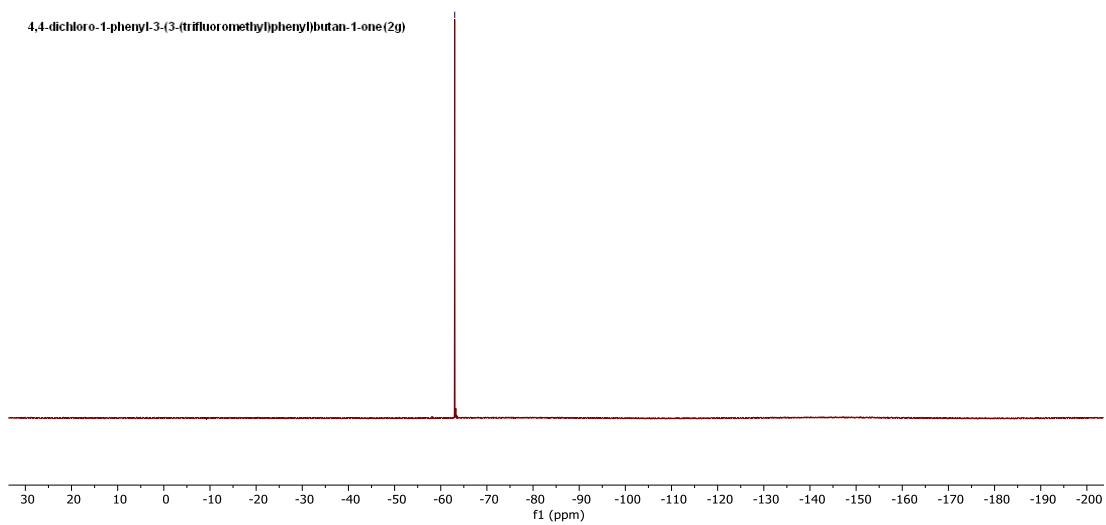
Supplementary Figure 59. NMR spectrum of 2g.

19F NMR

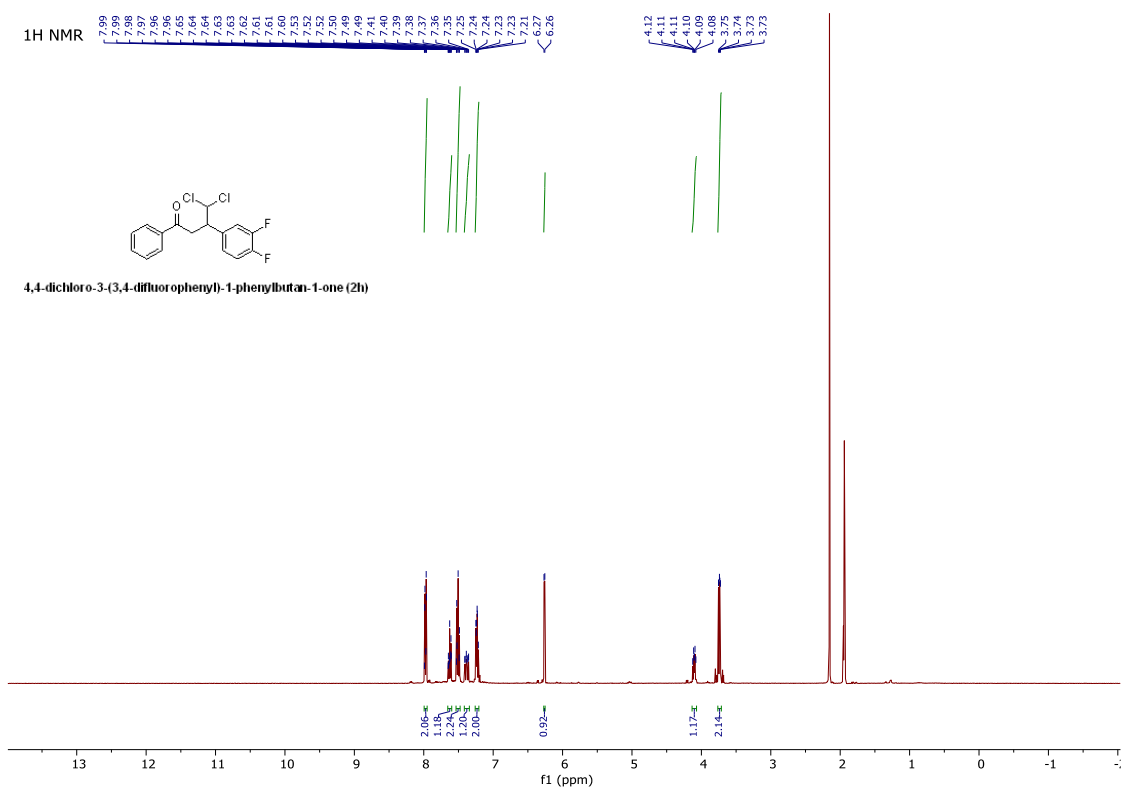
63.03



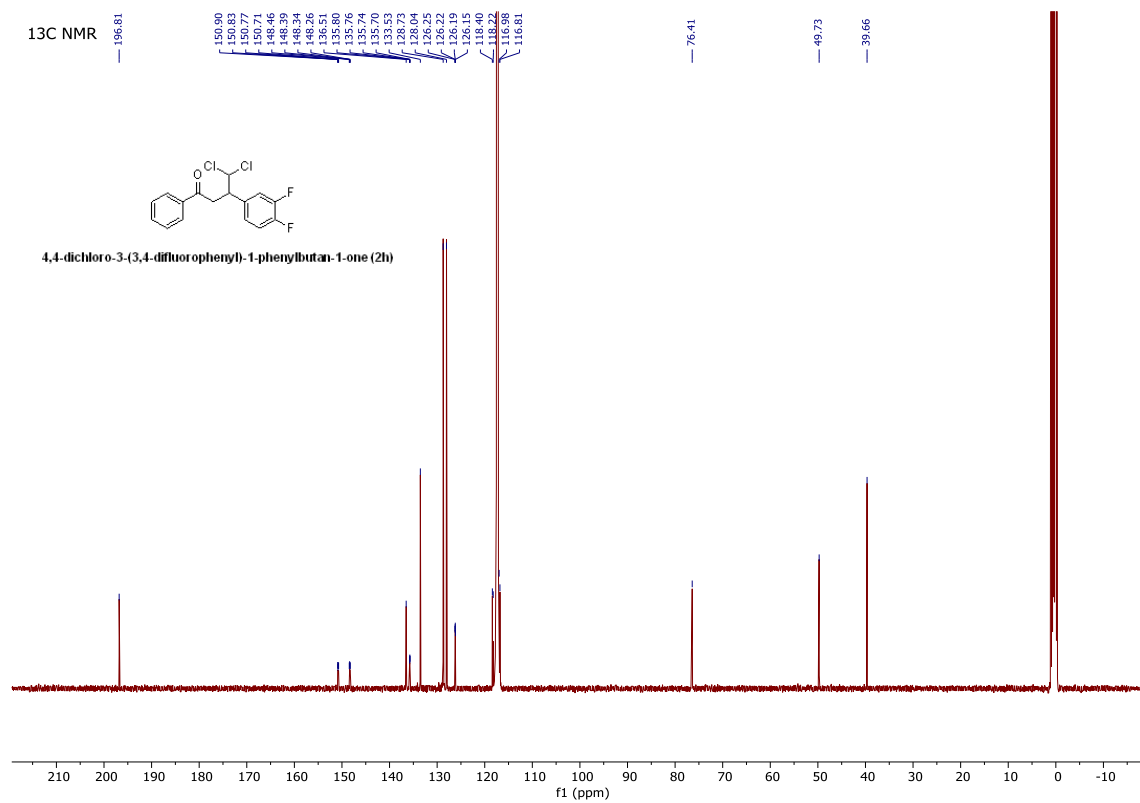
4,4-dichloro-1-phenyl-3-(3-(trifluoromethyl)phenyl)butan-1-one (2g)



Supplementary Figure 60. NMR spectrum of 2g.

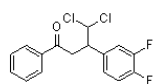


Supplementary Figure 61. NMR spectrum of 2h.

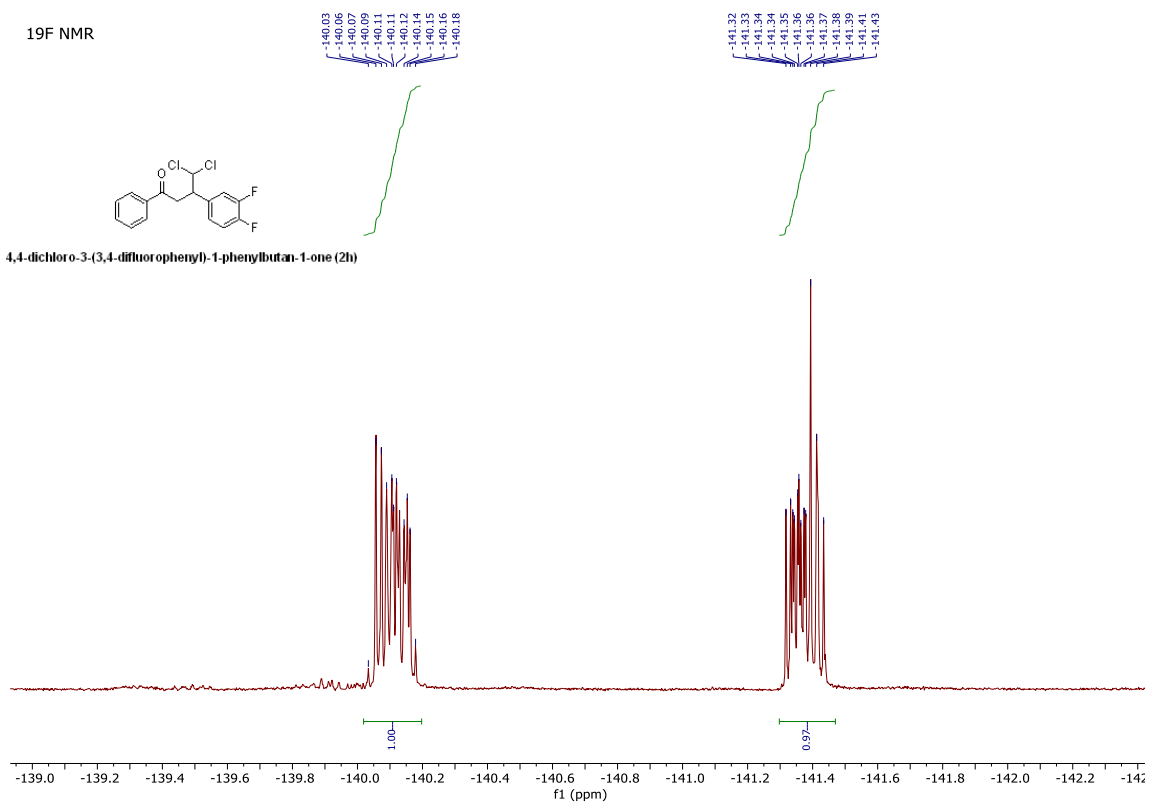


Supplementary Figure 62. NMR spectrum of 2h.

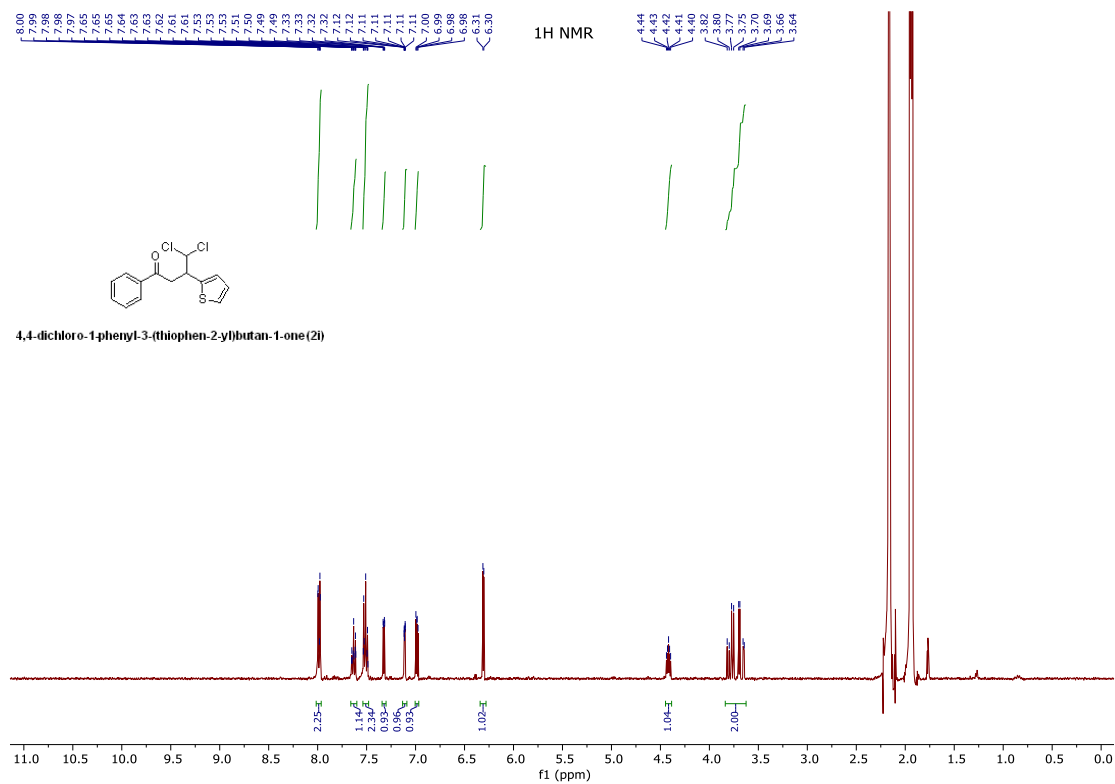
19F NMR



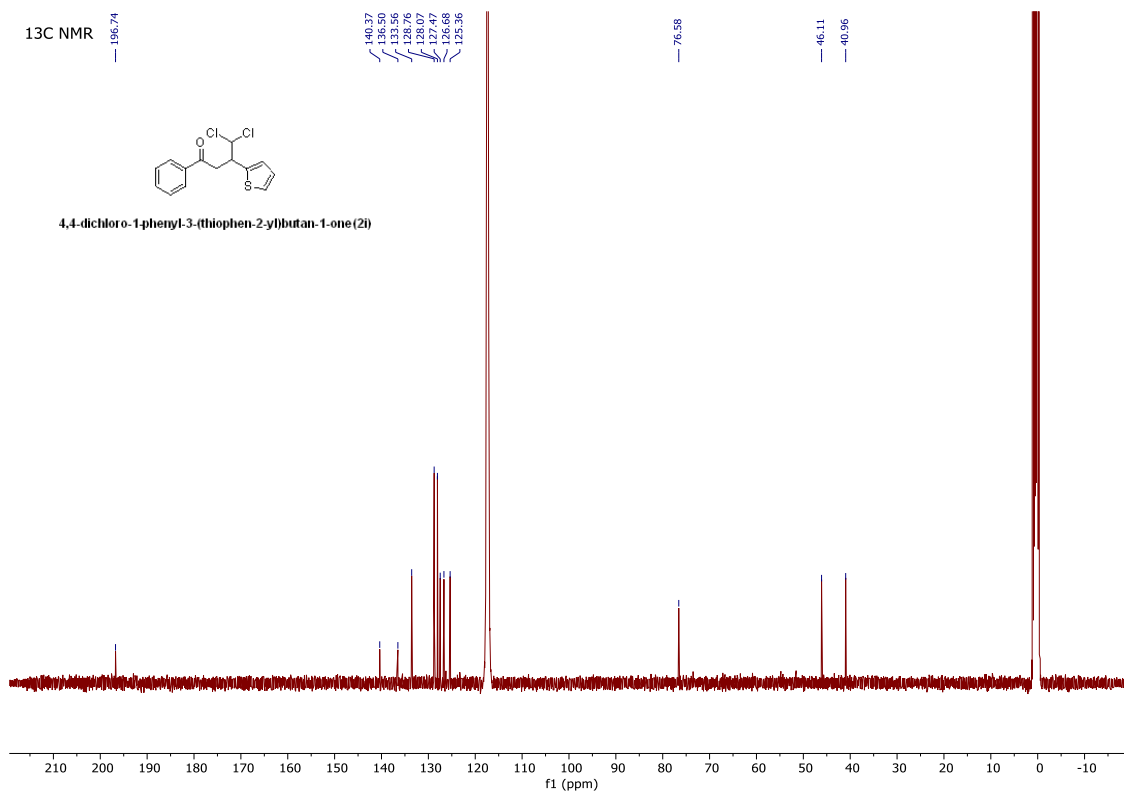
4,4-dichloro-3-(3,4-difluorophenyl)-1-phenylbutan-1-one (2h)



Supplementary Figure 63. NMR spectrum of 2h.

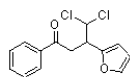


Supplementary Figure 64. NMR spectrum of 2i.

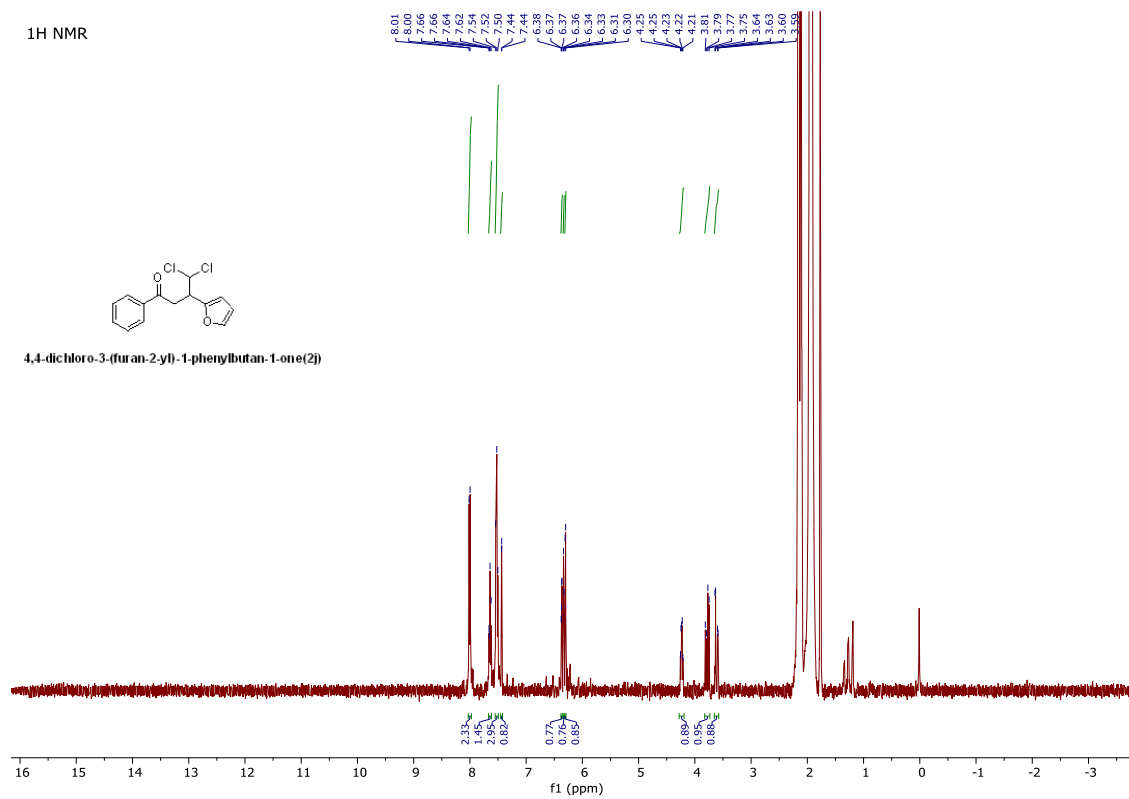


Supplementary Figure 65. NMR spectrum of 2i.

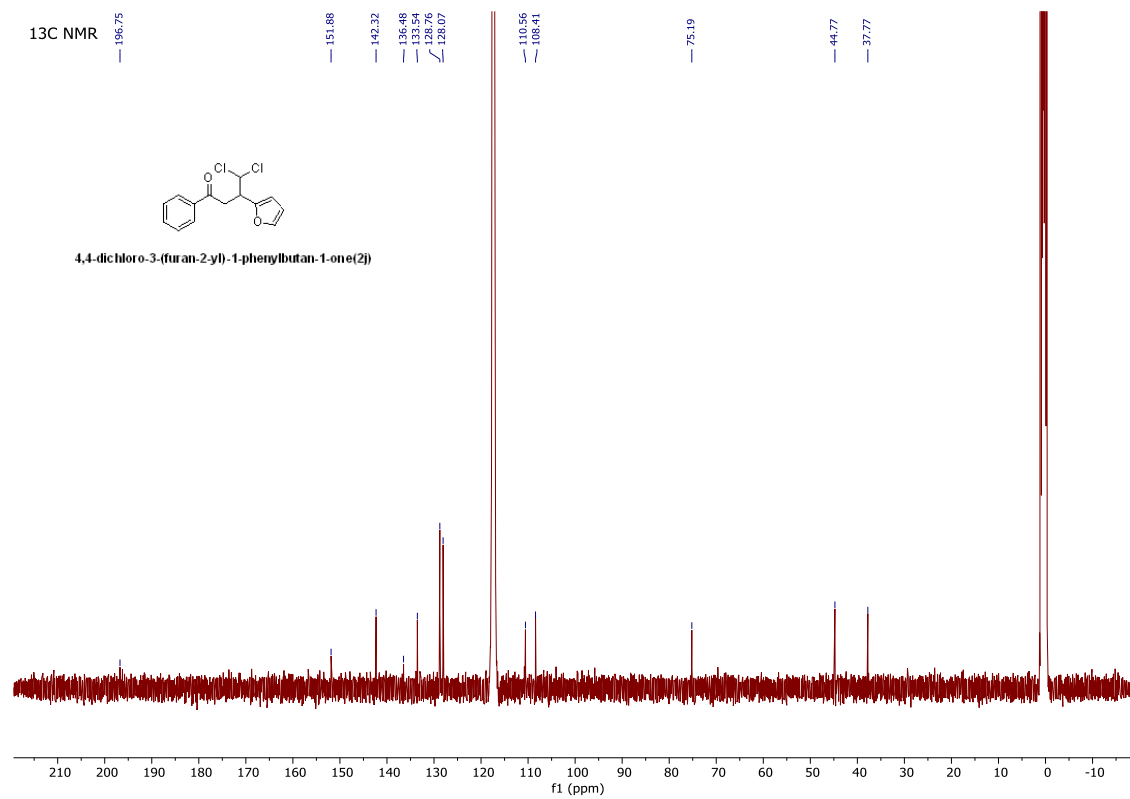
¹H NMR



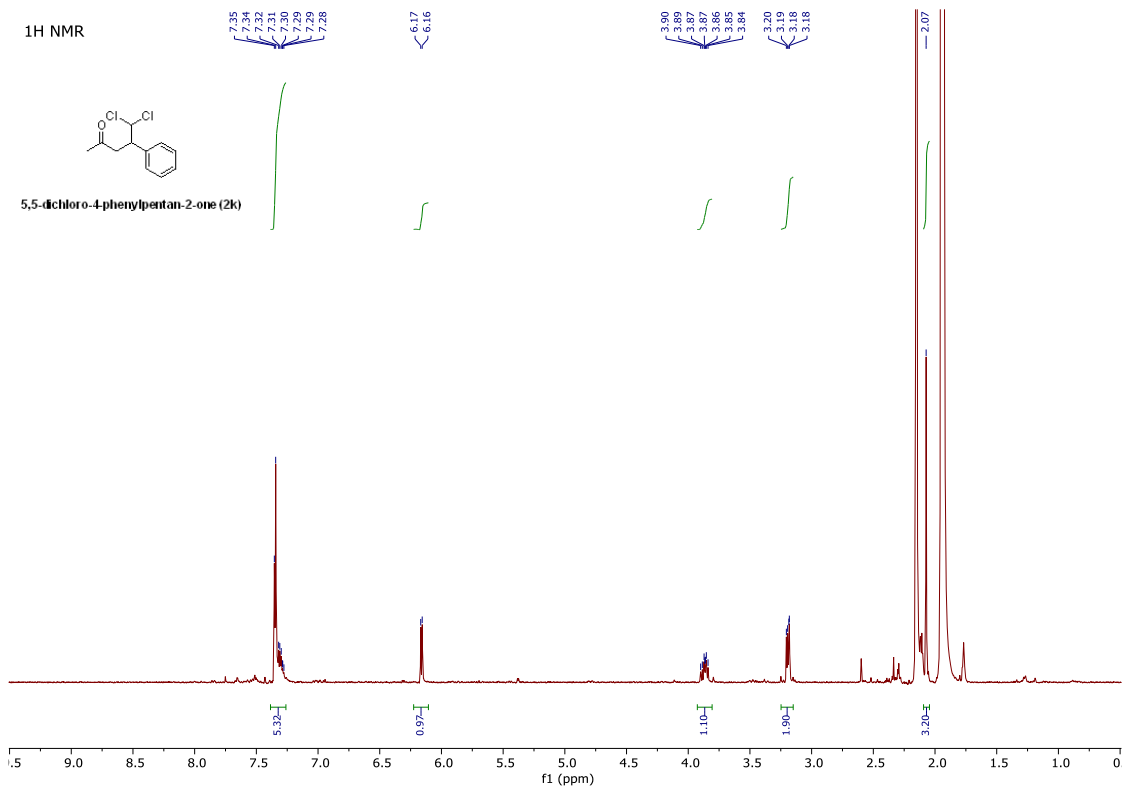
4,4-dichloro-3-(furan-2-yl)-1-phenylbutan-1-one(2j)



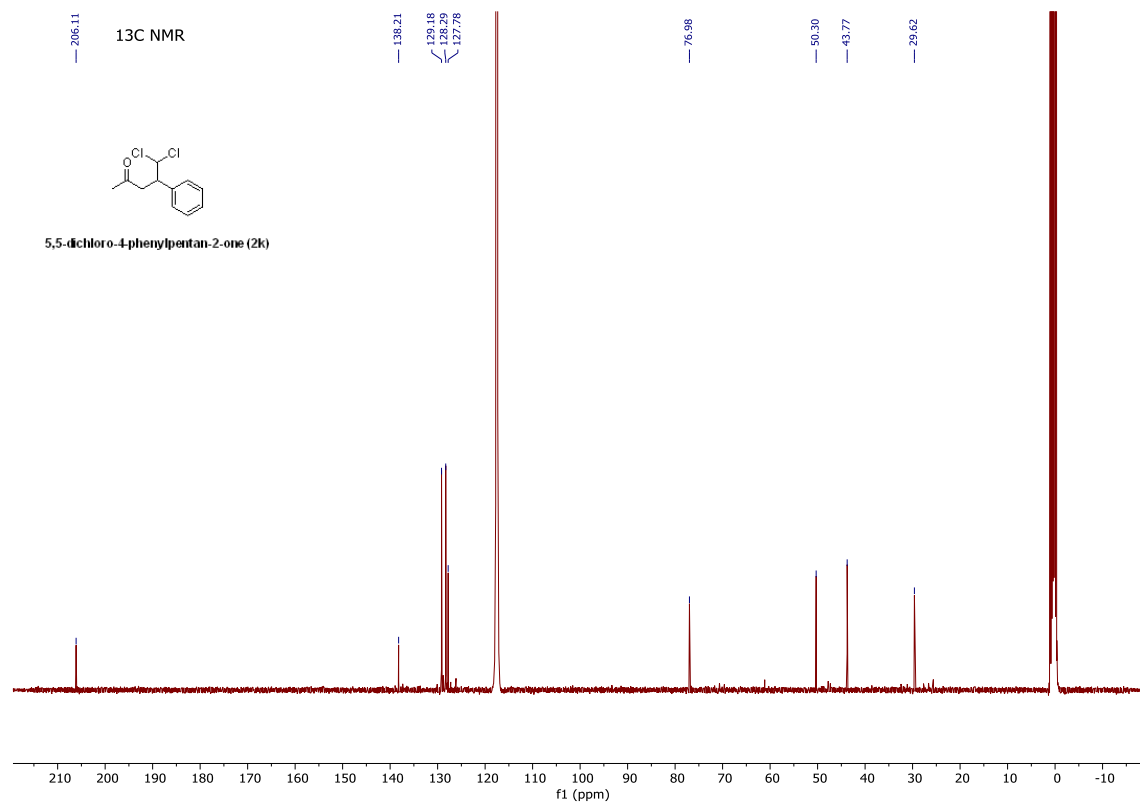
Supplementary Figure 66. NMR spectrum of 2j.



Supplementary Figure 67. NMR spectrum of 2j.

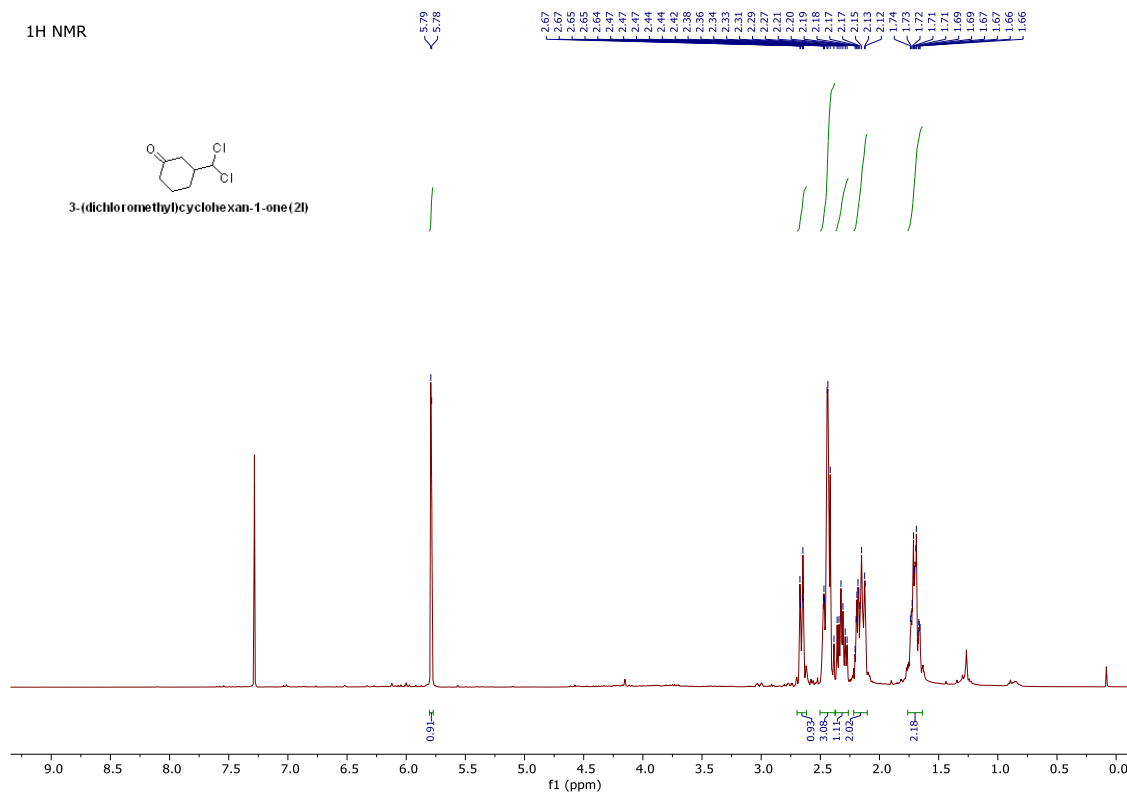


Supplementary Figure 68. NMR spectrum of 2k.

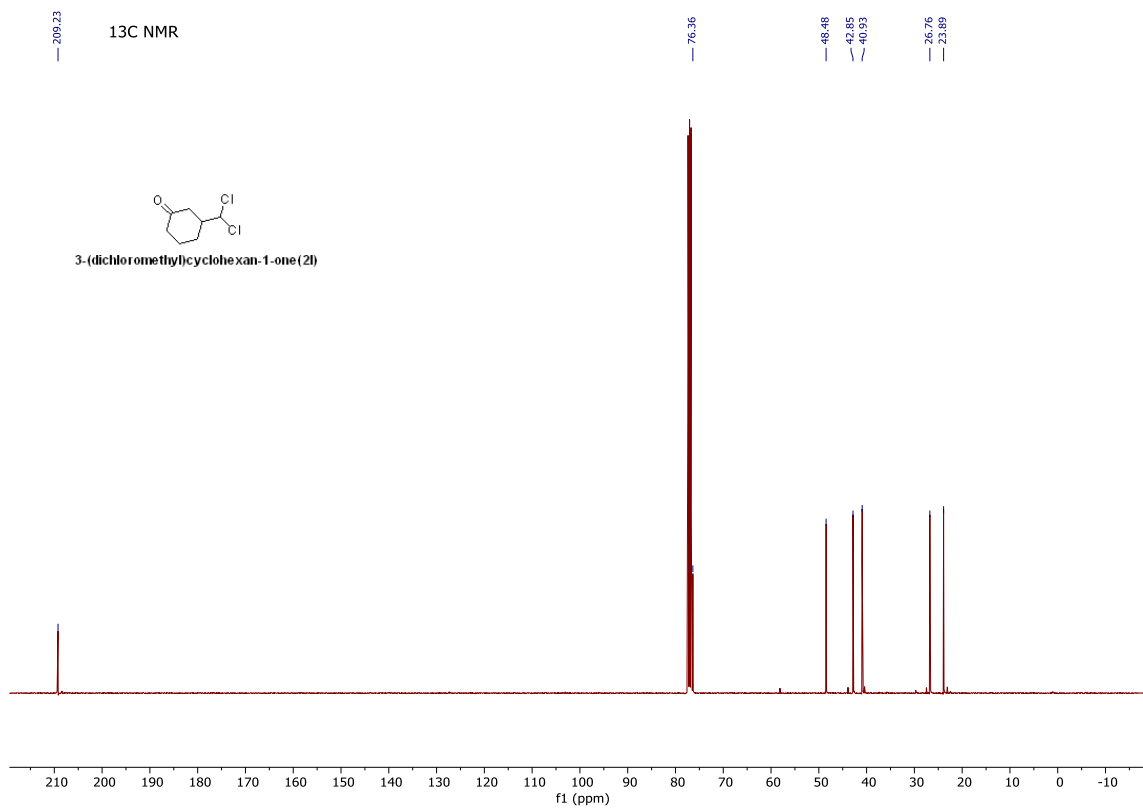


Supplementary Figure 69. NMR spectrum of 2k.

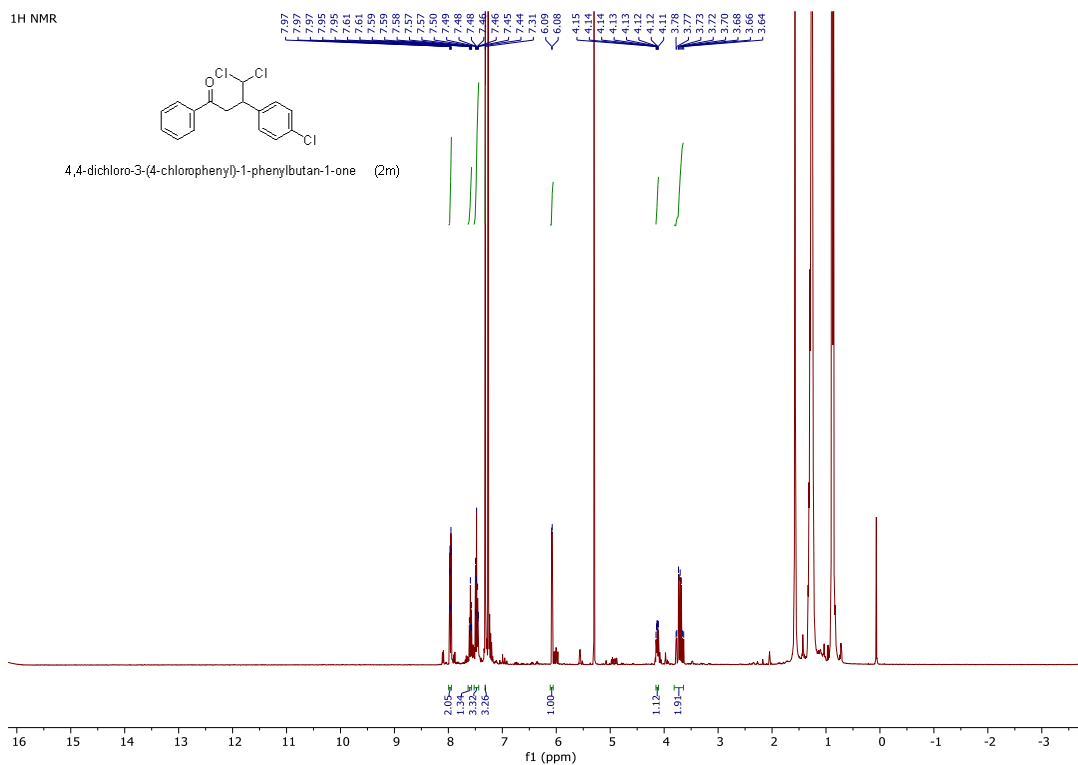
1H NMR



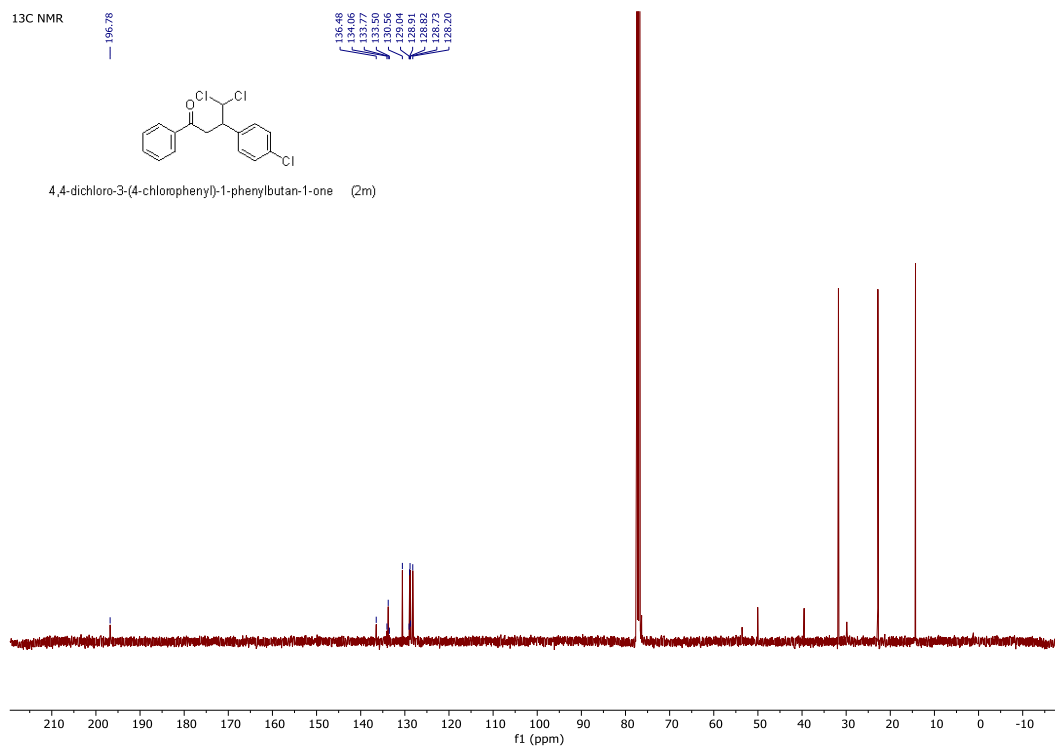
Supplementary Figure 70. NMR spectrum of **21**.



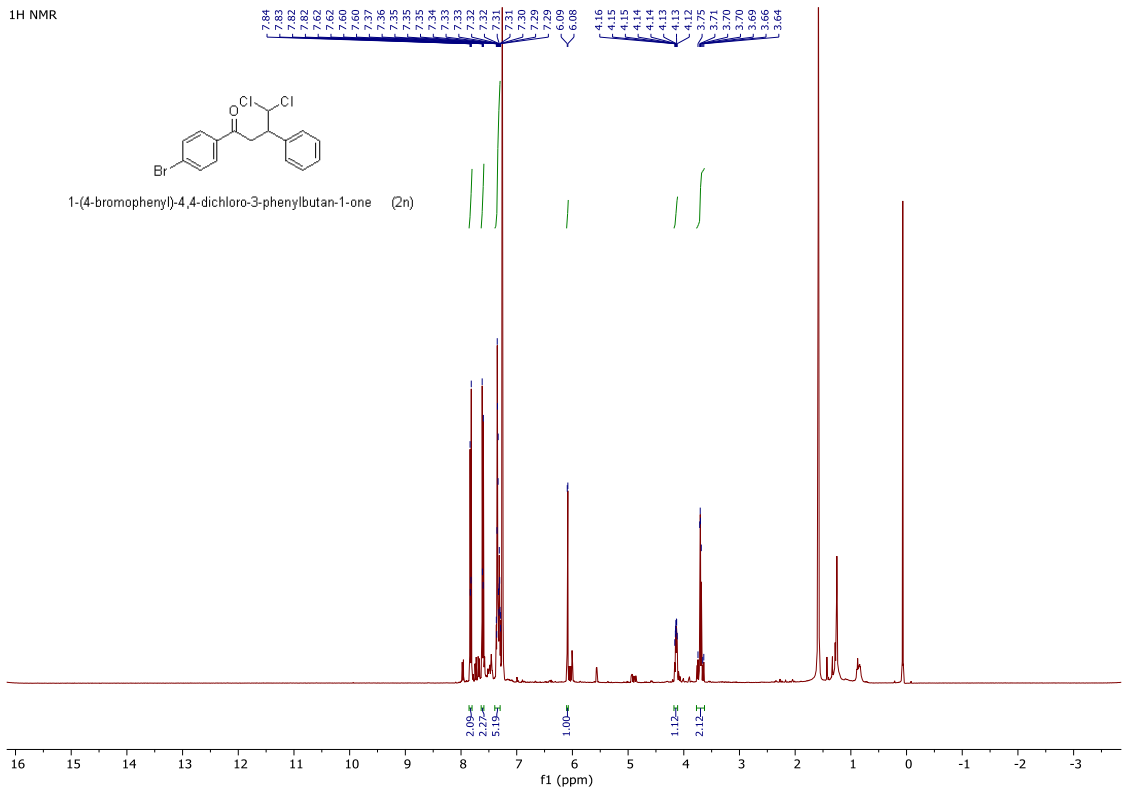
Supplementary Figure 71. NMR spectrum of 2.



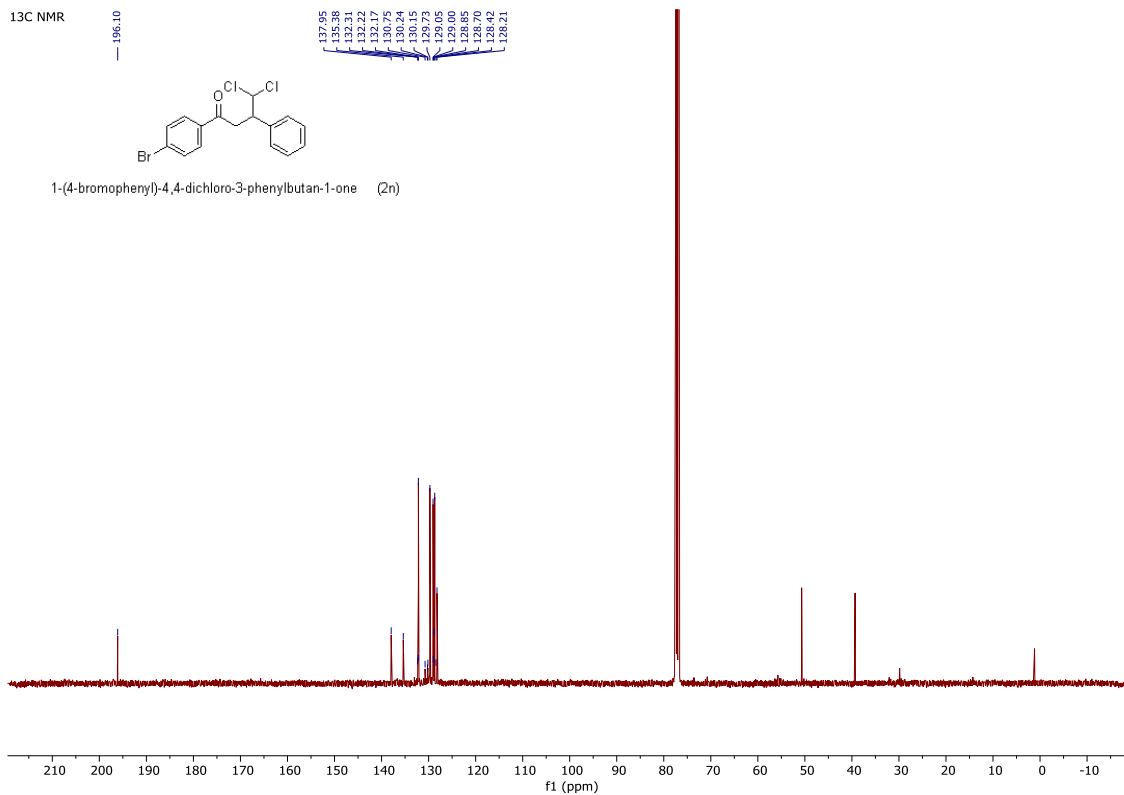
Supplementary Figure 72. NMR spectrum of 2m.



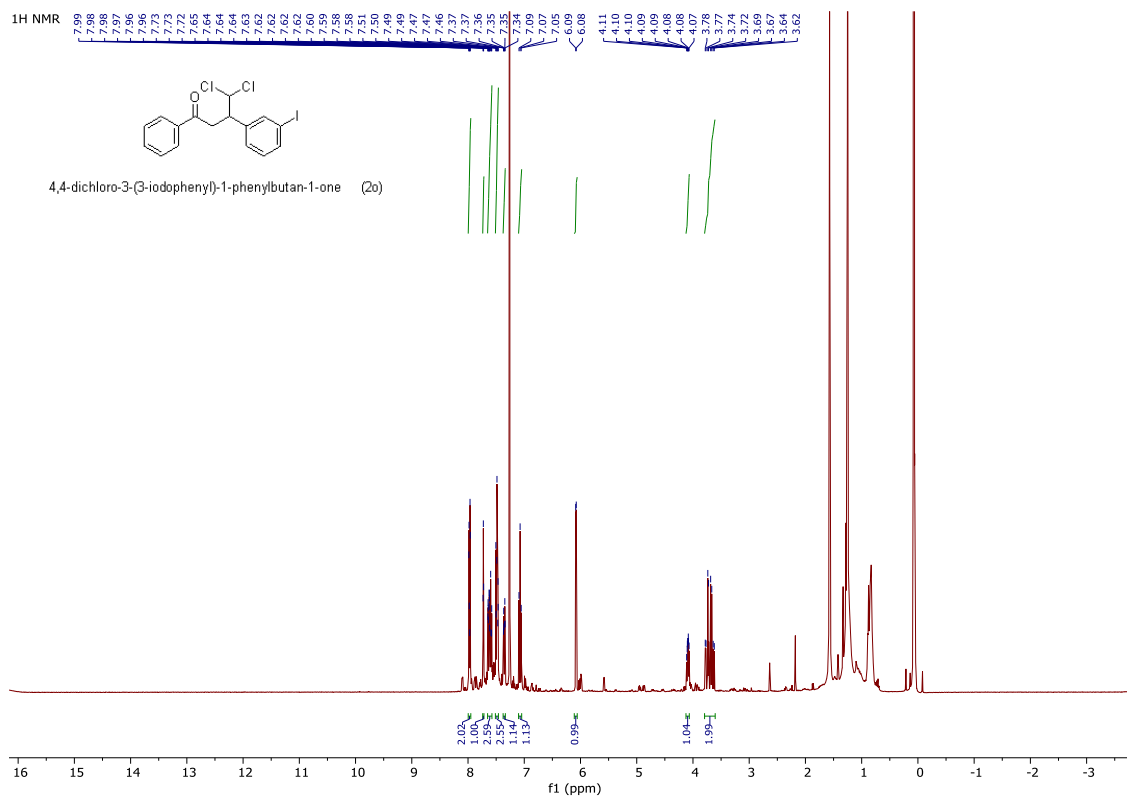
Supplementary Figure 73. NMR spectrum of 2m.



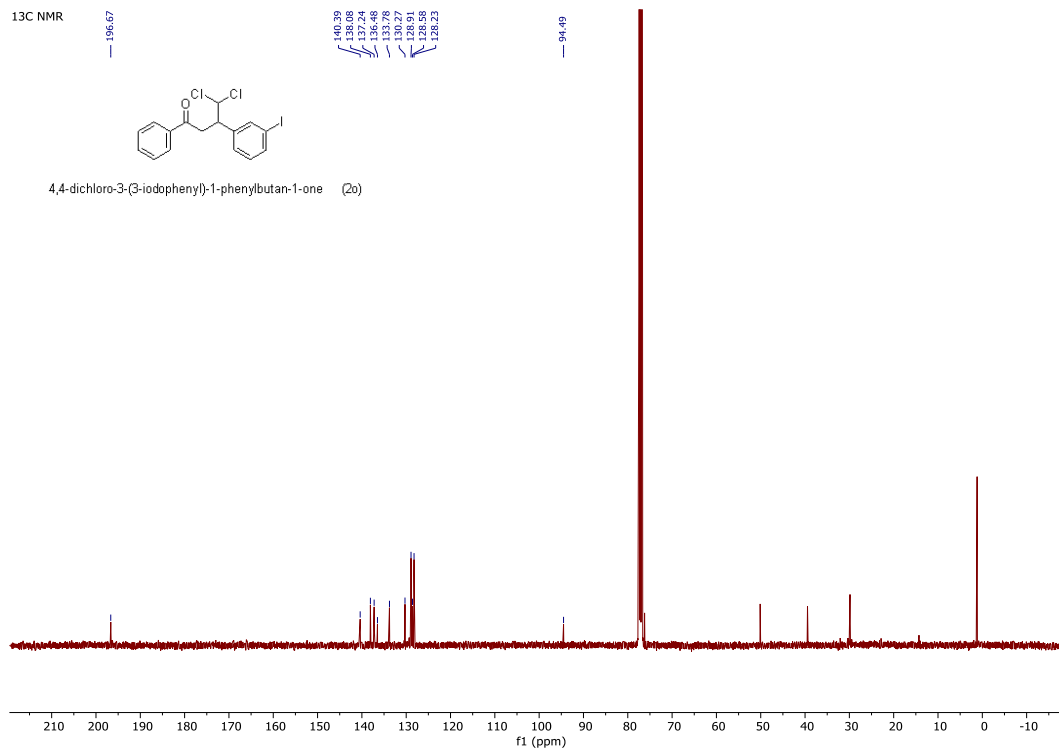
Supplementary Figure 74. NMR spectrum of 2n.



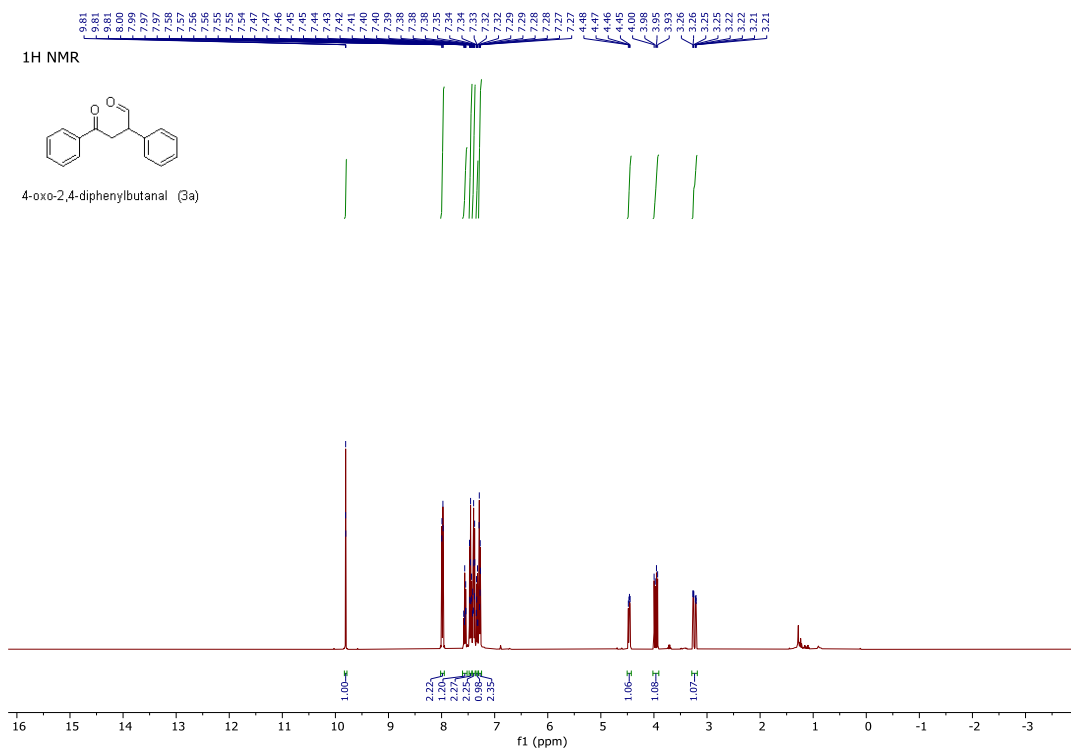
Supplementary Figure 75. NMR spectrum of 2n.



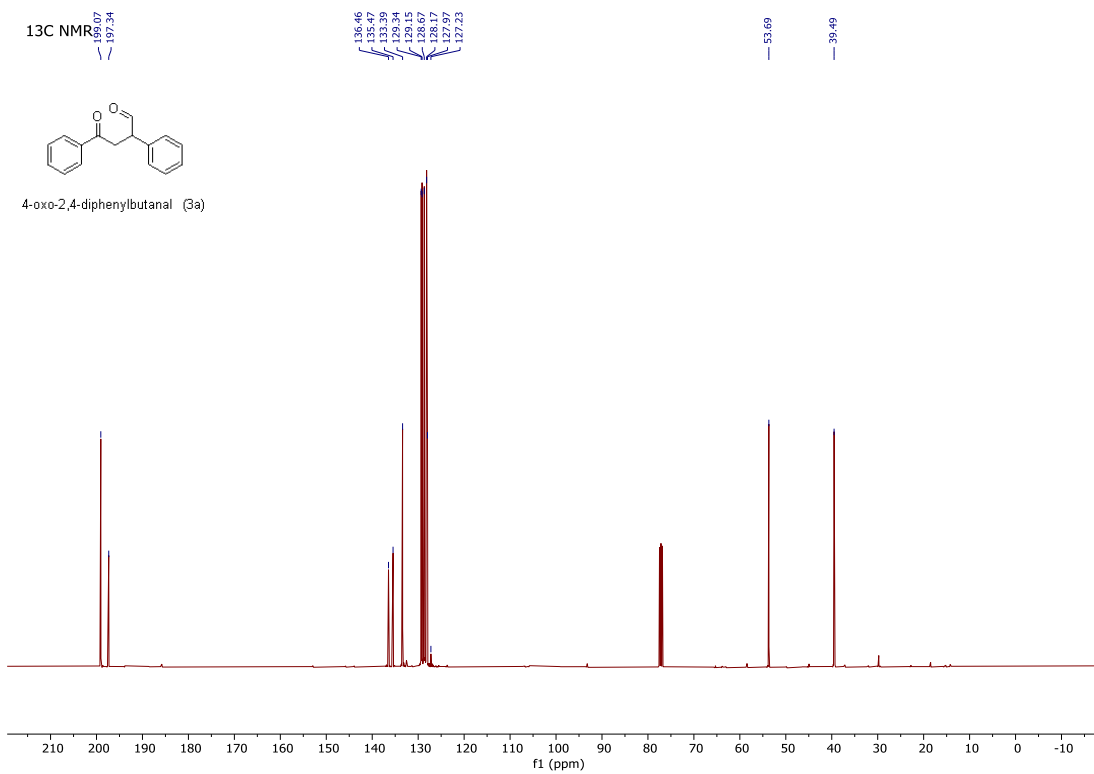
Supplementary Figure 76. NMR spectrum of 2o.



Supplementary Figure 77. NMR spectrum of 2o.

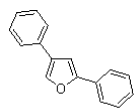


Supplementary Figure 78. NMR spectrum of 3a.

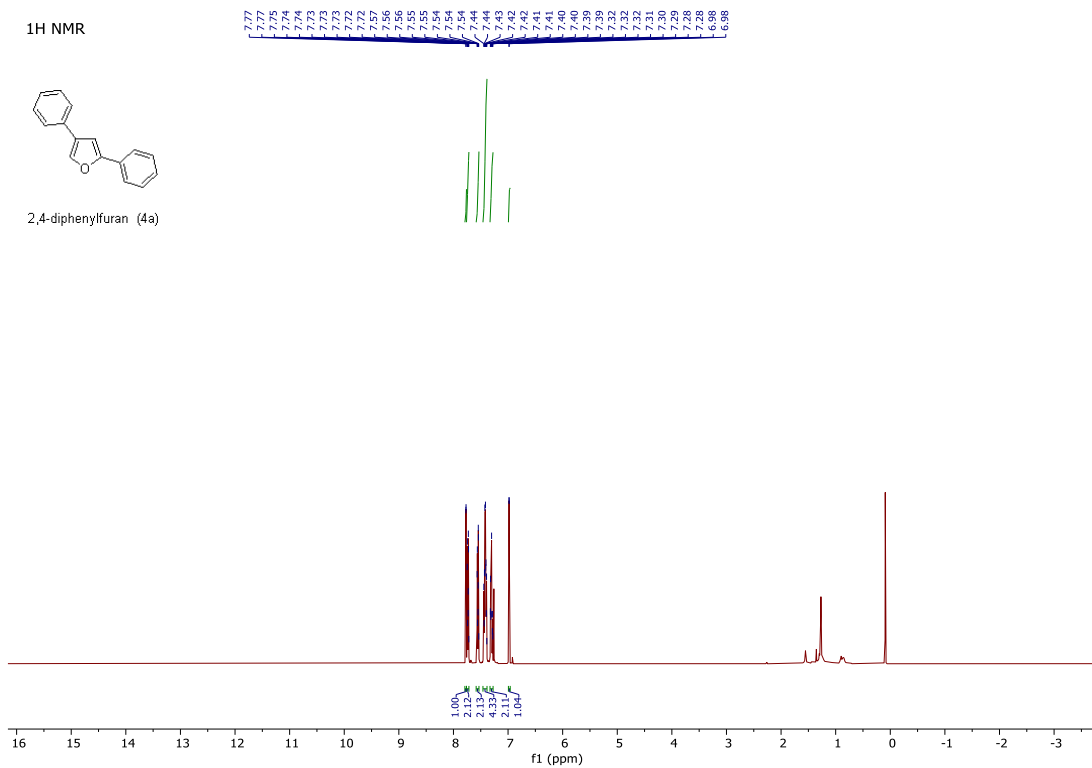


Supplementary Figure 79. NMR spectrum of 3a.

¹H NMR

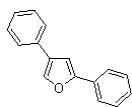


2,4-diphenylfuran (4a)

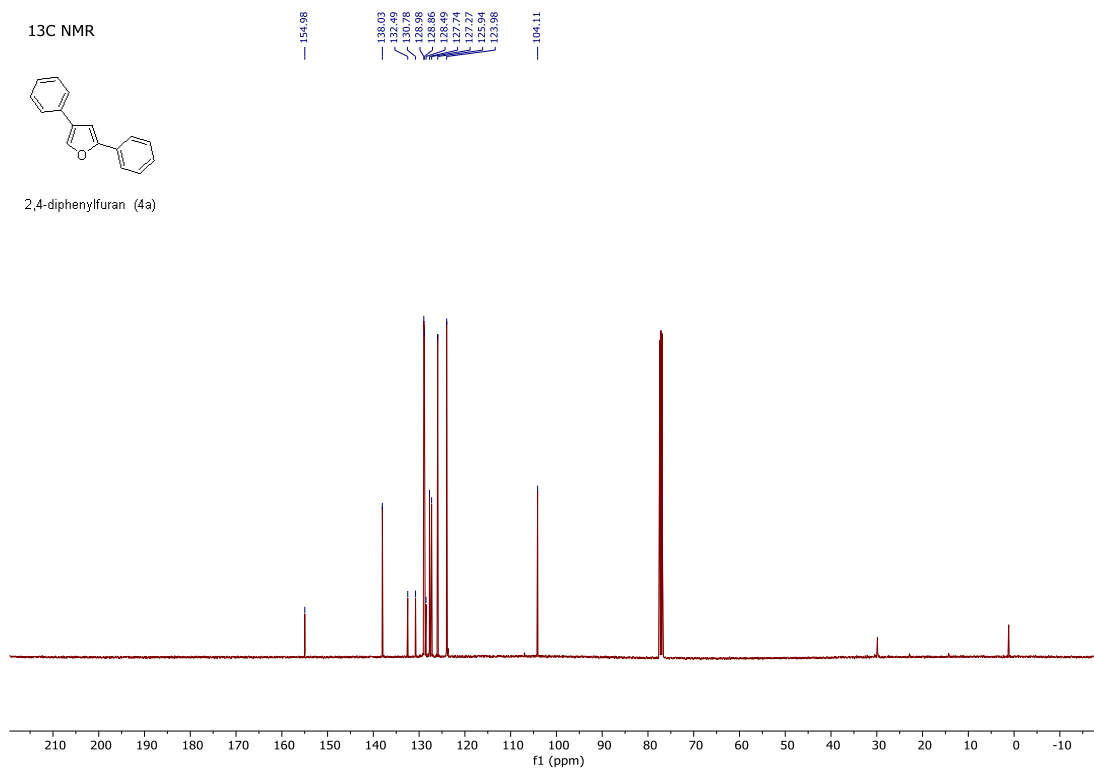


Supplementary Figure 80. NMR spectrum of 4a.

13C NMR

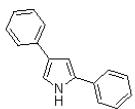


2,4-diphenylfuran (4a)

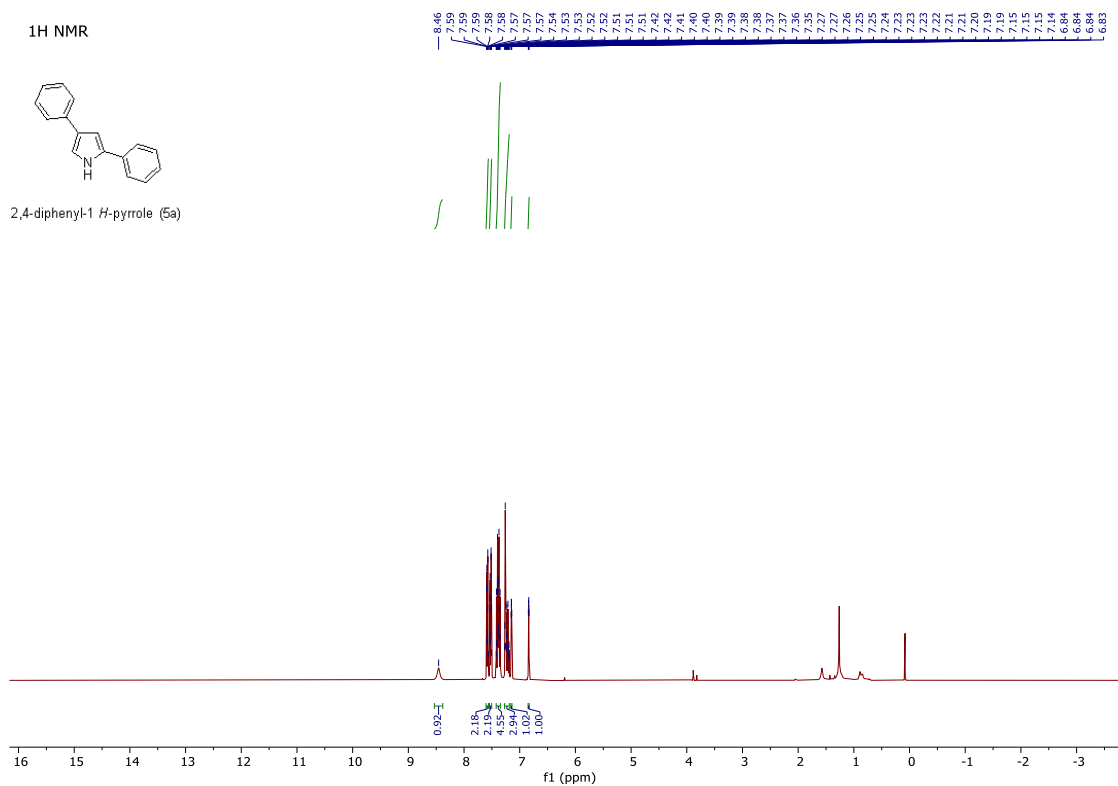


Supplementary Figure 81. NMR spectrum of 4a.

¹H NMR

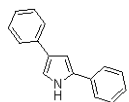


2,4-diphenyl-1 H-pyrrole (5a)

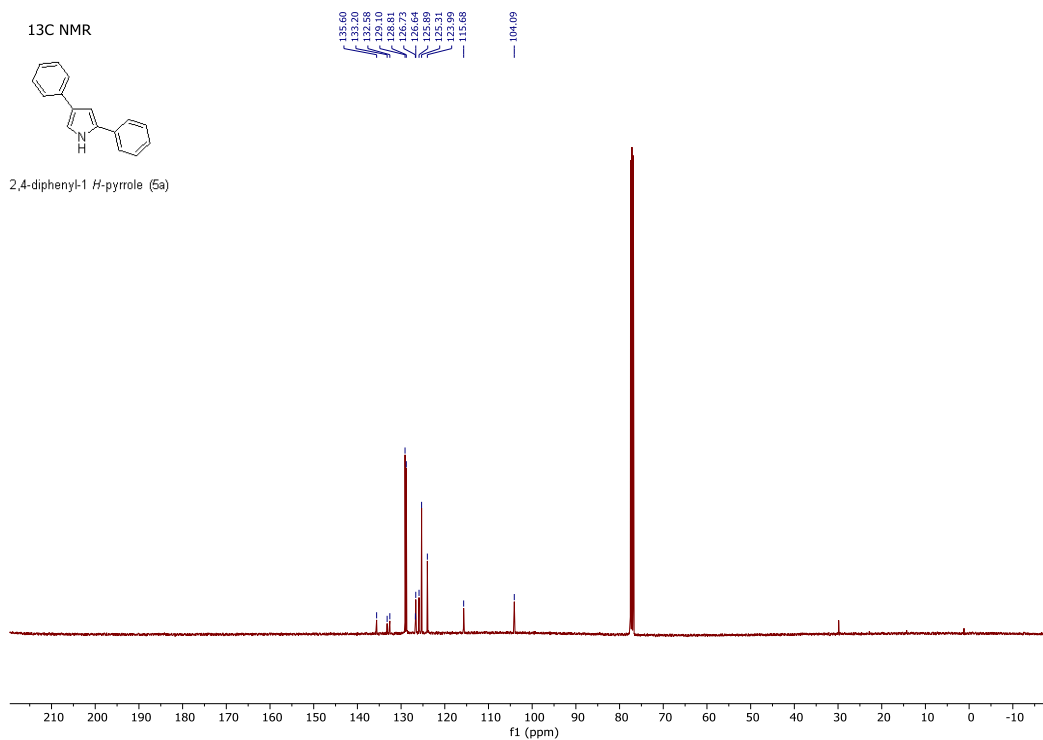


Supplementary Figure 82. NMR spectrum of 5a.

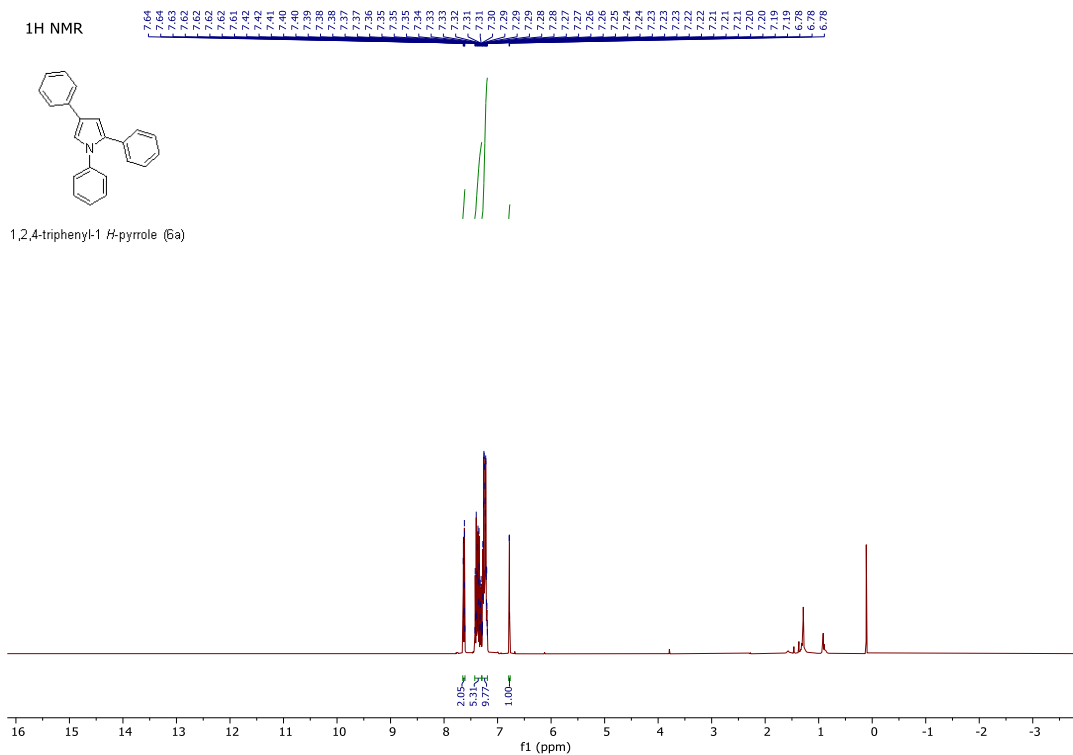
¹³C NMR



2,4-diphenyl-1H-pyrrole (5a)

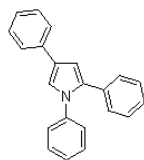


Supplementary Figure 83. NMR spectrum of 5a.



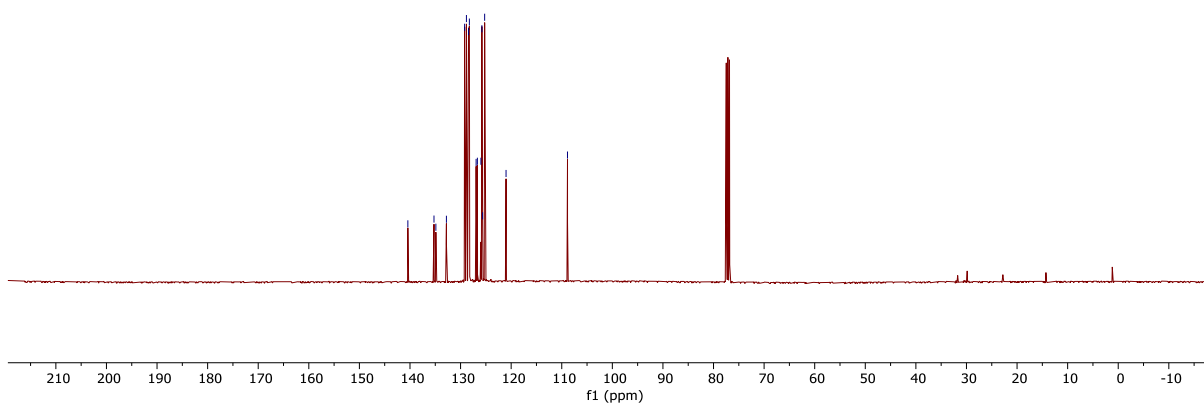
Supplementary Figure 84. NMR spectrum of 6a.

¹³C NMR

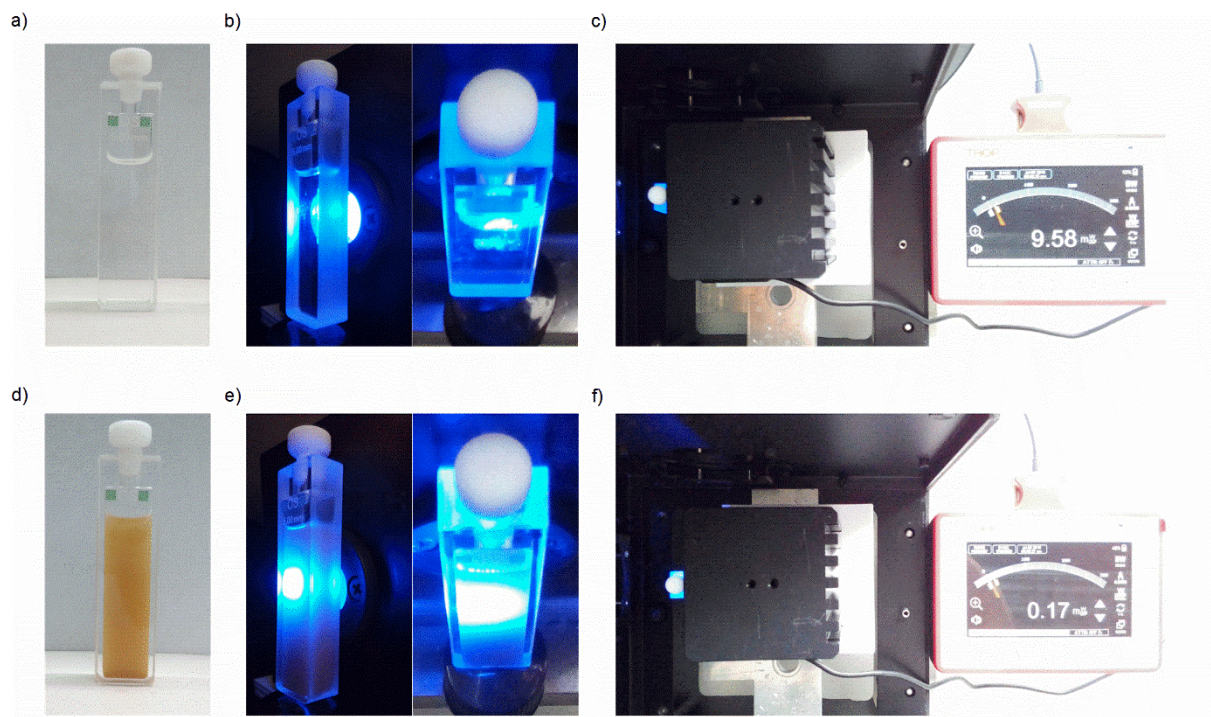


1,2,4-triphenyl-1 H-pyrrole (6a)

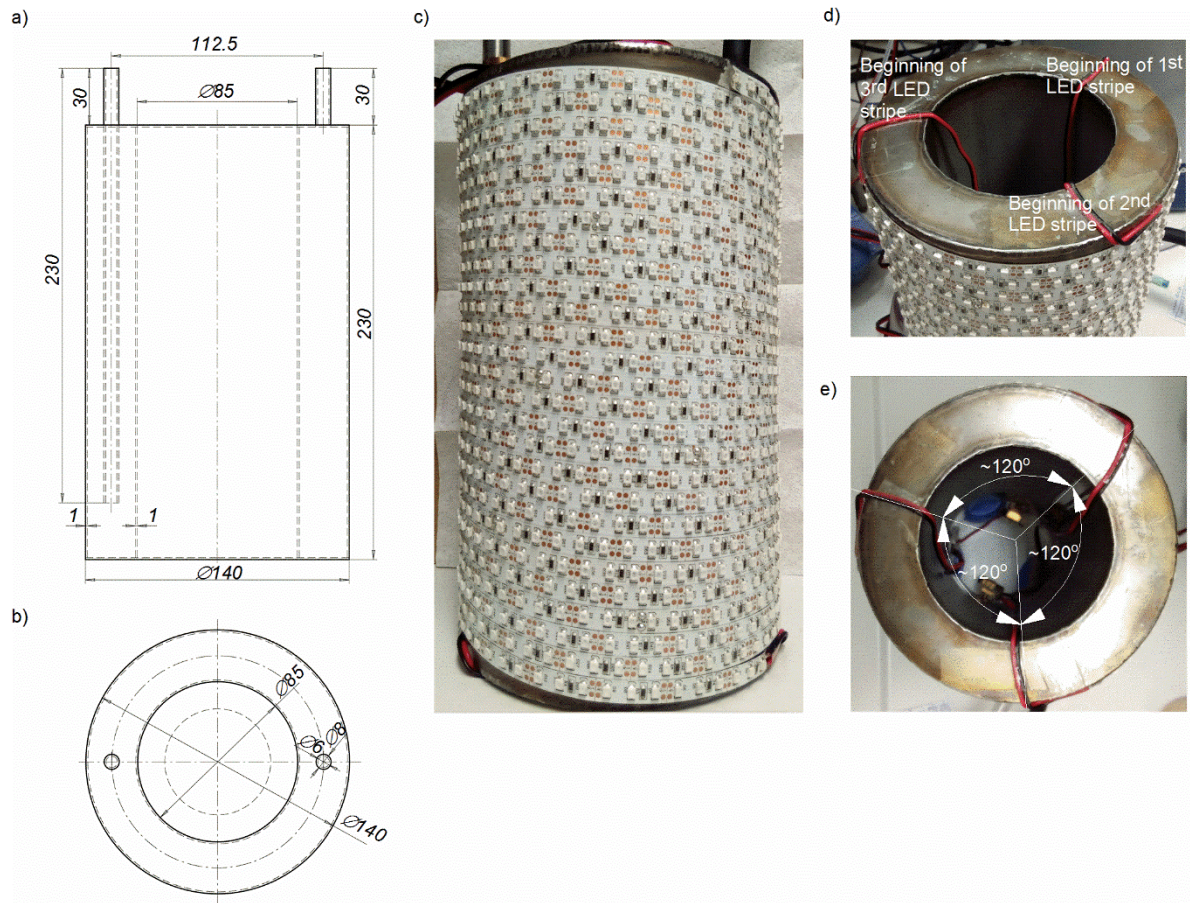
140.92
139.92
134.68
132.80
129.20
128.84
128.43
128.26
126.65
126.68
125.98
125.79
125.65
125.24
121.01
108.86



Supplementary Figure 85. NMR spectrum of 6a.



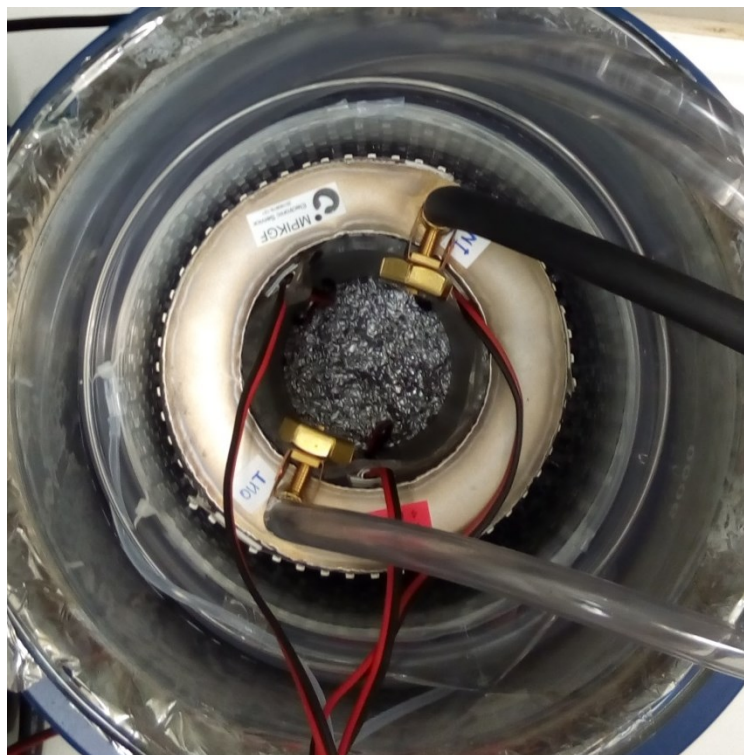
Supplementary Figure 86. Light scattering by K-PHI suspension. a) 5 mm cuvette filled with CHCl₃:DMSO (9:1) under day light; b) 5 mm cuvette filled with CHCl₃:DMSO (9:1) under 461±20 nm ($I_0 = 10.6 \text{ mW cm}^{-2}$) does not scatter light (no halo in the middle of the cuvette); c) Measurement of light intensity transmitted through a 5 mm cuvette filled with CHCl₃:DMSO (9:1). Integrating sphere S142C connected to PM400 Optical Power and Energy Meter with readings on the left are shown; d) 5 mm cuvette filled with a suspension of K-PHI (2.5 mg mL⁻¹) in CHCl₃:DMSO (9:1) under day light; e) 5 mm cuvette filled with a suspension of K-PHI (2.5 mg mL⁻¹) in CHCl₃:DMSO (9:1) under 461±20 nm ($I_0 = 10.6 \text{ mW cm}^{-2}$) scatters light strongly (strong halo in the middle of the cuvette); f) Measurement of light intensity transmitted through a 5 mm cuvette filled with a suspension of K-PHI (2.5 mg mL⁻¹) in CHCl₃:DMSO (9:1). Integrating sphere S142C connected to PM400 Optical Power and Energy Meter with readings on the left are shown.



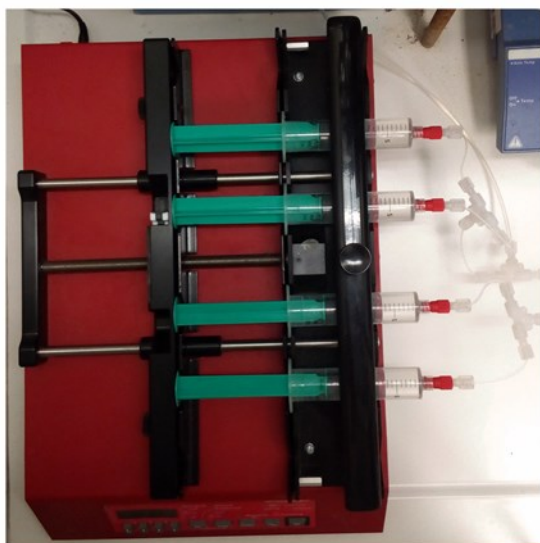
Supplementary Figure 87. a) Side view of the steel cylinder; b) Top view of the steel cylinder; c) Side view of the assembled light source; d) and e) Bottom view of the assembled light source. Displacement of ca. 120° between the leading ends of the LED stripes is shown.



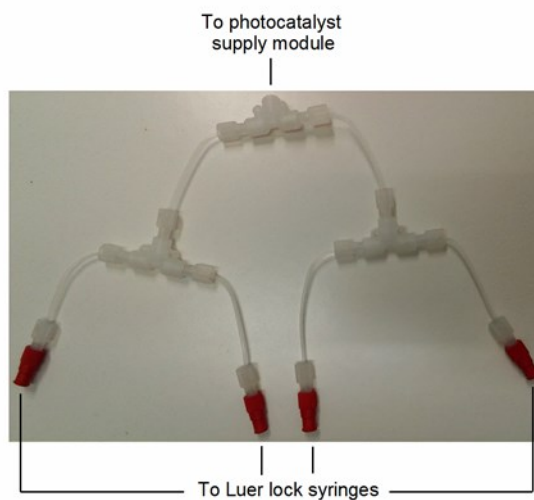
Supplementary Figure 88. Flow photoreactor tubing.



Supplementary Figure 89. External shell of the flow photoreactor.

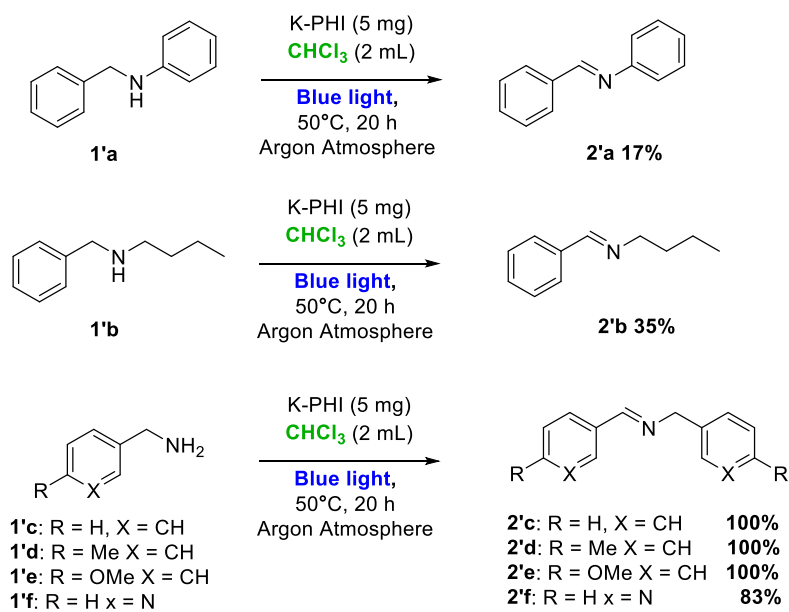


Supplementary Figure 90. Reaction mixture supply module.

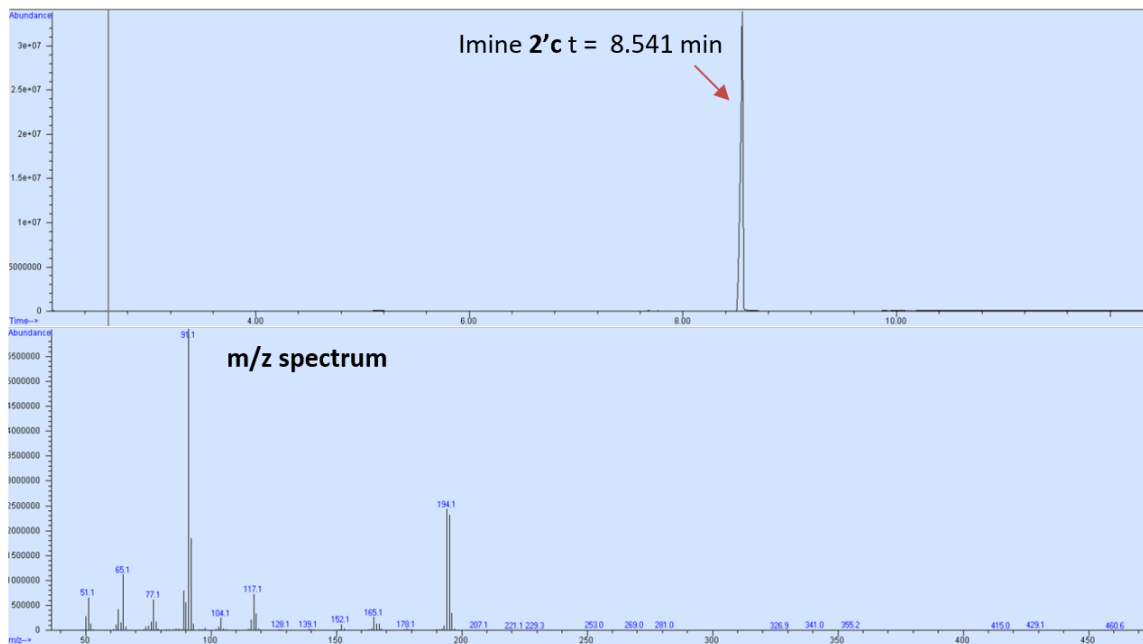




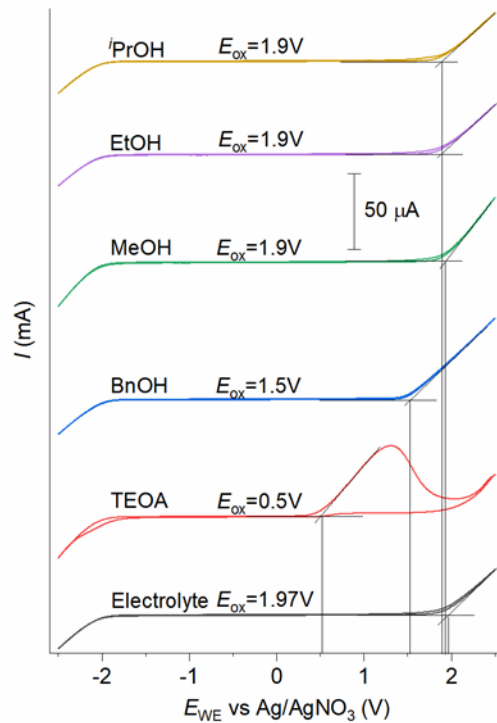
Supplementary Figure 91. Photocatalyst supply module.



Supplementary Figure 92. Scope of imines. Yields were calculated by GC-MS

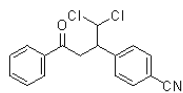


Supplementary Figure 93. Typical chromatogram after imine formation.

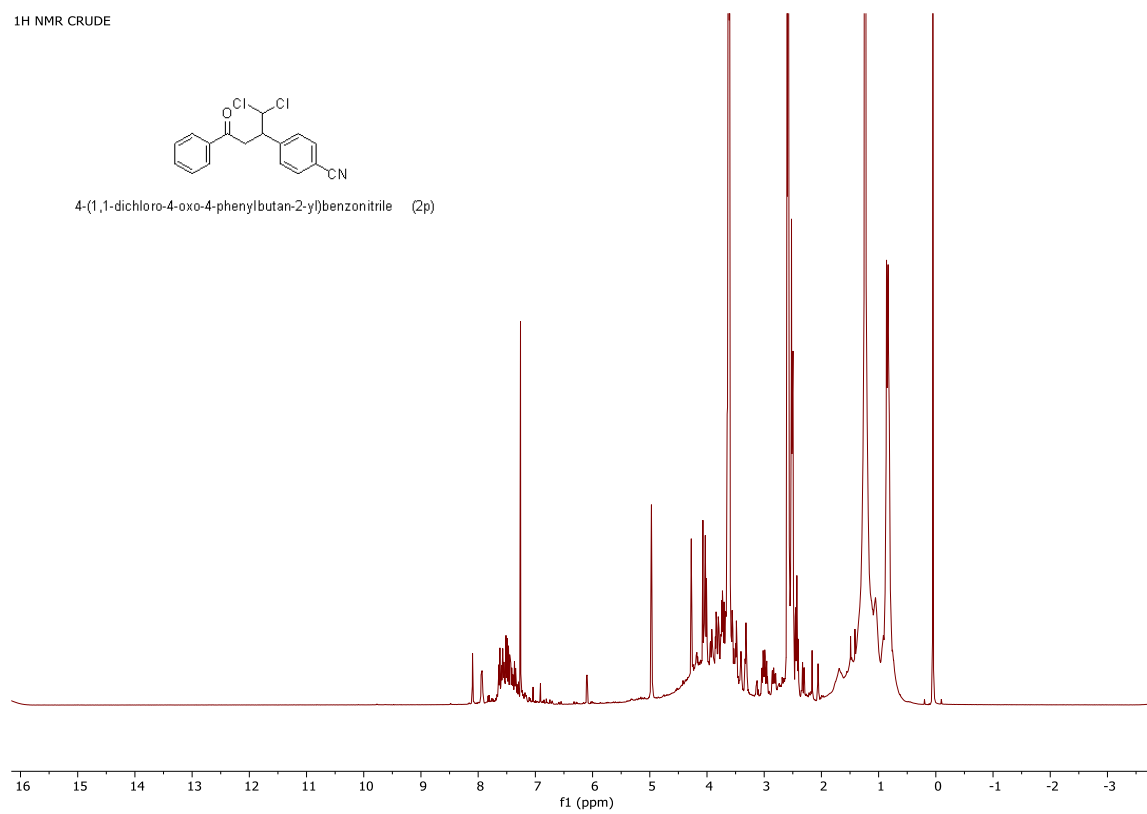


Supplementary Figure 94. Cyclic voltammograms of different hole scavengers. From bottom to top: a) electrolyte $(nBu)_4N^+ ClO_4^-$ in chloroform (0.1M) purged with Ar; b) TEOA solution (50 mM) in electrolyte shows $E_{ox} = +0.5 V$; c) BnOH solution (50 mM) in electrolyte shows $E_{ox} = +1.5 V$; d) MeOH solution (50 mM) in electrolyte shows $E_{ox} = +1.9 V$; e) EtOH solution (50 mM) in electrolyte shows $E_{ox} = +1.9 V$; f) iPrOH solution (50 mM) in electrolyte shows $E_{ox} = +1.9 V$.

¹H NMR CRUDE

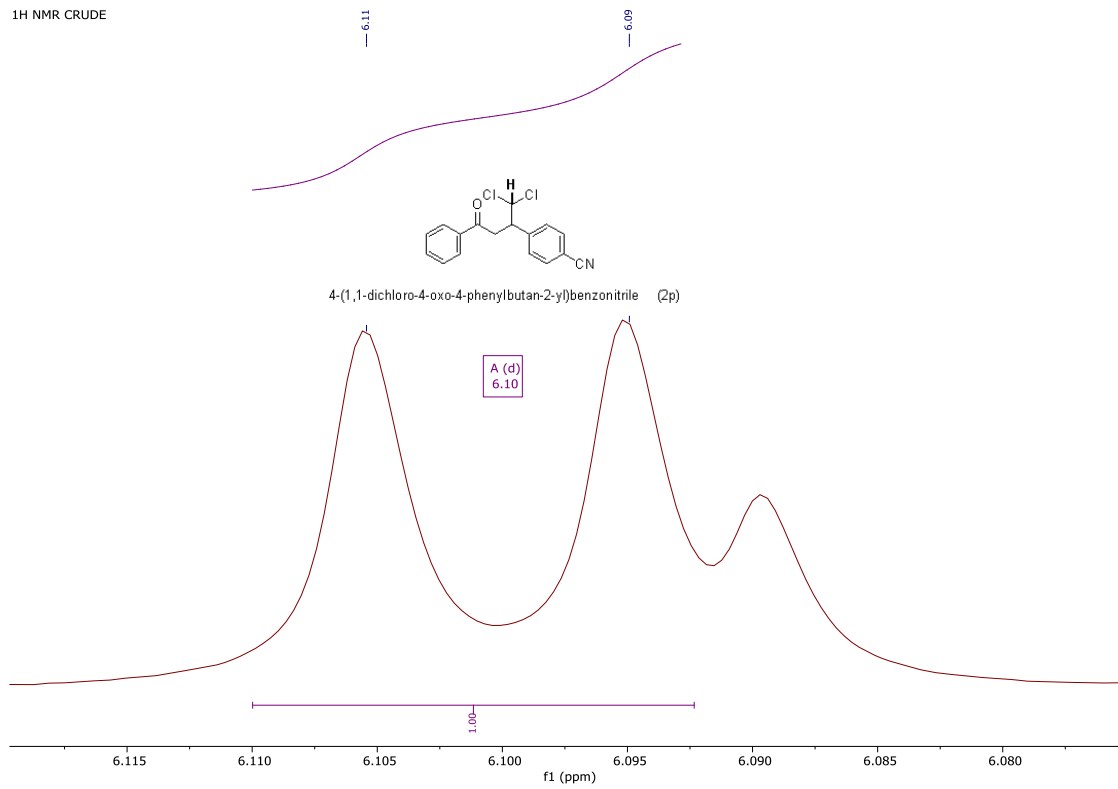


4-(1,1-dichloro-4-oxo-4-phenylbutan-2-yl)benzonitrile (2p)



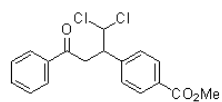
Supplementary Figure 95 - NMR spectrum of 2p.

1H NMR CRUDE

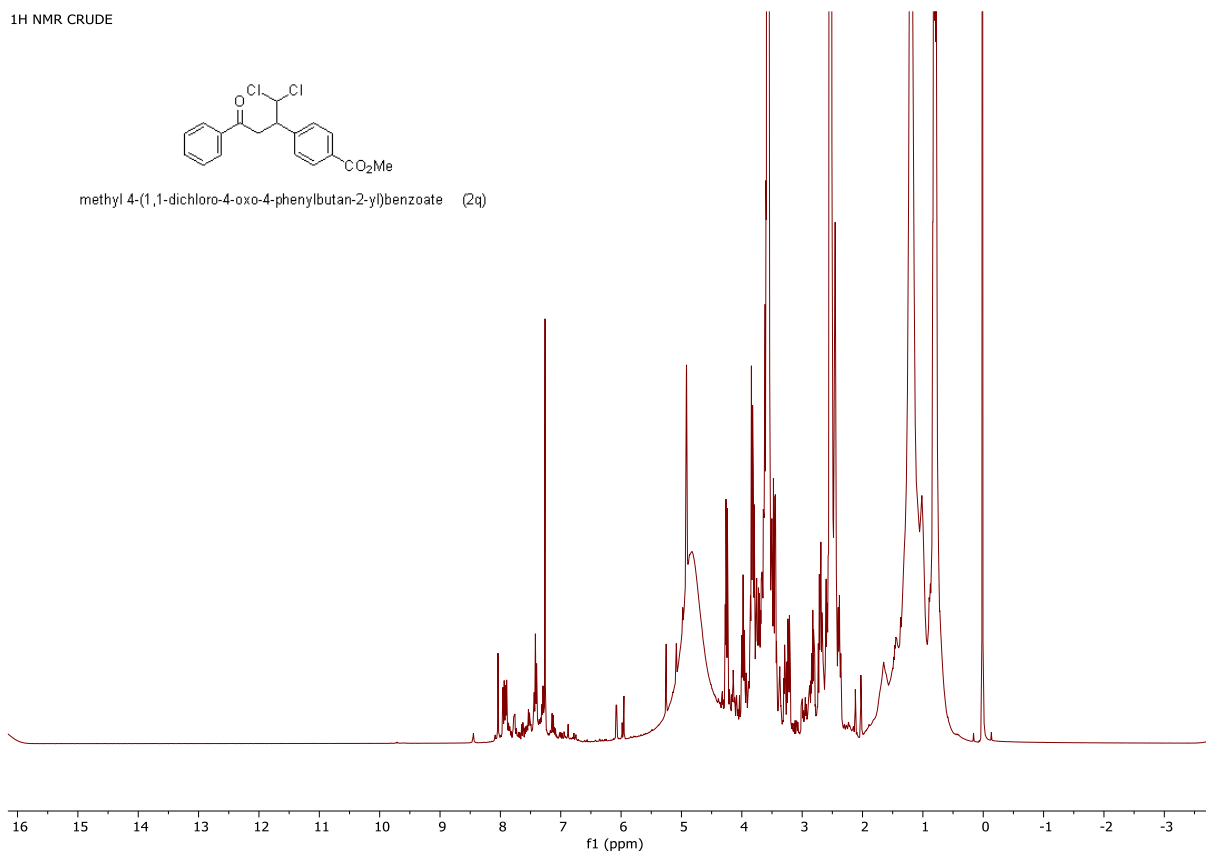


Supplementary Figure 96 - NMR spectrum of 2p.

¹H NMR CRUDE

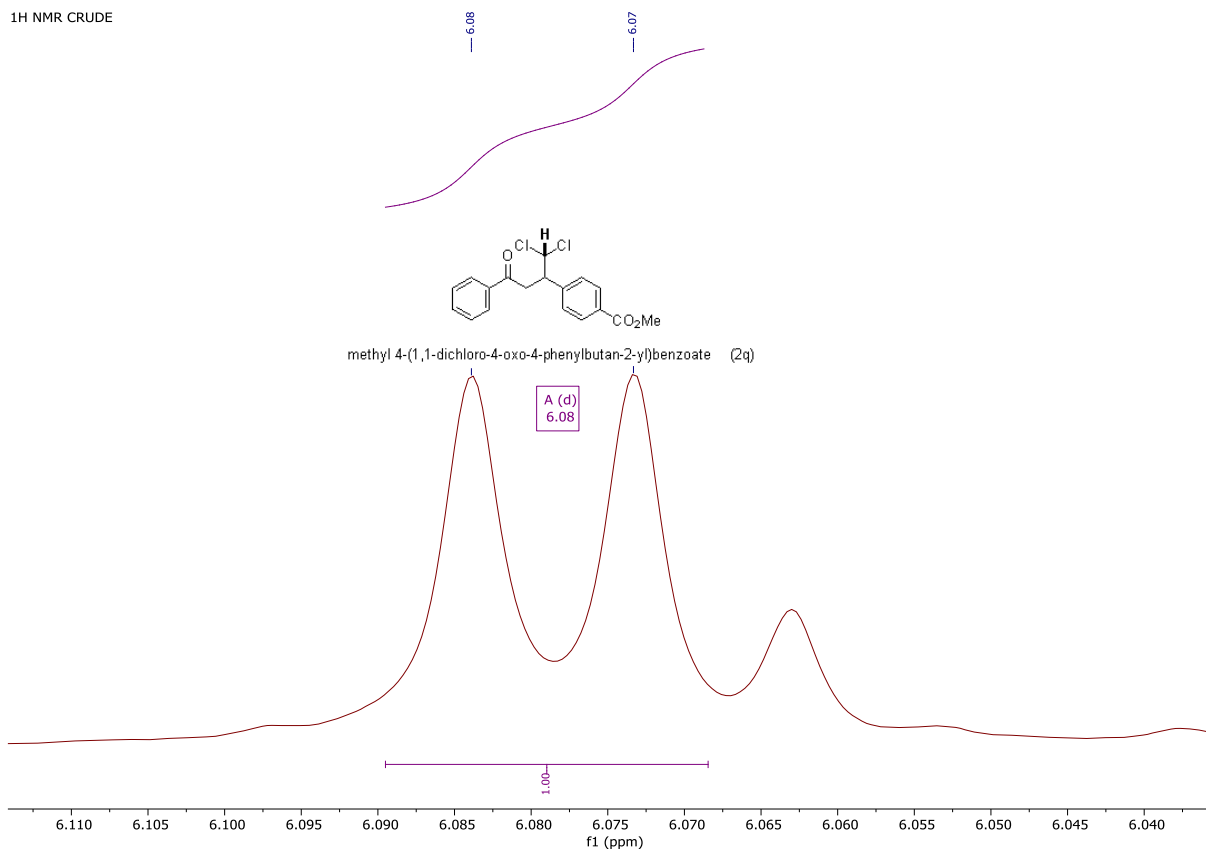


methyl 4-(1,1-dichloro-4-oxo-4-phenylbutan-2-yl)benzoate (2q)



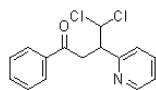
Supplementary Figure 97 - NMR spectrum of 2q.

1H NMR CRUDE

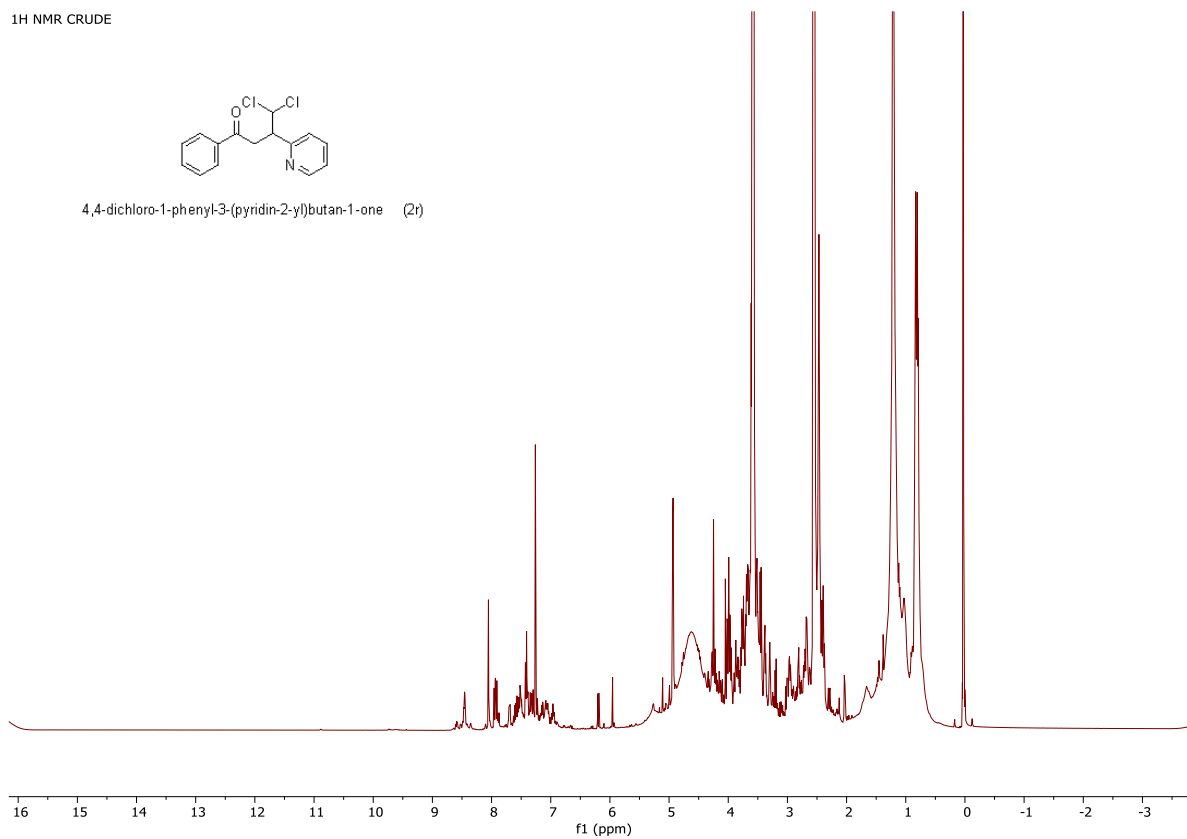


Supplementary Figure 98 - NMR spectrum of 2q.

1H NMR CRUDE

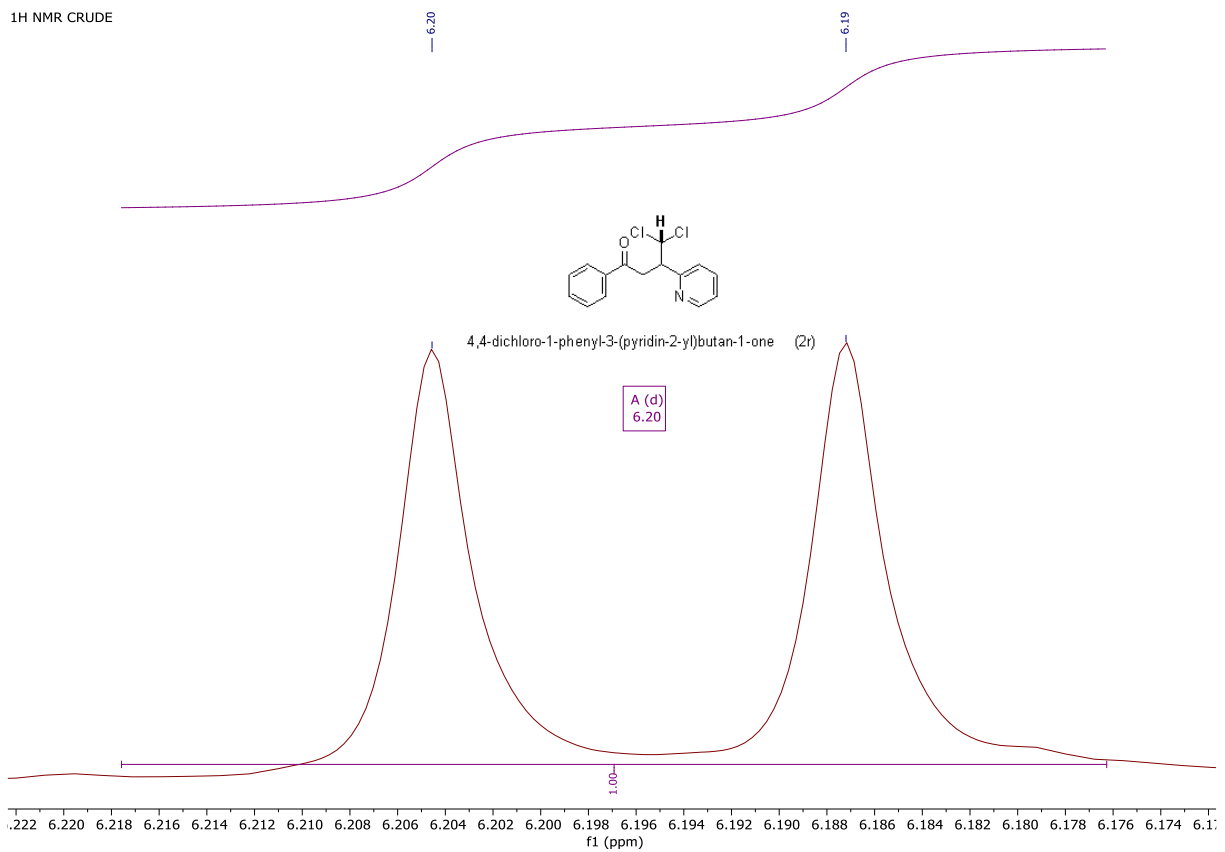


4,4-dichloro-1-phenyl-3-(pyridin-2-yl)butan-1-one (2r)

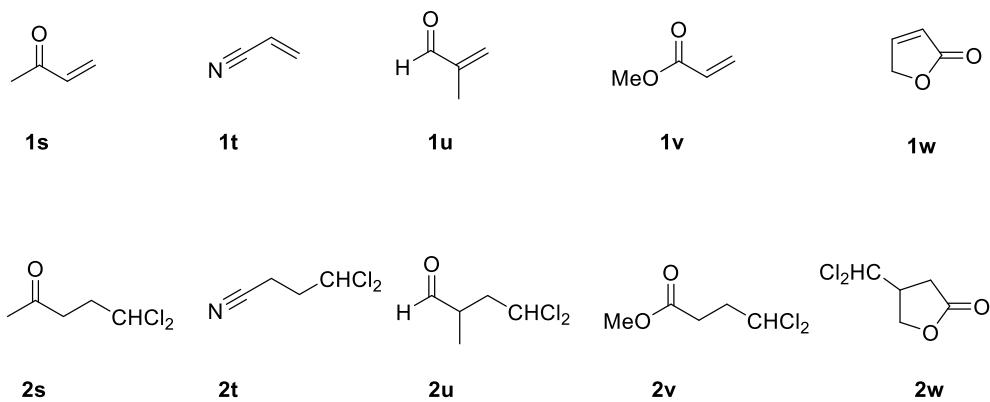


Supplementary Figure 99 - NMR spectrum of 2r.

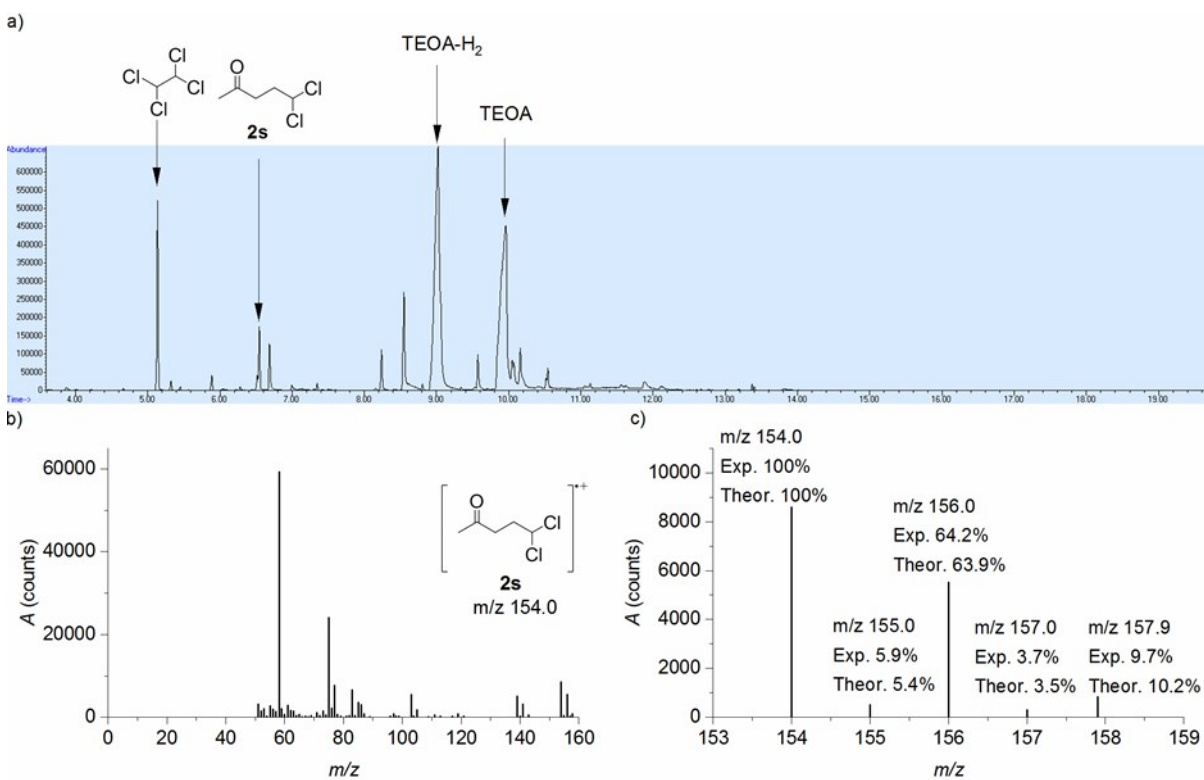
1H NMR CRUDE



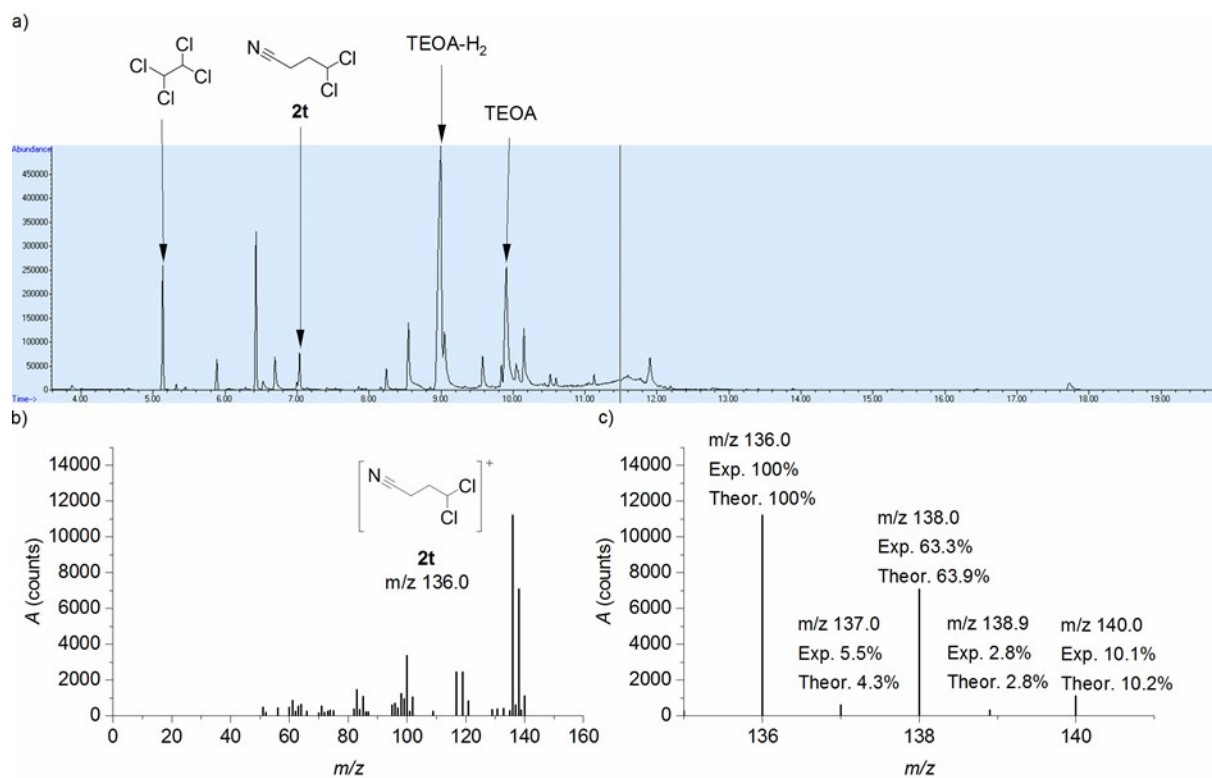
Supplementary Figure 100 - NMR spectrum of 2r.



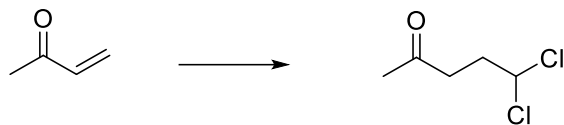
Supplementary Figure 101 – Scope of other Michael acceptors



Supplementary Figure 102 - GC-MS chromatogram of **2s**. (a) GC-MS chromatogram of the reaction mixture using methyl vinyl ketone **1s** as a reagent in dichloromethylation reaction. Main reaction mixture components peaks are labeled. b) Mass-spectrum of **2s** radical cation with the theoretical m/z value. c) Zoomed in area of the mass spectrum. Experimental and theoretical m/z intensities with respect to the intensity of **2s** radical cation (m/z 154.0) are shown.



Supplementary Figure 103 - GC-MS chromatogram of **2t**. (a) GC-MS chromatogram of the reaction mixture using acrylonitrile **1t** as a reagent in dichloromethylation reaction. Peaks in GC of the main components of the reaction mixture are labeled. (b) Mass spectrum of **2t** cation with the theoretical m/z value. (c) Zoomed in area of the mass spectrum. Experimental and theoretical m/z intensities with respect to the intensity of **2t** cation (m/z 136.0) are shown.



Reaction Structure structure variable only at spe... > reactions (0)

REACTIIONS: REACTION STRUCTURE

Structure Editor:

Java Non-Java

Search Type:

- Allow variability only as specified
- Substructure

Click image to change structure or view detail.

Import CXF

Search

Advanced Search

ChemDraw Launch a SciFinder substance or reaction

Reaction Structure structure variable only at spe... > reactions (0)

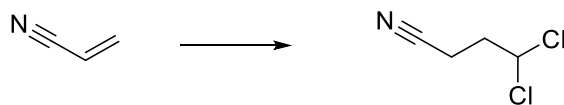
REACTIIONS

Analyze Refine

Analyze by:

No reactions available

Supplementary Figure 104 – SciFinder outcome for preparation of 2s



Reaction Structure structure variable only at spe... > reactions (0)

REACTIIONS: REACTION STRUCTURE

Structure Editor:

Java Non-Java

Search Type:

- Allow variability only as specified
- Substructure

Click image to change structure or view detail.

Import CXF

Search

Advanced Search

ChemDraw Launch a SciFinder substance or reaction

Reaction Structure structure variable only at spe... > reactions (0)

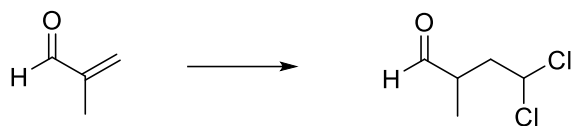
REACTIIONS

Analyze Refine

Analyze by:

No reactions available

Supplementary Figure 105 – SciFinder outcome for preparation of 2t



REACTIONS: REACTION STRUCTURE

Structure Editor:

Search Type:

- Allow variability only as specified
- Substructure

Click image to change structure or view detail.

Import CDF

Search

Advanced Search

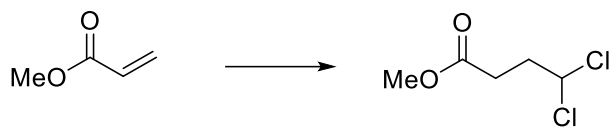
REACTIONS

Find Additional Reactions

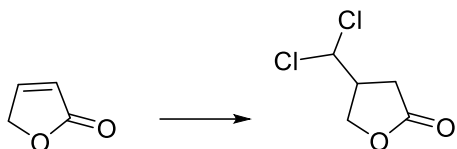
Analyze by:

No reactions available

Supplementary Figure 106 – SciFinder outcome for preparation of 2u



Supplementary Figure 107 – SciFinder outcome for preparation of 2v



Supplementary Figure 108 – SciFinder outcome for preparation of 2w

Reaxys® Quick search Query builder Results Synthesis planner History Stefano Mazzanti

Results for

New Edit

0 Reactions Reaction Query : as drawn
Edit in Query Builder Create Alert

0 Reactions Reaction Query : average similarity; included: tautomers, only absolute stereo, additional ring closures allowed, salts, mixtures, isotopes, charges, radicals
Edit in Query Builder Create Alert

Structure

Press ESC to close

ELSEVIER Copyright © 2019 Elsevier Life Sciences IP Limited. Terms and Conditions Privacy policy About content Performance Page Cookies are used by this site. To decline or learn more, visit our Cookies page RELX Group™

Supplementary Figure 109 – Reaxys outcome for the preparation of 2s

Reaxys® Quick search Query builder Results Synthesis planner History Stefano Mazzanti

Results for

New Edit

0 Reactions Reaction Query : as drawn
Edit in Query Builder Create Alert

0 Reactions Reaction Query : average similarity; included: tautomers, only absolute stereo, additional ring closures allowed, salts, mixtures, isotopes, charges, radicals
Edit in Query Builder Create Alert

Structure

Press ESC to close

ELSEVIER Copyright © 2019 Elsevier Life Sciences IP Limited. Terms and Conditions Privacy policy About content Performance Page Cookies are used by this site. To decline or learn more, visit our Cookies page RELX Group™

Supplementary Figure 110 – Reaxys outcome for the preparation of 2t

Reaxys® Quick search Query builder Results Synthesis planner History Stefano Mazzanti

Results for [] New Edit

0 Reactions Reaction Query : as drawn
 Edit In Query Builder Create Alert

0 Reactions Reaction Query : average similarity; included: tautomers, only absolute stereo, additional ring closures allowed, salts, mixtures, isotopes, charges, radicals
 Edit In Query Builder Create Alert

Structure

Press ESC to close

ELSEVIER Copyright © 2019 Elsevier Life Sciences IP Limited. Terms and Conditions Privacy policy About content Performance Page Cookies are used by this site. To decline or learn more, visit our Cookies page RELX Group™

Supplementary Figure 111 – Reaxys outcome for the preparation of 2u

Reaxys® Quick search Query builder Results Synthesis planner History Stefano Mazzanti

Results for [] New Edit

0 Reactions Reaction Query : as drawn
 Edit In Query Builder Create Alert

0 Reactions Reaction Query : average similarity; included: tautomers, only absolute stereo, additional ring closures allowed, salts, mixtures, isotopes, charges, radicals
 Edit In Query Builder Create Alert


Structure

Press ESC to close

ELSEVIER Copyright © 2019 Elsevier Life Sciences IP Limited. Terms and Conditions Privacy policy About content Performance Page Cookies are used by this site. To decline or learn more, visit our Cookies page RELX Group™

Supplementary Figure 112 – Reaxys outcome for the preparation of 2v

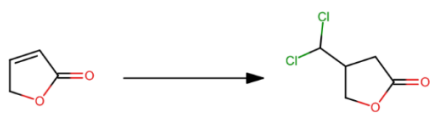
Reaxys Quick search Query builder Results Synthesis planner History Stefano Mazzanti

Results for  New Edit

0 Reactions Reaction Query: as drawn
Edit in Query Builder Create Alert

0 Reactions Reaction Query: average similarity; included: tautomers, only absolute stereo, additional ring closures allowed, salts, mixtures, isotopes, charges, radicals
Edit in Query Builder Create Alert

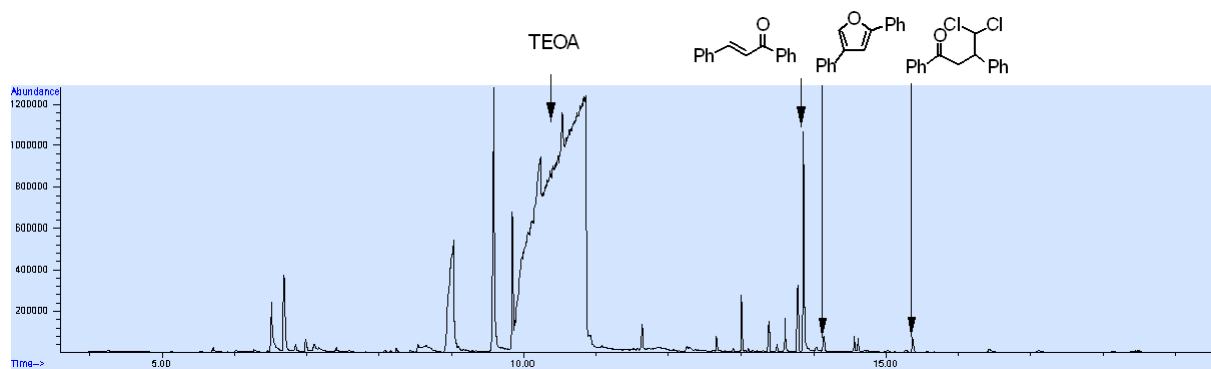
Structure



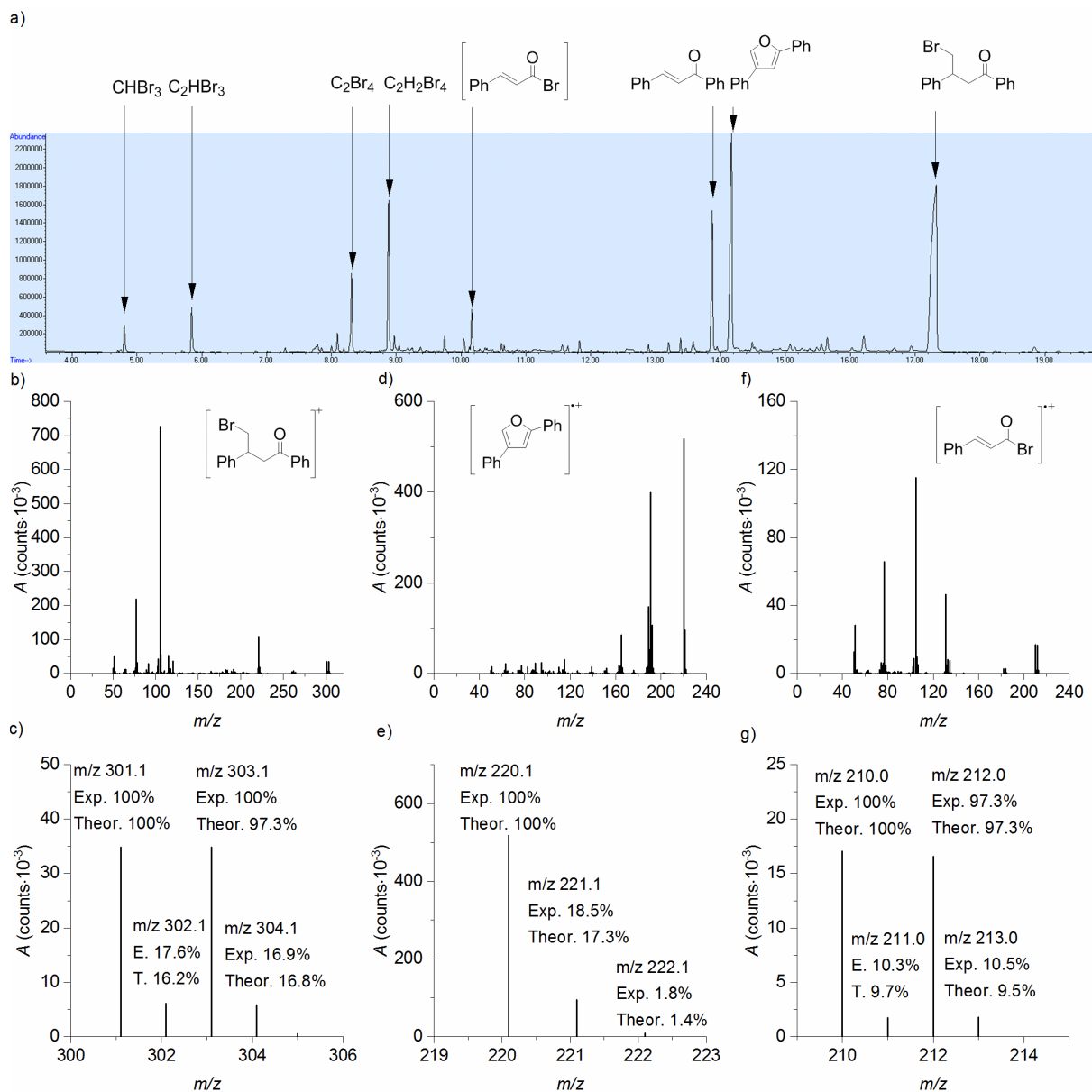
Press ESC to close

ELSEVIER Copyright © 2019 Elsevier Life Sciences IP Limited. Terms and Conditions Privacy policy About content Performance Page Cookies are used by this site. To decline or learn more, visit our Cookies page. RELX Group

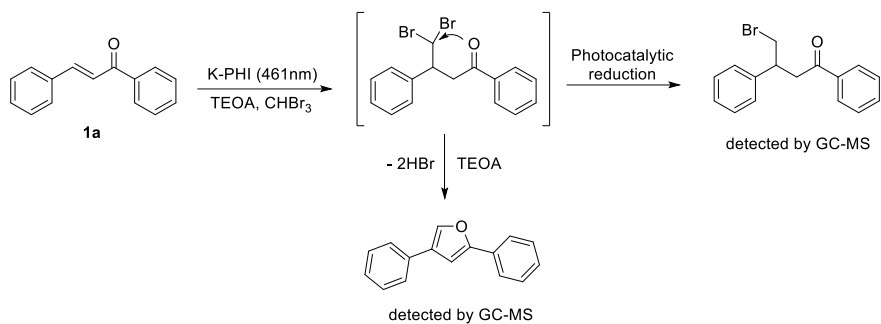
Supplementary Figure 113 – Reaxys outcome for the preparation of **2w**



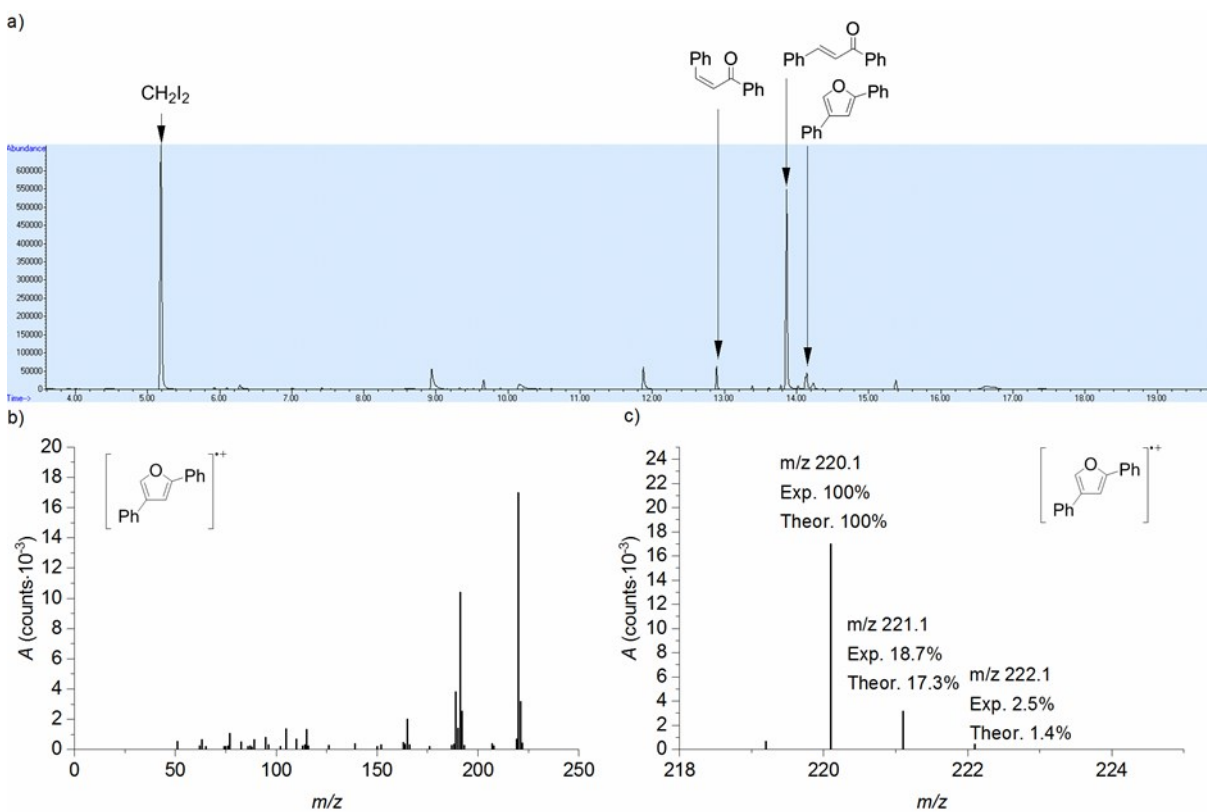
Supplementary Figure 114 - GC-MS data of the reaction mixture using dichloromethane as solvent.



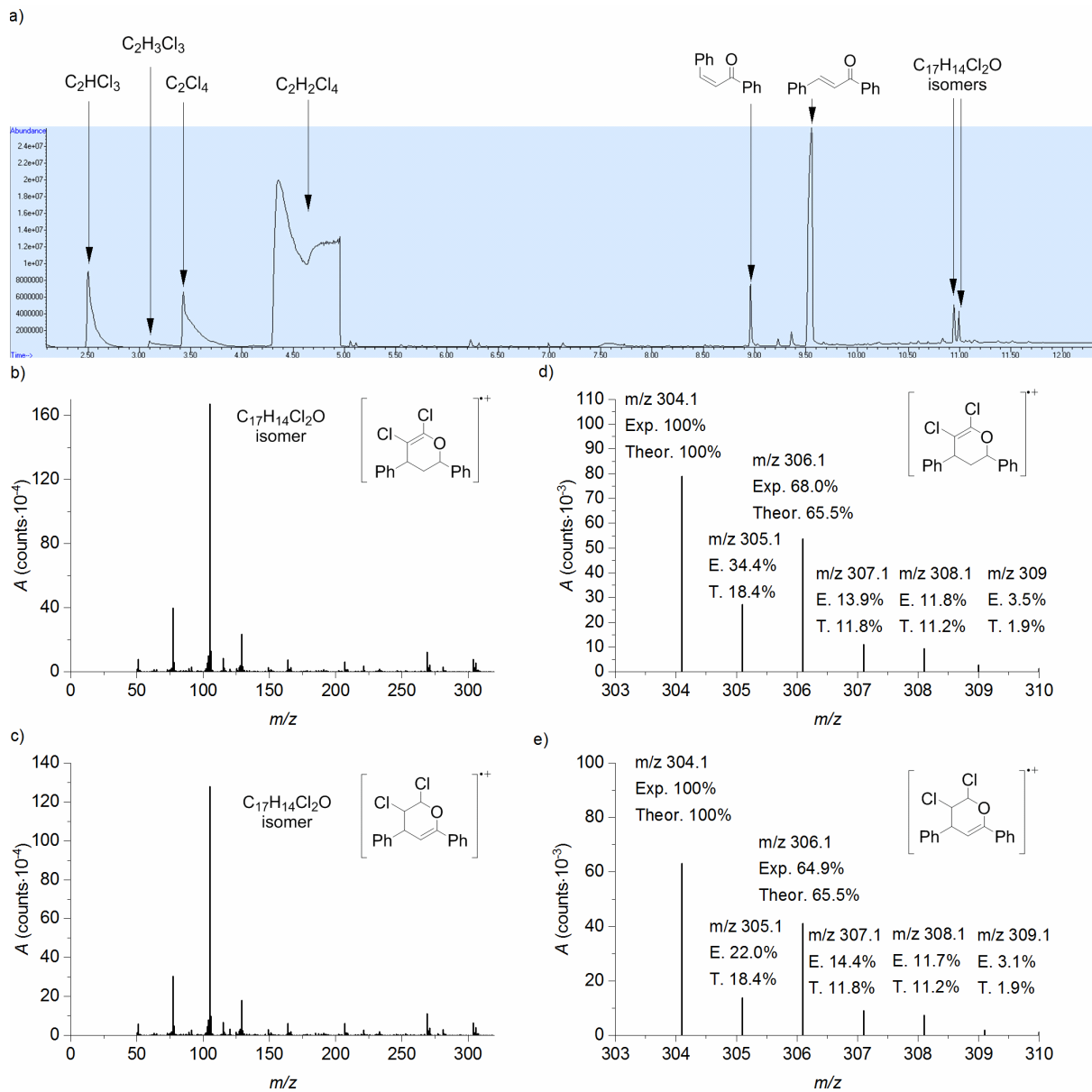
Supplementary Figure 115 - GC-MS data of the reaction mixture using bromoform as solvent. a) Gas chromatogram. b) Mass spectrum of the GC peak corresponding to 4-bromo-1,3-diphenylbutan-1-one cation. c) Zoomed in mass spectrum of 4-bromo-1,3-diphenylbutan-1-one cation. d) Mass spectrum of the GC peak corresponding to 2,4-diphenylfuran radical cation. e) Zoomed in mass spectrum of 2,4-diphenylfuran radical cation. f) Mass spectrum of the GC peak corresponding to the compound with a tentative structure of cinnamoyl bromide radical cation. g) Zoomed in mass spectrum of cinnamoyl bromide radical cation.



Supplementary Figure 116 – Proposed mechanism using bromoform as solvent

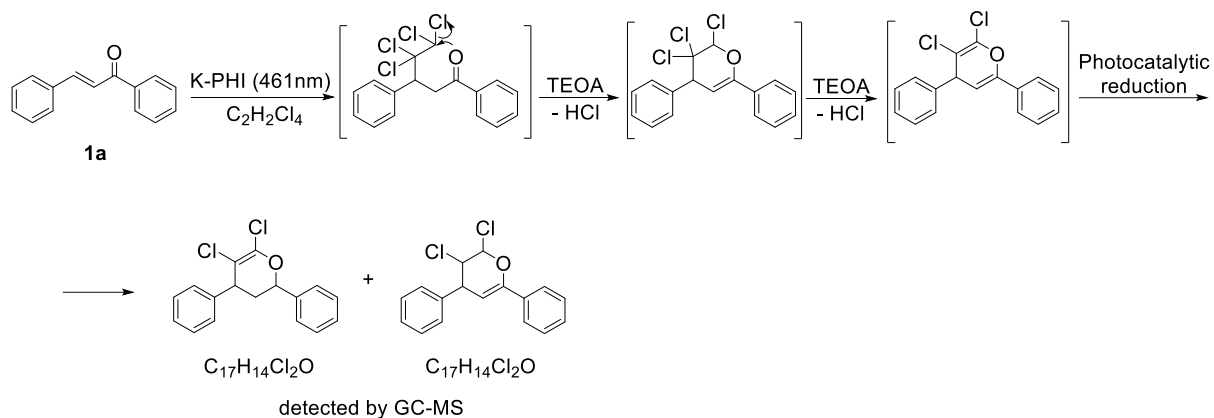


Supplementary Figure 117 - GC-MS data of the reaction mixture using iodoform in dichloromethane. a) Gas chromatogram. b) Mass spectrum of the GC peak corresponding to 2,4-diphenylfuran radical cation. c) Zoomed in mass spectrum of 2,4-diphenylfuran radical cation.

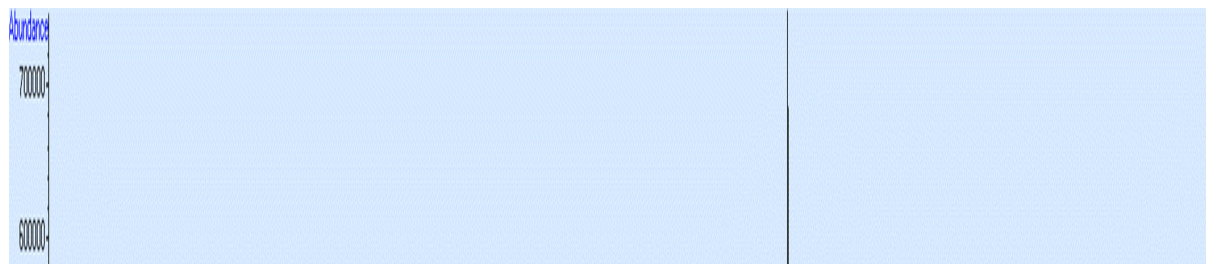


Supplementary Figure 118 - GC-MS data of the reaction mixture using 1,1,2,2-tetrachloroethane as solvent. a) Gas chromatogram. b) Mass spectrum of the GC peak (retention time 10.950 min) corresponding to the compound with brutto formula

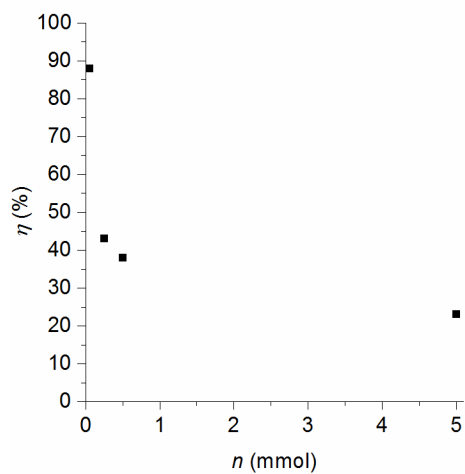
$C_{17}H_{14}Cl_2O$ radical cation. One of possible chemical structures is shown. c) Zoomed in mass spectrum of $C_{17}H_{14}Cl_2O$ radical cation. d) Mass spectrum of the GC peak (retention time 10.996 min) corresponding to the compound with brutto formula $C_{17}H_{14}Cl_2O$ radical cation. One of possible chemical structures is shown. e) Zoomed in mass spectrum of $C_{17}H_{14}Cl_2O$ radical cation.



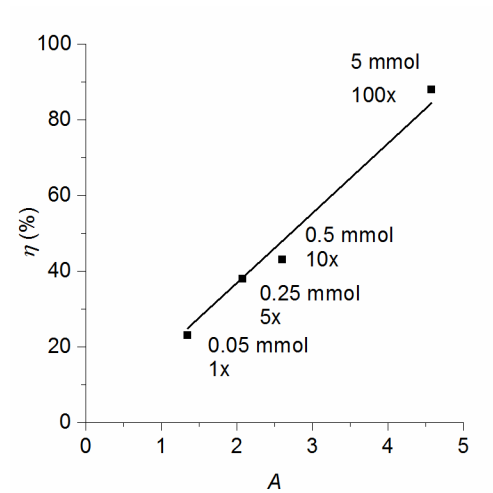
Supplementary Figure 119 – Proposed mechanism using 1,1,2,2-tetrachloroethane as solvent



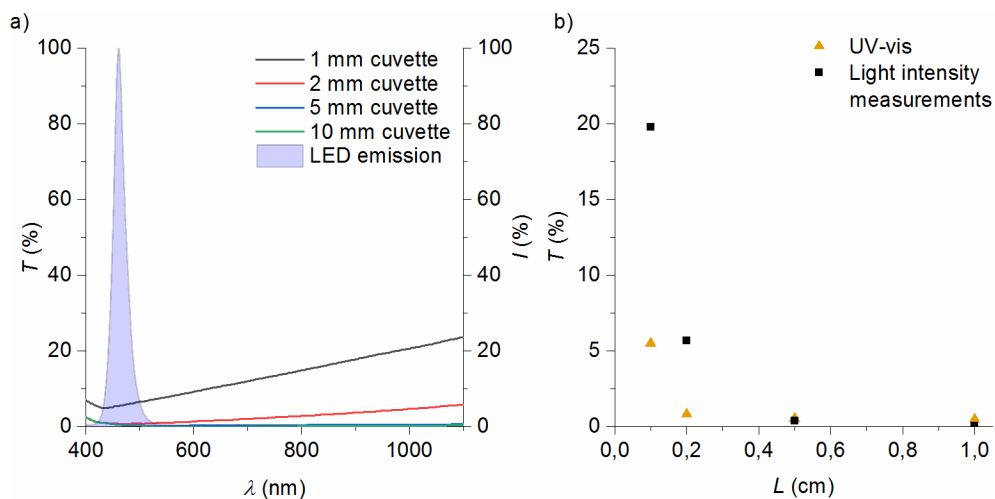
Supplementary Figure 120 - GC-MS data of the reaction mixture using tetrachloromethane as solvent.



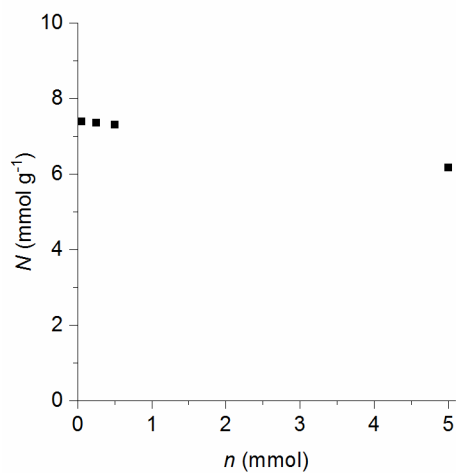
Supplementary Figure 121 – Yield of **2a** varying substrate loading in scale-up experiments



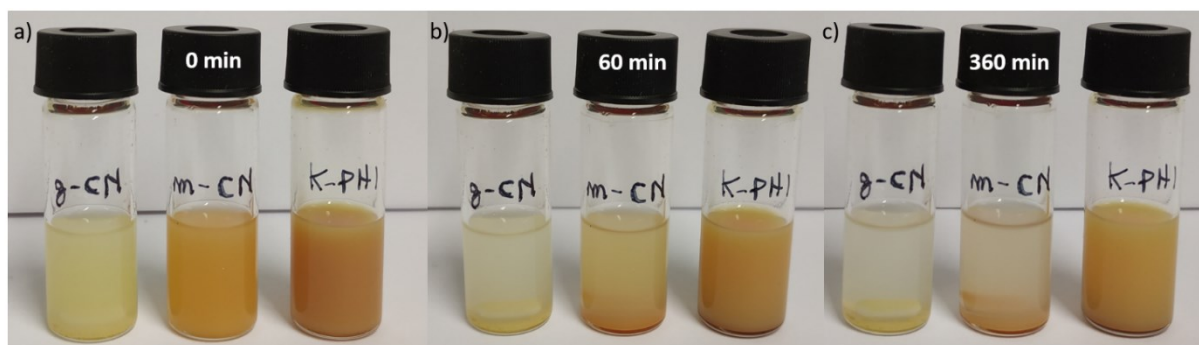
Supplementary Figure 122 – Yield of **2a** varying surface-volume ratio (A)



Supplementary Figure 123 – Light penetration tests. a) Transmittance (T) of the K-PHI suspension in CHCl_3 :DMSO (9:1) versus incident light wavelength measured using UV-vis spectrometer and LED emission spectrum (used in the photocatalytic experiments in this work); b) Transmittance (T) of the K-PHI suspension in CHCl_3 :DMSO (9:1) at $\lambda = 461$ nm versus cuvette optical path. Triangles denote data points obtained using UV-vis spectrometer. Squares denote data points obtained by measuring fraction of light ($\lambda = 461 \pm 20$ nm, $I_0 = 10.6 \text{ mW cm}^{-2}$) from the external source passed through the cuvette filled with K-PHI suspension.



Supplementary Figure 124 – Specific absolute yield (N) of **2a** varying substrate loading



Supplementary Figure 125 – Suspension stability test for different photocatalysts. From left to right, respectively, $g\text{-C}_3\text{N}_4$, $m\text{pg-CN}$, $K\text{-PHI}$. Pictures taken after different times: a) immediately after stop stirring; b) after 60 minutes; c) after 360 minutes

7.3 Photocatalysis Goes Thinner Than a Hair: Carbon Nitride Thin Films as All-in-one Technology for Photocatalysis

Time-correlated single photon counting (TCSPC) measurements of samples were using a PicoQuant FluoTime 250 with 375 nm laser diode excitation.

Emission spectra, Internal and External Quantum Efficiency (IQE/EQE) were recorded on Jasco FP-8300 instrument. The excitation wavelength was set at 375 nm.

EPR study was conducted on Bruker EMXnano benchtop X-Band EPR spectrometer. The following settings have been used for all spectra acquisition unless other is specified: Center Field 3444.05 G, Sweep Width 200 G, Receiver Gain 60 dB, Modulation Amplitude 1.000 G, Number of Scans 1, Microwave Attenuation 10 dB. Sample were placed and flame-sealed in EPR capillaries (IntraMark, volume 50 μ L, ID 0.86 mm), inside EPR tubes (ID 3 mm, OD 4 mm, length 250 mm)

In-situ EPR measurements of photocatalytic experiments have been performed coupling Thorlabs M415F3 Fiber-Coupled LED ($64 \text{ mW}\cdot\text{cm}^{-2}$ measured at 0 cm distance) with Thorlabs DC2200 High-Power LED controller.

Emission spectra of LED modules were measured using Avantes spectrometer Avaspec-ULS2048CL-EVO-R5 coupled with Thorlabs optical fiber M113L01 - $\text{\O}400 \mu\text{m}$.

Transient absorption spectroscopy was collected in transmission geometry. An amplified femtosecond laser (Light Conversion Pharos) generated pulses of ~ 280 fs centered at 1024 nm. A broadband white light probe is generated by focusing the pulses into a thin sapphire plate. At short delays (< 5 ns) the third harmonic of the fundamental provided the pump light (343 nm , $85 \mu\text{J}\cdot\text{cm}^{-2}$). At long delays (> 1 ns) pump light at 355 nm was provided by the third harmonic of a Q-switched Nd:YVO₄ laser (Innolas Picolo) which was electronically triggered and synchronised to the femtosecond laser via an electronic delay.

The data acquired in the two time regimes were combined together, with a small scaling factor applied to overlap signal amplitudes between 2 and 4 ns.

Data analysis was conducted using Matlab. tr-PL decays were fitted starting from 4 ns ignoring IRF (IRF at 4 ns is 2 order of magnitude lower than its peak value). TAS decays were fitted starting from time equal 0. Fitting has been conducted minimizing the square distance among the fitting function and the data. The minimization has been done using Matlab fminsearch that uses Nelder-Mead simplex algorithm. [266]

MarvinSketch was used for calculating **Molecular Surface Areas** of homogeneous photocatalysts (3D, Wan der Waals), Marvin 21.3, ChemAxon (<https://www.chemaxon.com>)

Atomic force microscopy analysis have been conducted on Veeco Dimension 3100 atomic force microscope.

Flow Reactor custom made from Little Things Factory. Microreactor Type KOE, Material: Quartz, Dimension of half cell: 90 x 54 x 2 ±0,3 mm, Throughput connection via SwageLok screws, Internal volume (whole cell): 1.0 ml, Permitted particle size: 250 µm

General procedure for carbon nitride thin film coated materials

Synthetic Procedure for CN Thin Films by CVD: The preparation of CN thin films was conducted with a planarGROW-3S-OS CVD System for Organic Semiconductor, provided by planarTECH, with a 3 inches quartz tube. The chosen material was placed vertically in the center of the second CVD oven and a glass boat containing melamine (5 g) in the center of the first one. Then, the vacuum was pulled down to 10 Torr and the temperature at the substrate was raised to 550 °C, with 50 sccm nitrogen flow as carrier gas. As soon as the substrate was at 550 °C, the melamine was heated up to 300 °C at a rate of 10 °C min⁻¹, and kept for additional 30 min. The substrates were kept for additional 30 min at 550 °C after the first oven heating program was finished. The samples were let cool down naturally and

collected at room temperature. Of note, the melamine was in all cases completely consumed during the experiments.

General procedure for photocatalytic benzyl alcohol oxidation

In a 4 mL vial coated with carbon nitride thin film, benzylic alcohol (1.04 μL , 0.01 mmol) in CD_3CN (3 mL) were added to the vial and closed with a rubber screw cap. The solution was flushed via double needle technique with O_2 for 2 minutes. A rubber balloon was filled with O_2 and attached to the vial via needle connection, in order to keep constant O_2 pressure due to small gas leaks. The vial was placed under irradiation between two LED modules 400 nm (50 W electric power, 460 $\text{mW}\cdot\text{cm}^{-2}$ output measured at 1 cm distance), placed at 1 cm distance. The reaction was cooled with a fan, keeping temperature at 40 $^\circ\text{C}$. After 24 hours, the reaction was stopped and analyzed by NMR. Products were identified comparing crude ^1H NMR spectra with pure compounds. Yield and conversion have been quantified using 1,3,5-trimethoxybenzene as internal standard.

Photocatalytic TEMPO detection experiment

A solution of 2,2,6,6-tetramethylpiperidine (TEMP) (5 μL , 0.03 mmol) in CH_3CN (3 mL) was prepared in 4 mL glass vial. The solution was flushed via double needle technique with O_2 for 2 minutes. A carbon nitride coated capillary (IntraMark, volume 50 μL , purchased from BRAND GMBH + CO KG) was sealed in the flame of gas burner from one side. The capillary was charged with an aliquot of the TEMP solution in CH_3CN (20 μL , 0.01 $\text{mol}\cdot\text{L}^{-1}$). The opened end of the capillary was sealed in the flame of gas burner and placed into an EPR tube (ID 3 mm, OD 4 mm, length 250 mm). EPR spectrum was acquired and used as a reference

(0 min, in dark). Afterwards the sample was directly irradiated using a 415 nm LED module equipped with optic fiber, to perform in-situ measurements. EPR spectra were acquired immediately when turning light ON and after 30 minutes. The acquired spectra were compared with spectra obtained under the same conditions, but using clean uncoated glass capillaries (control experiments).

Photocatalytic DMPO-O₂^{•-} detection experiment

A solution of 5,5-Dimethyl-1-pyrroline *N*-oxide (DMPO) (5 µg, 0.04 mmol) in CH₃CN (3 mL) was prepared in 4 mL glass vial. The solution was flushed via double needle technique with O₂ for 2 minutes. A carbon nitride coated capillary (IntraMark, volume 50 µL, purchased from BRAND GMBH + CO KG) was sealed in the flame of gas burner from one side. The capillary was charged with an aliquot of DMPO solution in CH₃CN (20 µL, 0.01 mol·L⁻¹). The opened end of the capillary was sealed in the flame of gas burner and placed into an EPR tube (ID 3 mm, OD 4 mm, length 250 mm). EPR spectrum was acquired and used as a reference (0 min, in dark). Afterwards the sample was directly irradiated using a 415 nm LED module equipped with optic fiber, to perform in-situ measurements. EPR spectra were acquired immediately after turning the light source ON and after 30 minutes. The acquired spectra were compared with the spectra obtained under the same conditions, but using clean uncoated glass capillaries (control experiments).

General procedure for photocatalytic benzyl alcohol oxidation in flow

Scheme of the setup is presented in Figure S12. Individual components of the setup are shown in Figure S13 with the details in the caption. The entire system was build using FEP tubing 0.8 x 1.6 mm, to minimize dead volume. Short piece of tubing 1.6 x 3.2 mm was used at the inlet and outlet of the reactor. Cooling with fan was used to avoid overheating of the

reactor. During the experiment reaction temperature remained below 50 °C (measured with infrared thermometer Scantemp 385 in the reactor channels). A 5 mL vial with rubber septum was used as a tank for reaction mixture recirculation. Prior the photocatalytic experiment it was filled with reaction mixture (3 mL) containing benzylalcohol (same concentration as reported in the general procedure, using non-deuterated CH₃CN). Once the reaction started, immediately after consumption of the initial volume, other 2 mL of CH₃CN were added to ensure that all pipes were filled. Flow details: Liquid flow 50 μL·min⁻¹, O₂ 50 μL·min⁻¹, pressure 1 atm (open air system, the vial was connected to air). The reaction progress over time was analyzed by GC-MS (Table S6).

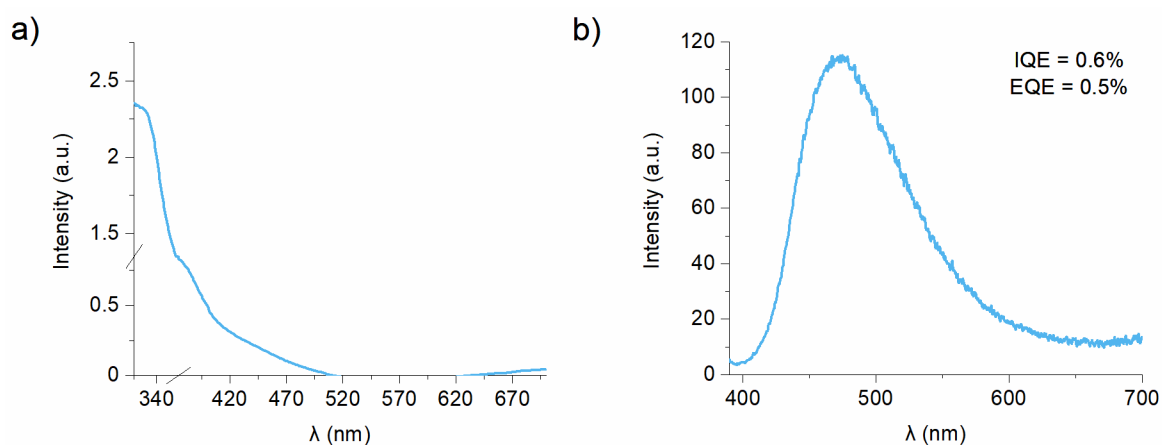


Figure S1 – Steady-state spectroscopy of Vis-BWR. a) UV-Vis absorption spectrum; b) Photoluminescence spectrum ($\lambda_{\text{Ex}} = 375 \text{ nm}$). Spectra were acquired by placing the vial coated with the CN film into the chamber of the spectrometers.

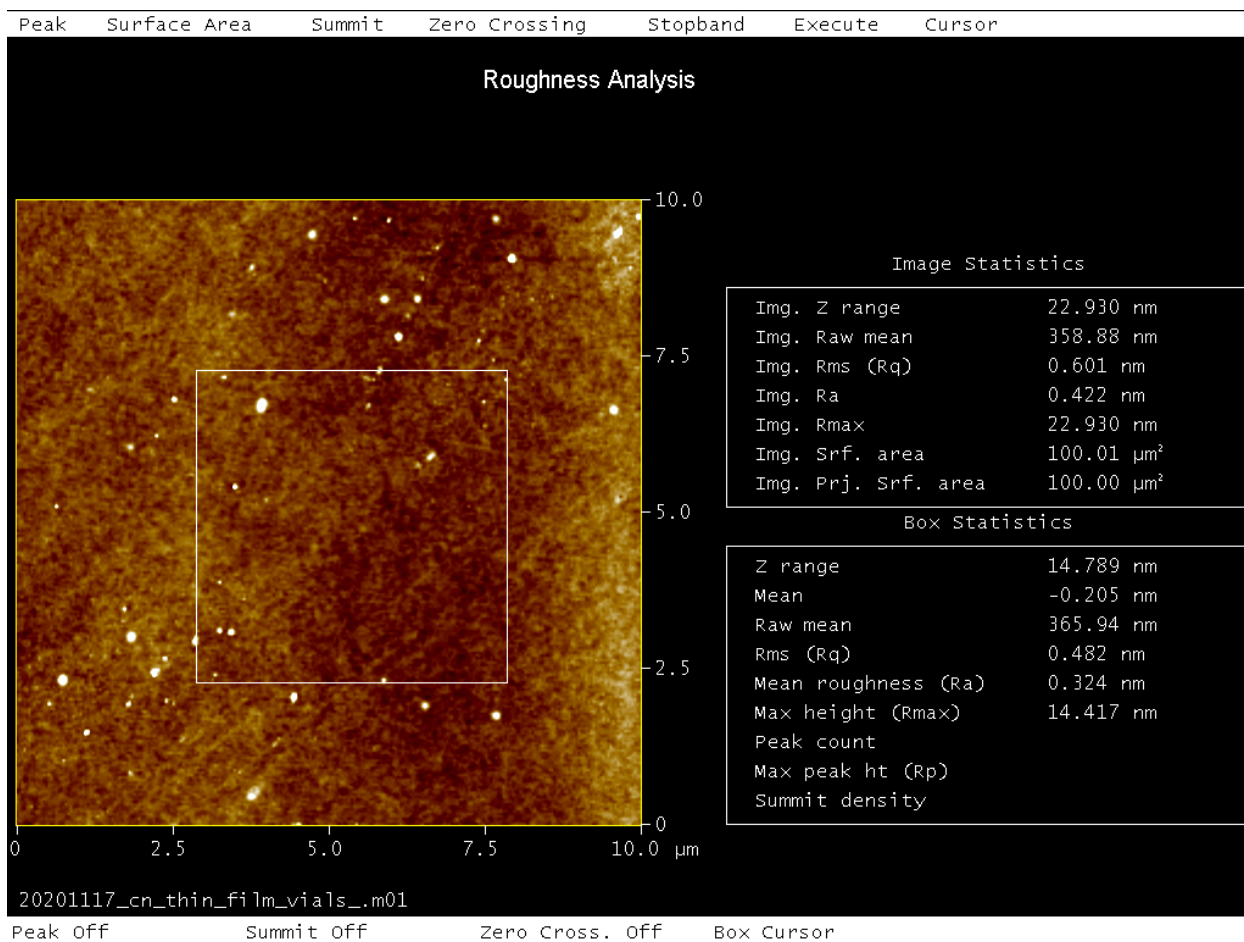


Figure S2 –Analysis of the CN film roughness deposited at the glass vial via AFM to determine homogeneity of the surface.

Analysis was performed using a small piece of glass after crushing a vial.

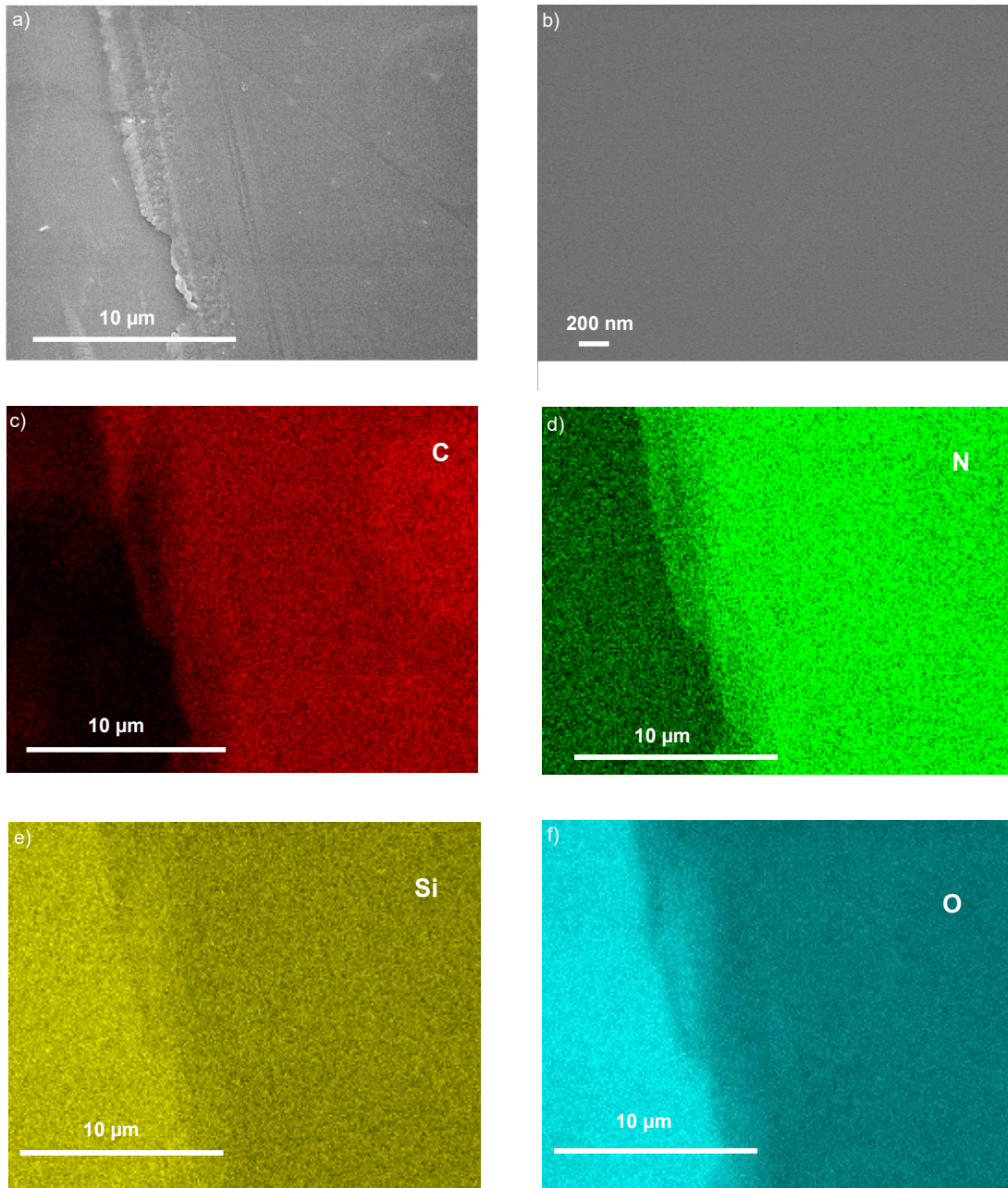


Figure S3 – SEM and SEM-EDX mapping images of carbon nitride coated vials. Analysis was performed using a small piece of glass after crushing a vial. A scratch was indented with a cutter to locally remove the film .a) SEM image of carbon nitride thin

films with mechanical scratch (the left part highlight only the glass substrate, whereas on the right the film is present) b) SEM image of the undamaged part of the CN thin films c) Carbon (C) SEM-EDX d) Nitrogen (N) SEM-EDX e) Silicon (Si) SEM-EDX f) Oxygen (O) SEM-EDX images.

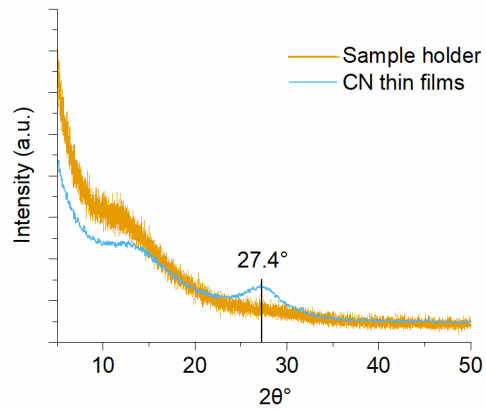
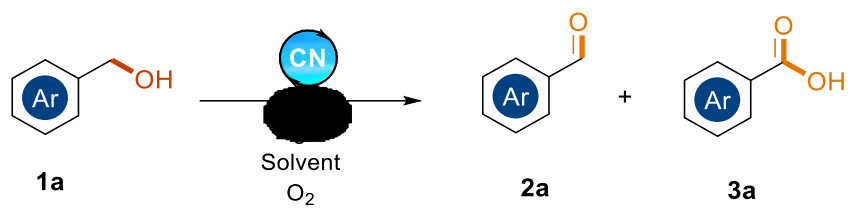


Figure S4 – PXR D pattern of the CN thin film deposited at the glass vial. Analysis was performed sampling material by scratching a CN coated glass vial with a steel spatula



Entry	BA (mmol)	Solvent	Time (h)	Light	Yield 2a (%)	Yield 3a (%)
1	0.05	CH ₃ CN	20	365 nm	3	n.d.
2	0.05	CH ₃ CN	20	400 nm	10	n.d.
3	0.05	CH ₃ CN	20	White	-	n.d.
4	0.05	CH ₃ CN	20	525 nm	-	n.d.
5	0.025	CH ₃ CN	20	400 nm	14	n.d.
6	0.025	EtOH	20	400 nm	7	n.d.
7	0.025	<i>i</i> PrOH	20	400 nm	8	n.d.
8	0.025	H ₂ O	20	400 nm	7	n.d.
9 ^a	0.025	CH ₃ CN	20	400 nm	29	n.d.
10 ^{ab}	0.025	CH ₃ CN	20	400 nm	27	n.d.
11 ^{abc}	0.025	CH ₃ CN	20	400 nm	38	n.d.
12 ^{abc}	0.025	CH ₃ CN	20	400 nm x2	56	15
13 ^d	0.01	CH ₃ CN	24	400 nm x2	14	81 (87)
14 ^{d,e}	0.01	CH ₃ CN	24	400 nm x2	-	-
15 ^{d,f}	0.01	CH ₃ CN	24	No light	-	-

Table S2 – Optimization of reaction conditions of benzyl alcohol (BA) oxidation. Yields have been estimated via GC-MS and in parenthesis via ¹H NMR with internal STD a) 2 cm distance from the LED b) Without stirring. c) Carbon nitride layer that was deposited in the CVD furnace on the outer surface of the vial was removed by sequential treatment with DMSO, followed by polishing with paper cloth and glass paper. d) reaction conditions as reported in the general procedure for benzyl alcohol oxidation e) reaction performed using a glass vial without CN coating f) vial was wrapped in aluminum foil



Figure S5 - Carbon nitride coated Glass vial coated with the CN film under UV light. Bottom part of the vial was scratched due to mechanical friction caused by the magnetic stirrer used during the reaction

Entry	Catalyst	Amount	Surface area	Yield 2a (%)	Yield 3a (%)	X (%)	TOA (mmol·m ⁻²)
1	Vis-BWR	n.a.	8 m ²	14	81	100	9.5
2	mpg-CN ^a	1 mg	180 m ² ·g ⁻¹	32	68	100	5.5*10 ⁻²
3 ^b	TiO ₂ ^c	1 mg	50 m ² ·g ⁻¹	34	66	100	2.0*10 ⁻¹
4	K-PHI ^d	1 mg	89 m ² ·g ⁻¹	29	-	29	3.2*10 ⁻²
5	CdS ^e	1 mg	65 m ² ·g ⁻¹	5	-	5	7.7*10 ⁻³
6	Ir(ppy) ₃ ^f	0.41 mg (2.5 mol%)	693 Å ² ·molecule ⁻¹	20	-	20	1.9*10 ⁻⁶
7	[Ru(bpy) ₃ Cl] ₂ ^g	0.47 mg (2.5 mol%)	875 Å ² ·molecule ⁻¹	64	-	64	4.9*10 ⁻⁶

Table S2 – Catalysts screening. Yield and conversion have been estimated via GC-MS. TOA stands for Turnover area, meaning converted mmol of benzyl alcohol (BA) per m² of catalytic surface in the general reaction conditions reported above. a) Surface area and preparation according to literature ^[115]. b) Experiment performed under 365 nm light. c) TiO₂ (purchased from Sigma-Aldrich, rutile nanopowder 10 x 40 nm). d) Surface area and preparation according to literature. ^[115] e) CdS, (purchased from Sigma-Aldrich), surface area measured via N₂ physisorption (see experimental procedure above). f) Homogeneous photocatalysts specific surface area employed has been calculated using MarvinSketch (see experimental procedure above). g) [Ru(bpy)₃Cl]₂ stands for abbreviation of [Ru(bpy)₃Cl]₂·6H₂O

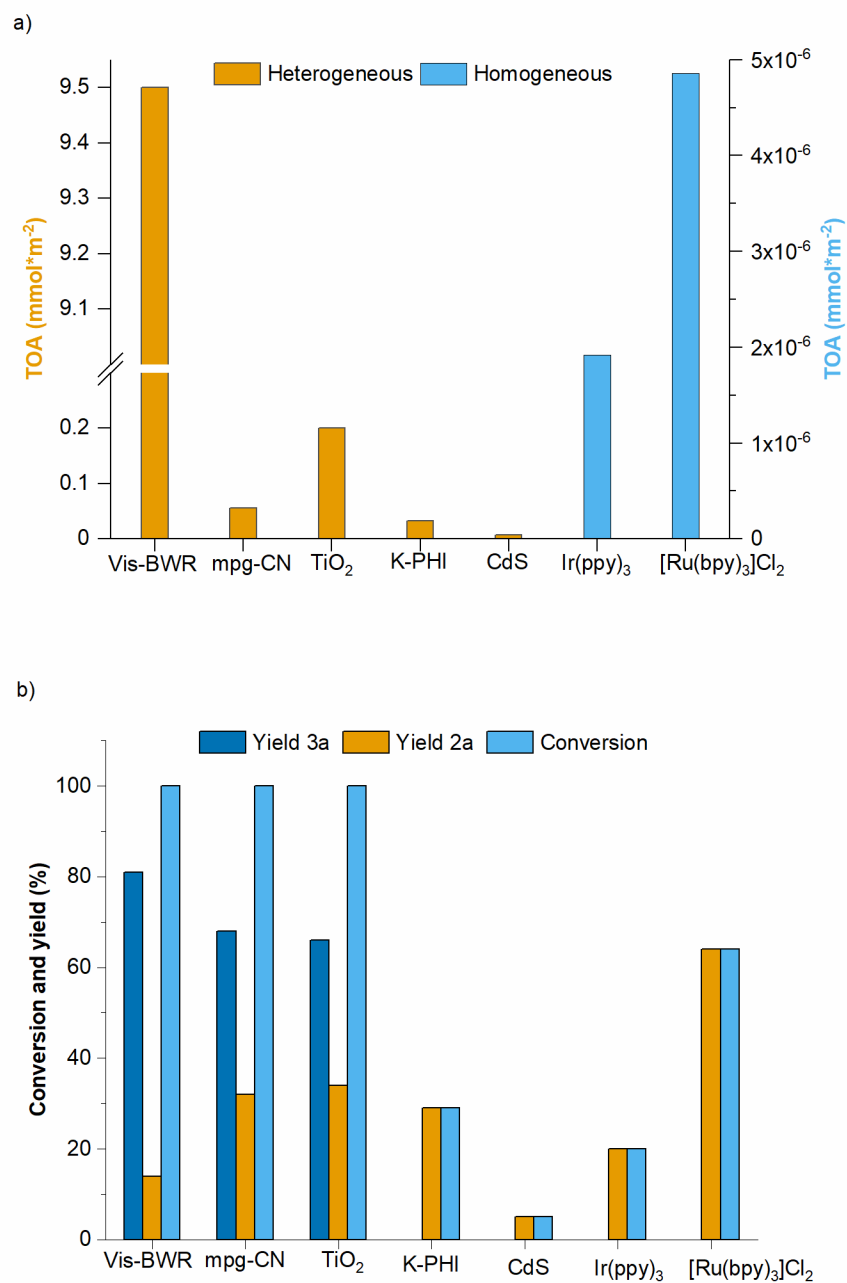


Figure S6 – Catalyst screening. TOA and yields comparison. Reaction details as reported in Table S2

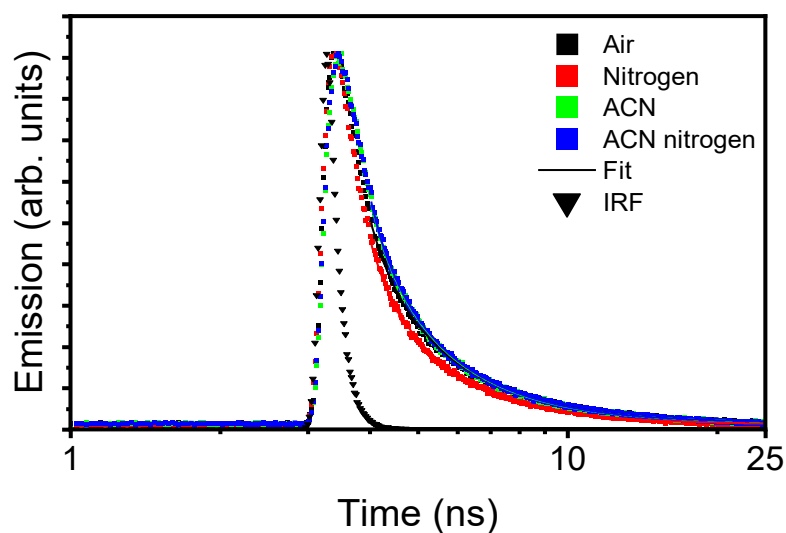


Figure S6 - TCSPC fluorescence decay curve ($\lambda_{\text{Ex}} = 375 \text{ nm}$, bandwidth 10 nm at 479.4 nm). In different colors with squares are shown the fluorescence decay curves of the sample under different conditions (the vial coated with the CN film in air, the vial filled with nitrogen the vial filled with acetonitrile, the vial filled with degassed acetonitrile). Fitting is shown with solid line (calculated from 4 ns onward, when IRF is 2 order of magnitudes lower than its peak). The black triangles represent the IRF.

Sample	Intensity (arb. units)	τ (ps)	Baseline (arb. units)	R ²
Air	9940	658	164	0.999
Nitrogen	9355	582	125	0.999
ACN	11224	593	170	0.999
ACN nitrogen	11289	598	173	0.999

Table S3 - Results of single stretched exponential fitting using a $\beta = \frac{1}{2}$.

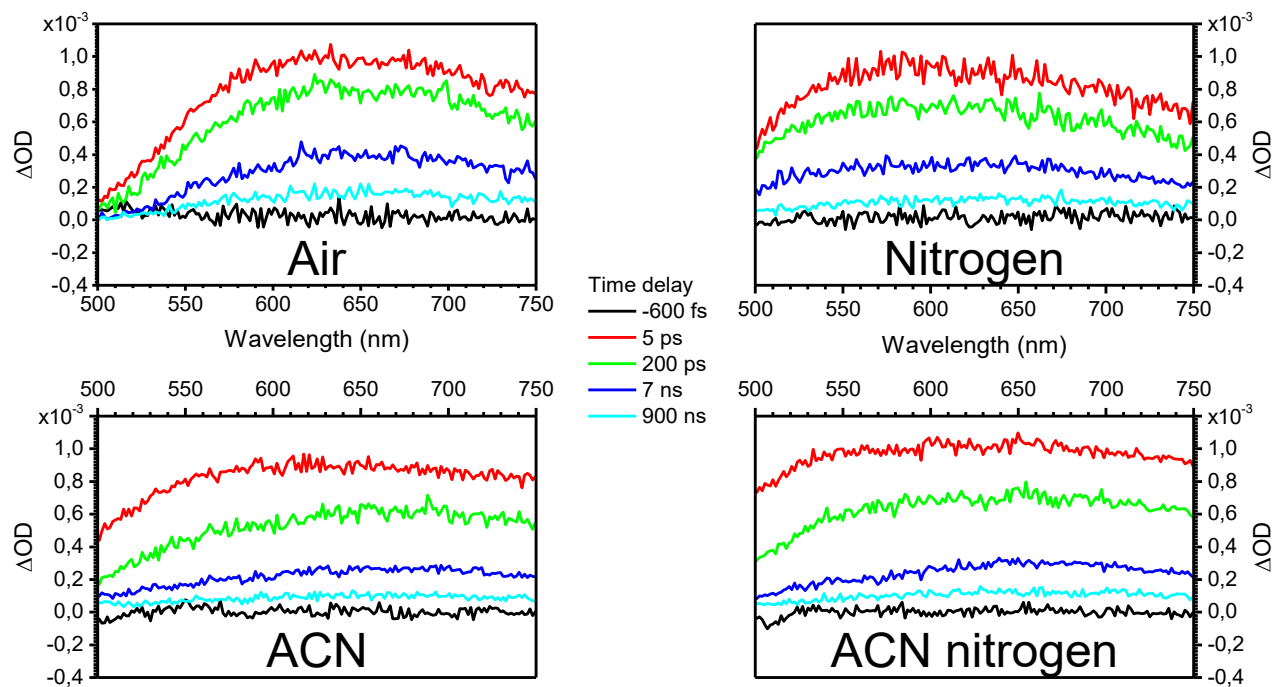


Figure S7 -TA spectra of CN thin films at different time delays. Spectra were acquired by placing a fragment of the vial coated with the CN film into a cuvette. Air – the cuvette was filled with air; Nitrogen – the cuvette was filled with nitrogen; ACN – the cuvette was filled with acetonitrile; ACN nitrogen – the cuvette was filled with degassed nitrogen. The black lines (-600 fs) represent the ground state.

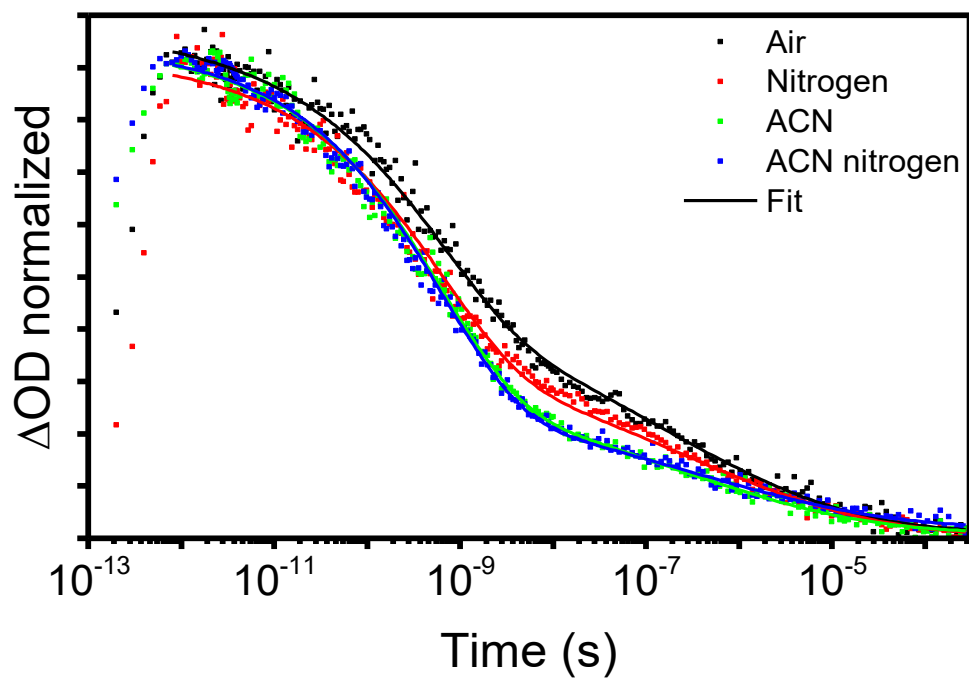


Figure S8 – Time-dependent evolution of signal (arithmetic mean between 550-750 nm) acquired by placing a fragment of the vial coated with the CN film into a cuvette. Air – the cuvette was filled with air; Nitrogen – the cuvette was filled with nitrogen; ACN – the cuvette was filled with acetonitrile; ACN nitrogen – the cuvette was filled with degassed nitrogen. The curves were normalized in the range 0-1.

Sample	A ₁ (arb. units)	τ ₁ (ns)	β ₁	A ₂ (arb. units)	τ ₂ (ns)	β ₂	R ²
Air	0.446	0.6	½	0.612	158	0.2	0.996
Nitrogen	0.541	0.6	½	0.484	238	0.2	0.994
ACN	0.646	0.6	½	0.376	265	0.2	0.996
ACN nitrogen	0.716	0.6	½	0.327	850	0.2	0.997

Table S4 - Results of TA data fitting shown in Figure S9 using 2 stretched exponential decay function $-\frac{\Delta T}{T} = A_1 e^{-\left(\frac{t}{\tau_1}\right)^{\beta_1}} + A_2 e^{-\left(\frac{t}{\tau_2}\right)^{\beta_2}}$. Given the very low β , difference in τ_2 between ACN and ACN nitrogen samples is most probably due to fitting artifacts and not reasonable observing the curves.

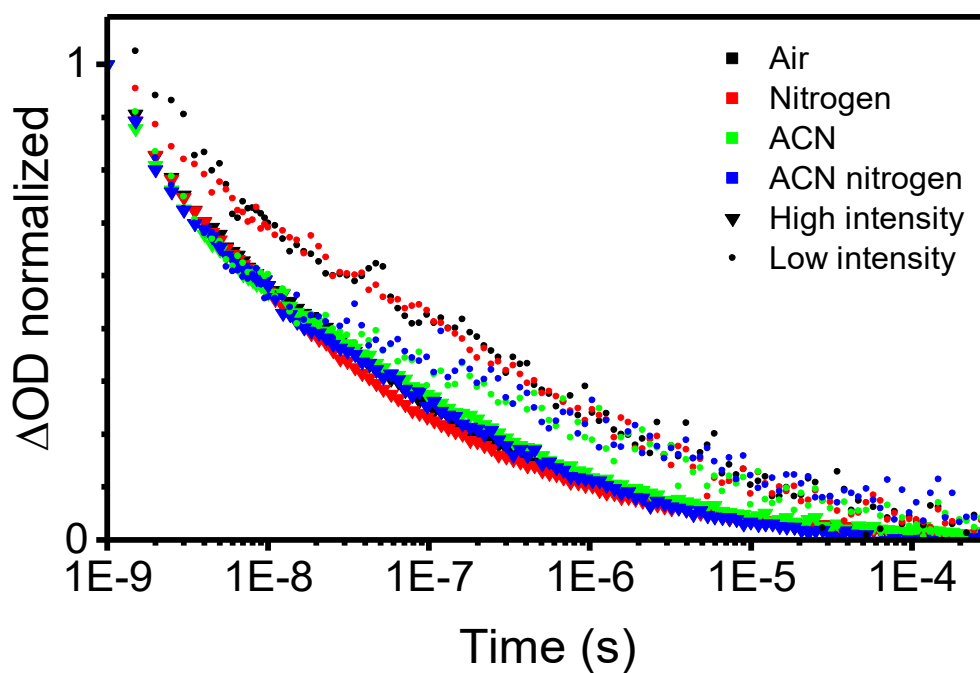


Figure S9 - Time-dependent evolution of signal (arithmetic mean between 550-750 nm) in the ns-ms regime using low and high intensity excitation. The decay curves have been acquired by placing a fragment of the vial coated with the CN film into a cuvette.

Air – the cuvette was filled with air; Nitrogen – the cuvette was filled with nitrogen; ACN – the cuvette was filled with acetonitrile; ACN nitrogen – the cuvette was filled with degassed nitrogen. The curves were normalized in the range 0-1.

Sample	A ₁ (arb. units)	τ ₁ (ns)	β ₁	A ₂ (arb. units)	τ ₂ (ns)	β ₂	R ²
Air	0.932	0.6	½	1.35	12.3	0.2	0.998
Nitrogen	1.04	0.6	½	1.35	9.62	0.2	0.997
ACN	1.08	0.6	½	1.13	27.3	0.2	0.998
ACN nitrogen	1.00	0.6	½	1.25	15.7	0.2	0.999

Table S5 - Results of the TA data fitting shown in Figure S12 under high intensity pump using 2 stretched exponential decay

$$\text{functions } -\frac{\Delta T}{T} = A_1 e^{-\left(\frac{t}{\tau_1}\right)^{\beta_1}} + A_2 e^{-\left(\frac{t}{\tau_2}\right)^{\beta_2}}$$

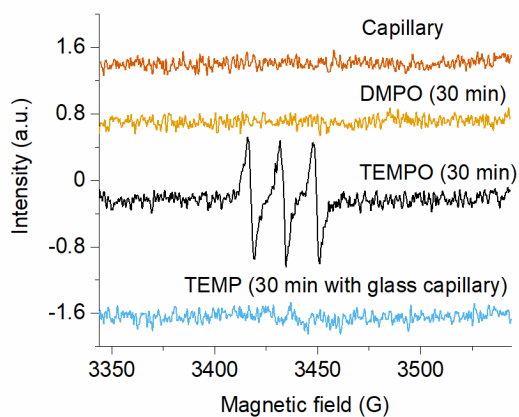


Figure 10 - In situ EPR investigation of TEMPO and DMPO-O₂^{•-} generation with control experiments. Analysis have been conducted using coated capillaries and uncoated capillaries (for control experiments)

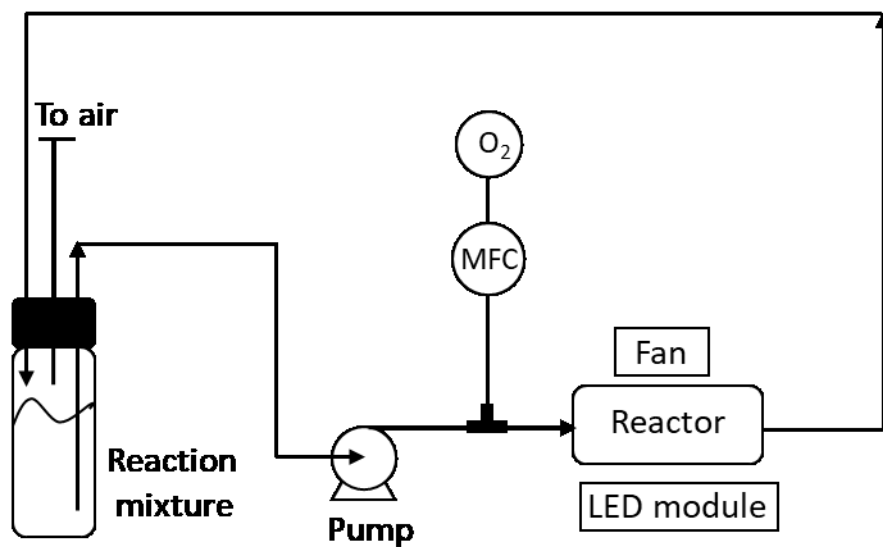


Figure S11 – Scheme of the reaction setup employed to perform the experiment in flow.

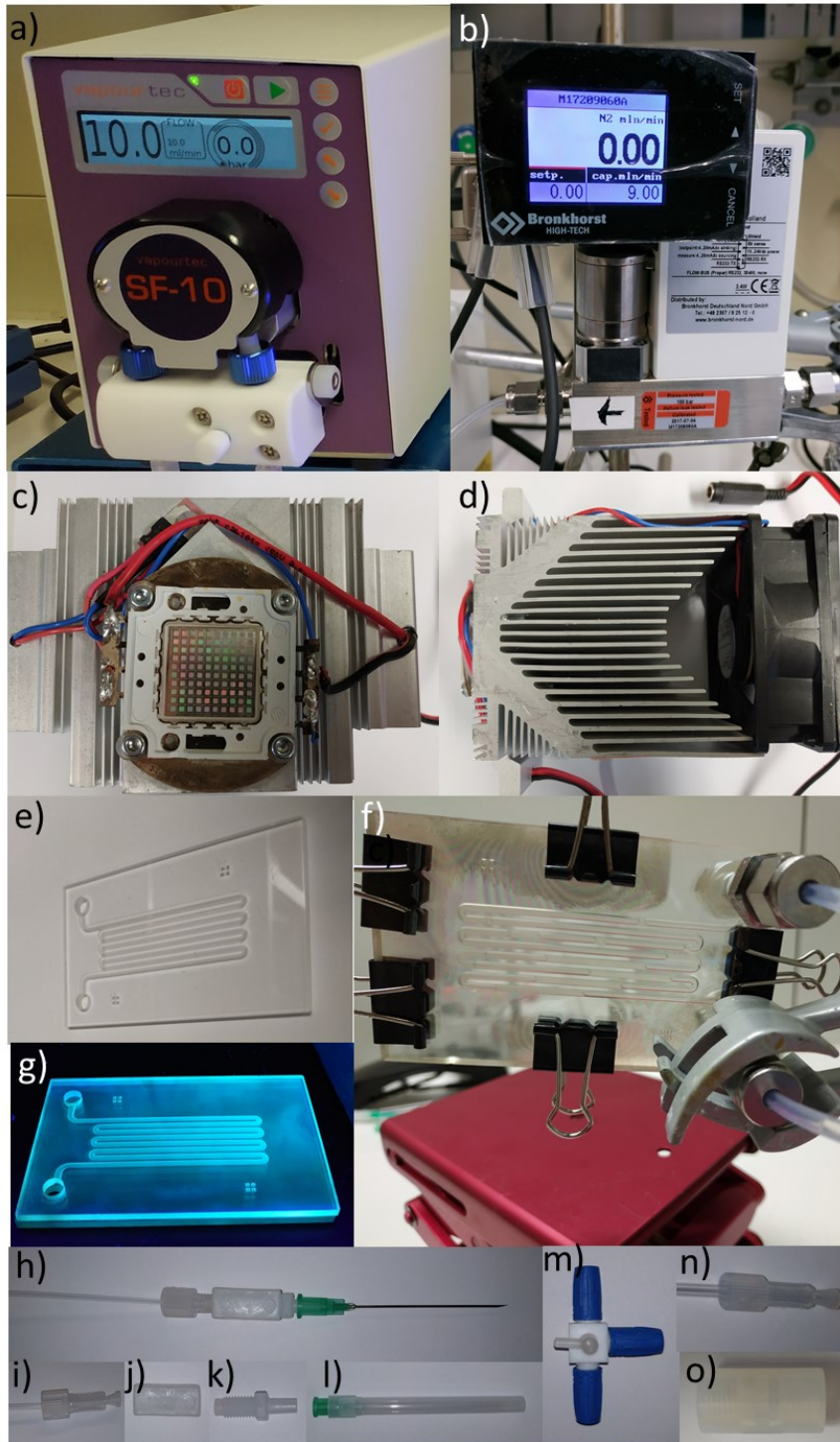


Figure 12 - a) SF-10 reagent pump (Vapourtec). b) Mass flow controller (MFC, Bronkhorst). MFC calibrated for N₂ was used to provide steady flow of O₂. The difference between N₂ and O₂ physical properties has been taken into account using database provided by the MFCs (<https://www.fluidat.com/>). c) 400 nm LEDs module, front view. d) 400 nm LEDs module, top view. e) Quartz reactor under visible light (half-cell, uncoated). f) Quartz reactor, coated and mounted in the flow system. g) Quartz reactor under 365 nm light (half-cell, coated). h) Input and output of flow system (assembled, see i-l for single specific parts). i) connector unit, composed of FEP tubing 0.8 x 1.6 mm, nut and ferrule of the respective diameter. j) Union, threaded, 1/4"-28 (trhu-threads). k) Luer adapter, female luer to 1/4-28. l) Syringe needle ID 0.8 mm, 5 cm. m) T-connector with valve, 3-way, single key, bore 1.5 mm. n) connector unit, composed by FEP tubing 1.6 x 3.2 mm, nut and ferrule of the respective diameter. o) Union, threaded, 1/4"-28 (flat bottom, female).

Cycles	τ (min)	Yield (%)
0	0	0
1	13	16
3	40	54
5	67	75
6	80	89
7	93	96

Table S6 – Flow experiment data. Yield of **2a** was determined by GC-MS.

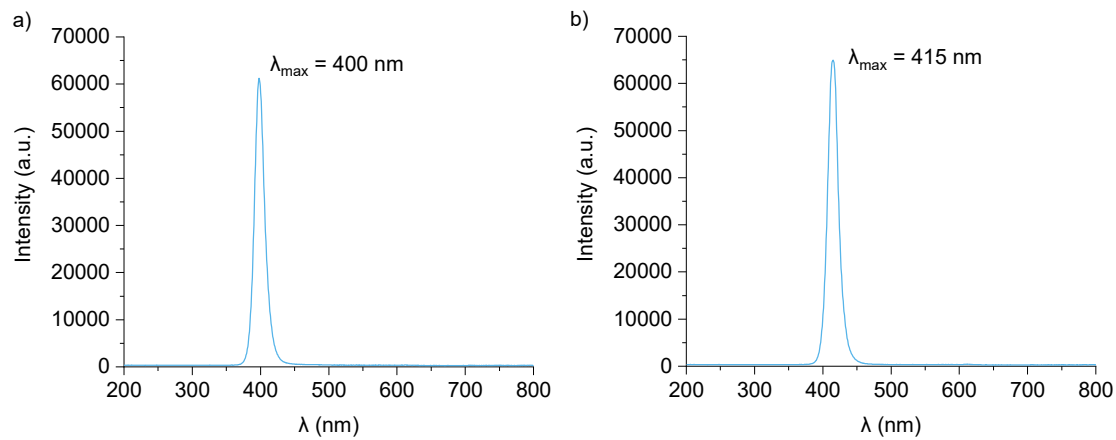


Figure S13 – Emission spectra of the light sources used in the photocatalytic experiments in this work. a) 400 nm LED module used for photocatalytic experiments; b) 415 nm LED module used for in-situ EPR experiments

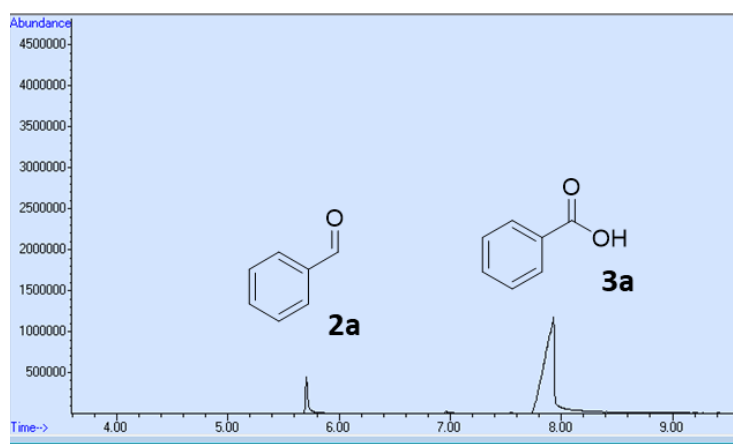


Figure 14 – Typical GC-MS chromatogram of photocatalytic oxidation of benzyl alcohol during screening of the reaction conditions (Table S1)

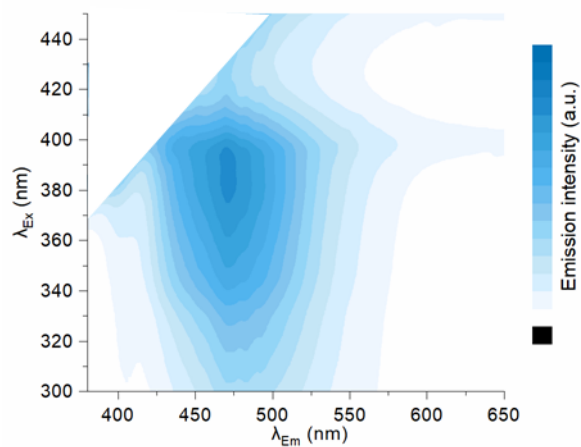
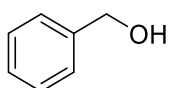


Figure 15 – Contour plot of photoexcitation wavelength versus emission spectra of CN thin films.

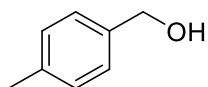
^1H NMR and ^{13}C NMR



phenylmethanol (1a)

^1H NMR (400 MHz, CD_3CN) δ 6.09 (d, $J = 4.4$ Hz, 4H), 6.01 (q, $J = 4.4$ Hz, 1H), 3.32 (d, $J = 5.9$ Hz, 2H).

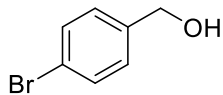
^{13}C NMR (101 MHz, CD_3CN) δ 143.08, 129.21, 127.92, 127.62, 64.66.



p-tolylmethanol (1b)

^1H NMR (400 MHz, CD_3CN) δ 7.21 (d, $J = 7.9$ Hz, 2H), 7.15 (d, $J = 7.9$ Hz, 2H), 4.51 (d, $J = 5.8$ Hz, 2H), 2.31 (s, 3H).

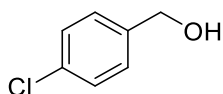
^{13}C NMR (101 MHz, CD_3CN) δ 140.06, 137.58, 129.79, 127.76, 64.55, 21.09.



(4-bromophenyl)methanol (1c)

^1H NMR (400 MHz, CD_3CN) δ 7.49 (d, J = 8.2 Hz, 2H), 7.26 (d, J = 8.1 Hz, 2H), 4.53 (d, J = 5.8 Hz, 2H).

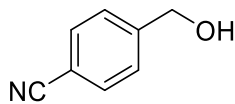
^{13}C NMR (101 MHz, CD_3CN) δ 142.46, 132.12, 129.54, 121.03, 63.84.



(4-chlorophenyl)methanol (1d)

^1H NMR (400 MHz, CD_3CN) δ 7.39 – 7.28 (m, 4H), 4.55 (d, J = 5.9 Hz, 2H).

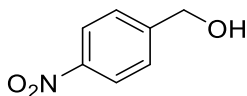
^{13}C NMR (101 MHz, CD_3CN) δ 142.02, 132.97, 129.23, 129.16, 63.83.



4-(hydroxymethyl)benzonitrile (1e)

^1H NMR (400 MHz, CD_3CN) δ 7.73 – 7.65 (m, 2H), 7.49 (dq, J = 7.4, 0.8 Hz, 2H), 4.64 (s, 2H).

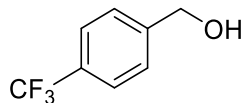
^{13}C NMR (101 MHz, CD_3CN) δ 148.83, 133.12, 127.88, 119.87, 111.19, 63.79.



(4-nitrophenyl)methanol (1f)

^1H NMR (400 MHz, CD_3CN) δ 8.22 – 8.14 (m, 2H), 7.59 – 7.50 (m, 2H), 4.70 (d, J = 5.8 Hz, 2H).

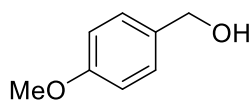
^{13}C NMR (101 MHz, CD_3CN) δ 150.97, 147.96, 127.91, 124.34, 63.58.



(4-(trifluoromethyl)phenyl)methanol (1g)

^1H NMR (400 MHz, CD_3CN) δ 7.65 (d, J = 8.1 Hz, 2H), 7.55 – 7.47 (m, 2H), 4.66 (d, J = 4.7 Hz, 2H).

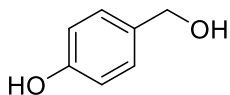
^{13}C NMR (101 MHz, CD_3CN) δ 147.81, 127.80, 126.91, 126.04 (q, J = 3.9 Hz), 124.22, 63.87.



(4-methoxyphenyl)methanol (1h)

^1H NMR (400 MHz, CD_3CN) δ 7.30 – 7.22 (m, 2H), 6.93 – 6.85 (m, 2H), 4.49 (d, J = 5.7 Hz, 2H), 3.77 (s, 3H).

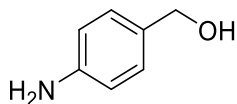
^{13}C NMR (101 MHz, CD_3CN) δ 46.57, 21.84, 16.09, 1.32, -48.81, -57.41.



4-(hydroxymethyl)phenol (1i)

^1H NMR (400 MHz, CD_3CN) δ 7.20 – 7.12 (m, 2H), 6.80 – 6.72 (m, 2H), 4.45 (s, 2H).

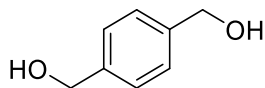
^{13}C NMR (101 MHz, CD_3CN) δ 157.00, 134.27, 129.45, 115.86, 64.48.



1,4-phenylenedimethanol (1j)

^1H NMR (400 MHz, CD_3CN) δ 7.09 – 7.01 (m, 2H), 6.64 – 6.56 (m, 2H), 4.38 (s, 2H).

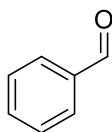
^{13}C NMR (101 MHz, CD_3CN) δ 148.14, 131.65, 129.34, 115.15, 64.83.



(4-aminophenyl)methanol (1k)

^1H NMR (400 MHz, CD_3CN) δ 7.30 (s, 4H), 4.55 (d, J = 5.9 Hz, 4H).

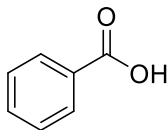
^{13}C NMR (101 MHz, CD_3CN) δ 141.85, 127.66, 64.53.



benzaldehyde (2a)

^1H NMR (400 MHz, CD_3CN) δ 10.00 (s, 1H), 7.89 (dd, J = 7.8, 1.6 Hz, 2H), 7.74 – 7.65 (m, 1H), 7.57 (t, J = 7.6 Hz, 2H).

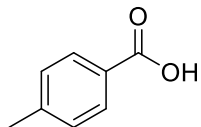
^{13}C NMR (101 MHz, CD_3CN) δ 193.70, 137.54, 135.39, 130.40, 130.05.



benzoic acid (3a)

^1H NMR (400 MHz, CD_3CN) δ 8.01 (dd, J = 7.7, 1.6 Hz, 2H), 7.63 (t, J = 7.4 Hz, 1H), 7.49 (t, J = 7.8 Hz, 2H).

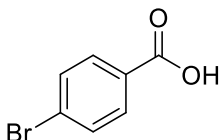
^{13}C NMR (101 MHz, CD_3CN) δ 168.12, 134.18, 130.86, 130.54, 129.52.



4-methylbenzoic acid (3b)

$^1\text{H NMR}$ (400 MHz, CD_3CN) δ 7.89 (d, $J = 8.0$ Hz, 2H), 7.30 (d, $J = 7.8$ Hz, 2H), 2.40 (s, 3H).

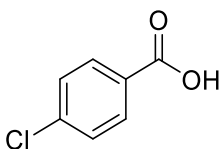
$^{13}\text{C NMR}$ (101 MHz, CD_3CN) δ 168.10, 145.09, 130.62, 130.13, 128.09, 21.62.



4-bromobenzoic acid (3c)

$^1\text{H NMR}$ (400 MHz, CD_3CN) δ 7.92 – 7.86 (m, 2H), 7.69 – 7.63 (m, 2H).

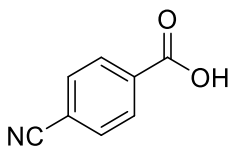
$^{13}\text{C NMR}$ (101 MHz, CD_3CN) δ 166.99, 132.74, 132.35, 130.15, 128.47.



4-chlorobenzoic acid (3d)

$^1\text{H NMR}$ (400 MHz, CD_3CN) δ 7.97 (d, $J = 8.5$ Hz, 2H), 7.50 (d, $J = 8.5$ Hz, 2H).

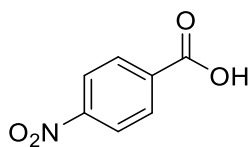
$^{13}\text{C NMR}$ (101 MHz, CD_3CN) δ 166.86, 139.82, 132.24, 129.74, 129.71.



4-cyanobenzoic acid (3e)

$^1\text{H NMR}$ (400 MHz, CD_3CN) δ 8.15 – 8.07 (m, 2H), 7.88 – 7.80 (m, 2H).

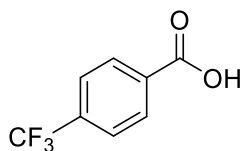
$^{13}\text{C NMR}$ (101 MHz, CD_3CN) δ 166.36, 134.94, 133.50, 131.08, 118.97, 117.06.



4-nitrobenzoic acid (3f)

$^1\text{H NMR}$ (400 MHz, CD_3CN) δ 8.32 – 8.24 (m, 2H), 8.22 – 8.14 (m, 2H).

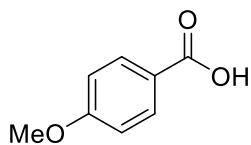
$^{13}\text{C NMR}$ (101 MHz, CD_3CN) δ 166.09, 151.71, 136.51, 131.80, 124.58.



4-(trifluoromethyl)benzoic acid (3g)

$^1\text{H NMR}$ (400 MHz, CD_3CN) δ 8.16 (ddt, $J = 7.6, 1.7, 0.9$ Hz, 2H), 7.82 – 7.79 (m, 2H).

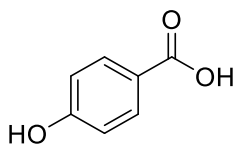
$^{13}\text{C NMR}$ (101 MHz, CD_3CN) δ 166.62, 134.72 (d, $J = 7.0$ Hz), 131.23, 126.49 (q, $J = 3.9$ Hz), 126.27, 123.57.



4-methoxybenzoic acid (3h)

$^1\text{H NMR}$ (400 MHz, CD_3CN) δ 8.11 – 7.82 (m, 2H), 7.17 – 6.90 (m, 2H), 3.85 (s, 3H).

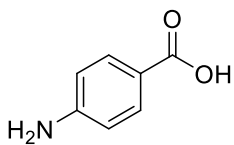
$^{13}\text{C NMR}$ (101 MHz, CD_3CN) δ 167.67, 164.58, 132.66, 123.11, 114.71, 56.24.



4-hydroxybenzoic acid (3i)

$^1\text{H NMR}$ (400 MHz, CD_3CN) δ 7.92 – 7.84 (m, 2H), 6.91 – 6.83 (m, 2H).

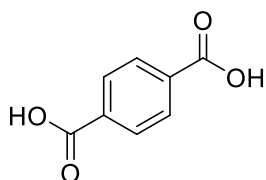
^{13}C NMR (101 MHz, CD_3CN) δ 168.16, 162.38, 132.94, 122.35, 116.08.



terephthalic acid (3j)

^1H NMR (400 MHz, CD_3CN) δ 7.77 – 7.70 (m, 2H), 6.67 – 6.60 (m, 2H).

^{13}C NMR (101 MHz, CD_3CN) δ 168.53, 153.90, 132.64, 114.06.



4-aminobenzoic acid (3k)

^1H NMR (400 MHz, DMSO) δ 13.31 (s, 4H), 8.04 (s, 2H).

^{13}C NMR (101 MHz, DMSO) δ 157.10, 124.84, 119.88.

Crude ^1H NMR

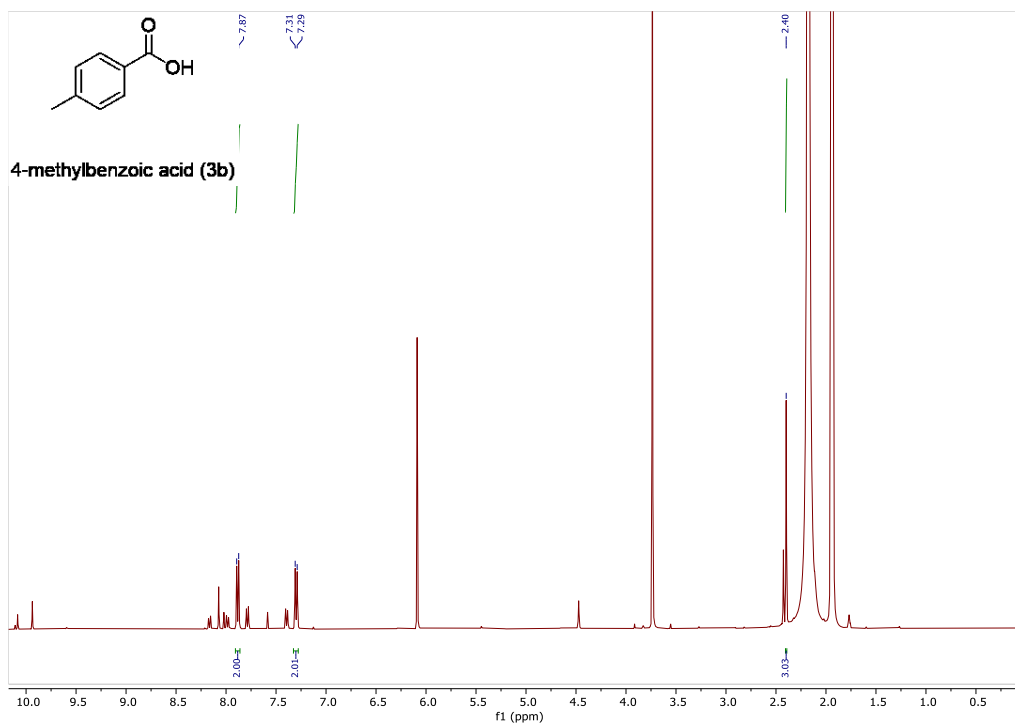


Figure S17 – Crude ¹H NMR spectrum of **3b**

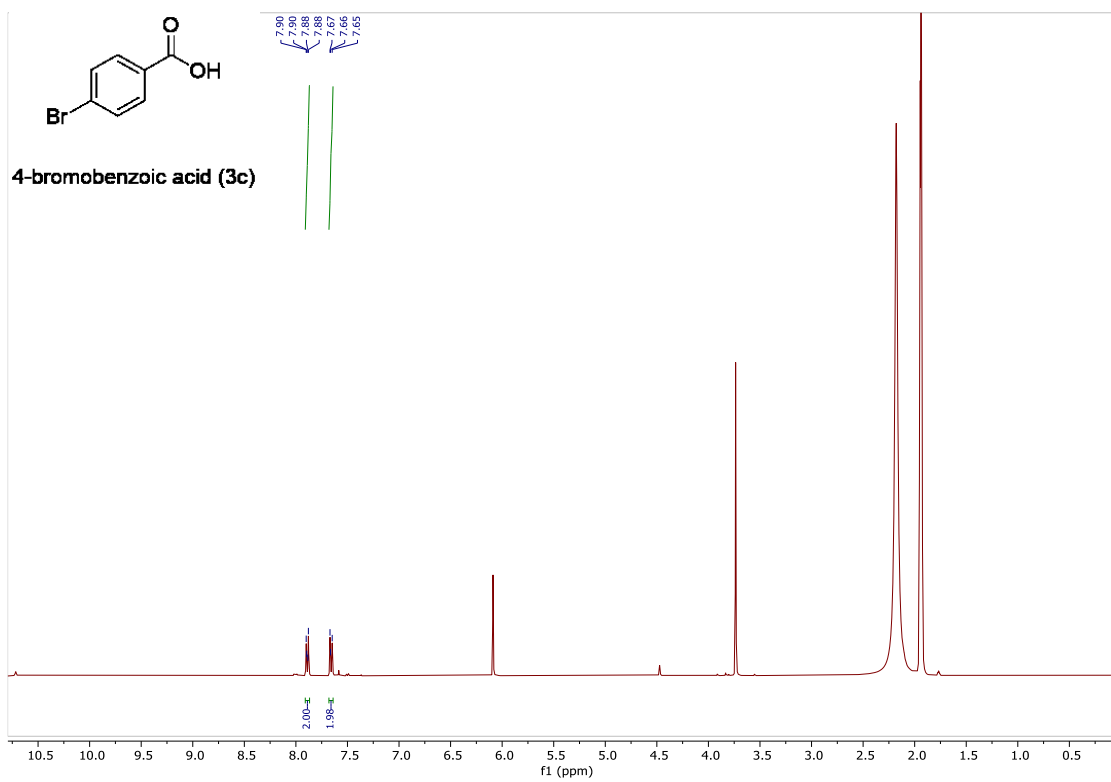


Figure S18 – Crude ¹H NMR spectrum of **3c**

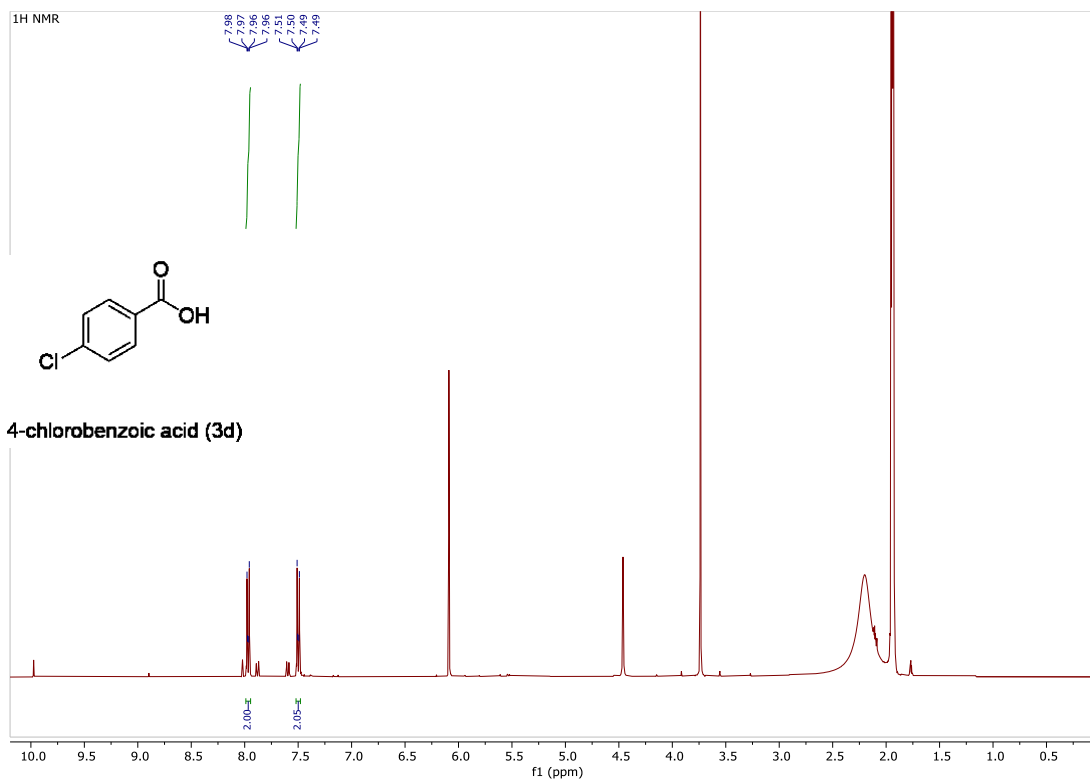


Figure S19 – Crude ^1H NMR spectrum of **3d**

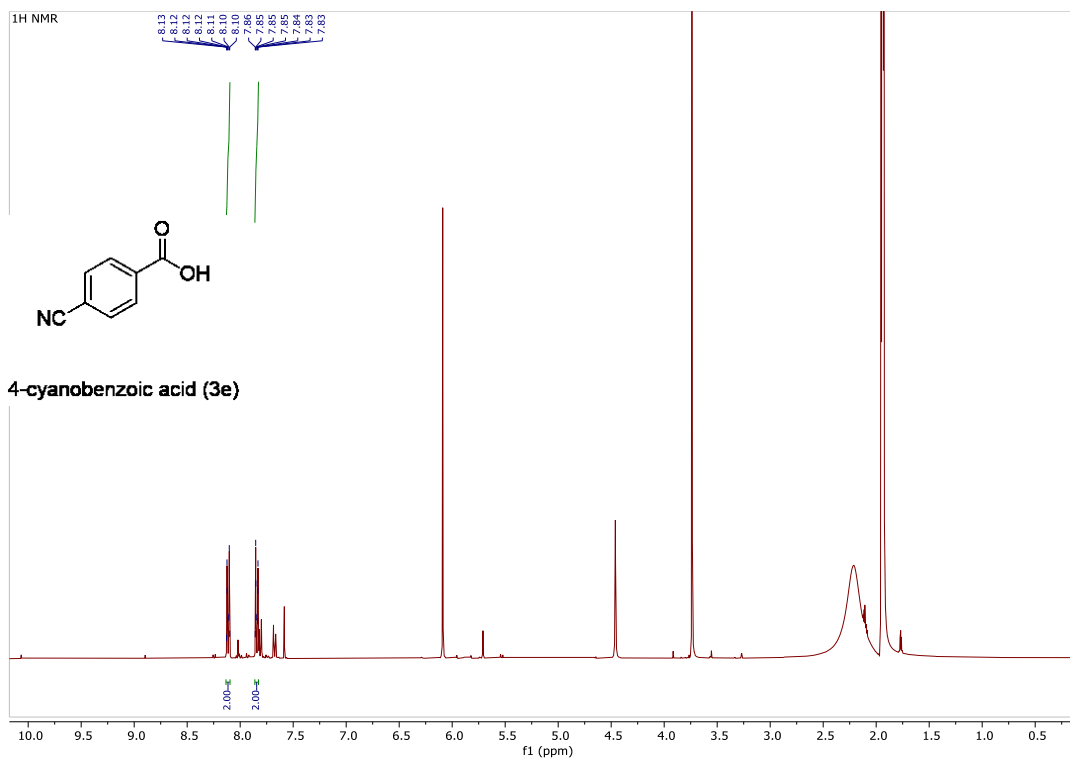


Figure S20 – Crude ¹H NMR spectrum of **3e**

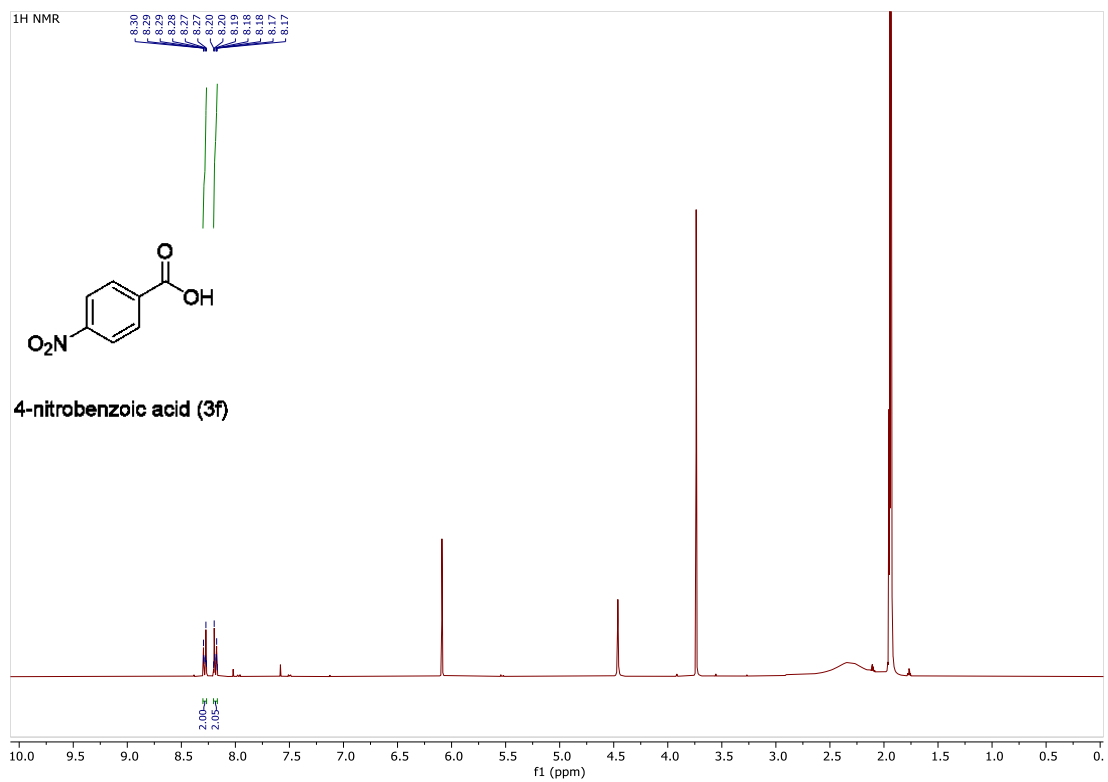


Figure S21 – Crude ¹H NMR spectrum of **3f**

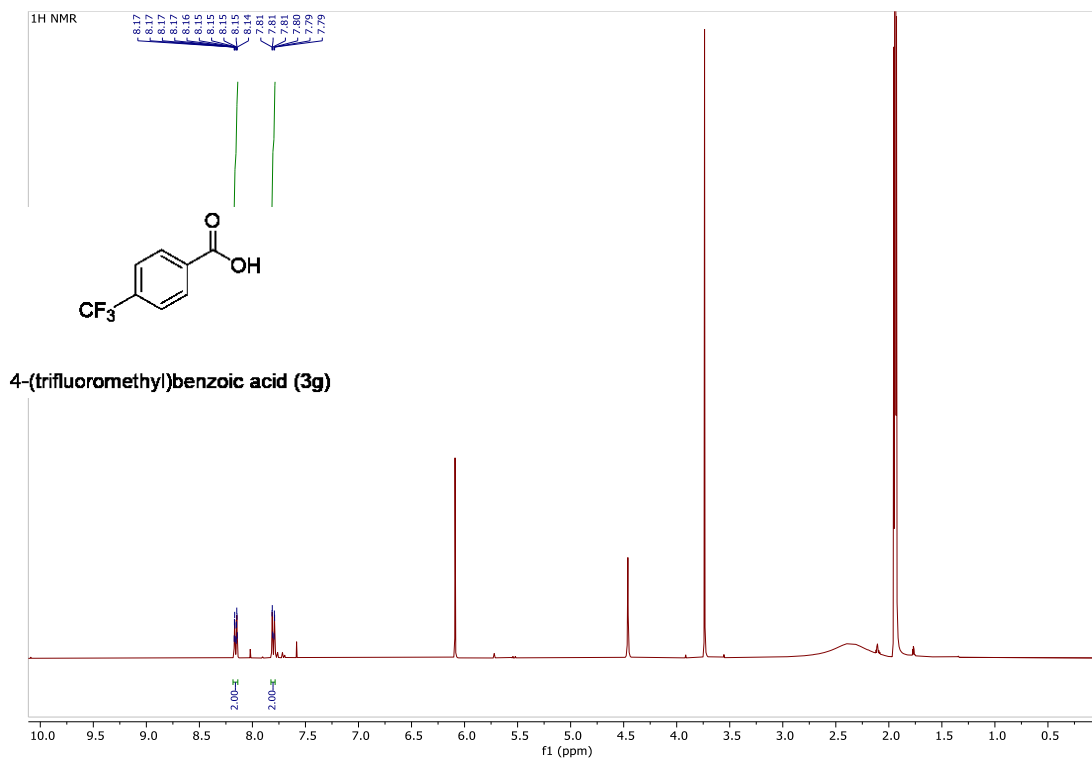


Figure S22 – Crude ^1H NMR spectrum of **3g**

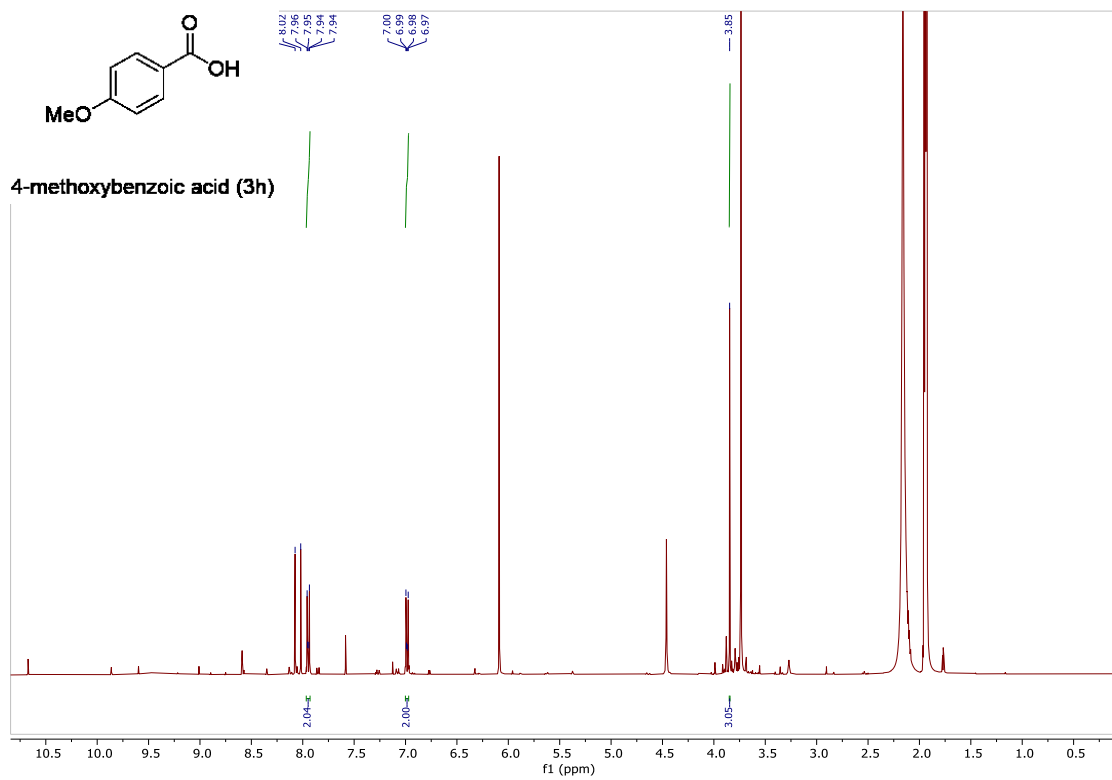


Figure S23 – Crude ^1H NMR spectrum of **3h**

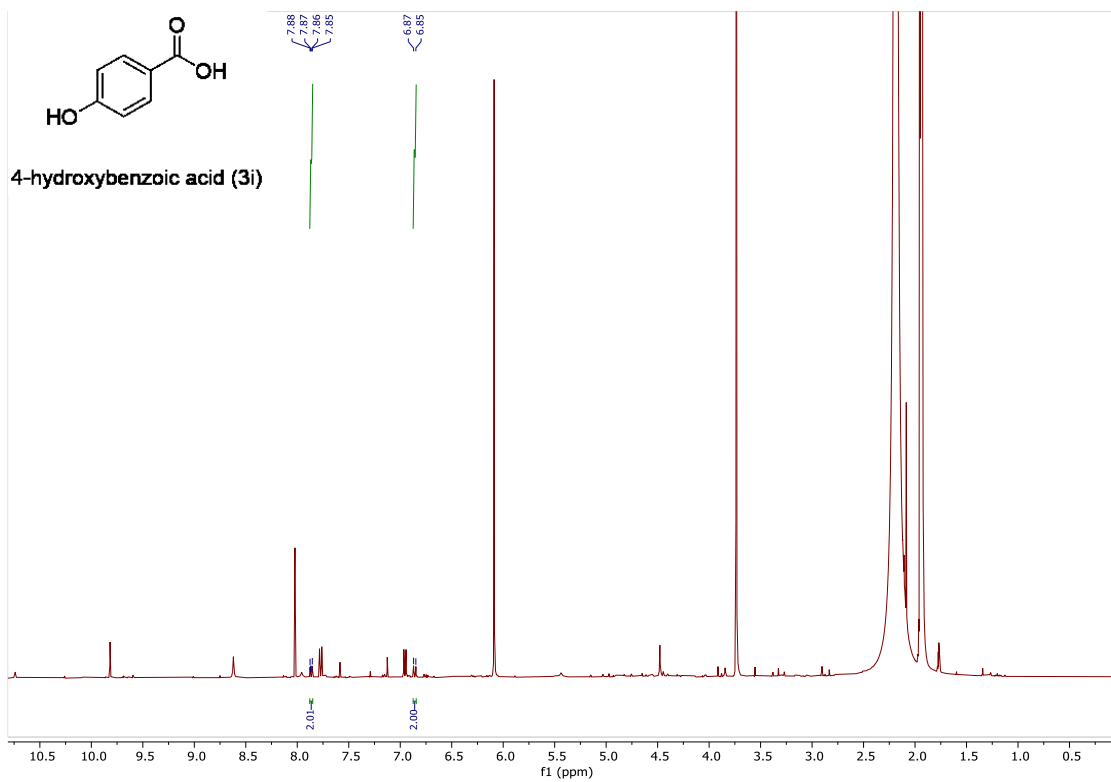


Figure S24 – Crude ¹H NMR spectrum of **3i**

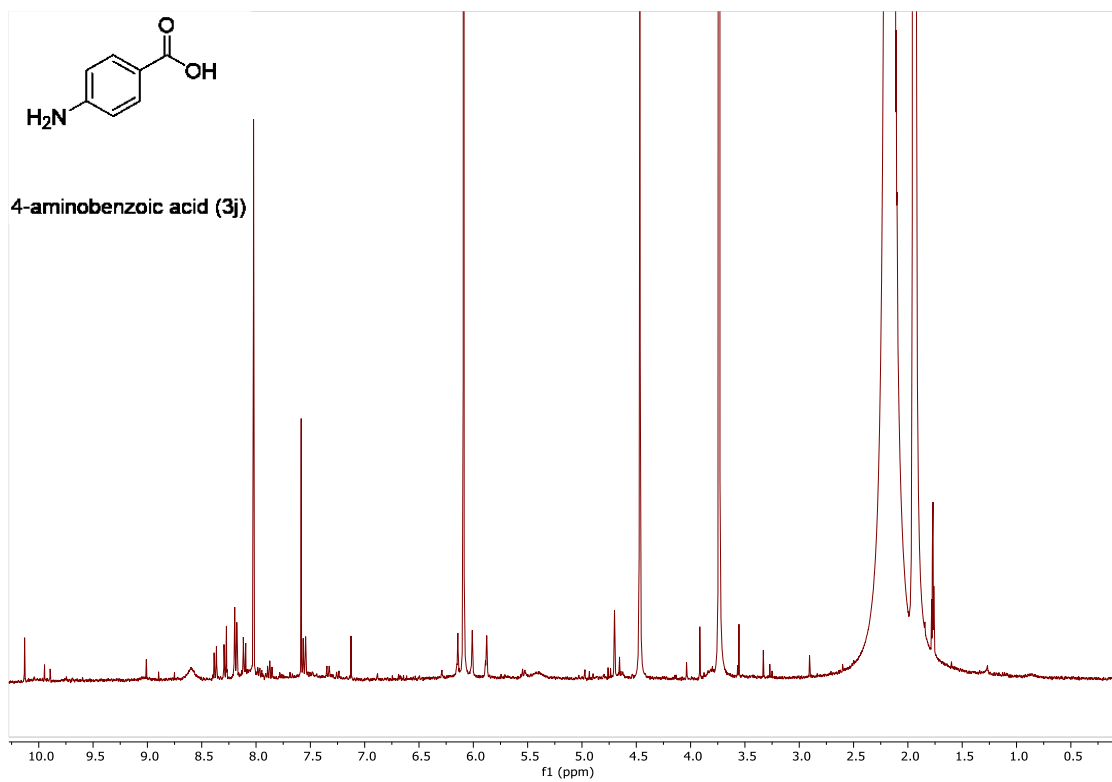


Figure S25 – Crude ¹H NMR spectrum of **3j**

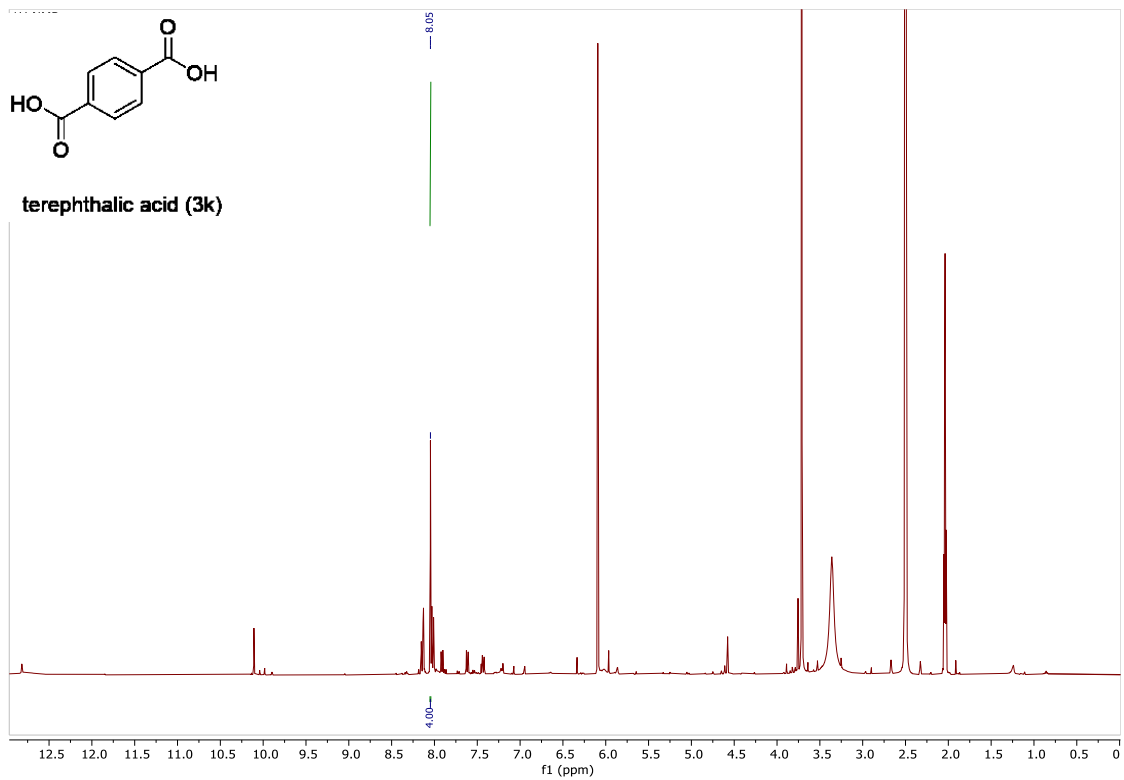


Figure S26 – Crude ^1H NMR spectrum of **3k**

^1H NMR and ^{13}C NMR of pure compounds

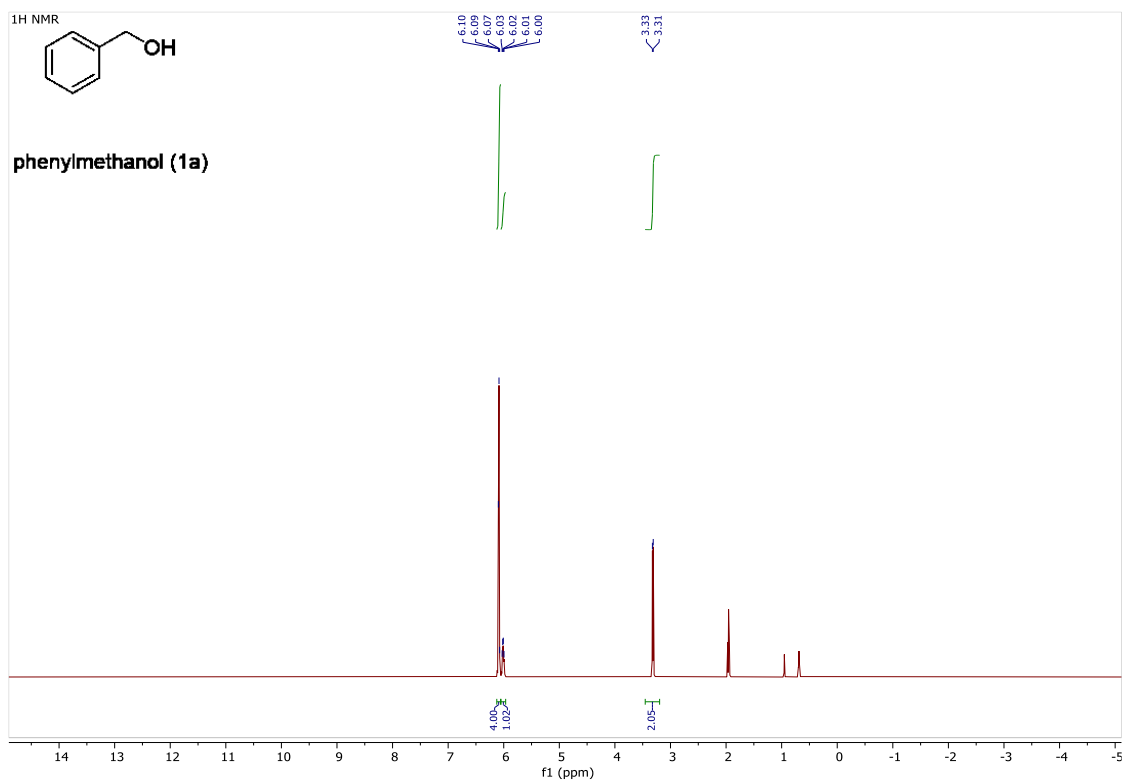


Figure S27 – ^1H NMR spectrum of **1a**

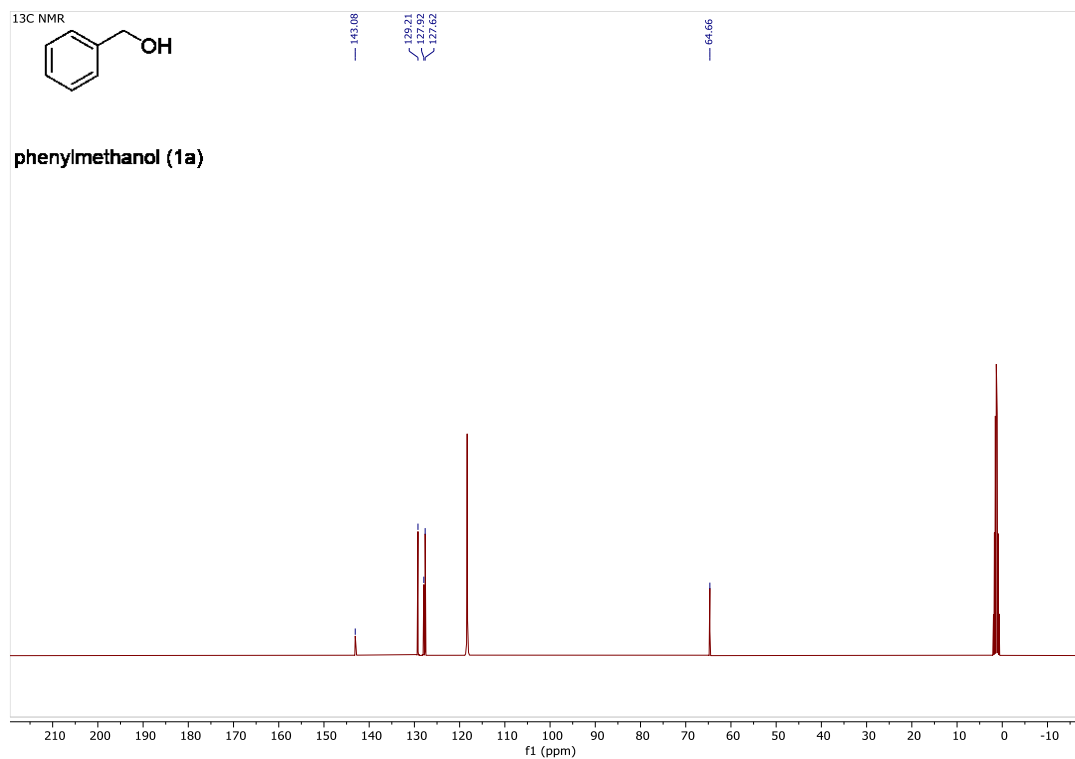


Figure S28 – ¹³C NMR spectrum of **1a**

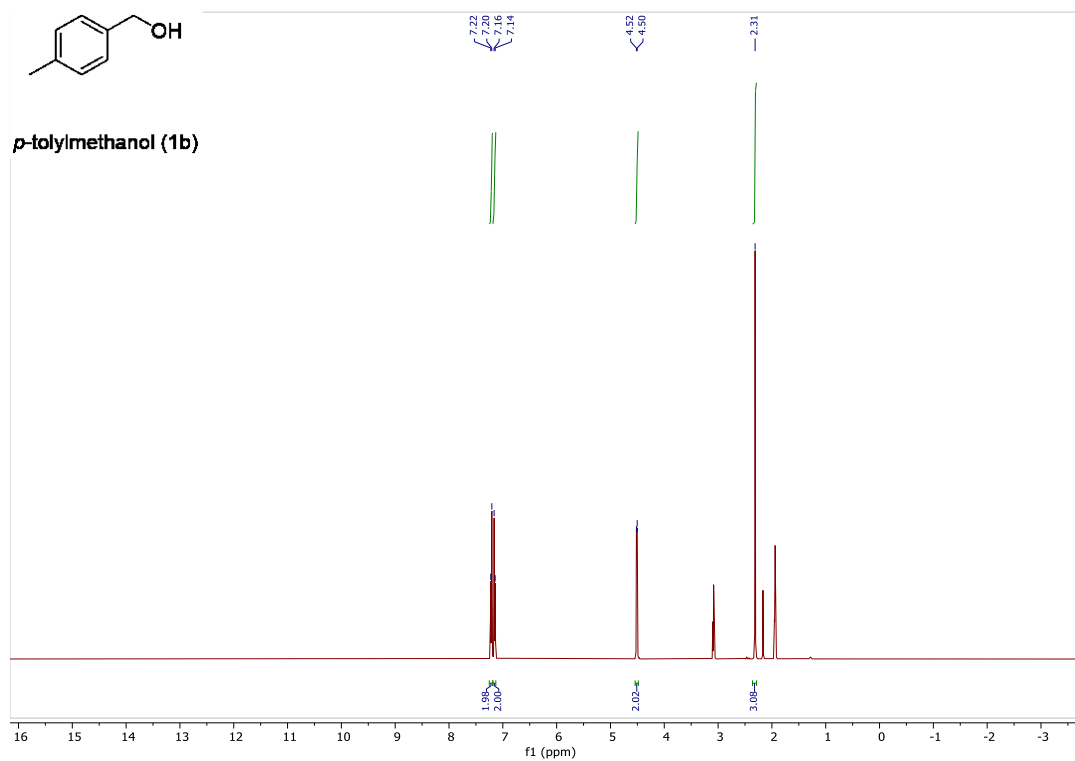


Figure S29 – ¹H NMR spectrum of **1b**

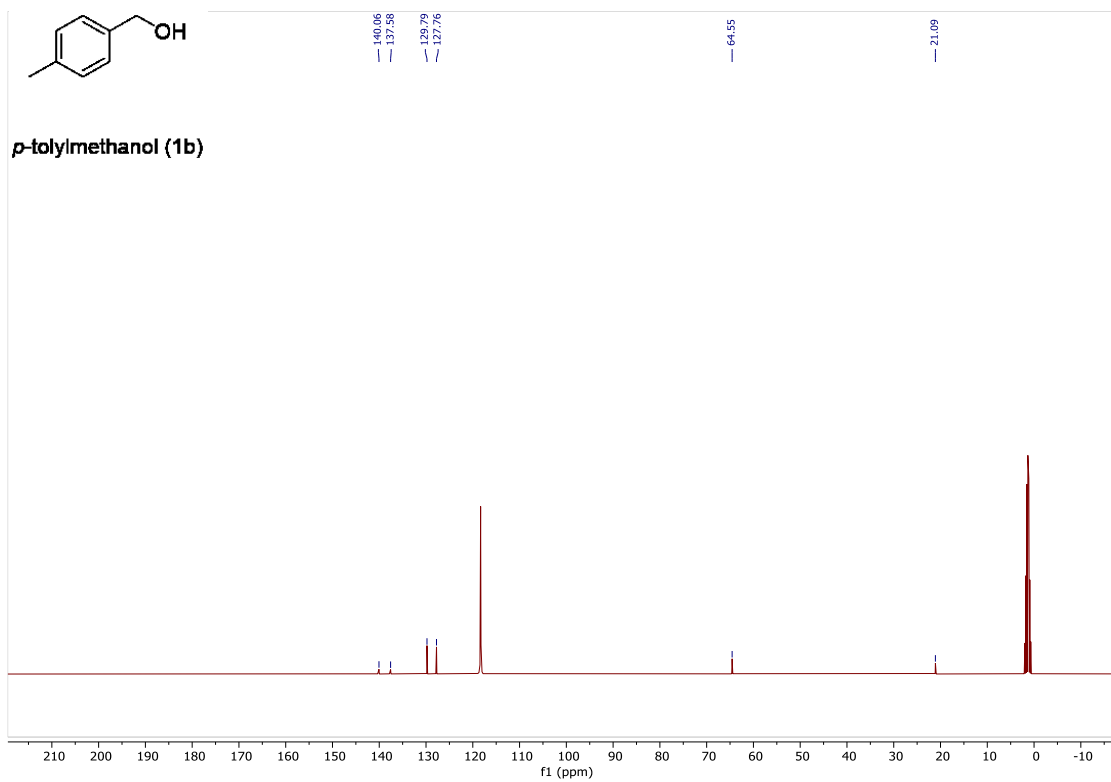


Figure S30 – ^{13}C NMR spectrum of **1b**

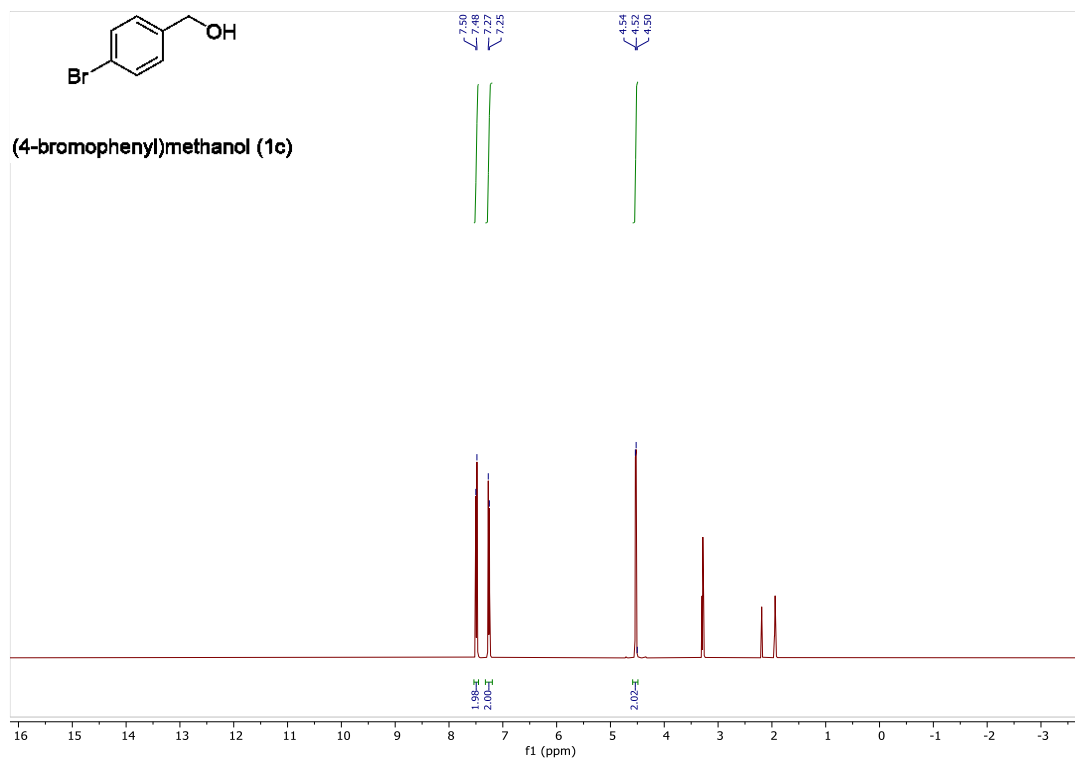


Figure S31 – ^1H NMR spectrum of **1c**

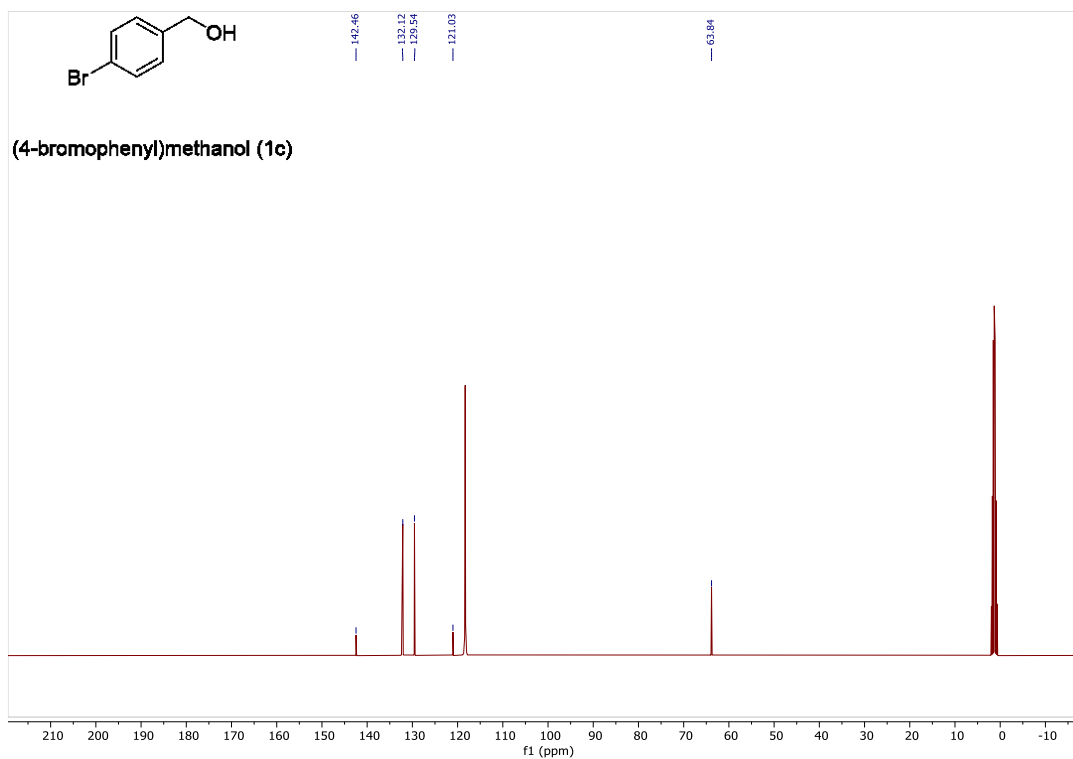


Figure S32 – ^{13}C NMR spectrum of **1c**

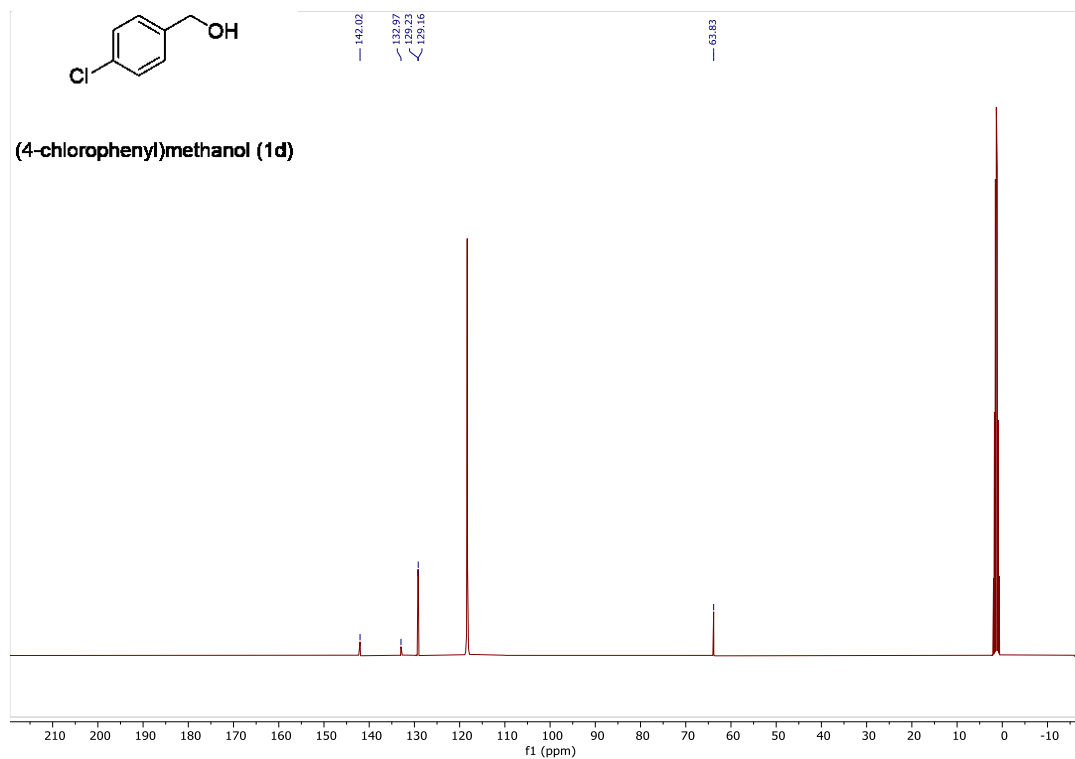


Figure S33 – ^1H NMR spectrum of **1d**

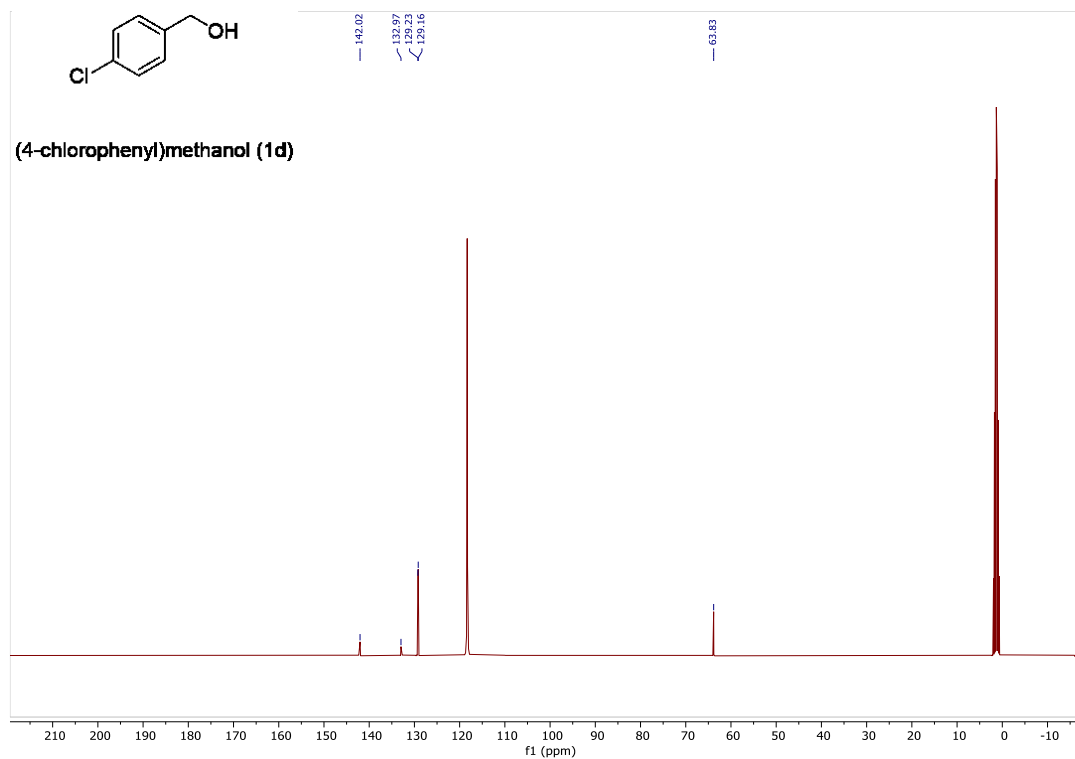


Figure S34 – ^{13}C NMR spectrum of **1d**

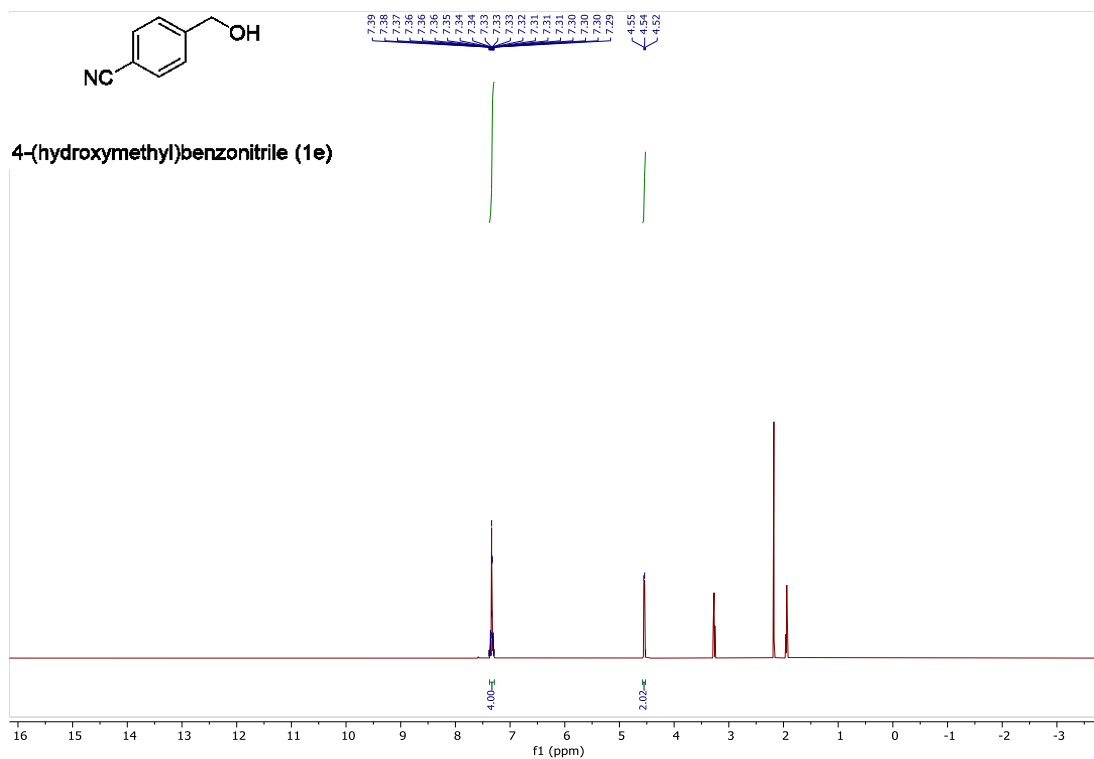


Figure S35 – ¹H NMR spectrum of **1e**

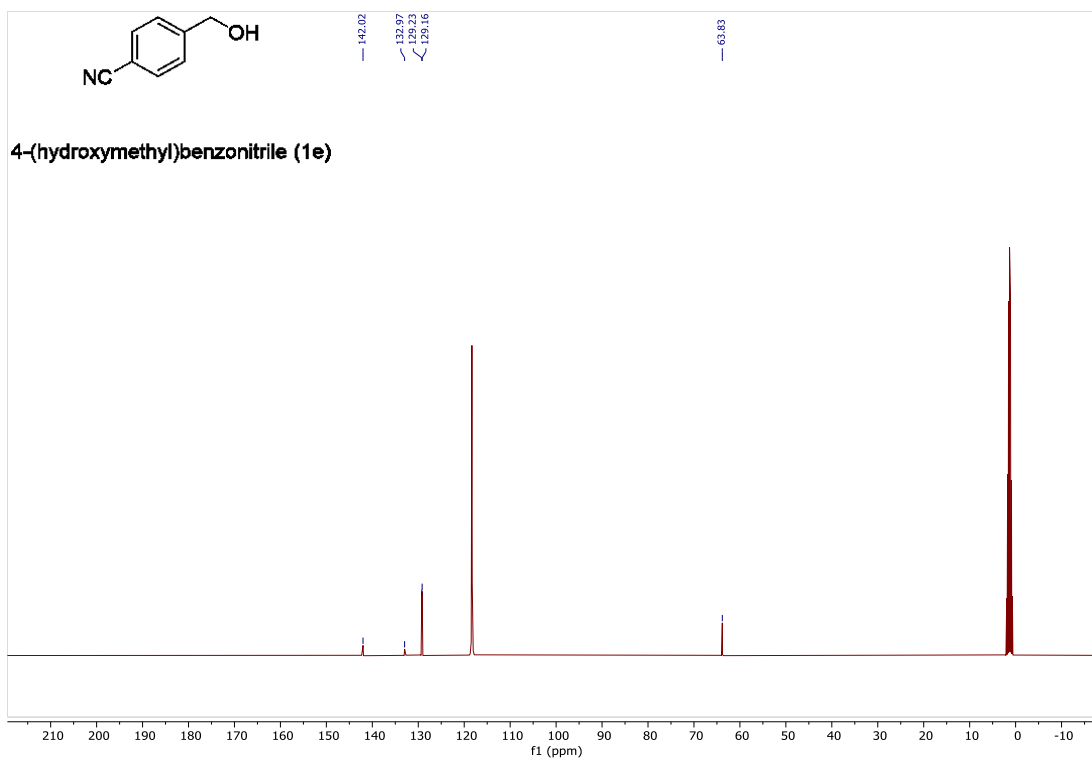


Figure S36 – ^{13}C NMR spectrum of **1e**

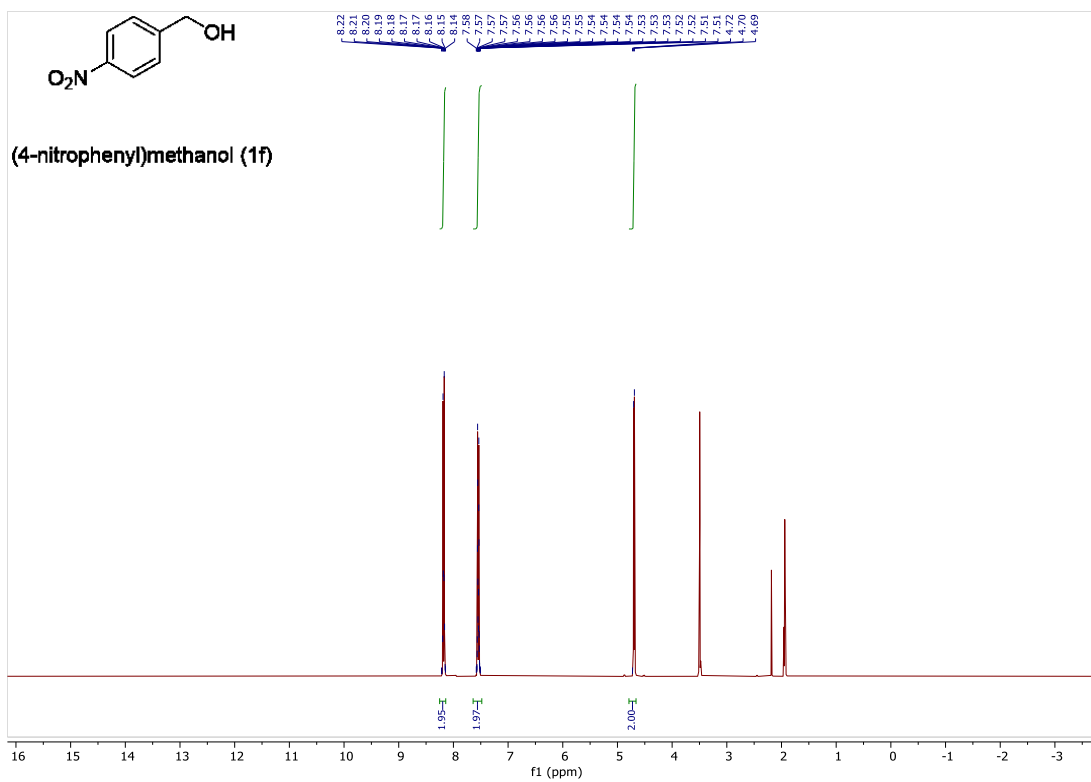


Figure S37 – ^1H NMR spectrum of **1f**

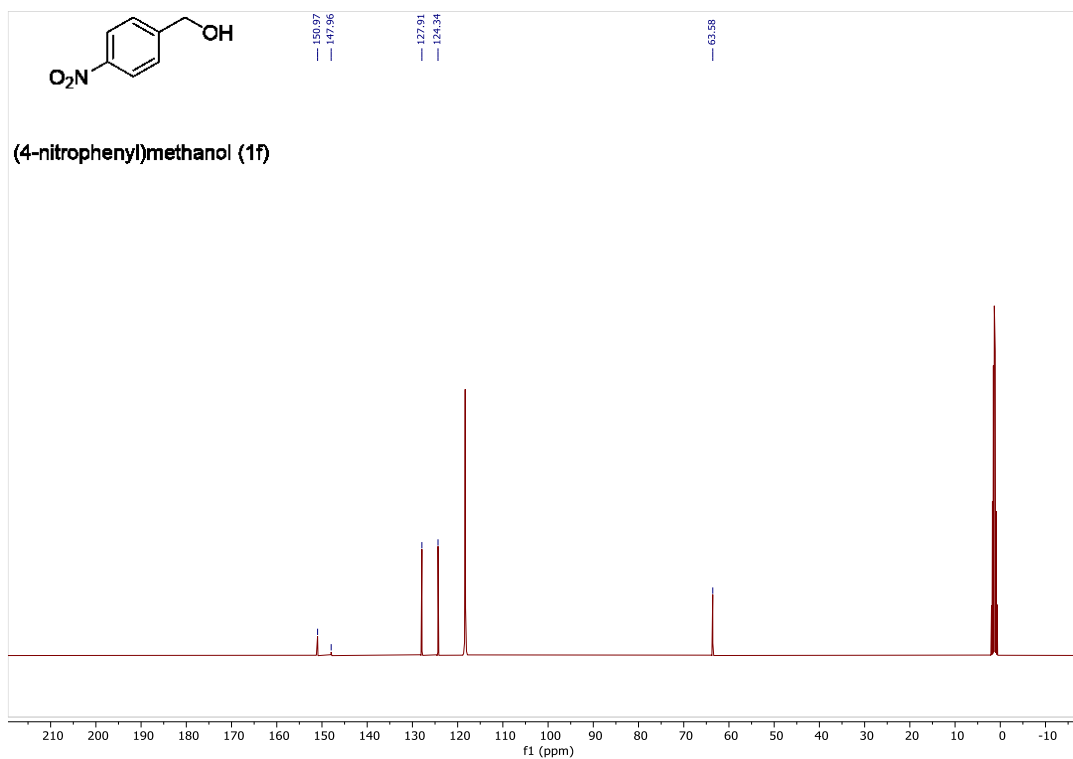


Figure S38 – ^{13}C NMR spectrum of **1f**

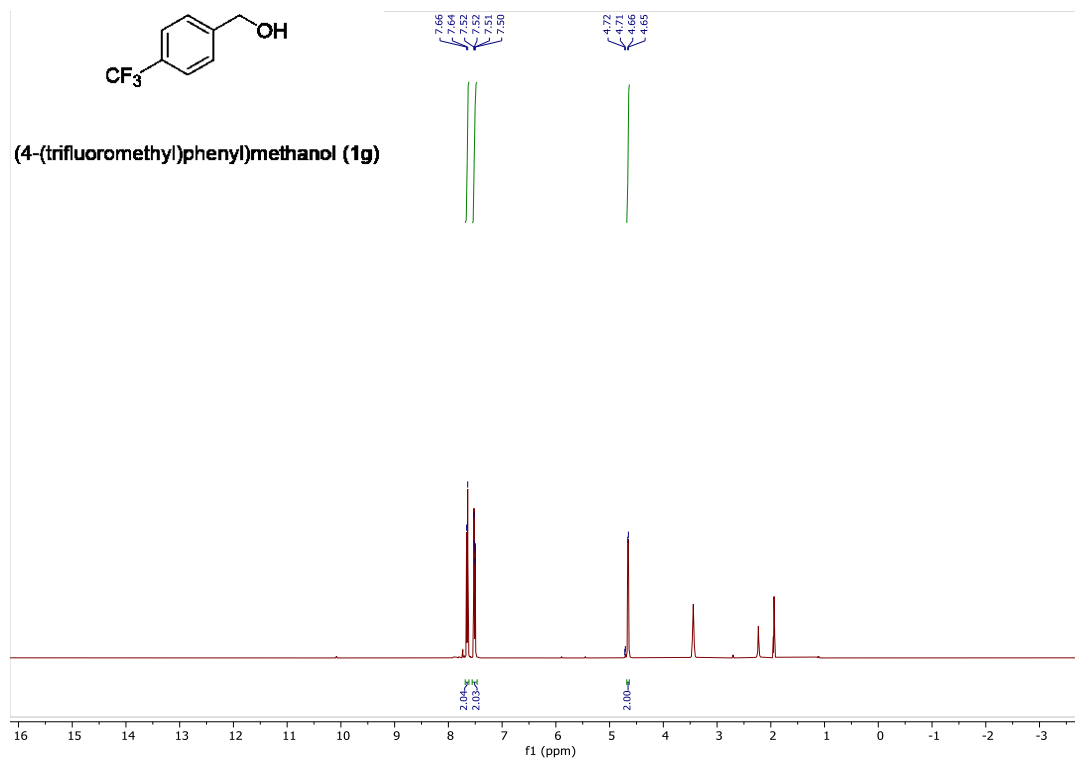


Figure S39 – ¹H NMR spectrum of **1g**

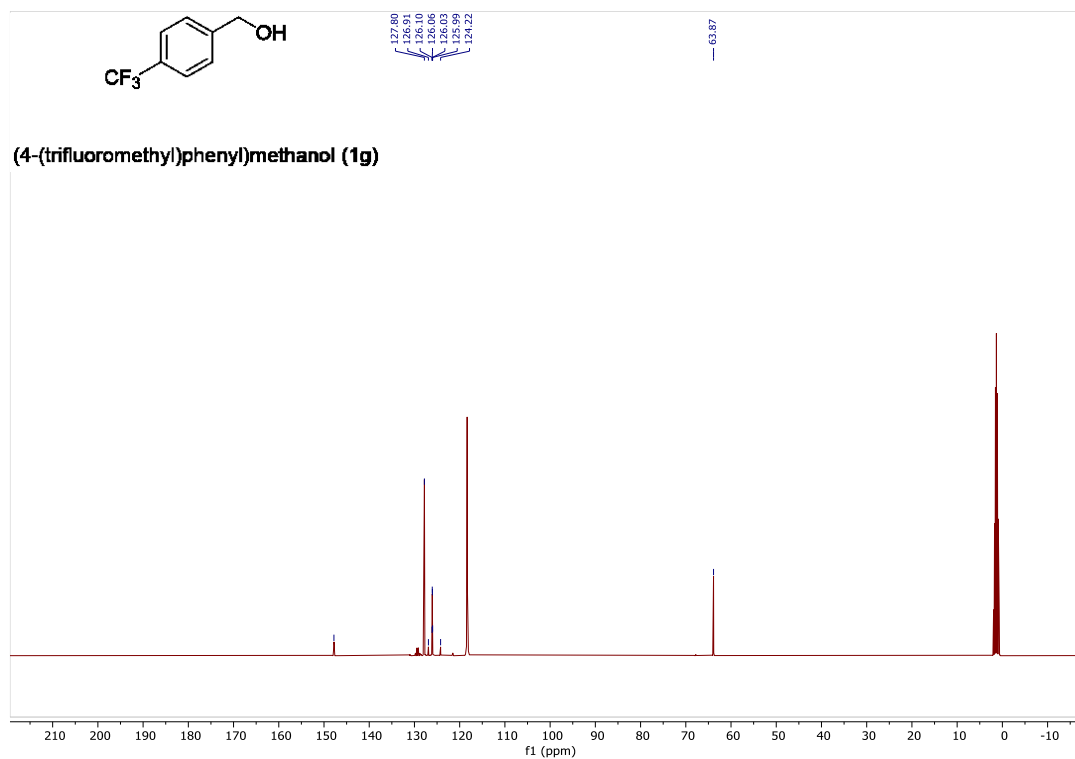


Figure S40 – ^{13}C NMR spectrum of **1g**

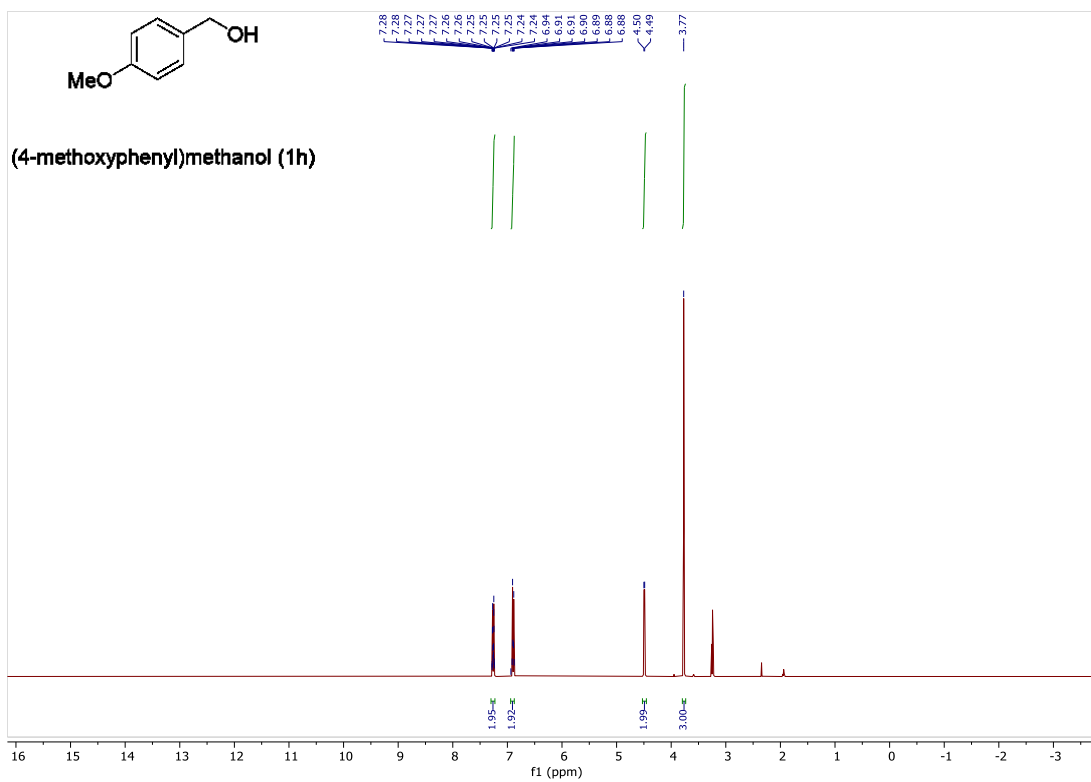


Figure S41 – ^1H NMR spectrum of **1h**

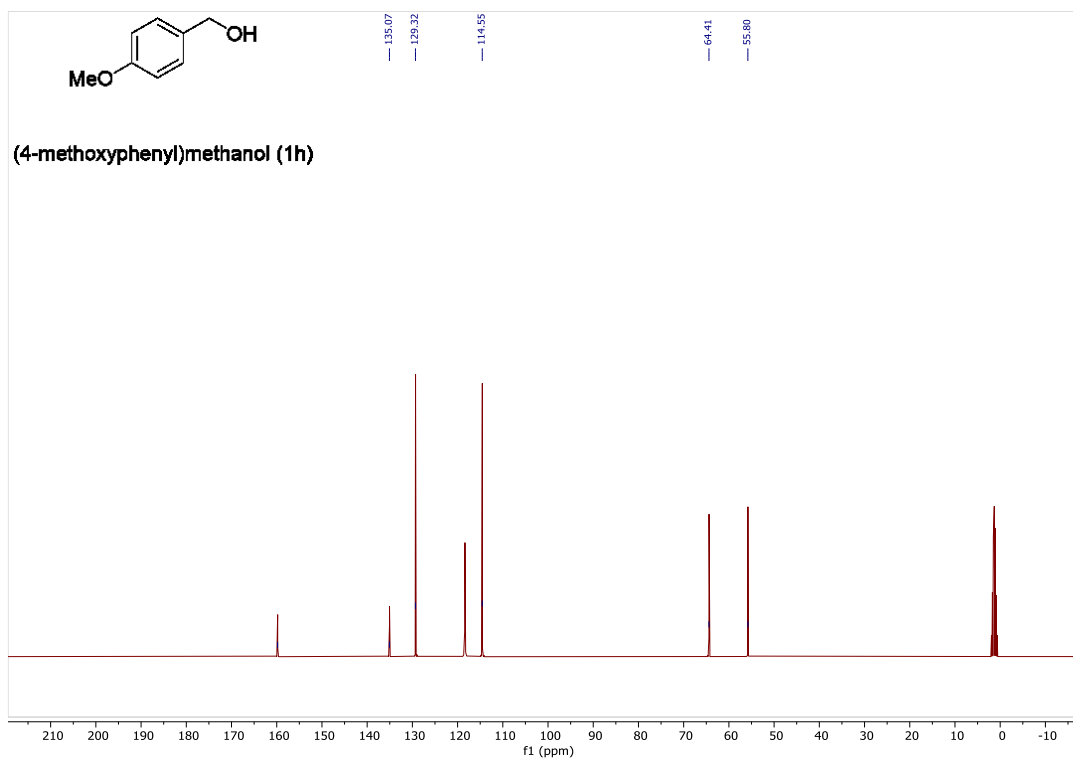


Figure S42 – ^{13}C NMR spectrum of **1h**

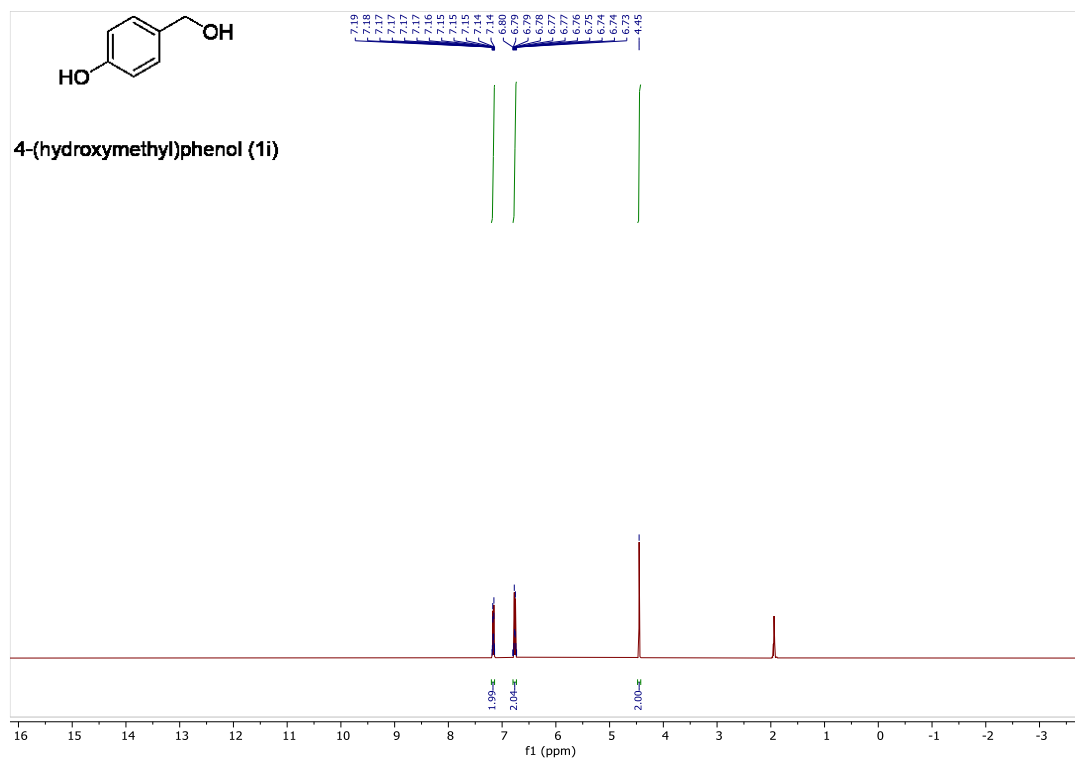


Figure S44 – ¹H NMR spectrum of **1i**

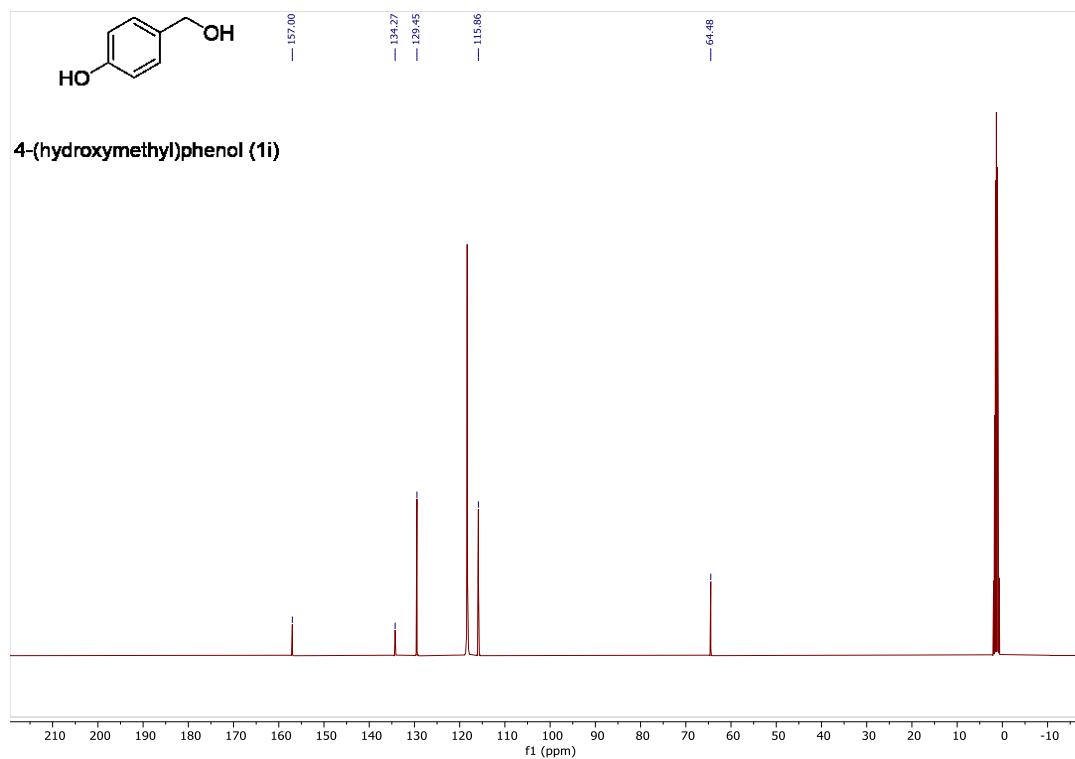


Figure S43 – ^{13}C NMR spectrum of **1i**

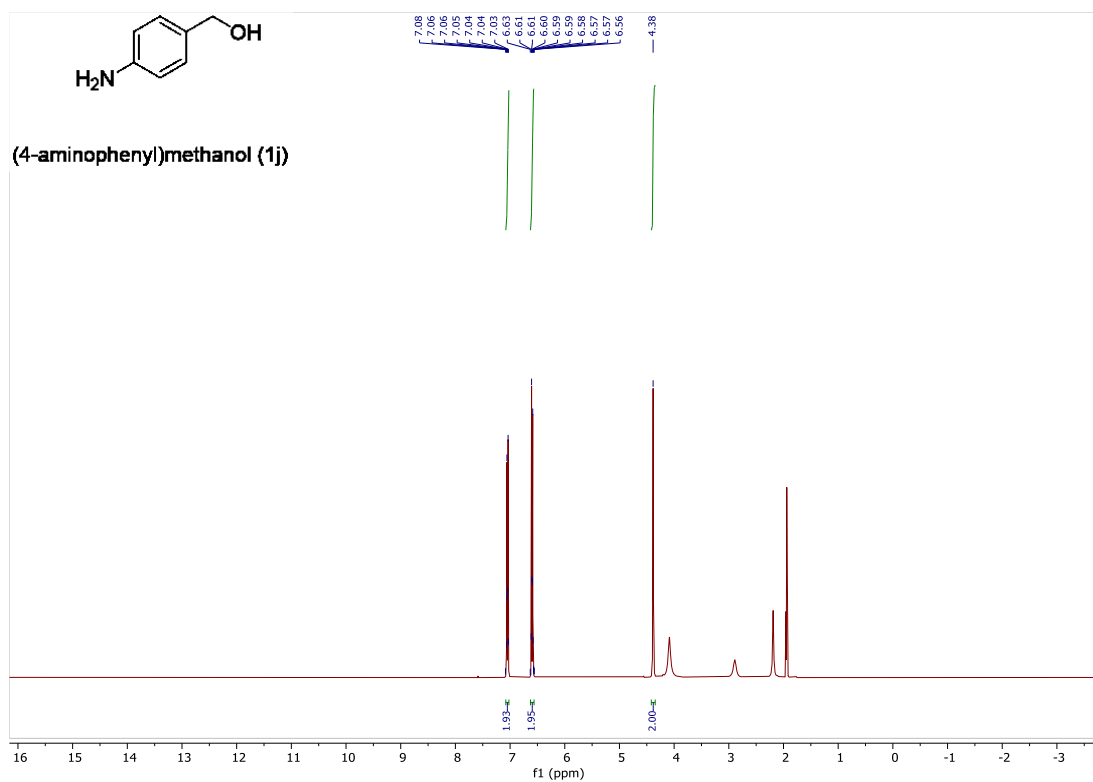


Figure S44 – ¹H NMR spectrum of **1j**

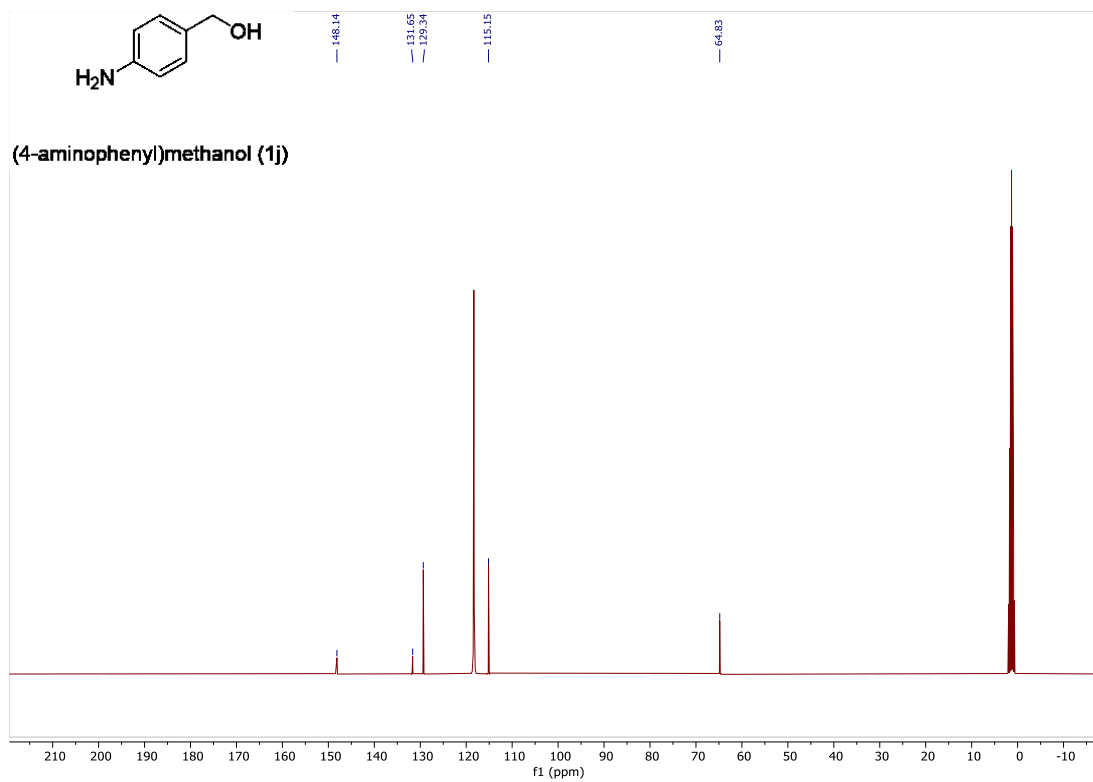


Figure S45 – ^{13}C NMR spectrum of **1j**

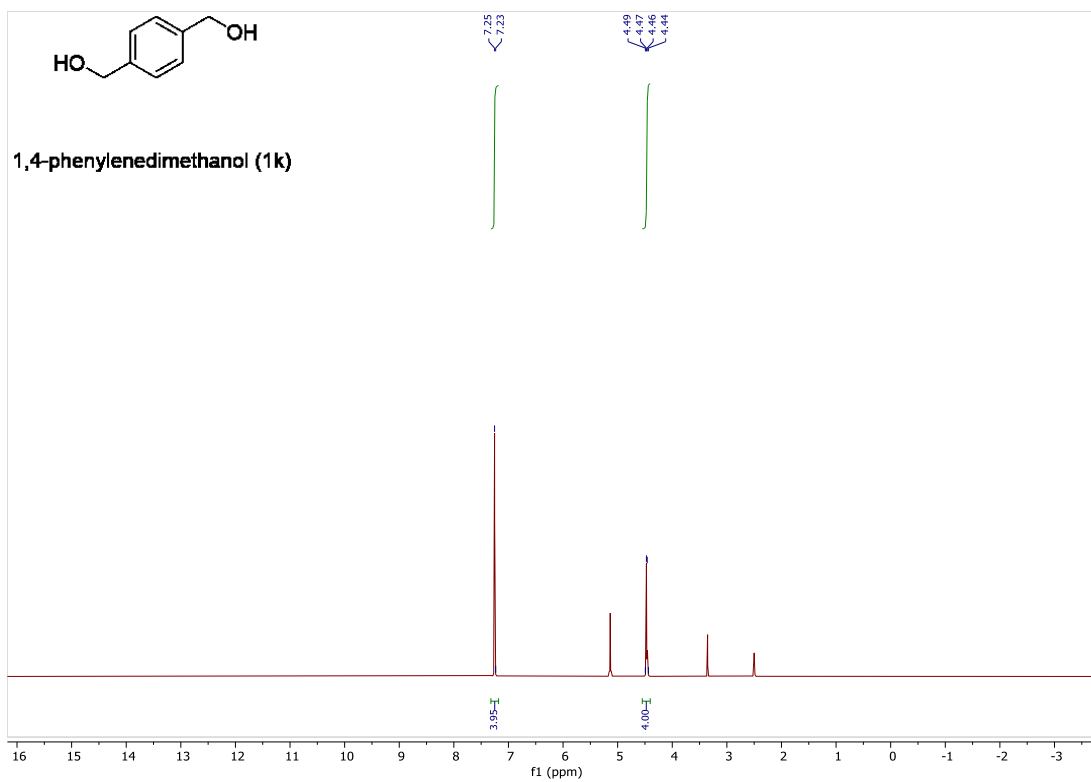


Figure S46 – ^1H NMR spectrum of **1k**

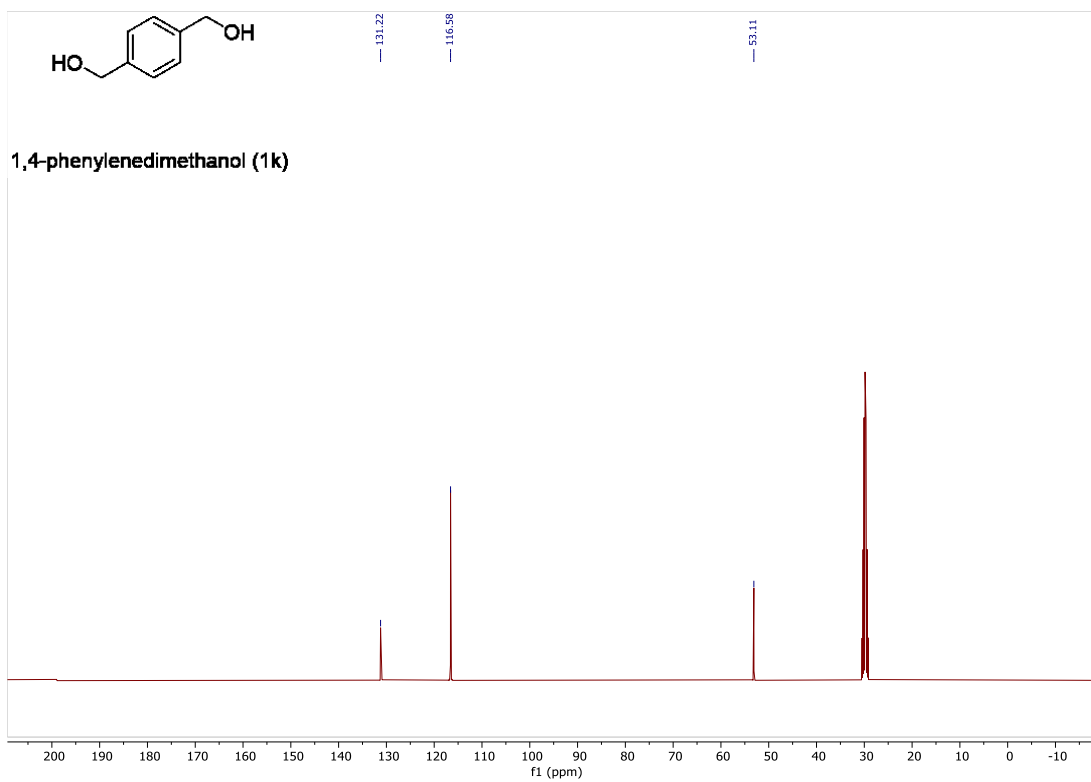


Figure S47 – ^{13}C NMR spectrum of **1k**

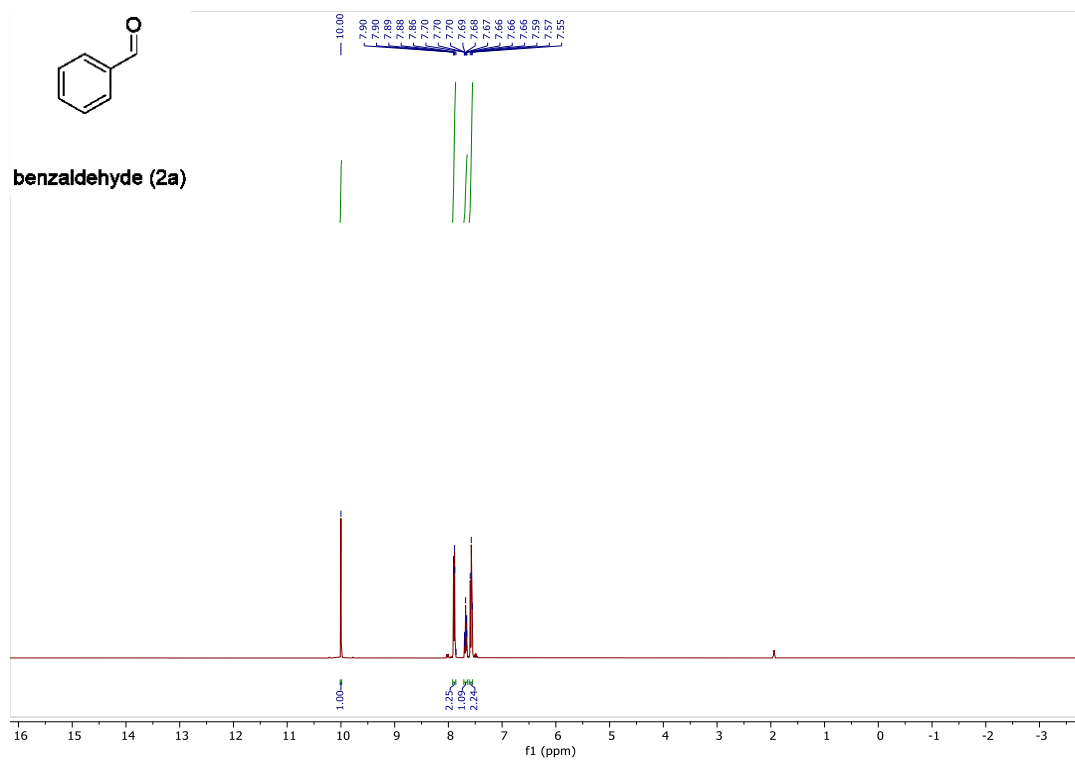


Figure S48 – ¹H NMR spectrum of **2a**

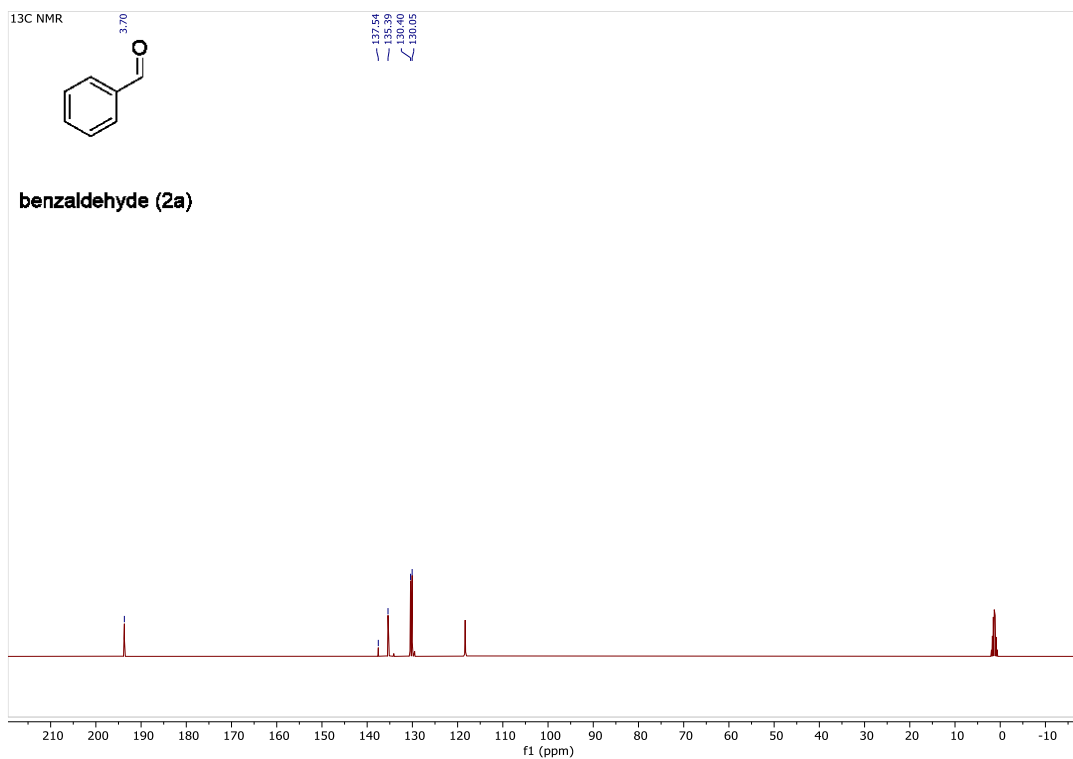


Figure S49 – ¹³C NMR spectrum of **2a**

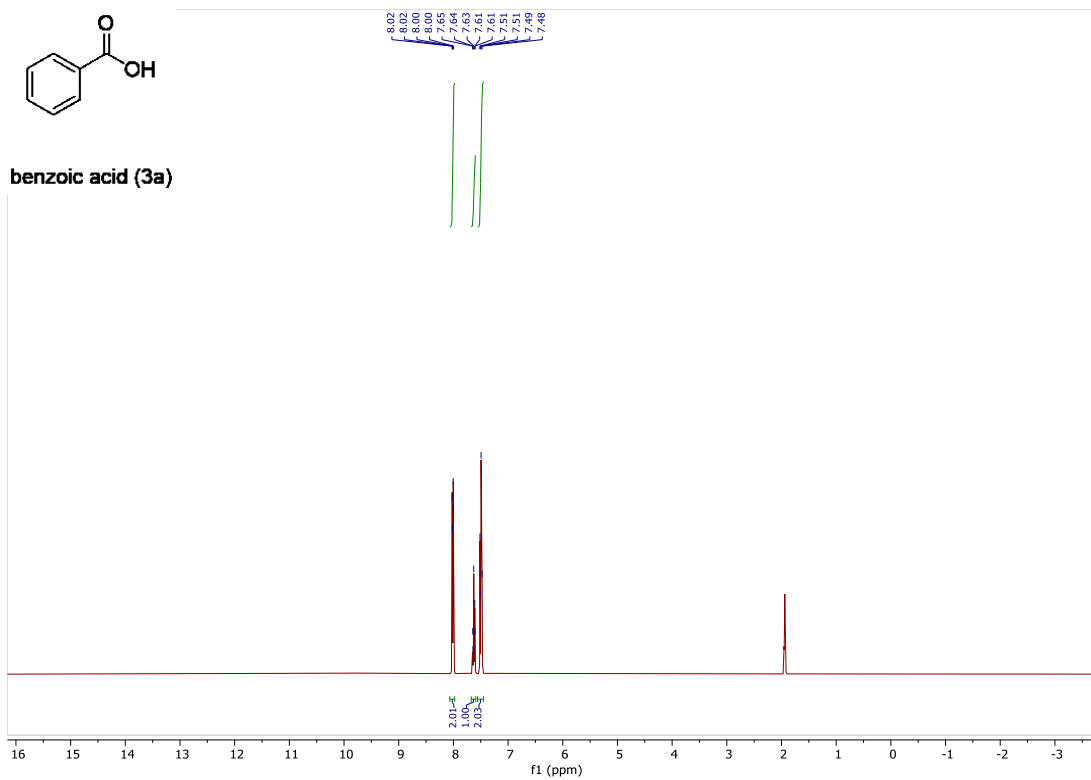


Figure S50 – ¹H NMR spectrum of **3a**

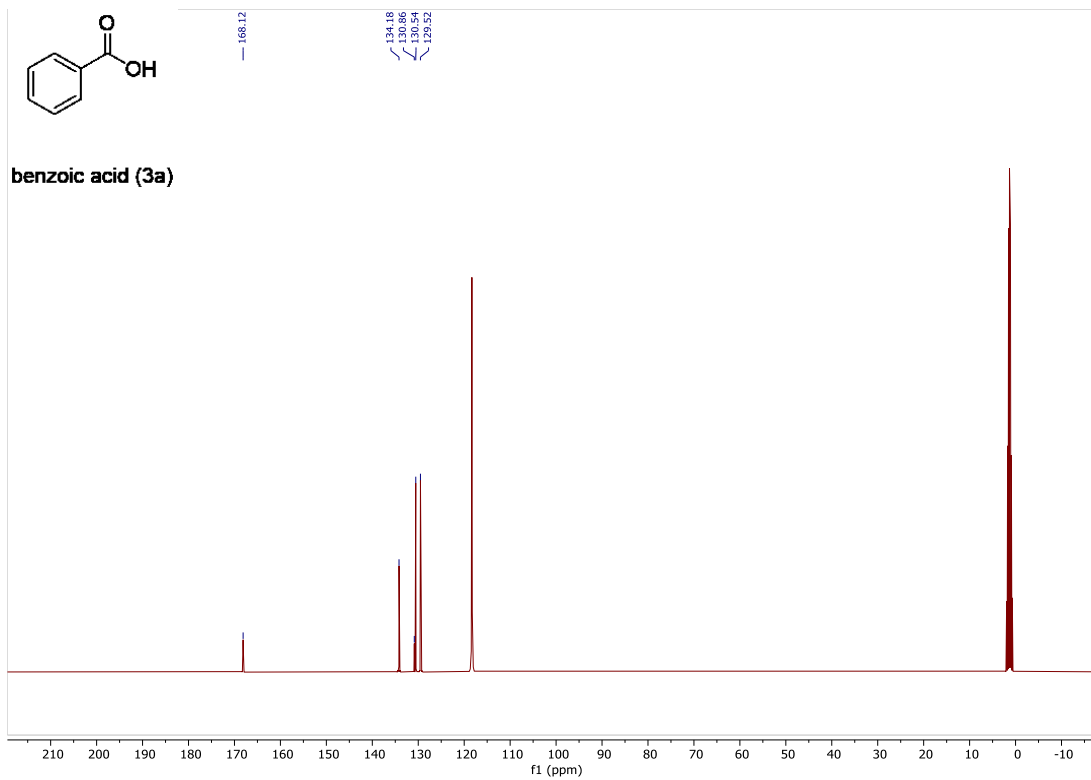


Figure S51 – ^{13}C NMR spectrum of **3a**

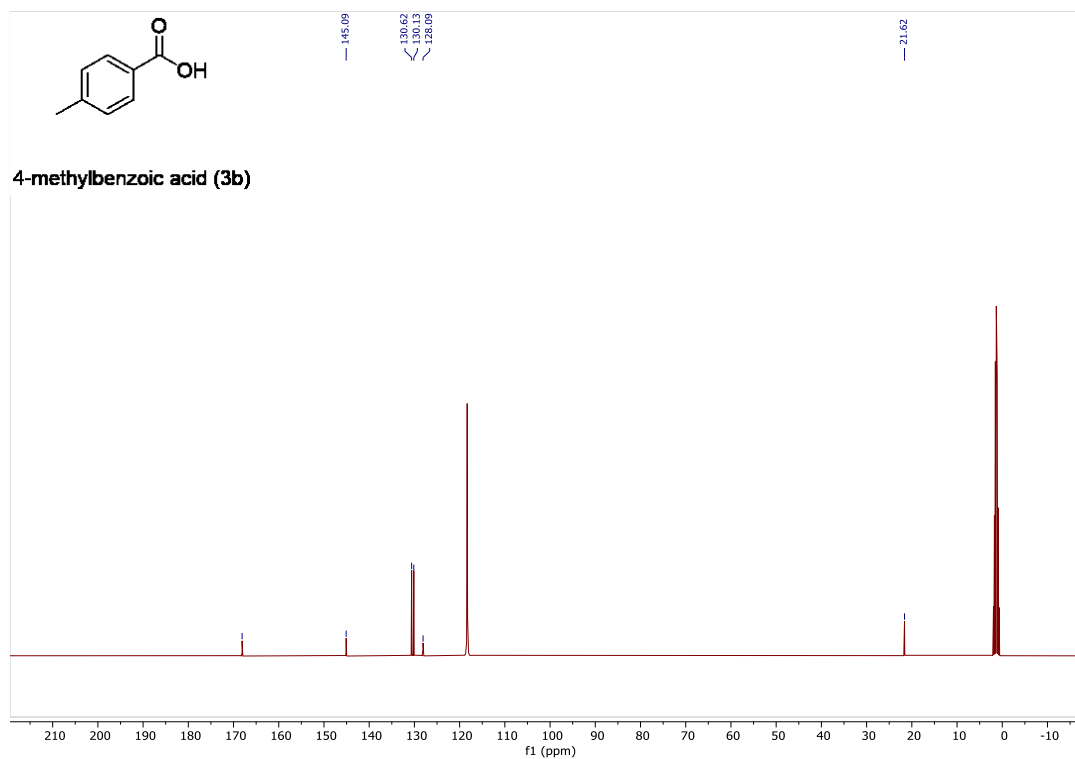


Figure S52 – ^{13}C NMR spectrum of **3b**

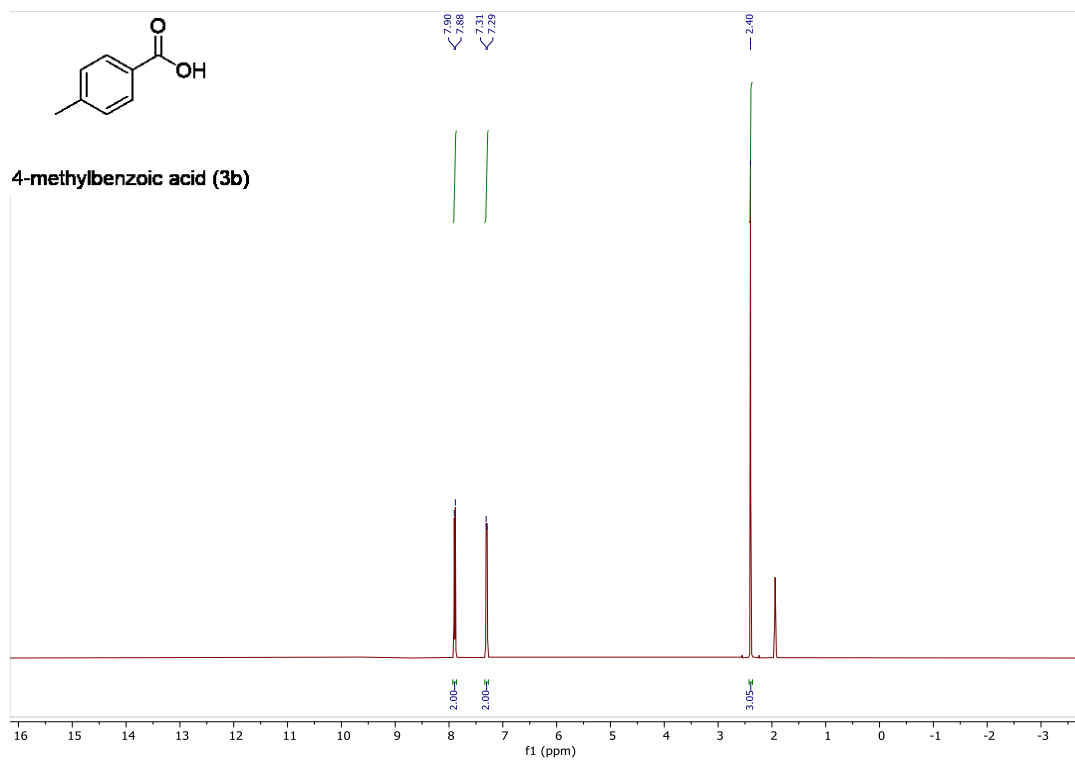


Figure S53 – ^1H NMR spectrum of **3b**

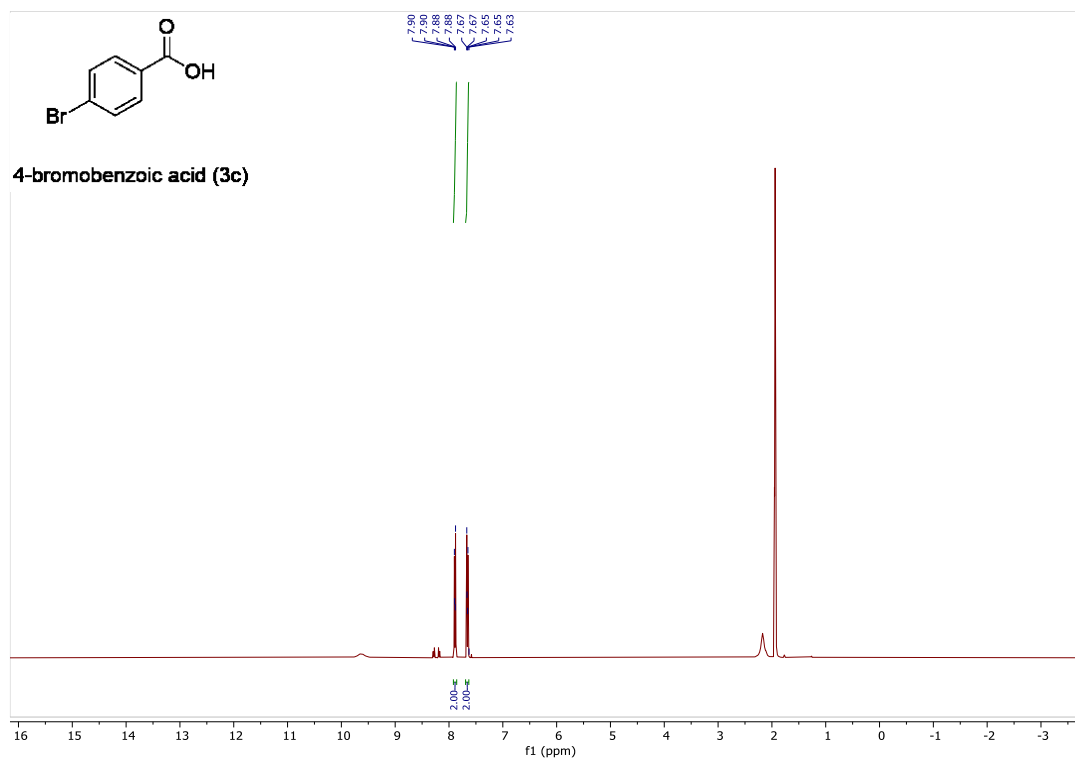


Figure S54 – ¹H NMR spectrum of **3c**

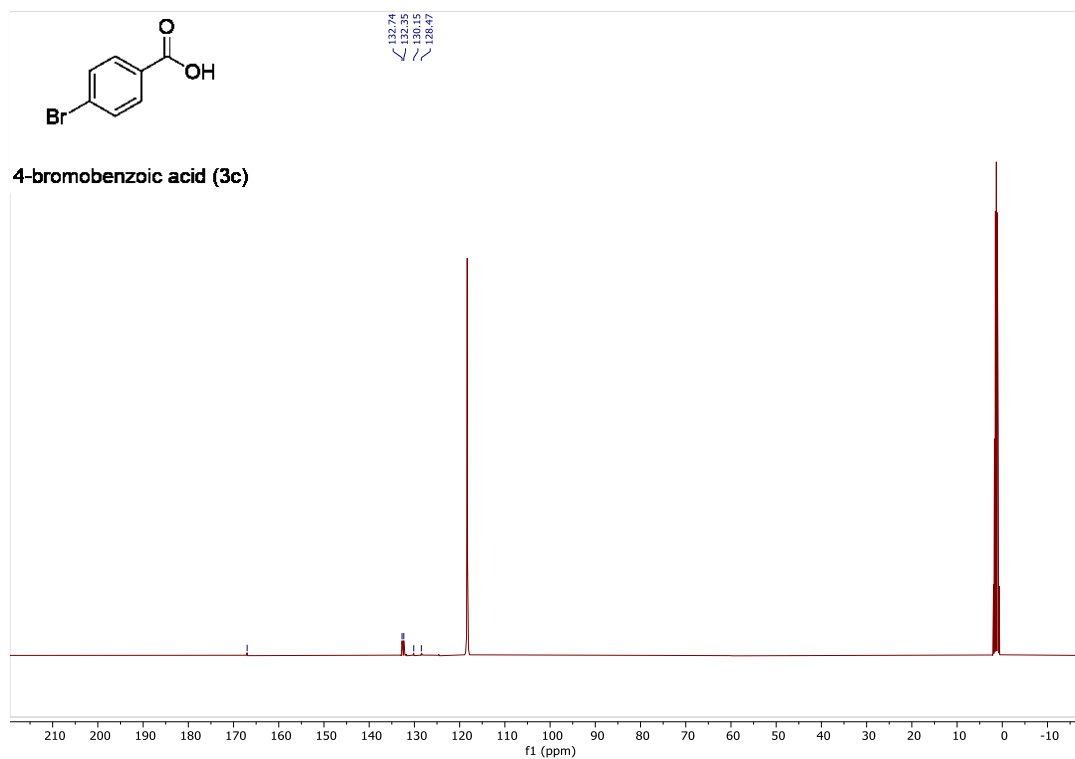


Figure S55 – ^{13}C NMR spectrum of **3c**

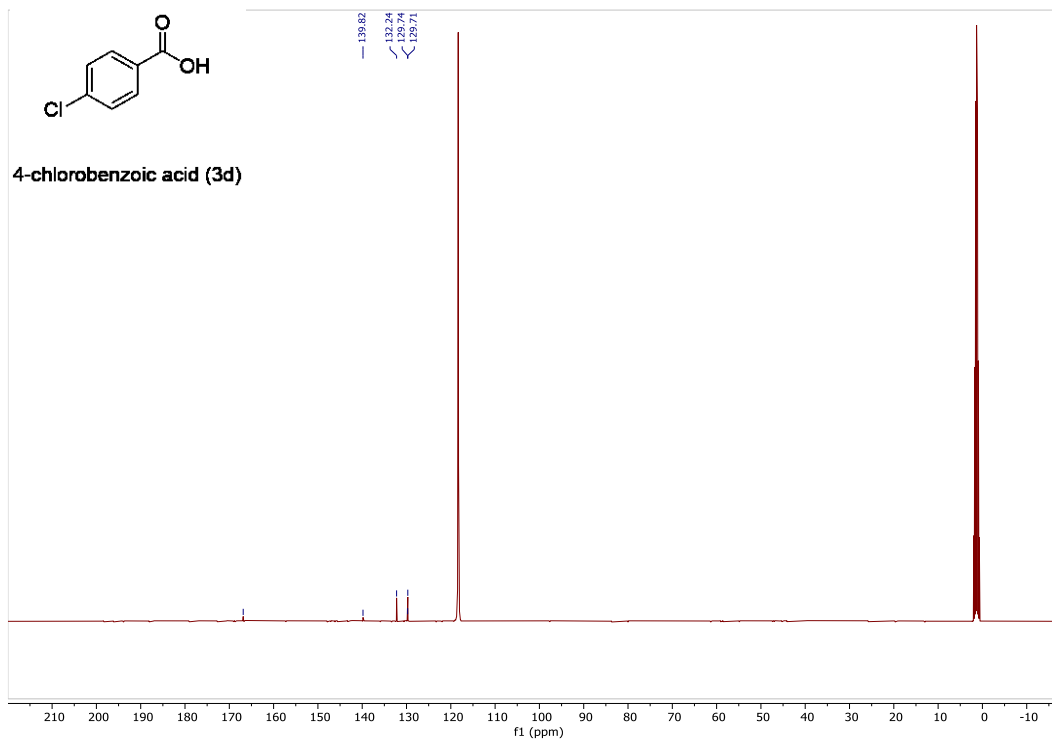


Figure S56 – ^{13}C NMR spectrum of **3d**

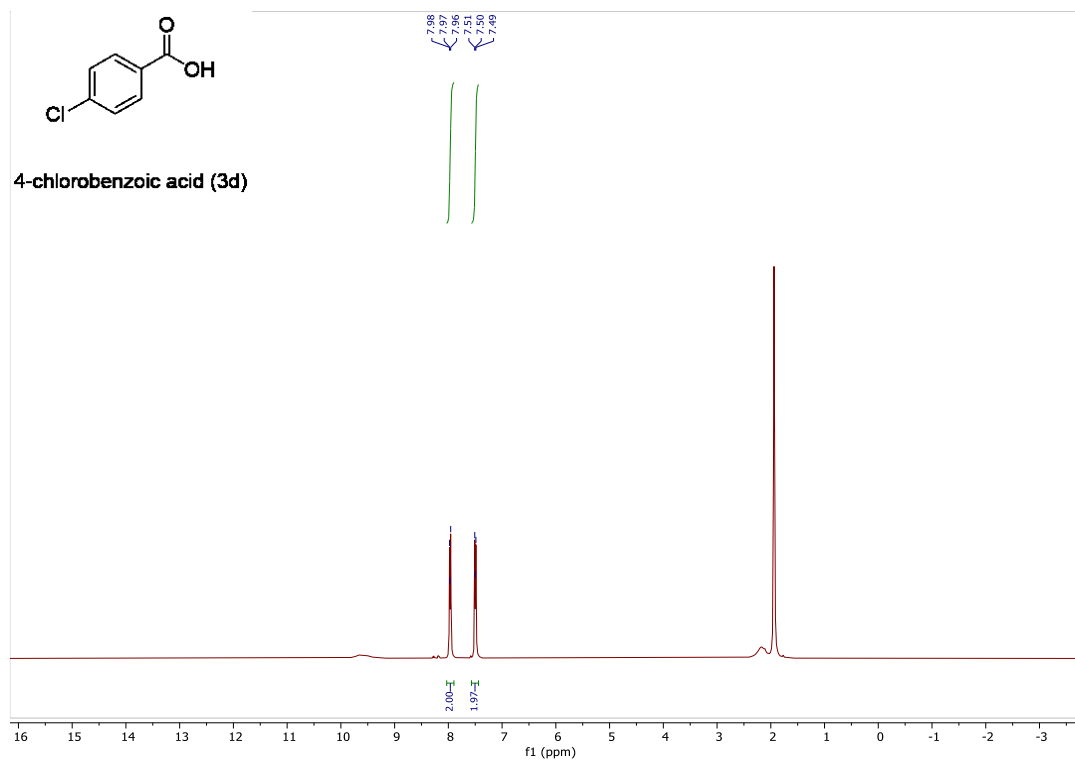


Figure S57 – ¹H NMR spectrum of **3d**

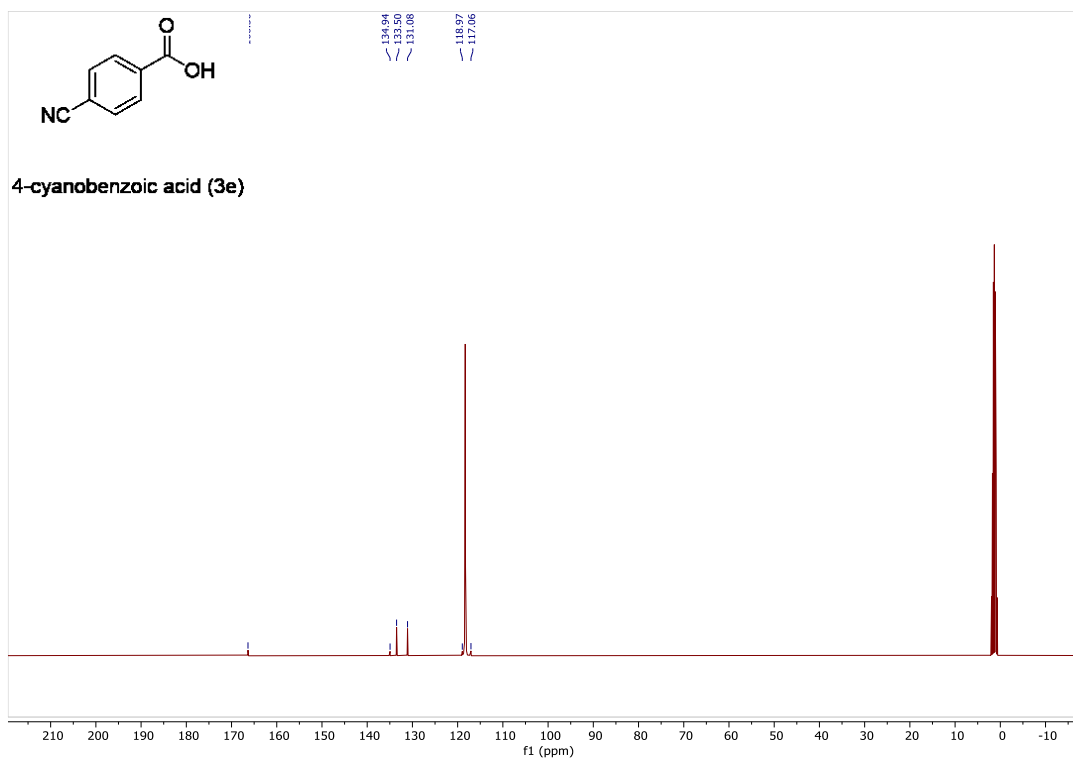


Figure S59 – ^{13}C NMR spectrum of **3e**

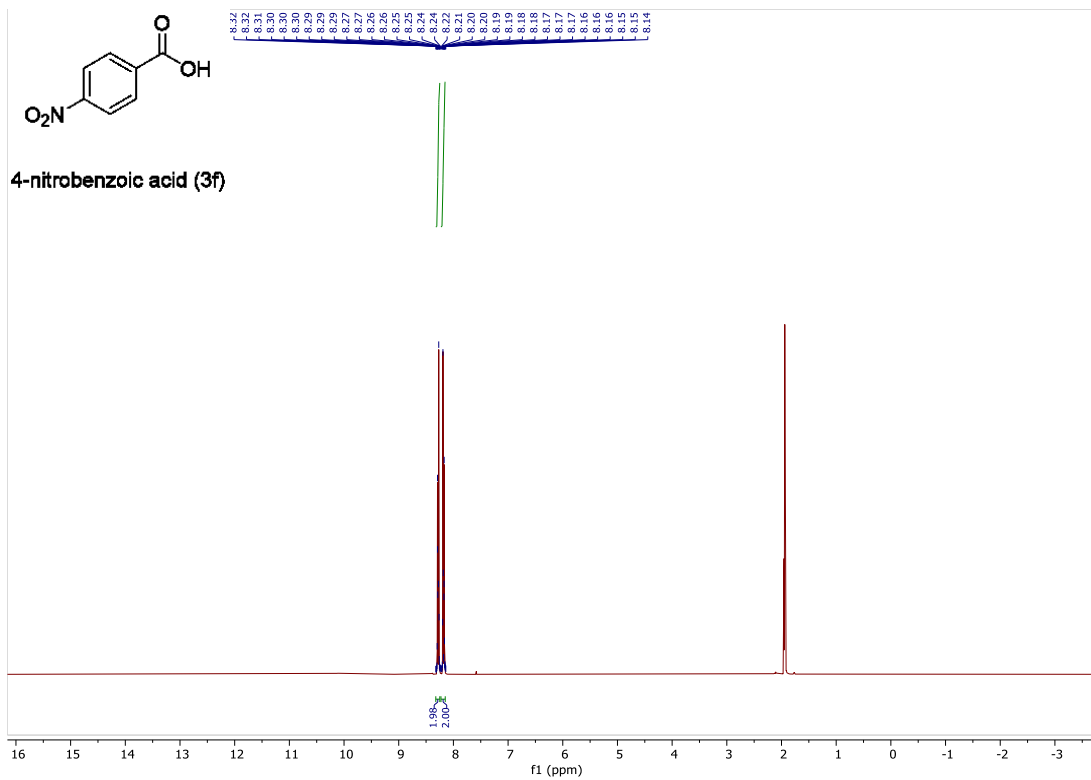


Figure S60 – ¹H NMR spectrum of **3f**

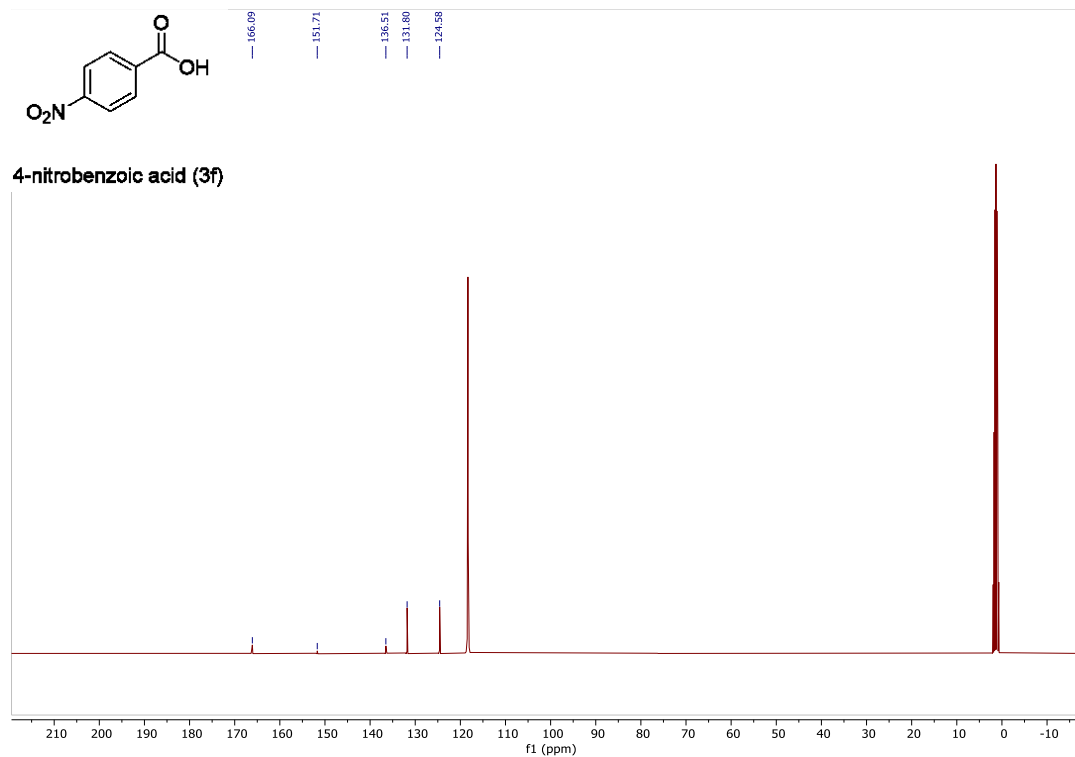


Figure S61 – ^{13}C NMR spectrum of **3f**

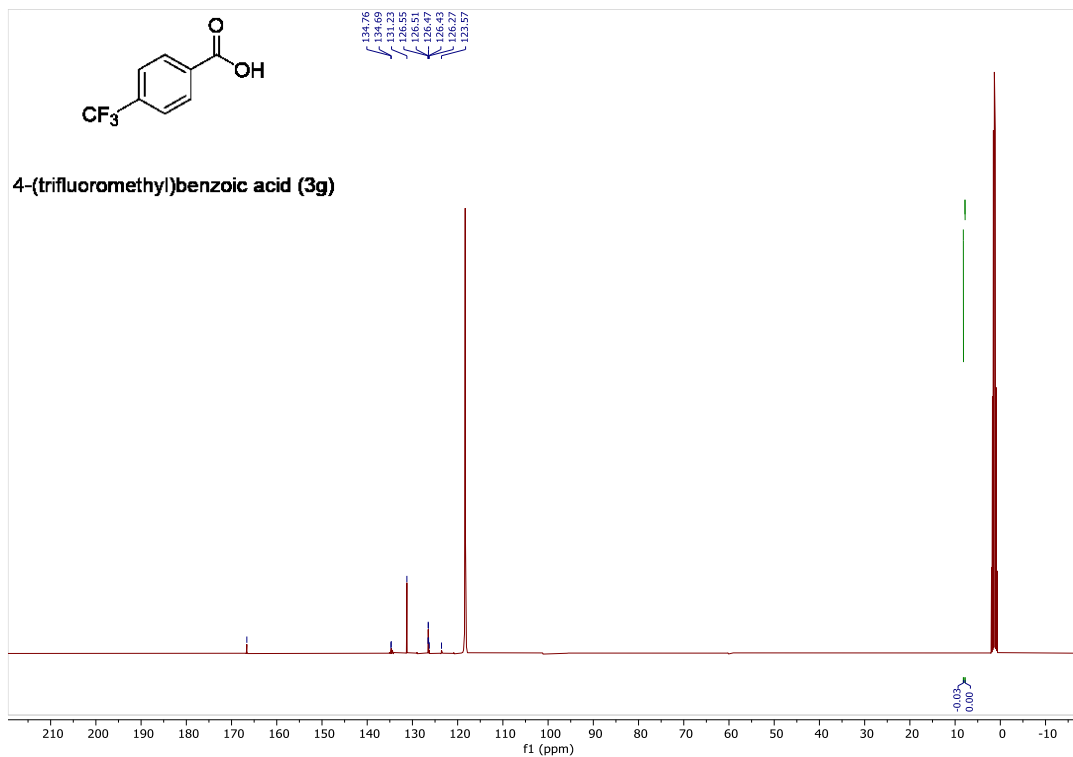


Figure S63 – ^{13}C NMR spectrum of **3g**

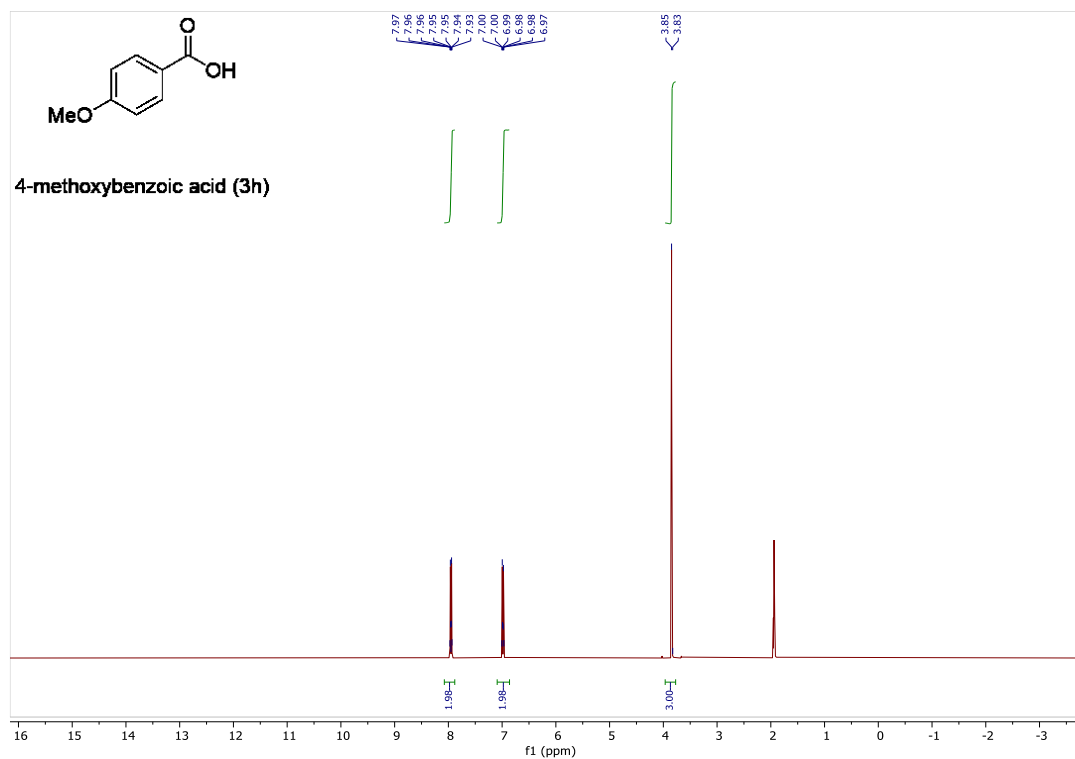


Figure S64 – ^1H NMR spectrum of **3h**

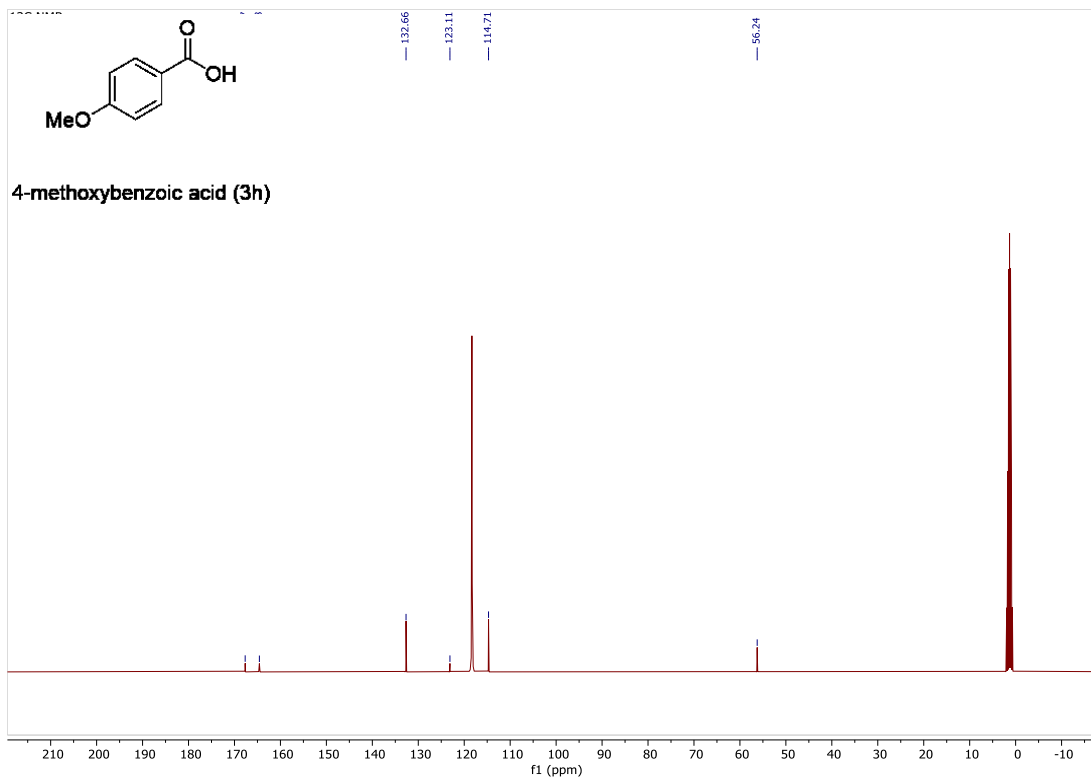


Figure S65 – ^{13}C NMR spectrum of **3h**

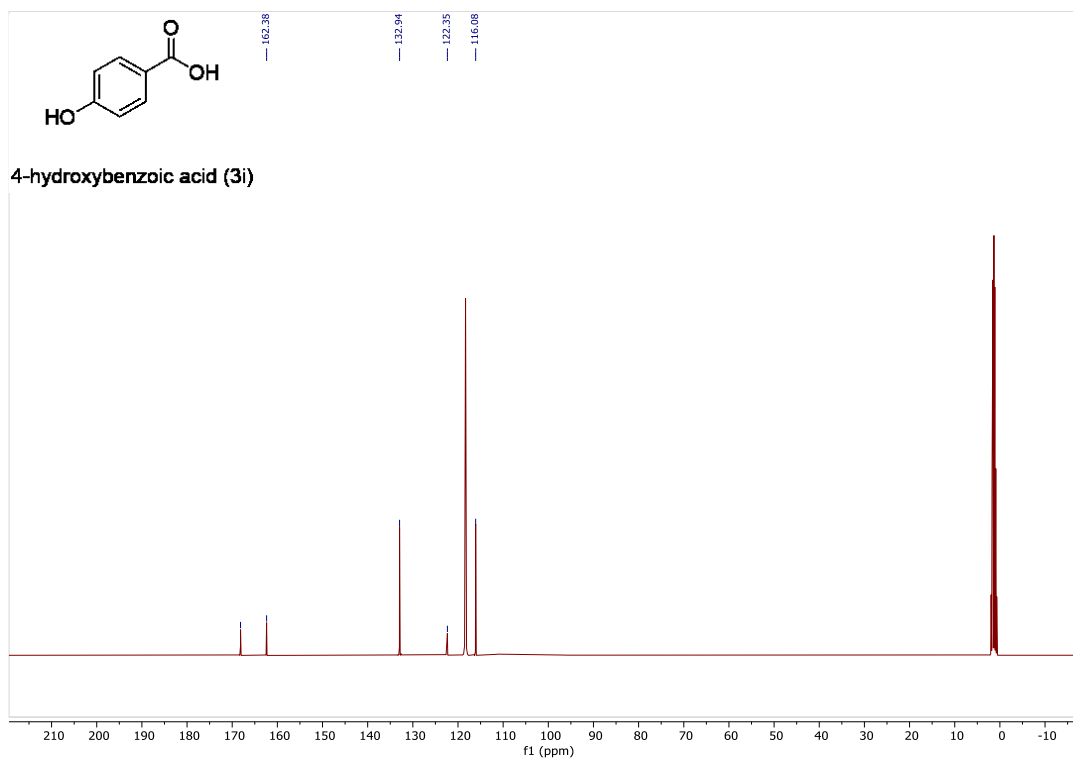


Figure S66 – ^{13}C NMR spectrum of **3i**

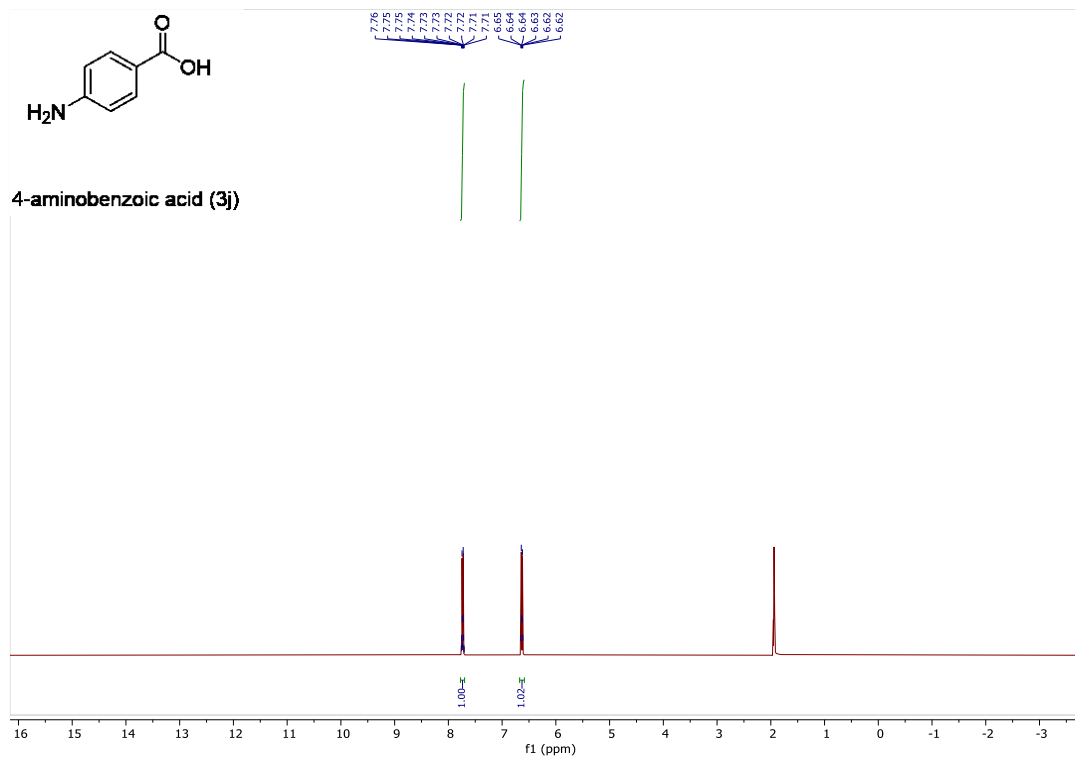


Figure S67 – ^1H NMR spectrum of **3j**

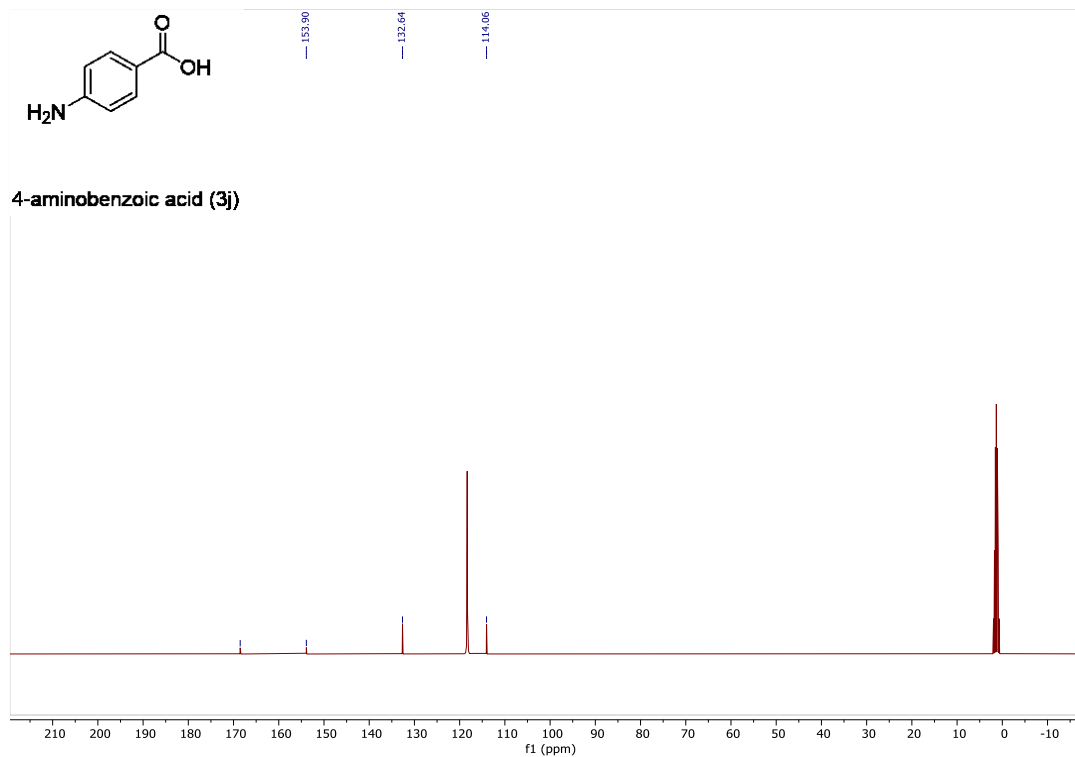


Figure S68 – ¹³C NMR spectrum of **3j**

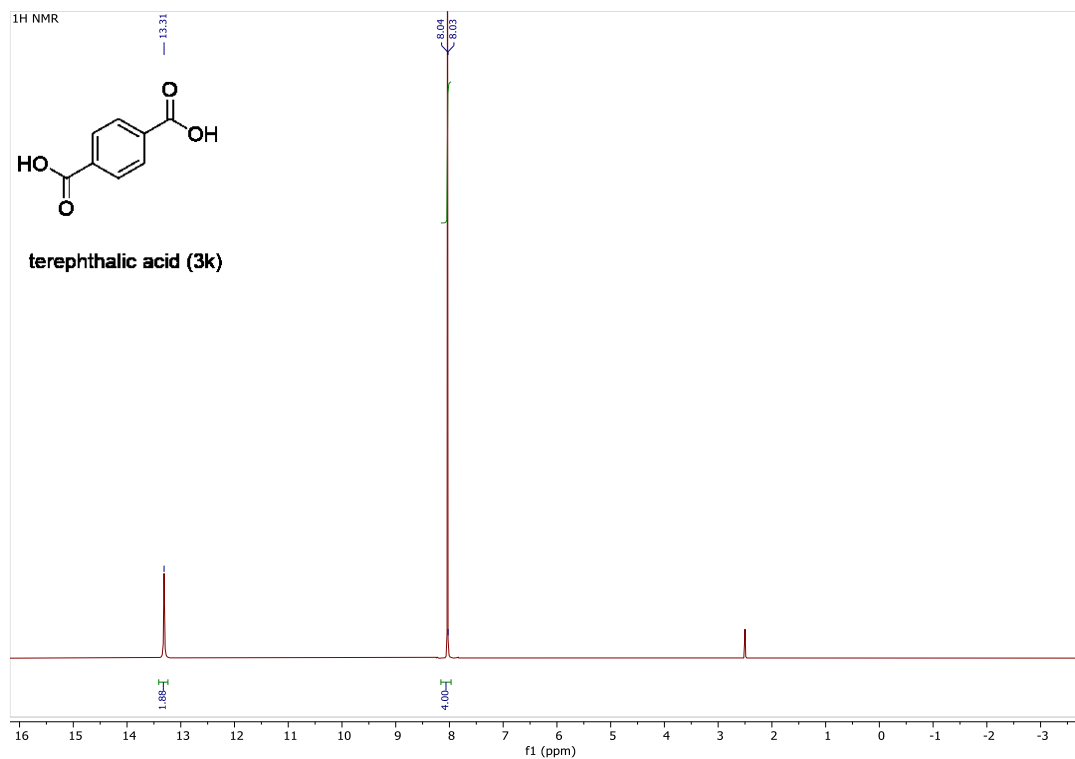


Figure S69 – ¹H NMR spectrum of **3k**

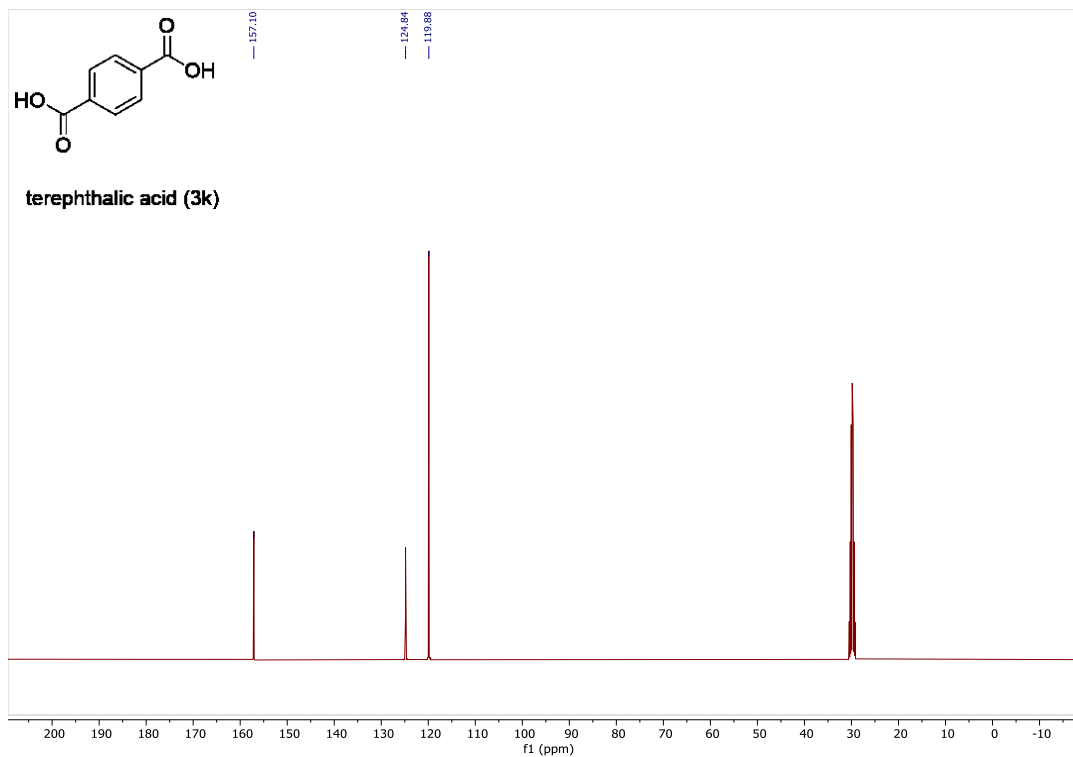


Figure S70 – ¹³C NMR spectrum of **3k**

7.4. Multisite Proton Coupled Electron Transfer with Long-lived Radicals of Poly(Heptazine Imide)s for Uphill Organic Synthesis

Materials. TiO₂ was purchased from Sigma-Aldrich (99.5%, CAS number [1317-80-2](#), rutile, nanopowder 10x40 nm, specific surface area 50 m²g⁻¹).

Cyclic voltammetry (CV) measurements were performed in a glass single-compartment electrochemical cell. Glassy carbon (diameter 3 mm) was used as a working electrode (WE), Ag wire in AgNO₃ (0.01M) as a reference electrode (RE), Pt wire as a counter electrode. Each compound was studied in a 10 mM concentration in a 0.1 M tetrabutylammonium perchlorate (TBAP) and DMSO electrolyte solution (10 mL). Before voltammograms were recorded, the solution was purged with Ar, and an Ar flow was kept in the headspace volume of the electrochemical cell during CV measurements. A potential scan rate of 0.050 V s⁻¹ was chosen, and the potential window ranging from +2.5 V to -2.5 V (and backwards) was investigated. Cyclic voltammetry was performed under room-temperature conditions (~20-22 °C).

Standard procedure for photocatalytic dehalogenation in dark conditions

In a 8 mL vial with stirrer (3 cm length, vertically placed), 80 mg of K-PHI, 4 mL of DMSO and 560 µL of DIPEA were added. The vial was closed with a rubber cap. The solution was degassed for 2 minutes via double needle technique, fluxing nitrogen. The reaction vessel was irradiated (light conditions) with a 50 W Blue light LED module at 1 cm distance (0.46 W·cm⁻²), cooled with a fan for 24 hours (T₁, τ₁). Afterwards, 1 mL DMSO solution (degassed as above) containing 0.05 mmol of aryl halide (**1a-1t**) was added. Then, the vial was placed in an oil bath (1 cm deep) at 80 °C for 20 hours (T₂, τ₂), wrapped in aluminum foil, without any light irradiation (dark conditions). At the end, the sample has been analyzed via GC-MS to determine the yield. See Figure S5 for schematic overview.

Standard procedure for photocatalytic generation of ketyl radical in dark conditions

In a 8 mL vial with stirrer (3 cm length, vertically placed), 80 mg of K-PHI, 4 mL of DMSO and 560 μL of DIPEA were added. The vial was closed with a rubber cap. The solution was degassed for 2 minutes via double needle technique, fluxing nitrogen. The reaction vessel was irradiated (light conditions) with a 50 W Blue light LED module at 1 cm distance ($0.46 \text{ W}\cdot\text{cm}^{-2}$), cooled with a fan for 24 hours (T_1, τ_1). Afterwards, 1 mL DMSO solution (degassed as above) containing chalcone **3a** (0.05 mmol, 10.4 mg) was added. Then, the vial was placed in an oil bath (1 cm deep) at 80 °C for 20 hours (T_2, τ_2), wrapped in aluminum foil, without any light irradiation (dark conditions). At the end, the sample has been analyzed via GC-MS to determine the yield.

Standard procedure for photocatalytic reduction of aniline in dark conditions

In a 8 mL vial with stirrer (3 cm length, vertically placed), 80 mg of K-PHI, 4 mL of DMSO and 560 μL of DIPEA were added. The vial was closed with a rubber cap. The solution was degassed for 2 minutes via double needle technique, fluxing nitrogen. The reaction vessel was irradiated (light conditions) with a 50 W Blue light LED module at 1 cm distance ($0.46 \text{ W}\cdot\text{cm}^{-2}$), cooled with a fan for 24 hours (T_1, τ_1). Afterwards, 1 mL DMSO solution (degassed as above) containing nitrobenzene **5a** (0.05 mmol, 5.13 μL) was added. Then, the vial was placed in an oil bath (1 cm deep) at 80 °C for 20 hours (T_2, τ_2), wrapped in aluminum foil, without any light irradiation (dark conditions). At the end, the sample has been analyzed via GC-MS to determine the yield.

2. Supplementary tables

Entry	Semiconductor	Amine	DMSO (mL)	τ_1 (h)	τ_2 (h)	T ₁ (°C)	T ₂ (°C)	Yield (%)
1	K-PHI (20 mg)	TEA (350 μ L)	1	25	20	RT	50	6
2	mpg-CN (20 mg)	TEA (350 μ L)	1	25	20	RT	50	Traces
3	g-CN (20 mg)	TEA (350 μ L)	1	25	20	RT	50	Traces
4	Na-PHI (20 mg)	TEA (350 μ L)	1	25	20	RT	50	Traces
5	K-PHI (40 mg)	TEA (350 μ L)	1	25	20	RT	50	15
6	K-PHI (80 mg)	TEA (350 μ L)	1	25	20	RT	50	22
7	K-PHI (20 mg)	TEA (350 μ L)	1	16	5	RT	80	14

Table S3 – Screening of semiconductors. Reactions were performed following the standard procedure. Parameters deviated from STD conditions are reported.

Entry	Substrate	K-PHI	Amine	DMSO	τ_1 (h)	τ_2 (h)	Yield (%)
1	0.025 mmol	20 mg	TEA (3.5 μ L)	1 mL	23	19	Traces
2	0.025 mmol	20 mg	TEA (7 μ L)	1 mL	23	19	12
3	0.025 mmol	20 mg	TEA (14 μ L)	1 mL	23	19	24
4	0.025 mmol	20 mg	TEA (28 μ L)	1 mL	23	19	25
5	0.025 mmol	20 mg	TEA (112 μ L)	1 mL	23	18	31
6	0.025 mmol	20 mg	TEA (168 μ L)	1 mL	23	18	28
7	0.025 mmol	20 mg	THIQ (102 μ L)	1 mL	26	17	16
8	0.025 mmol	20 mg	TEOA (106 μ L)	1 mL	26	17	25
9	0.025 mmol	20 mg	DIPEA (106 μ L)	1 mL	26	17	40
10	0.025 mmol	20 mg	1-phenylpyrrolidine (118 (μ L)	1 mL	26	17	7

Table S4 – Amines screening. Reactions were performed following the standard procedure. Parameters deviated from STD conditions are reported.

Entry	Substrate	DIPEA	Light distance	DMSO	K-PHI	τ_1 (h)	τ_2 (h)	Yield (%)
1	0.025 mmol	140 μ L	1 cm	1 mL	20 mg	22	19	67
2	0.025 mmol	140 μ L	1 cm	1 mL	80 mg	22	19	31
3	0.025 mmol	140 μ L	1 cm	3 mL	80 mg	22	20	71

Table S5 – Studying the effect of dilution and K-PHI loading. Reactions were performed following the standard procedure. Parameters deviated from STD conditions are reported.

Entry	DIPEA	DMSO	K-PHI	Light (at 1 cm)	τ_1 (h)	τ_2 (h)	Yield (%)
1	140 μ L	1 mL	20 mg	Blue (465 nm)	20	5	34
2	140 μ L	1 mL	20 mg	Purple (410 nm)	20	5	11
3	140 μ L	1 mL	20 mg	UV (365 nm)	20	5	52

Table S6 – Studying the effect of photon energy. Reactions were performed following the standard procedure. Parameters deviated from STD conditions are reported.

Entry	Substrate	K-PHI	DIPEA (μ L)	DMSO	τ_1 (h)	τ_2 (h)	Yield (%)
1	0.025 mmol	40 mg	140	2 mL	23	22	63
2	0.025 mmol	40 mg	180	2 mL	23	22	51
3	0.025 mmol	40 mg	100	2 mL	23	22	69
4	0.025 mmol	40 mg	280	2 mL	23	22	100

Table S7 – Screening the amount of DIPEA. Reactions were performed following the standard procedure. Parameters deviated from STD conditions are reported.

Entry	τ_1 (h)	τ_2 (h)	Yield (%)
1	8	24	80
2	20	24	100
3	24	24	100
4	24	8	70
5	24	20	100
6	24	20	100

Table S8 – Reaction time screening. Reactions were performed following the standard procedure. Parameters deviated from STD conditions are reported.

Entry	Catalyst	Light	T ₂ (°C)	Yield (%)
1	K-PHI (80 mg)	Blue	80	100%
2	K-PHI (80 mg)	Blue	RT	7%
3	K-PHI (80 mg)	None	80	Traces
4	None	Blue	80	Traces
5	Na-PHI (80 mg)	Blue	80	61
6	g-CN (80 mg)	Blue	80	Traces
7	Mpg-CN (80 mg)	Blue	80	12
8	TiO ₂ (12.8 mg)	UV	80	Traces
9 ^a	K-PHI (80 mg)	Blue	/	100
10	K-PHI (80 mg) ^b	Blue	80	49%

Table S9 – Reactions were performed following the standard procedure. Parameters deviated from STD conditions are reported.

a) Reaction performed with the substrate added before irradiation. Reaction was stopped after the light phase. b) Recycled catalyst.

Entry	Solvent	Co-solvent	Yield (%)
1	DMSO	/	100
2	CH ₃ CN	/	0
3	CH ₃ CN	80 μ L H ₂ O	0
4	DMF	/	7
5	Toluene	/	0
6	DMSO	/	100
7	DMSO ^a	20 μ L H ₂ O	90
8	DMSO ^a	40 μ L H ₂ O	97
9	DMSO ^a	80 μ L H ₂ O	100

Table S10 – Reactions were performed following the standard procedure. Parameters deviated from STD conditions are reported.

a) Using a new bottle of dry DMSO.

Entry	Storage after 24 h irradiation	Yield (%)
1	3 days	75
2	7 days	10
3	7 days ^a	51

Table S11 – Reactions were performed following the standard procedure. Parameters deviated from STD conditions are reported.

a) Kept in freezer at -25 °C

Entry	Substrate	E _{Red} (vs. SCE)
1	1a	-1.18 V
2	1o	-1.20 V

Table S10 – Cyclic voltammetry experiments.

3. Supplementary figures

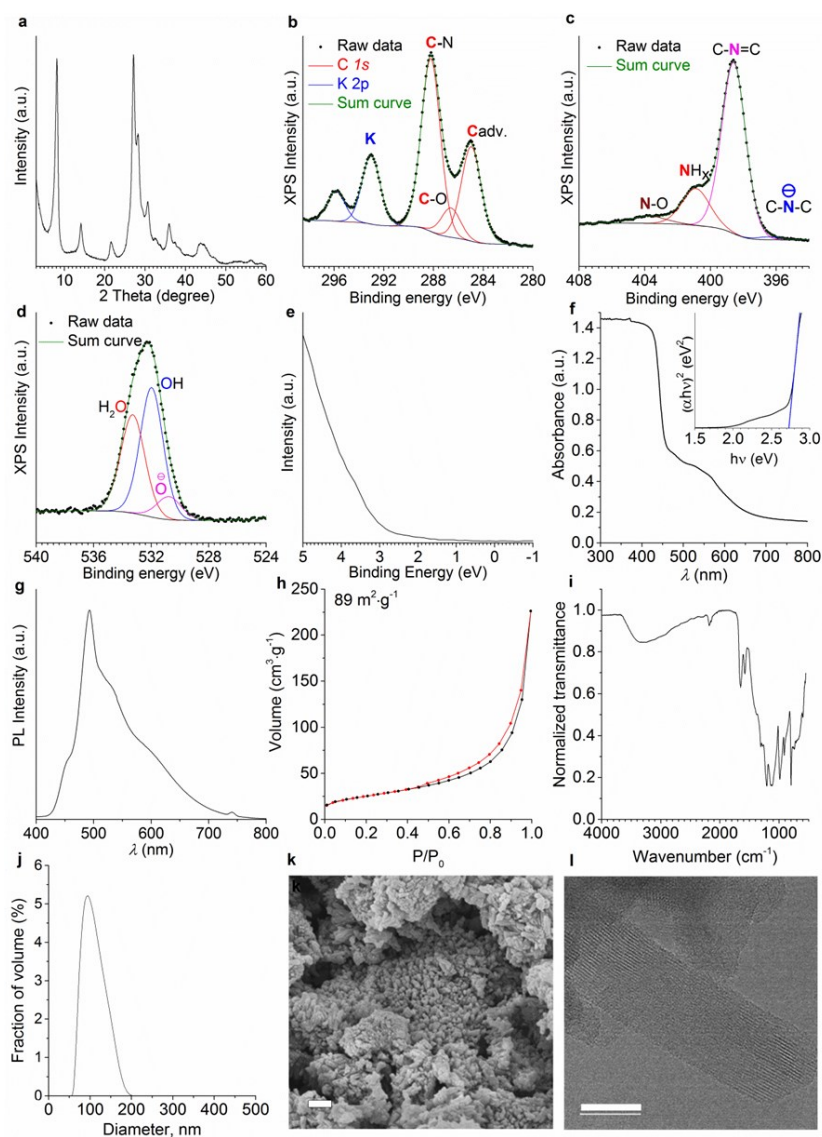


Figure S1 - K-PHI characterization. a) PXRD pattern of K-PHI; b) XPS C 1s and K 2p spectra of K-PHI; c) XPS N 1s spectrum of K-PHI; d) XPS O 1s spectrum of K-PHI; e) UPS spectrum of K-PHI; f) UV-vis absorption spectrum of K-PHI with Tauc plot as inset assuming that K-PHI is a direct semiconductor; g) room temperature PL spectrum of K-PHI obtained upon excitation with 350 nm wavelength; h) N_2 sorption isotherm measured at 77 K. BET surface area; i) FT-IR spectrum of K-PHI; j) DLS analysis of K-PHI

suspension in water; k) representative SEM image of K-PHI photocatalyst. Scale bar 200 nm; l) AC-HRTEM image of K-PHI photocatalyst. Scale bar 20nm.

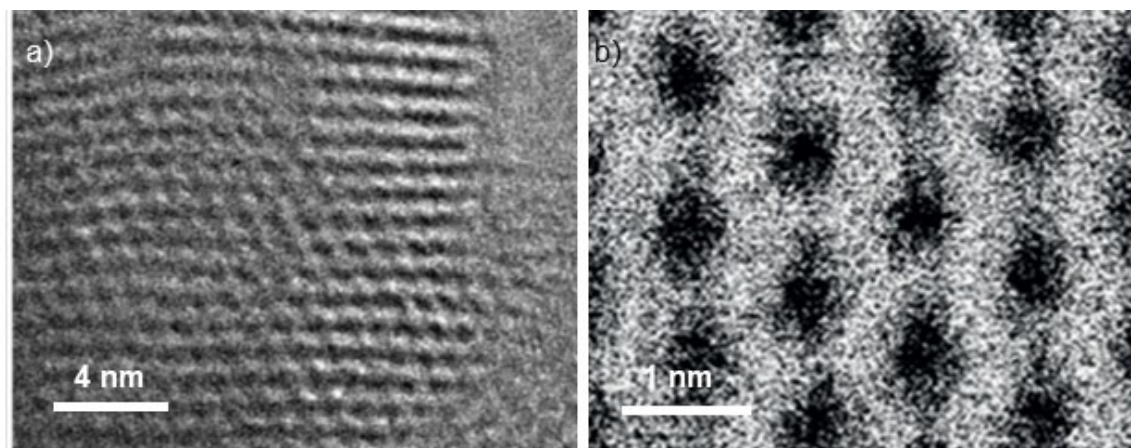


Figure S2 – AC-HRTEM images of K-PHI microporous structure. Reproduced with permission from [106, 139]

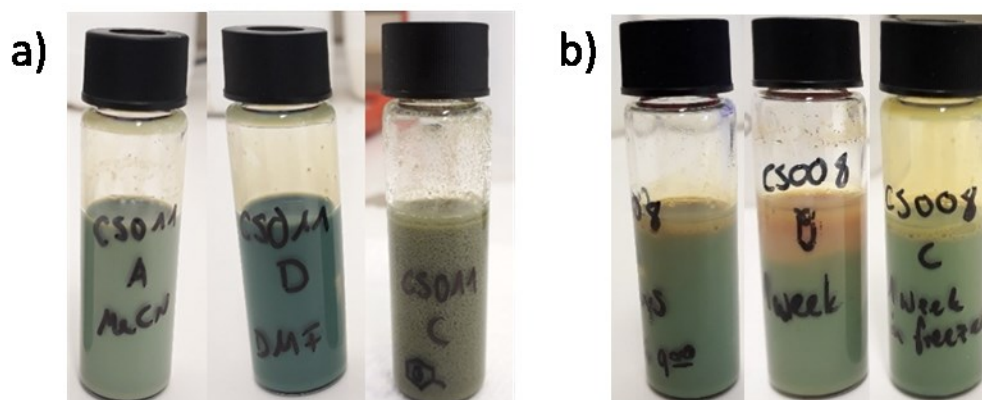


Figure S3 – a) Samples after irradiation in different solvent: CH_3CN , DMF and toluene, respectively from left to right. b) Samples after irradiation stored for 3 days, 7 days and 7 days in freezer, respectively from left to right

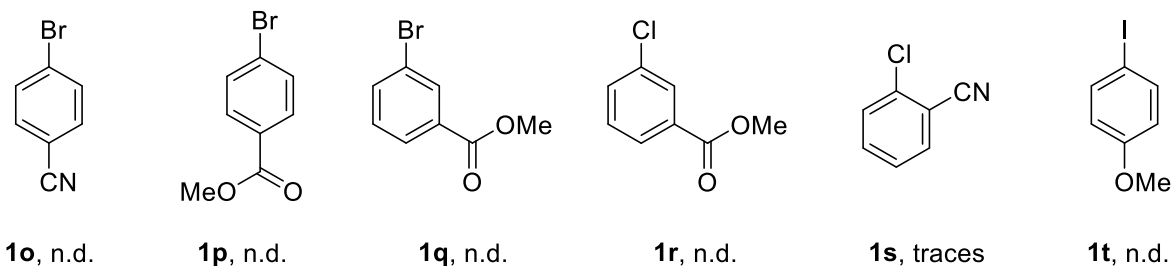


Figure S4 – Structure of aryl halides that did not react under the standard conditions. n.d. – the product of arylhalide reduction was not detected in the GC-MS chromatograms.

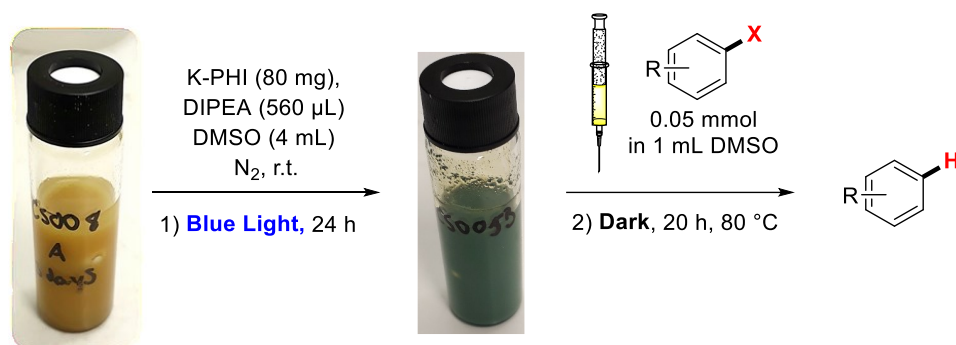
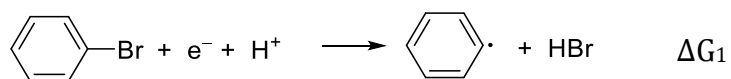


Figure S5 – General procedure of dark photocatalytic aryl halide dehalogenation

Thermochemical calculations

1. Reduction of phenyl radical from bromobenzene via MS-PCET by e^-/H^+ .

Reduction of bromobenzene to phenyl radical via MS-PCET by e^-/H^+ can be described by the equation (1):



which is a combination of equations (2), (3) and (4):

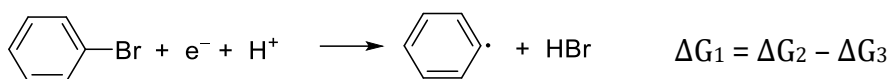
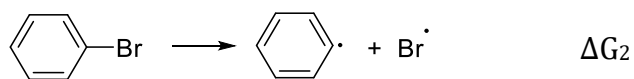
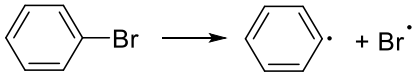
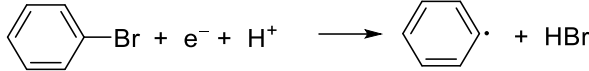


Table S11. Reported and estimated BDFE values.

	Reaction	ΔG or BDFE, kcal mol ⁻¹	Comment
(2)		$\Delta G_2 = 74.6$	Gas phase, 298 K. Calculated from the equation $\Delta G_2 = \text{BDE} - T\Delta S$ (BDE = 82.3 kcal mol ⁻¹ from the reference [222] (computed value), $\Delta S = 0.026$ kcal mol ⁻¹ from the reference [221]).
(3)	$\text{HBr} = \text{Br}\cdot + \text{H}\cdot$	$\Delta G_3 = 79.8$	Gas phase, 298 K. Calculated from the equation $\Delta G_2 = \text{BDE} - T\Delta S$ (BDE = 87.54 kcal mol ⁻¹ from the reference [221] (experimental value), $\Delta S =$

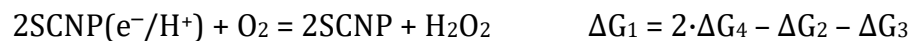
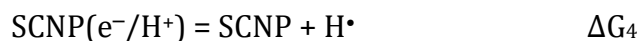
			0.026 kcal mol ⁻¹ from the reference [221]).
(1)		$\Delta G_3 = -5.2$	Gas, 298K. Calculated based on values of ΔG_2 and ΔG_3 .

2. Reduction of O₂ to H₂O₂ by e⁻/H⁺ stored in the semiconductor.^{[121],[206]}

Reduction of O₂ to H₂O₂ by e⁻/H⁺ stored in the semiconductor nanoparticle (SCNP) can be described by the equation (1):



which is a combination of equations (2), (3) and (4):



ΔG_2 , ΔG_3 and ΔG_4 – are the BDFE of the corresponding compounds in kcal mol⁻¹.

The condition for reduction of O₂ to H₂O₂ by e⁻/H⁺ stored in the SCNP is that $\Delta G_1 < 0$. The upper limit of ΔG_4 can be estimated from the relation:

$$\Delta G_4 < \frac{1}{2}(\Delta G_2 + \Delta G_3)$$

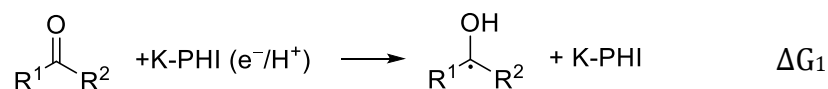
The results for different conditions (gas or water) are summarized in the Table S12.

Table S12. Reported and estimated BDFE values.

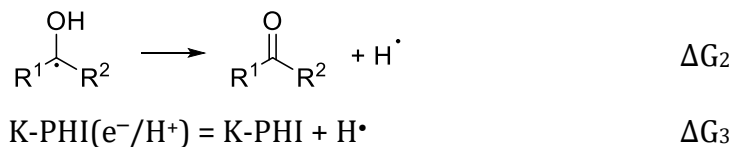
	Equation	BDFE, kcal mol ⁻¹	Comment
(1)	$\text{HO}_2^\bullet = \text{O}_2 + \text{H}^\bullet$		
		$\Delta G_2 = 42.7$	Gas, 298K. Data from reference [[228]].
		$\Delta G_2 = \sim 58$	DMSO, 298 K. Data from reference [[228]].
		$\Delta G_2 = 60.6$	H ₂ O, 298 K. Data from reference [[228]].
(2)	$\text{H}_2\text{O}_2 = \text{HO}_2^\bullet + \text{H}^\bullet$		
		$\Delta G_3 = 79.6$	Gas, 298K. Data from reference [[228]].
		$\Delta G_3 = 91.0$	H ₂ O, 298 K. Data from reference [[228]].
(3)	$\text{SCNP}(e^-/\text{H}^+) = \text{SCNP} + \text{H}^\bullet$		
		$\Delta G_4 < 61.2$	Gas, 298K. Estimated based on values of ΔG_2 and ΔG_3 .
		$\Delta G_4 < 75.8$	H ₂ O, 298 K. Estimated based on values of ΔG_2 and ΔG_3 .

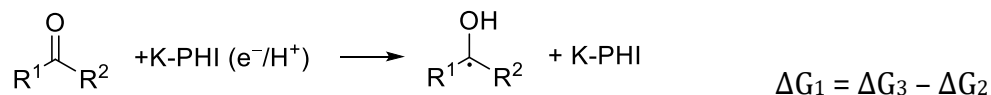
3. Reduction of ketone to ketyl radical by e⁻/H⁺ stored in K-PHI.^[110]

Reduction of ketone to ketyl radical by e⁻/H⁺ stored in K-PHI can be described by the equation (1):



which is a combination of equations (2) and (3):





$\Delta G_2, \Delta G_3$ – are the BDFE of the corresponding compounds in kcal mol⁻¹.

The condition for reduction of ketone to its ketyl radical by e⁻/H⁺ stored in K-PHI is that $\Delta G_1 < 0$. The upper limit of ΔG_3 can be estimated from the relation:

$$\Delta G_3 < \Delta G_2$$

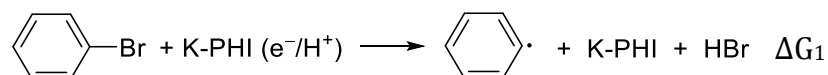
The results are summarized in the Table S13.

Table S13. Reported and estimated BDFE values.

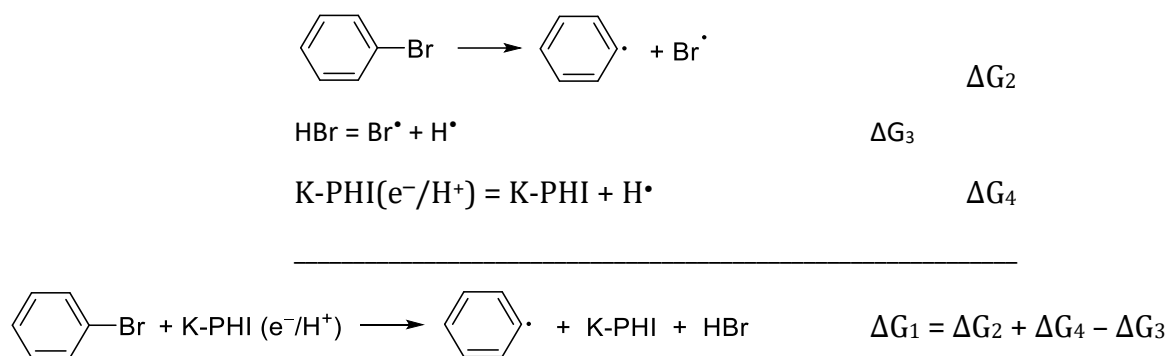
	Equation	BDFE, kcal mol ⁻¹	Comment
(1)	$R^1-\dot{C}(OH)-R^2 \longrightarrow R^1-C(=O)-R^2 + H^\bullet$	$\Delta G_2 = 25.69$	Calculated value for acetophenone ketyl radical. Data from reference [227].
(2)	$K\text{-PHI} (e^-/H^+) = K\text{-PHI} + H^\bullet$	$\Delta G_3 < 25.69$	Estimated based on the value of ΔG_2 .

4. Generation of phenyl radical from bromobenzene using e⁻/H⁺ stored in K-PHI via MS-PCET (this work).

Reduction of bromobenzene to phenyl radical by e⁻/H⁺ stored in K-PHI can be described by the equation (1):



which is a combination of equations (2), (3) and (4):



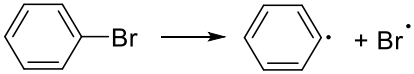
$\Delta G_2, \Delta G_3, \Delta G_4$ – are the BDFE of the corresponding compounds in kcal mol⁻¹.

The condition for reduction of bromobenzene to phenyl radical by e⁻/H⁺ stored in K-PHI is that $\Delta G_1 < 0$. Therefore, the upper limit of ΔG_4 can be estimated from the relation:

$$\Delta G_4 < \Delta G_3 - \Delta G_2$$

The results for different conditions (gas or water) are summarized in the Table S14.

Table S14. Reported and estimated BDFE values.

	Reaction	BDFE, kcal mol ⁻¹	Comment
(2)		$\Delta G_2 = 74.6$	Gas phase, 298 K. Calculated from the equation $\Delta G_2 = \text{BDE} - T\Delta S$ (BDE = 82.3 kcal mol ⁻¹ from the reference [222] (computed value), $\Delta S = 0.026$ kcal mol ⁻¹ from the reference [221]).
		$\Delta G_2 = 73.2$	H ₂ O, 298K. Computed value. Data from the reference [222].

(3)	$\text{HBr} = \text{Br}^\bullet + \text{H}^\bullet$	$\Delta G_3 = 79.8$	Gas phase, 298 K. Calculated from the equation $\Delta G_2 = \text{BDE} - T\Delta S$ (BDE = 87.54 kcal mol ⁻¹ from the reference [[221]] (experimental value), $\Delta S = 0.026$ kcal mol ⁻¹ from the reference [[221]]).
(4)	$\text{K-PHI}(e^-/\text{H}^+) = \text{K-PHI} + \text{H}^\bullet$	$\Delta G_4 < 5.2$	Gas phase, 298 K. Estimated based on values of ΔG_2 and ΔG_3 .

Table S15. Correlation of SCNPs doping degree with the yield of **2a** under the optimized conditions.

Entry	SCNP	Diameter, nm	Doping degree, [electrons]·cm ⁻³	Yield of 2a , %
1	K-PHI	100	ca. 10 ²¹ [a]	100%
2	mpg-CN	–	ca. 6·10 ¹⁹ [a]	12%
3	TiO ₂	–	ca. 10 ¹⁸ [b]	Traces[d]
4	ZnO	4.6	2·10 ¹⁹ [c]	–[e]

[a] Calculated using the equation: $N = d \cdot C \cdot N_A$, where d – density of carbon nitride, 2.336 g cm⁻³, [232] C – concentration of electrons in the carbon nitride, mol g⁻¹. Data is taken from the reference [[111]]. N_A – Avogadro number, 6.02·10²³ mol⁻¹. [b] Data is taken from the reference [[230]]. [c] Data is taken from the reference [[231]]. [d] Commercial TiO₂. [e] Not evaluated in this work.

7.5. All-organic Z-scheme photoreduction of CO₂ with water as the donor of electrons and protons

Materials. Acrylamide ($\geq 99\%$), PEDOT:PSS 1.3 wt. % dispersion in H₂O conductive grade, N,N-methylenebisacrylamide (99%), N,N,N',N'-tetramethylethylenediamine (99%) were purchased from Aldrich. (NH₄)₂S₂O₈ ($\geq 98.0\%$) was purchased from Fluka. Chemicals for Flavin syntheses were purchased from Aldrich and used as received without further purification. Petri dishes (diameter 150 mm, depth 25 mm, soda lime glass) were purchased from Duran Group. Copper gauze, 60 mesh woven from 0.19 mm diameter wire was purchased from Alfa Aesar. Glass slides (76 x 26 x 1 mm) were purchased from Marienfeld. Parafilm "M" (width 100 mm), laboratory film was purchased from Bemis.

Airbrush. Fengda Model: BD-186, cup capacity 5 mL, nozzle diameter 0.3 mm

Cyclic voltammetry (CV) measurements of flavins (F1, F2, F3) were performed in a glass single-compartment electrochemical cell. Glassy carbon (diameter 3 mm) was used as a working electrode (WE), Ag wire in AgNO₃ (0.01M) with tetrabutylammonium perchlorate (0.1M) in MeCN as a reference electrode (RE), Pt wire as a counter electrode. Each compound was studied in a 2 mM concentration in a 0.1 M tetrabutylammonium perchlorate (TBAP)/MeCN electrolyte solution (10 mL). Before voltammograms were recorded, the solution was purged with Ar, and an Ar flow was kept in the headspace volume of the electrochemical cell during CV measurements. A potential scan rate of 0.050 V s⁻¹ was chosen, and the potential window ranging from +2.0 to -2.0 V (and backwards) was investigated. Cyclic voltammetry was performed under room-temperature conditions (~20-22 °C).

Thermal response measurements were carried out by using an optical calorimeter (InfraSORP Technology by Fraunhofer/Rubotherm). For the adsorption and desorption cycling measurements for CO₂ physisorption at 298 K, the materials (~ 10 mg) were placed

in the sample cell, followed by purging with N₂ gas until the temperature stabilized. Then, the sample was subjected to the CO₂ test gas for 100 s. After 60 s of by-pass time to remove the gas from the lines between each injection, a N₂ gas flow was subjected to the sample for the duration of 200 s, resulting in the decrease of temperature due to the desorption of the test gas. All test and purging gas flows were maintained in 70 ml/min at 1 bar. The adsorption and desorption cycling repeated 3 times for all samples.

The measurement with wet CO₂ and He as the test gas were performed under the similar conditions to CO₂ except that the injection time for both adsorption and desorption was 1000 s. The total uptake of samples was obtained from the integrated peak area of each adsorption and desorption area in the thermal response curve. This area was divided by the sample mass to compare the normalized uptake of the samples. The peak areas and the baseline of the thermal response curve were obtained using OriginPro 2019 software.

Preparation procedure and characterization of K-PHI

Synthesis and characterization of potassium poly(heptazine imide) was performed according to previous works [1-8]. [108-112, 115, 248, 267]

Preparation and characterization of flavins F1, F2, F3

Flavin **F1** has been synthesized by using the procedure reported by Patrick Pasau and coworkers [9].^[268] The synthesis of **F1** and **F2** are shown in Figure S1 and **F3** is shown in Figure S2.

Synthesis of F1

To a solution of riboflavin (1.13 g, 3 mmol) in acetic acid (30.0 mL) and acetic anhydride (30.0 mL) at room temperature, perchloric acid (1 mL, 70 %) was added dropwise. After complete dissolution of the solid, the reaction mixture was stirred 5 minutes at room

temperature and water (200 mL) was added carefully. The mixture was stirred for another 5 minutes at room temperature and the product was extracted with dichloromethane (3 x 60 mL). The combined organic layers were dried over Na₂SO₄, filtered and concentrated to 5.0 mL. After the addition of a cold solution of diethyl ether (50.0 mL), the orange precipitate was filtered and dried over the weekend in a desiccator protected from light. The desired product **F1** (82 %, 1.34 g) was obtained pure as an orange solid.

¹H NMR (400 MHz, CDCl₃) δ 8.64 (s, 1H), 8.02 (s, 1H), 7.56 (s, 1H), 5.66 (d, *J* = 8.8 Hz, 1H), 5.54 – 5.29 (m, 2H), 4.88 (s, 1H), 4.43 (dd, *J* = 12.4, 2.9 Hz, 1H), 4.24 (dd, *J* = 12.3, 5.7 Hz, 1H), 2.56 (s, 3H), 2.48 – 2.37 (m, 3H), 2.28 (s, 3H), 2.21 (s, 3H), 2.07 (s, 3H), 1.75 (s, 3H).

¹³C NMR (101 MHz, CDCl₃) δ 170.75, 170.43, 170.01, 169.85, 159.43, 154.59, 150.84, 148.27, 137.15, 133.10, 131.37, 115.67, 70.61, 69.57, 69.14, 62.02, 45.17, 21.61, 21.19, 20.94, 20.84, 20.47, 19.60.

HRMS (ESI) = calcd for C₂₅H₂₈N₄O₁₀: 545.1878, found: 545.1889 (+H⁺).

Synthesis of F2

p-Bromobenzoyl chloride (3.150 g, 6 equiv.) was added to an inert solution of riboflavin (0.900 g, 2.39 mmol) at 0 °C containing triethyl amine (2mL, 6.0 equiv.) and DMAP (0.098 g, cat.) in anhydrous DCM (30 mL). After stirring for 12 hours at ambient temperature, the residue was dissolved in H₂O (25 mL) and extracted with DCM (4 x 50 mL). The organic layer was washed with brine (1 x 30 mL), dried over Na₂SO₄, the combined organic solvent was removed under vacuum, and the residue was purified by column chromatography (SiO₂, EtOAc: pet ether; 3: 7) to afford **F2** (1.7 g, 55%) as an orange solid.

¹H NMR (300 MHz, CDCl₃) δ 8.16 (d, *J* = 7.6 Hz, 2H), 8.08 – 7.78 (m, 7H), 7.68 (s, 1H), 7.64 – 7.29 (m, 12H), 6.28 (s, 1H), 6.24 – 6.14 (m, 1H), 6.10 – 5.99 (m, 1H), 4.95 (dd, *J* = 12.3, 3.0 Hz, 1H), 4.63 (dd, *J* = 12.2, 6.0 Hz, 1H), 2.25 (s, 5H), 1.81 (d, *J* = 31.8 Hz, 2H).

Synthesis of F3

Compound **2** (1.496 g, 7 mmol) was dissolved in glacial acetic acid (20 mL). Alloxan (1.0 g, 7 mmol) and boron oxide (0.98 g, 14 mmol) were added. After flushing the system with argon, the reaction mixture was stirred at 60 °C for 4 hours. Water (50 mL) was added, and a small amount was re-dissolved via heating. On cooling, a yellow /green precipitate formed. The solid was collected by vacuum filtration the solid recrystallized from absolute ethanol. The desired product **F3** (62 %, 1.380 g) was obtained pure as an orange solid.

¹H NMR (400 MHz, DMSO-*d*₆) δ 11.40 (s, 1H), 8.18 (dd, *J* = 8.2, 1.5 Hz, 1H), 7.75 (ddd, *J* = 8.7, 7.2, 1.6 Hz, 1H), 7.70 – 7.47 (m, 3H), 7.42 – 7.20 (m, 2H), 6.78 (dd, *J* = 8.6, 1.2 Hz, 1H), 2.77 (q, *J* = 7.6 Hz, 2H), 1.31 (t, *J* = 7.6 Hz, 3H).

¹³C NMR (101 MHz, DMSO-*d*₆) δ 159.59, 155.59, 151.84, 145.50, 139.48, 134.76, 133.68, 131.37, 129.59, 127.59, 125.98, 116.86, 27.96, 15.36.

HRMS (ESI) = calcd for C₁₈H₁₄N₄O₂: 319.1190, found: 319.1195 (+H⁺).

Synthesis of compounds 1 and 2 (F3 precursors)

Preparation of *N*-(4-ethylphenyl)-2-nitroaniline (1): 1-Floro-2-nitrobenzene (5 g, 35.4 mmol), 4-ethyl aniline (4.079 g, 33.6 mmol) and potassium fluoride (4.112 g, 70.8 mmol) were heated to 140°C in 50 mL DMF for 16 h. The crude reaction mixture was diluted with ethyl acetate, filtered through a Celite®-pad and washed with brine and the organic solvent was removed in rota vap. The crude mixture was further purified using column chromatography (silica gel) to get the pure product **1** (7.207 g, 88%).

¹H NMR (300 MHz, CDCl₃) δ 9.47 (s, 1H), 8.20 (dd, *J* = 8.6, 1.6 Hz, 1H), 7.44 – 7.07 (m, 6H), 6.74 (ddd, *J* = 8.5, 6.9, 1.3 Hz, 1H), 2.68 (q, *J* = 7.6 Hz, 2H), 1.27 (t, *J* = 7.6 Hz, 3H).

¹³C NMR (75 MHz, Chloroform-*d*) δ 143.81, 142.23, 136.23, 135.80, 132.96, 129.25, 126.77, 124.95, 117.23, 116.12, 28.55, 15.75.

***N*¹-(4-ethylphenyl)benzene-1,2-diamine (2)**: Palladium on charcoal [0.878 g; (10%)] was added to a solution of 2.0 g (8.25 mmol) *N*-(4-ethylphenyl)-2-nitroaniline in 30 ml of ethyl acetate and shaken at room temperature for 2h in 3 bar H₂ pressure. After completion of the reaction, the reaction solution was filtered off and concentrated to dryness. After drying in vacuo, product was purified through column chromatography to obtained **2**; Yield: (1.682 g, 92%), as a dark red solid.

¹H NMR (300 MHz, CDCl₃) δ 7.18 – 6.92 (m, 4H), 6.92 – 6.62 (m, 4H), 5.12 (s, 1H), 3.76 (s, 2H), 2.58 (q, *J* = 7.6 Hz, 2H), 1.22 (t, *J* = 7.6 Hz, 3H).

¹³C NMR (75 MHz, CDCl₃) δ 142.90, 141.42, 135.48, 129.39, 128.65, 125.16, 123.99, 119.21, 116.15, 115.75, 28.05, 15.92.

HRMS (ESI) = calcd for C₁₄H₁₆N₂: 213.1386, found: 213.1390 (+H⁺)

Preparation of composites C1 (K-PHI/F-1 2:1), C2 (K-PHI/F-2 2:1), C3 (K-PHI/F-3 2:1)

In a 100 mL flask, 0.1 mmol of flavin (54.45 mg of F1 for **C1**, 129.14 mg of F2 for **C2**, 31.83 mg of F3 for **C3**) and 0.2 mmol of K-PHI (100 mg) were dissolved in 25 mL of methanol. Suspension was stirred for 30 minutes. MeOH was evaporated, the solid was transferred into a mortar, ground and put into a porcelain crucible. Solids were heated at 150 °C for 6 hours in oven in air.

CO₂ Photoreduction

General procedure for photocatalytic CO₂ reduction

Photocatalytic CO₂ reduction tests were carried out in a two-necked 200 mL Pyrex glass reactor. A 350 W Xe arc lamp with an AM 1.5 filter was used as the light source. In a typical photocatalytic experiment, 20 mg of the sample was dispersed in 10 mL of deionized water, and dried at 80 °C for 4 h to form a uniform film on the bottom surface of the reactor. Next, NaHCO₃ (0.084 g) was carefully put into a groove on one of the necks. Then these two necks

were sealed with the rubber plugs. After that, this reactor was purged with nitrogen for 1 h to thoroughly remove the air. The CO₂ gas was generated from a simple reaction between H₂SO₄ and NaHCO₃ in the sealed reactor. Particularly, 0.5 mL of 2 M H₂SO₄ was elaborately injected into the groove to react with NaHCO₃. After irradiation, the resulting gas species were monitored and recorded by a gas chromatography (GC-14C, SHIMADZU, JAPAN). No noticeable amount of H₂ has formed due to the fact that the investigated system is free of transition metal co-catalyst, which otherwise would facilitates hydrogen evolution. In the control experiment under the standard conditions employing N₂ saturated with water vapor without addition of CO₂ no carbon-contained species were formed.

Electrochemistry

Preparation of devices for electrochemical measurements using conductive hydrogel.

Synthesis of hydrogel

Hydrogel was synthesized according to the modified procedure reported earlier [10]. [269]PEDOT:PSS solution (1.2 mL, 1.3 wt. % in water), deionized water (1.2 mL), acrylamide (2.6 g), freshly prepared solution of N,N-methylenebisacrylamide in water (0.3 mL, 10 g L⁻¹) and N,N,N,N-tetramethylethylenediamine (15 μL) were mixed. The mixture was stirred for 20 min to obtain homogeneous solution. (NH₄)₂S₂O₈ (0.1 g) was added in one portion to a stirred solution at room temperature. The solution was stirred for 1 min until (NH₄)₂S₂O₈ has completely dissolved. Stir bar was removed and solution was poured into a Petri dish (diameter 143 mm, height 12 mm). The Petri dish was covered with a glass lid. The reaction mixture has self heated and gelled. In 1 h the chamber was sealed with parafilm and left standing at room temperature for 1 week. Hydrogel was obtained as a round piece (diameter 143 mm, thickness 1 mm). Hydrogel was cut into rectangular pieces (height 30 mm, width 20 mm) using scalpel right before assembly of the electrochemical device.

Spray-coating of FTO glass electrodes with photocatalysts

For spray coating of the FTO glass electrodes with the materials, formulations specified in the Table S3 have been used.

Each mixture was sonicated for 10 min to obtain fine dispersion (entries 1-4) or transparent solution (entry 5-7).

A piece of FTO glass (20 mm x 30 mm) was cleaned by sonicating in deionized water for 1 min, followed by rinsing with acetone and drying with pressurized air. FTO glass was placed on the heating plate. The temperature of the plate was maintained at 35°C during the spray-coating procedure. A specified in the Table volume of the specific mixture (0.44-0.96 mL) was loaded into the air brush container. The mixture was sprayed onto the conductive side of the FTO glass. The rate of material deposition was monitored visually to ensure that only fine droplets are deposited on the surface of FTO-glass.

Assembly of the electrochemical device

The device was assembled from the following elements:

1. FTO glass electrode coated with the respective material – 1 piece;
2. hydrogel (height 30 mm, width 20 mm) – 3 pieces;
3. copper wire (diameter 0.19 mm, length 30 mm) – 1 piece;
4. copper gauze (height 30 mm, width 20 mm) – 1 piece;
5. glass slide (height 25 mm, width 20 mm, thickness 1 mm) – 1 piece.
6. Parafilm stripes (width 5 mm, length)

The device was assembled in the following order stacking the elements above each other:

1. FTO glass electrode, coated side up (working electrode);
2. A piece of hydrogel
3. Copper wire (pseudo-reference electrode)
4. A piece of hydrogel

5. Copper gauze (counter electrode)
6. A piece of hydrogel
7. Glass slide

Attention was paid to ensure the absence of air bubbles in the assembled device and absence of the direct electric contact of the copper wire (reference electrode of the device) with working electrode and counter electrode. In principle, pieces of hydrogel provide good adhesion of the elements of the device without additional bracing. Nevertheless, to ensure good electric contact between the elements, the top and bottom sides of the device were wrapped with parafilm stripes (see figures below for appearance of the assembled device). The devices are stable for at least 24 h without obvious signs of copper corrosion. Extended storage of the devices results in oxidation of copper that is observed as green solid. Therefore, the lifetime of the device is tentatively limited to 24 h. Using of platinum gauze and platinum wire as counter electrode and pseudo-reference electrode respectively could increase the life time of the device. However, due to much lower cost, copper was used in the present study.

Electrochemical tests

The tests were performed using only freshly prepared devices. For reference, a clean FTO glass was used as a working electrode. In the electrochemical tests, FTO glass was used as the WE, copper wire as the RE and copper gauze as CE. During the tests fan was used to blow air at the device (glass slide side) and maintain the device temperature at 25-30°C. White LED with optical power 467 mW cm⁻² at the electrode surface (FTO glass slide) was used as the light source.

Composite C3 long-term stability tests

Stability of the composite C3 has been assessed based on OCP and chronoamperometry experiments of freshly prepared photoelectrodes and after storage for 3 hours (Figure S23). In OCP test, photoelectrode retained its light response after storage for 3 hours (Figure S23a). In CA experiment, dark current increased (ca. 16 times) that could be explained by decrease of the conductivity of the electrochemical cell. The amplitude of photocurrent in CA experiment increased by 7 times after storage the photoelectrode for 3 hours.

Given that in this study, hydrogel was used as a conductive medium instead of liquid electrolyte, these results could be explained by gradual increase of the interface area between the photoactive layer of the electrode and a layer of hydrogel.

In this study the designed electrochemical cell was used to evaluate response of the composites and their components to light rather than use them as photoelectrodes in bulk electrochemical synthesis. A series of materials have been tested under the same conditions (time, electrochemical measurements parameters, light intensity, etc.) that ensures comparison of data.

Thermogravimetric analysis (TGA)

TGA of the composite C2 shows loss of the mass between 250-350°C that matches to the onset of decomposition temperature for pure flavin F2 (Figure S19). However, the percentage of the mass lost in the composite C2 is ca. 20 %, while the calculated value for the composite C2 (assuming homogeneous mixing of two components) is ca. 36 wt.%. The difference (ca. 16%) implies that the shell made on K-PHI nanoparticles stabilizes flavin core.

DFT Calculations

DFT calculations were carried out using the Vienna Ab Initio Simulation Package (VASP) [11, 12] [270] [271] employing the Bayesian error estimation functional with van der Waals corrections (BEEF-vdW) [13, 14][272] the projector-augmented wave (PAW) potentials [15, 16] and energy cutoff of 450 eV.[273]

Bulk K-PHI was optimized with unit cell $K_3C_{12}N_{17}$, interlayer distance was found to be 3.514 Å. After that slab of 2*2 unitcells was used in calculation of flavin F3 adsorption. To reduce computational costs, flavin F3 has been chosen due to smaller number of atoms. All atoms of K-PHI were frozen, while all atoms of flavin – relaxed. Flavin was placed over C_6N_7 -unit and stayed there during the optimization.

To estimate charge transfer 2 different approaches were used: 1) charge density difference was calculated by subtracting charge densities of individual subparts (Flavin molecule and K-PHI slab) from charge density of whole system (VTST-scripts [17] was used for manipulating with CHGCAR files and VMD [18] for visualization). On Figure S35 red isosurface corresponds to decrease of charge density and green/yellow one – to increase. Both isosurfaces plotted with cutoff 0.0015 (First) 0.002 (Second). One can see that charge density shifts occurs on flavin, but shift to K-PHI is very small.

2) Bader charges were calculated using VTST-scripts and bader-code [19].[274] It was found that charge shift between flavin and K-PHI is small (0.023 electron).

Supplementary Figures

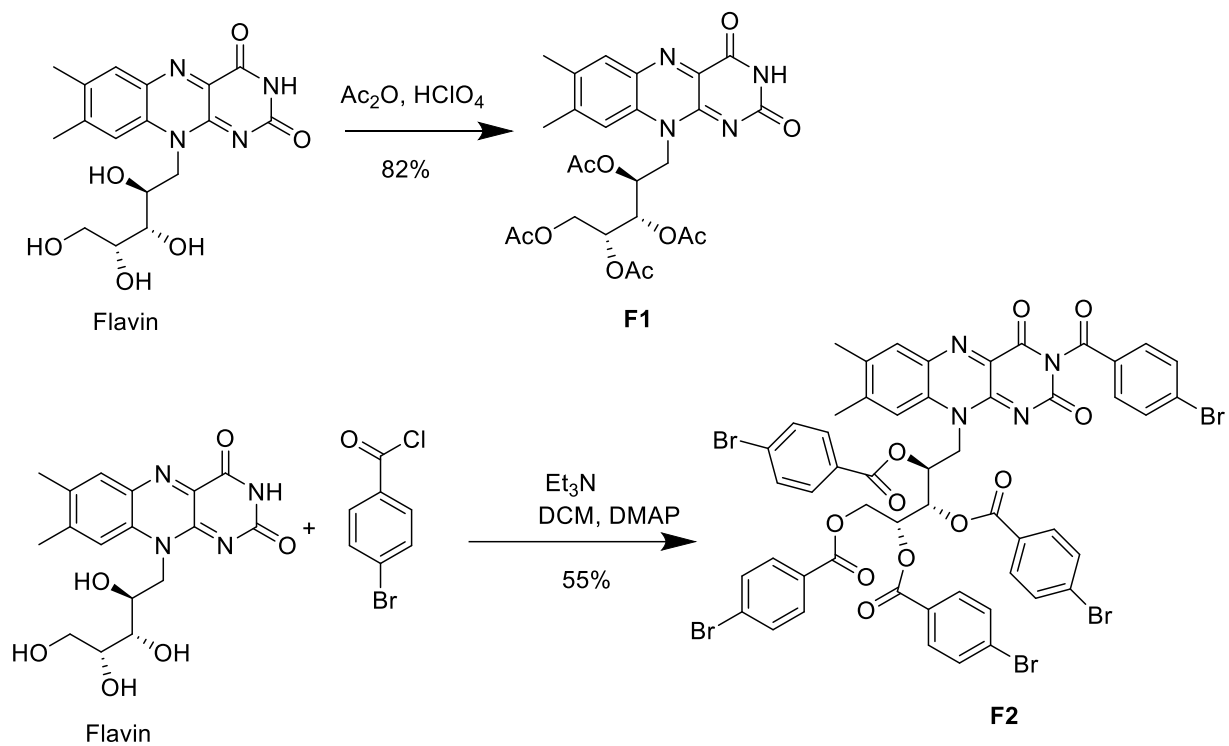


Figure S1. Scheme for the preparation of F1 and F2

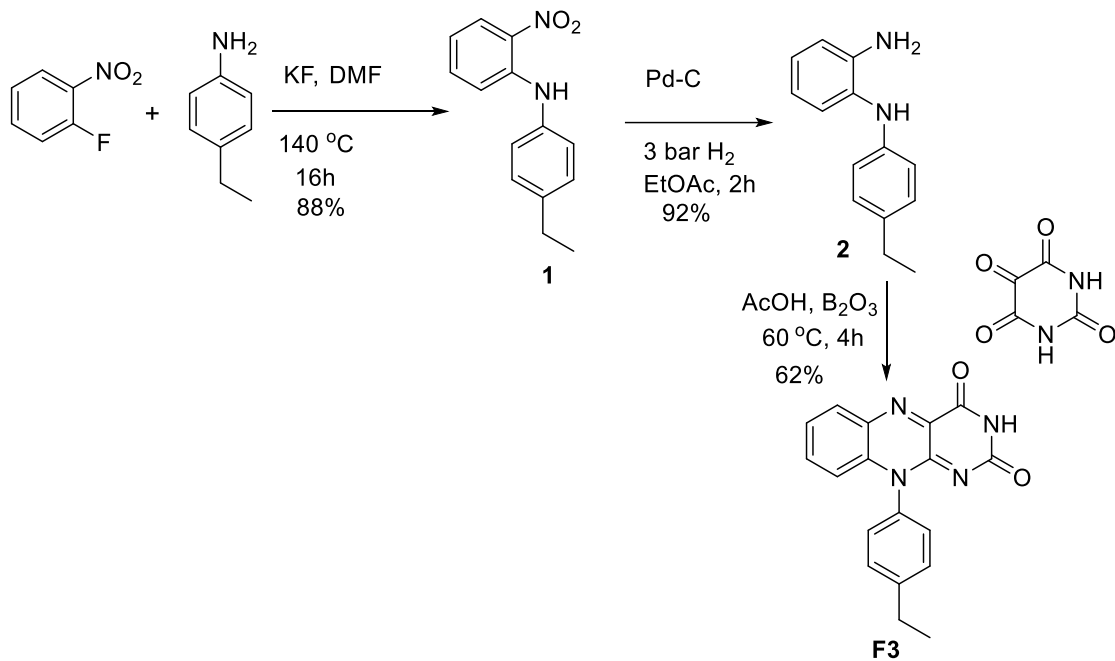


Figure S2. Scheme for the preparation of F3

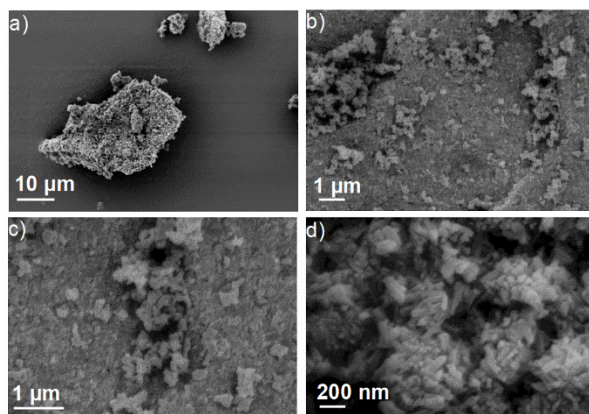


Figure S3. SEM images of K-PHI

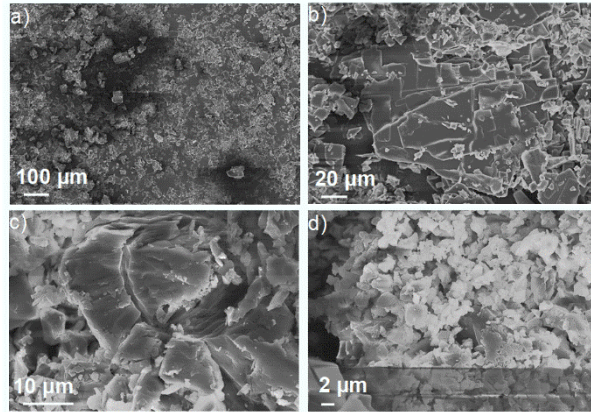


Figure S4. SEM images of F1

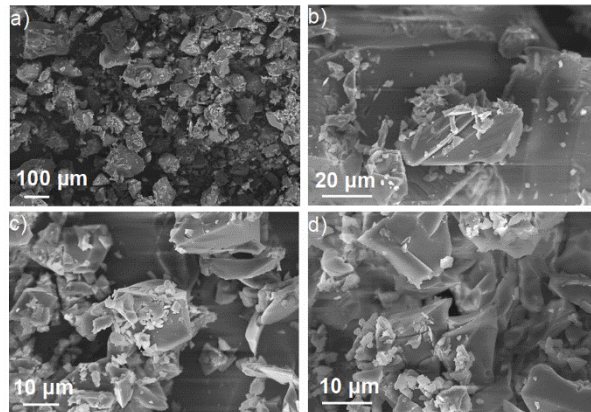


Figure S5. SEM images of F2

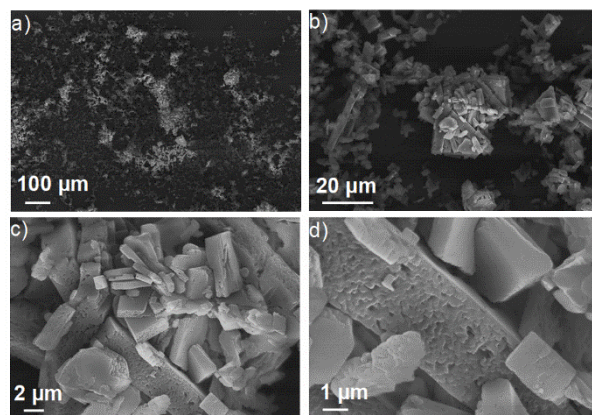


Figure S6. SEM images of F3

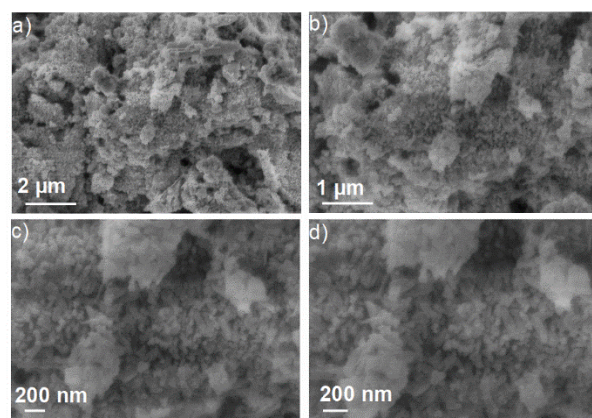


Figure S7. SEM images of C1

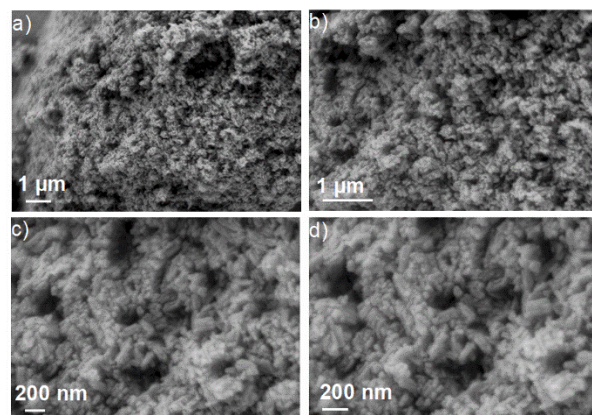


Figure S8. SEM images of C2

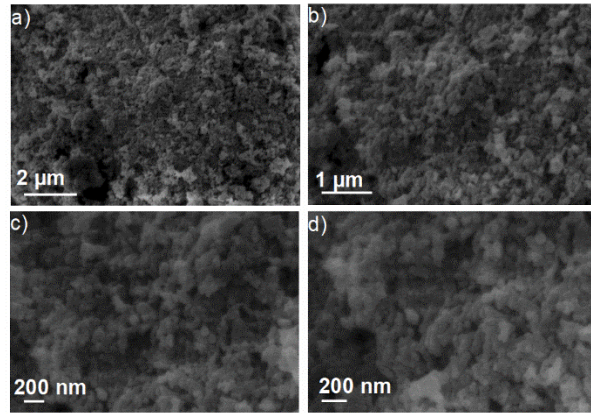


Figure S9. SEM images of C3

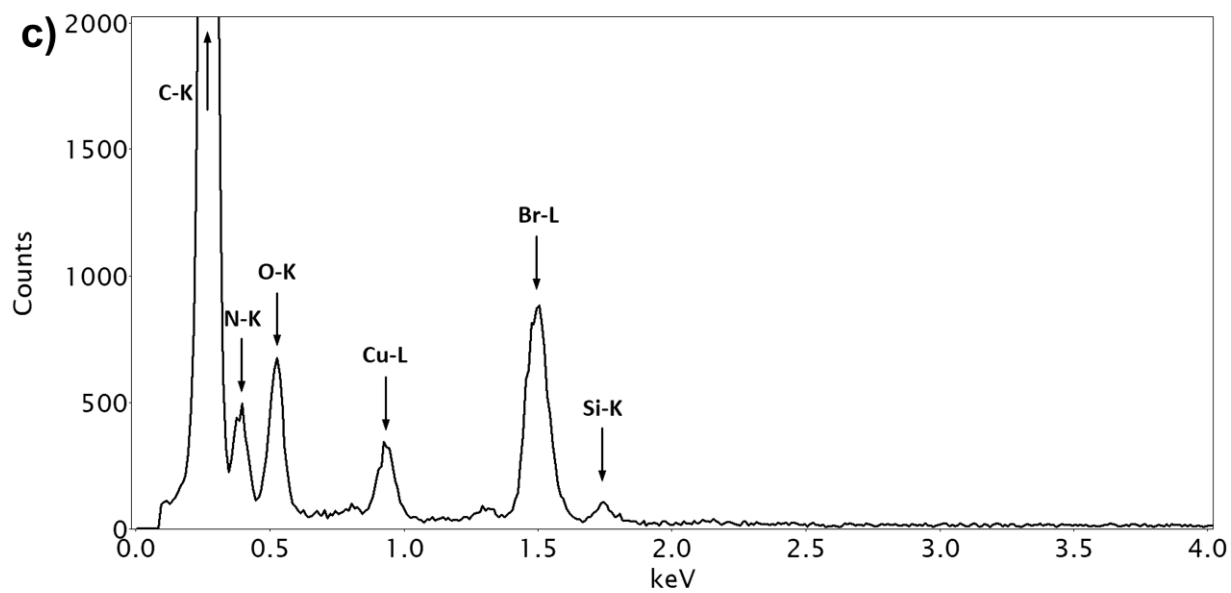
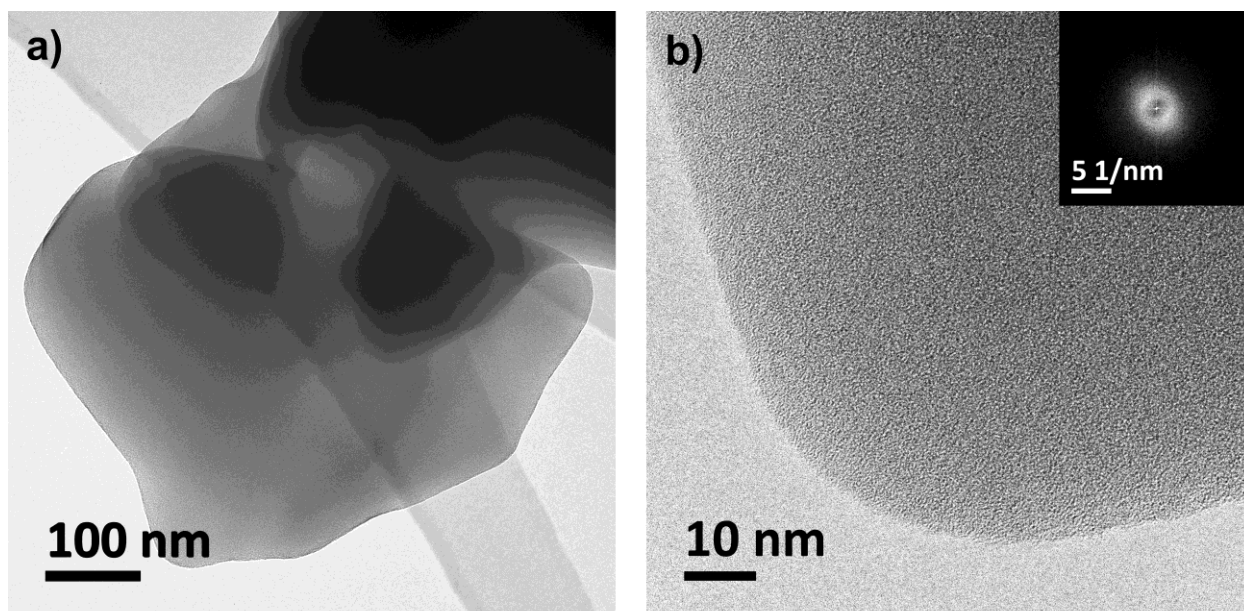


Figure S10. TEM (a,b) and TEM-EDX (c) spectra of the flavin F2.

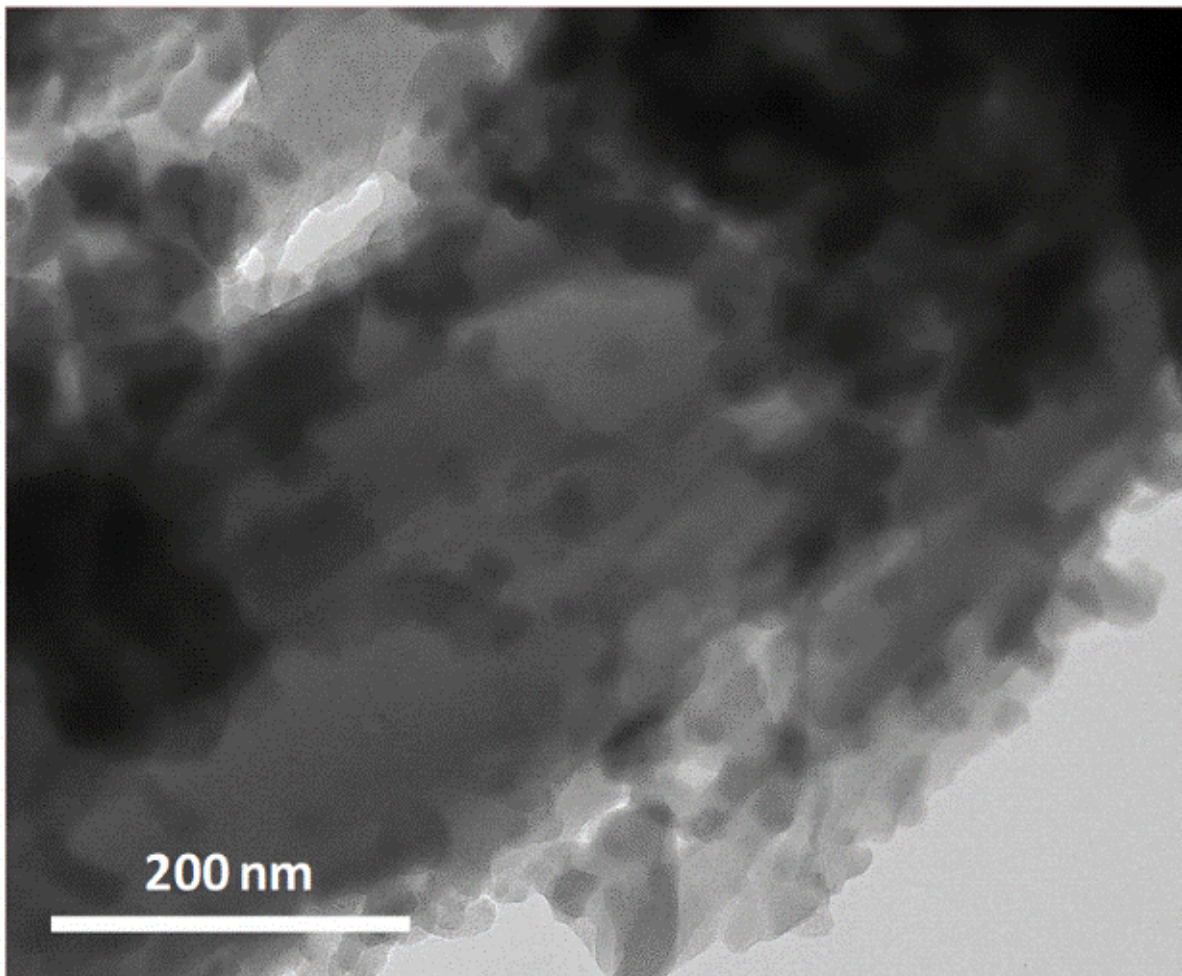


Figure S11. TEM image of composite C2. Overview of the composite material

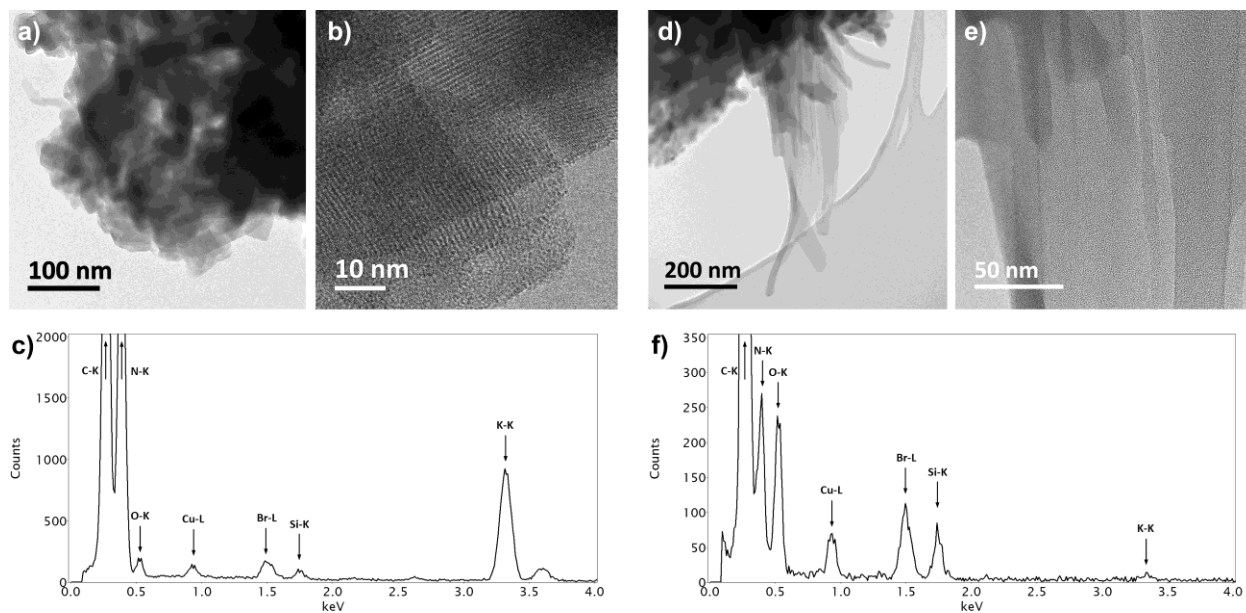


Figure S12. TEM images of K-PHI-rich region (a,b) and flavin-rich region (d,e) of the composite C2. TEM-EDX spectra of the K-PHI-rich region (c) and the flavin-rich region (f) of the composite C2.

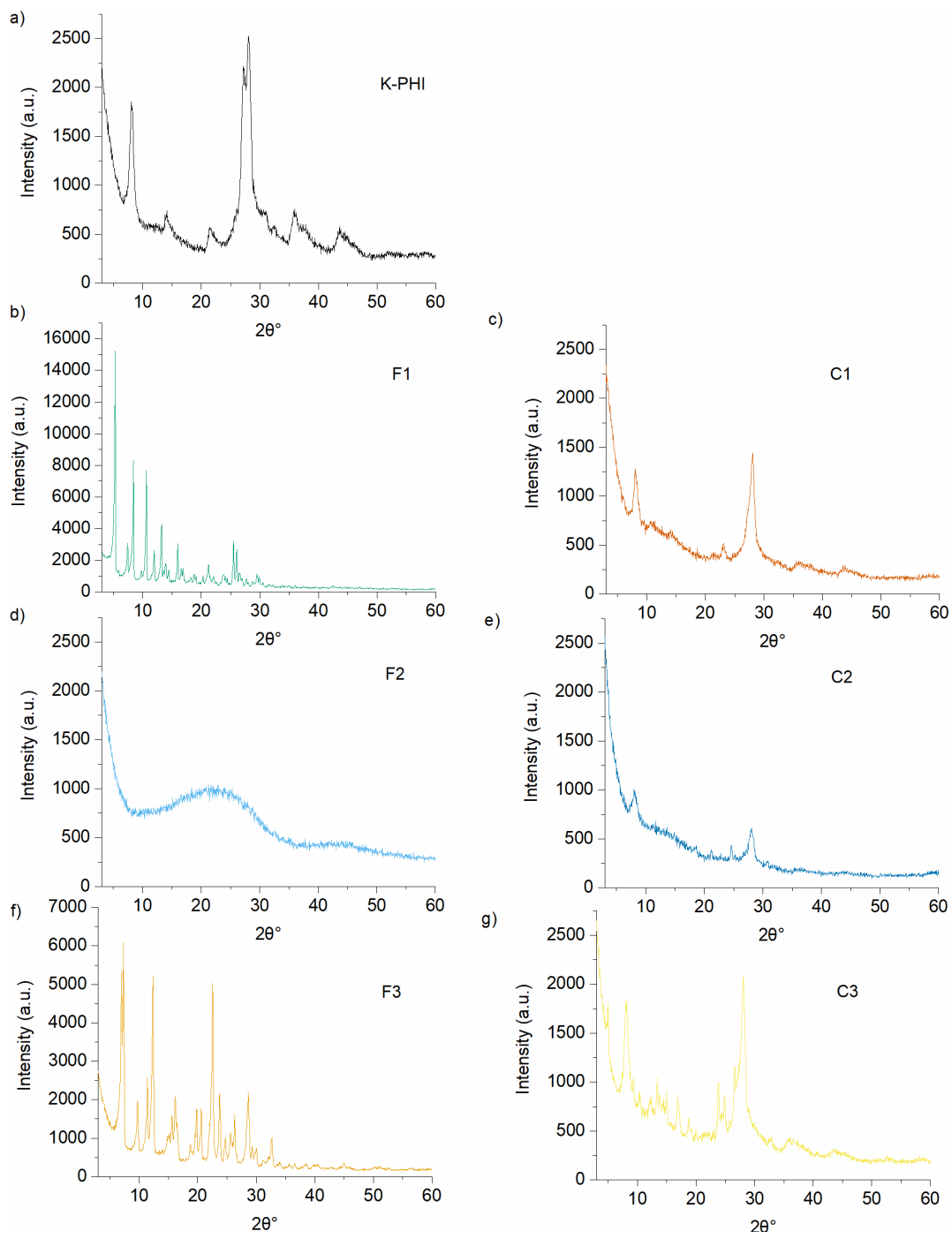


Figure S13. XRD analysis

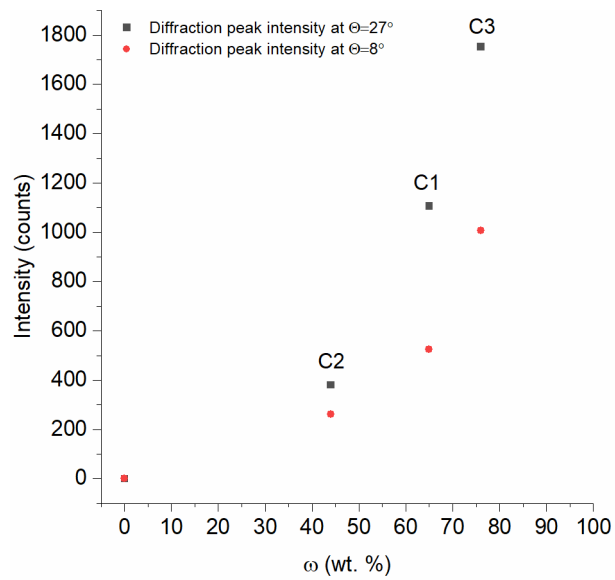


Figure S14. Dependence of K-PHI diffraction peaks intensities at $\theta=8^\circ$ and $\theta=27^\circ$ versus K-PHI content in the composites.

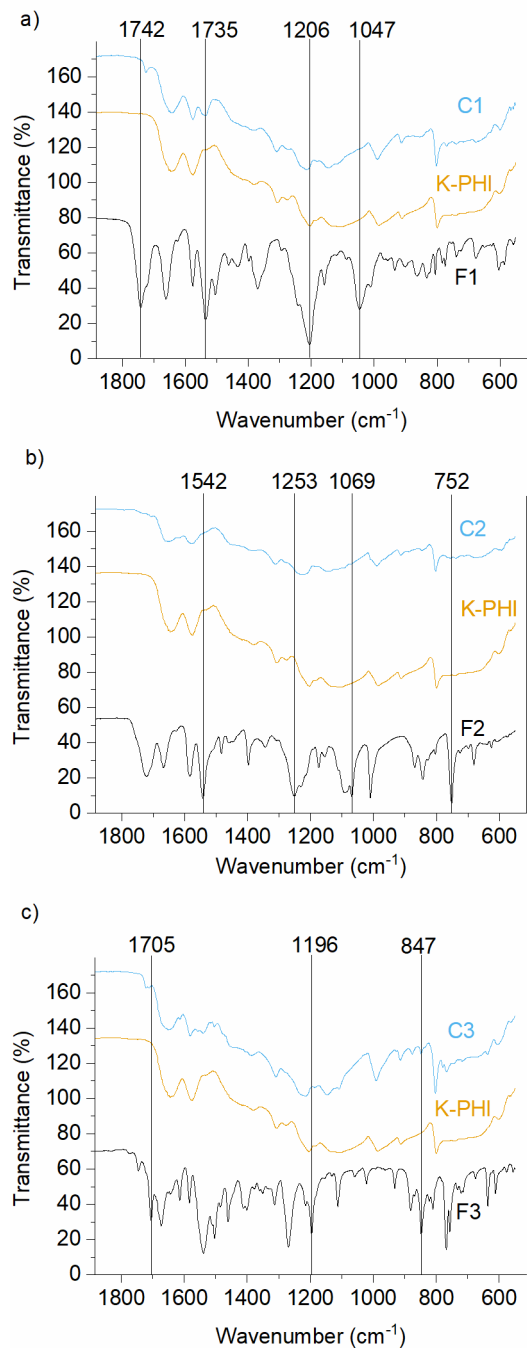


Figure S15. IR spectra

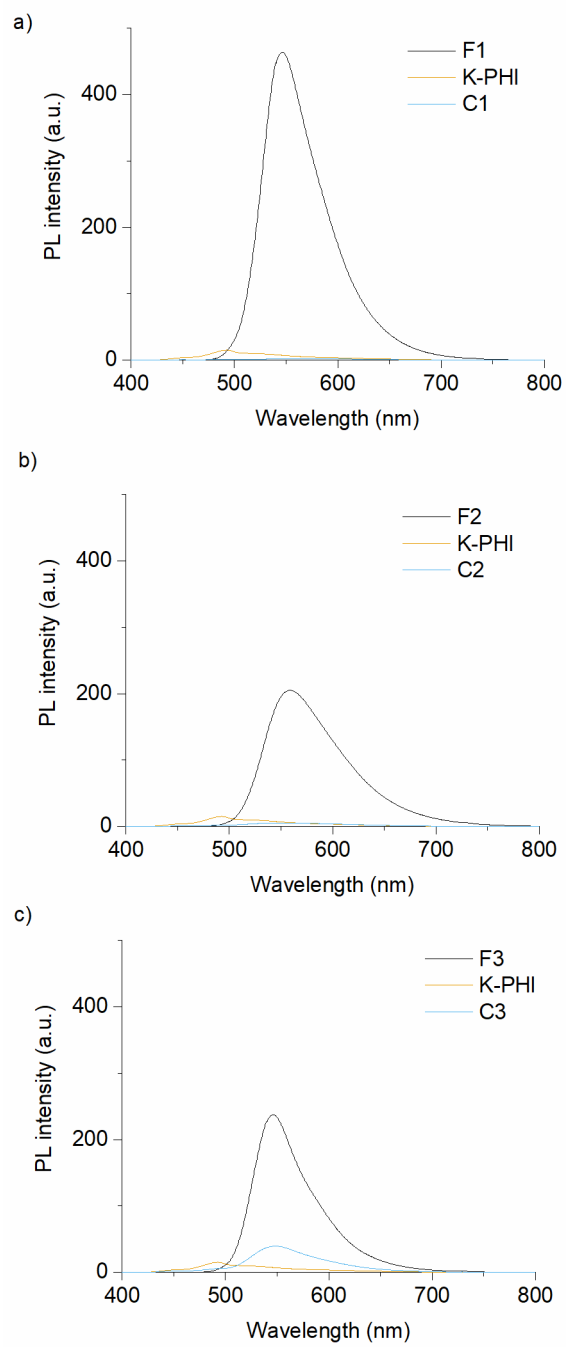


Figure S16. Emission spectra in solid state

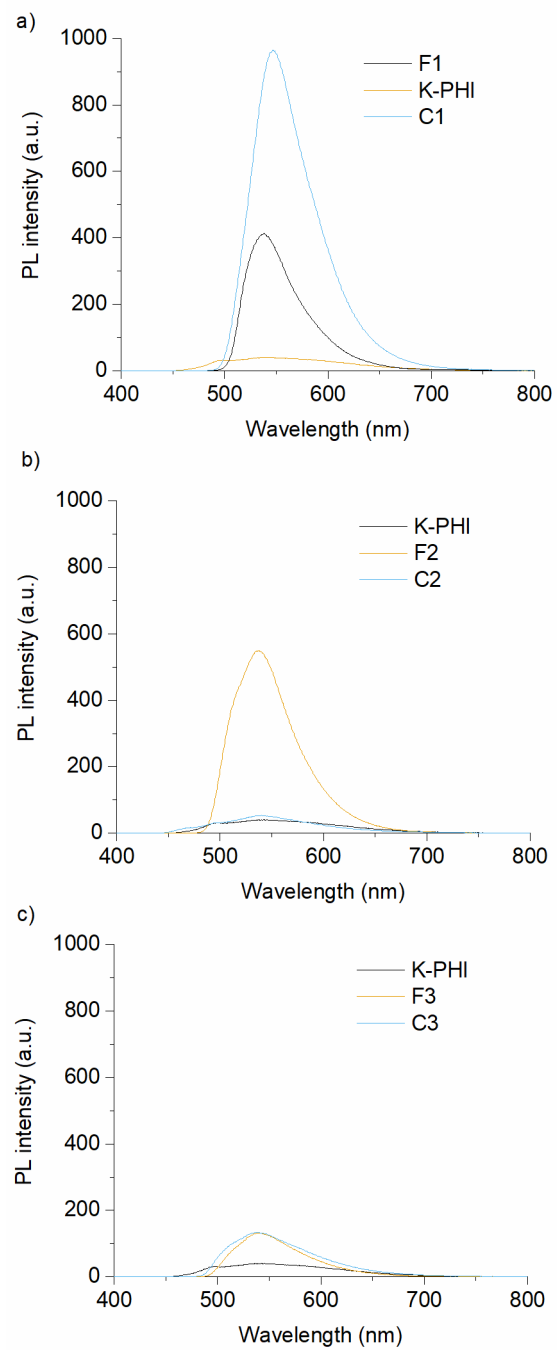


Figure S17. Emission spectra in solution/dispersion

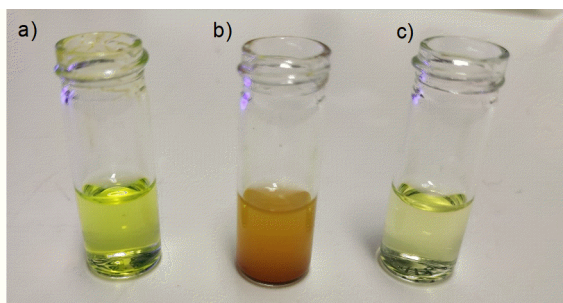


Figure S18. Filtration test pictures. a) Dissolved F1; b) Dispersed C1 c) Solution containing F1 after filtration

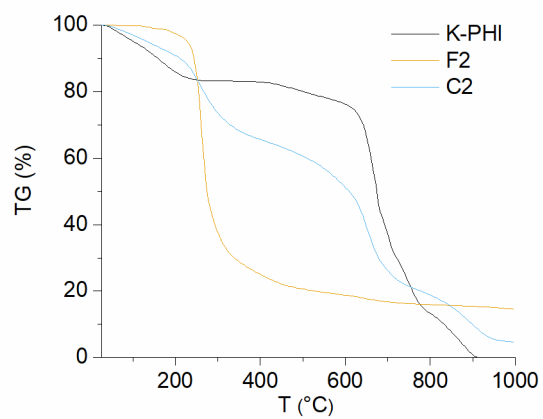


Figure S19. Thermogravimetric analysis of K-PHI, F2 and C2

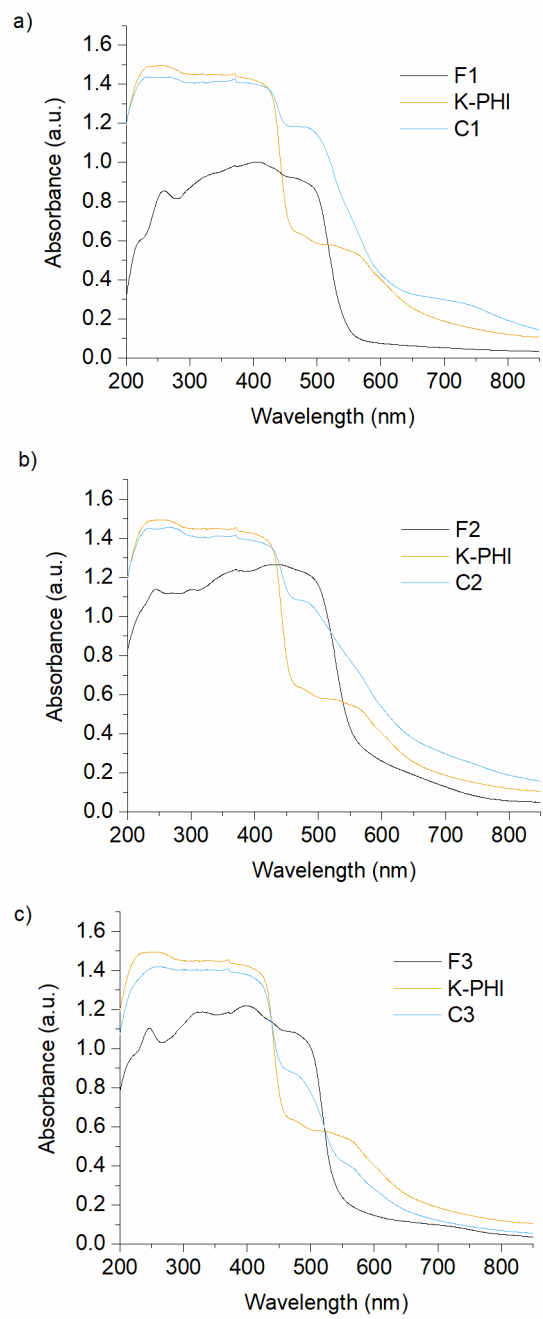


Figure S20. Absorption spectra

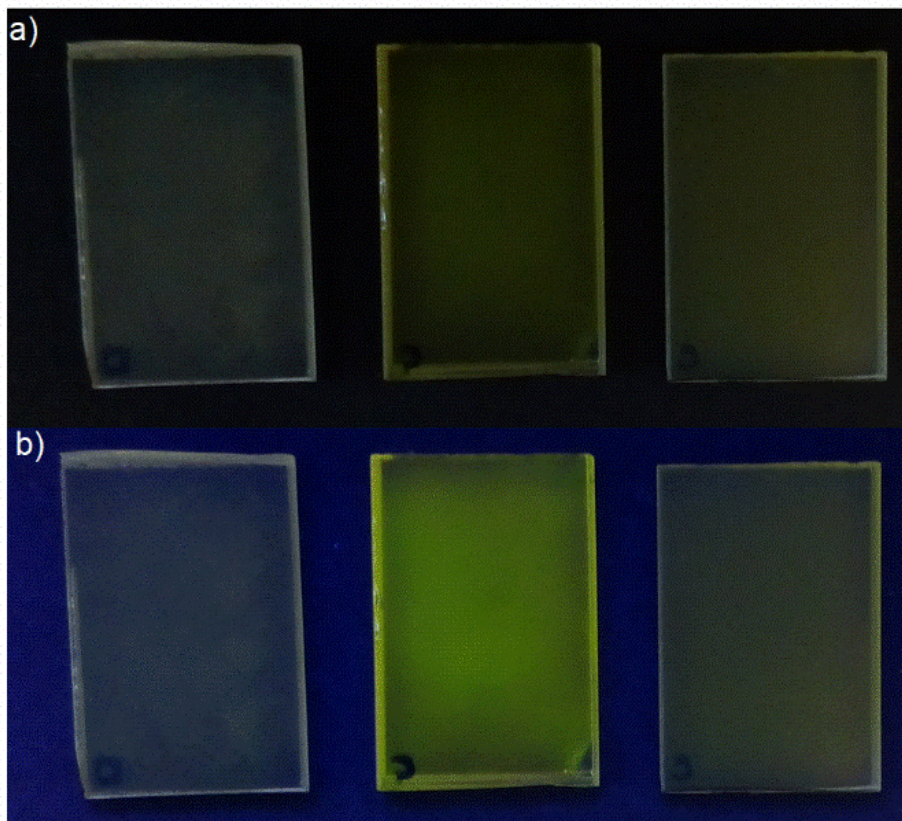


Figure S21. Representative pictures of homemade photo-cathodes; from left to right: K-PHI, F1, C1. a) under visible light irradiation
b) under irradiation at 366 nm

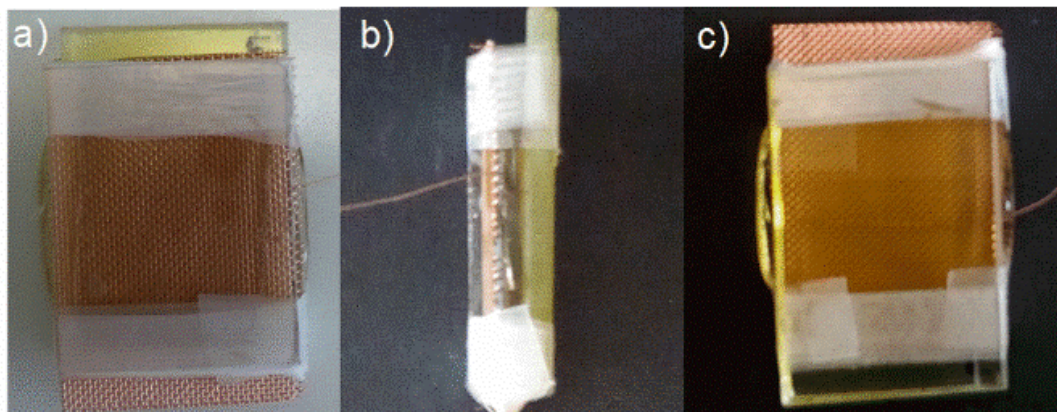


Figure S22. Representative pictures of homemade built photoelectrochemical device: a) Front side view, showing the counter electrode in copper; b) Left side view, showing the sandwich layers composition; c) back side view, showing the photo-cathode made with semiconducting material

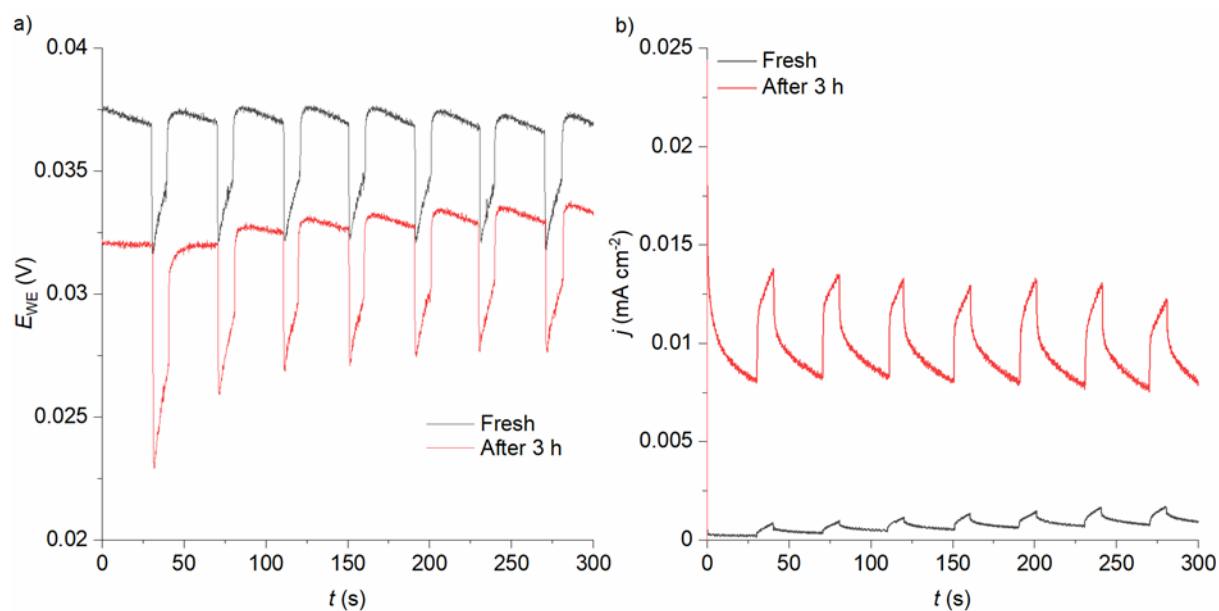


Figure S23. Long-term stability test of the electrochemical device based on the composite C3. Electrochemical device was cooled with axial fan. Irradiation using White LED 467 mW/cm² at 3 cm distance. a) Open circuit voltage. b) Chronoamperometry. Voltage 0.5 V.

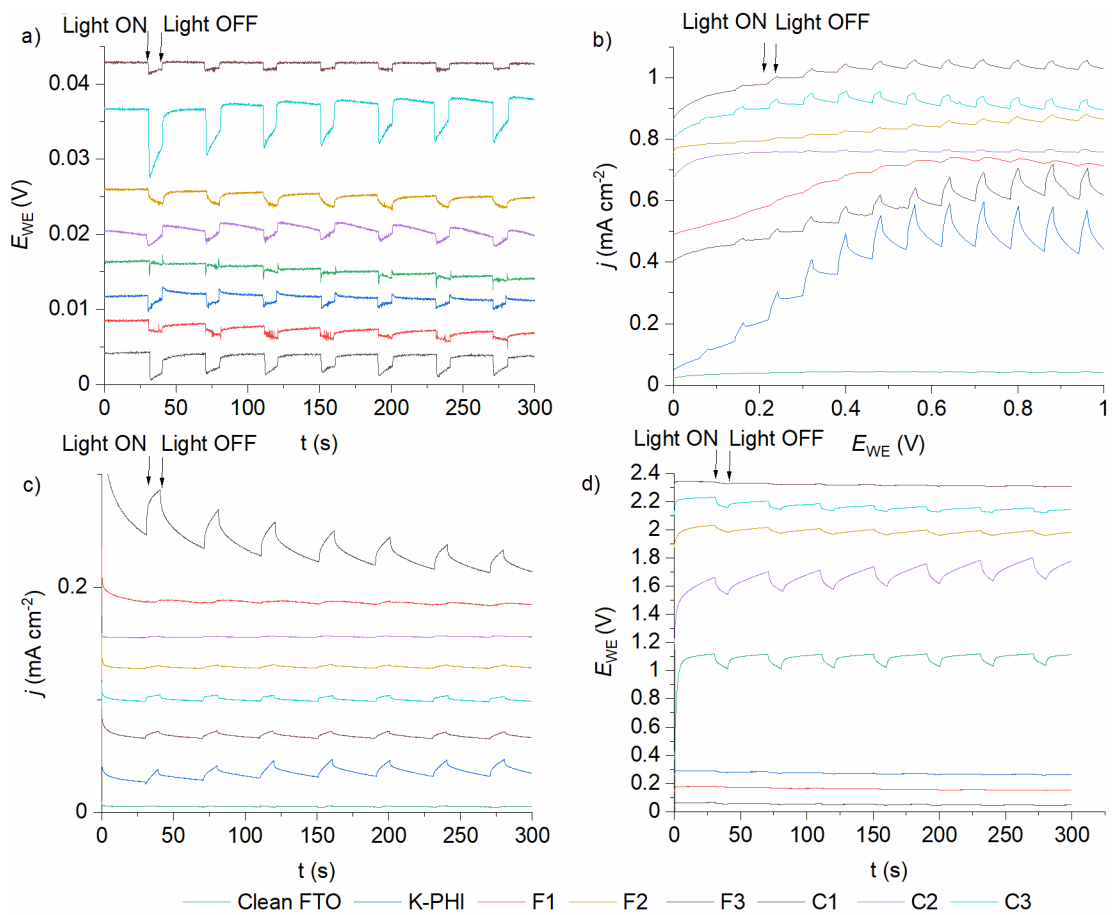


Figure S24. Electrochemical measurements. Herein data is plotted in stack. Electrochemical device was cooled with axial fan. Irradiation using White LED 467 mW/cm² at 3 cm distance. a) Open circuit voltage. b) Linear sweep Voltammetry c) Chronoamperometry. Voltage 0.5 V. d) Chronopotentiometry. Current 10 μ A.

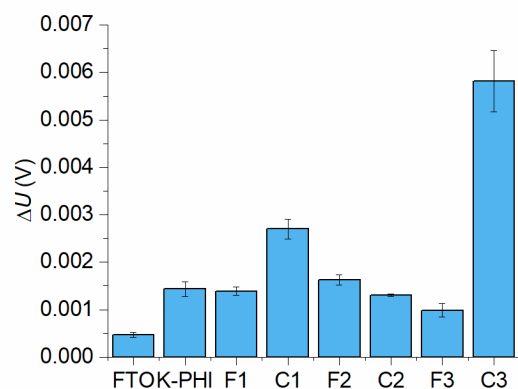


Figure S25. OCP change under light irradiation. Mean values were calculated based on 7 cycles. Error bars correspond to standard deviation calculated based on the data of 7 cycles.

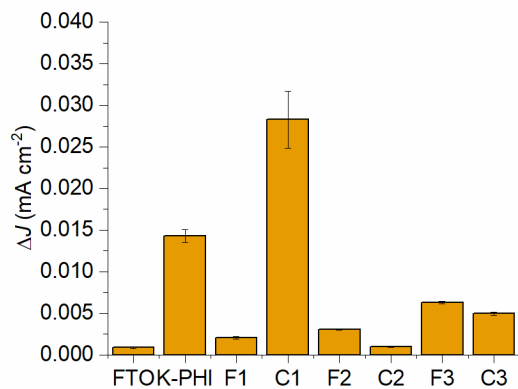


Figure S26. Photocurrent density change in the chronoamperometry (CA) experiments. Mean values were calculated based on 7 cycles. Error bars correspond to standard deviation calculated based on the data of 7 cycles. Larger error bars in case of composite C1 is explained by lower stability of the electrode during the electrochemical measurements.

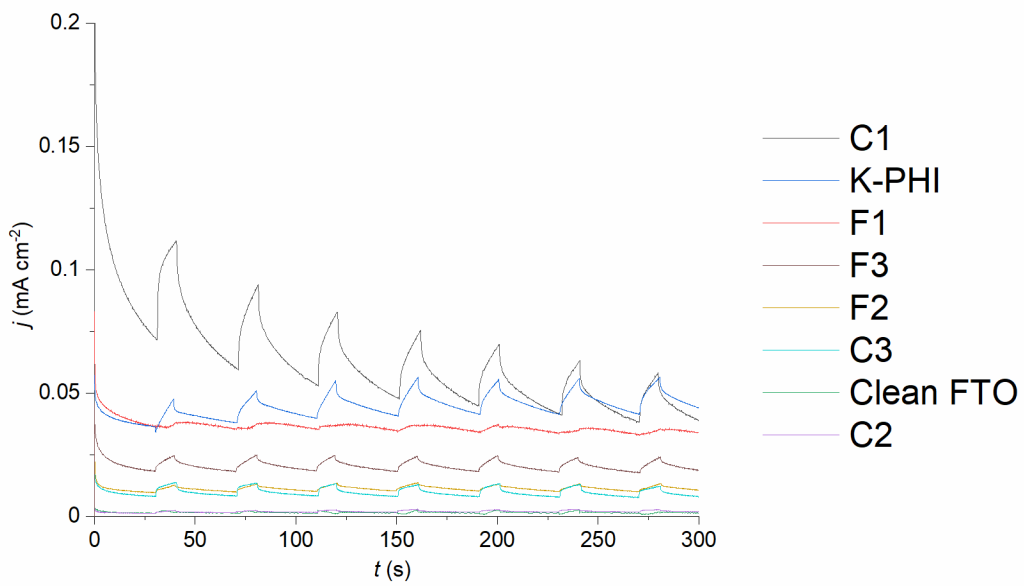
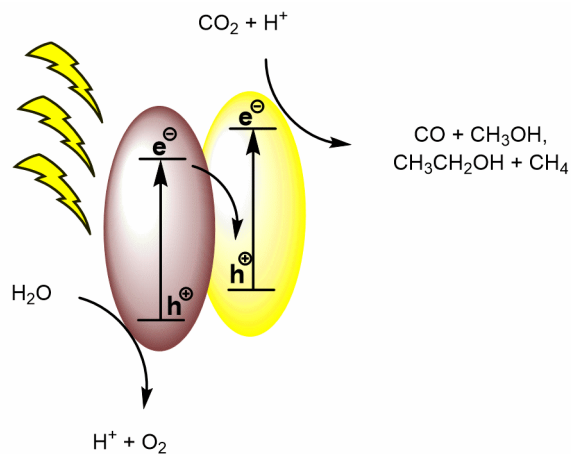


Figure S27. Chronoamperometry. Voltage 0.5 V. Absolute values are shown.



	E_{Red} (V vs. NHE)
$\text{CO}_2 + e^- \longrightarrow \text{CO}_2^{\cdot-}$	-1.90
$2\text{H}_2\text{O} \longrightarrow \text{O}_2 + 4\text{H}^+ + 4e^-$	+0.81
$\text{CO}_2 + 2\text{H}^+ + 2e^- \longrightarrow \text{CO} + \text{H}_2\text{O}$	-0.53
$\text{CO}_2 + 6\text{H}^+ + 6e^- \longrightarrow \text{CH}_3\text{OH} + \text{H}_2\text{O}$	-0.38
$2\text{CO}_2 + 12\text{H}^+ + 12e^- \longrightarrow \text{CH}_3\text{CH}_2\text{OH} + 3\text{H}_2\text{O}$	+0.08
$\text{CO}_2 + 8\text{H}^+ + 8e^- \longrightarrow \text{CH}_4 + 2\text{H}_2\text{O}$	-0.24

Figure S28. Proposed mechanism and Redox potential of CO_2 ; All potentials are reported from reference [20]^[275] and [21]^[276]

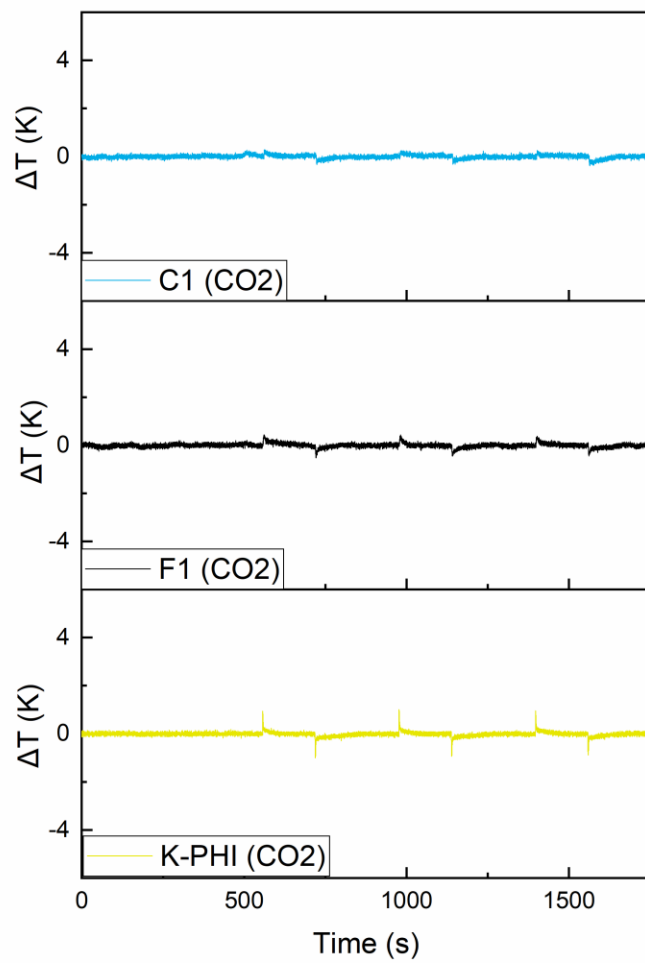


Figure S29. Thermal response of materials to dry CO₂.

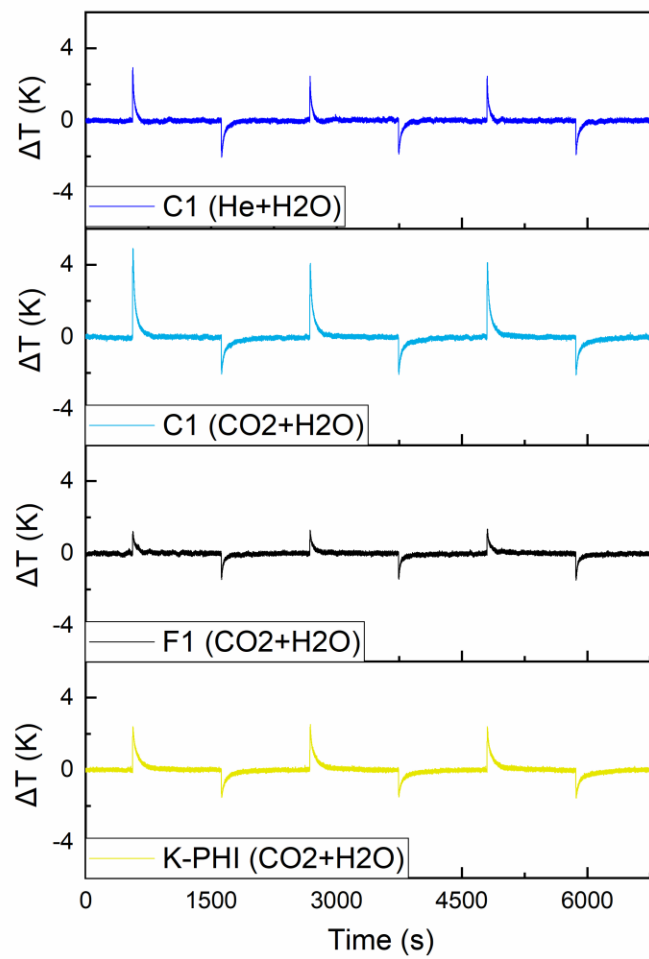


Figure S30. Thermal response of materials to wet CO₂.

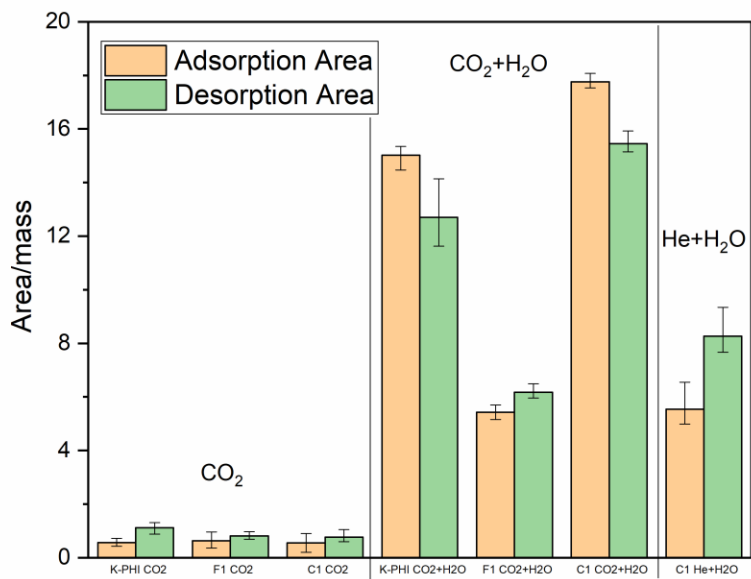


Figure S31. Peaks areas summary.

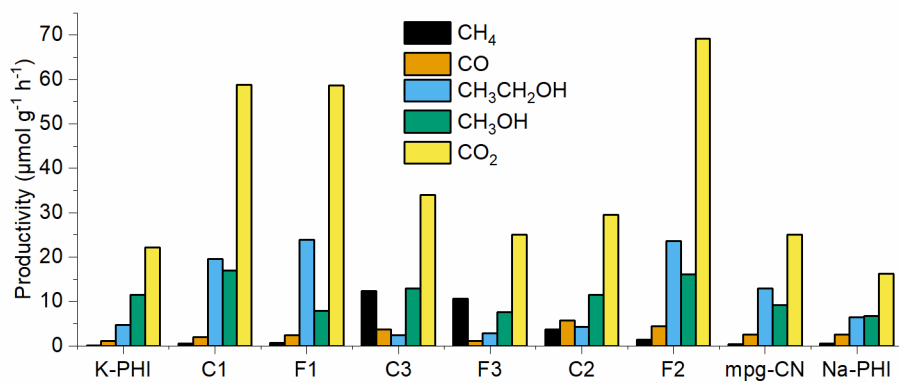


Figure S32. CO₂ Photoreduction results in the gas/solid photoreactor

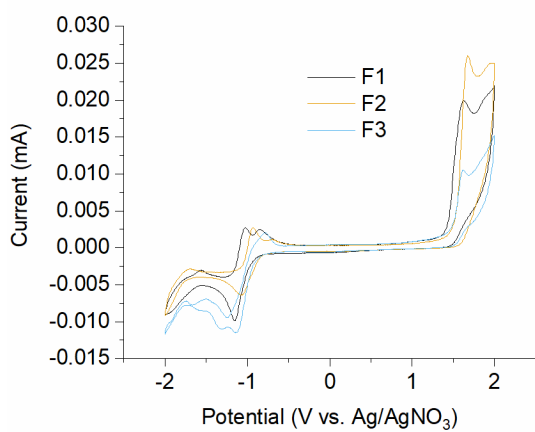


Figure S33. CV measurements of flavins to determine oxidation and reduction potentials

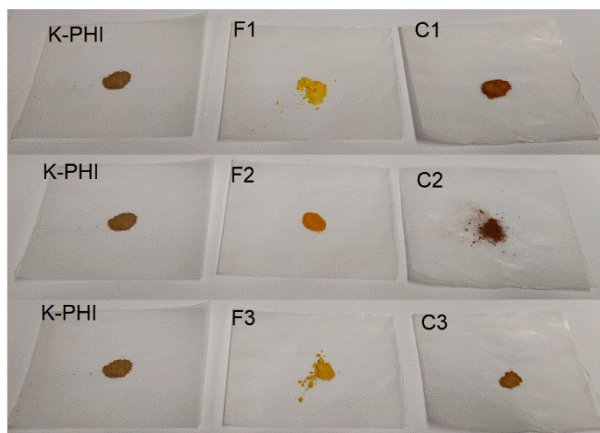


Figure S34. Pictures of compounds used in this work in comparison

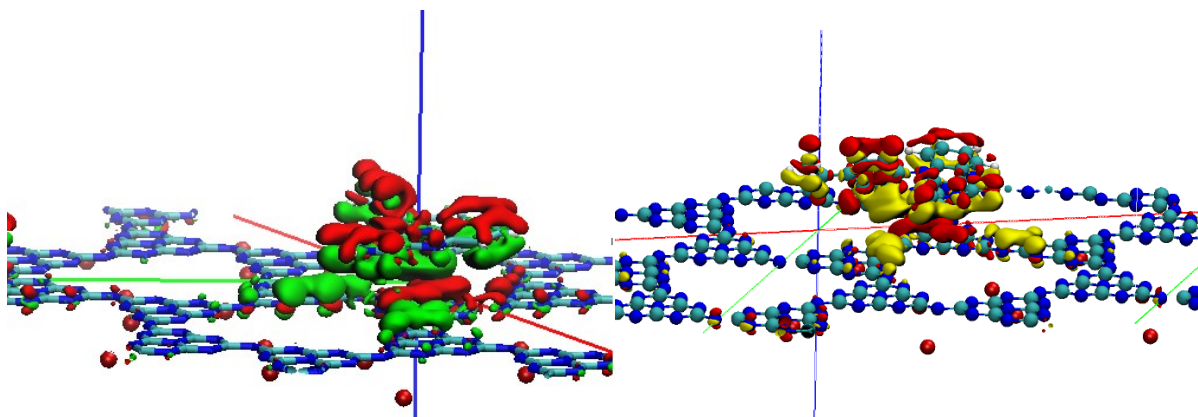


Figure S35. a) Charge density difference. b) visualizations of the same isosurface

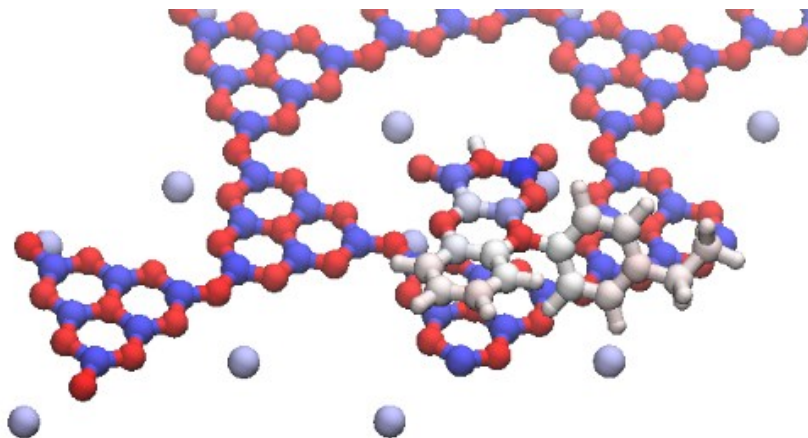


Figure S36. Coloring of structure by bader-charges

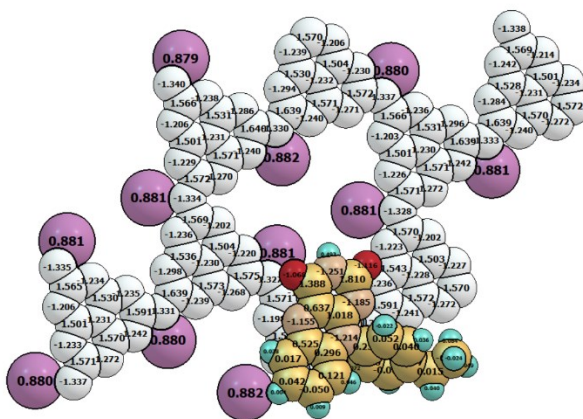


Figure S37. Bader charges

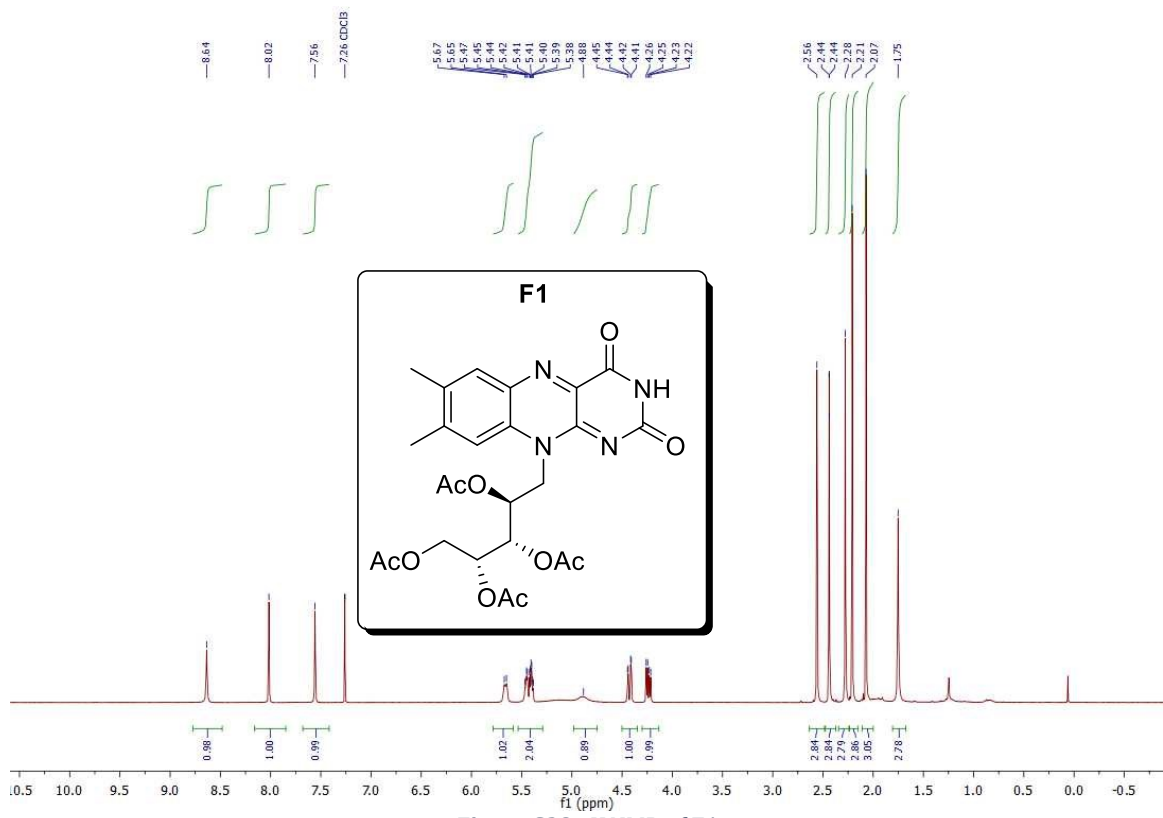


Figure S38. ¹H NMR of F1

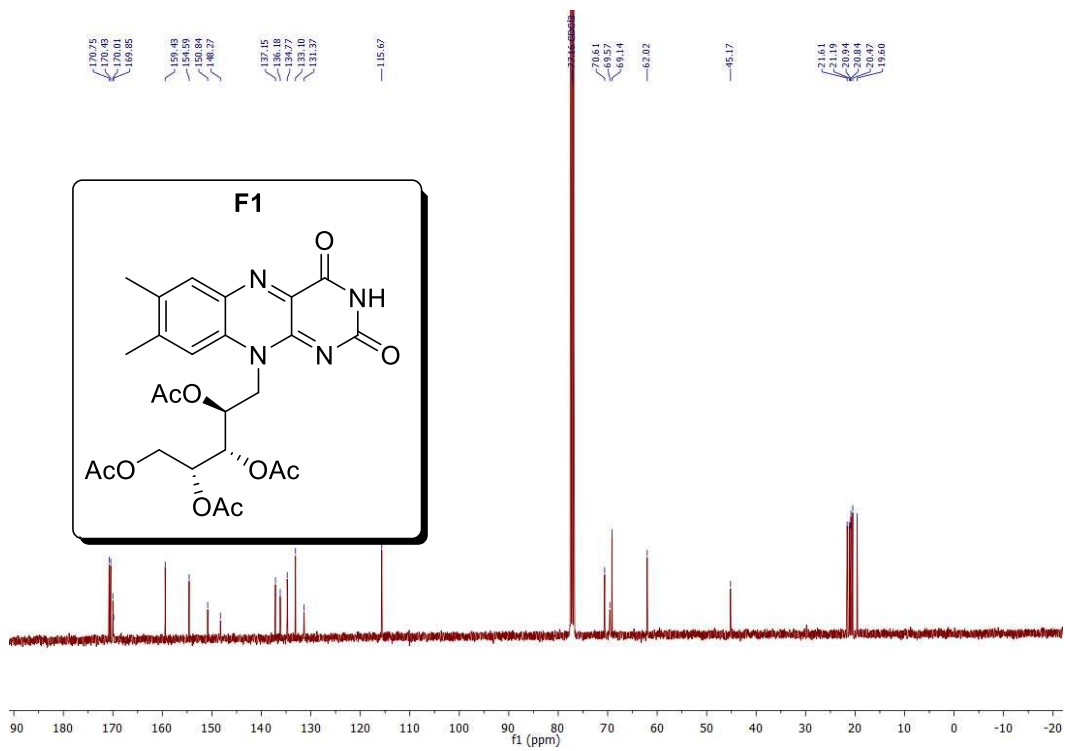


Figure S39. ¹³C NMR of F1

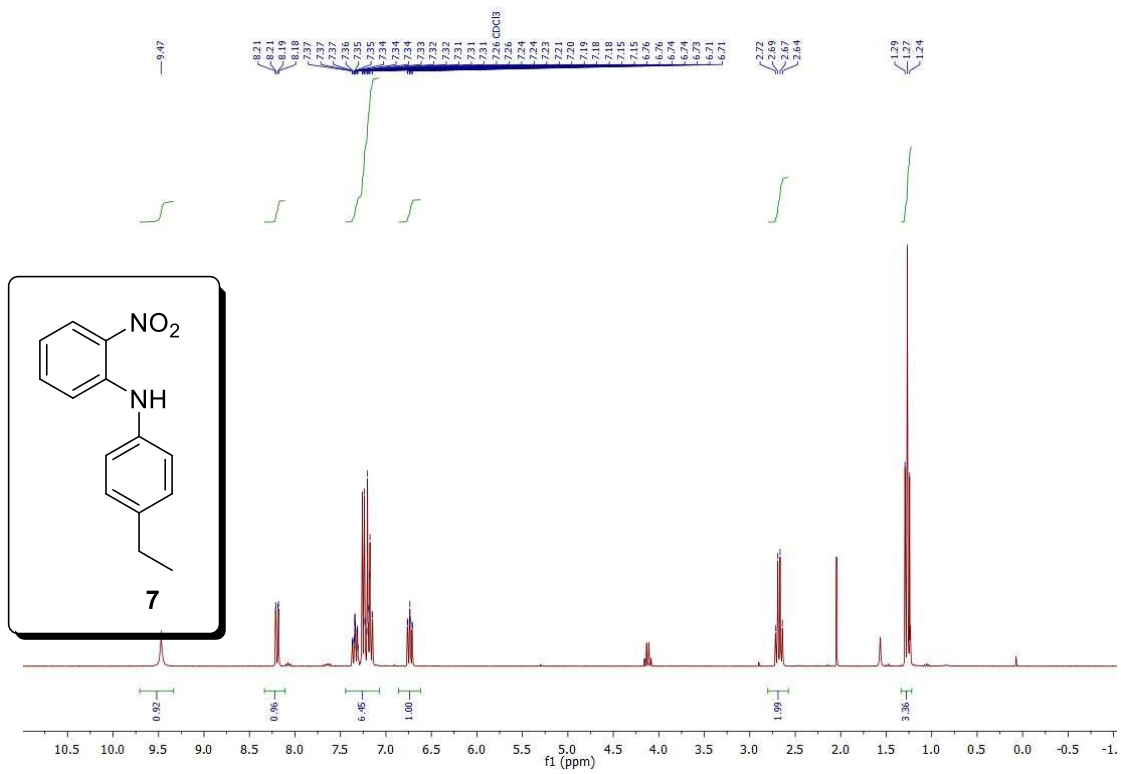


Figure S41. ¹H NMR of 1

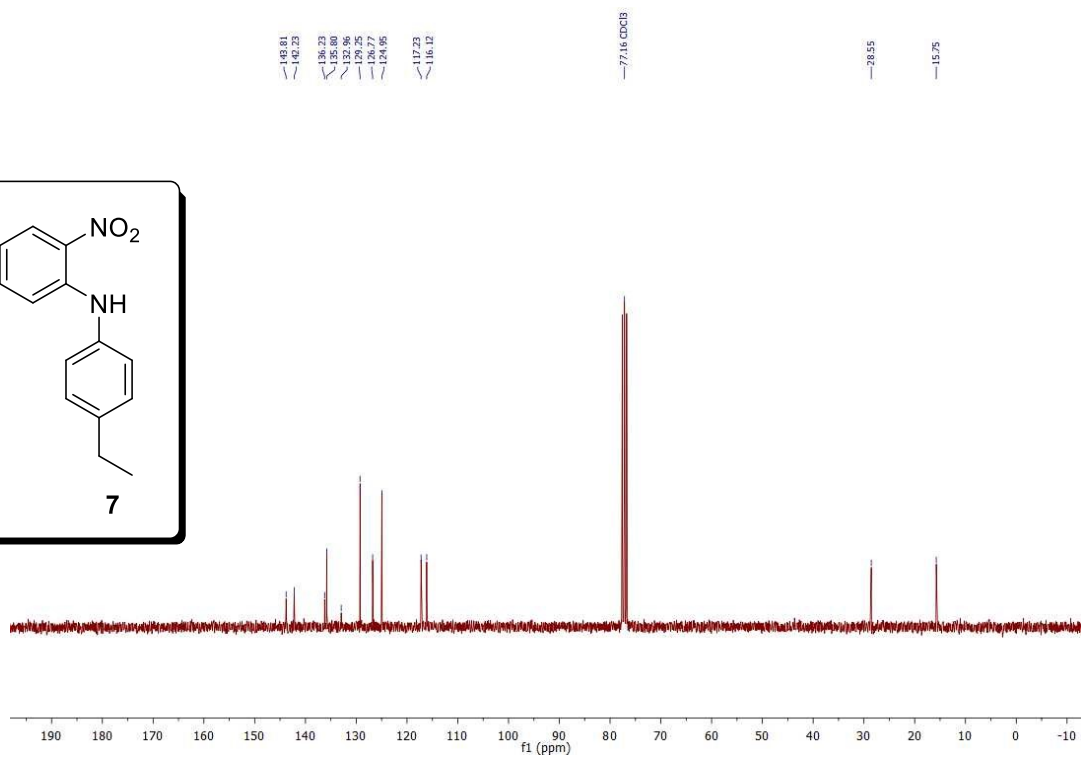
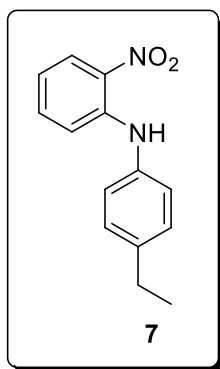


Figure S42. ¹³C NMR of **1**

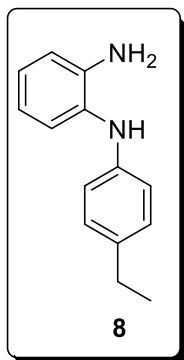
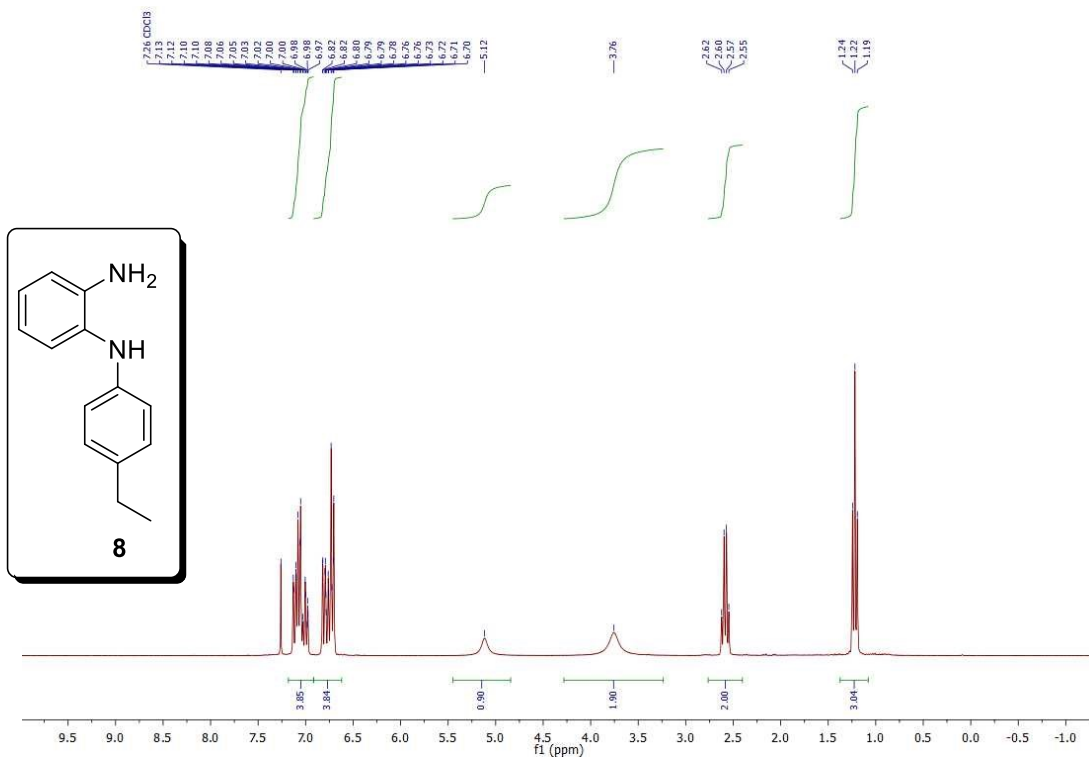


Figure S43. ¹H NMR of 2

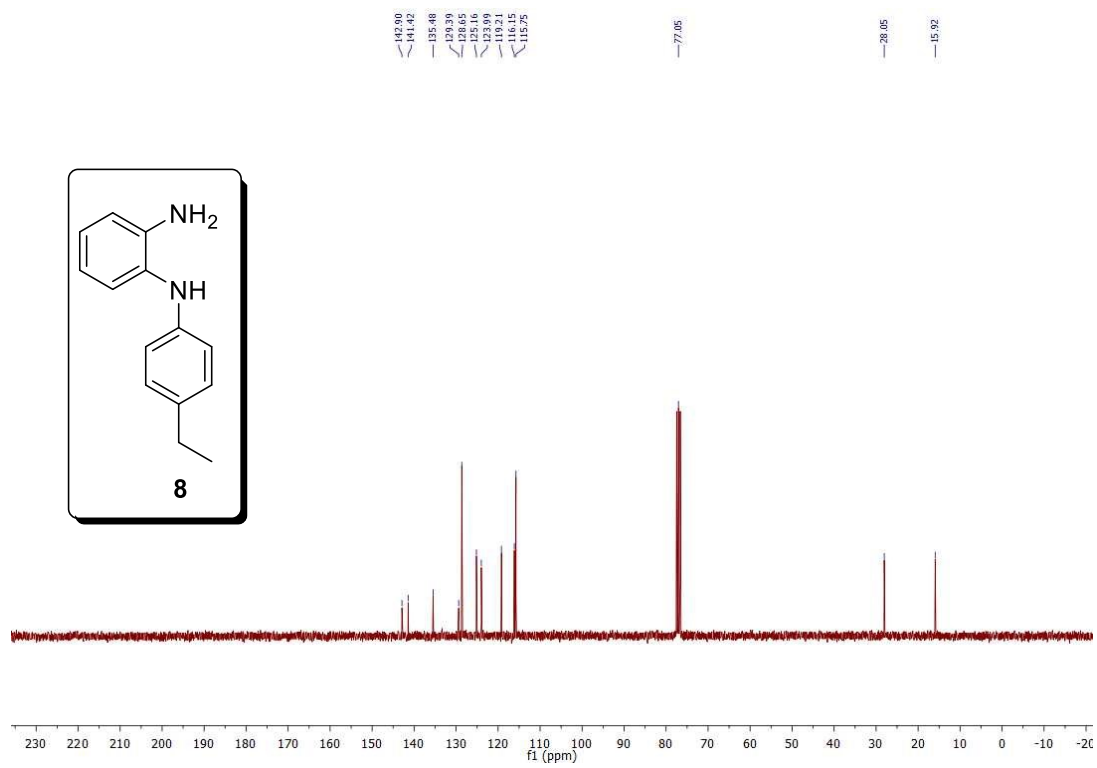


Figure S44. ¹³C NMR of **2**

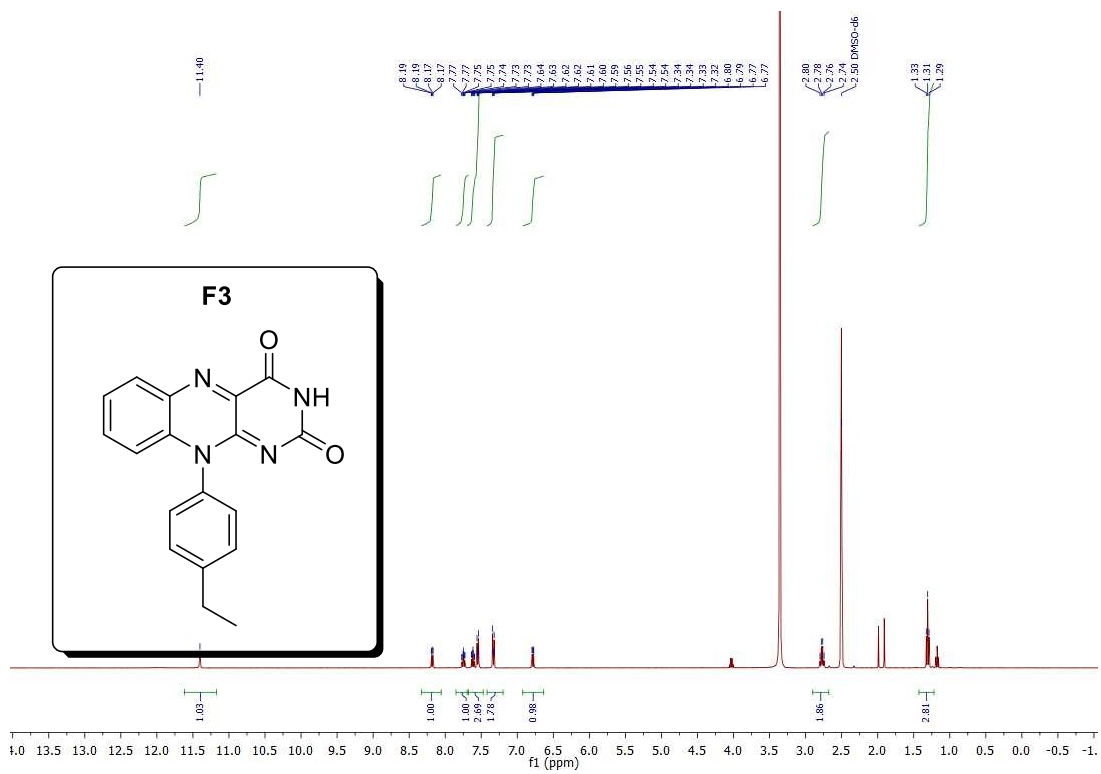


Figure S45. ¹H NMR of F3

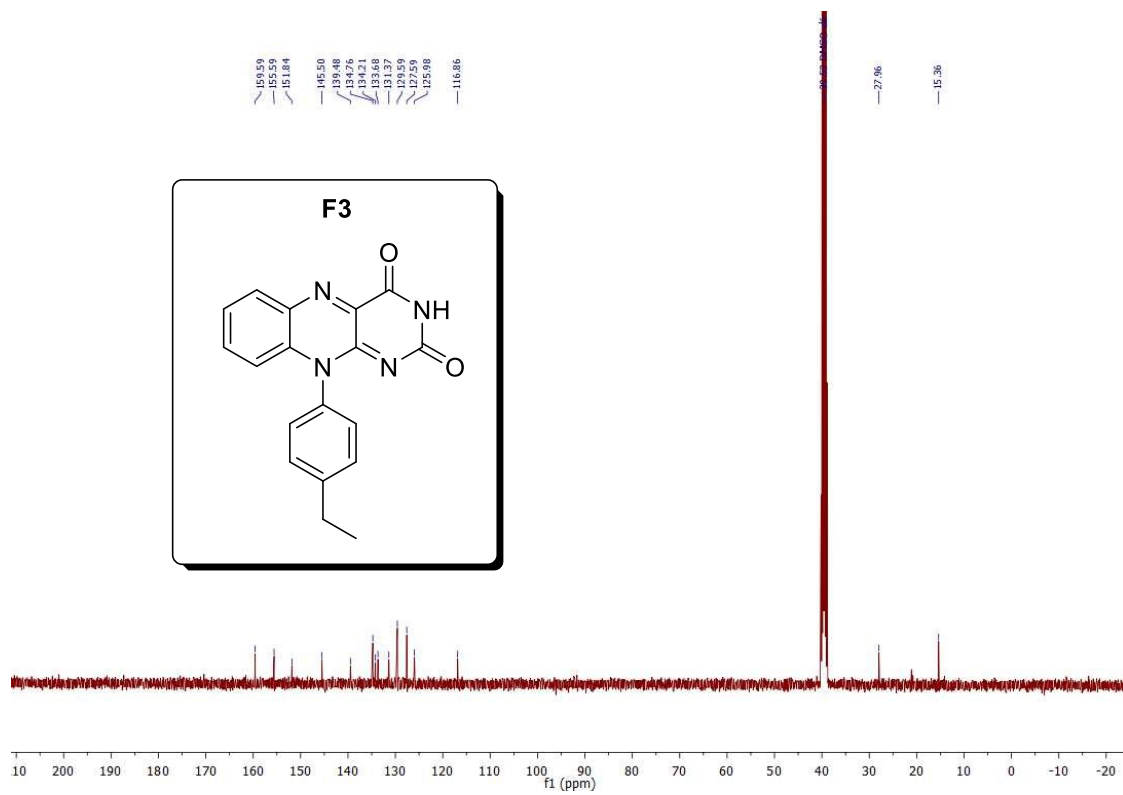


Figure S46. ^{13}C NMR of F3

Supplementary Tables

Entry	Composite	K-PHI content, mol. %	K-PHI content, wt. %
1	C1	67	65
2	C2	67	44
3	C3	67	76

Table S1. Formulations of the composites and K-PHI content in molar % and weight %.

Material	EQE (%)	IQE (%)
K-PHI	0.17	0.19
C1	0.08	0.12
C2	0.19	0.26
C3	0.39	0.43
F1	6.94	7.66
F2	2.20	2.44
F3	1.80	2.00

Table S2. EQE and IQE values

Entry	Composite label	K-PHI	Flavin	Solvent	Volume ^a	Mass ^b
1	C1	5.4 mg	F1 2.7 mg	Acetone:Water (1:1) 5 mL	0.5 mL	0.81 mg
2	C2	4.0 mg	F2 5.1 mg	Acetone:Water (1:1) 5 mL	0.44 mL	0.81 mg
3	C3	6.0 mg	F3 1.9 mg	EtOH:Water (1:1)	0.51 mL	0.81 mg
4	-	K-PHI 8.1 mg	-	Acetone:Water (1:1) 5 mL	0.5 mL	0.81 mg
5	-	-	F1 8.1 mg	Acetone 5 mL	0.5 mL	0.81 mg
6	-	-	F2 8.1 mg	Acetone 5 mL	0.5 mL	0.81 mg

7	-	-	F3 2.1 mg	Ethanol 2.5 mL	0.96 mL	0.81 mg
---	---	---	-----------	----------------	---------	---------

Table S3. Formulations for FTO glass electrodes spray-coating. a) volume of the mixture taken for spray-coating. b) theoretical mass of the material deposited on the FTO glass.

Bulk.

CIF-format:

```

data_image0
_cell_length_a 13.0504
_cell_length_b 13.0504
_cell_length_c 3.51378
_cell_angle_alpha 89.9941
_cell_angle_beta 90.0044
_cell_angle_gamma 120

_symmetry_space_group_name_H-M "P 1"
_symmetry_int_tables_number 1

loop_
_symmetry_equiv_pos_as_xyz
'x, y, z'

loop_
_atom_site_label
_atom_site_occupancy
_atom_site_fract_x
_atom_site_fract_y
_atom_site_fract_z
_atom_site_thermal_displace_type
_atom_site_B_iso_or_equiv
_atom_site_type_symbol
C1 1.0000 0.61059 0.10827 0.95508 Biso 1.000 C
C2 1.0000 0.54727 0.24209 0.95621 Biso 1.000 C
C3 1.0000 0.38941 0.49767 0.95517 Biso 1.000 C
C4 1.0000 0.45273 0.69482 0.95598 Biso 1.000 C
C5 1.0000 0.89173 0.50232 0.95548 Biso 1.000 C
C6 1.0000 0.75791 0.30518 0.95598 Biso 1.000 C
C7 1.0000 0.49767 0.38940 0.95539 Biso 1.000 C
C8 1.0000 0.69482 0.45273 0.95635 Biso 1.000 C
C9 1.0000 0.10827 0.61060 0.95563 Biso 1.000 C
C10 1.0000 0.24209 0.54727 0.95615 Biso 1.000 C
C11 1.0000 0.50232 0.89173 0.95519 Biso 1.000 C
C12 1.0000 0.30518 0.75792 0.95648 Biso 1.000 C
N1 1.0000 0.33334 0.66667 0.95683 Biso 1.000 N
N2 1.0000 0.46306 0.27093 0.95564 Biso 1.000 N
N3 1.0000 0.51990 0.12944 0.95601 Biso 1.000 N
N4 1.0000 0.59913 1.00000 0.95383 Biso 1.000 N

```

N5	1.0000	0.53694	0.80787	0.95514	Biso	1.000	N
N6	1.0000	0.48008	0.60952	0.95582	Biso	1.000	N
N7	1.0000	0.72907	0.19213	0.95509	Biso	1.000	N
N8	1.0000	0.87056	0.39048	0.95588	Biso	1.000	N
N9	1.0000	1.00000	0.59913	0.95453	Biso	1.000	N
N10	1.0000	0.80785	0.53694	0.95582	Biso	1.000	N
N11	1.0000	0.60952	0.48008	0.95621	Biso	1.000	N
N12	1.0000	0.40087	0.40087	0.95404	Biso	1.000	N
N13	1.0000	0.27092	0.46306	0.95538	Biso	1.000	N
N14	1.0000	0.12944	0.51992	0.95609	Biso	1.000	N
N15	1.0000	0.66666	0.33333	0.95682	Biso	1.000	N
N16	1.0000	0.19214	0.72908	0.95609	Biso	1.000	N
N17	1.0000	0.39047	0.87056	0.95633	Biso	1.000	N
K1	1.0000	0.99997	0.74686	0.45418	Biso	1.000	K
K2	1.0000	0.74688	0.00002	0.45367	Biso	1.000	K
K3	1.0000	0.25311	0.25313	0.45380	Biso	1.000	K

Slab:

```

direct lattice vectors
26.100900244 0.000000000 0.000000000
-13.050450122 22.603930942 0.000000000
0.000000000 0.000000000 20.000000000

```

Element order and number of atoms:

```

C H K N O
66 14 12 72 2

```

ACF.dat of bader-analysis:

#	X	Y	Z	CHARGE	MIN DIST	ATOMIC VOL
1	20.312477	1.223641	19.842480	2.428666	0.351544	10.535410
2	18.612891	2.736070	19.846560	2.429672	0.343840	17.476099
3	14.884991	5.624649	19.843180	2.360977	0.341303	17.085201
4	14.424936	7.852809	19.846140	2.463758	0.339157	20.885474
5	21.410125	5.677249	19.844000	2.434536	0.367835	11.162517
6	20.950174	3.449179	19.845680	2.498841	0.365253	13.221521
7	17.004371	4.400985	19.843800	2.409422	0.341461	21.139801
8	19.163972	5.116739	19.847120	2.469735	0.339282	18.594441
9	10.479185	6.900958	19.845040	2.424675	0.351761	8.678474
10	12.638774	6.185227	19.846760	2.427229	0.343844	14.602552
11	13.787278	10.078279	19.843460	2.430636	0.367793	16.611387
12	12.087692	8.565940	19.848020	2.495780	0.365464	14.030490
13	13.787252	12.525607	19.843180	2.428288	0.351600	22.699906
14	12.087640	14.038036	19.847280	2.428895	0.343881	26.162934
15	8.359766	16.926615	19.843900	2.360764	0.341364	22.572394
16	7.899698	19.154752	19.846840	2.470047	0.339245	20.374730
17	14.884913	16.979191	19.844700	2.433977	0.367915	18.829954
18	14.424949	14.751145	19.846400	2.498926	0.365315	26.351066
19	10.479120	15.702951	19.844520	2.359839	0.341498	22.752165
20	12.638721	16.418704	19.847820	2.468661	0.339323	22.674125
21	3.953960	18.202923	19.845760	2.427910	0.351824	22.987679
22	6.113522	17.487192	19.847460	2.429184	0.343923	26.213103
23	7.262027	21.380245	19.844160	2.430182	0.367872	12.855708
24	5.562441	19.867906	19.848720	2.495942	0.365547	23.902559
25	7.261988	1.223619	19.841900	2.429966	0.351473	7.810975
26	5.562389	2.736070	19.846000	2.437395	0.343737	13.105855
27	1.834489	5.624649	19.842620	2.408543	0.341298	8.658267
28	1.374447	7.852786	19.845560	2.457164	0.338963	12.384681
29	8.359635	5.677226	19.843420	2.428999	0.367771	7.734329
30	7.899685	3.449156	19.845100	2.500431	0.365174	13.240334
31	3.953882	4.400963	19.843240	2.410240	0.361083	7.673708
32	6.113483	5.116716	19.846520	2.475403	0.339190	13.321858
33	-2.571304	6.900935	19.844480	2.429903	0.351733	10.819699
34	-0.411716	6.185204	19.846180	2.428376	0.343792	12.415339
35	0.736789	10.078256	19.842880	2.430119	0.367775	11.054516
36	-0.962797	8.565918	19.847420	2.496677	0.365423	16.026783
37	0.736763	12.525584	19.842620	2.428548	0.351529	17.199474
38	-0.962836	14.038036	19.846700	2.428695	0.343801	26.419351
39	-4.690736	16.926615	19.843320	2.361125	0.341355	12.734467
40	-5.150804	19.154752	19.846280	2.472042	0.339225	12.880793
41	1.834410	16.979191	19.844140	2.433838	0.367828	23.939489
42	1.374460	14.751122	19.845820	2.498775	0.365234	27.327961
43	-2.571356	15.702951	19.843940	2.360710	0.341424	19.100308
44	-0.411768	16.418682	19.847240	2.469449	0.339232	22.988375
45	-9.096529	18.202900	19.845180	2.427652	0.351792	12.523341

46	-6.936967	17.487170	19.846900	2.429799	0.343872	14.842943
47	-5.788436	21.380222	19.843580	2.430733	0.367829	8.326597
48	-7.488048	19.867883	19.848140	2.498926	0.365506	12.659215
49	8.711971	1.928364	15.930120	3.982512	0.526136	51.509931
50	8.451641	0.592743	15.686160	3.957970	0.567009	61.938036
51	7.125741	0.178458	15.461340	4.050280	0.533413	40.265193
52	6.067415	1.073054	15.519700	3.879057	0.530575	33.015828
53	3.913217	2.938308	15.964540	3.744757	0.472448	9.939657
54	2.981310	3.428858	15.052560	3.948012	0.512480	31.139382
55	1.647763	3.032611	15.150820	3.959901	0.518629	43.277401
56	1.218507	2.149521	16.151080	4.076829	0.536863	18.517097
57	2.183941	1.663288	17.041620	4.009280	0.512686	23.693523
58	3.516300	2.045000	16.959580	3.889886	0.513604	12.779062
59	-0.222301	1.699816	16.296640	3.984729	0.615474	12.350538
60	-1.278814	2.517129	15.549140	4.035570	0.575981	23.236431
61	7.660784	2.869366	15.973060	3.475204	0.370562	21.029012
62	6.314134	2.429312	15.812300	3.703801	0.372280	13.964295
63	7.008118	5.063959	16.158500	3.363419	0.342455	16.767467
64	5.586297	4.728200	16.107440	2.981672	0.343885	10.085982
65	4.870989	6.921527	16.364300	2.189976	0.277276	7.484182
66	7.350379	6.525393	16.242940	2.611808	0.335251	13.427770
67	9.717678	2.300854	16.091560	0.961602	0.292592	159.665806
68	-3.790203	22.476693	15.657760	0.951172	0.237213	247.941669
69	-6.132354	21.742812	15.239160	0.990513	0.319060	319.479331
70	5.057454	0.728457	15.350400	0.954010	0.290502	65.715315
71	3.285046	4.131886	14.289020	1.021741	0.305193	200.216682
72	0.939789	3.441675	14.439160	0.963698	0.210158	137.376307
73	1.896387	0.977213	17.832120	1.032904	0.286013	26.525960
74	4.230395	1.670453	17.676580	0.928068	0.196081	7.909222
75	-0.468237	1.704133	17.364200	0.983698	0.274333	23.255245
76	-0.292082	0.650157	15.980240	0.960232	0.311262	157.129504
77	23.825463	2.127595	15.775020	0.995652	0.303958	196.218522
78	-1.255284	3.568731	15.849380	0.915757	0.259386	111.597999
79	-1.141758	2.464959	14.464180	1.024011	0.327498	316.834330
80	6.389892	8.322677	16.406460	0.507435	0.150199	159.523662
81	8.176655	8.441031	1.597000	6.118731	1.141645	290.191310
82	22.797440	0.000316	1.594240	6.120350	1.139734	275.408988
83	14.701932	2.860934	1.595140	6.119594	1.169220	327.154433
84	1.651417	19.742974	1.597720	6.119982	1.142116	349.755395
85	16.272215	11.302282	1.594940	6.119399	1.140202	373.611269
86	8.176707	14.162900	1.595860	6.118291	1.169747	348.565981
87	21.227066	8.441009	1.596440	6.118704	1.141268	324.023772
88	9.746950	0.000294	1.593640	6.118332	1.139306	266.662228
89	1.651443	2.860912	1.594580	6.121634	1.168838	247.908224
90	14.701815	19.742974	1.597140	6.121077	1.141744	299.266952
91	3.221725	11.302259	1.594360	6.118627	1.139787	326.013097
92	-4.873795	14.162900	1.595280	6.118675	1.169341	342.783351
93	13.050489	7.534681	19.849160	6.230085	0.749933	34.201758
94	17.325777	3.062064	19.844660	6.241865	0.683864	80.167361
95	18.990858	1.462926	19.845820	6.272014	0.700019	65.799626
96	20.869340	0.000000	19.838000	6.336679	0.738186	33.943947
97	14.786290	9.130496	19.843200	6.235517	0.714395	104.290801
98	15.338507	6.888819	19.845480	6.297983	0.685648	86.811915
99	21.311450	2.171492	19.842500	6.232546	0.737522	40.534849
100	21.863706	4.413146	19.845320	6.205779	0.746833	48.568796
101	9.141005	6.771369	19.841220	6.326752	0.738281	23.758324
102	20.089693	6.068455	19.845260	6.234499	0.714855	89.841542
103	17.872382	5.425802	19.846680	6.234603	0.656805	76.760075
104	15.666217	4.530574	19.839140	6.330927	0.699760	52.099413

105	13.564572	5.233511	19.843980	6.238898	0.683830	54.490087
106	11.347092	5.876141	19.846580	6.267750	0.699874	49.435598
107	19.575649	3.767307	19.848720	6.230900	0.750004	34.839318
108	10.800618	8.240014	19.846680	6.219698	0.737583	46.139102
109	12.465725	9.839016	19.847520	6.201510	0.746899	63.493960
110	6.525264	18.836647	19.849880	6.232326	0.749878	44.014600
111	10.800552	14.364030	19.845360	6.239862	0.683894	82.414497
112	12.465620	12.764869	19.846520	6.270172	0.700057	73.938091
113	14.344115	11.301965	19.838700	6.333781	0.738208	83.544684
114	8.261078	20.432439	19.843920	6.239264	0.714543	57.066802
115	8.813295	18.190762	19.846180	6.294140	0.656873	69.956653
116	14.786225	13.473457	19.843200	6.229060	0.737549	110.138929
117	15.338494	15.715089	19.846020	6.206250	0.746855	81.725375
118	2.615793	18.073312	19.841940	6.336846	0.738303	64.721001
119	13.564468	17.370420	19.845960	6.238063	0.714976	64.761414
120	11.347131	16.727768	19.847400	6.286004	0.656865	71.312600
121	9.140992	15.832539	19.839860	6.330398	0.699785	67.192502
122	7.039347	16.535476	19.844700	6.240213	0.683861	88.311399
123	4.821867	17.178106	19.847300	6.271346	0.699907	81.982489
124	13.050398	15.069272	19.849440	6.230525	0.749974	47.995341
125	4.275393	19.541980	19.847400	6.230106	0.737614	90.656086
126	5.940500	21.140982	19.848240	6.205827	0.746931	72.956319
127	0.000000	7.534659	19.848600	6.228497	0.749974	32.371997
128	4.275288	3.062042	19.844080	6.245110	0.683871	28.041470
129	5.940369	1.462904	19.845220	6.283001	0.700025	37.664090
130	-5.231599	22.603908	19.837420	6.338054	0.738183	25.010449
131	1.735801	9.130474	19.842620	6.223244	0.714292	39.595581
132	2.288018	6.888797	19.844900	6.236452	0.685616	41.440672
133	8.260961	2.171469	19.841900	6.229463	0.737520	36.945703
134	8.813217	4.413124	19.844720	6.197620	0.746765	41.883131
135	22.191416	6.771347	19.840660	6.334809	0.738306	54.311012
136	7.039204	6.068432	19.844680	6.237733	0.714791	32.599150
137	4.821893	5.425780	19.846120	6.231082	0.656809	36.960335
138	2.615728	4.530551	19.838560	6.325598	0.699774	21.579473
139	0.514070	5.233511	19.843400	6.241448	0.683770	37.277373
140	-1.703397	5.876118	19.846000	6.272053	0.699837	46.550903
141	6.525160	3.767284	19.848140	6.234992	0.750087	24.251649
142	-2.249871	8.239992	19.846120	6.226739	0.737604	83.400449
143	-0.584765	9.838994	19.846960	6.201594	0.746842	69.440335
144	-6.525225	18.836624	19.849300	6.230990	0.749919	31.093394
145	-2.249950	14.364030	19.844780	6.241814	0.683920	110.101999
146	-0.584882	12.764869	19.845940	6.271692	0.700082	81.578353
147	1.293626	11.301943	19.838120	6.328325	0.738205	37.986702
148	-4.789424	20.432439	19.843340	6.241840	0.714413	45.827639
149	-4.237207	18.190762	19.845600	6.284452	0.656808	55.463497
150	1.735736	13.473435	19.842620	6.226371	0.737546	73.586213
151	2.287992	15.715089	19.845440	6.202789	0.746795	85.682425
152	15.666191	18.073312	19.841360	6.339752	0.738331	43.050248
153	0.513966	17.370420	19.845380	6.236181	0.714927	71.009497
154	-1.703345	16.727768	19.846820	6.295923	0.656862	65.290275
155	-3.909510	15.832539	19.839260	6.332712	0.699772	70.067442
156	-6.011155	16.535476	19.844100	6.240145	0.683799	87.576987
157	-8.228622	17.178083	19.846720	6.271698	0.699870	64.517539
158	-0.000065	15.069250	19.848860	6.230210	0.750030	48.507479
159	-8.775110	19.541980	19.846820	6.234410	0.737636	46.580168
160	-7.109990	21.140959	19.847660	6.214262	0.746873	46.013681
161	5.294646	3.372280	15.929820	6.213937	0.733964	13.976837
162	7.977779	4.192555	16.129620	6.154525	0.696117	62.080877
163	4.595925	5.574581	16.228800	6.185060	0.664373	25.999189

164	6.228654	7.326273	16.342100	6.250874	0.693765	48.492846
165	4.001307	7.781833	16.462260	7.115988	0.668599	218.758167
166	8.487921	6.976726	16.194020	7.067764	0.748365	296.484684

VACUUM CHARGE: 0.0000
VACUUM VOLUME: 0.0000
NUMBER OF ELECTRONS: 734.0000

8. Abbreviations

AC-HRTEM	Aberration corrected high resolution transmission electron microscopy
AC-iDPC TEM	aberration corrected integrated differential phase contrast transmission electron microscopy
ACN	Acetonitrile
AFM	Atomic force microscopy
AQY	Apparent quantum yield
BA	Benzyl alcohol
BET	Brunauer-Emmett-Teller
CB	Conduction band
CN	carbon nitride
COF	Covalent organic frameworks
CP	Cyclic potentiometry
CV	cyclic voltammetry
CVD	Chemical vapor deposition
DFT	Density functional theory
DIPEA	N,N-Diisopropylethylamine
DMF	Dimethylformamide
DMPO	5,5-Dimethyl-1-pyrroline N-oxide
DMSO	Dimethylsulfoxide
DSC	Differential scanning calorimetry
Ec	Energy of the conduction band
ED	Electron acceptor
ED	electron donor
EDG	Electron'donatign group
EDX	Energy dispersive X-ray

EELS	Electron energy loss spectroscopy
E_f	Fermi energy level
EnT	Energy transfer
EPR	Electron paramagnetic spectroscopy
EPR	Electron paramagnetic spectroscopy
EQE	External quantum efficiency
ESA	Excited state absorption
ET	electron transfer
EtOH	Ethanol
EWG	Electron-withdrawing group
FRET	Förster resonance energy transfer
FT-IR	Fourier transformed infrared
GC-MS	Gas chromatography mass spectrometry
g-CN	graphitic carbon nitride
GSB	Ground state bleaching
Hal	Halogen
HAT	Hydrogen atom transfer
HER	Hydrogen evolution reaction
HOMO	Highest occupied molecular orbital
HR-MS	High resolution mass spectrometry
IDEAS	Illumination-Driven Electrons Accumulation in Semiconductor
IDEASE	Illumination-Driven Electrons Accumulation in Semiconductor and Exploitation
<i>i</i> Pr	<i>Iso</i> -propanol
IQE	Internal quantum efficiency
IR	Infrared

ISC	Intersystem crossing
K-PHI	potassium poly(heptazine imide)
LED	Light emitting diode
LSV	Linear sweep voltammetry
LUMO	Lowest unoccupied molecular orbital
MeCN	Acetonitrile
MeOH	Methanol
MOF	metal organic frameworks
mpg-CN	mesoporous graphitic carbon nitride
M-PHI	Metal poly(heptazine imide)
MS-PCET	Multi-site proton coupled electron transfer
MV	Methyl viologen
Na-PHI	sodium poly(heptazine imide)
NCN_xCN_x	cyanamide surface-functionalized melon-type carbon nitride
NHE	Normal hydrogen electrode
NMR	Nuclear magnetic resonance
OCP	Open circuit potentiometry
OCV	Open circuit voltammetry
OD	Optical density
OER	Oxygen evolution reaction
OLED	Organic light emitting diode
ORR	Oxygen reduction reaction
PC	Photoatalysts
PC*	Excited state photocatalyst
PCET	Proton-coupled electron transfer
PEC	Photoelectrochemical water-splitting

PET	Photoinduced electron transfer
PHI	poly(heptazine imide)
PL	Photoluminescence
PT	Proton transfer
PTI	poly(triazine imide)
PXRD	Powder X-ray diffraction
QE	Quantum efficiency
RF	Riboflavin
RHE	Reference hydrogen electrode
S ₀	Ground state
S ₁	Singlet excited state
SCE	Saturated calomel electrode
SCNPs	Semiconductor nanoparticles
SET	Single electron transfer
SMBR	Serial micro batch reactor
ST	Singlet'triplet
T ₁	Triplet excited state
TA	Transient absorption
TAS	Transient absorption spectroscopy
<i>t</i> BuOH	<i>Tert</i> -butanol
TC-SPC	Time-correlated single photon counting
TEA	Triethylamine
TEM	Transmission electron microscopy
TEMP	2,2,6,6-Tetramethylpiperidine
TEMPO	2,2,6,6-Tetramethylpiperidine 1-oxyl
TEOA	Triethanolamine

TGA	Thermal gravimetric analysis
THF	Tetrahydrofurna
THIQ	Tetrahydroisoquinoline
TOA	Turnover area
TRPL	Time resolved photoluminescene
TRPL	Time resolved photoluminescence
tr-PL	Time-resolved photoluminescence
TTA	Triplet'triple annihilation
UV	Ultraviolet
VB	Valence band
Vis	Visible
Vis-BWR	Visible batch wall reaction
Vis-FWR	Visible flow wall reactor
XPS	X-ray photoelectron spectroscopy
τ_{Fl}	Fluorescence lifetime
τ_{Ph}	Phosphorescence lifetime

9. References

- [1] K. Kubota, Y. Pang, A. Miura, H. Ito, *Science* 2019, 366, 1500.
- [2] M. Ghosh, V. S. Shinde, M. Rueping, *Beilstein Journal of Organic Chemistry* 2019, 15, 2710; E. J. Horn, B. R. Rosen, P. S. Baran, *ACS Central Science* 2016, 2, 302; M. D. Kärkäs, *Chemical Society Reviews* 2018, 47, 5786.
- [3] D. A. Nicewicz, D. W. C. MacMillan, *Science* 2008, 322, 77.
- [4] D. S. Achilleos, W. Yang, H. Kasap, A. Savateev, Y. Markushyna, J. R. Durrant, E. Reisner, *Angewandte Chemie International Edition* 2020, 59, 18184; T. Uekert, H. Kasap, E. Reisner, *Journal of the American Chemical Society* 2019, 141, 15201.
- [5] T. Koike, M. Akita, *Synlett* 2013, 24, 2492; S. Crespi, M. Fagnoni, *Chemical Reviews* 2020, 120, 9790.
- [6] J. P. Barham, B. König, *Angewandte Chemie International Edition* 2020, 59, 11732.
- [7] L. Marzo, S. K. Pagire, O. Reiser, B. König, *Angewandte Chemie International Edition* 2018, 57, 10034.
- [8] R. H. Verschueren, W. M. De Borggraeve, *Molecules* 2019, 24.
- [9] A. García, C. Fernandez-Blanco, J. R. Herance, J. Albero, H. García, *Journal of Materials Chemistry A* 2017, 5, 16522.
- [10] F. Strieth-Kalthoff, M. J. James, M. Teders, L. Pitzer, F. Glorius, *Chemical Society Reviews* 2018, 47, 7190.
- [11] F. Glaser, C. Kerzig, O. S. Wenger, *Angewandte Chemie International Edition* 2020, 59, 10266.
- [12] A. Pannwitz, O. S. Wenger, *Chemical Communications* 2019, 55, 4004.
- [13] T. S. Teets, *ChemPhotoChem* 2018, 2, 380; D. M. Hedstrand, W. H. Kruizinga, R. M. Kellogg, *Tetrahedron Letters* 1978, 19, 1255; H. Cano-Yelo, A. Deronzier, *Tetrahedron Letters* 1984, 25, 5517.
- [14] O. S. Wenger, *Journal of the American Chemical Society* 2018, 140, 13522; C. Förster, K. Heinze, *Chemical Society Reviews* 2020, 49, 1057; A. Hossain, A. Bhattacharyya, O. Reiser, *Science* 2019, 364, eaav9713.
- [15] V. Mojr, E. Svobodová, K. Straková, T. Neveselý, J. Chudoba, H. Dvořáková, R. Cibulka, *Chem Commun (Camb)* 2015, 51, 12036.
- [16] J. Zelenka, E. Svobodová, J. Tarábek, I. Hoskovcová, V. Boguschová, S. Bailly, M. Sikorski, J. Roithová, R. Cibulka, *Organic Letters* 2019, 21, 114; I. K. Sideri, E. Voutyritsa, C. G. Kokotos, *Organic & Biomolecular Chemistry* 2018, 16, 4596.
- [17] D. A. Nicewicz, T. M. Nguyen, *ACS Catalysis* 2014, 4, 355.
- [18] K. A. Korvinson, G. N. Hargenrader, J. Stevanovic, Y. Xie, J. Joseph, V. Maslak, C. M. Hadad, K. D. Glusac, *The Journal of Physical Chemistry A* 2016, 120, 7294; D. Friedmann, A. Hakki, H. Kim, W. Choi, D. Bahnemann, *Green Chemistry* 2016, 18, 5391; S. Kohtani, A.

Kawashima, H. Miyabe, *Frontiers in Chemistry* 2019, 7; D. W. Manley, J. C. Walton, *Beilstein Journal of Organic Chemistry* 2015, 11, 1570.

[19] S. Sohrabi, M. K. Moraveji, D. Iranshahi, *Reviews in Chemical Engineering* 2020, 36, 687.

[20] K. Fuku, N. Wang, Y. Miseki, T. Funaki, K. Sayama, *ChemSusChem* 2015, 8, 1593; H. Tateno, Y. Miseki, K. Sayama, *ChemElectroChem* 2017, 4, 3283.

[21] G. Beck, M. Sieland, J. F. Beleites, R. Marschall, B. M. Smarsly, *Inorganic Chemistry* 2019, 58, 2599.

[22] A. L. Luna, F. Matter, M. Schreck, J. Wohlwend, E. Tervoort, C. Colbeau-Justin, M. Niederberger, *Applied Catalysis B: Environmental* 2020, 267, 118660.

[23] M. Monai, T. Montini, P. Fornasiero, *Catalysts* 2017, 7; T. Montini, M. Melchionna, M. Monai, P. Fornasiero, *Chemical Reviews* 2016, 116, 5987.

[24] Y. Lin, J. Guo, J. San Martin, C. Han, R. Martinez, Y. Yan, *Chemistry – A European Journal* 2020, 26.

[25] A. Dhakshinamoorthy, A. M. Asiri, H. Garcia, *Advanced Materials* 2019, 31, 1900617; D. Mateo, A. Santiago-Portillo, J. Albero, S. Navalón, M. Alvaro, H. García, *Angewandte Chemie International Edition* 2019, 58, 17843; A. Dhakshinamoorthy, A. M. Asiri, H. Garcia, *ACS Catalysis* 2017, 7, 2896; X. Deng, Z. Li, H. García, *Chemistry – A European Journal* 2017, 23, 11189; S. Abednatanzi, P. Gohari Derakhshandeh, H. Depauw, F.-X. Coudert, H. Vrielinck, P. Van Der Voort, K. Leus, *Chemical Society Reviews* 2019, 48, 2535.

[26] B. Ohtani, *Catalysts* 2013, 3.

[27] D. Noureldine, K. Takanabe, *Catalysis Science & Technology* 2016, 6, 7656; K. Watanabe, A. Iwase, A. Kudo, *Chemical Science* 2020, 11, 2330.

[28] M. Weiss, B. Wirth, R. Marschall, *Inorganic Chemistry* 2020, 59, 8387.

[29] K. Kirchberg, R. Marschall, *Sustainable Energy & Fuels* 2019, 3, 1150; R. A. Henning, P. Uredat, C. Simon, A. Bloesser, P. Cop, M. T. Elm, R. Marschall, *The Journal of Physical Chemistry C* 2019, 123, 18240.

[30] K. Obata, Y. Shinohara, S. Tanabe, I. Waki, K. Kotsovos, K. Ohkawa, K. Takanabe, *Energy Technology* 2019, 7, 1900575; Y. Goto, T. Hisatomi, Q. Wang, T. Higashi, K. Ishikiriyama, T. Maeda, Y. Sakata, S. Okunaka, H. Tokudome, M. Katayama, S. Akiyama, H. Nishiyama, Y. Inoue, T. Takewaki, T. Setoyama, T. Minegishi, T. Takata, T. Yamada, K. Domen, *Joule* 2018, 2, 509.

[31] J. Byun, K. A. I. Zhang, *Materials Horizons* 2020, 7, 15.

[32] C. Krishnaraj, H. S. Jena, K. Leus, P. Van Der Voort, *Green Chemistry* 2020, 22, 1038.

[33] W. Huang, J. Byun, I. Rörich, C. Ramanan, P. W. M. Blom, H. Lu, D. Wang, L. Caire da Silva, R. Li, L. Wang, K. Landfester, K. A. I. Zhang, *Angewandte Chemie International Edition* 2018, 57, 8316.

[34] Z. J. Wang, S. Ghasimi, K. Landfester, K. A. I. Zhang, *Journal of Materials Chemistry A* 2014, 2, 18720.

- [35] L. Wang, W. Huang, R. Li, D. Gehrig, P. W. M. Blom, K. Landfester, K. A. I. Zhang, *Angewandte Chemie International Edition* 2016, 55, 9783.
- [36] R. Li, B. C. Ma, W. Huang, L. Wang, D. Wang, H. Lu, K. Landfester, K. A. I. Zhang, *ACS Catalysis* 2017, 7, 3097.
- [37] R. Li, Z. J. Wang, L. Wang, B. C. Ma, S. Ghasimi, H. Lu, K. Landfester, K. A. I. Zhang, *ACS Catalysis* 2016, 6, 1113.
- [38] Z. J. Wang, S. Ghasimi, K. Landfester, K. A. I. Zhang, *Advanced Synthesis & Catalysis* 2016, 358, 2576.
- [39] X. Wang, S. Blechert, M. Antonietti, *ACS Catalysis* 2012, 2, 1596.
- [40] M. Shalom, S. Inal, C. Fettkenhauer, D. Neher, M. Antonietti, *Journal of the American Chemical Society* 2013, 135, 7118.
- [41] T. Jordan, N. Fechler, J. Xu, T. J. K. Brenner, M. Antonietti, M. Shalom, *ChemCatChem* 2015, 7, 2826.
- [42] L. Li, Y. Zhao, M. Antonietti, M. Shalom, *Small* 2016, 12, 6090.
- [43] J. Xu, T. J. K. Brenner, L. Chabanne, D. Neher, M. Antonietti, M. Shalom, *Journal of the American Chemical Society* 2014, 136, 13486.
- [44] J. Xu, H. Wang, C. Zhang, X. Yang, S. Cao, J. Yu, M. Shalom, *Angewandte Chemie International Edition* 2017, 56, 8426.
- [45] L. Li, M. Shalom, Y. Zhao, J. Barrio, M. Antonietti, *Journal of Materials Chemistry A* 2017, 5, 18502.
- [46] F. Dong, Z. Wang, Y. Sun, W.-K. Ho, H. Zhang, *Journal of Colloid and Interface Science* 2013, 401, 70; K. Maeda, X. Wang, Y. Nishihara, D. Lu, M. Antonietti, K. Domen, *The Journal of Physical Chemistry C* 2009, 113, 4940; G. Zhang, J. Zhang, M. Zhang, X. Wang, *Journal of Materials Chemistry* 2012, 22, 8083; H. Ji, F. Chang, X. Hu, W. Qin, J. Shen, *Chemical Engineering Journal* 2013, 218, 183.
- [47] S. C. Yan, Z. S. Li, Z. G. Zou, *Langmuir* 2009, 25, 10397.
- [48] H. Yan, *Chemical Communications* 2012, 48, 3430; X. Wang, K. Maeda, X. Chen, K. Takanebe, K. Domen, Y. Hou, X. Fu, M. Antonietti, *Journal of the American Chemical Society* 2009, 131, 1680; X. Chen, Y.-S. Jun, K. Takanebe, K. Maeda, K. Domen, X. Fu, M. Antonietti, X. Wang, *Chemistry of Materials* 2009, 21, 4093.
- [49] H. Yan, Y. Chen, S. Xu, *International Journal of Hydrogen Energy* 2012, 37, 125; Y. Guo, S. Chu, S. Yan, Y. Wang, Z. Zou, *Chem Commun (Camb)* 2010, 46, 7325; B. Kumru, M. Antonietti, B. V. K. J. Schmidt, *Langmuir* 2017, 33, 9897.
- [50] Z. Ding, X. Chen, M. Antonietti, X. Wang, *ChemSusChem* 2011, 4, 274; X. Wang, X. Chen, A. Thomas, X. Fu, M. Antonietti, *Advanced Materials* 2009, 21, 1609; Y. Zhang, M. Antonietti, *Chemistry – An Asian Journal* 2010, 5, 1307; S. C. Yan, Z. S. Li, Z. G. Zou, *Langmuir* 2010, 26, 3894; Y. Wang, Y. Di, M. Antonietti, H. Li, X. Chen, X. Wang, *Chemistry of Materials* 2010, 22, 5119; G. Liu, P. Niu, C. Sun, S. C. Smith, Z. Chen, G. Q. Lu, H.-M. Cheng, *Journal of the American Chemical Society* 2010, 132, 11642; G. Zhang, X. Wang, *Journal of Catalysis* 2013, 307, 246; J.

- Zhang, G. Zhang, X. Chen, S. Lin, L. Möhlmann, G. Dołęga, G. Lipner, M. Antonietti, S. Blechert, X. Wang, *Angewandte Chemie International Edition* 2012, 51, 3183; J. Zhang, X. Chen, K. Takanahe, K. Maeda, K. Domen, J. D. Epping, X. Fu, M. Antonietti, X. Wang *Angewandte Chemie International Edition* 2010, 49, 441; J. Barrio, M. Volokh, M. Shalom, *Journal of Materials Chemistry A* 2020, 8, 11075.
- [51] G. Zhang, M. Zhang, X. Ye, X. Qiu, S. Lin, X. Wang, *Advanced Materials* 2014, 26, 805.
- [52] J. Zhang, J. Sun, K. Maeda, K. Domen, P. Liu, M. Antonietti, X. Fu, X. Wang, *Energy & Environmental Science* 2011, 4, 675.
- [53] J. Zhang, M. Zhang, S. Lin, X. Fu, X. Wang, *Journal of Catalysis* 2014, 310, 24.
- [54] M. E. Lamanna, E. d. l. Horra, S. Jacobo, N. B. D'Accorso, *Reactive and Functional Polymers* 2009, 69, 759.
- [55] A. Savateev, S. Pronkin, J. D. Epping, M. G. Willinger, M. Antonietti, D. Dontsova, *Journal of Materials Chemistry A* 2017, 5, 8394.
- [56] S. N. Talapaneni, G. Singh, I. Y. Kim, K. AlBahily, A. a. H. Al-Muhtaseb, A. S. Karakoti, E. Tavakkoli, A. Vinu, *Advanced Materials* 2020, 32, 2070142.
- [57] M. R. Benzigar, S. N. Talapaneni, S. Joseph, K. Ramadass, G. Singh, J. Scaranto, U. Ravon, K. Al-Bahily, A. Vinu, *Chemical Society Reviews* 2018, 47, 2680.
- [58] G. P. Mane, S. N. Talapaneni, K. S. Lakhi, H. Ilbeygi, U. Ravon, K. Al-Bahily, T. Mori, D.-H. Park, A. Vinu, *Angewandte Chemie International Edition* 2017, 56, 8481.
- [59] I. Y. Kim, S. Kim, S. Premkumar, J.-H. Yang, S. Umapathy, A. Vinu, *Small* 2020, 16, 1903572.
- [60] W. Cha, I. Y. Kim, J. M. Lee, S. Kim, K. Ramadass, K. Gopalakrishnan, S. Premkumar, S. Umapathy, A. Vinu, *ACS Applied Materials & Interfaces* 2019, 11, 27192; T. Kesavan, T. Partheeban, M. Vivekanantha, N. Prabu, M. Kundu, P. Selvarajan, S. Umapathy, A. Vinu, M. Sasidharan, *ACS Applied Materials & Interfaces* 2020, 12, 24007.
- [61] G. Zhang, M. Liu, T. Heil, S. Zafeiratos, A. Savateev, M. Antonietti, X. Wang, *Angewandte Chemie International Edition* 2019, 58, 14950.
- [62] G. Zhang, L. Lin, G. Li, Y. Zhang, A. Savateev, S. Zafeiratos, X. Wang, M. Antonietti, *Angewandte Chemie International Edition* 2018, 57, 9372.
- [63] X.-N. Cao, S. Lian, Y. Tong, W. Lin, L. Jia, Y. Fang, X. Wang, *Chemical Communications* 2020, 56, 916.
- [64] P. Xia, S. Cao, B. Zhu, M. Liu, M. Shi, J. Yu, Y. Zhang, *Angewandte Chemie International Edition* 2020, 59, 5218.
- [65] Y. Zou, J.-W. Shi, L. Sun, D. Ma, S. Mao, Y. Lv, Y. Cheng, *Chemical Engineering Journal* 2019, 378, 122192.
- [66] Y. Zou, J.-W. Shi, D. Ma, Z. Fan, L. Cheng, D. Sun, Z. Wang, C. Niu, *ChemSusChem* 2018, 11, 1187.
- [67] Y. Zou, J.-W. Shi, D. Ma, Z. Fan, C. He, L. Cheng, D. Sun, J. Li, Z. Wang, C. Niu, *Catalysis Science & Technology* 2018, 8, 3883.

- [68] Q. Cao, B. Kumru, M. Antonietti, B. V. K. J. Schmidt, *Materials Horizons* 2020, 7, 762; N. Yandrapalli, T. Robinson, M. Antonietti, B. Kumru, *Small* 2020, 16, 2001180.
- [69] P. Giusto, B. Kumru, J. Zhang, R. Rothe, M. Antonietti, *Chemistry of Materials* 2020, 32, 7284.
- [70] G. Wu, Y. Hu, Y. Liu, J. Zhao, X. Chen, V. Whoehling, C. Plesse, G. T. M. Nguyen, F. Vidal, W. Chen, *Nature Communications* 2015, 6, 7258.
- [71] P. Giusto, D. Cruz, T. Heil, H. Arazoe, P. Lova, T. Aida, D. Comoretto, M. Patrini, M. Antonietti, *Advanced Materials* 2020, 32, 1908140.
- [72] B. Kumru, V. Molinari, M. Shalom, M. Antonietti, B. V. K. J. Schmidt, *Soft Matter* 2018, 14, 2655; B. Kumru, V. Molinari, M. Hilgart, F. Rummel, M. Schäffler, B. V. K. J. Schmidt, *Polymer Chemistry* 2019, 10, 3647; B. Kumru, M. Shalom, M. Antonietti, B. V. K. J. Schmidt, *Macromolecules* 2017, 50, 1862.
- [73] M. H. S. Nathan J. Gesmundo, Jack Twilton, John C. Tellis, David W. C. MacMillan, David A. Nicewicz, in *Desk Reference and User's Guide*, (Ed: M. KGaA), Merck KGaA, Darmstadt, Germany 2019, 60.
- [74] C. K. Prier, D. A. Rankic, D. W. C. MacMillan, *Chemical Reviews* 2013, 113, 5322.
- [75] N. A. Romero, D. A. Nicewicz, *Chemical Reviews* 2016, 116, 10075.
- [76] Y. Yoshimi, M. Masuda, T. Mizunashi, K. Nishikawa, K. Maeda, N. Koshida, T. Itou, T. Morita, M. Hatanaka, *Organic Letters* 2009, 11, 4652.
- [77] K. Ohkubo, A. Fujimoto, S. Fukuzumi, *Chemical Communications* 2011, 47, 8515.
- [78] W. Yang, S. Yang, P. Li, L. Wang, *Chemical Communications* 2015, 51, 7520.
- [79] M. Rueping, S. Zhu, R. M. Koenigs, *Chemical Communications* 2011, 47, 12709.
- [80] M. H. Shaw, J. Twilton, D. W. C. MacMillan, *The Journal of Organic Chemistry* 2016, 81, 6898.
- [81] G. Pandey, M. Karthikeyan, A. Murugan, *The Journal of Organic Chemistry* 1998, 63, 2867; G. Pandey, R. Sochanchingwung, *Journal of the Chemical Society, Chemical Communications* 1994, 1945.
- [82] G. Pandey, R. Laha, *Angewandte Chemie International Edition* 2015, 54, 14875; S. Hintz, J. Mattay, R. van Eldik, W.-F. Fu, *European Journal of Organic Chemistry* 1998, 1998, 1583.
- [83] A. J. Perkowski, C. L. Cruz, D. A. Nicewicz, *Journal of the American Chemical Society* 2015, 137, 15684.
- [84] H. Huang, Z. M. Strater, M. Rauch, J. Shee, T. J. Sisto, C. Nuckolls, T. H. Lambert, *Angewandte Chemie International Edition* 2019, 58, 13318.
- [85] X. Wu, C. Meng, X. Yuan, X. Jia, X. Qian, J. Ye, *Chemical Communications* 2015, 51, 11864.
- [86] T. Keshari, V. K. Yadav, V. P. Srivastava, L. D. S. Yadav, *Green Chemistry* 2014, 16, 3986.
- [87] A. Savateev, M. Antonietti, *ChemCatChem* 2019, 11, 6166.
- [88] S. Cao, J. Low, J. Yu, M. Jaroniec, *Advanced Materials* 2015, 27, 2150.

- [89] C. Qiu, Y. Xu, X. Fan, D. Xu, R. Tandiana, X. Ling, Y. Jiang, C. Liu, L. Yu, W. Chen, C. Su, *Advanced Science* 2019, 6, 1801403; Z. Zhang, J. Huang, Q. Yuan, B. Dong, *Nanoscale* 2014, 6, 9250; Z. Wu, H. Gao, S. Yan, Z. Zou, *Dalton Transactions* 2014, 43, 12013.
- [90] A. Savateev, S. Pronkin, M. G. Willinger, M. Antonietti, D. Dontsova, *Chemistry – An Asian Journal* 2017, 12, 1517.
- [91] Y. Zhao, M. Shalom, M. Antonietti, *Applied Catalysis B: Environmental* 2017, 207, 311.
- [92] B. Ni, B. Zhang, J. Han, B. Peng, Y. Shan, T. Niu, *Organic Letters* 2020, 22, 670; Y. Zhao, M. Antonietti, *Angewandte Chemie International Edition* 2017, 56, 9336; W.-J. Ong, L.-L. Tan, Y. H. Ng, S.-T. Yong, S.-P. Chai, *Chemical Reviews* 2016, 116, 7159; M. Baar, S. Blechert, *Chemistry – A European Journal* 2015, 21, 526; Y. Zheng, L. Lin, B. Wang, X. Wang, *Angewandte Chemie International Edition* 2015, 54, 12868; Y. Wang, X. Wang, M. Antonietti, *Angewandte Chemie International Edition* 2012, 51, 68.
- [93] Y. Cai, Y. Tang, L. Fan, Q. Lefebvre, H. Hou, M. Rueping, *ACS Catalysis* 2018, 8, 9471.
- [94] J. Qin, S. Wang, H. Ren, Y. Hou, X. Wang, *Applied Catalysis B: Environmental* 2015, 179, 1.
- [95] M. A. Bajada, A. Vijeta, A. Savateev, G. Zhang, D. Howe, E. Reisner, *ACS Applied Materials & Interfaces* 2020, 12, 8176.
- [96] J. Khamrai, I. Ghosh, A. Savateev, M. Antonietti, B. König, *ACS Catalysis* 2020, 10, 3526; F. Su, S. C. Mathew, G. Lipner, X. Fu, M. Antonietti, S. Blechert, X. Wang, *Journal of the American Chemical Society* 2010, 132, 16299; I. Ghosh, J. Khamrai, A. Savateev, N. Shlapakov, M. Antonietti, B. König, *Science* 2019, 365, 360.
- [97] M. Woźnica, N. Chaoui, S. Taabache, S. Blechert, *Chemistry – A European Journal* 2014, 20, 14624.
- [98] A. Vinu, K. Ariga, T. Mori, T. Nakanishi, S. Hishita, D. Golberg, Y. Bando, *Advanced Materials* 2005, 17, 1648.
- [99] L. Lin, Z. Lin, J. Zhang, X. Cai, W. Lin, Z. Yu, X. Wang, *Nature Catalysis* 2020, 3, 649; F. K. Kessler, W. Schnick, *Zeitschrift für anorganische und allgemeine Chemie* 2019, 645, 857; L. Lin, C. Wang, W. Ren, H. Ou, Y. Zhang, X. Wang, *Chemical Science* 2017, 8, 5506; Y. Ham, K. Maeda, D. Cha, K. Takanabe, K. Domen, *Chemistry – An Asian Journal* 2013, 8, 218.
- [100] Theo M. Suter, T. S. Miller, J. K. Cockcroft, A. E. Aliev, M. C. Wilding, A. Sella, F. Corà, C. A. Howard, P. F. McMillan, *Chemical Science* 2019, 10, 2519; T. S. Miller, T. M. Suter, A. M. Telford, L. Picco, O. D. Payton, F. Russell-Pavier, P. L. Cullen, A. Sella, M. S. P. Shaffer, J. Nelson, V. Tileli, P. F. McMillan, C. A. Howard, *Nano Letters* 2017, 17, 5891; E. Wirnhier, M. Döblinger, D. Gunzelmann, J. Senker, B. V. Lotsch, W. Schnick, *Chemistry – A European Journal* 2011, 17, 3213.
- [101] M. J. Bojdys, J.-O. Müller, M. Antonietti, A. Thomas, *Chemistry – A European Journal* 2008, 14, 8177.

- [102] Z. Chen, S. Pronkin, T.-P. Fellingner, K. Kailasam, G. Vilé, D. Albani, F. Krumeich, R. Leary, J. Barnard, J. M. Thomas, J. Pérez-Ramírez, M. Antonietti, D. Dontsova, *ACS Nano* 2016, 10, 3166.
- [103] L. Lin, Z. Lin, J. Zhang, X. Cai, W. Lin, Z. Yu, X. Wang, *Nature Catalysis* 2020.
- [104] H. Kasap, C. A. Caputo, B. C. M. Martindale, R. Godin, V. W.-h. Lau, B. V. Lotsch, J. R. Durrant, E. Reisner, *Journal of the American Chemical Society* 2016, 138, 9183.
- [105] S. Mazzanti, B. Kurpil, B. Pieber, M. Antonietti, A. Savateev, *Nature Communications* 2020, 11, 1387.
- [106] A. Savateev, N. V. Tarakina, V. Strauss, T. Hussain, K. ten Brummelhuis, J. M. Sánchez Vadillo, Y. Markushyna, S. Mazzanti, A. P. Tyutyunnik, R. Walczak, M. Oschatz, D. M. Guldi, A. Karton, M. Antonietti, *Angewandte Chemie International Edition* 2020, 59, 15061.
- [107] Y. Markushyna, P. Lamagni, J. Catalano, N. Lock, G. Zhang, M. Antonietti, A. Savateev, *ACS Catalysis* 2020, 10, 7336.
- [108] Y. Markushyna, C. Teutloff, B. Kurpil, D. Cruz, I. Lauermann, Y. Zhao, M. Antonietti, A. Savateev, *Applied Catalysis B: Environmental* 2019, 248, 211.
- [109] B. Kurpil, K. Otte, A. Mishchenko, P. Lamagni, W. Lipiński, N. Lock, M. Antonietti, A. Savateev, *Nature Communications* 2019, 10, 945.
- [110] B. Kurpil, Y. Markushyna, A. Savateev, *ACS Catalysis* 2019, 9, 1531.
- [111] Y. Markushyna, P. Lamagni, C. Teutloff, J. Catalano, N. Lock, G. Zhang, M. Antonietti, A. Savateev, *Journal of Materials Chemistry A* 2019, 7, 24771.
- [112] B. Kurpil, K. Otte, M. Antonietti, A. Savateev, *Applied Catalysis B: Environmental* 2018, 228, 97.
- [113] B. Kurpil, B. Kumru, T. Heil, M. Antonietti, A. Savateev, *Green Chemistry* 2018, 20, 838.
- [114] A. Savateev, B. Kurpil, A. Mishchenko, G. Zhang, M. Antonietti, *Chemical Science* 2018, 9, 3584.
- [115] A. Savateev, D. Dontsova, B. Kurpil, M. Antonietti, *Journal of Catalysis* 2017, 350, 203.
- [116] H. Schlomberg, J. Kröger, G. Savasci, M. W. Terban, S. Bette, I. Moudrakovski, V. Duppel, F. Podjaski, R. Siegel, J. Senker, R. E. Dinnebier, C. Ochsenfeld, B. V. Lotsch, *Chemistry of Materials* 2019, 31, 7478.
- [117] F. Podjaski, J. Kröger, B. V. Lotsch, *Advanced Materials* 2018, 30, 1705477.
- [118] V. W.-h. Lau, D. Klose, H. Kasap, F. Podjaski, M.-C. Pignié, E. Reisner, G. Jeschke, B. V. Lotsch, *Angewandte Chemie International Edition* 2017, 56, 510.
- [119] V. W.-h. Lau, I. Moudrakovski, T. Botari, S. Weinberger, M. B. Mesch, V. Duppel, J. Senker, V. Blum, B. V. Lotsch, *Nature Communications* 2016, 7, 12165.
- [120] Z. Chen, A. Savateev, S. Pronkin, V. Papaefthimiou, C. Wolff, M. G. Willinger, E. Willinger, D. Neher, M. Antonietti, D. Dontsova, *Advanced Materials* 2017, 29, 1700555.
- [121] H. Ou, C. Tang, X. Chen, M. Zhou, X. Wang, *ACS Catalysis* 2019, 9, 2949.
- [122] G. Zhang, G. Li, Z.-A. Lan, L. Lin, A. Savateev, T. Heil, S. Zafeiratos, X. Wang, M. Antonietti, *Angewandte Chemie International Edition* 2017, 56, 13445.

- [123] D. Dontsova, S. Pronkin, M. Wehle, Z. Chen, C. Fettkenhauer, G. Clavel, M. Antonietti, *Chemistry of Materials* 2015, 27, 5170.
- [124] L. Lin, H. Ou, Y. Zhang, X. Wang, *ACS Catalysis* 2016, 6, 3921.
- [125] J. Albero, E. M. Barea, J. Xu, I. Mora-Seró, H. Garcia, M. Shalom, *Advanced Materials Interfaces* 2017, 4, 1600265.
- [126] H. Wang, S. Jiang, S. Chen, X. Zhang, W. Shao, X. Sun, Z. Zhao, Q. Zhang, Y. Luo, Y. Xie, *Chemical Science* 2017, 8, 4087.
- [127] C. Merschjann, S. Tschierlei, T. Tyborski, K. Kailasam, S. Orthmann, D. Hollmann, T. Schedel-Niedrig, A. Thomas, S. Lochbrunner, *Advanced Materials* 2015, 27, 7993.
- [128] A. Savateev, N. V. Tarakina, V. Strauss, T. Hussain, K. Ten Brummelhuis, J. M. Sanchez Vadiillo, Y. Markushyna, S. Mazzanti, A. P. Tyutyunnik, R. Walczak, M. Oschatz, D. Guldi, A. Karton, M. Antonietti, *Angew Chem Int Ed Engl* 2020.
- [129] R. Godin, Y. Wang, M. A. Zwijnenburg, J. Tang, J. R. Durrant, *Journal of the American Chemical Society* 2017, 139, 5216.
- [130] H. Kisch, *Accounts of Chemical Research* 2017, 50, 1002; H. Hennig, *Angewandte Chemie International Edition* 2015, 54, 4429; H. Kisch, *Angewandte Chemie International Edition* 2013, 52, 812.
- [131] A. Meyer, M. van Gestel, *The Journal of Physical Chemistry A* 2011, 115, 1939.
- [132] T. Hirakawa, P. V. Kamat, *Journal of the American Chemical Society* 2005, 127, 3928.
- [133] P. V. Kamat, *The Journal of Physical Chemistry Letters* 2012, 3, 663.
- [134] T. Hirakawa, P. V. Kamat, *Langmuir* 2004, 20, 5645; X. Wang, T. Wu, H. Wang, X. Su, *Materials Research Bulletin* 2016, 73, 423.
- [135] J. N. Schrauben, R. Hayoun, C. N. Valdez, M. Braten, L. Fridley, J. M. Mayer, *Science* 2012, 336, 1298; T. Cai, Y. Liu, L. Wang, S. Zhang, J. Ma, W. Dong, Y. Zeng, J. Yuan, C. Liu, S. Luo, *ACS Applied Materials & Interfaces* 2018, 10, 25350; I. A. MacKenzie, L. Wang, N. P. R. Onuska, O. F. Williams, K. Begam, A. M. Moran, B. D. Dunietz, D. A. Nicewicz, *Nature* 2020, 580, 76.
- [136] J. W. Verhoeven, *Pure and Applied Chemistry* 1996, 68, 2223.
- [137] N. H. Damrauer, G. Cerullo, A. Yeh, T. R. Boussie, C. V. Shank, J. K. McCusker, *Science* 1997, 275, 54.
- [138] T. P. Yoon, M. A. Ischay, J. Du, *Nature Chemistry* 2010, 2, 527; T. Gensch, M. Teders, F. Glorius, *The Journal of Organic Chemistry* 2017, 82, 9154.
- [139] A. Savateev, I. Ghosh, B. König, M. Antonietti, *Angewandte Chemie International Edition* 2018, 57, 15936.
- [140] H. Zhang, A. Yu, *The Journal of Physical Chemistry C* 2014, 118, 11628; J. Xu, M. Shalom, *ChemPhotoChem* 2019, 3, 170; J. Xu, M. Shalom, F. Piersimoni, M. Antonietti, D. Neher, T. J. K. Brenner, *Advanced Optical Materials* 2015, 3, 913; Q. Cui, J. Xu, X. Wang, L. Li, M. Antonietti, M. Shalom, *Angewandte Chemie International Edition* 2016, 55, 3672.
- [141] J. Han, H. Y. Zou, M. X. Gao, C. Z. Huang, *Talanta* 2016, 148, 279.

- [142] H. Wang, S. Jiang, S. Chen, D. Li, X. Zhang, W. Shao, X. Sun, J. Xie, Z. Zhao, Q. Zhang, Y. Tian, Y. Xie, *Advanced Materials* 2016, 28, 6940.
- [143] M. B. Plutschack, B. Pieber, K. Gilmore, P. H. Seeberger, *Chemical Reviews* 2017, 117, 11796.
- [144] C. G. Thomson, A.-L. Lee, F. Vilela, *Beilstein Journal of Organic Chemistry* 2020, 16, 1495.
- [145] C. Sambigiato, T. Noël, *Trends in Chemistry* 2020, 2, 92; G. Vilé, S. Richard-Bildstein, A. Lhuillery, G. Rueedi, *ChemCatChem* 2018, 10, 3786; G. Laudadio, Y. Deng, K. van der Wal, D. Ravelli, M. Nuño, M. Fagnoni, D. Guthrie, Y. Sun, T. Noël, *Science* 2020, 369, 92; L. Amini-Rentsch, E. Vanoli, S. Richard-Bildstein, R. Marti, G. Vilé, *Industrial & Engineering Chemistry Research* 2019, 58, 10164.
- [146] J. P. Barham, E. Koyama, Y. Norikane, N. Ohneda, T. Yoshimura, *The Chemical Record* 2019, 19, 188; J. P. Barham, S. Tamaoki, H. Egami, N. Ohneda, T. Okamoto, H. Odajima, Y. Hamashima, *Organic & Biomolecular Chemistry* 2018, 16, 7568; E. Koyama, N. Ito, J.-i. Sugiyama, J. P. Barham, Y. Norikane, R. Azumi, N. Ohneda, Y. Ohno, T. Yoshimura, H. Odajima, T. Okamoto, *Journal of Flow Chemistry* 2018, 8, 147; J. P. Barham, S. Tanaka, E. Koyama, N. Ohneda, T. Okamoto, H. Odajima, J.-i. Sugiyama, Y. Norikane, *The Journal of Organic Chemistry* 2018, 83, 4348; S. Tortoioli, A. Friedli, A. Prud'homme, S. Richard-Bildstein, P. Kohler, S. Abele, G. Vilé, *Green Chemistry* 2020, 22, 3748.
- [147] T. Noël, M. Escriba Gelonch, K. Huvaere, in *Photochemical Processes in Continuous-Flow Reactors*, WORLD SCIENTIFIC (EUROPE), 2016, 245.
- [148] K. C. Harper, E. G. Moschetta, S. V. Bordawekar, S. J. Wittenberger, *ACS Central Science* 2019, 5, 109.
- [149] D. Cambié, C. Bottecchia, N. J. W. Straathof, V. Hessel, T. Noël, *Chemical Reviews* 2016, 116, 10276.
- [150] J. J. Douglas, M. J. Sevrin, C. R. J. Stephenson, *Organic Process Research & Development* 2016, 20, 1134.
- [151] Y. Dai, C. Li, Y. Shen, T. Lim, J. Xu, Y. Li, H. Niemantsverdriet, F. Besenbacher, N. Lock, R. Su, *Nature Communications* 2018, 9, 60.
- [152] A. Ufer, D. Sudhoff, A. Mescher, D. W. Agar, *Chemical Engineering Journal* 2011, 167, 468.
- [153] C. Yang, R. Li, K. A. I. Zhang, W. Lin, K. Landfester, X. Wang, *Nature Communications* 2020, 11, 1239.
- [154] B. Pieber, M. Shalom, M. Antonietti, P. H. Seeberger, K. Gilmore, *Angewandte Chemie International Edition* 2018, 57, 9976.
- [155] I. Krivtsov, D. Mitoraj, C. Adler, M. Ilkaeva, M. Sardo, L. Mafra, C. Neumann, A. Turchanin, C. Li, B. Dietzek, R. Leiter, J. Biskupek, U. Kaiser, C. Im, B. Kirchhoff, T. Jacob, R. Beranek, *Angewandte Chemie International Edition* 2020, 59, 487.

- [156] C. Rosso, S. Gisbertz, J. D. Williams, H. P. L. Gemoets, W. Debrouwer, B. Pieber, C. O. Kappe, *Reaction Chemistry & Engineering* 2020, 5, 597.
- [157] O. Levenspiel, *Chemical Reaction Engineering*, John Wiley & Sons, 1998.
- [158] Y. D. Gabriele Laudadio, Klaas van der Wal, Davide Ravelli, Manuel Nuño, Maurizio Fagnoni, Duncan Guthrie, Yuhan Sun, Timothy Noël, *Science* 2020, 369, 92.
- [159] B. Pieber, J. A. Malik, C. Cavedon, S. Gisbertz, A. Savateev, D. Cruz, T. Heil, G. Zhang, P. H. Seeberger, *Angewandte Chemie International Edition* 2019, 58, 9575.
- [160] I. Ghosh, J. Khamrai, A. Savateev, N. Shlapakov, M. Antonietti, B. König, *Science* 2019, 365, 360.
- [161] M. Baar, S. Blechert, *Chemistry* 2015, 21, 526.
- [162] R. Filler, Y. Kobayashi, L. Yagupolskii, *Organofluorine Compounds in Medicinal Chemistry and Biomedical Applications*, Elsevier Science LTD, University of Michigan 1993; Y. Zafrani, D. Yeffet, G. Sod-Moriah, A. Berliner, D. Amir, D. Marciano, E. Gershonov, S. Saphier, *J Med Chem* 2017, 60, 797.
- [163] V. H. Mai, G. I. Nikonov, *ACS Catalysis* 2016, 6, 7956.
- [164] S. B. Waghmode, G. Mahale, V. P. Patil, K. Renalson, D. Singh, *Synthetic Communications* 2013, 43, 3272; N. A. Rebacz, P. E. Savage, *Phys Chem Chem Phys* 2013, 15, 3562.
- [165] J. Zhang, C. Xing, B. Tiwari, Y. R. Chi, *Journal of the American Chemical Society* 2013, 135, 8113.
- [166] P. Kohls, D. Jadhav, G. Pandey, O. Reiser, *Organic Letters* 2012, 14, 672; L. Ruiz Espelt, E. M. Wiensch, T. P. Yoon, *Journal of Organic Chemistry* 2013, 78, 4107; L. Ruiz Espelt, I. S. McPherson, E. M. Wiensch, T. P. Yoon, *Journal of the American Chemical Society* 2015, 137, 2452; J. J. Murphy, D. Bastida, S. Paria, M. Fagnoni, P. Melchiorre, *Nature* 2016, 532, 218.
- [167] W. Jones, D. J. Martin, A. Caravaca, A. M. Beale, M. Bowker, T. Maschmeyer, G. Hartley, A. Masters, *Applied Catalysis B: Environmental* 2019, 240, 373.
- [168] S. Samanta, S. Khilari, D. Pradhan, R. Srivastava, *ACS Sustainable Chemistry & Engineering* 2017, 5, 2562; M. Bajada, A. Vijeta, A. Savateev, G. Zhang, D. Howe, E. Reisner, *ACS Appl Mater Interfaces* 2020.
- [169] Z. Chen, A. Savateev, S. Pronkin, V. Papaefthimiou, C. Wolff, M. G. Willinger, E. Willinger, D. Neher, M. Antonietti, D. Dontsova, *Adv Mater* 2017, 29.
- [170] K. Maruoka, I. Shimada, H. Imoto, H. Yamamoto, *Synlett* 1994, 1994, 519.
- [171] N. Serpone, *Journal of Photochemistry and Photobiology A: Chemistry* 1997, 104, 1.
- [172] I. Francesconi, W. D. Wilson, F. A. Tanious, J. E. Hall, B. C. Bender, R. R. Tidwell, D. McCurdy, D. W. Boykin, *Journal of Medicinal Chemistry* 1999, 42, 2260; B. B. Thompson, J. Montgomery, *Organic Letters* 2011, 13, 3289.
- [173] F. Su, S. C. Mathew, L. Mohlmann, M. Antonietti, X. Wang, S. Blechert, *Angew Chem Int Ed Engl* 2011, 50, 657.

- [174] X. Q. Hu, X. Qi, J. R. Chen, Q. Q. Zhao, Q. Wei, Y. Lan, W. J. Xiao, *Nat Commun* 2016, 7, 11188.
- [175] K. Rajeshwar, A. Thomas, C. Janáky, *The Journal of Physical Chemistry Letters* 2015, 6, 139.
- [176] R. Li, F. Zhang, D. Wang, J. Yang, M. Li, J. Zhu, X. Zhou, H. Han, C. Li, *Nature Communications* 2013, 4, 1432.
- [177] L. Li, P. A. Salvador, G. S. Rohrer, *Nanoscale* 2014, 6, 24.
- [178] S. Mazzanti, A. Savateev, *ChemPlusChem* 2020, n/a.
- [179] O. Ola, M. M. Maroto-Valer, *Journal of Photochemistry and Photobiology C: Photochemistry Reviews* 2015, 24, 16.
- [180] R. Shwetharani, H. R. Chandan, M. Sakar, G. R. Balakrishna, K. R. Reddy, A. V. Raghu, *International Journal of Hydrogen Energy* 2020, 45, 18289.
- [181] P. Giusto, D. Cruz, T. Heil, H. Arazoe, P. Lova, T. Aida, D. Comoretto, M. Patrini, M. Antonietti, *Adv Mater* 2020, 32, 1908140.
- [182] D. Dvoranova, Z. Barbierikova, V. Brezova, *Molecules* 2014, 19, 17279.
- [183] The reaction was conducted without stirring (Table S1 entry 9).
- [184] M. Sankar, E. Nowicka, E. Carter, D. M. Murphy, D. W. Knight, D. Bethell, G. J. Hutchings, *Nature Communications* 2014, 5, 3332.
- [185] B. Burger, P. M. Maffettone, V. V. Gusev, C. M. Aitchison, Y. Bai, X. Wang, X. Li, B. M. Alston, B. Li, R. Clowes, N. Rankin, B. Harris, R. S. Sprick, A. I. Cooper, *Nature* 2020, 583, 237.
- [186] R. Gérardy, N. Emmanuel, T. Toupy, V. E. Kassin, N. N. Tshibalonza, M. Schmitz, J. C. M. Monbaliu, *European Journal of Organic Chemistry* 2018, 2018, 2301.
- [187] J. C. Phillips, *Journal of Non-Crystalline Solids* 2011, 357, 3853.
- [188] O. V. Mikhnenko, F. Cordella, A. B. Sieval, J. C. Hummelen, P. W. M. Blom, M. A. Loi, *The Journal of Physical Chemistry B* 2008, 112, 11601.
- [189] W. Jia, Q. Wang, H. Shi, Z. An, W. Huang, *Chemistry – A European Journal* 2020, 26, 4437.
- [190] R. Arcas, E. Peris, E. Mas-Marzá, F. Fabregat-Santiago, *Sustainable Energy & Fuels* 2021, 5, 956.
- [191] F. E. Osterloh, *ACS Energy Letters* 2017, 2, 445.
- [192] E. C. Gentry, R. R. Knowles, *Accounts of Chemical Research* 2016, 49, 1546.
- [193] S. Y. Reece, D. G. Nocera, *Annual Review of Biochemistry* 2009, 78, 673.
- [194] J. P. Roth, J. M. Mayer, *Inorganic Chemistry* 1999, 38, 2760.
- [195] D. C. Miller, K. T. Tarantino, R. R. Knowles, *Topics in Current Chemistry* 2016, 374, 30.
- [196] R. F. Howe, M. Gratzel, *The Journal of Physical Chemistry* 1985, 89, 4495.
- [197] B. H. Meekins, P. V. Kamat, *The Journal of Physical Chemistry Letters* 2011, 2, 2304.
- [198] P. V. Kamat, I. Bedja, S. Hotchandani, *The Journal of Physical Chemistry* 1994, 98, 9137.
- [199] S. Mazzanti, A. Savateev, *ChemPlusChem* 2020, 85, 2499.

- [200] F. Podjaski, B. V. Lotsch, *Advanced Energy Materials* 2021, 11, 2003049.
- [201] I. K. Levy, M. A. Brusa, M. E. Aguirre, G. Custo, E. S. Román, M. I. Litter, M. A. Grela, *Physical Chemistry Chemical Physics* 2013, 15, 10335.
- [202] C. Y. Liu, A. J. Bard, *The Journal of Physical Chemistry* 1989, 93, 3232.
- [203] R. H. Joel N. Schrauben, Carolyn N. Valdez, Miles Braten, Lila Fridley, James M. Mayer, *Science* 2012, 336, 1298.
- [204] M. Mokhtarifar, D. T. Nguyen, M. V. Diamanti, R. Kaveh, M. Asa, M. Sakar, M. Pedferri, T.-O. Do, *New Journal of Chemistry* 2020, 44, 20375.
- [205] F. Feng, W. Yang, S. Gao, C. Sun, Q. Li, *ACS Sustainable Chemistry & Engineering* 2018, 6, 6166.
- [206] Z. Zeng, X. Quan, H. Yu, S. Chen, Y. Zhang, H. Zhao, S. Zhang, *Applied Catalysis B: Environmental* 2018, 236, 99.
- [207] A. U. Meyer, V. W.-h. Lau, B. König, B. V. Lotsch, *European Journal of Organic Chemistry* 2017, 2017, 2179.
- [208] A. Savateev, M. Antonietti, *ACS Catalysis* 2018, 8, 9790.
- [209] H. Schlomberg, J. Kroger, G. Savasci, M. W. Terban, S. Bette, I. Moudrakovski, V. Duppel, F. Podjaski, R. Siegel, J. Senker, R. E. Dinnebier, C. Ochsenfeld, B. V. Lotsch, *Chem Mater* 2019, 31, 7478.
- [210] A. Savateev, Y. Markushyna, C. M. Schüßlbauer, T. Ullrich, D. M. Guldi, M. Antonietti, *Angewandte Chemie International Edition* 2020, n/a.
- [211] H. Tanaka, K. Sakai, A. Kawamura, K. Oisaki, M. Kanai, *Chemical Communications* 2018, 54, 3215.
- [212] L. Capaldo, D. Ravelli, *European Journal of Organic Chemistry* 2017, 2017, 2056.
- [213] Z.-Y. Dai, Z.-S. Nong, P.-S. Wang, *ACS Catalysis* 2020, 10, 4786.
- [214] Z.-J. Li, S. Li, E. Hofman, A. Hunter Davis, G. Leem, W. Zheng, *Green Chemistry* 2020, 22, 1911.
- [215] N. Kvasovs, V. Gevorgyan, *Chemical Society Reviews* 2021, 50, 2244.
- [216] T. Kawamoto, A. Sato, I. Ryu, *Chemistry – A European Journal* 2015, 21, 14764.
- [217] C. G. López-Calixto, M. Liras, V. A. de la Peña O'Shea, R. Pérez-Ruiz, *Applied Catalysis B: Environmental* 2018, 237, 18.
- [218] H. G. Roth, N. A. Romero, D. A. Nicewicz, *Synlett* 2016, 27, 714.
- [219] J. D. Nguyen, E. M. D'Amato, J. M. R. Narayanam, C. R. J. Stephenson, *Nature Chemistry* 2012, 4, 854.
- [220] I. Ghosh, T. Ghosh, J. I. Bardagi, B. König, *Science* 2014, 346, 725.
- [221] S. J. Blanksby, G. B. Ellison, *Accounts of Chemical Research* 2003, 36, 255.
- [222] D. Sadowsky, K. McNeill, C. J. Cramer, *Environmental Science & Technology* 2013, 47, 14194.
- [223] Being a protic solvent.
- [224] Slightly decreased yield of 2a.

- [225] N. G. W. Cowper, C. P. Chernowsky, O. P. Williams, Z. K. Wickens, *J Am Chem Soc* 2020.
- [226] M. Nakajima, E. Fava, S. Loescher, Z. Jiang, M. Rueping, *Angewandte Chemie International Edition* 2015, 54, 8828.
- [227] S. Shi, R. Szostak, M. Szostak, *Organic & Biomolecular Chemistry* 2016, 14, 9151.
- [228] J. J. Warren, T. A. Tronic, J. M. Mayer, *Chemical Reviews* 2010, 110, 6961.
- [229] Y. Markushyna, A. Völkel, A. Savateev, M. Antonietti, S. Filonenko, *Journal of Catalysis* 2019, 380, 186.
- [230] B. C. O'Regan, J. R. Durrant, *Accounts of Chemical Research* 2009, 42, 1799.
- [231] W. K. Liu, K. M. Whitaker, A. L. Smith, K. R. Kittilstved, B. H. Robinson, D. R. Gamelin, *Physical Review Letters* 2007, 98, 186804.
- [232] <https://www.americanelements.com/graphitic>.
- [233] C. D. Windle, R. N. Perutz, *Coordination Chemistry Reviews* 2012, 256, 2562.
- [234] B. AlOtaibi, S. Fan, D. Wang, J. Ye, Z. Mi, *ACS Catalysis* 2015, 5, 5342.
- [235] S. Gao, B. Gu, X. Jiao, Y. Sun, X. Zu, F. Yang, W. Zhu, C. Wang, Z. Feng, B. Ye, Y. Xie, *J Am Chem Soc* 2017, 139, 3438.
- [236] J. L. White, M. F. Baruch, J. E. Pander Iii, Y. Hu, I. C. Fortmeyer, J. E. Park, T. Zhang, K. Liao, J. Gu, Y. Yan, T. W. Shaw, E. Abelev, A. B. Bocarsly, *Chem Rev* 2015, 115, 12888.
- [237] K. A. Ahrendt, C. J. Borths, D. W. C. MacMillan, *Journal of the American Chemical Society* 2000, 122, 4243.
- [238] T. Hering, B. Muhlendorf, R. Wolf, B. König, *Angew Chem Int Ed Engl* 2016, 55, 5342.
- [239] B. Muhlendorf, R. Wolf, *ChemCatChem* 2017, 9, 920.
- [240] J. Dad'ová, E. Svobodová, M. Sikorski, B. König, R. Cibulka, *ChemCatChem* 2012, 4, 620; G. de Gonzalo, M. W. Fraaije, *ChemCatChem* 2013, 5, 403; S. J. S. Düsel, B. König, *The Journal of Organic Chemistry* 2018, 83, 2802; H. Iida, Y. Imada, S. I. Murahashi, *Org Biomol Chem* 2015, 13, 7599; R. Lechner, S. Kummel, B. König, *Photochem Photobiol Sci* 2010, 9, 1367; J. B. Metternich, R. Gilmour, *J Am Chem Soc* 2016, 138, 1040.
- [241] P. Dongare, I. MacKenzie, D. Wang, D. A. Nicewicz, T. J. Meyer, *Proc Natl Acad Sci U S A* 2017, 114, 9279.
- [242] N. Jürgensen, M. Ackermann, T. Marszalek, J. Zimmermann, A. J. Morfa, W. Pisula, U. H. F. Bunz, F. Hinkel, G. Hernandez-Sosa, *ACS Sustainable Chemistry & Engineering* 2017, 5, 5368.
- [243] B. König, Ed. *CHEMICAL PHOTOCATALYSIS*, DE GRUYTER, Göttingen 2013.
- [244] J. K. Indrajit Ghosh, Aleksandr Savateev, Nikita Shlapakov, Markus Antonietti, Burkhard König, *Science* 2019, 365, 360; C. Cavedon, A. Madani, P. H. Seeberger, B. Pieber, *Organic Letters* 2019, 21, 5331; L. Möhlmann, S. Blechert, *Advanced Synthesis & Catalysis* 2014, 356, 2825.
- [245] Y. Markushyna, C. A. Smith, A. Savateev, *European Journal of Organic Chemistry* 2020, 2020, 1294.

- [246] C. Yang, B. C. Ma, L. Zhang, S. Lin, S. Ghasimi, K. Landfester, K. A. Zhang, X. Wang, *Angew Chem Int Ed Engl* 2016, 55, 9202; Z. A. Lan, G. Zhang, X. Chen, Y. Zhang, K. A. I. Zhang, X. Wang, *Angew Chem Int Ed Engl* 2019, 58, 10236.
- [247] G. Zhang, L. Lin, G. Li, Y. Zhang, A. Savateev, S. Zafeiratos, X. Wang, M. Antonietti, *Angew Chem Int Ed Engl* 2018, 57, 9372.
- [248] B. Kurpil, A. Savateev, V. Papaefthimiou, S. Zafeiratos, T. Heil, S. Özenler, D. Dontsova, M. Antonietti, *Applied Catalysis B: Environmental* 2017, 217, 622.
- [249] A. M. Díez-Pascual, D. García-García, M. P. San Andrés, S. Vera, *RSC Advances* 2016, 6, 19686.
- [250] Y. Chen, J. W. Y. Lam, R. T. K. Kwok, B. Liu, B. Z. Tang, *Materials Horizons* 2019, 6, 428.
- [251] A. B. Jorge, D. J. Martin, M. T. S. Dhanoa, A. S. Rahman, N. Makwana, J. Tang, A. Sella, F. Corà, S. Firth, J. A. Darr, P. F. McMillan, *The Journal of Physical Chemistry C* 2013, 117, 7178.
- [252] Z. Pan, G. Zhang, X. Wang, *Angew Chem Int Ed Engl* 2019, 58, 7102; L. Zhao, X. Chen, X. Wang, Y. Zhang, W. Wei, Y. Sun, M. Antonietti, M. M. Titirici, *Adv Mater* 2010, 22, 3317.
- [253] F. Le Formal, K. Sivula, M. Grätzel, *The Journal of Physical Chemistry C* 2012, 116, 26707; R. C. I. MacKenzie, C. G. Shuttle, M. L. Chabiny, J. Nelson, *Advanced Energy Materials* 2012, 2, 662.
- [254] H. N. D. Z. Chen, E. Miller, 2013, *Photoelectrochemical Water Splitting*.
- [255] M. Oschatz, M. Leistner, W. Nickel, S. Kaskel, *Langmuir* 2015, 31, 4040.
- [256] D. M. Arias-Rotondo, J. K. McCusker, *Chemical Society Reviews* 2016, 45, 5803; S. S. Meryem, S. Nasreen, M. Siddique, R. Khan, *Reviews in Chemical Engineering* 2018, 34, 409.
- [257] G. Filippini, F. Longobardo, L. Forster, A. Criado, G. Di Carmine, L. Nasi, C. D'Agostino, M. Melchionna, P. Fornasiero, M. Prato, *Science Advances* 2020, 6, eabc9923.
- [258] J. Montes-Avila, S. P. Diaz-Camacho, J. Sicairos-Felix, F. Delgado-Vargas, I. A. Rivero, *Bioorg Med Chem* 2009, 17, 6780.
- [259] F. Hayat, A. Salahuddin, S. Umar, A. Azam, *Eur J Med Chem* 2010, 45, 4669.
- [260] F. Fang, Y. Li, S.-K. Tian, *European Journal of Organic Chemistry* 2011, 2011, 1084.
- [261] R. U. Braun, M. Ansorge, T. J. Muller, *Chemistry* 2006, 12, 9081.
- [262] V. Kumar, S. Kumar, M. Hassan, H. Wu, R. K. Thimmulappa, A. Kumar, S. K. Sharma, V. S. Parmar, S. Biswal, S. V. Malhotra, *J Med Chem* 2011, 54, 4147.
- [263] B. C. Ranu, R. Jana, *J Org Chem* 2005, 70, 8621.
- [264] A. L. Gottumukkala, J. F. Teichert, D. Heijnen, N. Eisink, S. van Dijk, C. Ferrer, A. van den Hoogenband, A. J. Minnaard, *J Org Chem* 2011, 76, 3498.
- [265] S. Gupta, J. A. Melanson, L. Vaillancourt, W. A. Nugent, G. J. Tanoury, G. Schatte, V. Snieckus, *Org Lett* 2018, 20, 3745.
- [266] J. A. R. Jeffrey C. Lagarias, Margaret H. Wright, P. E. Wright, *Society for Industrial and Applied Mathematics* 1998, 9, 112.
- [267] A. Savateev, B. Kurpil, A. Mishchenko, G. Zhang, M. Antonietti, *Chem Sci* 2018, 9, 3584.
- [268] M. Lesieur, C. Genicot, P. Pasau, *Org Lett* 2018, 20, 1987.

- [269] L. Han, L. Yan, M. Wang, K. Wang, L. Fang, J. Zhou, J. Fang, F. Ren, X. Lu, *Chemistry of Materials* 2018, 30, 5561.
- [270] G. Kresse, J. Furthmüller, *Physical Review B* 1996, 54, 11169.
- [271] G. Kresse, J. Furthmüller, *Computational Materials Science* 1996, 6, 15.
- [272] J. J. Mortensen, K. Kaasbjerg, S. L. Frederiksen, J. K. Nørskov, J. P. Sethna, K. W. Jacobsen, *Phys Rev Lett* 2005, 95, 216401; J. Wellendorff, K. T. Lundgaard, A. Møgelhøj, V. Petzold, D. D. Landis, J. K. Nørskov, T. Bligaard, K. W. Jacobsen, *Physical Review B* 2012, 85.
- [273] P. E. Blochl, *Phys Rev B Condens Matter* 1994, 50, 17953.
- [274] E. Sanville, S. D. Kenny, R. Smith, G. Henkelman, *J Comput Chem* 2007, 28, 899.
- [275] M. Syeda Shaima, N. Sadia, S. Maria, K. Romana, *Reviews in Chemical Engineering* 2018, 34, 409.
- [276] N. Sagara, S. Kamimura, T. Tsubota, T. Ohno, *Applied Catalysis B: Environmental* 2016, 192, 193.

From Italy to a PhD in Germany, what a journey!

In the life of a human being, many memories are shortly stored in our brain, while others, are unforgettable. My arrival at Golm Bahnhof is definitely among them.

I will never forget about that intense dark grey sky. It was not a good start.

On the contrary, it was a sign of how lucky I have been to do my PhD in such an environment.

At the Colloid Chemistry department, words such as “boring” are not part of the vocabulary.

I remember, after sending many applications for a PhD, I ended up to be chosen from Sasha and Markus. I am still surprised when I think about it, how my life would have been completely different and the life of others that surrounded me.

Thanks to Markus and Sasha, I can say that we have accomplished much together.

Special thanks go to Coronavirus – Covid 2019.

Nonetheless, the deepest thanks go to my family “...and yet it is family that moves us. Family consumes us”.

Last but not least, I am grateful and I must thank the *Max Punk - ChezBriel* community to be my family for the great not sober time spent together, and for everything that you taught me. Everywhere I will go, I'll make sure to export *ChezBriel* with me.